NEUTRON-FRAGMENT COINCIDENCE MEASUREMENTS IN $^{14}N + ^{165}Ho$ AND ^{14}N + Ni REACTIONS AT 35 MeV/NUCLEON

By

Bruce Allen Remington

A DISSERTATION

Submitted to
Michigan State University
in partial fulfillment of the requirements
for the degree of

DOCTOR OF PHILOSOPHY

Department of Physics and Astronomy
1986

ABSTRACT

NEUTRON-FRAGMENT COINCIDENCE MEASUREMENTS IN $^{14}N + ^{165}Ho$ AND ^{14}N + Ni REACTIONS AT 35 MeV/NUCLEON

By

Bruce Allen Remington

We have studied $^{14}N + ^{165}Ho$ and ^{14}N + Ni collisions at 35 MeV/nucleon by detecting neutrons in coincidence with light fragments. Strong preequilibrium neutron emission is observed at forward and middle angles. The preequilibrium component of the neutron spectra is symmetric about the beam axis for all but the most peripheral interactions, where more neutrons are observed on the side of the beam opposite the detected light fragment. The moving-sources picture is utilized to extract systematic trends with light-fragment angle in the preequilibrium component of the neutron spectra and in the component from the target-like source. The target-like source multiplicity is compared with predictions from the statistical code CASCADE, revealing an angle-dependent difference between calculated and measured multiplicity. Comparisons with a two-body calculation show that there is considerable "missing momentum", only part of which can be accounted for by preequilibrium neutron emission.

For Güzide

PREFACE

This work is the culmination of two neutron--light-fragment coincidence experiments. The first experiment was conducted in May, 1983 on the ^{14}N + ^{165}Ho system and the second in August, 1984 on the ^{14}N + ^{165}Ho, Ni, and C systems, both at 35 MeV/nucleon. These data have been and are continuing to be analyzed in various ways by the different members of our group. This thesis is based upon an analysis within the moving-sources picture of the neutron data from the 1984 experiment. The 1983 data has also been looked at in a similar manner in an independent analysis by other members of our group. Though the experimental arrangements for the two experiments were not identical, there was sufficient overlap to allow some comparisons of similar parameters arrived at through independent work. Where appropriate these comparisons are noted in the text and in the figures.

This thesis is organized into two sections: (1) the main text and (2) an extensive set of appendices. The reader not interested in excessive detail will not miss any of the essence of this work by reading only the main text and skipping the appendices. All experimental details not essential to an explanation of the physics extracted from the data, including a complete compilation of the data, are presented in the appendices at the end of the thesis.

Inevitably small redundancies exist between the main text and the appendices, especially in Appendices A-X and A-XI where all the data are presented. It is hoped, though, that separating out the crucial ideas from the experimental details in this manner makes this thesis a more readable document.

ACKNOWLEDGEMENTS

I wish to thank Dr. Aaron Galonsky, my research advisor, for his guidance, instruction, and supervision during my graduate career. Without his depth of vision and willingness to "gamble" on an initially very inexperienced student, my career in physics might never have begun. I am forever indebted to him for his efforts in molding a "raw" high school teacher into a nuclear physicist. His interest in me and my career is gratefully acknowledged.

It is a pleasure to thank Dr. Jirohta Kasagi for his constant encouragement, supervision, and concern in guiding me from my initial crude attempts at experimental physics through the completion of this thesis project. His participation in our work at M.S.U. meant frequent trips from Tokyo to East Lansing, and my deepest appreciation for his efforts is here acknowledged.

I owe special thanks to Dr. Greg Caskey for his encouragement and guidance, especially in matters of data analysis and computer manipulations. His patient handling of my never-ending stream of questions about bits, bytes, and the like is greatly appreciated.

I also express my sincere appreciation for the efforts

of Drs. Adam Kiss, Ferenc Deak, and Zolton Seres. Without their help in all aspects of this work, from the building and testing of the equipment to the analysis of the data, this thesis would not have been possible.

I am grateful for the expert support of the Cyclotron operations group and machine shop. When deadlines became imminent, people willing to work overtime on Saturdays and Sundays were always found. Such dedication is always necessary for the success of any major project and my gratitude is here sincerely acknowledged.

I would like to thank all members of the support personnel of the lab that make the many small but crucial contributions. Without their help this experimental work could not have been possible. Special appreciation is extended to Barb Pollack of the computer group and Len Morris of the mechanical design group.

I am also grateful for the generous financial support of the N.S.F and M.S.U. This was a very necessary ingredient of my graduate career.

I have the deepest gratitude for the constant support and interest of my family. They had to listen to occasional tirades about nuclear physics and accompanying subjects without having any interest except in my success. This type of support can only be offered by family, and I acknowledge my sincere appreciation.

But above all, I have nothing but the deepest appreciation and gratitude for the help of my wife Güzide.

She has offered support, understanding, and encouragement through even the "darkest" moments of my graduate years at M.S.U. She not only was willing to tolerate my long hours at the lab, but actively joined in, helping out with anything she could. My graduate work would never have even taken root, let alone blossom to fruition without her continuous support and unfaltering dedication to this cause. Love knows perhaps no stronger test than the strains created in graduate school, and Güzide has held strong always.

Allah ondan razi olsun.

TABLE OF CONTENTS

LIST OF FIGURES

LIST OF TABLES

I. INTRODUCTION

In concert with developments in heavy-ion accelerator technology, heavy-ion nuclear reactions have largely been studied at low energies ($E_{beam} \leq$ 10 MeV/nucleon) and at high energies ($E_{beam} \geq$ 100 MeV/nucleon). The low energy regime corresponds to beam-energies/nucleon lower than either the speed of sound in nuclear matter (equivalent to about 15 MeV/nucleon) or the mean Fermi energy of nucleons in a nucleus (about 28 MeV) (Ge 78, Sc 81). The time scale of the interaction is hence long compared to the nuclear relaxation time. As a result low energy nuclear collisions have been successfully described by theories based upon equilibrium, as in the statistical model (Pü 77) and theories incorporating mean-field phenomena, such as the TDHF approach (Ne 82, Da 84). On the other hand, high energy collisions occur on a time scale which is short compared to the nuclear relaxation time. Successful theories for the high energy regime typically divide the colliding nuclei into participant and spectator zones, as in the fireball model (We 76), or assume the reactions to consist of a series of free nucleon-nucleon collisions, as in the intranuclear cascade model (Cu 82).

With the advent of intermediate energy heavy-ion accelerators, data are now emerging in the transition region (10 MeV/nucleon $\leq E_{beam} \leq$ 100 MeV/nucleon). The simplifying

assumptions of interaction time being either long or short compared to the nuclear relaxation time no longer apply. Much theoretical activity is taking place to extend current high energy and low energy theories into the transition region (Ai 85, Kr 85, Bl 85) and to develop "new" approaches such as the Fermi-jet (Bo 80, Le 85) or hot spot (Ga 80, Go 77, Mo 80, We 77) models. ("New" approaches should be qualified since Bethe pointed out the possibility of preequilibrium particle emission from an evolving hot spot in 1938 (Be 38)). Incumbent upon the experimental community is the task of producing data that can cleanly distinguish between currently emerging theories, and indeed, establish clear landmarks and systematics by which the theorists can be guided.

One such landmark of the intermediate energy regime is the onset of preequilibrium particle emission. As beam energies exceed the "threshold" of $(E_{cm} - V_c)/\mu \approx 8$ MeV/nucleon, a distinct non-equilibrium or preequilibrium component of particle emission appears. Although various models have been proposed to explain preequilibrium particle emission (exciton model (Gr 67, Bl 75, Ma 76), Fermi-jet model (Bo 80, Le 85), hot spot model (Ga 80, Go 77, Mo 80, We 77), piston model (Gr 77), "tangental friction" model (Ge 77, Ts 82), Harp-Miller-Berne model or Boltzmann master equation model (Ha 68, Bl 81)), no one single approach can yet explain the systematic behavior of preequilibrium

particle spectra over a broad energy and angular range. One notable common denominator of all preequilibrium emission, though, is the success of a thermal parameterization.

It has been shown in inclusive measurements that a single, relatively hot, intermediate-rapidity source (IRS) can reproduce the energy and angular distributions of light particles (Sy 80, Aw 81, Aw 82) and of complex fragments (We 82, Ja 83, We 84) as long as the forward-most angles are excluded. Preequilibrium light particle spectra taken in coincidence with fission fragments (Aw 79, Ba 80, Aw* 81) or with projectile-light fragments (Yo 80, Ha 85) have also been successfully parameterized with a hot IRS. A particularly "clean" reflection of the nuclear reaction is contained in the energy and angular distributions of the emitted neutrons, since they are not subject to Coulomb distortions. For this reason numerous studies of neutrons in coincidence with evaporation residues (Hi 81, Ga 81, Hi 83, Ho 83, Ga 83, Hi 84), with fission fragments (Ka 81, Hi 81, Hi 83, Ho 83, Hi 84), and with projectile-like fragments (Hi 79, Ge 80, Hi 81, Ga 81, Ts 82, Ja* 83, Hi 83, Wa 83, Ch 83, Hi 84, Ca 85, Pe 85, Lü 85) have been reported. In all the studies where preequilibrium neutron emission was observed (Ge 80, Hi 81, Ga 81, Ts 82, Hi 83, Hi 84, Ca 85, Pe 85), the preequilibrium component to the neutron spectra could be parameterized with a hot thermal source. The pervasive success of the moving source model in parameterizing preequilibrium particle emission leads one to

consider whether the IRS carries more fundamental information about the reaction mechanism. Indeed, one cannot help but wonder if an understanding of this thermal appearance of preequilibrium spectra might not be the link between the participant-spectator thermal description (fireball) of high energies and the compound nucleus thermal (statistical) description of low energies. Until this question is answered with a suitable theory, experimental interest will remain keen in mapping out the systematics of the transitional energy region.

Of particular relevance to the present study is a recent experiment carried out on the ^{14}N + ^{165}Ho system at 35 MeV/nucleon (Ca 85, Re 85, Ki 86, De 86). In that work, neutrons were detected in coincidence with projectile-like fragments near and beyond the grazing angle. Considerable evidence for preequilibrium neutron emission in coincidence with both quasi-elastic and strongly damped fragments was observed (Ca 85). This preequilibrium component was parameterized by assuming thermal emission from a localized hot source moving at a velocity of about half the beam velocity. One interesting feature observed was that for very peripheral collisions, the preequilibrium neutron spectra showed a distinct asymmetry at middle angles. More high energy neutrons were observed on the side of the beam opposite to that of the detected projectile-like fragment. For neutrons in coincidence with low energy fragments, such

an asymmetry was not observed. This asymmetry was reproduced within the thermal-source parameterization by requiring the hot source to move off axis towards the side of the beam opposite the detected projectile-like fragment. For reactions leading to strongly damped fragments, the hot source was shown to move on the average straight down the beam axis, thus creating no asymmetry. Asymmetry effects in preequilibrium particle emission have been observed before in both charged particle--projectile-like fragment coincidence studies (Ge 77, Si 84) and in neutron--projectile-like fragment coincidence studies (Ts 82, Pe 85). No systematic trend has yet been established, and results often depend on the method of isolating the preequilibrium component.

Motivated by these results, we conducted an experiment using a 35 MeV/nucleon beam of ^{14}N provided by the K500 cyclotron at the National Superconducting Cyclotron Laboratory at Michigan State University in East Lansing. To try to understand the target dependence of preequilibrium neutron emission, we selected targets of Ho as a relatively large nucleus and Ni as a significantly smaller nucleus. If the observed asymmetry was due to a shadowing effect, then the size of the target nucleus might be a pertinent parameter. In the earlier neutron study (Ca 85) fragments were detected at two angles, 10° and 30°, with the above-mentioned asymmetry observed only for coincident fragments

resulting from quasi-elastic interactions. Such fragments were observed at 10° (which is near the grazing angle) but not at 30°. To try to understand the dependence on impact parameter, as reflected in the angle of the coincident fragment, we placed an array of fragment telescopes both inside and outside the grazing angle (8°) for the ^{14}N + ^{165}Ho system and near the grazing angle (4°) for the ^{14}N + Ni system.

In this paper we present a systematic study of neutrons detected in coincidence with light fragments (LF) in ^{14}N-induced reactions on targets of Ho and Ni at 35 MeV/nucleon incident energy. In the next section of this paper we describe the experimental details. Since neutrons were detected in coincidence with fragments, a short discussion of the fragment energy, angle and Z distributions is given in Section III. The neutron spectra are discussed in Section IV, and the results from a moving source analysis are presented in Section V. Also contained in Section V are the results of a two-body calculation and of multiplicity calculations done with CASCADE, as well as a discussion of the "size" of the hot source. A summary of our results and our conclusions are given in Section VI.

II. EXPERIMENTAL SETUP

As a detailed description of the experimental setup can be found in the appendices, only the salient features will be mentioned here. The detector arrangement is shown in Fig. 1. Ten neutron detectors were placed around the outside of the scattering chamber, and six triple-element Si telescopes placed inside. The scattering chamber was made from steel, had a 3 mm wall thickness and a 0.91 m diameter. The ten neutron detectors were identical to those described in Ref. De 86. Each one consisted of 1 liter of NE213 liquid scintillator contained in a sealed glass cell about 12.7 cm in diameter by 7.6 cm thick. Each cell was preceeded by a 6 mm thick NE102A proton veto paddle to eliminate events due to high energy protons that traveled through the chamber wall and into the neutron detector.

The coincident light fragments were detected in one of six triple-element Si telescopes. The four forward-most telescopes consisted of a 100 μm surface barrier Si detector serving as the ΔE detector, and the combination of a 5 mm and a 1 mm Li drifted Si detector serving together as the E detector. For the two largest fragment angles (18° and 23°), the detector thicknesses were 30 μm, 100 μm, and 5 mm. The first two elements were intended for particle identification of the lower-energy, higher-Z fragments that would be stopped in the middle detector. All the telescopes were cooled to about -10°C by circulating refrigerated

Figure 1. Experimental setup. Ten neutron detectors, together with their proton veto detectors, are located around the chamber at symmetric angle pairs of ±10°, ±30°, ±70°, ±110°, and ±160°. Also shown on a direct path from the target to the detectors are the shadow bars, which periodically throughout the run were placed in the locations indicated. Six triple-element Si telescopes were placed inside the chamber at polar angles of 7°, 10°, 15°, 18°, and 23° in the horizontal plane, and at 14° directly below the beam direction. The line in the upper right-hand corner corresponds to a length of 1 m.

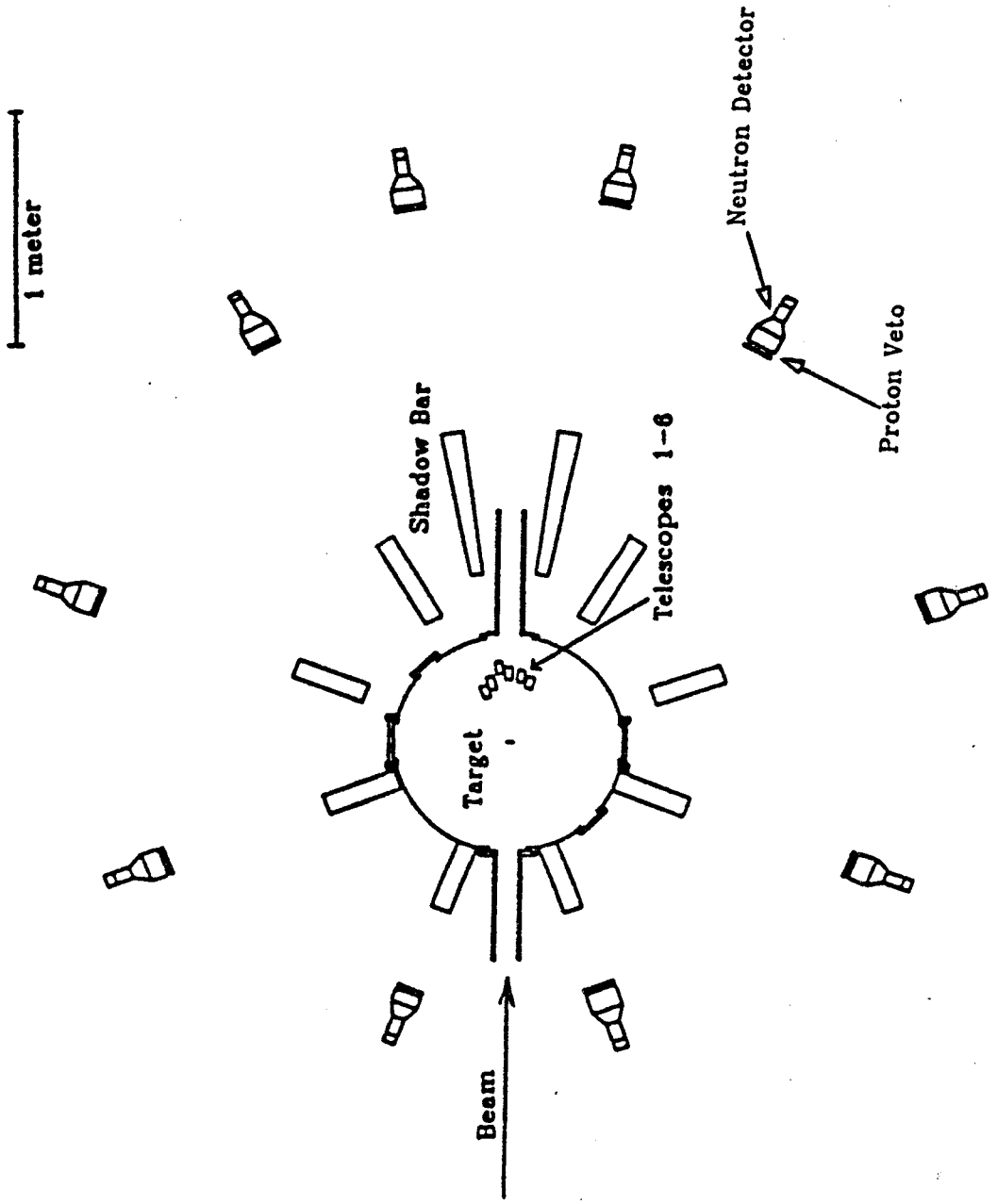
1 meter
Neutron Detector
Proton Veto
Shadow Bar
Telescopes 1-6
Target
Beam

Figure 1.

liquid methanol. This reduced the leakage current, and hence the noise, resulting from radiation damage in the Si.

The neutron detectors were placed in a horizontal plane at angles of ±10°, ±30°, ±70°, ±110°, and ±160° at distances ranging from 1.14 m at ±160° to 2.42 m at ±10°. The time resolution of the detectors was about 1ns at the ^{60}Co Compton edge. Combining this with the flight path and detector thickness allowed energy resolutions which, for 5 and 50 MeV neutrons, varied from 14% and 20% at the back angles to 6% and 8% at the forward angles. The fragment telescopes were placed at angles of 7°, 10°, 15°, 18°, and 23° in the horizontal plane and 14° out of this plane directly below the beam axis. The distances from the target of five of the six telescopes ranged from 21 to 25 cm, and 12.7 mm collimators were placed in front of each telescope. The telescope at 7° was placed at 30 cm from the target with a 4.0 mm collimator. With the typical beam intensity of 2 x 10^{10}/sec the live time was about 90%. To inhibit secondary electrons knocked out of the target by the beam from entering the Si detectors, rare-earth Co magnets were mounted in front of each telescope.

The targets used were 8.9 mg/cm^2 Ho, 4.6 mg/cm^2 Ni, 3.1 mg/cm^2 C, and 3.2 mg/cm^2 mylar. A run with the carbon target gave us the data with which to subtract a possible contribution from ^{14}N - carbon reactions in case there was

any appreciable carbon buildup on the Ni and Ho targets. Similarly, in case of oxidation of targets, a short run with the mylar target was conducted to determine the contribution from ^{14}N - O reactions. As was determined in a separate α-particle back-scattering experiment done on the tandem Van de Graaff system at the University of Notre Dame, the level of carbon buildup on our targets was $\leq$ 1 $\mu g/cm^2$ and the oxygen contamination was about 4 $\mu g/cm^2$. From our measurements taken with the carbon target, we determined that the cross sections for neutron production from ^{14}N + C reactions were typically less than for the corresponding reactions resulting from the ^{14}N + Ni and ^{14}N + Ho systems. So compared to the 8.9 - 4.6 mg/cm^2 thickness of targets used, the contamination level was completely negligible.

To reduce the level of background neutrons, the amount of (potential scattering) material in the chamber and beamline near the target was kept low, and extensive shielding was installed around the beam dump. To know the background contribution to our measured neutron spectra, periodically throughout the experiment data were taken with shadow bars placed as shown in Fig. 1. The background contribution was typically less than 10% of the total.

The time structure of the beam was not suitable for timing the neutron against the cyclotron rf signal, so instead neutrons were recorded in coincidence with and

"timed against" a fragment in any one of the six Si telescopes. Neutron--gamma-ray discrimination was accomplished with commercially available pulse-shape discrimination modules (Sp 74), using standard two-dimensional neutron--gamma-ray discrimination techniques (On 75, Pe 79). For each event, the following information was written onto magnetic tape: timing, pulse-shape discrimination, and light signals from the neutron detector; ΔE, E, and timing signals from the Si telescope; and a bit mask that recorded which combination of detectors fired. Downscaled fragment singles events were also recorded. The data were written onto tape with the aid of a CAMAC multiparameter data acquisition system incorporating an MC68010 microprocessor, with typical acquisition rates of 800 events/sec (Va 85).

The thick Si detectors at angles $\theta \leq 15°$ were calibrated with the peak from elastically scattered beam particles. For the two telescopes at $\theta \geq 18°$, where we could not observe an elastic peak, the high energy calibration was transferred from the small-angle detectors with the aid of a pulser. The ΔE detectors were calibrated with α-particle sources and a pulser used in combination with a calibrated charge terminator.

III. FRAGMENT SPECTRA

Since neutrons were recorded only in coincidence with fragments, a discussion of the fragment spectra will be useful. Figures 2 and 3 show linearized ΔE - E fragment identification plots for the Ho target for singles fragments at angles of 10° and 23°, respectively. One can see that we had excellent element separation and in many cases good isotope separation. In sorting the neutron data, gates were set across the fragment element groups of Li, Be, B, and C. Figures 4 and 5 show the singles fragment energy spectra at angles of 7°, 10°, 15°, 18°, 23°, and 30° for the Ho target and angles of 7°, 15°, 18°, and 23° for the Ni target. The 30° fragment data for the Ho target were taken during an earlier experiment (Ca 85, Ki 86, De 86). Fragment singles data at 10° for the Ni target were not obtained due to a difficulty in the downscaling electronics. (The 10° fragment coincidence data were unaffected by this problem.) The low energy (LE) and high energy (HE) gates set across the fragment spectra in sorting the neutron data are indicated in both Figs. 4 and 5. These gates were set by inspecting the coincidence fragment spectra, which were very similar to the singles spectra. The fragment energy gates used at 10° for the Ni target are listed in Table 1.

By examining Figs. 2-5, one can obtain qualitative information about the reaction mechanism as a function of fragment angle. In Fig. 2 (for fragments at 10° for the Ho

Table 1. Energy gates for fragments at 10° for the Ni target.

Fragment	LE(MeV)	HE(MeV)
Li	30-100	140-250
Be	40-140	170-300
B	60-180	220-400
C	74-210	260-436

target), two features stand out clearly. First, all fragments are most prominent at energies near the beam-energy/nucleon. Second, the N fragments stand out as distinct, with essentially no high energy fragments with Z > 7 being observed. Evidently, the processes leading to high energy fragments strongly favor $Z \leq Z_{beam}$. This skewing of the charge distribution to $Z \leq Z_{beam}$ has also been observed for fragments near the grazing angle in the $^{12}C + ^{158}Gd$ and $^{20}Ne + ^{150}Nd$ systems at slightly lower beam energies (9-16 MeV/nucleon) (Pe 85), and is consistent with the systematics for asymmetric systems (Si 79). Processes such as projectile fragmentation (Go 74, Fr 83) and stripping (Si 85) would be possible candidates for the reaction mechanism. On the other hand, an examination of Fig. 3 shows that neither Z = 7 nor the beam-energy/nucleon occupies a unique position, indicating that memory of the entrance channel has been lost. Suitable candidates for this process might be partial orbiting (Wi 73, La 78) or fragment emission from a localized hot source (We 82, Ja 83, We 84, Fi 84, Ha 85).

Figure 2. Linearized ΔE-E fragment identification plot for fragment singles at 10° resulting from collisions with the Ho target nucleus. The various element groups are identified in the left hand column. The units are MeV/nucleon on the X-axis and an arbitrary fragment identification unit on the Y-axis.

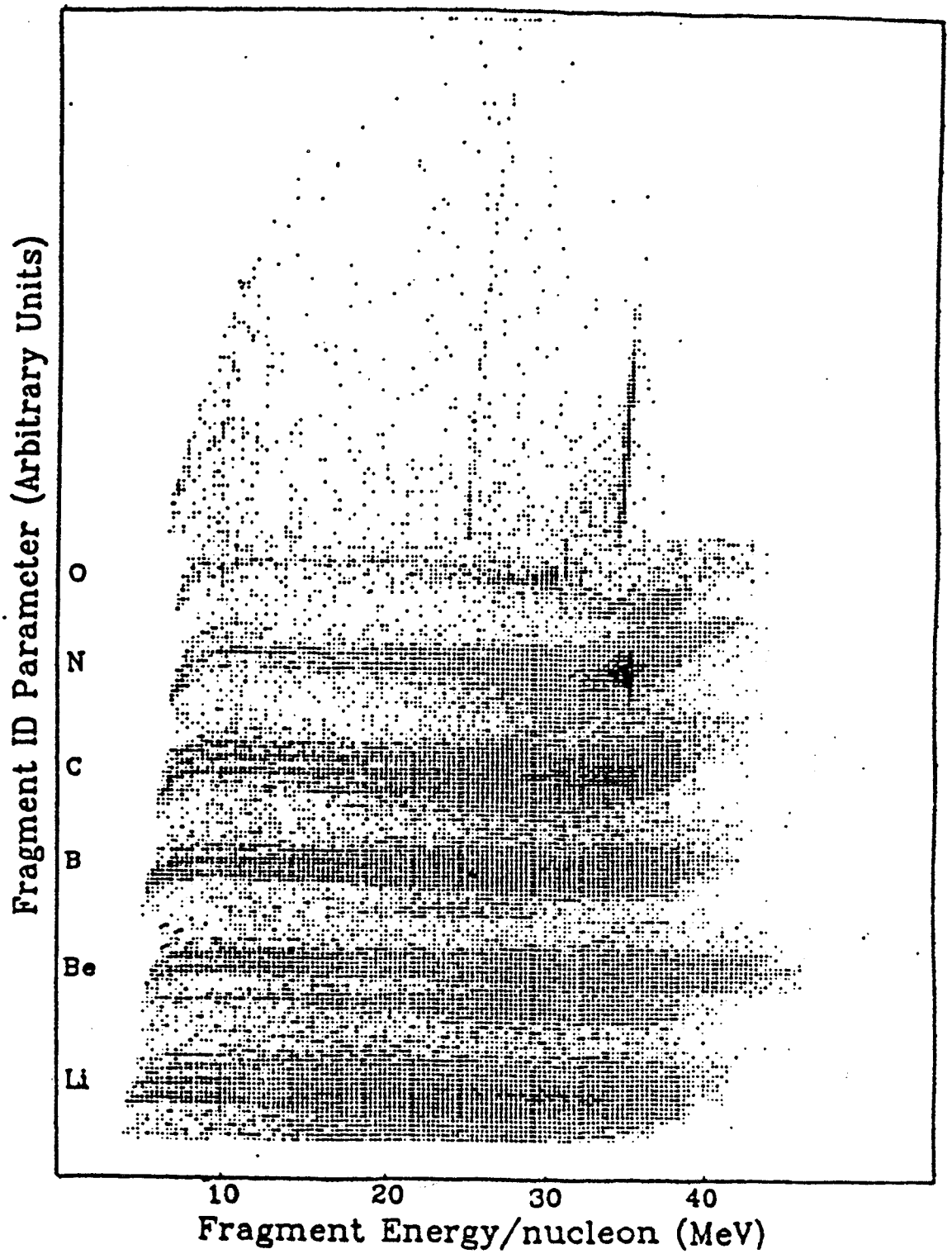
Fragment ID Parameter (Arbitrary Units)
O
N
C
B
Be
Li
10
20
30
40
Fragment Energy/nucleon (MeV)

Figure 2.

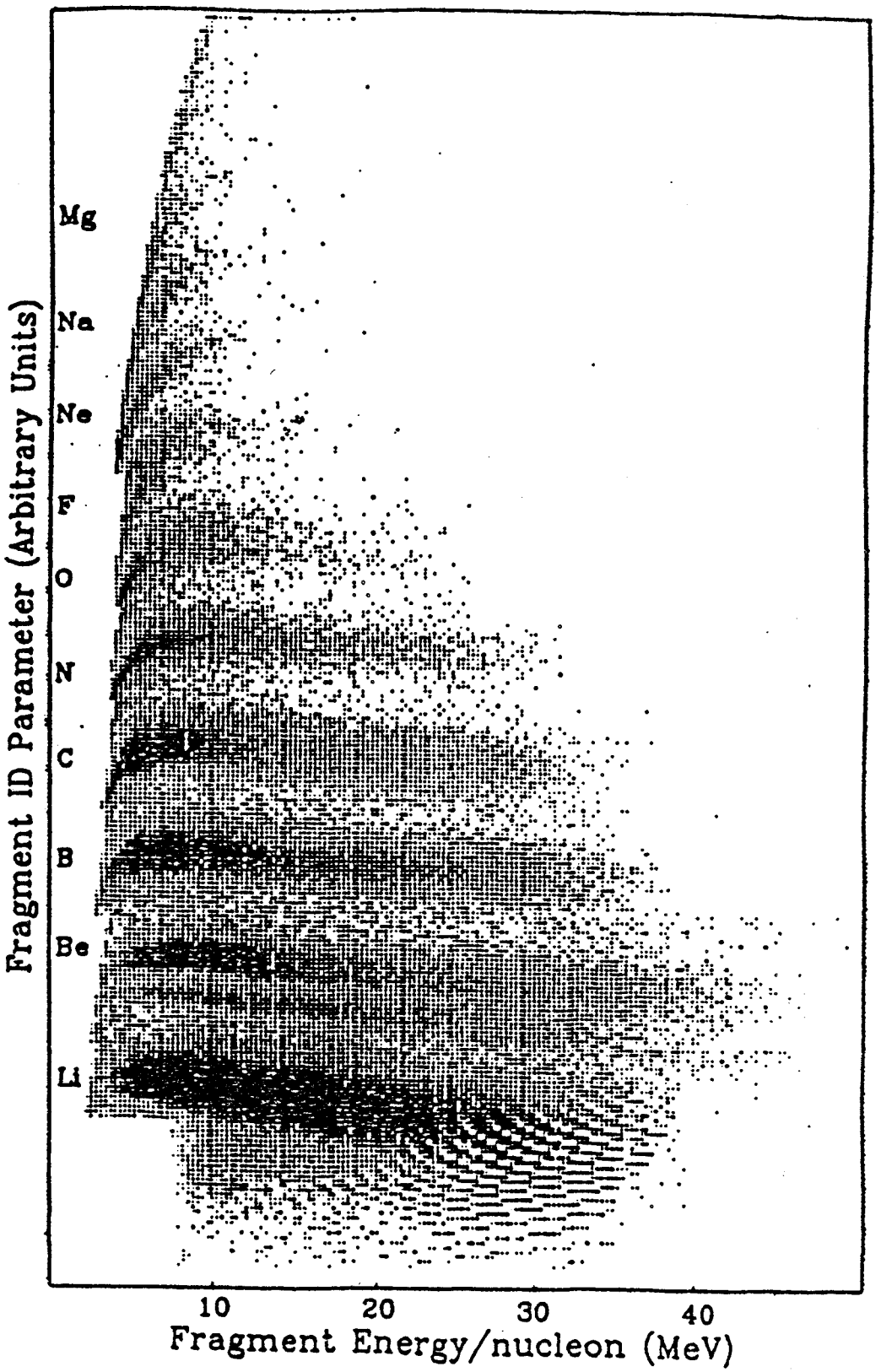

Figure 3. Same as Fig. 2 except for fragments at 23°.

The fragment energy spectra displayed in Fig. 4 for the Ho target show the transformation of spectral shape as a function of angle. For fragments near the grazing angle, 8°, one sees the spectra dominated by a broad peak at energies corresponding to near-beam velocities. This dominating component corresponds to the quasi-elastic peak from projectile fragmentation in very peripheral collisions (Go 74, Fr 83). As the fragment angle increases, one sees the quasi-elastic component steadily decrease and essentially disappear for fragment angles of 23° and larger. The strongly damped component corresponding to low energy fragments from more central collisions exists at all the angles studied. At 30° this is the only component present and the spectrum seems to be falling off nearly exponentially with energy. We notice a rapid transition in spectral shape between 15° and 18°, and speculate that 15° corresponds to a transition angle beyond which quasi-elastic reactions become negligible.

The fragment spectra for the Ni target presented in Fig. 5 show the same qualitative features as discussed for the Ho target data in Fig. 4. The rapid transition now occurs between 7° and 15°. The transition angle is about half the value for Ho, and the grazing angle, 4°, is also half the Ho value.

We point out the possibility of misidentifying ^{7}Li in our fragment telescopes from the reaction ^{8}Be $\rightarrow 2\alpha$ if both

Figure 4. Singles energy spectra for the Ho target for fragments of Li, Be, B and C. From top to bottom, the angle of the fragment is 7°, 10°, 15°, 18°, 23° and 30°. Indicated on each spectrum are the high energy (HE) and low energy (LE) gates used for the coincident neutron spectra.

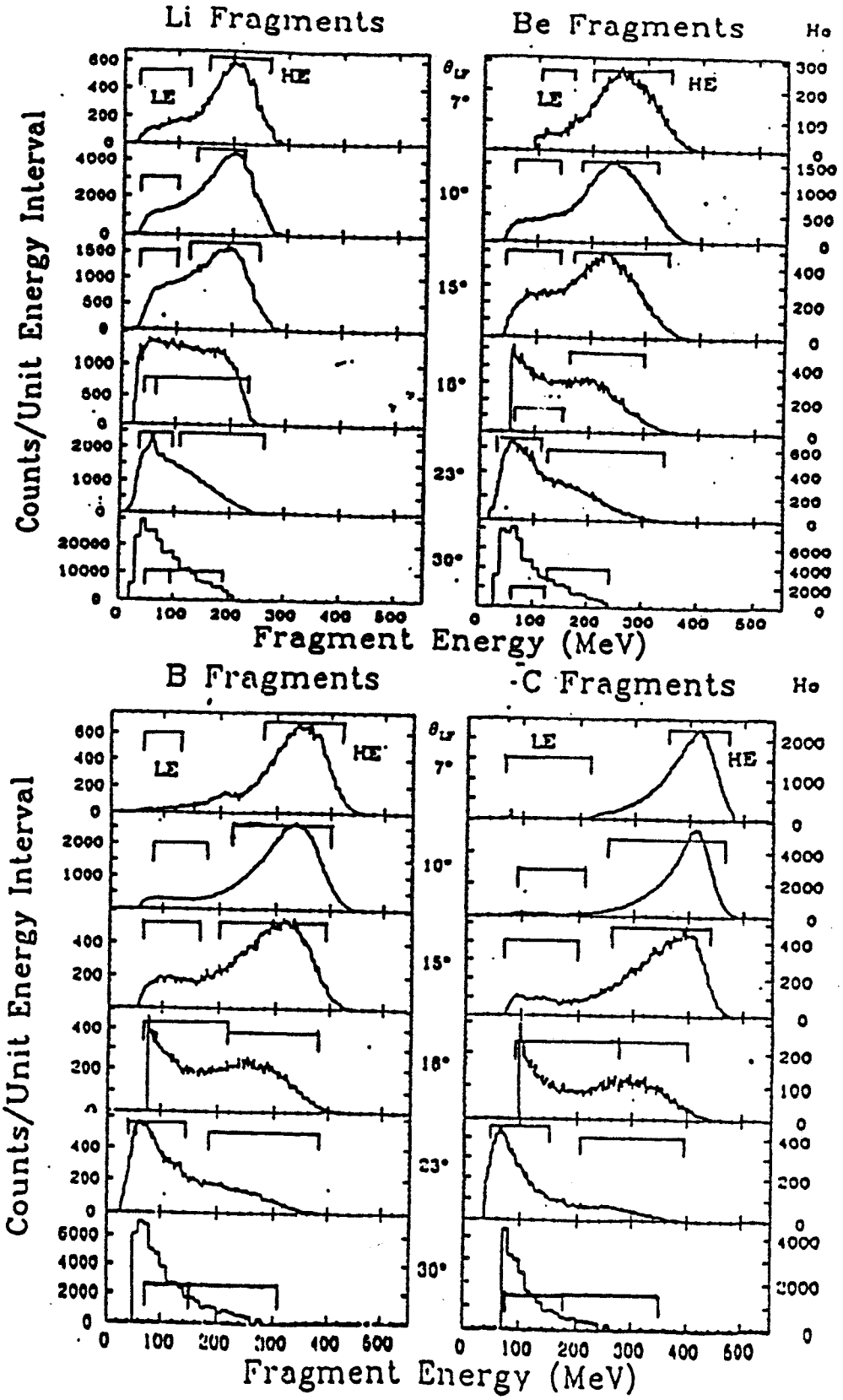
Li Fragments
Be Fragments
B Fragments
C Fragments
LE
HE
Counts/Unit Energy Interval
Fragment Energy (MeV)
7°
10°
15°
18°
23°
30°

Figure 4.

Figure 5. Same as Fig. 5 except for the Ni target. (No 10° or 30° fragment singles data were obtained for the Ni target.)

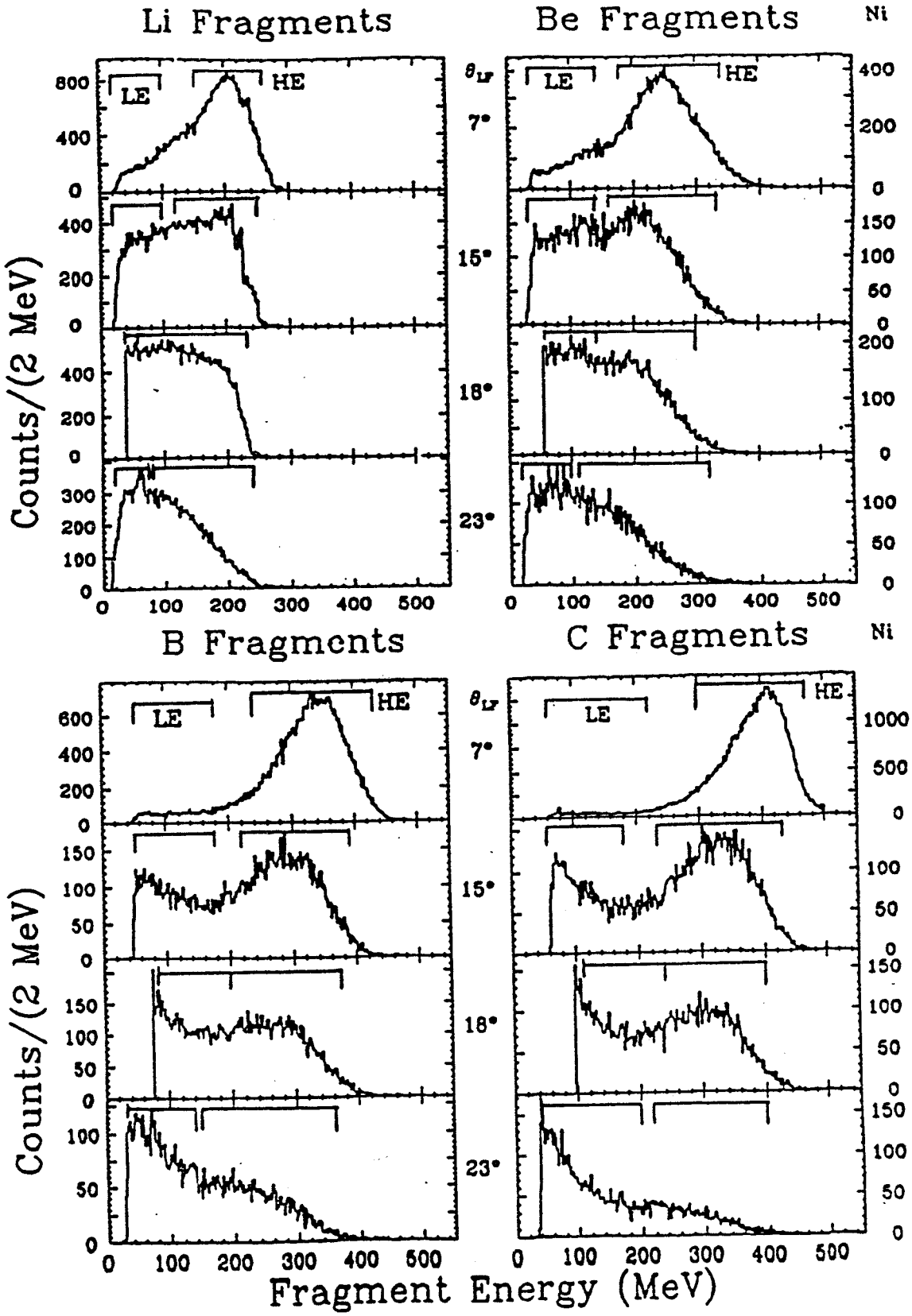
Li Fragments
Be Fragments
Ni
B Fragments
C Fragments
Ni
LE
HE
θLF
7°
15°
18°
23°
Counts/(2 MeV)
Fragment Energy (MeV)

Figure 5.

alpha particles enter the detector (Wo 74). Based on the solid angles of the collimators and the average energy of the Be fragments within the LE and HE gates, we estimate that less than 1% of all ^{8}Be fragments result in both alpha particles entering the same detector. Unless ^{8}Be is produced with an anomalously high abundance in comparison to neighboring isotopes, this effect is negligible for the present work.

IV. NEUTRON SPECTRA

The neutron energies were determined by the method of time-of-flight (TOF). A more detailed discussion of the data reduction process can be found in the appendices. As mentioned in Section II, the neutron was "timed against" the coincident fragment, with the flight time of the fragment added off-line to obtain the true neutron TOF. Figure 6 shows a neutron TOF spectrum along with the accidental coincidences (top) and background neutrons (middle). The final "true" TOF spectrum is shown at the bottom of the figure. The reference time in the neutron TOF spectra was determined by the position of the gamma-ray peak due to fragment--gamma-ray coincidences. The gamma-ray events have been suppressed in Fig. 6 using pulse shape discrimination, but the position of the gamma peak is indicated by an arrow. In the transformation from TOF spectra to energy spectra, the detector efficiency and attenuation correction were folded in. The efficiency was calculated with a Monte Carlo code developed by Cecil et al. (Ce 79) and then compared with the results from a calculation using a code developed earlier by Kurz (Ku 64). The two calculations agreed with one another very well, and both agree with data to better than 10%. Although the efficiency is energy dependent, a typical value is 10%. The attenuation factor corrects for the attenuation of neutron flux by material lying between

Figure 6. Neutron time-of-flight (TOF) spectra showing the various stages of processing the data. The data are for neutrons at -10° in coincidence with high energy Li fragments at +10°. The top spectrum is the raw neutron TOF data, with the counts due to accidental coincidences indicated by circles. The middle plot has had the accidental coincidences subtracted out. The background (scattered) neutrons are indicated by triangles. The bottom spectrum has had the background counts subtracted out and represents the "true" neutron TOF spectrum. The gamma-ray events have been supressed off-line using pulse-shape discrimination, but the position of the gamma-ray peak is indicated by the arrow.

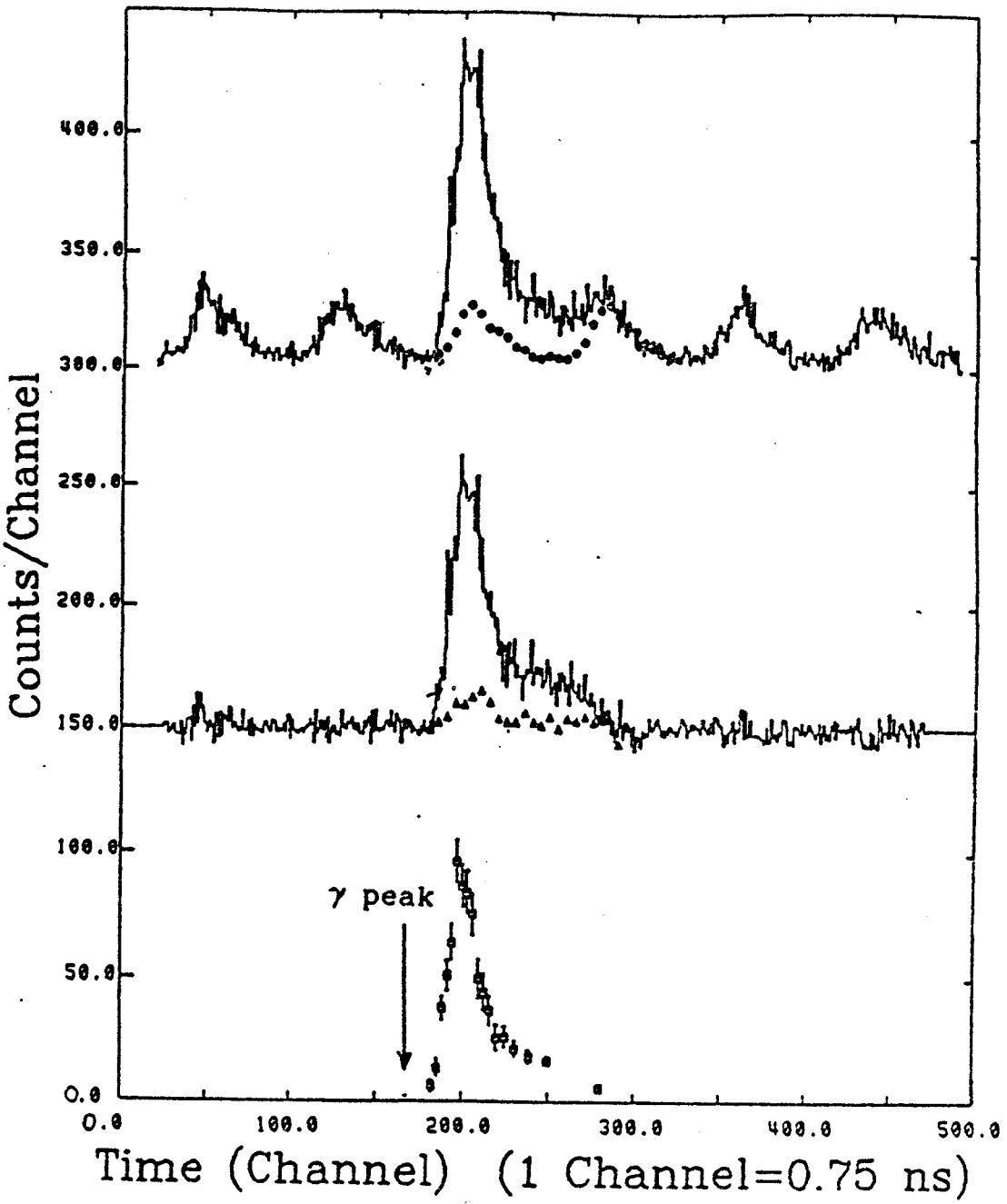
Counts/Channel
400.0
350.0
300.0
250.0
200.0
150.0
100.0
50.0
0.0
γ peak
0.0
100.0
200.0
300.0
400.0
500.0
Time (Channel) (1 Channel=0.75 ns)

Figure 6.

the target and detector. This correction is also energy dependent, but again 10% is a typical value.

Figure 7 shows a two dimensional scatter plot of neutron velocities for coincident high energy boron fragments at 10°. The arrow in the figure indicates the average velocity vector of the fragment. The cross section is proportional to the darkness of the lines. One notices that there are many high velocity neutrons at the forward angles, especially at $\theta_n = \pm 10°$, whereas at the back angles, there are very few high velocity neutrons. A very interesting feature can be seen at the middle angles of $\theta_n = \pm 70°$ and $\pm 110°$. There are more high velocity neutrons at middle angles on the side of the beam opposite to that of the detected fragment, verifying an earlier observation (Ca 85). In the very peripheral collisions represented here, the projectile most probably does not pass by the target nucleus closely enough for the nuclear force of attraction to initiate partial orbiting (Wi 73, La 78). So one would expect the side of the beam on which the fragment was detected to coincide with the side of the target nucleus the projectile interacted with. Furthermore, one might consider the source of high energy neutrons at middle angles to be the "hot" overlap region between the projectile and target nuclei, sometimes called a surface "hot spot" (Ga 80, Go 77, Mo 80, We 77). Then for neutrons to be detected at middle angles on the side opposite the coincident fragment, these

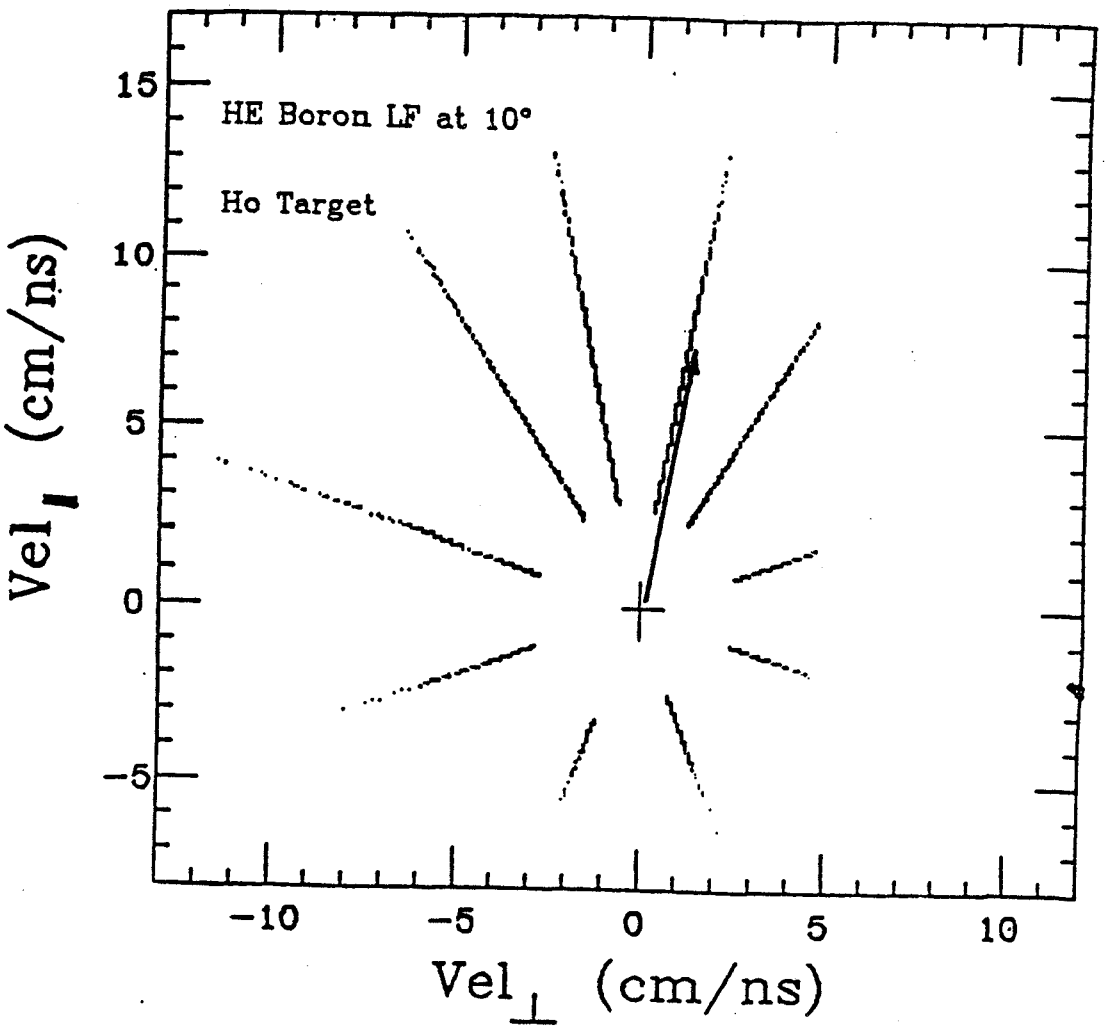

Figure 7. Neutron velocity scatter plot of invariant cross section. Intensity of the lines is proportional to the yield. The coincident fragments were high energy borons at 10° for the Ho target. The Y-axis plots the component of neutron velocity parallel to the beam direction and the X-axis the component perpendicular to the beam direction. The arrow indicates the average velocity vector of the boron fragments.

neutrons would first have to traverse the nuclear matter of the large target nucleus. Hence, one might expect to see a dearth of neutrons on the side opposite the detected fragment as compared to the same side, which is just the opposite of what is observed!

Figure 8 shows the same data as in Fig. 7, but here the data is presented as a contour plot in the rapidity plane. This representation is useful for understanding the various sources of the neutrons observed. Due to the additivity of rapidity, concentric circular contours of invariant cross section in the rapidity plane indicate the presence of a source emitting isotropically in its rest frame. A vector from the origin to the center of such concentric circles indicates the rapidity of the emitting source. One notices concentric, circular contours centered around the tip of the average rapidity vector of the boron fragment. These contours correspond to neutrons emitted from excited boron fragments. Also, there are contours centered around the origin which fall roughly equally in all directions, indicating a source nearly at rest emitting neutrons isotropically. This component corresponds to the contribution from a slowly moving, target-like source (TLS). The conspicuous bulge at middle angles corresponds to the same asymmetry seen in the velocity scatter plot of Fig. 7. Within the moving-sources parameterization, this asymmetry can be reproduced by introducing an IRS moving to the side of the beam opposite the detected fragment.

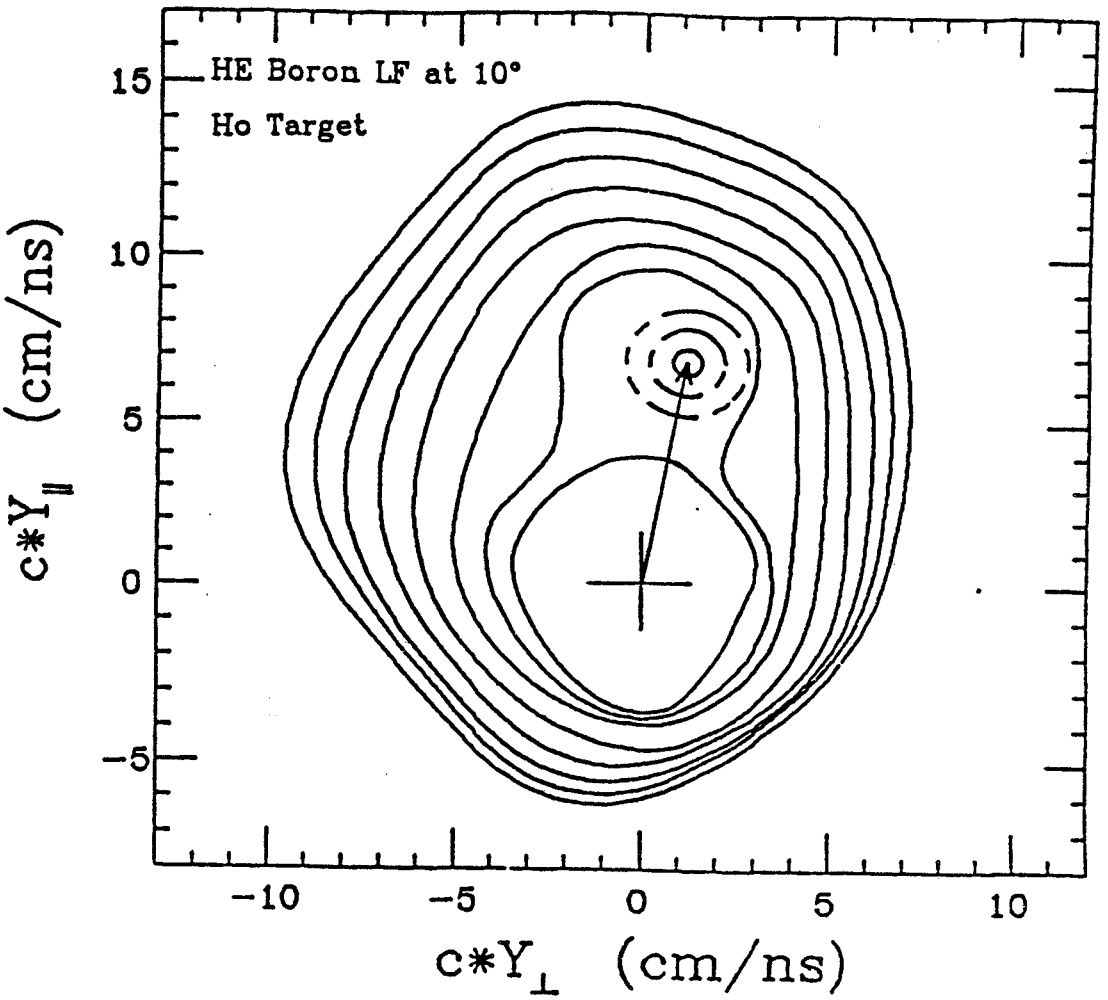

Figure 8. Rapidity contour plot for the same system of Fig. 7. Each contour is offset by a factor of $1/\sqrt{5}$ in invariant cross section, and the arrow represents the average rapidity of the boron fragments. The dashes in the circular contours at the tip of the arrow indicate regions of smooth interpolation.

Examples of neutron energy spectra are given in Figs. 9 and 10 for the Ni target and in Figs. 11 and 12 for the Ho target. The solid and dashed lines in Figs. 9, 10 and 12 correspond to moving-source fits which will be discussed below. The ordinates in Figs. 9 and 10 are differential associated multiplicity in units of neutrons/(MeV·sr) per detected fragment. To obtain multiplicity, neutron coincidence cross section was divided by the fragment singles cross section for the appropriate fragment gate. The fragment singles cross sections used in this transformation are listed in Table 2.

The coincident fragments in Fig. 9 are high energy carbons at 7°, and the inset gives the spectrum. In this figure one can identify three distinct components of the neutron spectra. A low energy, nearly isotropic component dominates at $\theta_n = \pm 160°$; it corresponds to neutrons evaporated from a TLS. At $\theta_n = \pm 10°$ one can see definite structure at energies between 15 and 45 MeV. This structure results from neutrons emitted from specific discrete states of excited projectile-like fragments of carbon nuclei (Ki 86, Re 85). The structure is centered around 30 MeV, the energy corresponding to the average velocity of the carbon fragments. The spread results from the addition of source and neutron velocities. With the gate used for the coincident high energy carbon fragments, a decay energy of only 2 MeV is sufficient to produce laboratory neutron

Table 2. Fragment singles cross sections.

	Ho Target		Ni Target	
Fragment	$\frac{d\sigma}{d\Omega}$ ($\frac{mb}{sr}$)-LE	$\frac{d\sigma}{d\Omega}$ ($\frac{mb}{sr}$)-HE	$\frac{d\sigma}{d\Omega}$ ($\frac{mb}{sr}$)-LE	$\frac{d\sigma}{d\Omega}$ ($\frac{mb}{sr}$)-HE
θ =7°				
Li	219.5	972.5	145.7	720.2
Be	75.6	586.2	92.0	437.3
B	61.5	1405.4	80.0	880.3
C	96.1	3045.0	80.9	1329.5
θ =10°				
Li	120.1	425.7	115.4	399.2
Be	42.0	241.4	70.0	166.3
B	40.4	436.0	57.1	306.8
C	27.8	630.0	53.0	405.4
θ =15°				
Li	92.1	191.9	99.3	175.3
Be	41.9	64.7	54.9	71.9
B	33.0	72.9	45.6	75.6
C	23.0	47.3	35.6	75.0
θ =18°				
Li	35.4	195.9	36.9	222.1
Be	36.2	39.4	43.5	59.5
B	35.0	28.3	58.6	47.3
C	20.5	12.7	30.8	37.1
θ = 23°				
Li	75.3	64.8	53.3	93.4
Be	28.0	22.3	31.6	39.2
B	26.9	12.0	33.6	27.6
C	17.7	5.1	37.2	12.5
θ = 14° Out-of-Plane				
Li	106.5	291.3	99.7	240.0
Be	42.0	104.7	53.3	106.6
B	41.0	125.3	47.7	105.0
C	25.7	101.8	36.8	101.2

Figure 9. Neutron differential multiplicity spectra (neutrons/MeV·sr per detected fragment) for a coincident fragment of high energy carbon at 7° for the Ni target. The spectra are plotted in symmetric angle pairs, each offset from the next by a factor of 100, with the spectra at the top having the scale as indicated. The curves correspond to moving-source fits with a TLS and an IRS. The open symbols and dashed lines correspond to the same side of the beam as the detected fragment, while the solid symbols and solid lines correspond to the opposite side. The gate set across the fragment energy is shown as the hatched region in the inset. The multiplicity, temperature, energy/nucleon and angle of the TLS (IRS) are 0.35 (0.34), 3.40 MeV (10.00 MeV), 0.12 MeV (11.00 MeV) and -18.5° (-10.5°).

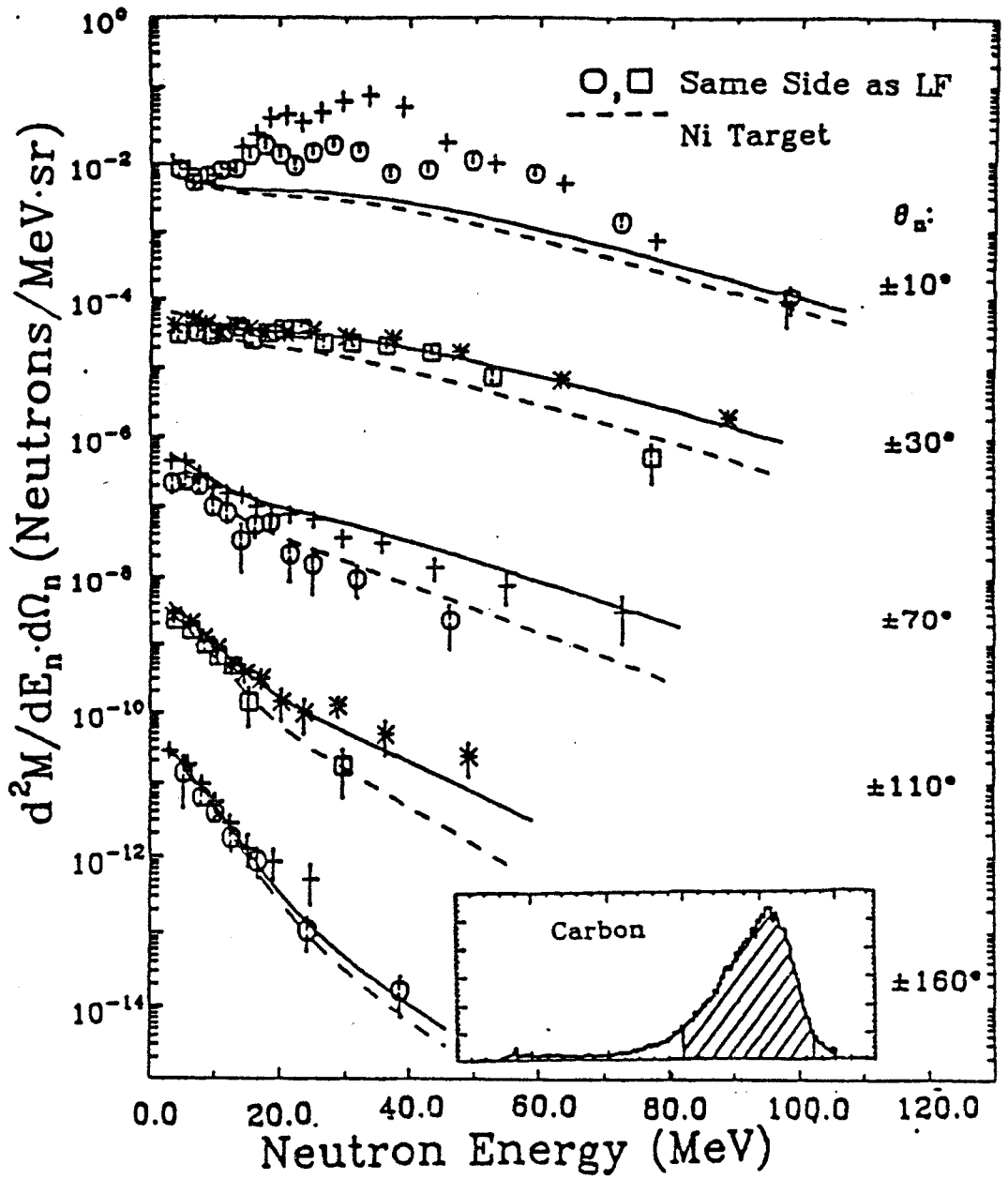
O,□ Same Side as LF
Ni Target
θn:
±10°
±30°
±70°
±110°
±160°
Carbon
d²M/dEn·dΩn (Neutrons/MeV·sr)
Neutron Energy (MeV)
10⁰
10⁻²
10⁻⁴
10⁻⁶
10⁻⁸
10⁻¹⁰
10⁻¹²
10⁻¹⁴
0.0
20.0
40.0
60.0
80.0
100.0
120.0

Figure 9.

energies between 15 and 45 MeV. Emission from discrete states of the projectile-like fragment has been seen by others for neutrons (Ga 81, Hi 81, Lü 85, Ch 83) and for α-particles (Ge 79, Ho* 83). In addition to the TLS and the light-fragment components, one can see at middle angles in Fig. 9 a very distinct third component of high energy neutrons. This component appears thermal in shape, has a much flatter slope than the TLS component, and exhibits a very interesting asymmetry at ±70° and probably at ±110°. There are more high energy neutrons seen at 70° on the side opposite the detected fragment than on the same side. This asymmetry was seen in an earlier study of the N + Ho system for very peripheral collisions (Ca 85), and now we have observed it in the N + Ni system, also for peripheral collisions.

Figure 10 shows the neutron spectra in coincidence with low energy Li fragments at 23°. Again three components can be identified. The low energy, nearly isotropic TLS component is most easily distinguished at $\theta_n = \pm 160°$. The contribution from discrete neutron emitting states of the light fragment causes a small "peak" at about 8 MeV in the neutron detector at +30° (this is the neutron detector nearest to the fragment direction of +23°). The "peak" is roughly centered around the average energy/nucleon of the detected fragment. The third component, corresponding to high energy neutrons at middle angles, is prominent in this

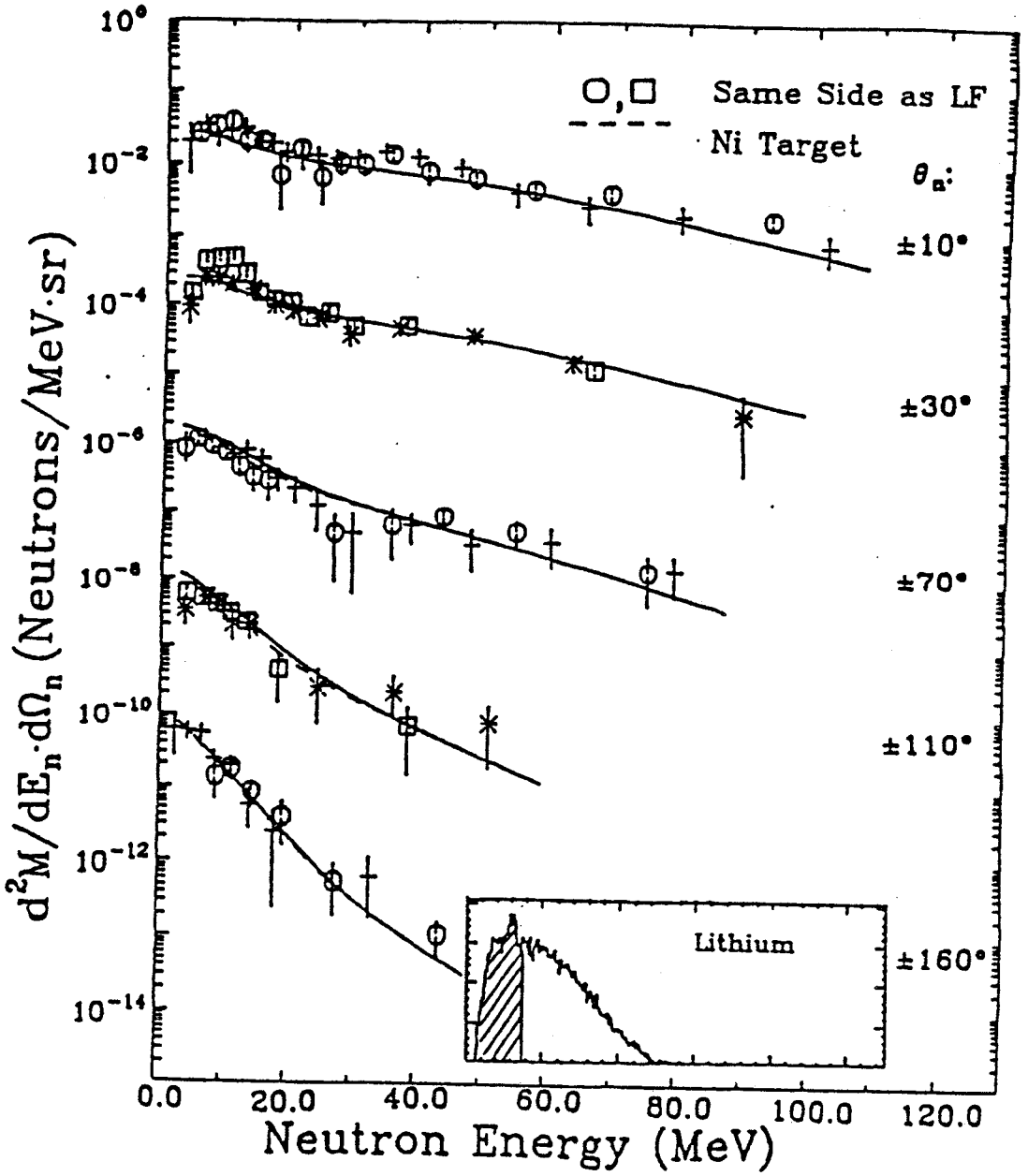

Figure 10. Same as Fig. 9 except for coincident low energy lithium fragments at 23°. The inset shows the energy of the coincident fragments. The multiplicity, temperature, energy/nucleon and angle of the TLS (IRS) are 1.63 (1.07), 4.23 MeV (12.27 MeV), 0.58 MeV (12.11 MeV), and -7.6° (0.0°).

spectrum, too, with the one notable exception that there is no asymmetry at $\theta_n = \pm 70°$. This lack of asymmetry is also consistent with the systematics of the N + Ho system (Ca 85), where a neutron asymmetry was observed only when the coincident fragment was a quasi-elastic fragment.

Summarizing the systematics of the asymmetry, we have observed for the Ho target that the asymmetry exists only for high energy fragments at 7° and 10°, whereas the grazing angle is about 8°. For the Ni target the asymmetry was seen only for high energy fragments at 7°, whereas the grazing angle is about 4°. For both targets the asymmetry is strongest for fragments of mass just below, or equal to, the projectile mass. Since the asymmetry is strongest for high energy, near-projectile-mass fragments close to the grazing angle, it seems to be associated with the most peripheral interactions.

One needs to consider whether the observed asymmetry is a trivial instrumental effect caused by the neutrons traversing more material on one side of the chamber than on the other. This is not the case. Only at 10°, where there was a fragment telescope on one side of the beam but not the other, was there a difference in the attenuating material. That difference was small and was corrected for, as mentioned above.

An angular misalignment of the neutron detectors with respect to the beam could also cause an asymmetry. By

examining the neutron spectra at symmetric angle pairs for a coincident fragment at 14° out-of-plane directly below the beam, we were able to check the alignment. Examples of such spectra are displayed in Fig. 11. As all of the coincident Li, Be, B, and C fragments were used, the statistical accuracy of the comparison is high. There is no asymmetry in these spectra.

If there were extensive carbon or oxygen contamination on the target, then scattering of the projectile off such small contaminant nuclei might yield a "TLS" moving at a high enough velocity to the side opposite the light fragment to create the observed asymmetry. But as mentioned in Section II, the target contamination was measured and found to be negligible compared to the thickness of the target.

A more subtle possible cause of an asymmetry arises from the recoil of the light fragment after it emits a particle. It has been shown (Ge 79, Yo 80, Hi 83, Ho 83, Wa 83, Pe 85) that under certain conditions, asymmetries in the same sense as we observe can be caused by the recoil of the emitter. Using the asymmetries in Fig. 9 as an example, we first note that the angular distribution of the parent fragments is very steeply falling. So there are many more fragments inside of 7° (the angle of the fragment detector) than outside of 7°. Therefore, more fragments recoil into the telescope from inside of 7° by emitting a neutron to the side opposite than recoil into the telescope from outside of 7° by emitting a neutron to the same side. This effect has

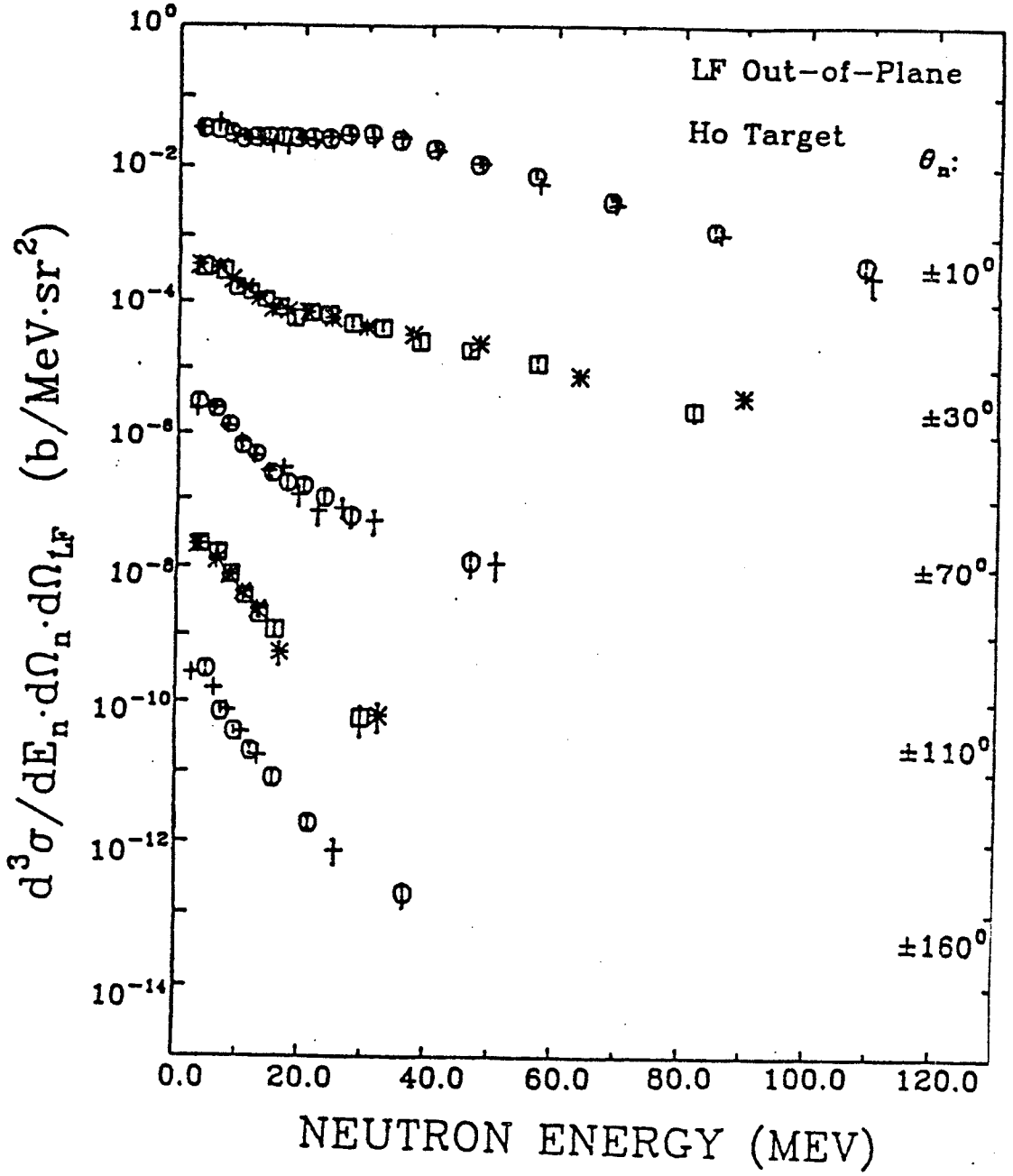

Figure 11. Neutron spectra in coincidence with all fragments with Z ≥ 3 moving at 14° out-of-plane. The spectra are plotted in symmetric angle pairs, each offset from the next by a factor of 100, with the spectra at the top having the scale as indicated.

been studied with a computer simulation (Ca* 85), and it has been found that even though an asymmetry of the sense observed can be created, it greatly lacks the energy and angular distribution of the data. In essence, a fragment moving at near-beam velocity towards the 7° telescope cannot contribute significantly to the high energy neutrons at middle angles, where the asymmetry is observed. That the light fragment contribution to neutrons at middle angles is small was also shown by Gavron in a Monte Carlo simulation (Ga* 81).

Having disposed of the trivial instrumental possibilities, we should consider the reaction models that quite obviously produce a left-right asymmetry, viz., the Fermi jet and the quasi-free knock-out (Ha 79, Ko 77) models. Unfortunately, the Fermi jet model has not been worked out for the case of a coincident fragment. But we were able to compute quasi-free scattering of target neutrons by the nitrogen projectile nucleus. As a sample set of data to compare with the calculation, we considered neutrons from Ho in coincidence with all inelastically scattered nitrogen fragments at 10°. As illustrated in Fig. 12, one again sees the asymmetry at 70° and 110° that was observed in neutron spectra gated by carbon and boron fragments (Ca 85). Selecting fragments of the same species as the projectile simplifies the calculation. If one ignores higher order processes, the coincidence cross section is

Figure 12. Comparison of a quasi-free scattering calculation (dot-dashed lines) to neutron spectra at ±30°, ±70°, and ±110° for nitrogen fragments at 10° for the Ho target. The solid and dashed lines are the results of moving source fits. The temperature, energy/nucleon and angle of the TLS (IRS) are 3.12 MeV (10.72 MeV), 0.16 MeV (9.00 MeV) and -35.5° (-17.6°). The spectra are plotted in symmetric angle pairs, each offset from the next by a factor of 100, with the spectra at the top having the scale as indicated.

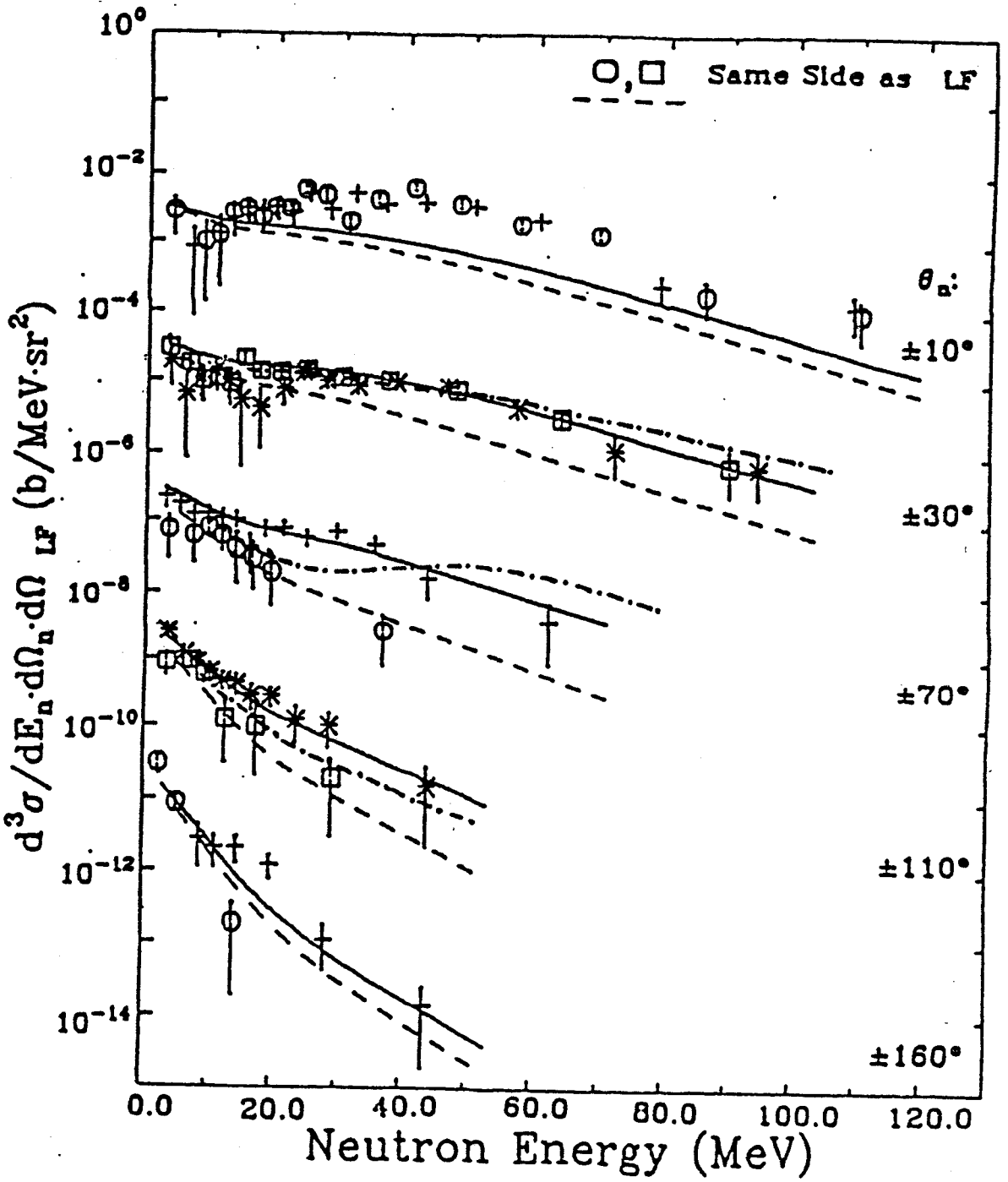
10⁰
10⁻²
10⁻⁴
10⁻⁶
10⁻⁸
10⁻¹⁰
10⁻¹²
10⁻¹⁴
O,□ Same Side as LF
θn:
±10°
±30°
±70°
±110°
±160°
d³σ/dEn·dΩn·dΩ LF (b/MeV·sr²)
0.0
20.0
40.0
60.0
80.0
100.0
120.0
Neutron Energy (MeV)

Figure 12.

$$\frac{d^3\sigma}{d\Omega_f d\Omega_n dE_n} = C \frac{d\sigma}{d\Omega}(E,\theta) \left[\phi(k)\right]^2 \rho, \qquad (1)$$

where C is an overall scale factor, and the subscripts f and n refer to the scattered nitrogen fragment and knocked-out neutron, respectively. The second factor in eq. (1), the differential cross section for elastic scattering between the ^{14}N projectile and a target neutron in the center-of-mass system of the projectile + target-neutron, was estimated using the optical model (Pa 76). The third factor in eq. (1) is the probability of having a neutron in the target nucleus at momentum k; a Gaussian momentum distribution was assumed (Ch 80). The fourth factor, ρ, is the three-body density of final states. The calculation was an attempt to reproduce only the asymmetry at middle angles. For each pair of neutron angles, the spectrum corresponding to the same side as the detected fragment was, therefore, assumed to be formed by other processes and to provide a symmetric background common to both sides of the beam. Then the quasi-free scattering process described above was added to this symmetric background. The results of this calculation are shown in Fig. 12 as the dot-dashed lines at $\theta_n = \pm 30°$, $\pm 70°$, and $\pm 110°$. For comparison the solid and dashed lines are the results of a moving source fit, as described at the end of this section. As we knew ab initio, there is an asymmetry in the same sense as that observed.

However, it peaks at too large an energy, and it does not quite match the angular distribution of the data. It has only one free parameter, the scale factor, but its success is limited and it deals only with a very small part of the data. For a comprehensive treatment of the data we now proceed with a model that necessarily has more parameters, and we seek regularities in the values of those parameters, hoping thereby to gain insight into the reaction mechanism.

We have seen that the neutrons seem to originate from three sources: excited light fragments, excited TLSs and a preequilibrium source. The light-fragment contribution is clearly not thermal, and it is confined to angles near the angle of the coincident fragment. Therefore, it is desirable and possible to treat it separately (Ki 86). In this paper we shall study the behavior of only the TLS and preequilibrium (IRS) neutrons as a function of the coincident fragment species, of its energy, and of its angle.

To arrive at some simple way of categorizing a large body of data, the moving source parameterization has been adopted, and both the TLS and IRS are assumed to be thermal sources. This parameterization is predicated upon the idea of thermal evaporation of nucleons from a "hot" nucleus. The spectrum takes the following form in the rest frame of the emitter (We 37, Bl 79):

$$N(E_n) \propto E_n^{\alpha} e^{-E_n/\tau} , \qquad (2)$$

where E_n is the energy of the neutron and τ is a temperature parameter. $\alpha = 1$ corresponds to single neutron "surface emission", whereas $\alpha = 1/2$ corresponds to volume sampling ("volume emission") of a hot Fermi gas (Go 78). In both cases, the temperature parameter τ is the temperature τ of the daughter nucleus after single neutron emission. $\alpha = 5/11$ corresponds to multiple neutron emission and then τ is an effective temperature parameter related to the temperature T of the daughter nucleus after the first neutron emission by $T = (12/11)\tau$ (Le 59).

The IRS is typically in a very excited state at an excitation-energy/nucleon near to or exceeding the binding energy, so volume emission (with $\alpha = 1/2$) should be the most suitable choice for this source. The TLS most probably emits more than one neutron, indicating that $\alpha = 5/11 \approx 1/2$. So we use the same prefactor of $\sqrt{E_n}$ for both sources. Each source introduced is assumed to emit neutrons isotropically in its rest frame. These spectra are then transformed into the lab frame, taking the motion of the emitting source into account. The sum of these two contributions , then, written as a differential multiplicity takes the following form:

$$\frac{d^2M}{dE_n d\Omega_n}(E_n,\theta_n) =$$

$$\sum_{i=1}^{2} \frac{M_i \sqrt{E_n}}{2(\pi\tau)^{3/2}} \exp\left\{-\left[\frac{E_n - 2\sqrt{(\varepsilon_i E_n)}\cos(\theta_i - \theta_n) + \varepsilon_i}{\tau_i}\right]\right\} \qquad (3)$$

where the index i sums over the two sources. Equation 3 predicts the number of neutrons/(MeV·sr) per detected light fragment. E_n and θ_n are the neutron energy and angle, respectively, while M_i, τ_i, ε_i, and θ_i are the neutron multiplicity, nuclear temperature parameter, energy per nucleon, and angle of the ith source. Equation 3 is then fitted to the data by minimizing the χ^2, thus allowing extraction of multiplicities, temperatures, and velocities for the TLS and IRS components of the reaction.

Neglecting the three angles nearest to the direction of the coincident light fragment, we fitted the data at seven angles. The solid and dashed lines in Figs. 9, 10 and 12 are the results of such moving two-thermal-source fits, and the parameters of the fits listed in the figure captions. The fits contained eight parameters and typical values of the χ^2/degree-of-freedom were between 1 and 2.

V. THE FIT PARAMETERS

The moving source parameterization allows one to extract systematic features from a large body of data. In this section we examine the resulting fit parameters for both the TLS and IRS as a function of the coincident fragment species, energy and angle. In such an examination we search for any striking behaviors or telling trends in the fit parameters that might serve as clues in the puzzle of unraveling the reaction mechanisms. First the TLS fit parameters will be discussed, along with the results from a two-body calculation and also from the statistical code CASCADE (PU 77). Then the IRS fit parameters will be examined.

Figures 13-15, 17, 19-21 and 23 are plots of the various fit parameters of the TLS and the IRS as a function of the angle of the coincident light fragment. In each of these figures the top four plots correspond to the coincident fragments of Li, Be, B, and C for the Ho target; the bottom four plots are for the same fragments, but the target is Ni. The points for the high energy fragment gate (HE LF) and for the low-energy fragment gate (LE LF) are plotted on the same graph. The method used for minimizing the χ^2 and producing a "best fit" (Fl 63) also produced a standard error matrix for each fit. The errors in the matrix are generally unrealistically small because they do

not account for the "structure" in the χ^2 - space. Therefore, we are allowing the scatter of the points to serve as a measure of the uncertainty of the various fitted parameters. Also included in these plots are fit parameters extracted from data from an earlier experiment (De 86) on the ^{14}N + ^{165}Ho system at 35 MeV/nucleon for fragment angles of 10° and 30°. So these parameters were extracted from an independent set of data in an independent analysis. Their deviations from the values of the present experiment are another measure of the errors.

TLS Parameters:

Figure 13 is a display of the TLS temperature parameter τ_{IRS} as a function of fragment angle. There seems to be no clear dependence of τ_{TLS} on either the angle or the energy of the fragment. For the present discussion we will ignore the difference between temperature T and temperature parameter τ as discussed in Section IV. The temperature of the TLS is approximately a constant between 2 and 3 MeV for the Ho target, whereas for the Ni target the temperature is higher at 3 to 4 MeV. To see if these temperatures are reasonable, we assume a very crude scenario where ΔA nucleons from the projectile are transferred to the target, depositing $\mu' \cdot (E_{cm} - V_c)/\mu$ MeV of excitation energy. Here E_{cm} is the beam energy in the center-of-mass system, V_c is

Figure 13. The temperature parameter τ_{TLS}, versus fragment angle for the Ho target (top) and Ni target (bottom). Each quadrant represents a different fragment. The diamond and cross plotting symbols correspond to an independent set of data and analysis (see text). Open symbols correspond to high energy light fragments (HE LF) and closed symbols to low energy light fragments (LE LF).

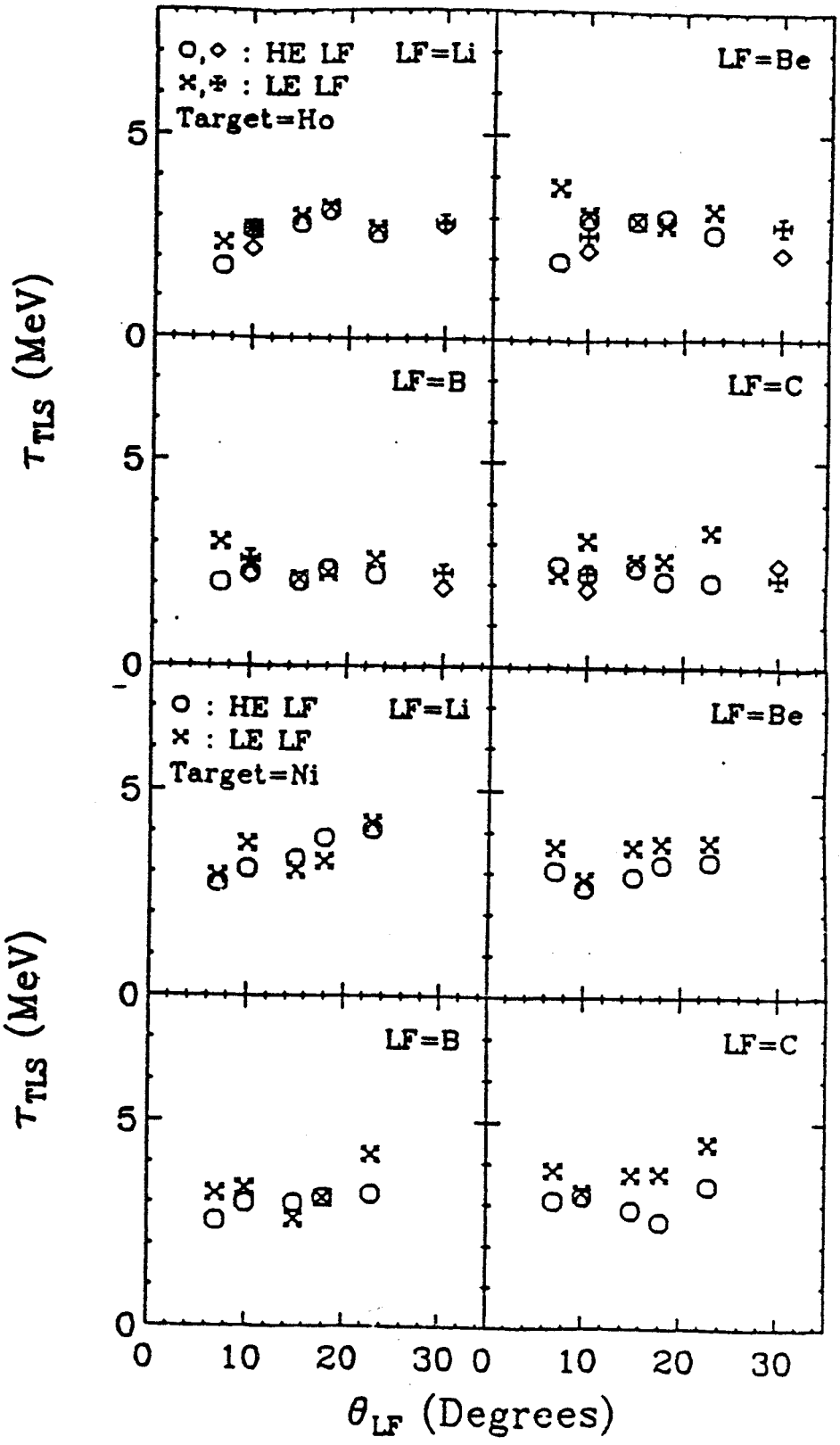
O,◇ : HE LF
×,✱ : LE LF
Target=Ho
LF=Li
LF=Be
LF=B
LF=C
O : HE LF
× : LE LF
Target=Ni
LF=Li
LF=Be
LF=B
LF=C
T_{TLS} (MeV)
T_{TLS} (MeV)
0
5
0
10
20
30
θ_{LF} (Degrees)

Figure 13.

the Coulomb barrier, and μ and μ' are the reduced masses of the projectile + target-nucleus system and of the transferred-mass + target-nucleus system, respectively. Then applying the simple thermodynamical relation (where the neutron separation energy has been neglected)

$$E^* = aT^2 \quad , \tag{4}$$

where $a = A/8$ is assumed for the density of states parameter, one can estimate the temperature for the Ho TLS ($A = 165 + \Delta A$) and for the Ni TLS ($A = 58 + \Delta A$). Letting $\Delta A =$ 2, 4, and 6 nucleons then gives temperatures of 1.7, 2.4 and 2.9 MeV, respectively, for the Ho TLS and 2.9, 3.9, and 4.7 MeV, respectively, for the Ni TLS. The temperatures of the Ni TLS are larger than those of the Ho TLS because a comparable excitation energy is shared by fewer nucleons. The estimated temperatures are in good agreement with the fitted temperatures, indicating that the fitted values correspond to physically reasonable results.

In Figure 14 is shown a plot of the angle of the TLS versus the angle of the detected light fragment. Since the TLS is moving very slowly, the direction of its motion cannot be determined very precisely, hence the angle parameter jumps around considerably. But the one notable feature of these plots for both the Ho and Ni targets is that with few exceptions, θ_{TLS} is always negative, positive

Figure 14. The fit parameter θ_{TLS} versus fragment angle. The dotted line corresponds to an angle of 0°. The format is the same as that of Fig. 13.

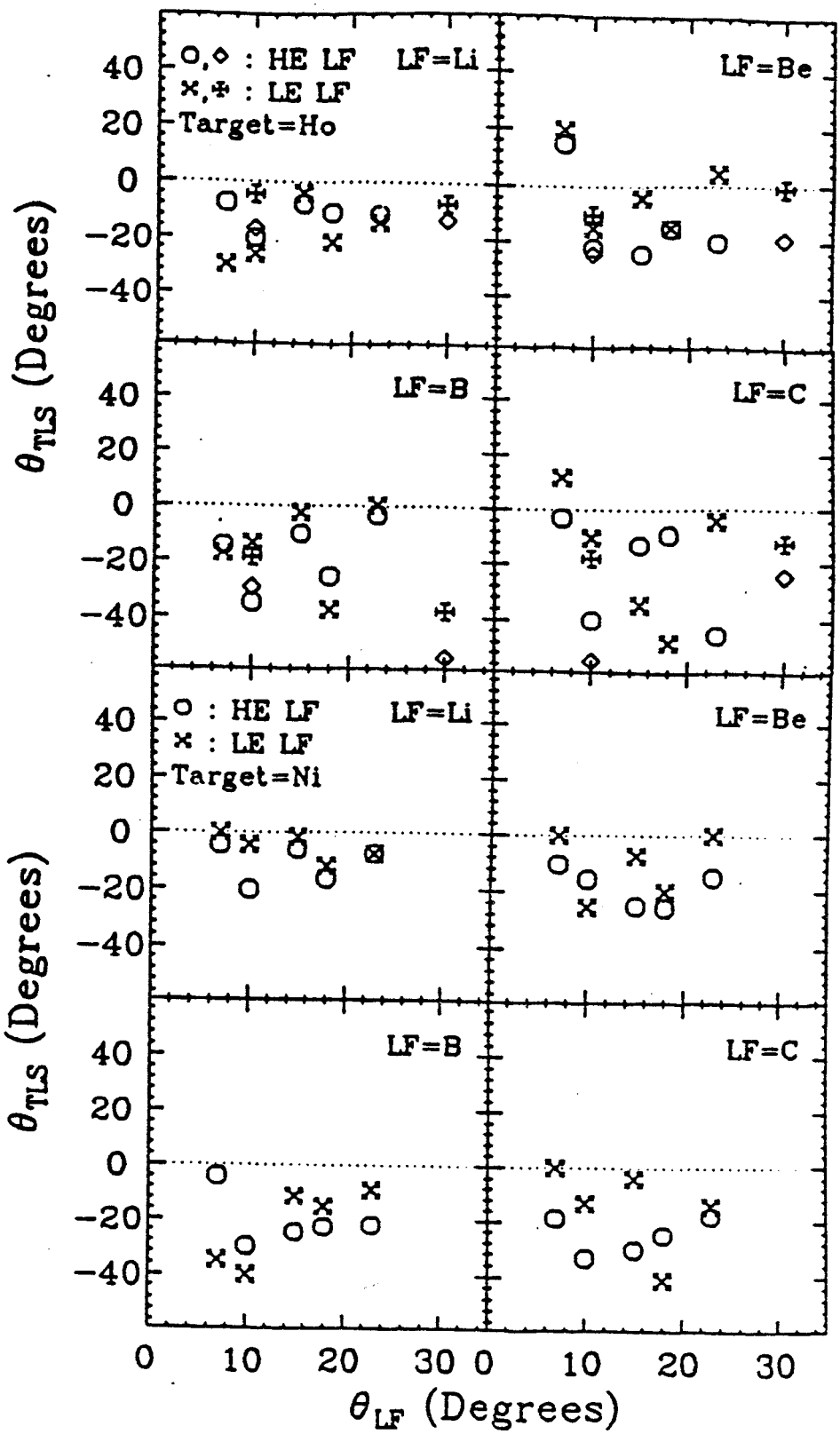
o,◇ : HE LF
×,+ : LE LF
Target=Ho
LF=Li
LF=Be
LF=B
LF=C
o : HE LF
× : LE LF
Target=Ni
LF=Li
LF=Be
LF=B
LF=C
40
20
0
−20
−40
0
10
20
30
θTLS (Degrees)
θLF (Degrees)

Figure 14.

being defined as the side of the detected light fragment. For a light fragment moving to one side of the beam, one would expect the TLS to move to the opposite side to help balance the transverse component of momentum, and this expectation is consistent with our observation.

Figure 15 shows the energy/nucleon of the target source plotted as a function of fragment angle. Extracting E/A_{TLS} (or the velocity-squared) from the neutron angular distribution for a slowly moving source is difficult, as was extracting θ_{TLS}. So a certain amount of scatter in the points is expected. For both targets, comparison of the values for the two fragment energy gates indicates the E/A_{TLS} is independent of the energy of the detected fragment. But E/A_{TLS} tends to increase with θ_{LF}. For a given fragment angle E/A_{TLS} for the Ni target is typically a factor of 5-10 larger than for the Ho target.

To establish a reference E/A_{TLS} we performed a two-body calculation. The reaction was assumed to be ^{14}N + target → LF + TLS. From the measured values of mass and energy of the LF at each LF angle, we determined its momentum, and by momentum conservation, the momentum of the TLS. With the two-body assumption, the mass of the LF gave us the mass of the TLS and, hence, its E/A. The solid and dashed lines in Fig. 15 are the results of these calculations for low energy and for high energy LFs respectively. The "structure" in

Figure 15. The fit parameter E/A_{TLS}, the energy/nucleon of the TLS versus fragment angle. The solid and dashed lines correspond to a two-body calculation, as described in the text. The format is the same as that of Fig. 13. (Note the difference in scale between the Ho and Ni data.)

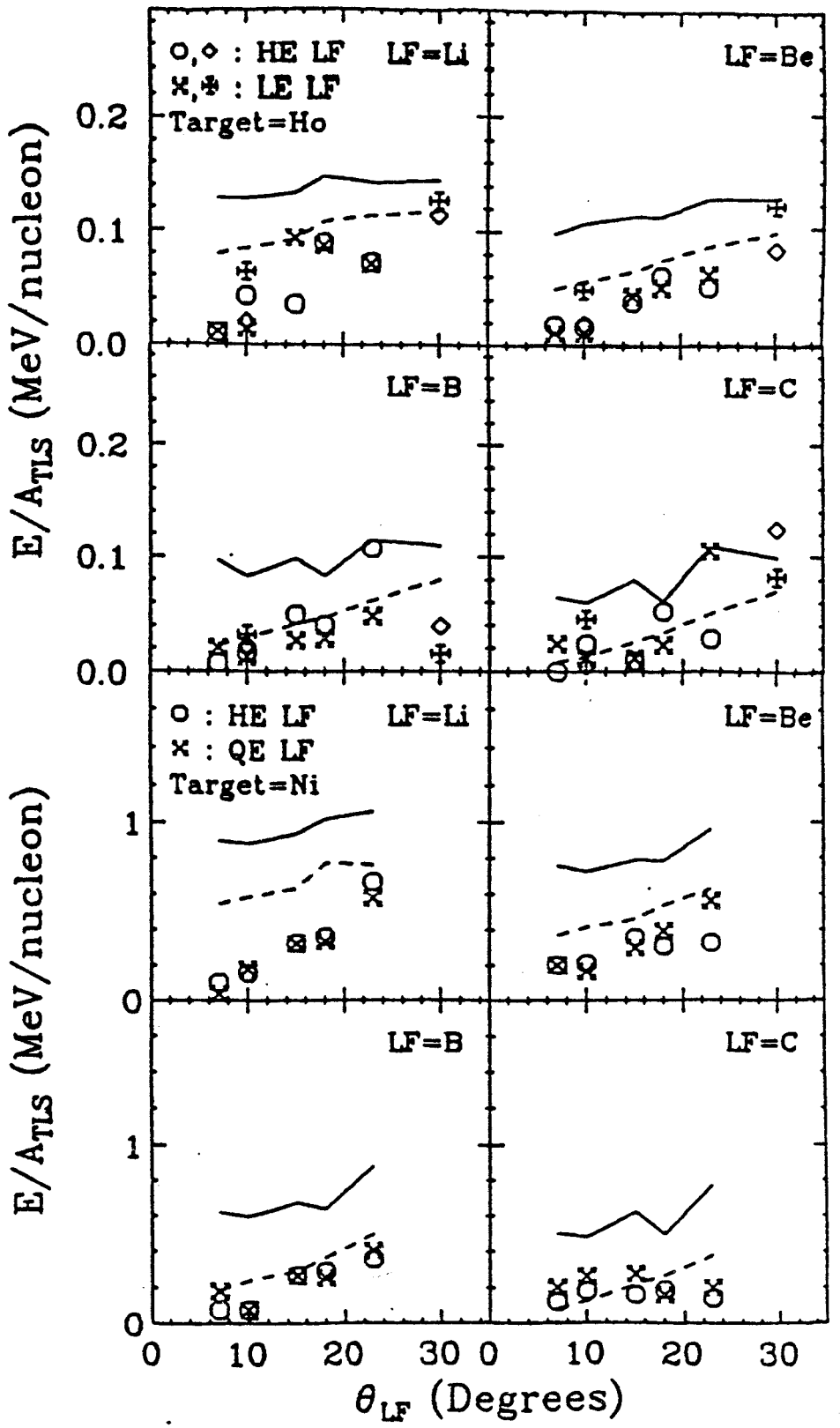
o,◇ : HE LF
×,✣ : LE LF
Target=Ho
LF=Li
LF=Be
LF=B
LF=C
o : HE LF
× : QE LF
Target=Ni
LF=Li
LF=Be
LF=B
LF=C
E/A_TLS (MeV/nucleon)
E/A_TLS (MeV/nucleon)
θ_LF (Degrees)
0.0
0.1
0.2
0
1
10
20
30

Figure 15.

the lines is due to the various gates set across the energy of the LF (see Figs. 4 and 5). With few exceptions the calculation predicts a larger E/A_{TLS} than is observed, the discrepancy being largest for low energy fragments. This discrepancy is a clear indication that the above assumed binary reaction is not a complete description. There is some component to the reaction carrying away momentum that is "missed" by our detectors.

Figure 16 is a plot of the fraction of "missing-momentum"/beam-momentum as a function of LF angle for the Ho target (top) and the Ni target (bottom). The missing-momentum is assumed to be parallel to the beam axis and corresponds to the difference between the calculated and observed values in Fig. 15. The large error bars in Fig. 16 are due to the inherent uncertainty in θ_{TLS} and E/A_{TLS}. The value of the fractional missing momentum varies between 0.5 and 0.0 for both targets and is largest when we detect a low energy fragment. In addition, for both targets the missing momentum is largest for Li fragments at small angles and smallest for C fragments. It appears that as the amount of LF energy damping increases, and also as $\Delta A = A_{projectile} - A_{LF}$ increases, so too does the amount of missing momentum. This is qualitatively very similar to what has been observed in projectile-like fragment--fission-fragment coincidence studies (Dy 79, Ba 80). In those investigations the missing momentum was seen to increase with projectile-like fragment

Figure 16. Fraction of the beam momentum "missing" versus fragment angle. The fraction was determined by the difference between a two-body calculation and the data. The format is the same as that of Fig. 13.

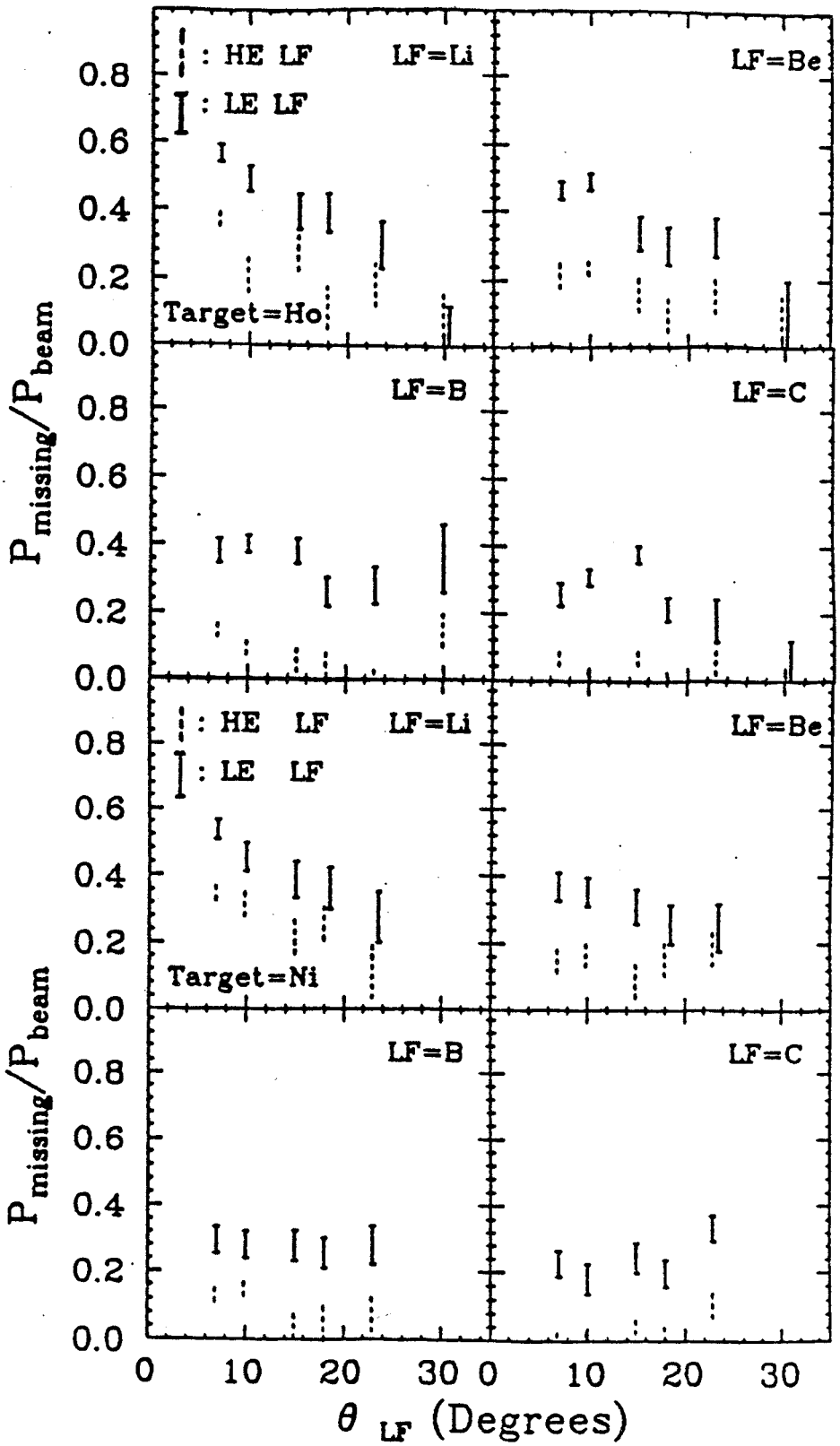
: HE LF
: LE LF
LF=Li
LF=Be
Target=Ho
LF=B
LF=C
: HE LF
: LE LF
LF=Li
LF=Be
Target=Ni
LF=B
LF=C
$P_{missing}/P_{beam}$
$P_{missing}/P_{beam}$
0.0
0.2
0.4
0.6
0.8
0
10
20
30
θ_{LF} (Degrees)

Figure 16.

momentum was seen to increase with projectile-like fragment damping, and was attributed to the emission of a "jet of particles preferentially into the forward direction" (Dy 79). We will take up consideration of the origin of the missing momentum in the discussion of Fig. 23, the IRS multiplicity.

Figure 17 shows the associated multiplicity of the TLS as a function of LF angle, where associated multiplicity is defined as the total number of neutrons emitted per detected LF. This is in contrast to absolute multiplicity, which is the total number of neutrons emitted per interaction. One immediately notices that the neutron multiplicities for Ho TLSs are much higher than those for Ni TLSs. But multiplicity varies directly with excitation energy. As discussed below, excitation energy can be calculated from the fitted temperature parameter, and estimates of E^*_{TLS} averaged over θ_{LF} give 150 and 100 MeV for the Ho and Ni TLS, respectively. So based upon excitation energy alone, one would expect the Ho TLS multiplicity to be larger than the Ni TLS multiplicity. In addition, due to the much lower Z of Ni, the Ni TLS has a much smaller Coulomb barrier than the Ho TLS, and proton or alpha emission can compete with neutron emission as a means of de-exciting.

There is a distinct increase in associated multiplicity with θ_{LF}, and the multiplicities for the low energy fragment gates are consistently larger than for the corresponding

Figure 17. Plot of M_{TLS}, the TLS associated multiplicity versus fragment angle. The format is the same as that of Fig. 13. (Note the difference in scale between the Ho and Ni data.)

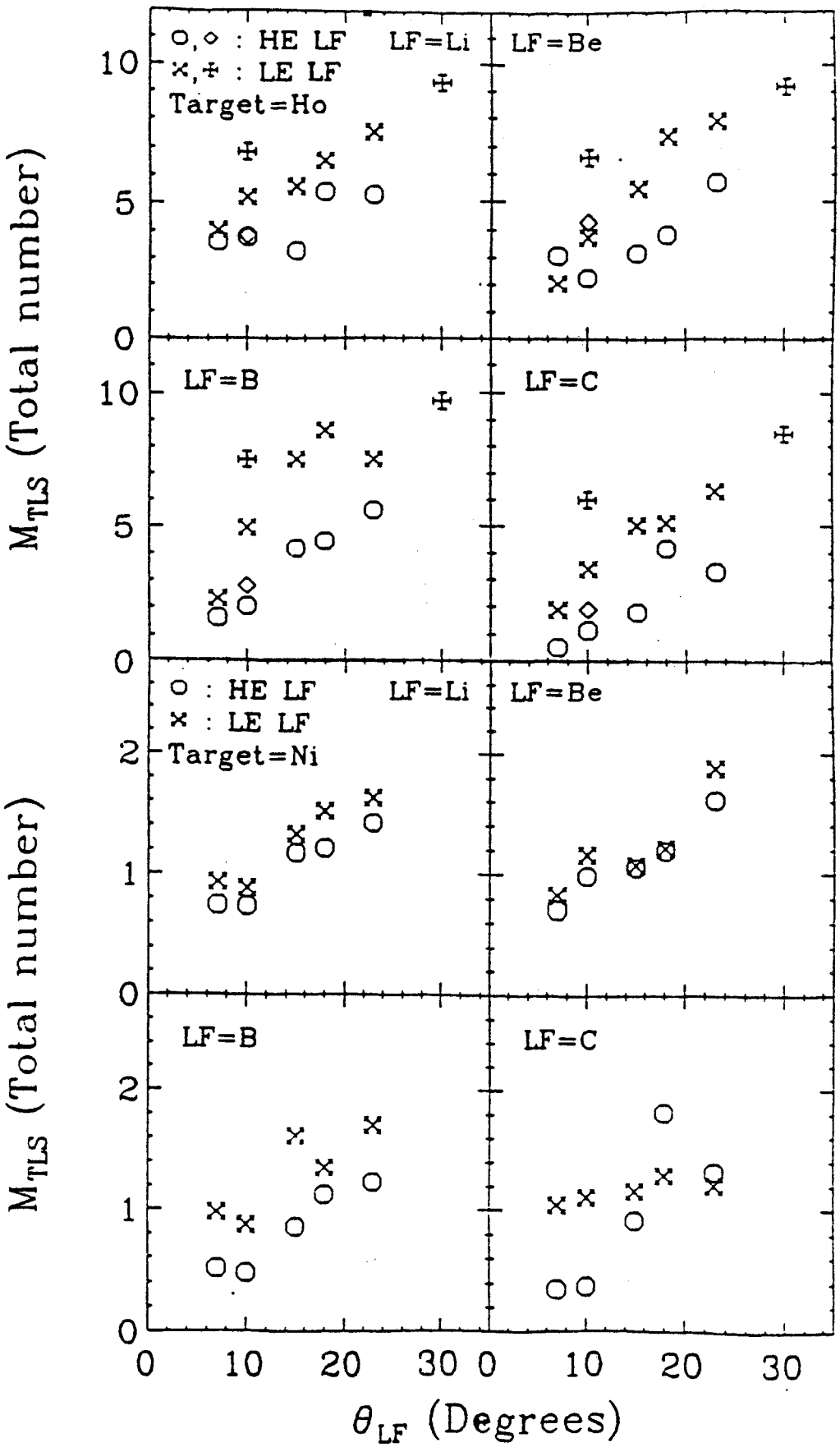
○,◇ : HE LF
×,+ : LE LF
Target=Ho
LF=Li
LF=Be
LF=B
LF=C
○ : HE LF
× : LE LF
Target=Ni
LF=Li
LF=Be
LF=B
LF=C
M_{TLS} (Total number)
M_{TLS} (Total number)
θ_{LF} (Degrees)

Figure 17.

it is quite possible for the reaction to produce a LF, especially a high energy LF, without producing a TLS; there is a competition between transfer reactions and projectile breakup. The observation that the temperature of the TLS is independent of θ_{LF} (Fig. 13) implies that the absolute multiplicity should also be independent of θ_{LF}. Therefore, we interpret a low observed associated multiplicity at small θ_{LF} as an indication that there are few excited TLSs formed per detected LF.

To obtain an estimate of the absolute multiplicity, we used the statistical code CASCADE (PÜ 77) to calculate the total neutron emission from a TLS. The most important input to CASCADE is the excitation energy. Using the fitted temperature parameter (corresponding to the TLS component of the neutron spectra) and the neutron separation energy S_n allows one to estimate the average TLS excitation energy E^*, before neutron emission. Modifying eq. (4) to include separation energy gives

$$E^* = aT^2 + S_n \quad , \tag{5}$$

where $a = A/8$ is the density of states parameter, $S_n = 8$ MeV, and $T = (12/11)\tau$ corresponds to the temperature of the daughter fragment after single neutron emission. $\tau_{TLS} = 4$

MeV is a typical TLS temperature parameter for the Ni target for a fragment angle of 23°, where the experimentally determined associated multiplicity of the Ni TLS is largest. Then with eq. (5) we estimate an excitation energy of about 150 MeV for ^{60}Ni and 125 MeV for ^{58}Ni. (For ^{58}Ni we used the single neutron emission formula, (α = 1 in eq. 2) after trial runs with CASCADE indicated a low neutron multiplicity). Using these values of excitation energy in the statistical calculation then gives a total neutron multiplicity averaged over the above two Ni isotopes of about 2.3 neutrons per excited Ni TLS. Figure 17 shows that the measured associated multiplicity of the TLS for low energy fragments at θ_{LF} = 23° is about 1.6, i.e., 70% of the calculated value. This statistical code was also run for the ^{14}N + ^{165}Ho system for an excitation energy of 195 MeV, and the resultant total neutron multiplicity was 12. The average measured value for a low energy gate on fragments at 30° (corresponding to the maximum associated multiplicity for the Ho TLS) is about 9.2, i.e., 77% of the calculated result.

Comparisons of CASCADE calculations with multiplicity data for systems at high excitation energy are not readily available, so we have no direct test as to the reliability of the predictions. But this code has been used often on systems with less excitation energy (St 85, Ka 85, Kh 85) with very favorable results. We tested the sensitivity of

the calculated neutron multiplicity on the angular momentum and excitation of the TLS for both Ni and Ho targets. The results are listed in Table 3. We find the multiplicity to be very sensitive to excitation energy, obviously, but insensitive to the angular momentum of the TLS. Based upon available information (St 85) and also on the above mentioned excitation-energy dependence, we believe our predicted values to about 20%, with an indication that they may be slightly overestimated (St* 85).

At this point we review some multiplicity results obtained by other investigators on similar systems. Tserruya et al. has studied the ^{86}Kr + ^{166}Er system at 11.9 MeV/nucleon (Ts 82) and extracted multiplicity as a function of excitation energy both for the target-like and projectile-like sources. They then compared their values to the results of a calculation using the Monte Carlo code JULIAN. For a TLS of A= 163 - 170 with E^* = 200 MeV, their observed TLS multiplicity was 8. Their calculated multiplicity using a = A/8 was 10.5 for 200 MeV excitation and 5.5 for 100 MeV excitation. These values are included in Table 3 for comparison, and one sees that their calculated multiplicity was also larger than their measured multiplicity. At this point, Tserruya et al. chose to adjust their density-of-states parameter to a = A/20 to bring the calculation into agreement with their data. The possibility remains, though, that the discrepancy was due to

TABLE 3. Calculated TLS multiplicities for central collisions using CASCADE, JULIAN[b] and PACE[c]

Nucleus	J (ħ)	E (MeV)	Multiplicity
^{58}Ni	40	83	1.2
^{58}Ni	5	125	1.6
^{58}Ni	40	125	1.7[a]
^{60}Ni	40	83	2.2
^{60}Ni	40	150	3.8[a]
^{165}Ho	80	100	7.7
^{165}Ho	80	195	12.0[a]
A = 163 - 170		100	5.5[b]
A = 163 - 170		200	10.5[b]
A = 64		60-80	3.0[c]

a Indicates the final values used

b Taken from Ref. Ts 82

c Taken from Ref. Lu 85

the difference between associated and absolute multiplicity, as discussed above, and not to the choice of the density-of-states parameter a. Lücking et al (Lü 85) have studied the $^{16}O + ^{64}Ni$ system at 7.5 - 12 MeV/nucleon, extracting experimental TLS and projectile-like fragment multiplicities and comparing with the evaporation code PACE. For a coincident O projectile-like fragment resulting in E^*_{TLS} = 60 - 80 MeV, their experimental and calculated TLS multiplicities were 3.2 ± 0.8 and 3.0, respectively. So in this work good agreement was achieved between measured and calculated multiplicity.

We have observed a dramatic dependence of TLS associated multiplicity on LF angle and have interpreted this as evidence for angle-dependent competition between reactions leading to a TLS (such as transfer or incomplete fusion) and reactions not appreciably exciting the target nucleus (such as knockout or projectile breakup). Competition between transfer and projectile breakup has been clearly demonstrated by Jahnke et al. (Ja* 83) for the $^{20}Ne + ^{197}Au$ system at 15 MeV/nucleon by measuring total neutron multiplicities using a 4π neutron-multiplicity counter. But we believe this is the first time a strong angle dependence has been demonstrated for this competition.

Taking the ratio of the measured TLS associated multiplicity to the calculated absolute multiplicity gives

one the fractional occurrence of a TLS per detected LF. This fraction, call it F, is plotted as a function of fragment angle and energy gate in Fig. 18. One notices that: 1) F increases steadily with θ_{LF} but at θ_{LF} = 23° or 30° is still less than one. (We note that adjustment of the density of states parameter could bring F closer to 1 at 23° or 30°, as was pointed out in Ref. Ts 82.) 2) F is larger for the low energy fragment gates than for the corresponding high energy gates. 3) At a given fragment angle, F is slightly larger for the Ni target than for the Ho target. 4) The smallest values of F for both targets occur for high energy C fragments. Observations (1) and (2) are consistent with the idea that larger fragment angle and greater energy damping indicate longer interaction time between the projectile and target nuclei (Sc 78, Hi 81). Longer interaction time creates a more favorable setting for transfer and partial fusion to occur, both of which lead to an excited TLS. Observation (3) is consistent with the fact that the grazing angle for the Ni target (4°) is smaller than for the Ho target (8°). So for fragments scattered through the same angle, the impact parameter had to be smaller and the projectile-target interaction greater for Ni than for Ho. Observation (4) maybe attributed to the fact that some of the high energy fragments result from quasi-elastic scattering. When the fragment is carbon rather than lithium, beryllium or boron, the smallest number of nucleons

Figure 18. The fraction F of excited TLSs per detected fragment as a function of fragment angle. The top two plots correspond to the LE and HE fragment gate for the Ho target, and the bottom two plots are for those gates for the Ni target. Each quadrant has F plotted for each of the four LFs (Li, Be, B, C).

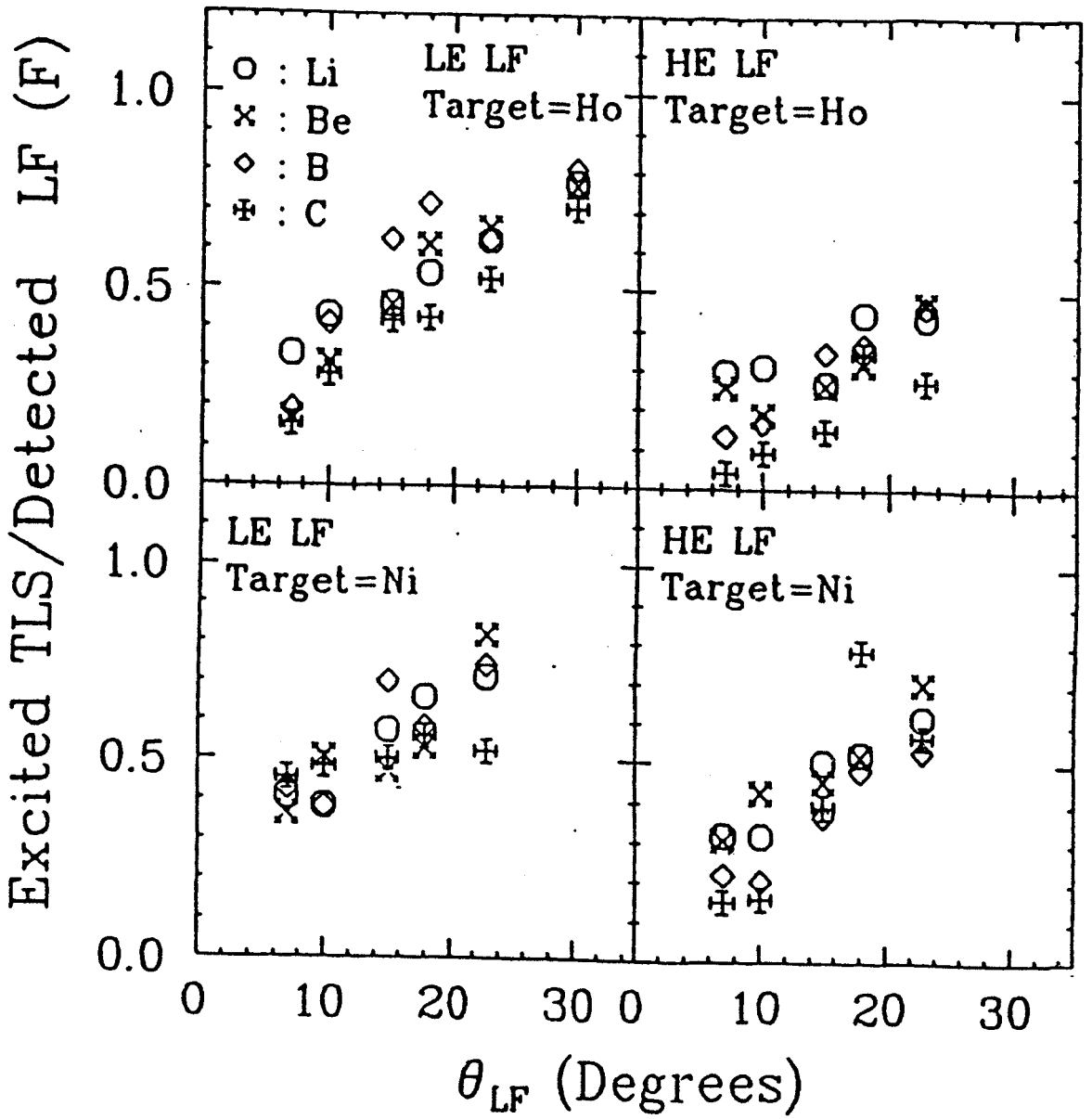
Excited TLS/Detected LF (F)
1.0
0.5
0.0
1.0
0.5
0.0
O : Li
× : Be
◇ : B
Ŧ : C
LE LF
Target=Ho
HE LF
Target=Ho
LE LF
Target=Ni
HE LF
Target=Ni
0
10
20
30
0
10
20
30
θLF (Degrees)

Figure 18.

are lost from the fragment, thus maximizing the chance of scattering without forming a TLS.

IRS Parameters:

Since the IRS is so successful in describing the preequilibrium neutrons, the question of whether it is just a convenient parameterization or harbors more "profound physical justification" (Ga 83) has to be faced. Indeed, the thermal "appearance" of preequilibrium emission is pervasive and quite remarkable. Some interpret the hot thermal source as a region where the nucleon velocities are "randomized in a rest frame different from the compound nucleus", TLS or projectile-like fragment rest frames (Aw 82). Others suggest a "local inhomogeneity of the energy density which is associated with a local temperature via an equation of state of nuclear matter" (We 77). Indeed, the original speculation on this matter of an "intense local heating that will then gradually spread over the whole nucleus" (Be 38) is amazingly close to the view we now hold. As such, the parameters we present that describe the IRS represent averages over both the extent and duration of the source. Nevertheless, we find it useful to examine the IRS fit parameters for any systematic trends that might yield insight into the physical significance of the IRS.

Figure 19 shows the temperature of the IRS as a function of fragment angle. There is no single clear trend

Figure 19. IRS temperature parameter τ_{IRS} versus fragment angle. Format is the same as that of Fig. 13.

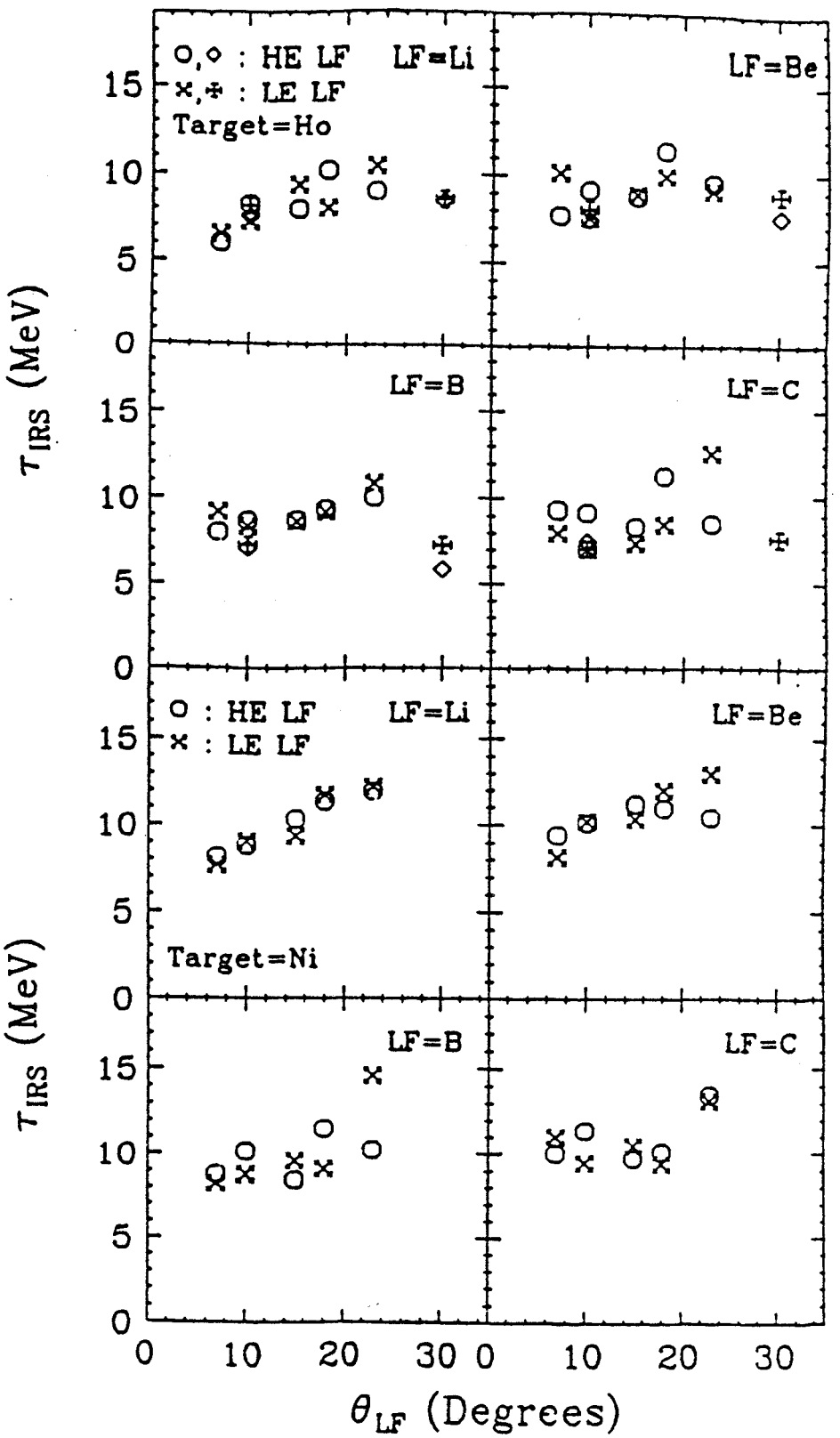
O,◇ : HE LF
×,+ : LE LF
Target=Ho
LF=Li
LF=Be
LF=B
LF=C
O : HE LF
× : LE LF
Target=Ni
LF=Li
LF=Be
LF=B
LF=C
τ_{IRS} (MeV)
τ_{IRS} (MeV)
0
5
10
15
0
10
20
30
θ_{LF} (Degrees)

Figure 19.

of τ_{IRS} with fragment angle common to both targets. In addition, there appears to be no significant difference in IRS temperature whether the gate is on fragments of low energy or high energy. The independence of τ_{IRS} on energy and angle of the fragment suggests that the IRS neutrons were produced at a very early stage of the reaction before the "final fate" of the projectile had been determined. Similar results were reported by Gemmeke et al. (Ge 80) in neutron--projectile-like fragment coincidence studies of the ^{16}O + Ni system at 6 MeV/nucleon as well as by Back et al. (Ba 80) and Awes et al. (Aw* 81) in light-particle--fission-fragment coincidence studies of ^{16}O + ^{238}U at 20 MeV/nucleon. For the Ni target, the temperatures of the IRS are systematically higher than for the corresponding cases for the Ho target. A typical value of τ_{IRS} for the Ho target is 8.5 MeV whereas for the Ni target the average τ_{IRS} is closer to 10 MeV.

To try to understand what these fitted temperatures mean, we can derive a reference temperature with which to "calibrate" τ_{IRS}. Adopting the approach of Awes et al. (Aw* 81), we equate the overlap region with an ideal Fermi gas consisting of equal contributions from the target and projectile nuclei. The assumption of thermal equilibrium then corresponds to thermalization in the nucleon-nucleon center of mass frame, and allows one to predict a

temperature (see eq. 14 in Ref. Aw* 81). With this method the predicted IRS temperature for both the Ho and Ni target is about 11 MeV, slightly higher than that derived from the data. If one instead assumes that the overlap region consists of two target nucleons for every projectile nucleon, then the predicted IRS temperature is about 7 MeV, slightly lower than that observed. So it appears that averaged over the lifetime of the hot source, each participating projectile nucleon interacts with between one and two target nucleons.

Figure 20 shows the kinetic-energy/nucleon of the IRS versus fragment angle. There appears to be no single clear trend for the Ho target, though on the average the velocity of the IRS for high energy is slightly higher than for the corresponding case of low energy fragments. Values of E/A_{IRS} for the Ho target range from 5 to 10 MeV/nucleon, with 8 MeV/nucleon being a representative average. For the Ni target, the IRS velocities are, on the average, slightly higher than for the Ho target. For high energy fragments from the Ni target, the average E/A_{IRS} is about 12 MeV/nucleon, whereas for low energy fragments, an average E/A_{IRS} would be closer to 8 MeV/nucleon. For comparison we calculate the E/A corresponding to the nucleon-nucleon center of mass velocity in the lab frame at the point of projectile--target-nucleus "contact", with the resulting values of 7.7 MeV/nucleon for Ho and 8.2 MeV/nucleon for Ni.

Figure 20. IRS energy/nucleon E/A_{IRS} versus fragment angle. Format is the same as that of Fig. 13.

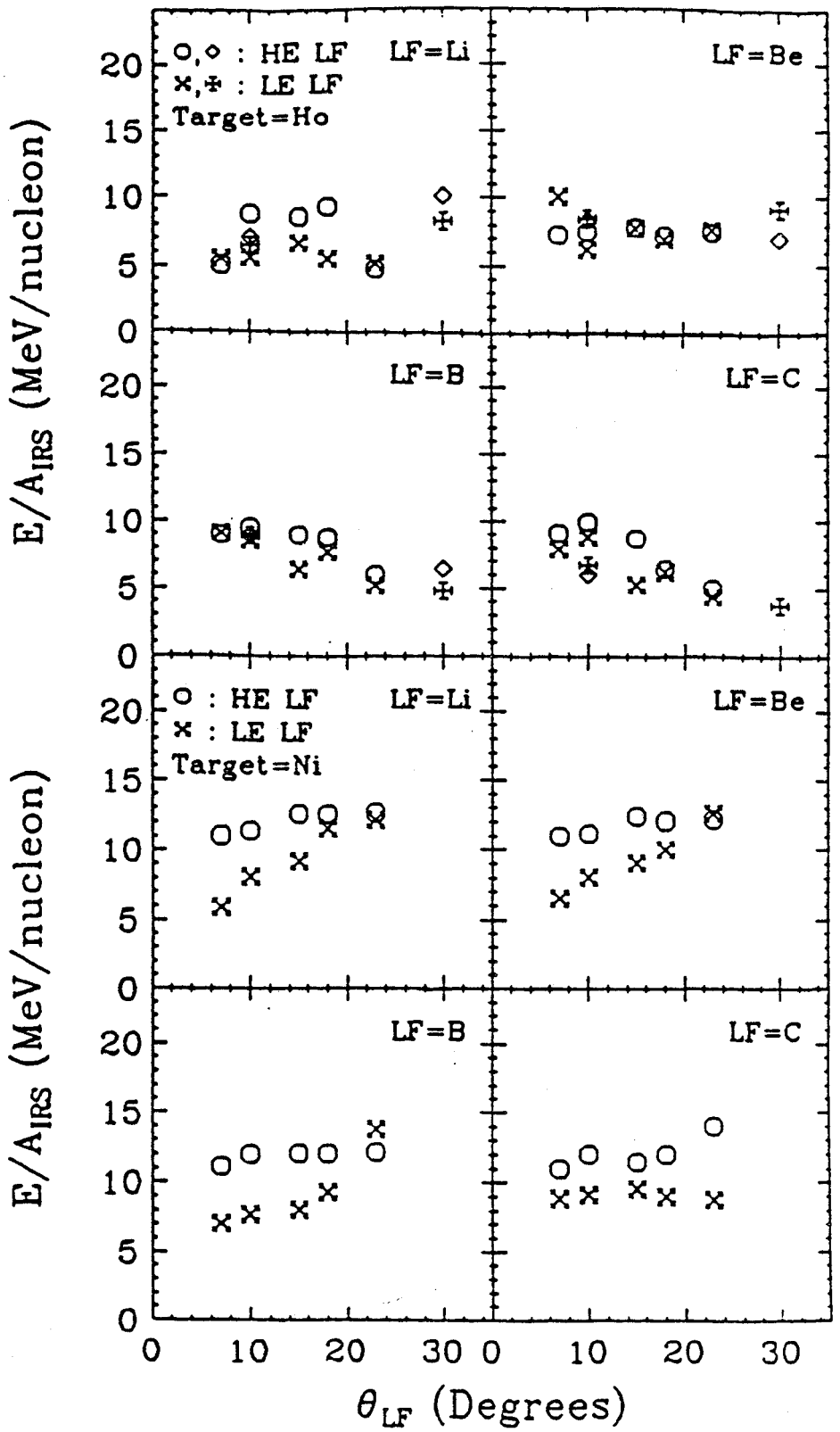
O,◇ : HE LF
×,+ : LE LF
Target=Ho
LF=Li
LF=Be
LF=B
LF=C
O : HE LF
× : LE LF
Target=Ni
LF=Li
LF=Be
LF=B
LF=C
E/A_IRS (MeV/nucleon)
E/A_IRS (MeV/nucleon)
θ_LF (Degrees)
0
5
10
15
20
0
10
20
30

Figure 20.

The difference in the two values is due to the difference in Coulomb barriers of the two systems. The calculated E/A_{IRS} corresponding to the velocities of the nucleon-nucleon centers of mass are contained within the ranges of the observed E/A_{IRS}. This agreement indicates emission after a very rapid local thermalization, perhaps after a single nucleon-nucleon collision (Hü 77, Aw* 81). For a given projectile, the observation that the IRS velocity is higher for a light target nucleus than for a heavy target nucleus has also be noted in charged particle work (Aw 82, Ha 85). This probably is due to a combination of lower Coulomb barrier plus larger projectile-nucleon to target-nucleon ratio in the interaction region for lighter systems.

At this point it is interesting to compare our parameters for the hot source (the IRS) with what other investigators have found in inclusive charged particle measurements for various systems. At slightly lower beam energies (10-20 MeV/nucleon) a moving hot source has been used to describe inclusive charged particle spectra, with resulting temperatures of 3-6 MeV (Aw 81). For the same beam energy as used in our investigation (35 MeV/nucleon) temperatures extracted for the IRS were typically 9-12 MeV (We 84); ours averaged 8.5 and 10 MeV for the two targets, in agreement with the charged particle result. At higher beam energies (100-150 MeV/nucleon) a "fireball" description of light charged particle spectra gave temperatures of 20-30

MeV (We 82), and still higher beam energies resulted in higher temperatures yet (Na 79). Awes et al. (Aw 81) have suggested a smooth relationship between $(E_{cm} - V_c)/\mu$ and τ_{IRS} that seems to work well for charged particle data. It has been pointed out, though, that neutrons may obey somewhat different systematics from protons (Ka 81), and indeed Gavron et al. (Ga 83) speculate that τ_{IRS} for neutrons might be independent of beam energy. The velocities of the hot thermal sources used in these various investigations were typically slightly less than half the beam velocity, about the same as we find.

Figure 21 shows the angle of the IRS as a function of the angle of the fragment. For the Ho target the only IRS angles that are significantly different from 0° occur for high energy fragments of B and C at θ_{LF} = 7° and 10°. For the Ni target, the only significant nonzero θ_{IRS} occurs for high energy C fragments at 7°. In the nonzero cases the angle of the IRS is always negative, indicating that it is moving towards the side of the beam opposite to the direction of motion of the fragment. This is how the moving IRS reproduces the asymmetry of high energy neutrons at middle angles. In each case of nonzero IRS angle, the fragment is detected close to the grazing angle (8° in the lab system for the Ho target and 4° for the Ni target). It

Figure 21. IRS angle θ_{IRS} versus fragment angle. Format is the same as that of Fig. 13.

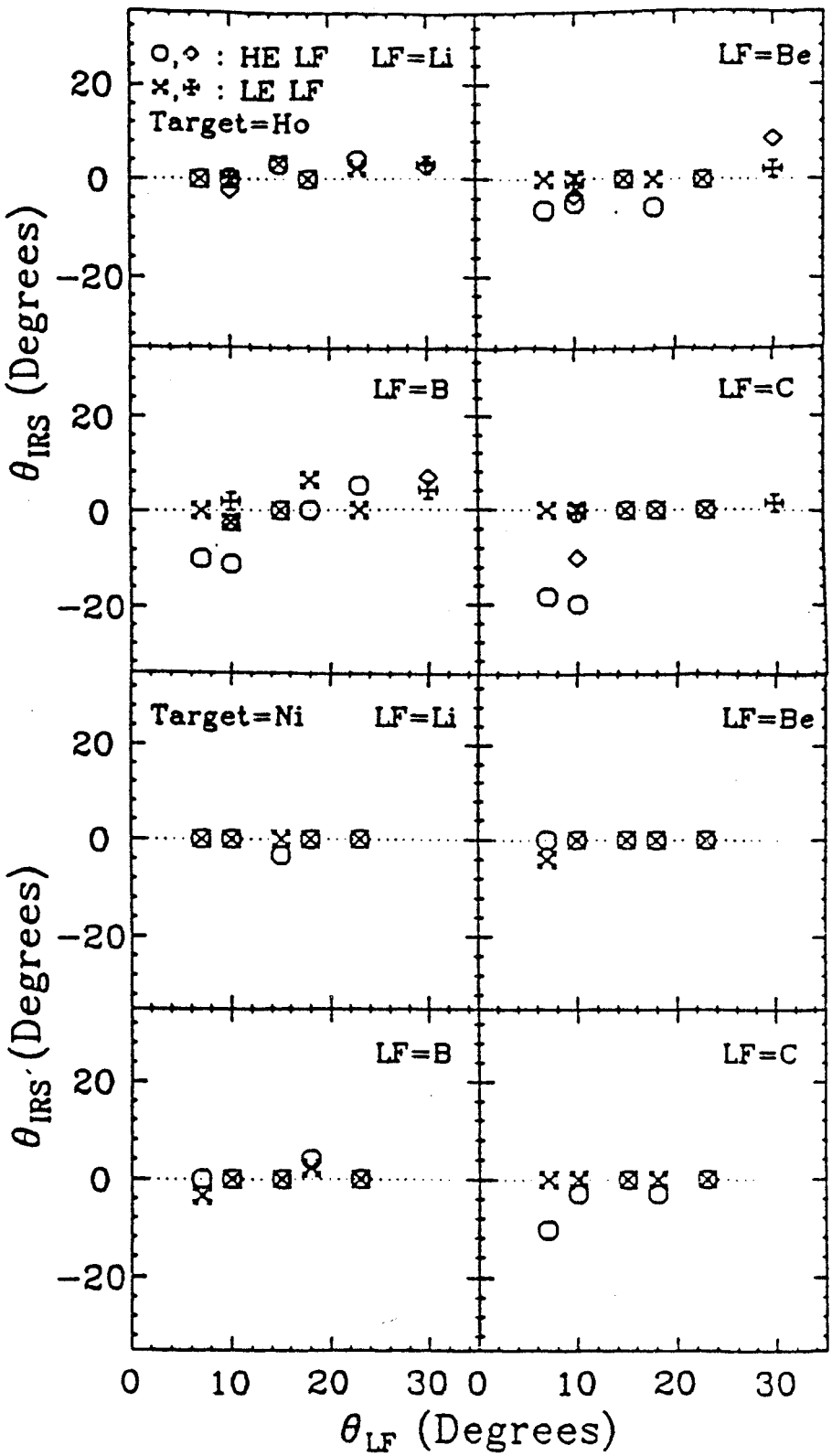
○,◇ : HE LF
×,✣ : LE LF
Target=Ho
LF=Li
LF=Be
LF=B
LF=C
Target=Ni
LF=Li
LF=Be
LF=B
LF=C
θIRS (Degrees)
θIRS' (Degrees)
θLF (Degrees)
20
0
−20
0
10
20
30

Figure 21.

appears that the asymmetry is associated only with the most peripheral collisions.

It is interesting to notice that such asymmetries in preequilibrium emission were not noticed until light particle--projectile-like fragment coincidence measurements were conducted. Asymmetric preequilibrium emission has now been seen in α-particle--projectile-like fragment coincidence measurements in the ^{16}O + Pb and ^{16}O + Au systems at 9 and 20 MeV/nucleon (Ge 77) and also in neutron--projectile-like fragment coincidence measurements of the ^{86}Kr + ^{166}Er system at 12 MeV/nucleon (Ts 82). Both investigators saw an enhancement of preequilibrium particles on the same side as the detected projectile-like fragment for quasi-elastic reactions and an enhancement on the opposite side for strongly damped collisions. They suggested that this asymmetry was consistent with a "tangental friction" model. A recent neutron--projectile-like fragment coincidence study (Pe 85) showed an asymmetry of preequilibrium neutrons in peripheral collisions of ^{12}C + ^{158}Gd at 16 MeV/nucleon. The enhancement was on the side opposite the detected projectile-like fragment, just as we observe but opposite to that of Refs. Ge 77 and Ts 82. Clearly, more coincidence studies of preequilibrium particle emission are necessary before we can start to unravel the dynamics of the early stages of the nuclear collision mechanism.

In an effort to elucidate the systematic behavior of the observed asymmetry of preequilibrium neutrons, we define an "asymmetry parameter" as the transverse component of the IRS velocity: $(V_{IRS})\sin\theta_{IRS}$. The asymmetry is the strongest for fragments at 10° for the Ho target, so this is the case we choose to study further. Shown in Fig. 22 is a plot of $(V_{IRS})\sin\theta_{IRS}$ versus Z_{LF}. One can see two systematic trends in the asymmetry parameter. First, it is large for peripheral reactions leading to high energy fragments but disappears for more central collisions resulting in low energy fragments. Second, it increases with the size of the coincident fragment and is maximum for carbon fragments. If one adopts the simple picture that in the most peripheral interactions the transverse momentum of the fragment is balanced mainly by that of the IRS, then the variation of the asymmetry parameter with Z_{LF} and hence A_{LF} can easily be understood. For the most peripheral collisions leading to high energy carbon fragments, only a few nucleon-nucleon collisions in the initial projectile--target-nucleus overlap region participate in transverse momentum conservation. Therefore, the average velocity of the localized interaction region must be strongly directed to the side opposite the detected fragment. At the opposite extreme, where we detect lithium fragments, more nucleons are contained in the initial overlap region. Also since A_{LF} is small, the amount of transverse momentum of the fragment

Figure 22. Plot of the IRS transverse velocity $(V_{IRS})\sin\theta_{IRS}$ versus fragment charge Z_{LF}. The symbols differentiate between gates set on high energy light fragments (HE LF) and low energy light fragments (LE LF) at an angle of 10° for the Ho target.

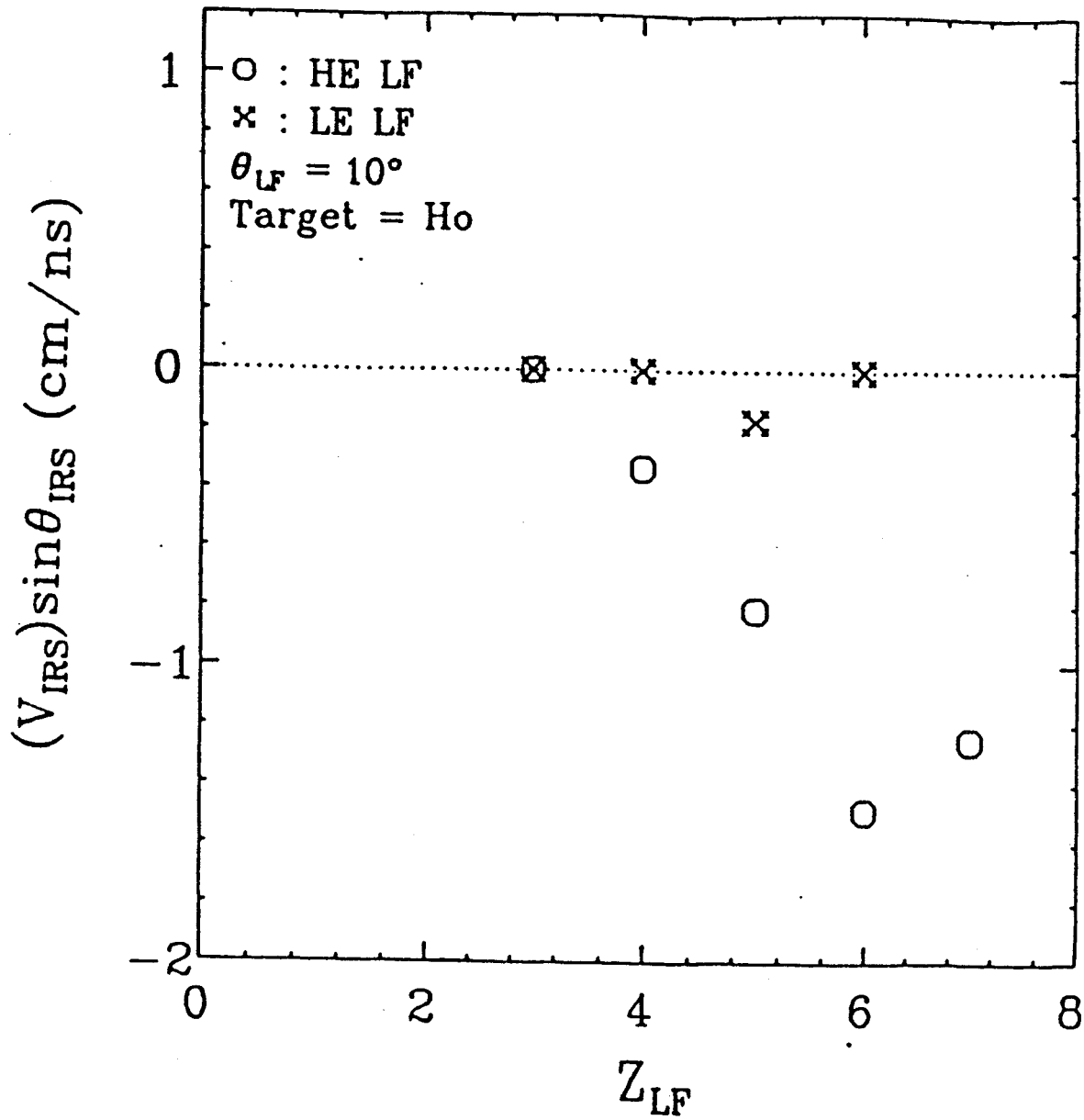
o : HE LF
× : LE LF
θ_{LF} = 10°
Target = Ho
1
0
−1
−2
0
2
4
6
8
$(V_{IRS})\sin\theta_{IRS}$ (cm/ns)
Z_{LF}

Figure 22.

needing to be balanced is less. So this "larger" localized region (IRS) can move more slowly to the side opposite. In collisions giving rise to low energy fragments there is larger kinetic energy loss, indicating a longer interaction time (Sc 78, Hi 81). Therefore, one might reasonably expect there to be more interaction between the projectile and the mean field of the target nucleus, meaning the target nucleus would participate more in balancing the momentum of the fragment.In this case, the direction of the IRS would not have to be correlated with the direction of the fragment, and the IRS could then move on the average straight down the beam axis.

The above discussion for peripheral collisions suggests a method for crudely estimating an average size of the localized region of randomization, viz., the size of the IRS. Neglecting the contribution of the TLS in balancing the transverse component of the fragment momentum allows one to write

$$A_{LF}\sqrt{(E/A_{LF})}\cdot\sin\theta_{LF} = A_{IRS}\sqrt{(E/A_{IRS})}\cdot\sin\theta_{IRS} \quad . \qquad (6)$$

Using average values for A_{LF} and E/A_{LF} estimated by examining Figs. 2, 4, and 5 and using the fit parameters for E/A_{IRS} and θ_{IRS} displayed in Figs. 20 and 21 allow one to solve this equation for A_{IRS}. We select the most peripheral

reactions as most nearly approximating the assumption of negligible contribution to momentum sharing from the TLS. For high energy C fragments at 7° for the Ni and Ho targets, eq. (6) gives A_{IRS} = 14 and 9, respectively. For high energy Be, B, C and N fragments at 10° for the Ho target one gets A_{IRS} = 32, 17, 11, and 15, respectively. The result for Be fragments at 10° clearly is much different from the other numbers. But the asymmetry parameter (Fig. 22) is quite small for Be and has a large relative error. If we neglect the Be value, we have left a close set of numbers whose average is about 13. If one also neglects the TLS contribution in balancing the parallel components of momenta, then

$$A_{beam}\sqrt{(E/A_{beam})} =$$

$$A_{LF}\sqrt{(E/A_{LF})}\cos\theta_{LF} + A_{IRS}\sqrt{(E/A_{IRS})}\cos\theta_{IRS} \qquad (7)$$

This equation then gives $\langle A_{IRS}\rangle \approx 5$, which is considerably smaller than the estimate from balancing transverse momenta. The difference is probably due to the TLS having non-negligible transverse momentum. At best we can say that $5 \leq A_{IRS} \leq 13$, where A_{IRS} represents the average size of the preequilibrium localization throughout its evolution into the target nuclear matter.

For central collisions, neglecting the TLS momentum is no longer valid, so the method used for estimating A_{IRS} for peripheral collisions cannot be extended to central collisions. Indeed, the picture becomes quite complicated if one tries to combine E^* and E/A for both the IRS and TLS, along with conservation of energy and momentum, to estimate A_{IRS}. The time scales for thermal neutron emission from the IRS and from the TLS are very different, due to their different temperatures (St 77). Hence, when one determines the velocities of the IRS and the TLS from the neutron emission spectra, one is determining the velocities at different times in the interaction. So a quantitative estimate of A_{IRS} for central collisions will not be attempted. Qualitatively, though, if one associates low energy fragments with central collisions and high energy fragments with peripheral collisions, then E/A_{IRS} on the average is slightly lower for central collisions (see Fig. 20). A lower E/A_{IRS} indicates that each nucleon in the overlap region originating from the projectile has on the average interacted with more nucleons originating from the target nucleus. Hence, one would expect the size of the IRS to be slightly larger for central collisions than for peripheral collisions.

To "calibrate" our experimentally determined values of A_{IRS}, we can calculate the size of the most probable overlap

region from purely geometrical considerations (Sc 81). Without differentiating between central and peripheral collisions, the most probable geometrical overlap gives 22 and 14 for the initial mass of the IRS in Ho and Ni, respectively. Compared to our experimentally deduced range of $5 \leq A_{IRS} \leq 13$ for peripheral collisions, then one can infer that considerable preequilibrium emission has occurred before the colliding nuclei reach the most probable overlap configuration. Gavron et al. (Ga 83) have also considered the size, or more appropriately the composition, of the IRS in a study of preequilibrium neutron emission in the C + Gd and Ne + Gd systems at 4-11 MeV/nucleon above the Coulomb barrier. Their finding for central collisions is that each projectile nucleon in the "hot spot" has interacted with approximately three target nucleons. Even though we did not make a quantitative estimate of A_{IRS} for central collisions, we can compare our results to Gavron's findings of the IRS composition by noting that our E/A_{IRS} for both central and peripheral collisions was near to the E/A corresponding to the velocity of the nucleon-nucleon center-of-mass. This indicates that preequilibrium neutrons are emitted after projectile nucleons have interacted on the average with only one target nucleon. In charged particle--projectile-like fragment coincidence studies of the ^{12}C + Au system at 30 MeV/nucleon (Ha 85), $A_{IRS} = 38$ was deduced from momentum

considerations. This estimate should be qualified, though, by noting that in order to conserve energy using the reported fit parameters for temperature, velocity, and source size requires that one adopt a rather nonstandard density-of-states parameter $a_{IRS} = A_{IRS}/\varepsilon$, where $\varepsilon > 20$.

Finally, the associated multiplicity of the IRS is plotted versus fragment angle in Fig. 23. It does seem significant that the same behavior observed for the TLS multiplicities is also evident here: 1) M_{IRS} increases with fragment angle; 2) M_{IRS} is larger for the low energy fragment gate than for the high energy gate; 3) M_{IRS} for the Ho target is larger than for the corresponding cases with the Ni target. The fact that the multiplicities of both sources exhibit the same behavior with angle and energy of the fragment and with target mass suggests that there is a very intimate relation between the IRS and the TLS. We feel this is a further indication that the neutrons parameterized by the IRS emerge very early in the interaction from a "hot" subset of the "cooler" target-like fragment nuclear matter (consistent with conclusions drawn from charged particle work (Aw* 81, Aw 82, Fi 84)). Then the Coulomb barrier effects mentioned in the discussion of Fig. 17 are valid here, too, explaining why the neutron multiplicity is greater for the Ho IRS than for the Ni IRS.

Having discussed the IRS parameters, we now return to the "missing-momentum" plot in Fig. 16. Dyer et al. (Dy

Figure 23. IRS associated multiplicity M_{IRS} versus fragment angle. Format is the same as that of Fig. 13. (Note the difference in scale between the Ho and Ni data).

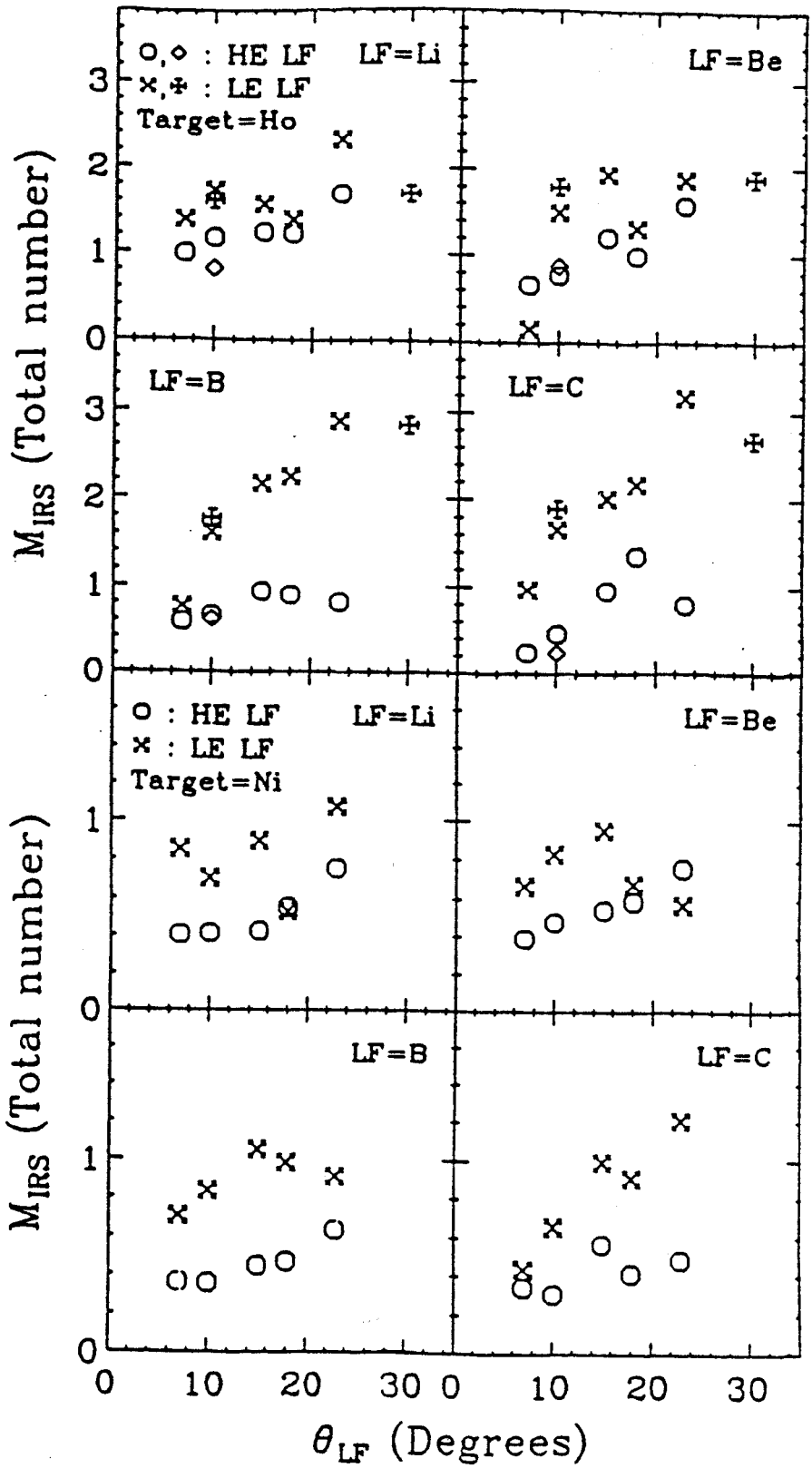
O,◇ : HE LF
×,✣ : LE LF
Target=Ho
LF=Li
LF=Be
LF=B
LF=C
O : HE LF
× : LE LF
Target=Ni
LF=Li
LF=Be
LF=B
LF=C
M_{IRS} (Total number)
M_{IRS} (Total number)
θ_{LF} (Degrees)
0
10
20
30
0
1
2
3

Figure 23.

79) ascribe their observed missing momentum (in fission studies) to a "jet of particles" in the forward direction. We have observed extensive preequilibrium neutron emission. Could the IRS be related to the forward angle "jet" of particles, and hence explain the missing momentum? It is noteworthy that the missing momentum observed both in this work (Fig. 16) and by Dyer et al. is largest for strongly damped reactions leading to low energy light fragments. These reactions are also where the IRS associated multiplicity is largest. But it is equally noteworthy that at small θ_{LF} where $P_{missing}$ is maximum is precisely where the IRS associated multiplicity is a minimum. Ascribing $P_{missing}$ to the IRS, then, is consistent with the dependence of $P_{missing}$ on the energy damping but not with its dependence on θ_{LF}.

VI. SUMMARY AND CONCLUSION

We have compiled an extensive set of neutron-fragment coincidence data for the ^{14}N + ^{165}Ho and ^{14}N + Ni systems at 35 MeV/nucleon. The fragment energy and angular distributions show a rather clear division into quasi-elastic processes leading to high energy fragments and strongly damped reactions leading to low energy fragments. To gain insight into the differences in their respective reaction mechanisms, we set gates across high energy and low energy fragments and examined the coincident neutron spectra. In all cases the neutron spectra consisted of three components: the projectile-like fragment and TLS components, and a preequilibrium component ascribed to an IRS. For the present work we neglected the projectile-like fragment contribution and focused on the TLS and IRS components.

The fit parameters describing the TLS were compared with a two-body calculation, with the observation that there was considerable missing momentum in the forward direction, especially for highly damped collisions. We have concluded that part of the missing momentum is due to preequilibrium particle emission. But the angular dependence of the missing momentum can only be explained by reactions such as projectile fragmentation that do not excite a TLS or an IRS. Comparison of the TLS associated multiplicities with

predictions from CASCADE indicates that many collisions resulting in a detected fragment do not necessarily excite the target fragment to energies above the neutron emission threshold. This is especially true for peripheral collisions, suggesting a strong angular dependence of the competition between transfer reactions and projectile breakup.

Examination of the IRS fit parameters shows that neither τ_{IRS} nor E/A_{IRS} exhibits a clear trend with E_{LF} or θ_{LF}. We interpret this as an indication that preequilibrium neutrons are emitted in the very early stages of the interaction before the "final fate" of the fragment has been determined. Estimates of the size of the IRS give evidence that it is an evolving localization of high excitation energy. Neutrons appear to be emitted early after its formation when the IRS is "hot and small", perhaps after participating projectile nucleons have undergone as few as 1-2 collisions. If composite particles are also emitted from the IRS, this happens later in the evolution of the IRS, after it has become "larger and cooler".

We acknowledge the efforts of the Operations Group at the National Superconducting Cyclotron Laboratory (NSCL). We would also like to thank D. Hilsher for his encouragement and many helpful discussions. This material is based on work supported by the National Science Foundation under

Grant Nos. PHY 83-12245, INT-80-15333, and PHY 84-16025 and by the Hungarian Academy of Sciences.

APPENDICES

A-1. Experimental Setup in More Detail

The experimental areas for the cyclotron lab at M.S.U. are shown in Fig. A-1. After the beam of 35 MeV/nucleon ^{14}N was extracted from the K500 cyclotron, it was steered with the "Hunter's Point" (HP) dipole switching magnet into the north vault. The beam passed through the S320 spectrograph, which served as an added focusing element, and was directed into the neutron chamber. The chamber was a thin-walled (3 mm) steel chamber with a 0.91 m diameter. After passing through the target at the center of the neutron chamber, the beam was deposited in and the charge collected in a Faraday cup well downstream from the target. To reduce the chance of neutrons scattered from the beam dump producing signals in the neutron detectors, the beam dump was extensively shielded (not shown in Fig. A-1).

Figure A-2 shows a photograph of the experimental setup just after the experiment, with the chamber, neutron detectors, target drive, and beam dump indicated in the picture. The extensive cabling to bring the signals from the detectors to the patch panel (hence to the data room) is also evident. The flange at the bottom of the photograph is where the beam enters the chamber, and the target is located at the center of the chamber. The detector arrangement inside the chamber is shown in Fig. A-3. One can see the

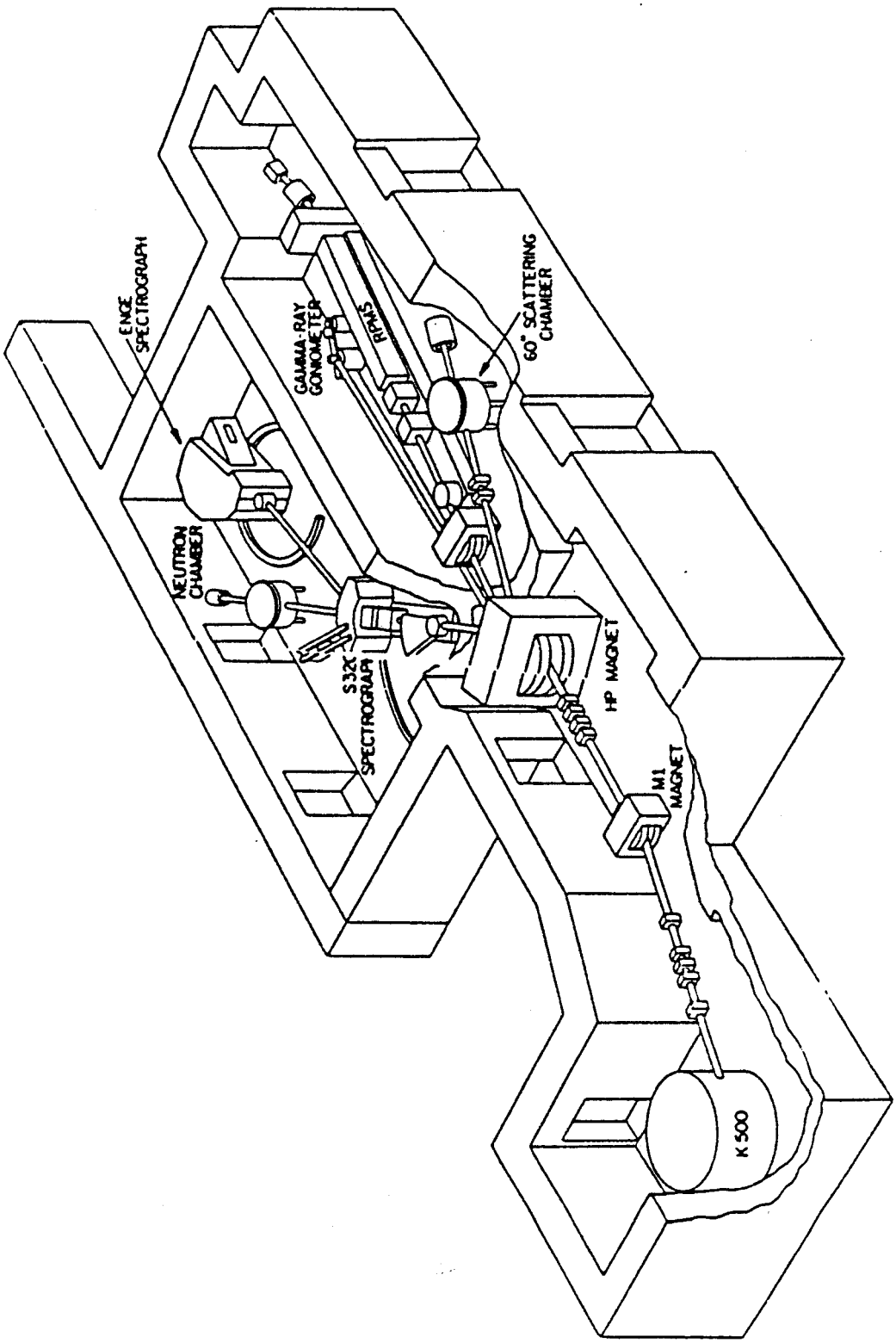

Figure A-1. Schematic of the experimental facilities.

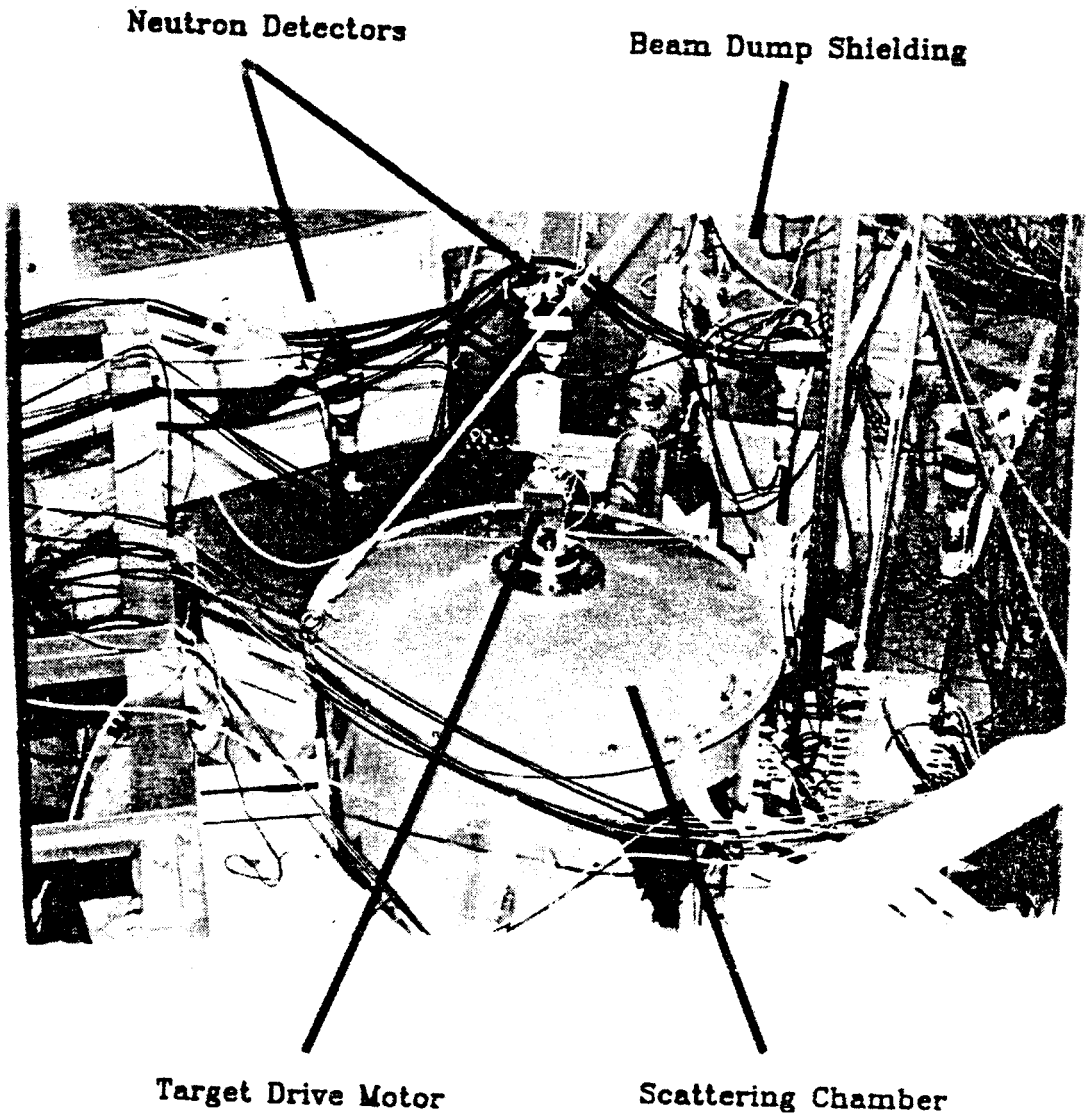

Figure A-2. The Chamber and neutron detector arrangement.

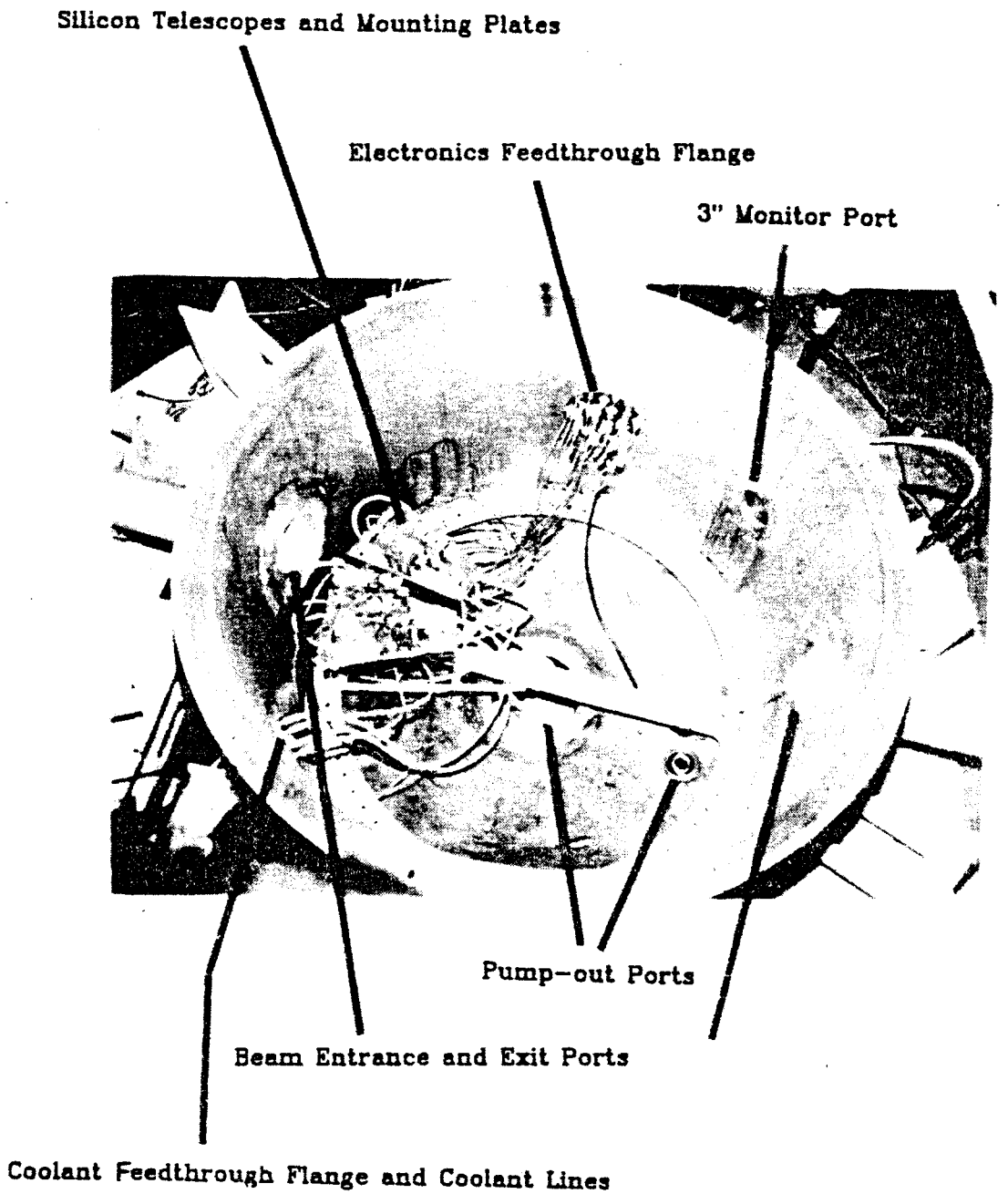

Figure A-3. The Si telescope arrangement inside the chamber.

beam entrance and exit ports, the electronics feed-through port, and the coolant (for the Si telescopes) feed-through port. At the bottom of the chamber is the main pumpout port where the cryopump was attached. Also on the bottom is a small rough-out pumping port.

A blow-up of the silicon detector arrangement is schematically illustrated in Fig. A-4. Each telescope contained three silicon detectors placed close together. The angles at which the detectors were placed are indicated in the figure, with the dashed lines corresponding to the one telescope that was placed out-of-plane. The shaded regions correspond to the solid angles subtended by the two neutron detectors at the forward-most angles (±10 degrees). One can see that neutrons detected in those two detectors have traversed the material contained in the silicon telescopes. Correction was made (see Appendix IV) for the attenuation of neutron flux due to this material.

Figure A-5 shows a "beam's-eye" view of the silicon telescopes. The picture was taken from just inside the entrance flange into the chamber, looking straight down the beam line towards the Faraday cup. The polyflo tubing entering from the flange at the far left in Fig. A-5 circulates the refrigerated methanol for cooling the silicon detectors. The black cables attached to the detectors at the top carry both the high voltage to and the output signals from the detectors. One can see the copper collimators placed in front of each detector, ensuring that

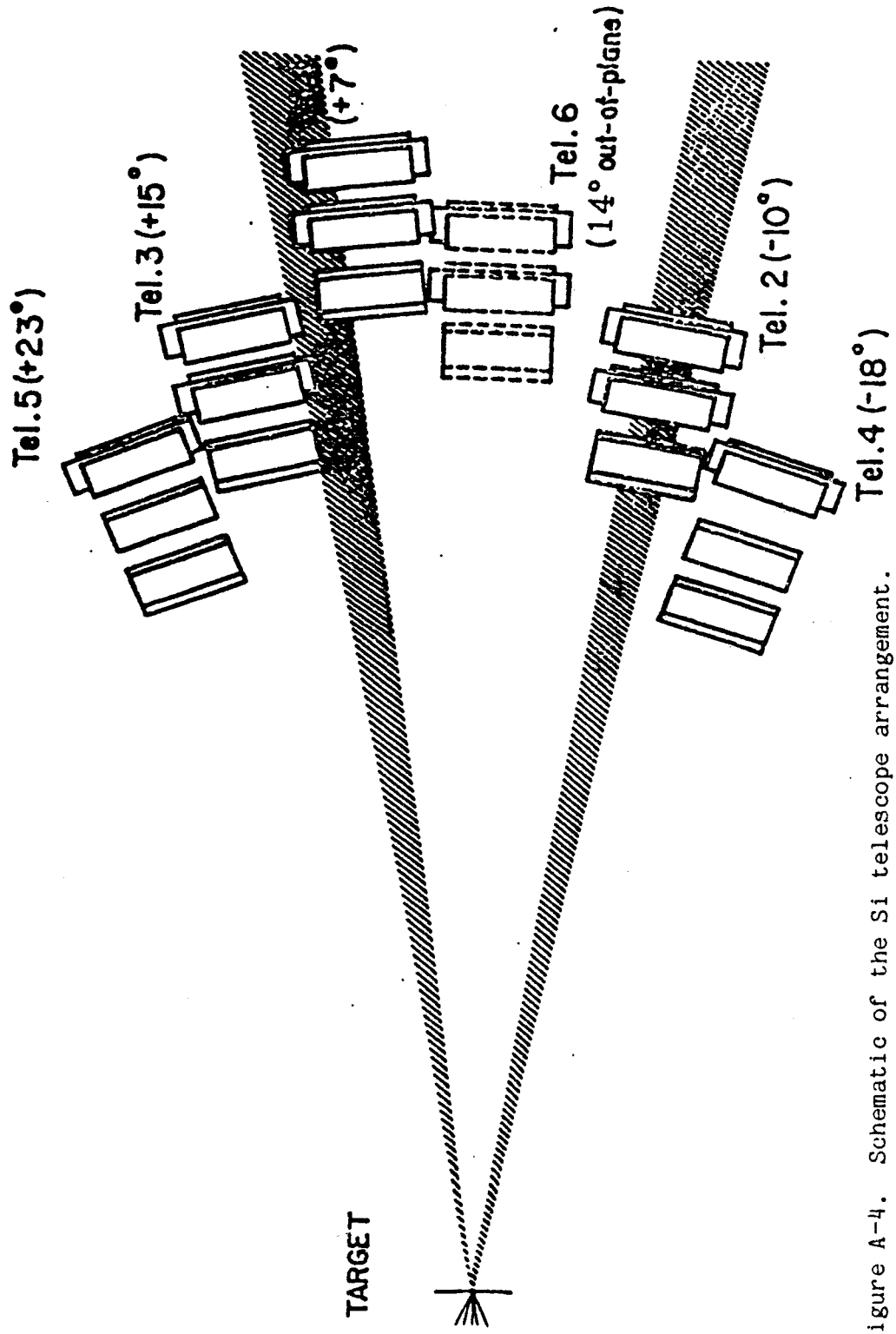

Figure A-4. Schematic of the Si telescope arrangement.

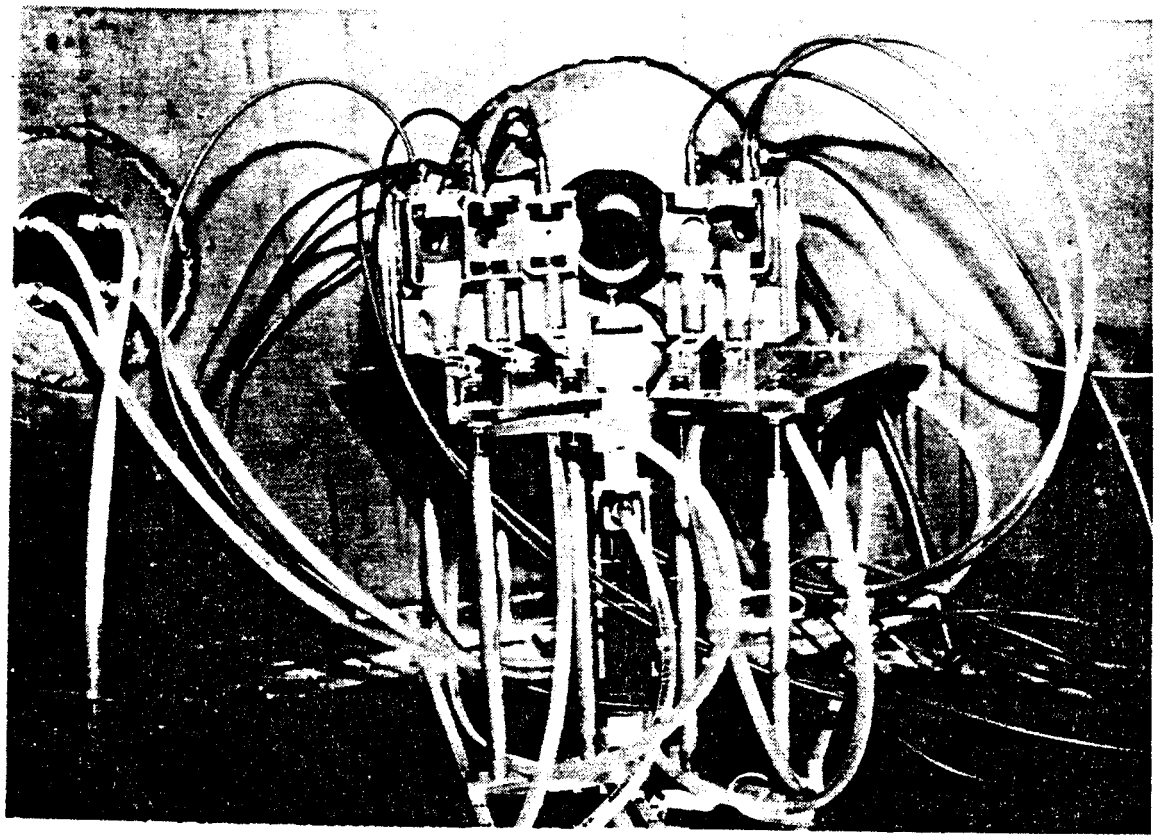

Figure A-5. Close-up of the Si telescope arrangement.

charged particles enter only the active region of the silicon. One can also see the cobalt magnets placed in front of the detectors. When the beam passes through the target, a spray of secondary electrons is created. To reduce the number of electrons entering the silicon (as unwanted charge), the permanent magnets create a vertical magnetic field in front of the detector which deflects the electrons away from the acceptance region. The charged particles being studied will undergo only a negligible deflection due to their much larger mass and enter the acceptance region of the Si detector.

Figure A-6 shows that portion of the beam line entering the beam dump and a neutron detector with its proton veto detector mounted in front of it. One can see that the beam dump is surrounded with extensive shielding. On either side of the Faraday cup sit two 20,000 pound, 18 inch thick slabs of steel, originating from the original University of Michigan cyclotron which operated during the 1930's and 1940's. The shielding is built up from below and built down from above with concrete blocks. The beam was stopped on a one inch thick piece of 1100 grade aluminum. Provision was made for cooling this Al block with forced air or water by attacking to it a 1/2 inch thick brass plate with fitted copper cooling lines. For the beam intensities used in this work (maximum of 40 ena for 35 MeV/nucleon ^{14}N), cooling the Faraday cup was not necessary. To moderate the neutrons

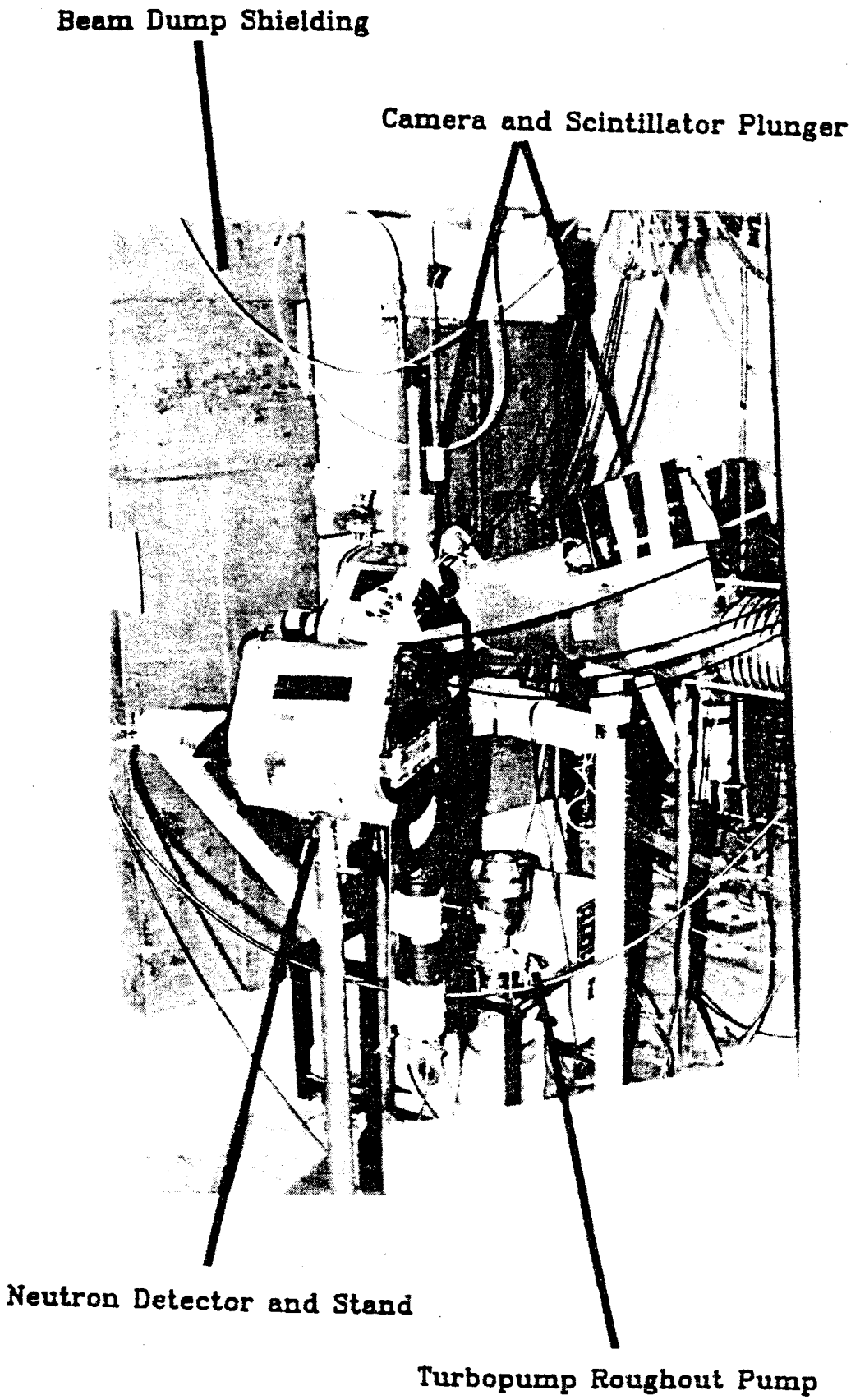

Figure A-6. A neutron detector and the beam dump.

formed when the beam was brought to a stop on the block of aluminum, paraffin was packed around the rear end of the Faraday cup. To reduce the number of gamma-rays formed in the beam dump from entering near-by neutron detectors, lead bricks were built into the shielding at the entrance to the beam dump. A plunger-scintillator-camera system was installed in the beam line just prior to the entrance to the beam dump, allowing one to remotely monitor the position of the beam at this point. The neutron detector at +10 degrees is also shown in Fig. A-6. One can see the neutron detector stand used, the aluminum protective casing around the detector, and the proton veto detector mounted on the front.

Figure A-7 shows the neutron detectors at an intermediate stage in their development. One-liter glass cells were made by the glass shop of the M.S.U. Chemistry Department. These cells have a small expansion bulb on the side to allow for thermal expansion of the liquid scintillator. The cells were then filled through the expansion bulb with NE213, a xylene-based liquid scintillator. The NE213 was then bubbled for about one hour with dry nitrogen by inserting a thin teflon tube into the liquid through the expansion bulb and attaching the other end of the tubing to a regulator and nitrogen bottle. This process removed the oxygen from the liquid by displacement. Oxygen in the NE213 hinders the pulse-shape discrimination (PSD) capabilities of the liquid, hence as much of the oxygen should be displaced out as possible. It should be

Figure A-7. The neutron detectors during assembly.

pointed out, though, that excessive bubbling may lead to a non-negligible change in the ratio of solvent to solute due to evaporation of solvent. This in turn may adversely affect the performance of the liquid's PSD capabilities (Pe 79). A second reason for wanting no oxygen in the NE213 is safety. NE213 is xylene-based with a relatively low flash point. Since one uses a torch to seal the cell at the expansion tube, then to minimize the possibility of an explosion, one would like as little oxygen present as possible. Various elegant methods of sealing have been used (Pe 79, Wi 85), but the one described here is very simple and effective (Hu 81). After the bubbling in the main cell was completed, the liquid in the expansion bulb was bubbled for 5-10 minutes. Since a certain amount of solute inevitably gets deposited onto the inner stem of the expansion bulb, a long-handled Q-tip was first dipped in methanol then inserted into the stem to clean it. The air was then displaced out of the stem region beyond the liquid in the bulb, and the stem was attached to a pump with a rubber hose. The pump was turned on until small bubbles started to form in the liquid in the cell, indicating a slight reduction of pressure inside the cell. At this point, the rubber hose was clamped off, maintaining the reduced pressure inside the cell at a constant value. Rags soaked in cold water were then wrapped around the expansion bulb. The stem about 1-2 inches above the bulb was then heated with a low flame on a small propane torch until it

became malleable and collapsed in on itself due to the reduced pressure inside the cell. The flame was then used to cut the stem and anneal the stub left until it was smooth. The cell thus produced was then glued onto a conical piece of highly polished ultraviolet-transmitting (UVT) lucite using NE581 optical epoxy. The free end of the lucite cone was then glued with optical epoxy onto an RCA-8575 photomultiplier (PM) tube. Both the cell and the lucite were then painted with NE560 white, high-reflectivity paint to increase the number of photons reaching the photocathode of the PM tube per scintillation in the liquid. The expansion bulb was painted with dull black paint to try and reduce internal reflection which might cause light formed in a scintillation in the expansion tube itself from finding its way into the cell and to the photocathode. The computed neutron detector efficiency did not include such events. To ensure the optimum cascade of electrons down the 12 dynodes of the PM tube, it was important to screen out any ambient magnetic fields. The area of the PM tube near to the photocathode is the most sensitive to stray magnetic fields, so that care was taken to have this region well shielded. The phototube was surrounded with high-permeability metal cylinders purchased from the μ-metal Company. The lucite cone was wrapped with layers of high-permeability Conetic followed by layers of high-saturation Netic purchased from the Perfection Mica Company.

Figure A-8 shows the proton veto detectors during their final stage of construction. These detectors consisted of 6 mm of NE102A plastic scintillator glued to two pieces of UVT lucite serving as a light guide to the photocathode of an RCA-8575 PM tube. The lucite was covered with (ungreased) aluminum foil to increase the amount of light reaching the photocathode per scintillation in the plastic. The PM tubes for the veto detectors were also wrapped in layers of Conetic and Netic to screen out magnetic fields.

EMI-Gencom PM bases were then used with all the PM tubes; an assembled detector is shown in Fig. A-6. Events where signals were created in both the veto detector and the neutron detector were interpreted as proton events and were vetoed in hardware.

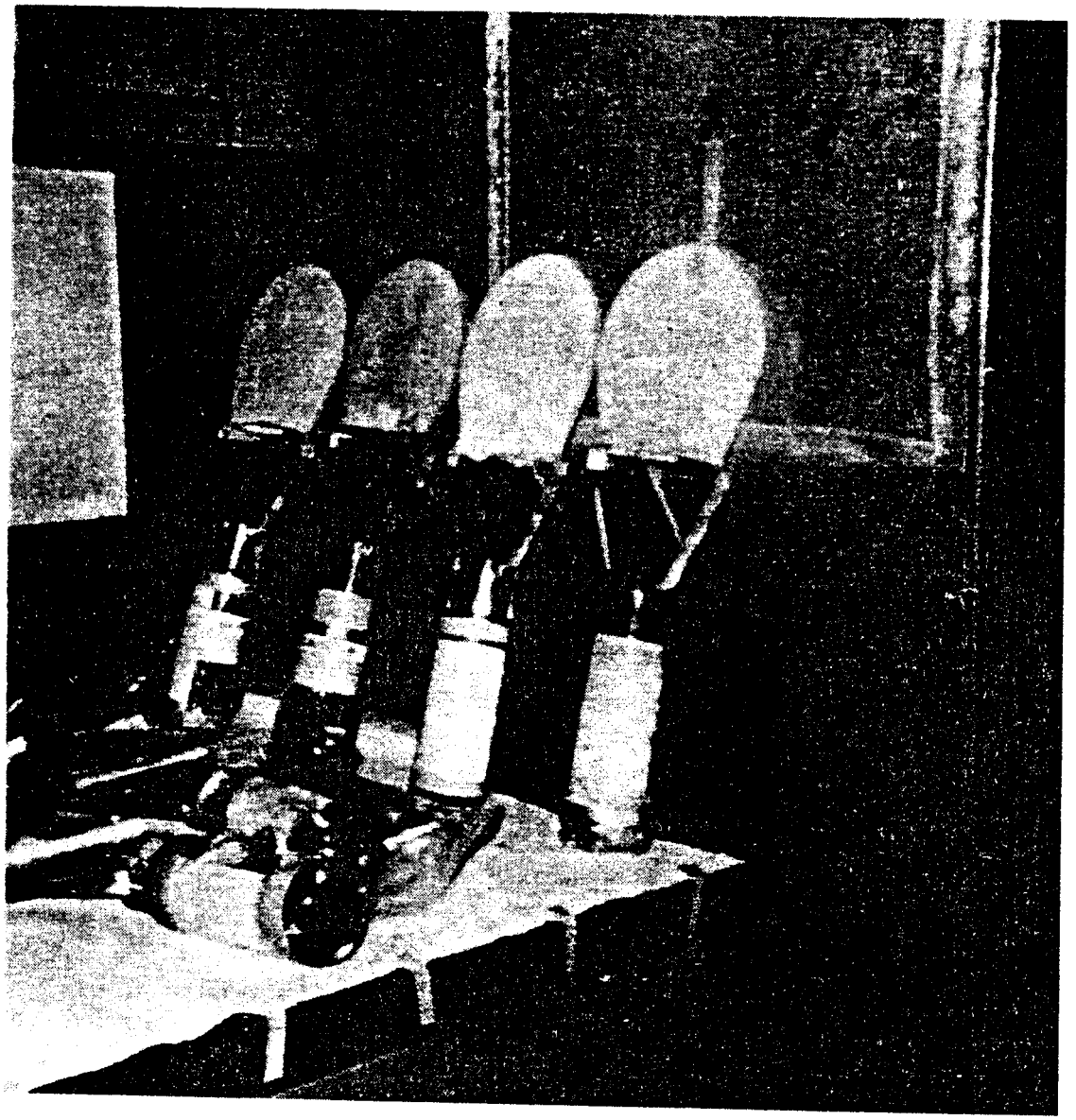

Figure A-8. The proton veto detectors during assembly.

A-II. The Electronics

Figure A-9 shows the block diagram of the electronics setup used in this work. The electronics were structured to record neutron-fragment coincidences where at least one neutron detector and one fragment telescope fired simultaneously. Down-scaled fragment singles events were also recorded.

The upper left side of Fig. A-9 shows the electronics for the neutron detectors, while the upper right side is for the Si telescopes. In the middle of the diagram are shown the coincidence requirements ensuring that within the 350 ns time gate there was both a neutron event in one of the ten neutron detectors and a fragment event in one of the six fragment telescopes. The downscaled fragment singles circuit is on the far right side of the diagram.

First considering the neutron detector electronics, one starts with the anode output from the photomultiplier tube (PM) base. The RCA-8575 photomultiplier tube consists of a 12 dynode chain which terminates at the anode. Electrons liberated from the photocathode (due to a scintillation in the NE213) cascade down the dynodes and are collected on an anode, forming a fast negative signal. Typical rise times were around 6 ns. To extract a signal that is directly proportional to the initial energy deposited upon the photocathode, a "linear" signal is often tapped from one of the earlier dynodes. If one operates the tube at a low

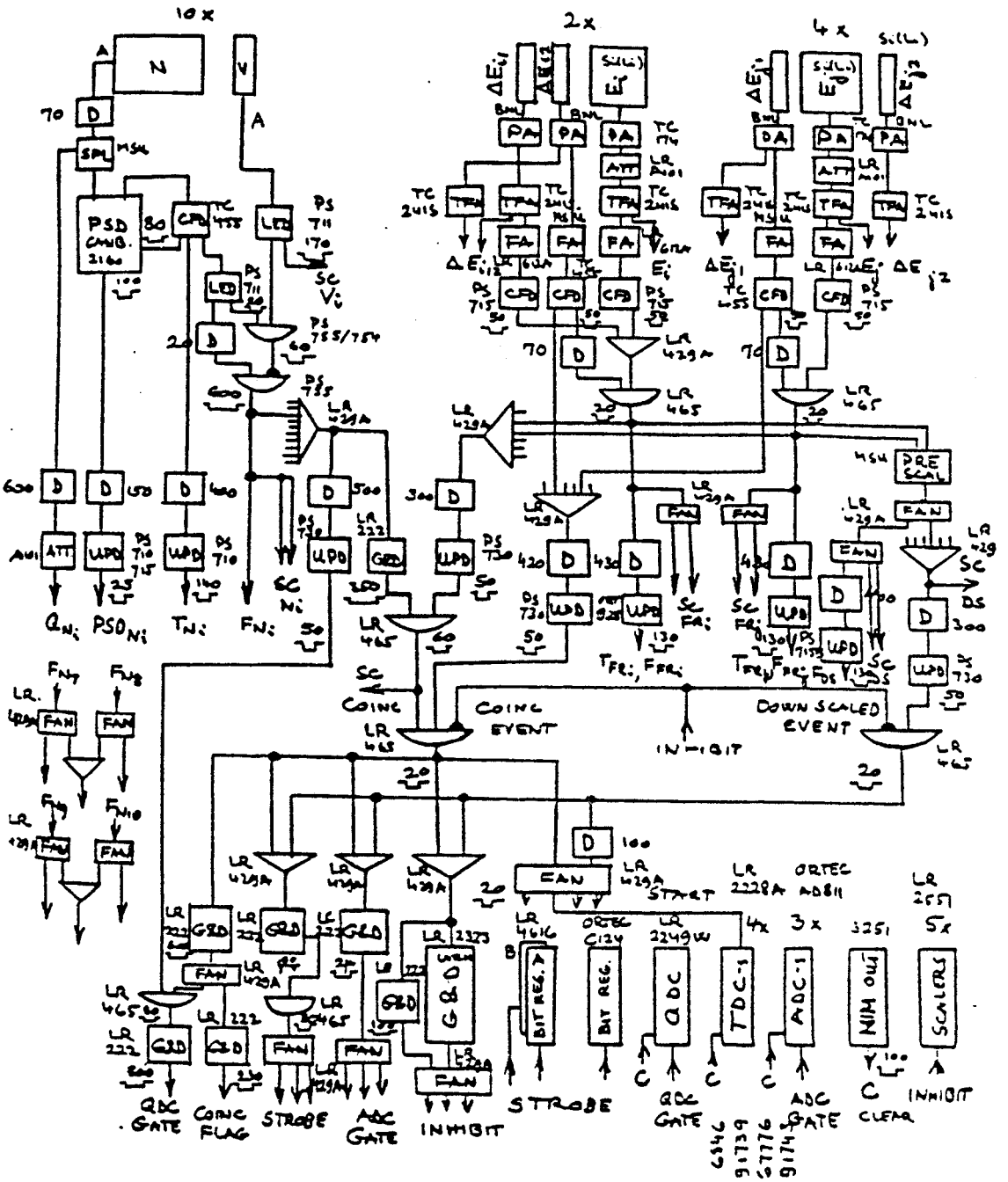

Figure A-9. Electronics block diagram.

enough voltage, one can integrate the anode signal in a charge sensing analog-to-digital converter (called a QDC) and extract similar information. We chose the latter method and split the anode signal three ways using 50-Ω splitters built in the NSCL Electronics Shop. One of these signals was sent directly to a LeCroy LR2249W QDC, where the total charge in the pulse was recorded.

The second anode signal was sent to a Tennelec 455 constant fraction discriminator (CFD) and served as the fast timing signal. The third signal was sent to a Canberra 2160 pulse-shape discriminator (PSD) and was used to distinguish between neutrons and gamma rays. (This technique will be discussed further in Appendix III.) The final element of the neutron detector electronics was the proton veto paddle. The anode pulse out of the phototube attached to this scintillator was passed through a Phillips 711 leading-edge discriminator (LED) creating a fast negative logic signal. This was then passed through an anticoincidence gate with the timing signal from the neutron detector thus creating a hardware veto.

From the fragment side of the electronics, one needs to be able to identify the fragment as to its Z and A and to determine its time of flight (TOF). One of the standard techniques for identifying the fragment is to record a ΔE and a total E signal. Off-line, when ΔE is plotted versus E, hyperbolic bands result which are separated, in accord with the relation

$$\Delta E \propto -\frac{A \cdot Z^2}{E} \quad .$$

Detector telescopes typically consist of a thin, transmission-type Si surface barrier ΔE detector followed by a thick Li drifted Si E stopping detector. The signal from the thin detector serves as the ΔE signal while the sum of the two signals is the total energy signal. In this work, to increase the dynamic range, triple element telescopes were used. Light, fast moving fragments penetrate the first two detectors and are stopped in the third so that fragment identification is accomplished by $\Delta E = E_1$ and $E_{total} = E_1 + E_2 + E_3$. On the other hand heavy, slowly moving fragments that are stopped in the second detector can still be identified by $\Delta E = E_1$ and $E_{total} = E_1 + E_2$. Knowing E_{total} for each fragment, as well as its mass and path length, allows one to calculate its TOF. This is added to the neutron-fragment time difference to obtain the absolute TOF of the neutron.

The signal from each Si detector in the telescope was passed through a preamp and a fast amplifier, then digitized in an analog-to-digital converter (ADC) and stored on magnetic tape. For the fast signal against which the neutrons were timed, special preamps made at the Lawrence Berkeley Laboratory were used. Coincidence gates were used to ensure that at least two of the three Si detectors in the

telescope fired, thus defining a fragment event. Each good fragment event signal was split. One of the signals was fed into a coincidence gate with signals from the neutron side. If there was no neutron-fragment coincidence, a fragment singles event was recorded.

If there was a neutron-fragment coincidence within approximately a 350 ns time window, then the neutron was "timed against" the fragment. The fragment signal was the common start of a LeCroy LR2228A time-to-digital converter (TDC), and the neutron signal stopped the TDC. For each good coincidence event, (1) the neutron-fragment time difference, (2) the neutron--gamma-ray PSD signal, (3) the neutron detector integrated charge, (4) the E_1, E_2 and E_3 fragment signals, and (5) a fragment self-timing signal were written onto magnetic tape. In addition, a bit register was set to record which neutron-detector--fragment-telescope combination fired. A bit in the bit register was also set to indicate coincidence events versus fragment singles events.

The events were stored in a data buffer via a Camac crate and a combination of LSI and MR8010 microprocessors (Va 85). These buffers were periodically dumped onto magnetic tape. Our counting rates were typically 800 events/sec, which resulted in approximately 10% dead time. The average beam current was generally 2-4 pna on target with a duty cycle of approximately 50% - 75%.

A-III. Pulse-Shape Discrimination

Neutrons are detected in NE213 liquid scintillator mainly through the ionization from protons resulting from n-p scattering. The scattered proton moving through the liquid ionizes molecules in its path, resulting in a scintillation when the electrons recombine with atoms. Similarly, a gamma-ray can Compton scatter off an electron in the liquid, causing the electron to move through the scintillator. The electron also ionizes molecules in its path causing a scintillation. The neutron detector has approximately equal efficiencies for detecting neutrons and gamma-rays. One needs to be able to distinguish the neutron events from gamma-ray events, and three ways of doing this will be discussed.

The first method exploits the fact that all gamma-rays travel at the same speed, which is always larger than the speed of neutrons. Measuring time of flight (TOF) alone will separate most of the gamma-ray events from neutron events. Unfortunately this technique does not give a clean separation of neutron and gamma-ray events for at least two reasons. First, the finite time resolution of the neutron detector means that the prompt gamma-ray spike has a finite width which merges with the signals from the highest energy neutrons. Second, there are non-negligible levels of delayed gamma-ray emission from neutron capture and other

processes which yield gamma-ray events in the time spectrum normally occupied by only neutrons.

A better method (the one used in this work) of separating out the two types of events is through pulse-shape discrimination. Idealized pulse shapes for neutron and gamma-ray initiated events are shown in Fig. A-10. The first feature that is evident is that the pulses appear to be made up of at least two components, one of short time constant and one of long time constant. The second feature to note is that the pulse shapes for neutron and gamma-ray events are essentially the same for the fast component, but differ in the slow-component, i.e., the trailing edge of the signal. To be able to differentiate between neutrons and gamma-rays, one can exploit the difference in trailing edge with suitable electronics. We used Canberra 2160 pulse-shape discriminator (PSD) modules and the method described in reference Sp 74.

Operation of the Canberra 2160 PSD is illustrated in Fig. A-11 (Sp 74). The anode signal (part (a) of the figure) is divided and one of the signals is first integrated to incorporate the difference in the trailing edge, then differentiated. The result after integration and differentiation is shown in part (b) of Fig. A-11 and one sees that the two types of events are now separated in time. To enhance this time separation, the signal is passed through a high gain amplifier (Fig. A-11 part c), then inverted (Fig. A-11 part d). The other anode signal is fed

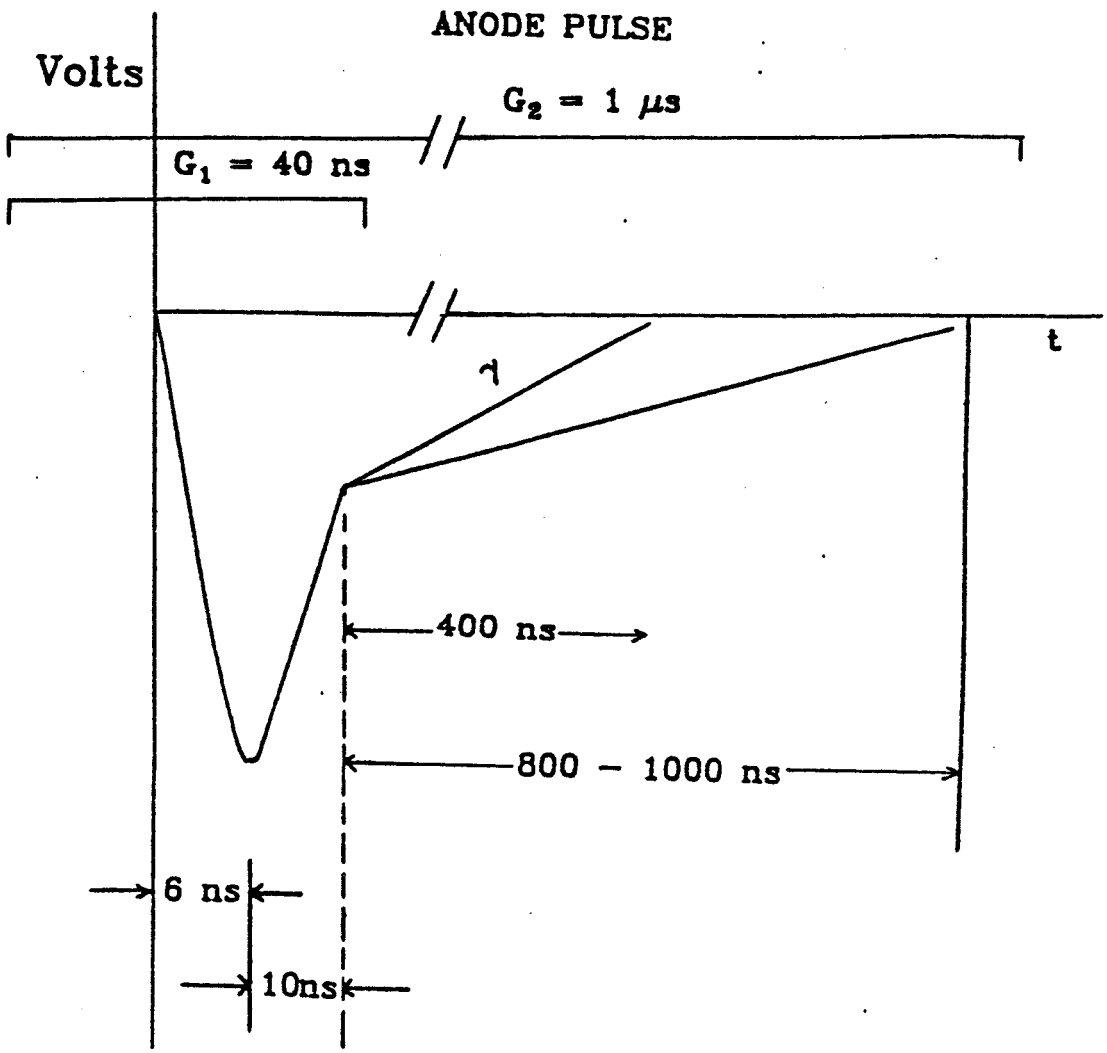

Figure A-10. Pulse shapes for neutrons and gamma rays.

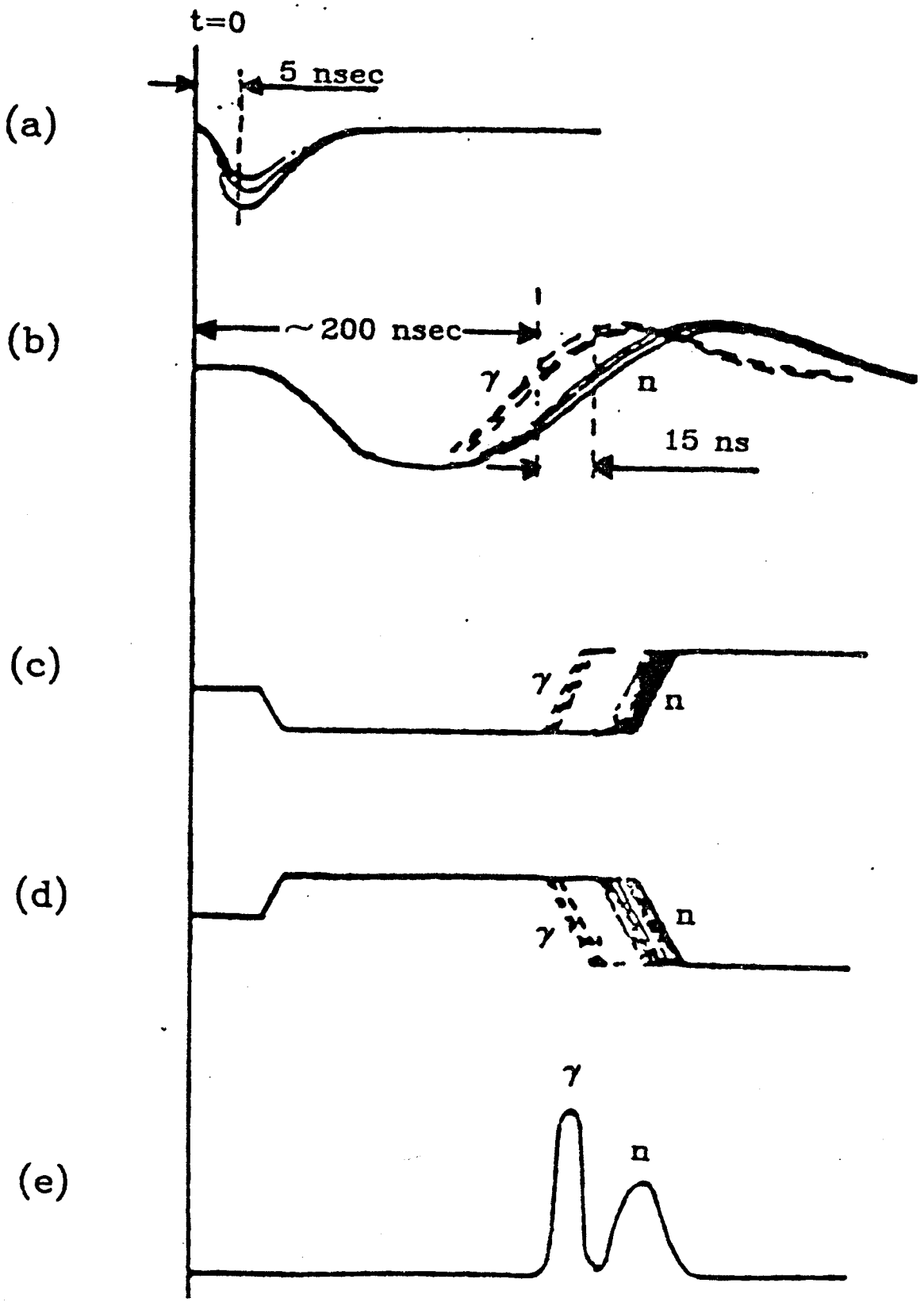

Figure A-11. Neutron--gamma-ray pulse-shape discrimination.

directly into a constant fraction discriminator (CFD). Since neutron and gamma-ray initiated signals do not differ appreciably at their leading edges, the relative time of the output from the CFD for the two signals will be the same. The output of the CFD is then used as the start signal for a time-to-digital converter (TDC) and the stop signal is taken from the output of the PSD. One then sees a clear division between the neutron and gamma-ray induced events as shown in part (e) of Fig. A-11. The separation of neutron and gamma-ray events can be further enhanced by displaying the output from the TDC on the x-axis and the total light output on the y-axis of a two dimensional plot. A contour plot of such a display is shown in Fig. A-12 (Sp 74). Discussion of this two-dimensional method can be found in references On 75 and Pe 79. The advantage of a two dimensional display is that one can set gates that follow the somewhat curved bands corresponding to neutron and gamma-ray events and get a cleaner separation.

Figure A-13 shows two TOF spectra for one of the detectors at the forward-most angle (10°). The top spectrum is for neutron events only, the gamma-ray events having been suppressed with pulse-shape discrimination. The bottom spectrum is for gamma-ray events only, the neutron events having been suppressed. Fig. A-14 is the same display, but it is for a detector at the backward-most angle (160°). The periodic structure is due to accidental coincidences and is discussed in Appendix IV. These spectra are "raw" data,

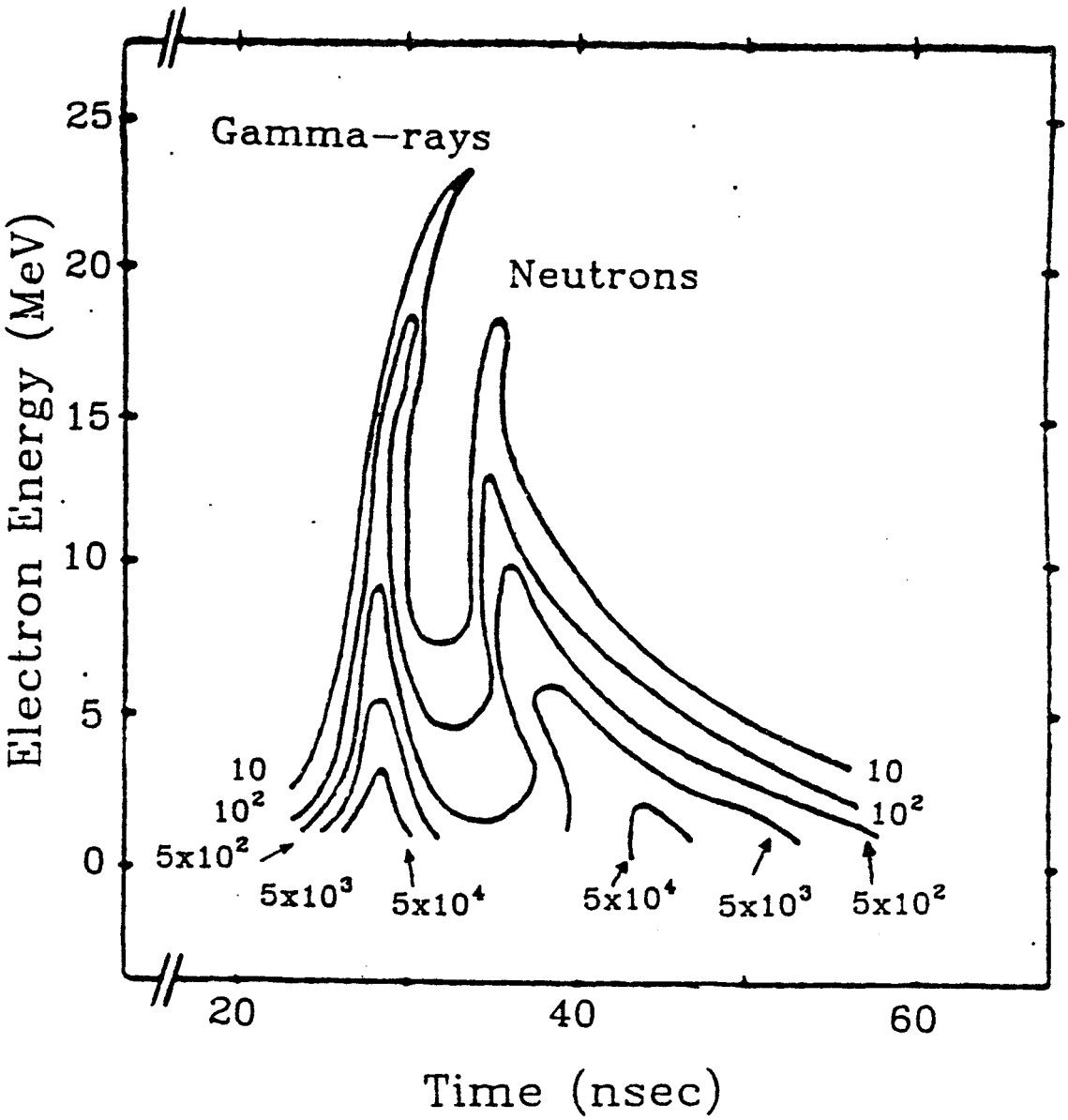

Figure A-12. Two-dimensional pulse-shape discrimination.

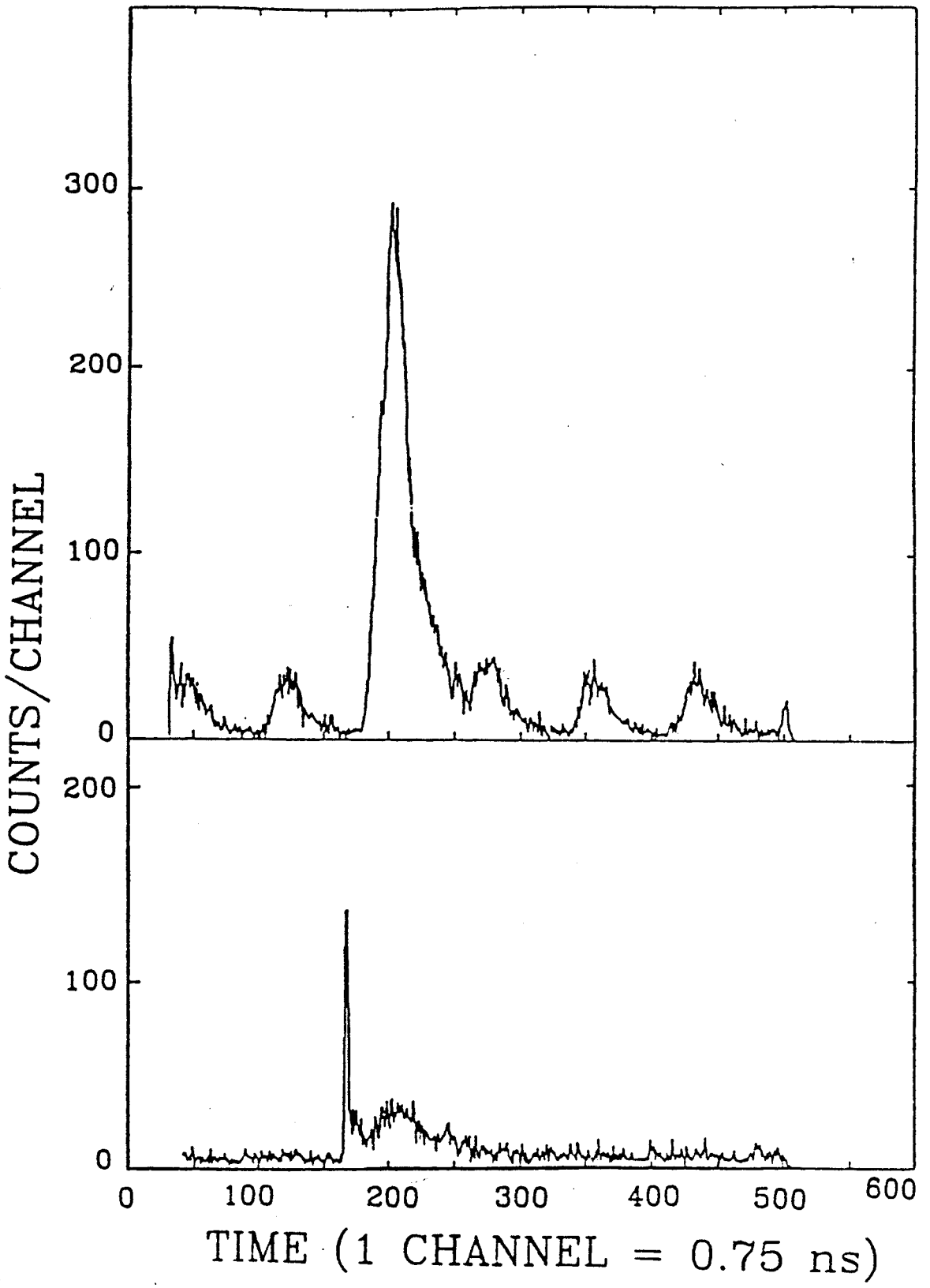

Figure A-13. Neutron and gamma ray TOF spectra at 10°.

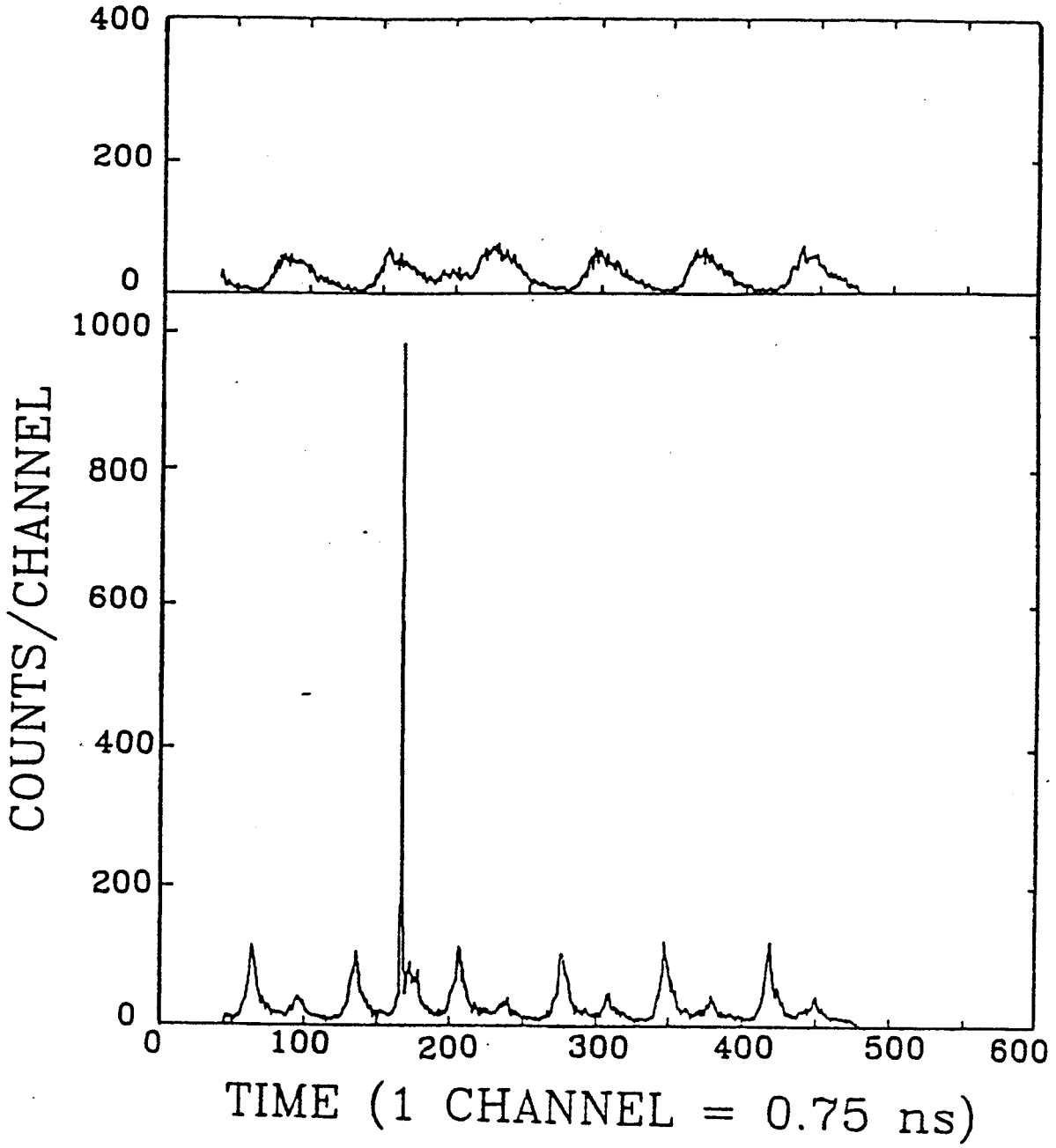

Figure A-14. Neutron and gamma ray TOF spectra at 16°.

having neither the detector efficiency nor attenuation taken into account. The gamma-ray emission is roughly isotropic, whereas the neutron spectra are forward peaked. So neutron events dominate gamma-ray events at the forward angles. But gamma-rays compete strongly with neutron events at the back angles. From these figures one clearly sees the necessity of being able to distinguish between neutron and gamma-ray events.

A third method of differentiating neutrons from gamma-rays uses two QDCs instead of the Canberra 2160 PSD units. Referring to Fig. A-10 again one can set QDC gate G1 across the fast component of the signal and gate G2 across the entire signal. When the outputs from these two QDCs are displayed on a two-dimensional plot, the neutron and gamma-ray events fall into well-separated bands, as shown in Fig. A-15. For this figure, gate G1 was 40 ns long and gate G2 was 1 μs long, and the source used was a Pu-Be neutron source. The gamma-rays from this source are predominantly 4.4 MeV from the decay of the first excited state of ^{12}C to its ground state. The anode pulses were passed through a LR612 photomultiplier amplifier, then into QDCs. The gain of the amplifier was adjusted in this figure so that the Compton edge for the 4.4 MeV gamma-ray was near to full scale. The gain on the amplifier used in Fig. A-15 is good for separating low energy neutrons and gamma-rays, but clearly would saturate for high energy events. In an

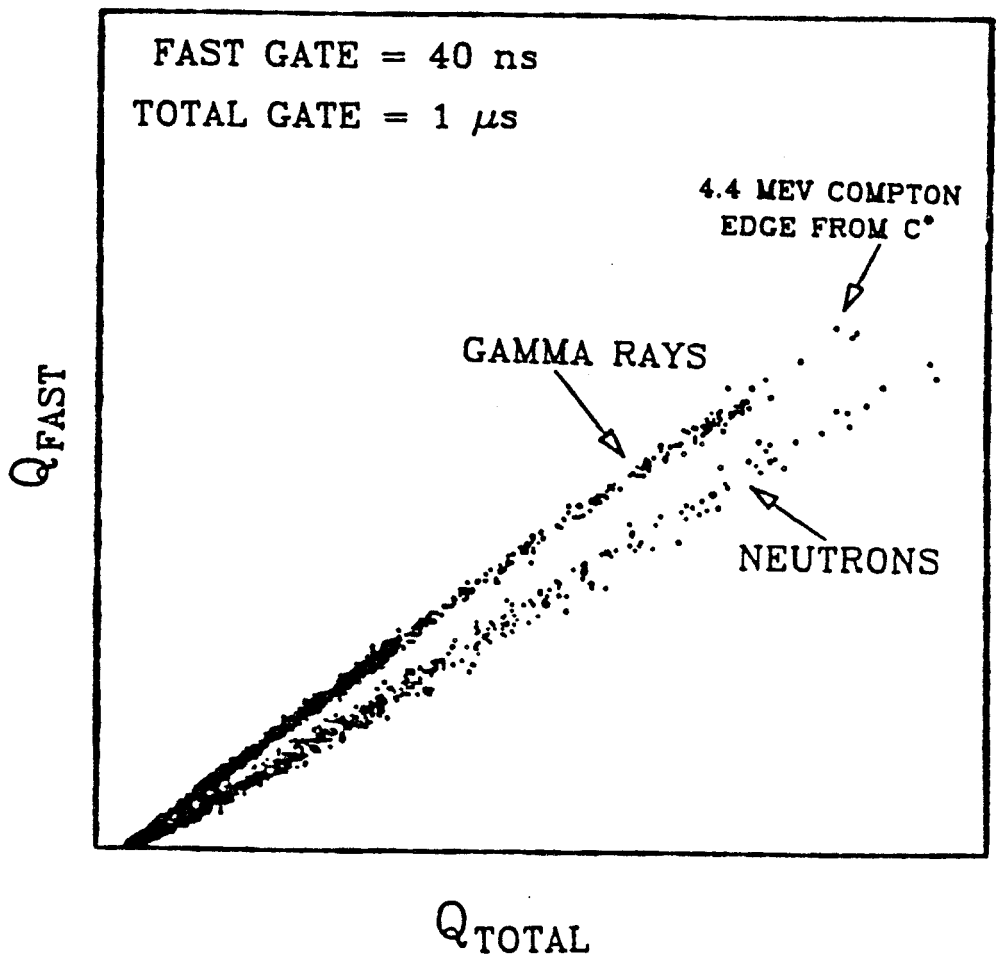

Figure A-15. Pulse-shape discrimination with QCDs.

experiment one has to use a second set of QDCs so that each event can be examined with both a high and a low amplification. One can then clearly separate neutrons from gamma-rays both at low and high energies. This method was recently employed in a neutron-fragment coincidence experiment (Be 85) with very good neutron--gamma-ray separation for both low energy and high energy events.

A-IV. The Method of Time-of-Flight

The method of time-of-flight (TOF) was used in this work to determine the energy of the neutrons. Since neutrons are neutral particles, they deposit energy in a scintillator only through the charged particles resulting from nuclear reactions such as (n,np) or (n,n3α). Therefore the amount of energy they deposit in a scintillating material is not directly proportional to their kinetic energy. But if a scintillation detector is placed at a known distance from the target, then by measuring the time it takes for the neutron to travel from the target to the detector, the velocity, and hence the energy can be determined.

What was recorded experimentally in this work was not the time-of-flight of the neutron directly, but rather the time difference between a "start" signal created in the fragment detector and a "stop" signal in the neutron detector (see Appendix II). From the fragment telescope one obtains a ΔE_f and an E_f signal. Since $\Delta E_f \propto \frac{m_f Z_f^2}{E_f}$, then the ΔE_f and E_f signals together allow one to determine the mass m_f of the fragment. Denoting the recorded time difference between the neutron detector and fragment telescope as Δt and the fragment flight path as ℓ_f, then

$$t = \Delta t + \frac{\ell_f}{(2E_f/m_f)^{1/2}} \quad .$$

Here t is proportional to the time between the occurrence of the nuclear reaction and the detection of the signal in the neutron detector. Note, due to the many delays incorporated in the electronics and due to the intrinsic delays of the modules themselves, t is not the absolute TOF of the neutron.

Figure A-16 shows a prompt gamma peak before and after the correction was made for the fragment flight time. (This figure is for the Ho target for events in the neutron detector at -160° in coincidence with fragments in the Si telescope at -10°.) One sees two striking features in Fig. A-16. First, the prompt gamma peak in the TOF spectrum is shifted to higher channels corresponding to longer neutron flight time after the correction. The amount of shift (- 5.5 ns) represents the average flight time of the fragment. And second, one also notices that the width of the gamma peak after the correction (FWHM = 1 ns) is considerably narrower than before the correction (FWHM = 2 ns). After the correction the width of the gamma peak represents the instrumental time resolution whereas before the correction the spread of the TOF of the various fragments is also included.

One obtains an absolute reference in the TOF spectrum from the position of the prompt gamma-ray peak. Letting Δt

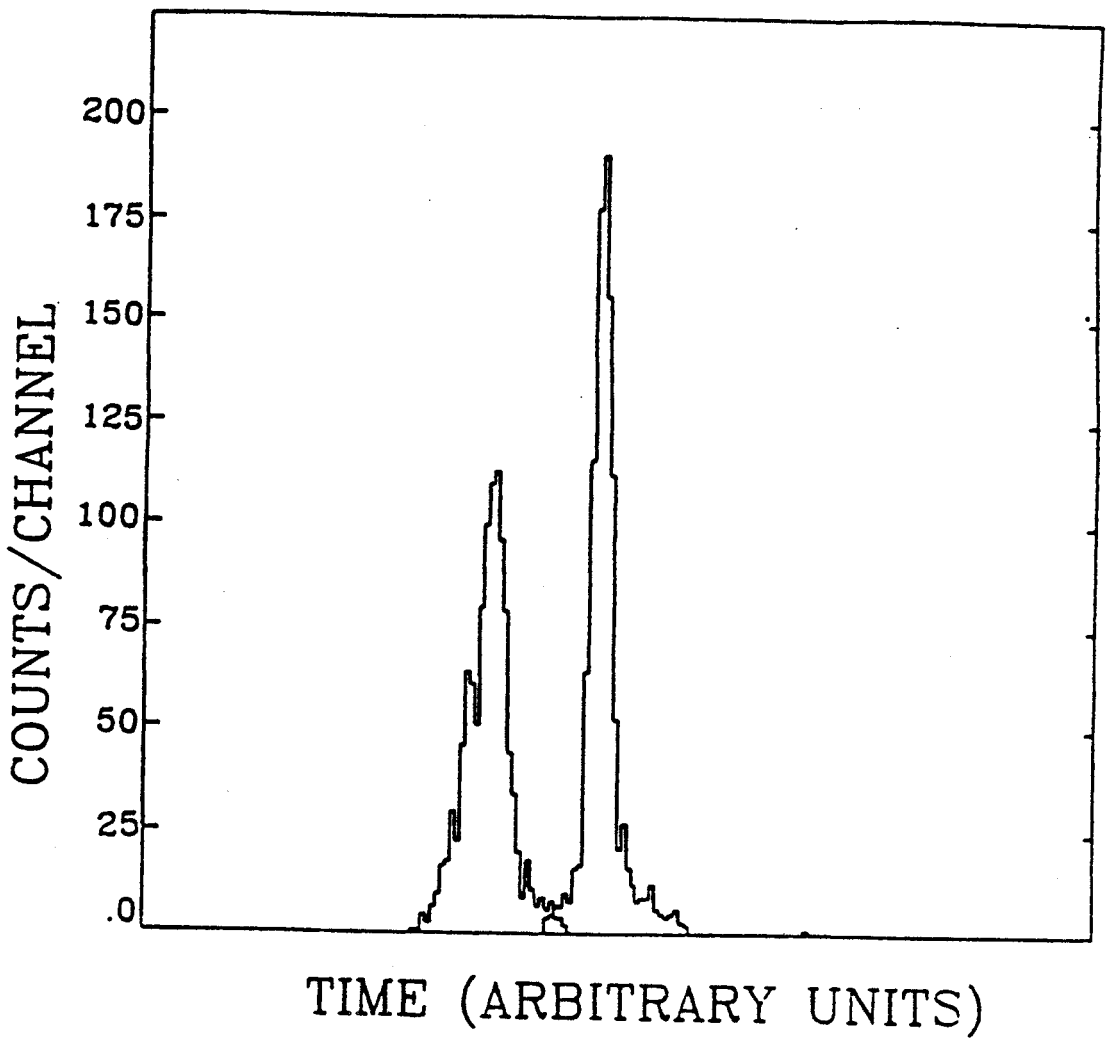

Figure A-16. Gamma-ray TOF peak before and after fragment correction.

be the difference between the TOF of the neutron, t_n, and the centroid of the gamma peak, t_γ, then

$$t_n = \Delta t + t_\gamma \quad ,$$

or

$$t_n = \Delta t + \ell_n/c \quad ,$$

where ℓ_n is the distance from the target to the center of the neutron detector and c is the speed of light. Then converting to kinetic energy, one gets

$$E_n = (\gamma - 1)\, m_n c^2$$

where c is the speed of light in vacuum, m_n is the rest mass of the neutron, $\gamma = 1/(1-\beta^2)^{1/2}$, $\beta = v_n/c$, and $v_n = \ell_n/t_n$. The relativistic formula is used because the beam energy of 490 MeV makes neutrons of over 100 MeV possible. For a 100 MeV neutron the relativistic correction, given by

$$\% \text{ Correction} = \frac{E_{Classical} - E_{Relativistic}}{E_{Relativistic}} \cdot 100\% \quad ,$$

is over 10%.

A-V. Detector Resolution

Two factors contributing to the energy resolution of the neutron detector are the finite thickness of the detector, $\Delta\ell$, and the finite time resolution of the electronics, ΔT. These two parameters are not completely independent of one another, but if one proceeds as if they were, then

$$\left|\frac{\Delta E}{E}\right| = \left\{\left[\left|\frac{\Delta E}{E}\right|\right]^2_{\Delta T} + \left[\left|\frac{\Delta E}{E}\right|\right]^2_{\Delta \ell}\right\}^{1/2}$$

where the subscripts ΔT and $\Delta\ell$ denote the two separate contributions. First, considering the effect of the finite time resolution of the system, a first order Taylor expansion gives

$$\Delta E = \frac{\partial E}{\partial t}\,\Delta T$$

$$\Delta E = \frac{\partial E}{\partial \gamma}\,\frac{\partial \gamma}{\partial \beta}\,\frac{\partial \beta}{\partial t}\,\Delta T \quad ,$$

making use of the chain rule of differentiation. But since $E = (\gamma - 1)\cdot m_n c^2$ gives the neutron kinetic energy, then the first factor in the above equation is

$$-\frac{\partial E}{\partial \gamma} = m_n c^2 \quad .$$

The second and third factors can be written as

$$-\frac{\partial \gamma}{\partial \beta} = \frac{\beta}{(1 - \beta^2)^{3/2}}$$

and

$$-\frac{\partial \beta}{\partial t} = \frac{-\ell}{ct^2}$$

where ℓ is the distance from the target to the center of the detector, t is the TOF of the neutron, and c is the speed of light in vacuum. Combining gives

$$\Delta E = m_n c^2 \cdot \frac{\beta}{(1 - \beta^2)^{3/2}} \cdot \frac{\ell}{ct^2} \cdot \Delta T$$

where the minus sign has been dropped, since it only indicates that β decreases as t increases. Dividing both sides of the above equation by $E = (\gamma - 1) \cdot m_n c^2$ gives, after some algebraic manipulation, the fractional energy resolution due to the finite time resolution ΔT of the circuit to be

$$\left[-\frac{\Delta E}{E}-\right]_{\Delta T} = -\frac{\gamma^3\beta^2}{(\gamma^2-1)}\cdot-\frac{\Delta T}{t}- \qquad (A-1)$$

Now the contribution to ΔE from the finite thickness of the detector, $\Delta \ell$, will be derived. Consider two monoenergetic neutrons incident upon the neutron detector, one interacting with the scintillator and creating a light pulse at the front face and the other at the back face. The time difference in the pulses arriving at the photocathode of the photomultiplier tube is given by

$$\Delta t = \Delta \ell \cdot \left(-\frac{1}{v_n}- - -\frac{n}{c}-\right)$$

where n is the index of refraction of the liquid scintillator, and v_n is the velocity of the neutron. Dividing both sides of the above equation by t and rearranging the right side gives

$$-\frac{\Delta t}{t}- = -\frac{\Delta \ell}{\ell}-\cdot(1 - n\beta)$$

where $\beta = v_n/c$. But equation A-1 relates time resolution to energy resolution, so,

$$\left(-\frac{\Delta E}{E}-\right)_{\Delta \ell} = -\frac{\gamma^3\beta^2}{(\gamma^2-1)}\cdot(1 - n\beta)\cdot-\frac{\Delta \ell}{\ell}- \qquad (A-2)$$

Combining the above two effects (equation A-1 and A-2) in quadrature gives

$$-\frac{\Delta E}{E}- = \frac{\gamma^3\beta^2}{(\gamma - 1)}\cdot\left\{\left(-\frac{\Delta T}{t}-\right)^2 + (1 - n\beta)^2\cdot\left(-\frac{\Delta \ell}{\ell}-\right)^2\right\}^{1/2} \qquad (A-3)$$

In the limit of nonrelativistic neutrons, this reduces to

$$-\frac{\Delta E}{E}- = 2\cdot\left\{\left(-\frac{\Delta T}{t}-\right)^2 + (1 - n\beta)^2\cdot\left(-\frac{\Delta \ell}{\ell}-\right)^2\right\}^{1/2} \qquad (A-4)$$

The actual energy resolution is slightly better than that predicted by equations A-3 and A-4. This is because the contribution due to the time uncertainty of the system and that due to the finite thickness of the detector are not completely independent effects, as adding in quadrature assumes. Also, in deriving the time uncertainty due to the finite thickness of the detector, the entire thickness was used as $\Delta\ell$, whereas something equivalent to a standard deviation should be used. In addition, for the scintillation occurring at the front face, the photons were assumed to travel in a straight line to the photocathode. However, one should use the average distance traveled by all photons reaching the photocathode. The net result of all the above mentioned effects is that the observed energy resolution is slightly better than the predicted value.

A-VI. Data Reduction

The neutron was "timed against" the light fragment (LF), with the flight time of the fragment corrected for off-line. Figure 6 (in the main text) shows such a corrected neutron time-of-flight (TOF) spectrum in various stages. The top plot shows the raw data. The dominating peak corresponds to prompt coincidences between neutrons and fragments arising from nuclear reactions within the same beam burst. The periodic structure on either side of the prompt coincidence peak corresponds to accidental coincidences between fragments and neutrons created in reactions from different beam bursts. The time gates of the TDCs were set at approximately 350 ns to allow five or six such accidental coincidence peaks. The prompt peak contains coincidence events due to fragments and neutrons from different reactions within the same beam burst. Therefore, the periodic structure of the neighboring accidental-coincidence neutrons is extended under the prompt peak (shown in the figure as circles) and subtracted out. The resulting spectrum is shown as the plot in the middle of Fig. 6. In addition to accidental coincidences, there are true coincidence events where instead of traveling undisturbed into the neutron detector, the neutron scattered off the floor or elsewhere. Since one cannot know the correct energy and angle of such a scattered neutron, their contributions (represented by triangles in the figure) are

measured by taking data with shadow bars in place. The shadow bar data is then scaled to the non-shadow bar data by the ratio of the dead-time corrected integrated beam current, then subtracted out. The length of time that data is taken with the shadow bars in place compared to that taken without shadow bars affects the statistical quality of the "true" TOF spectra. If T_1 and T_2 correspond to the length of time spent taking data with and without shadow bars, respectively, then the optimum sharing of beam time is given by

$$\frac{T_1}{T_2} = \left\{ \frac{R_1}{R_2} \right\}^{1/2}$$

Here R_1 and R_2 are the data acquisition rates with and without shadow bars, respectively. This relation is derived in Appendix VIII.

The final "true" TOF spectrum is shown at the bottom of Fig. 6. Using the position of the gamma-ray peak, indicated by an arrow in the figure, one can then transform TOF to neutron energy, as discussed in Appendix IV. The only quantity needed to do this is the calibration of the TDCs in, say, ns/channel. The periodic structure of the accidental coincidences was used to calibrate the neutron detector TDCs. The period of the accidental coincidence "peaks" is simply that of the rf of the cyclotron, which was

52.65 ns for this experiment. Since the period in channels of the accidental coincidences can be derived from the raw TOF spectra,one has a ready conversion from channels to nanoseconds. If one looks at the periodic behavior of the accidental coincidences with a gate on gamma-rays instead of neutrons, as shown in Fig. A-17, then one has an even sharper determination of the period of the cyclotron in channels. Both the neutron and gamma-ray TOF spectra were used in extracting the calibration of the TDCs. After transforming the neutron TOF to energy, one then has to transform the yield. To do this one uses conservation of counts per bin:

$$(Ht_1)(Width_1) = (Ht_2)(Width_2) \quad ,$$

where Ht_1 and $Width_1$ are the bin height and width in the TOF spectrum and Ht_2 and $Width_2$ are the same in the energy spectrum. To obtain yield, one only has to divide Ht_2 by the efficiency of the neutron detector at that energy, i.e.,

$$Yield(E) = Ht_2(E)/EFF(E) \quad .$$

The neutron detector efficiency can be calculated to an accuracy of better than or equal to 10% with a program called TOTEFF by R.J. Kurtz (Ku 64) or a Monte Carlo program

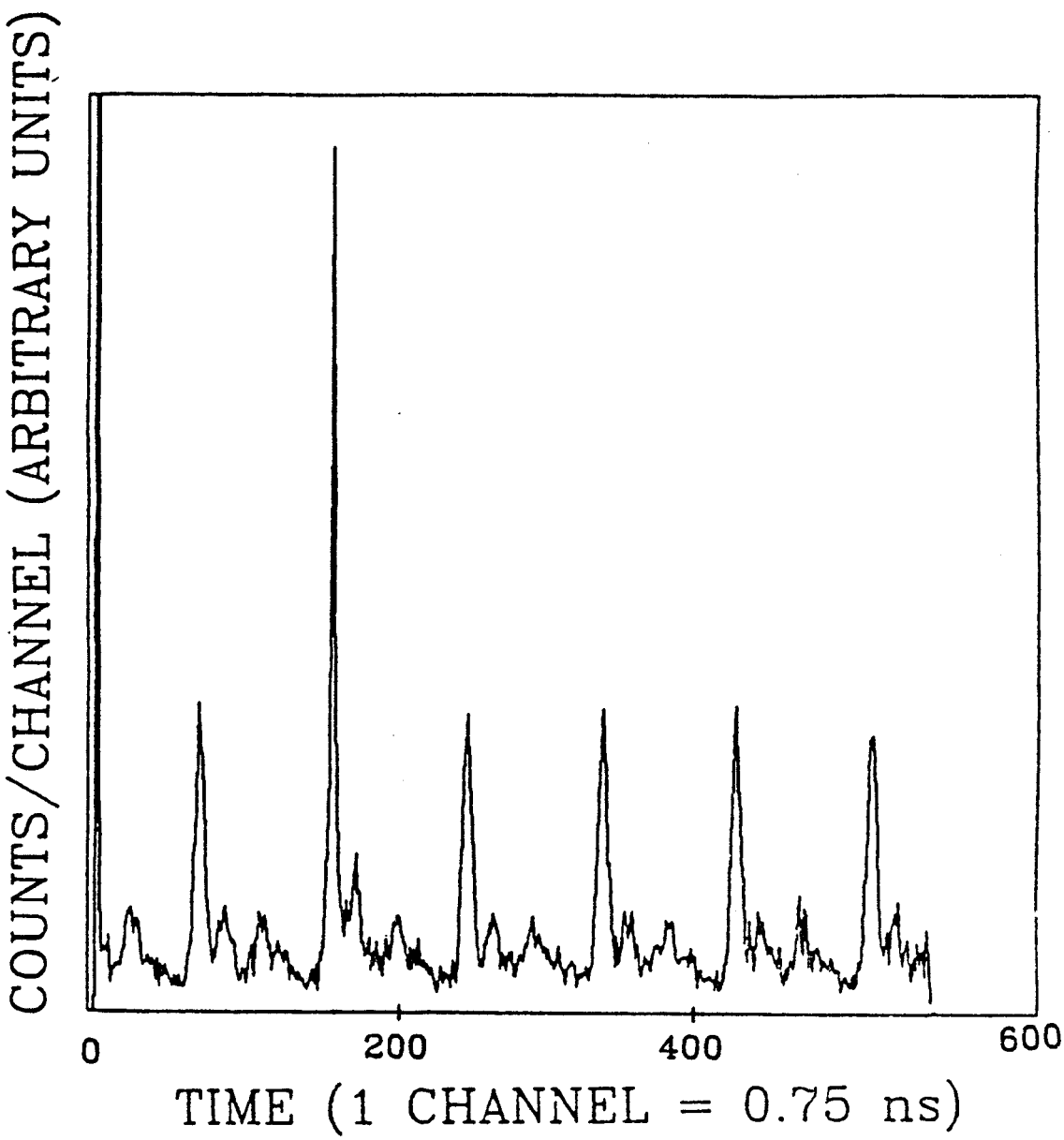

Figure A-17. Accidental coincidences in gamma-ray TOF spectrum.

written by Cecil et al. (Ce 79). A typical curve showing neutron efficiency as a function of energy calculated by both methods is shown in Fig. A-18 for the detector at 110° (to the right when facing the beam dump). The Monte Carlo result has had the attenuation function (see Appendix VII) folded in, whereas the TOTEFF calculation has not. Therefore, one can see that the two calculations agree well with one another and that the level of attenuation was small.

Both calculations require as input the detector threshold in equivalent electron energy. One could in principle state the detector threshold in terms of the lowest energy neutron detectable. Since neutrons are detected mainly through the proton resulting from n-p scattering, one could determine the neutron threshold energy by determining the lowest proton energy detectable. This would require some source of low-energy, monoenergetic protons, like a small accelerator. A much more convenient means of finding the detector threshold is through the use of gamma-ray sources. Gamma-rays are detected through the electron resulting from Compton scattering, so one can determine the lowest energy electron detectable. This can be related to the lowest energy proton (and hence neutron) detectable, as discussed in references Ve 68, Ta 70, but this correspondence has already been incorporated into the efficiency codes of Kurz (Ku 64) and Cecil et al. (Ce 79). One needs to determine the detector threshold only in

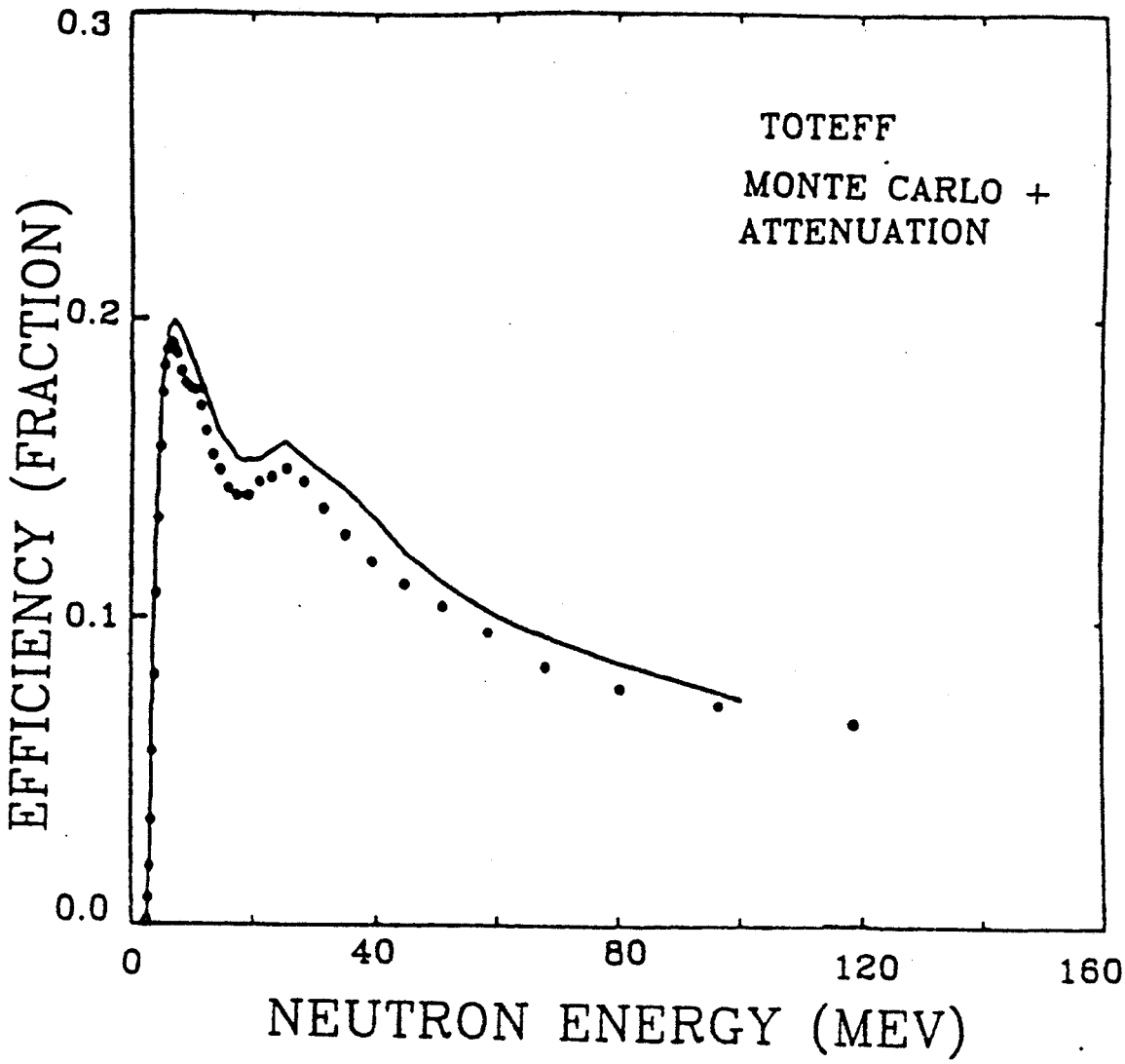

Figure A-18. Neutron detector efficiency calculations.

equivalent electron energy. The efficiency curve presented in Fig. A-18 had the threshold set at the Compton edge of a ^{60}Co gamma-ray source, i.e., 1.05 MeV equivalent electron energy.

We note here that in this experiment the prompt gamma-ray centroids shifted systematically to larger channel as the experiment progressed. Presumeably this is an indication that the charge collection time was affected as radiation damage developed within the Si crystals. So the centroids extracted by fitting the prompt gamma-ray peaks (with a Gaussian function with exponential tails) were beam-time dependent. Maximum shifts in gamma-centroid of about 1 ns from the beginning to the end of the experiment were observed.

A-VII. Corrections Applied to the Spectra

When one measures neutrons with the time-of-flight (TOF) technique, to ensure an acceptable energy resolution of the data, the neutron detectors cannot be placed too close to the target (see Appendix IV). In this experiment the flight path varied from 1.14 to 2.42 m. Necessarily, then neutrons detected in a detector have first passed through various materials like the 1/8" steel chamber wall, approximately 1.5 m of air, the 6 mm NE102A proton veto paddle, the 1/8" aluminum detector housing, and the 1/8" glass cell wall. Hence the neutron spectra contain distortions due to absorption and scattering, and these distortions should be corrected for. It is useful to divide the correction into an absorption and outscattering effect and an inscattering effect, as depicted in Fig. A-19. Outscattering means that neutrons created in the nuclear reaction and initially traveling towards a detector are scattered out of their path and are not detected in that detector. Fig. A-4 shows the telescope arrangement inside the chamber. The shaded regions represent the solid angles subtended at the target by the two neutron detectors at ±10°, i.e., the regions of outscattering due to the telescopes.

Inscattering, on the other hand, means that neutrons not initially moving towards a given detector are by some sequence of scattering (off the floor, chamber wall,

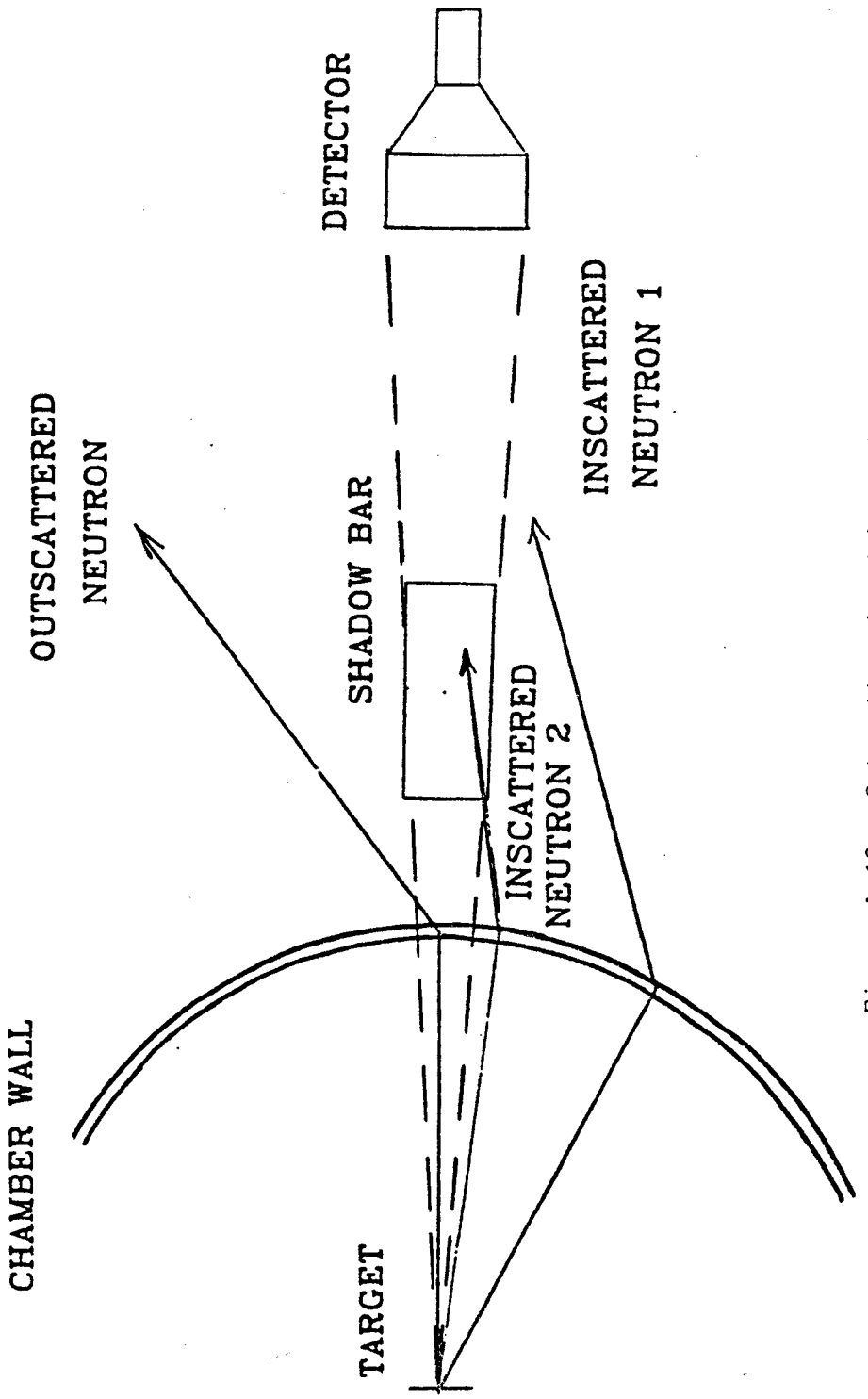

Figure A-19. Outscattered and inscattered neutron.

detector housing) detected in that detector. Inscattered neutrons are typically called background neutrons, and the standard technique for dealing with them is through the use of shadow bars. The placement of all shadow bars was approximately midway between the target and the detector in an attempt to minimize the added distortions the shadow bar itself can introduce to the neutron spectra. Transmission through the shadow bar as a function of neutron energy was studied (see the discussion below) and found to be negligible for the thicknesses of brass and steel chosen. The shadow bars used were 30 cm long by 7.62 cm diameter brass cylinders except at the forward angles where we had 41 cm long brass cylinders at ±30° and 46 cm long tapered steel cylinders at ±10°.

To make correct positioning of the shadow bar possible, the diameter of the bar was chosen such that at the target it subtended a solid angle slightly larger than that of the neutron detector. This "overshadowing" is greatest at the end of the shadow bar nearest to the target and smallest at the end nearest to the neutron detector. Due to "overshadowing" some of the "bad" or inscattered neutrons were also shadowed and not recorded during the shadow bar run of the experiment. Therefore, when the shadow bar data is subtracted from the raw data, these scattering events will not be subtracted out. The data must be corrected for these events, then, with a calculation.

The starting point for both the outscattering and inscattering correction calculations is the relation

$$N = N_o \, e^{-n\sigma_T x} \quad , \qquad (A-5)$$

where N_o is the number of neutrons/sec incident upon a thickness x of material and N is the number/sec transmitted. Here n is equal to the number of nuclei/cm^3 in the material and σ_T is the total neutron interaction cross section. Equation A-5 can be derived as follows. Let N neutrons/sec be incident upon a thickness dx of material, and let dN neutrons/sec undergo any type of interaction. Then the defining relation for total cross section, σ_T, is

$$dN = - \frac{N}{A} (n \cdot dx \cdot A) \sigma_T$$

$$dN = -N \cdot n \cdot dx \cdot \sigma_T$$

where A is the cross-sectional area of the bombarded material, and N/A is the incident flux of neutrons (i.e., number/(sec·cm^2)). Then (n·dx·A) is the total number of target nuclei in thickness dx that "see" the beam. The negative sign is to show that dN neutrons/sec are removed

from the incident flux, not added to it. Rearranging the above relation gives

$$-\frac{dN}{N} = n\sigma_T dx \quad ,$$

and integrating over the thickness, x, of the scattering material gives

$$\ell n\ N = -n\sigma_T x + \text{const}$$

After some rearranging this then gives the desired relation:

$$N = e^{-n\sigma_T x + \text{const}} \quad ,$$

or

$$N = N_o\, e^{-n\sigma_T x} \qquad \text{(A-5)}$$

where N_o corresponds to the incident neutrons/sec.

First the outscattering correction calculation will be discussed. Using eq. A-5, one can write down the neutrons/sec undergoing any type of interaction in thickness x of material as

$$N_{int} = N_o(1 - e^{-n\sigma_T x}) \quad .$$

But of those neutrons that interact,

$$N_{e\ell} = N_o(1 - e^{-n\sigma_T x})(\Delta\sigma_\ell/\sigma_T)$$

are the neutrons that elastically scatter through such a shallow angle that they still enter the detector. Here $\Delta\sigma_{e\ell}$ is given by

$$\Delta\sigma_{e\ell} = \int_{\theta=0}^{\theta_o} \frac{d\sigma_{e\ell}(\theta)}{d\Omega} 2\pi\sin\theta d\theta$$

and θ_o is the angle subtended by the edge of the neutron detector at the scattering material in question. To simplify the notation, we define F and f as

$$F = N/N_o$$

$$f = e^{-n\sigma_T x} \quad .$$

where N corresponds to the actual neutrons/sec detected and N_o to ideally what should have been detected had there been

no scattering or absorption. Considering both those neutrons transmitted through thickness x with no interaction and those elastically scattered through a small angle $\theta \leq \theta_o$, one can write down the fraction of neutrons detected as

$$F = f + (1 - f)(\Delta\sigma_{e\ell}/\sigma_T) \qquad (A-6)$$

If the scattering material is close to the neutron detector, it is possible that a neutron can inelastically scatter or undergo an (n,n'), (n,2n), (n,nα), or (n,p) interaction and still create a signal in the detector with a time-of-flight nearly the same as that of the original neutron. So the above cross sections, where available, have been included, and entered into the equation as follows:

$$F = f + (1 - f)\Delta\sigma_{e\ell}/\sigma_T + \sum_i (1 - f)\Delta\sigma_{T_i}/\sigma_T$$

where the sum over i runs over the above interactions for a scattering material close to the detector. This, so far, is for only a single outscattering material and considers only the outscattering correction. If there were J outscattering materials in the path of the neutrons going to a given detector, then the final result would be the product of their individual fractional contributions, i.e.,

$$F = \prod_{j=1}^{J} F_j$$

where F_j would be the fraction detected if there existed only the jth outscattering material.

The derivation for the inscattering contribution develops in a similar fashion. One has to calculate the inscattering effect from objects which are not included in subtraction of the shadow bar data due to overshadowing. The inscatterers contained in the overshadowed region are relatively far from the detectors. So inelastic scattering can be neglected and only elastic scattering need be considered.

Consider first just a single such inscatterer. If N_o is the neutron flux contained in the solid angle subtended at the target by the neutron detector, then let AN_o be the flux contained in the solid angle subtended by the inscatterer, where A is a scaling parameter. If the angular distribution of the incident neutrons is neglected, then A is just the ratio of the solid angle subtended by the inscatterer to the solid angle subtended by the neutron detector. If the inscatterer in question is of thickness x, has n nuclei/cm^3, and total cross section σ_T, then

$$N_{int} = AN_o(1 - e^{-n\sigma_T x})$$

is the number of neutrons undergoing any type of interaction. The probability that an interacting neutron elastically scatters into the detector can be written as $\Delta\sigma_{e\ell}/\sigma_T$, where

$$\Delta\sigma_{e\ell} = \frac{d\sigma_{e\ell}(\theta_o)}{d\Omega}\,\Delta\Omega \quad .$$

Here θ_o is the angle through which the neutrons must scatter from the inscatterer to move on a path towards the neutron detector, and $\Delta\Omega$ is the solid angle subtended by the detector at the inscatterer. So

$$N_{e\ell} = AN_o(1-e^{-n\sigma_T x})\Delta\sigma_{e\ell}/\sigma_T$$

gives those neutrons that scatter elastically from the inscatterer on a path towards the neutron detector. Finally, let F_{attn} be the attenuation factor resulting from the material between the target and the inscatterer and between the inscatterer and the neutron detector. F_{attn} is calculated in the same way as F in the outscattering calculation. The fraction of N_o neutrons detected at the detector due to inscattering can then be written as

$$F_{in} = N_{e\ell}/N_o$$

$$F_{in} = F_{attn} A(1 - e^{-n\sigma_T x})(\Delta\sigma_{e\ell}/\sigma_T)$$

So far this assumed a single inscatterer. For J inscatterers, the total fraction inscattered is just the sum of the individual contributions, i.e.,

$$(F_{in})_{total} = \sum_{j=1}^{J} (F_{in})_j$$

where $(F_{in})_j$ is the fraction due to the jth inscatterer.

If F_{in} is the total fraction of N_o neutrons arriving at the detector due to inscattering, then the final equation for the fraction of N_o neutrons detected in the detector is

$$N/N_o = F + F_{in} \quad .$$

N is the detected neutron flux and N_o is the desired undistorted flux. So the neutron energy spectra (after subtraction of shadow bar and accidental coincidence data) have to be multiplied by the energy dependent scaling factor

$$\text{scaling factor} = \frac{1}{F + F_{in}} \quad .$$

This calculation was carried out for each of the ten neutron detectors, and the results are displayed in Fig. A-20. Detectors 1, 3, 5, 7 and 9 in the figure titles refer to angles of 10°, 30°, 70°, 110° and 160°, respectively on the left side of the beam (when facing downstream). Detectors 2, 4, 6, 8 and 10 refer to the same angles on the right side of the beam. The scaling factors are energy dependent but typical values range from 80% detected for the low energy neutrons to 94% for the high energies for all the detectors except at ±10°. The largest corrections were for the two detectors at ±10°, with the results ranging from about 50% for low energy neutrons to 80% for high energy neutrons. Outscattering is the major contribution to the correction calculation, as can be seen in Fig. A-21 for the neutron detectors at 10° to the left of the beam. In this figure the squares are the correction calculation neglecting inscattering and the circles are the final results when both outscattering and inscattering are considered.

The basic shape of the correction curves can be understood by examining the total cross section curve. All neutrons detected have passed through at least the 1/8" steel chamber wall and the 6 mm thick NE102A proton veto detector. Figure A-22 displays total cross section and its elastic and nonelastic components for iron and carbon. The overall rise of the correction curve is the result of the overall decrease in total cross section as a function of energy exhibited by all of the scattering materials. The

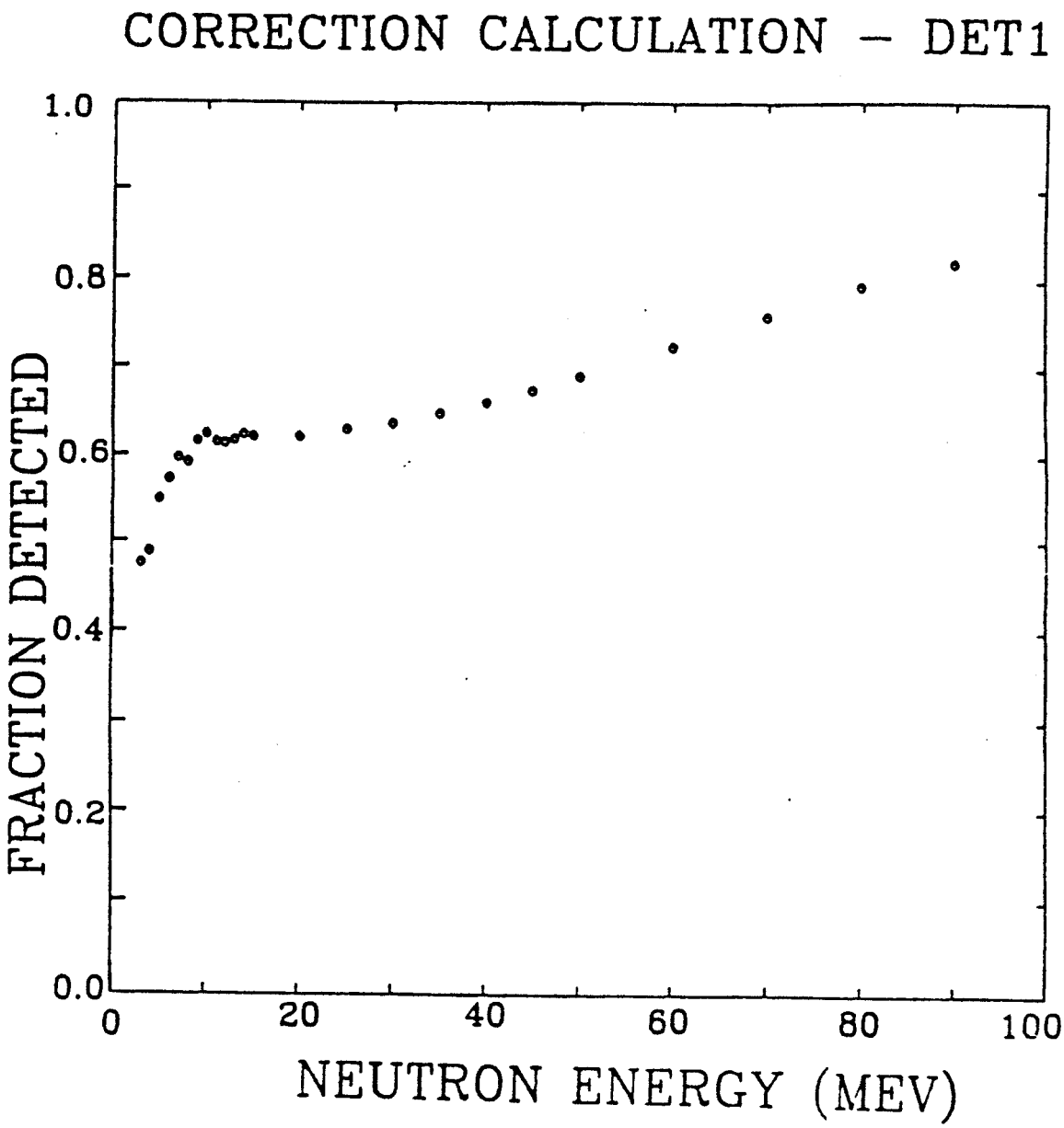

Figure A-20. Correction calculations for the ten neutron detectors.

Figure A-20. (continued)

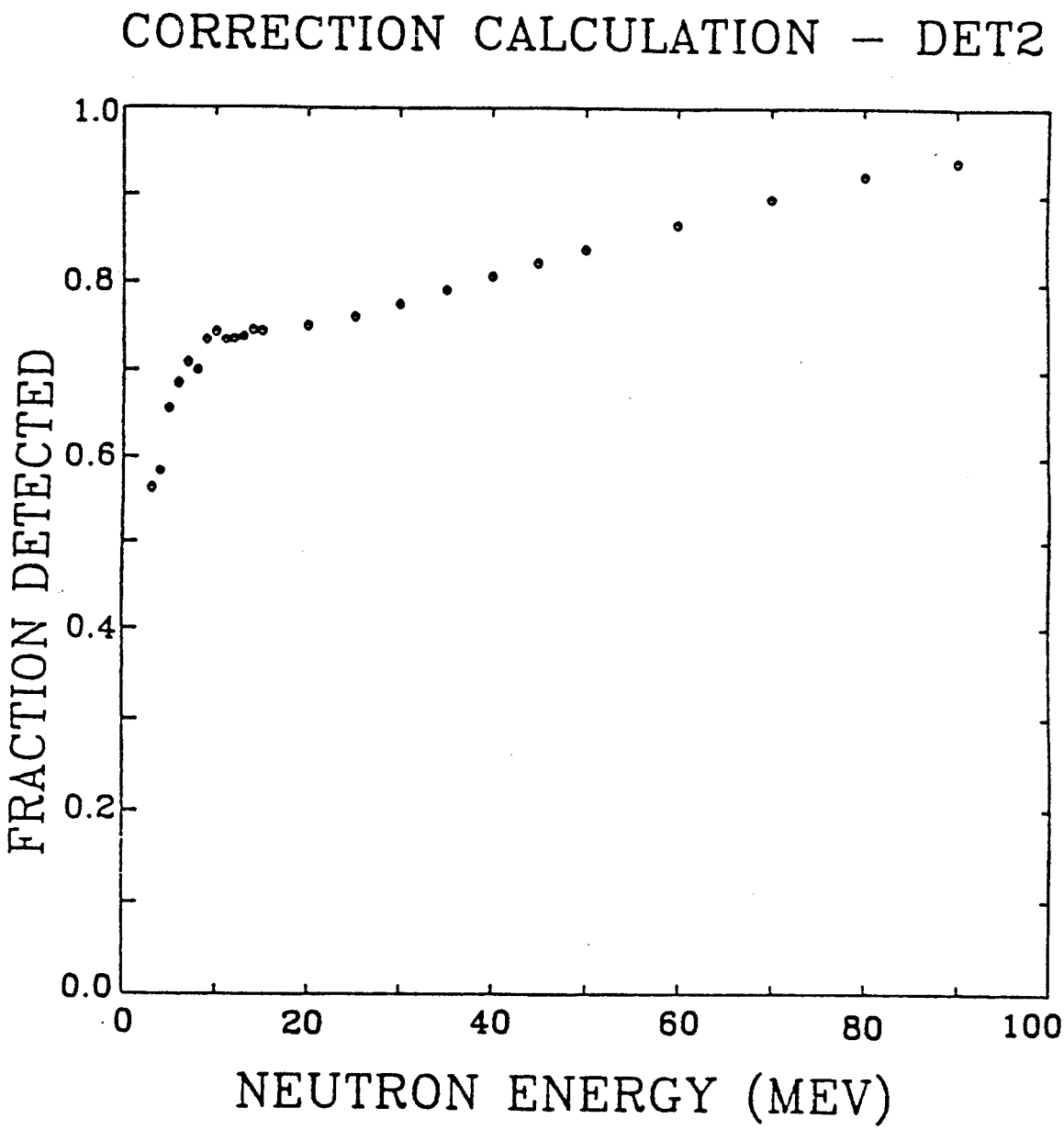

Figure A-20. (continued)

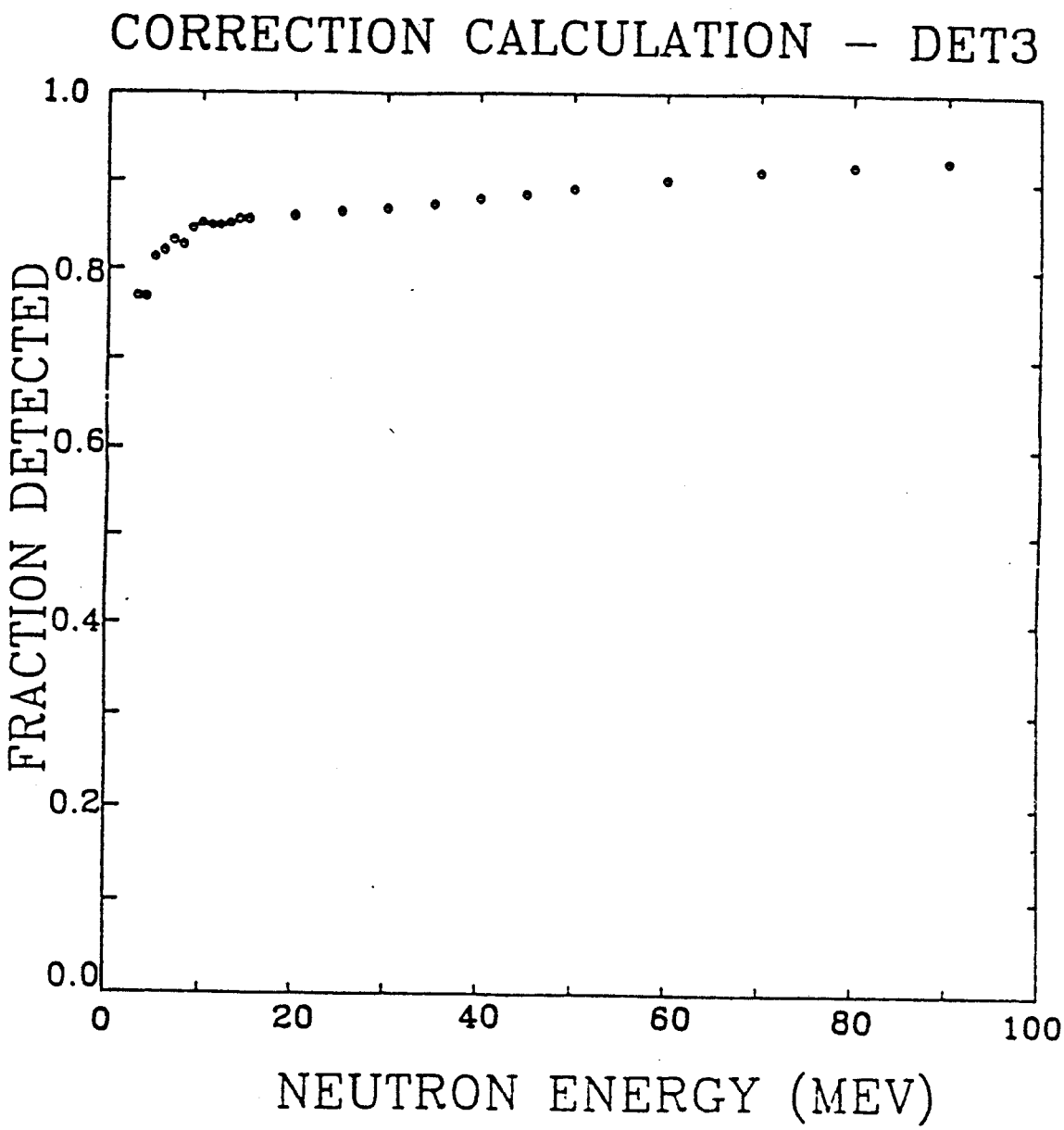

Figure A-20. (continued)

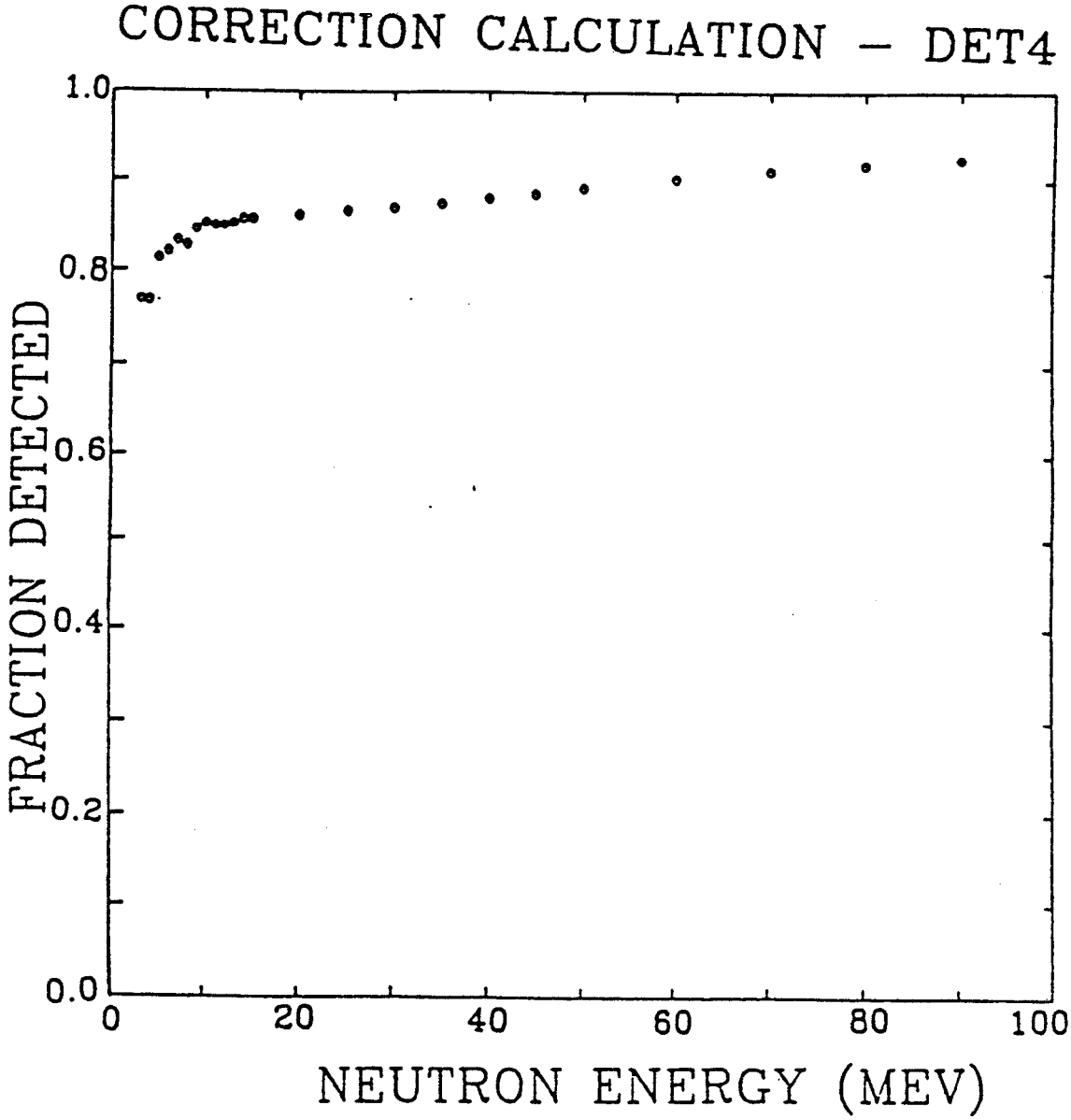

Figure A-20. (continued)

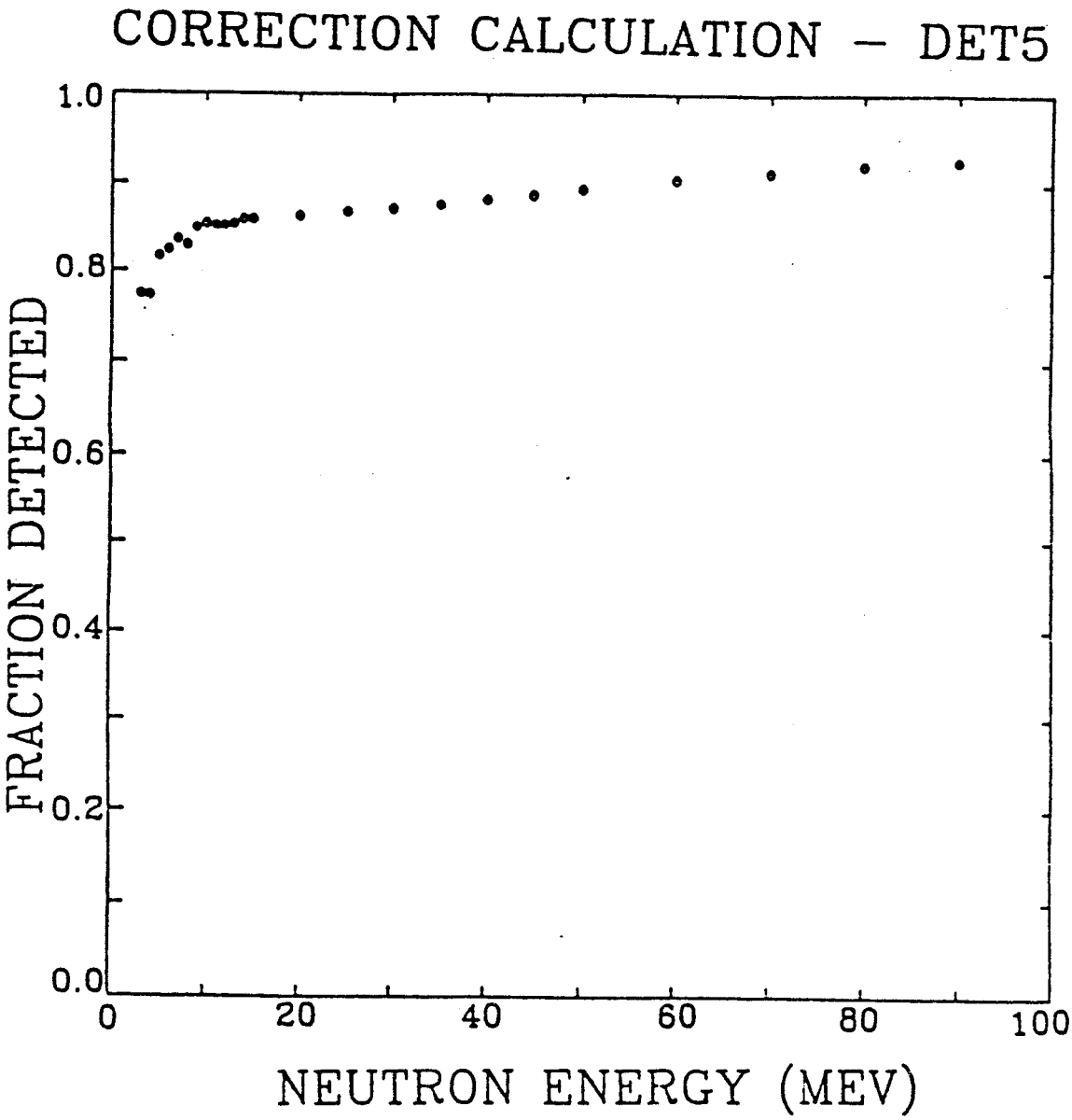

Figure A-20. (continued)

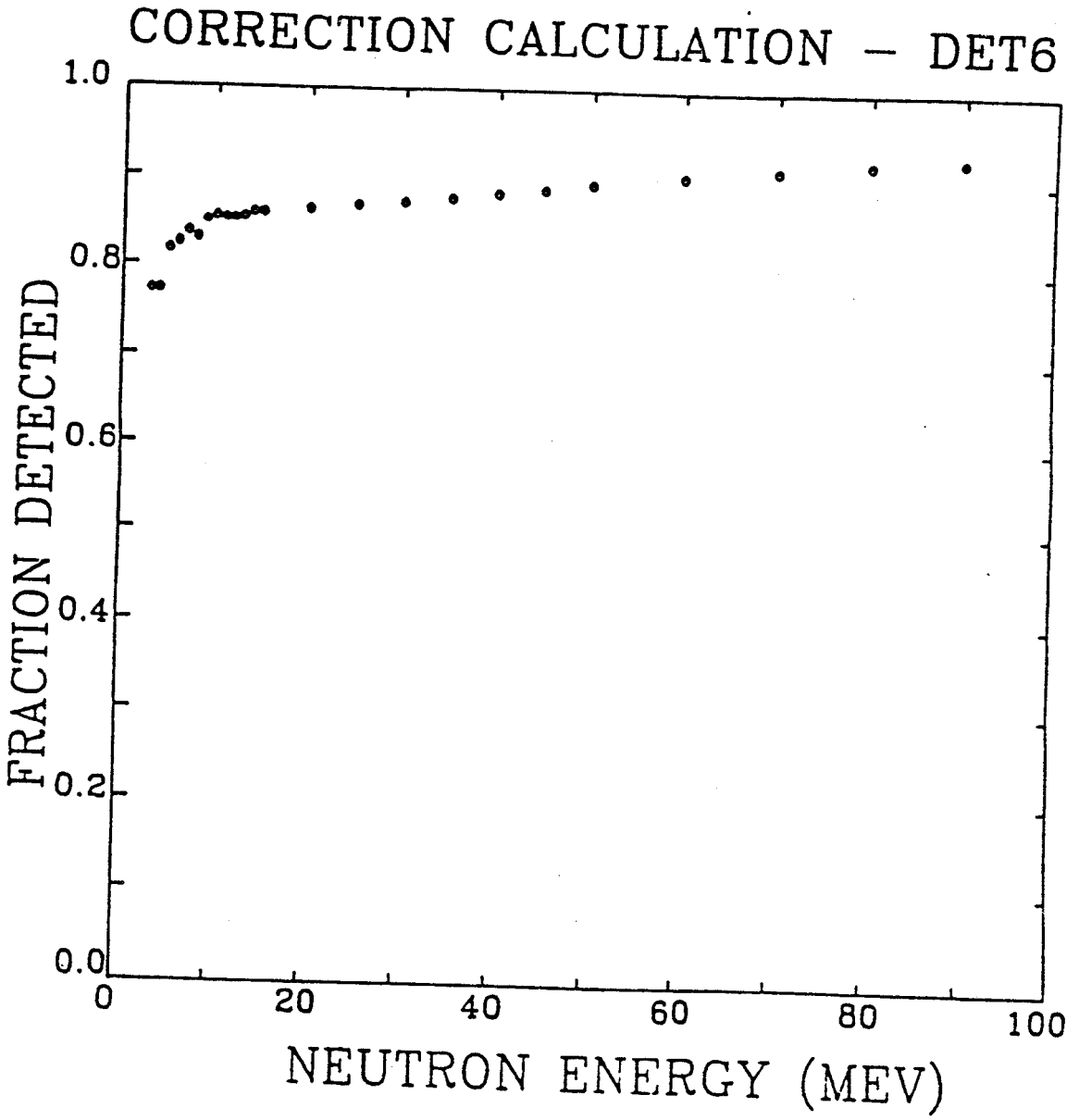

Figure A-20. (continued)

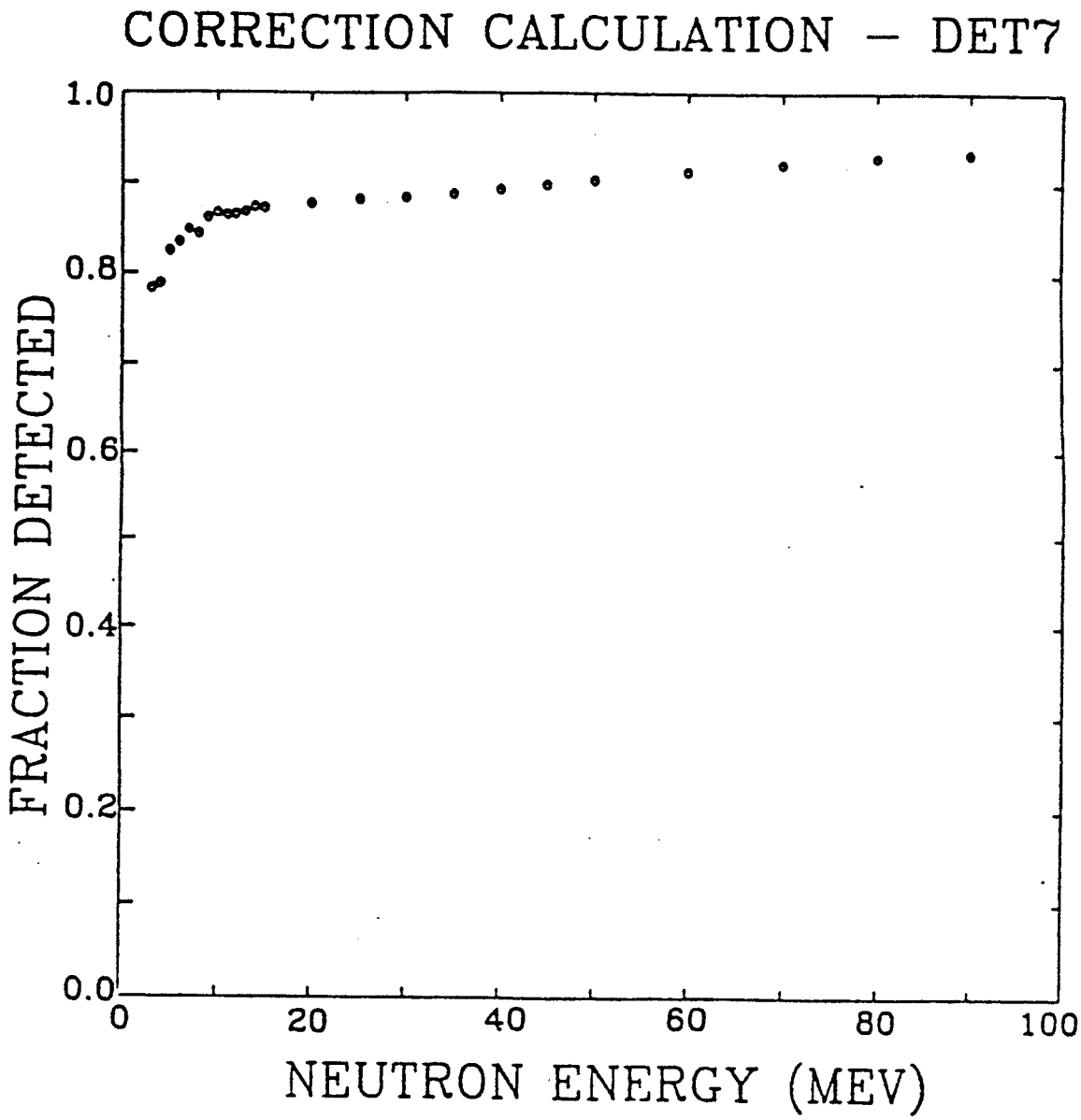

Figure A-20. (continued)

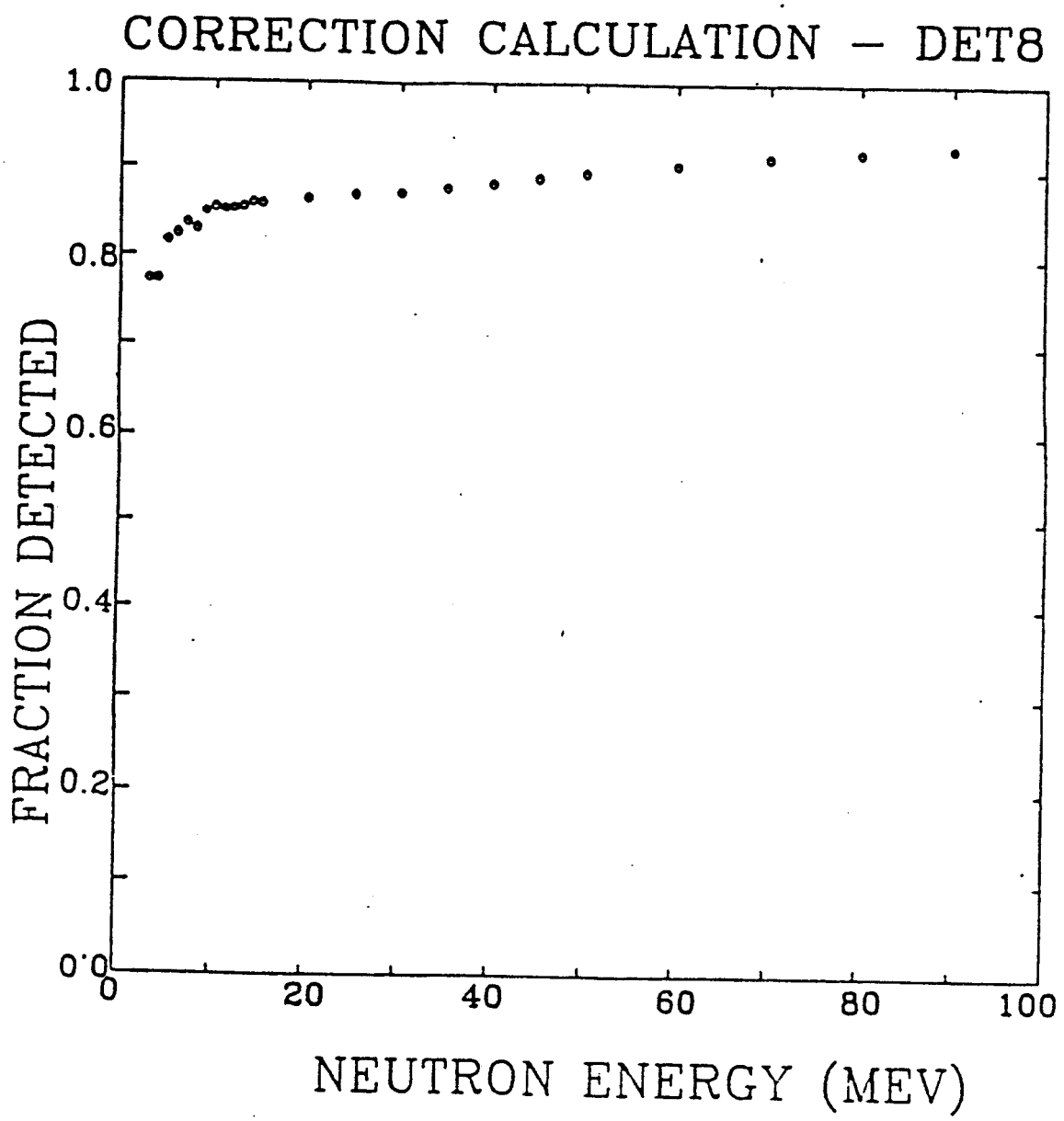

Figure A-20. (continued)

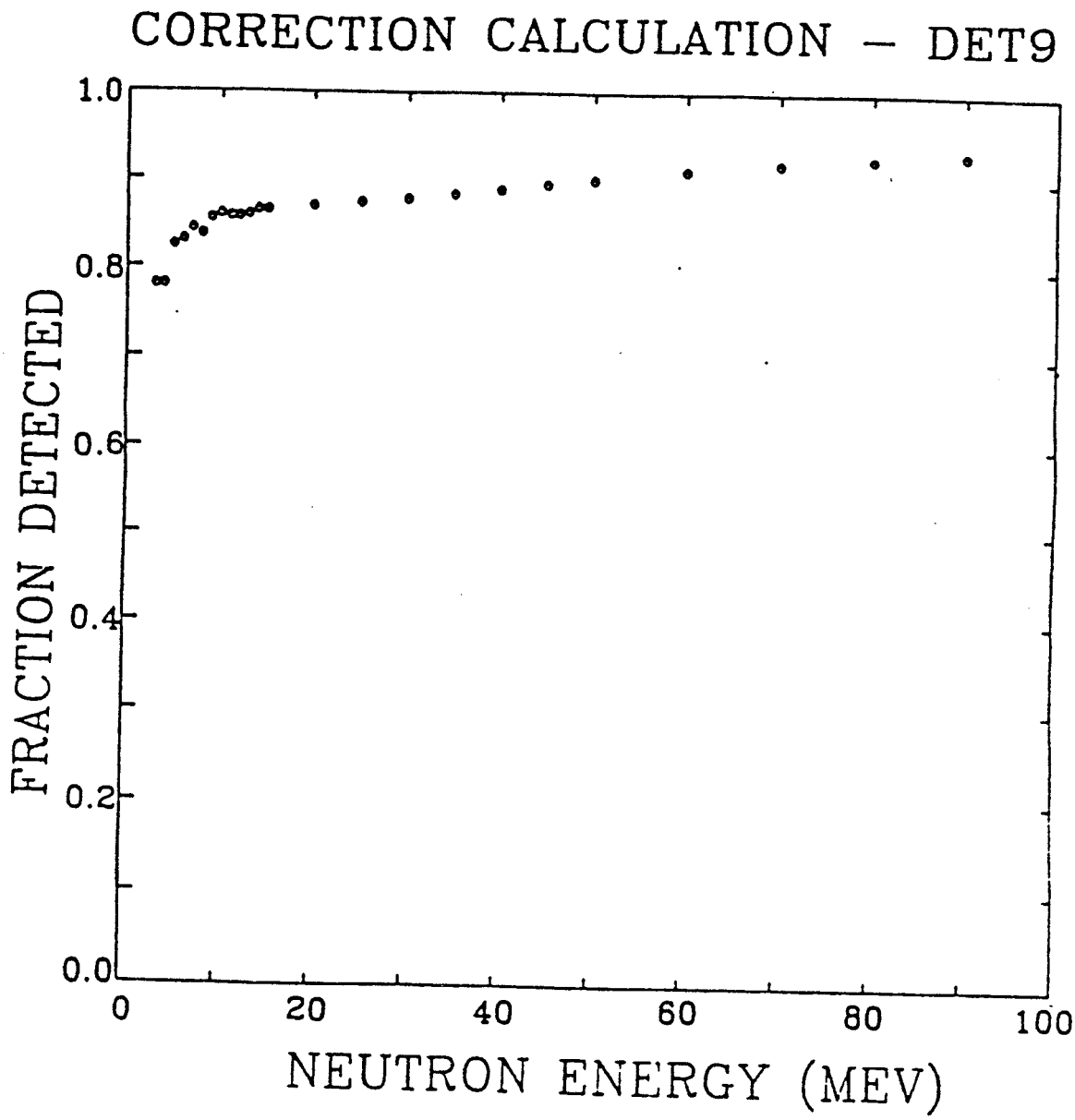

Figure A-20. (continued)

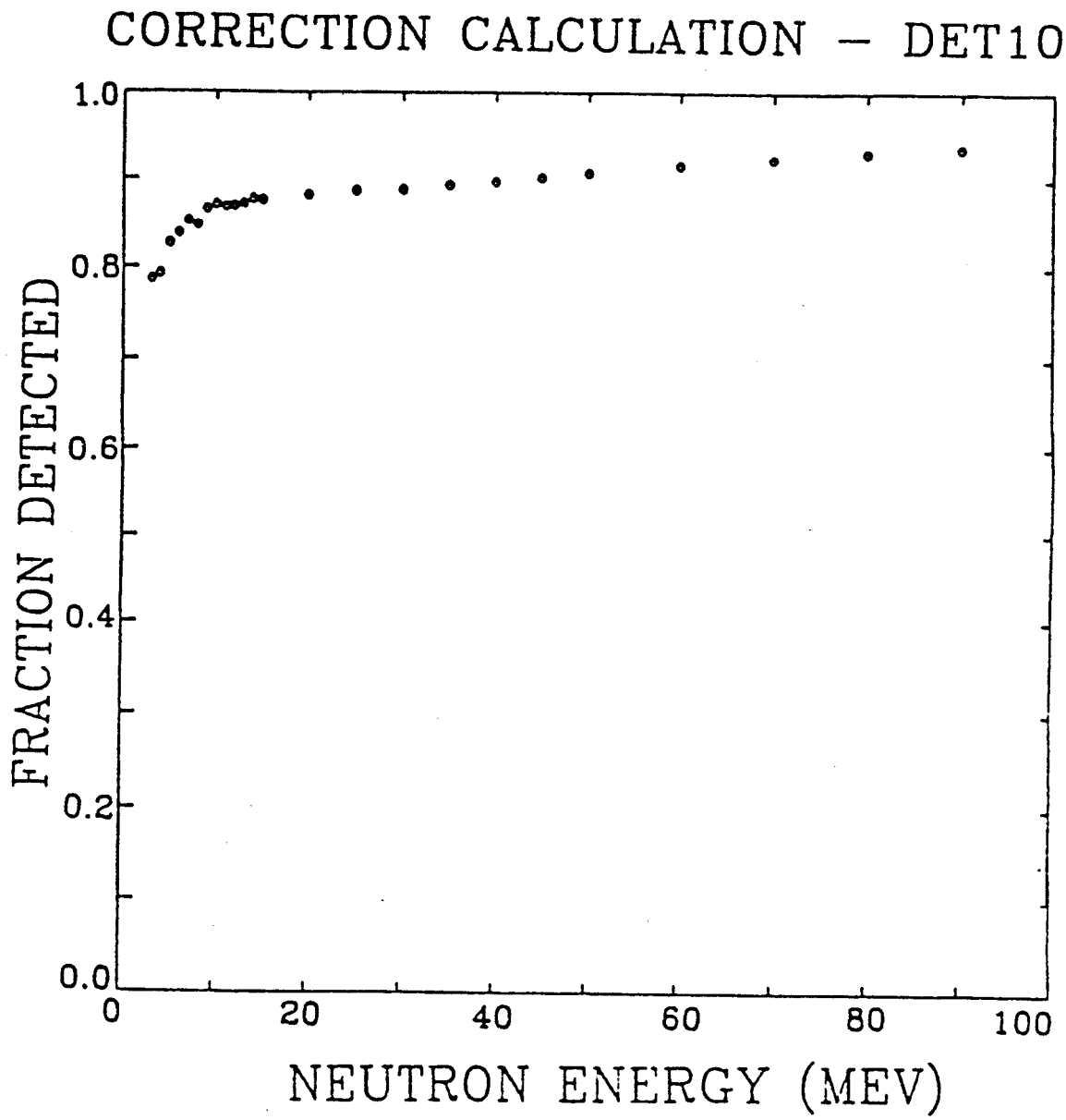

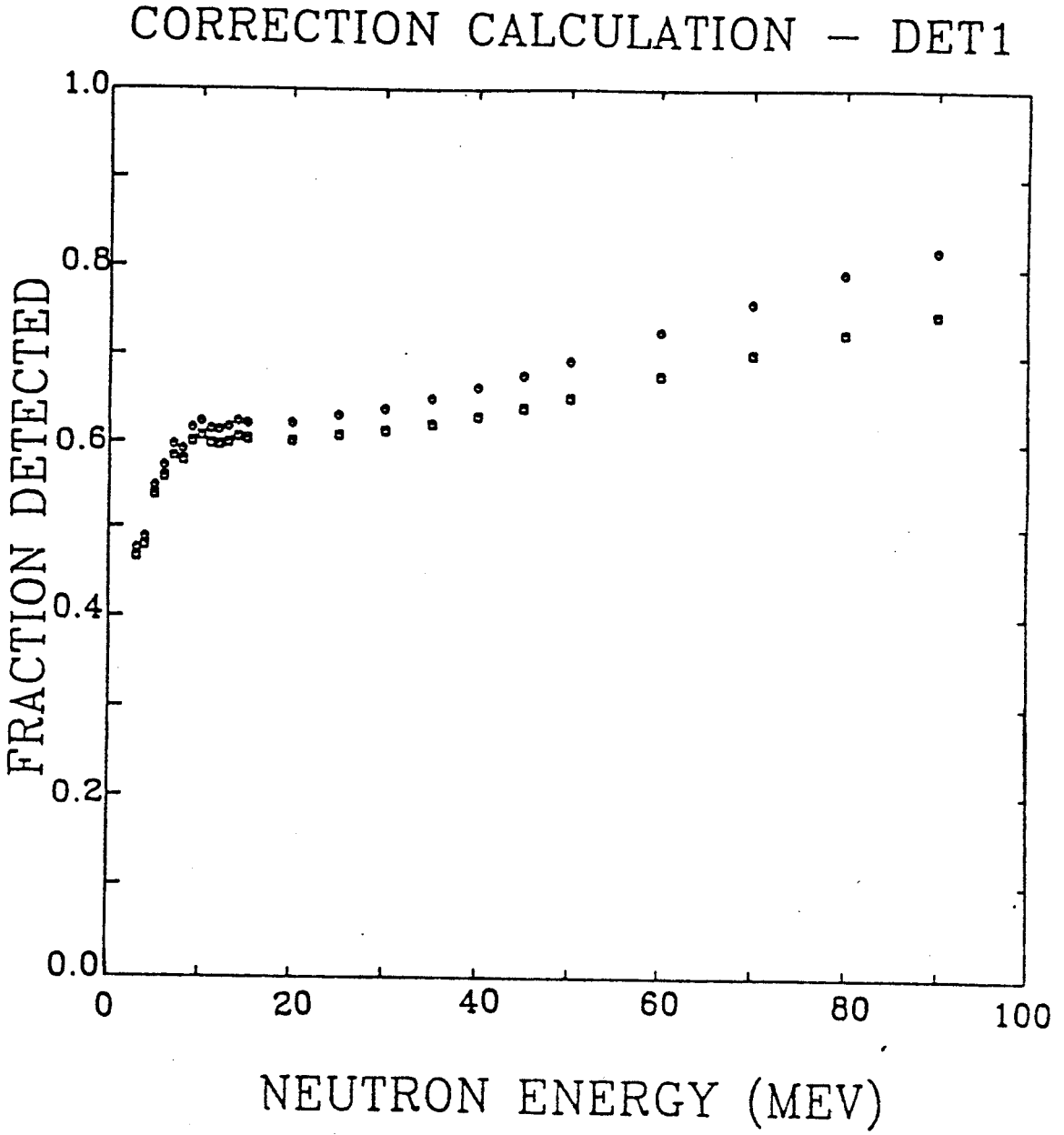

Figure A-21. Correction calculation with and without inscattering.

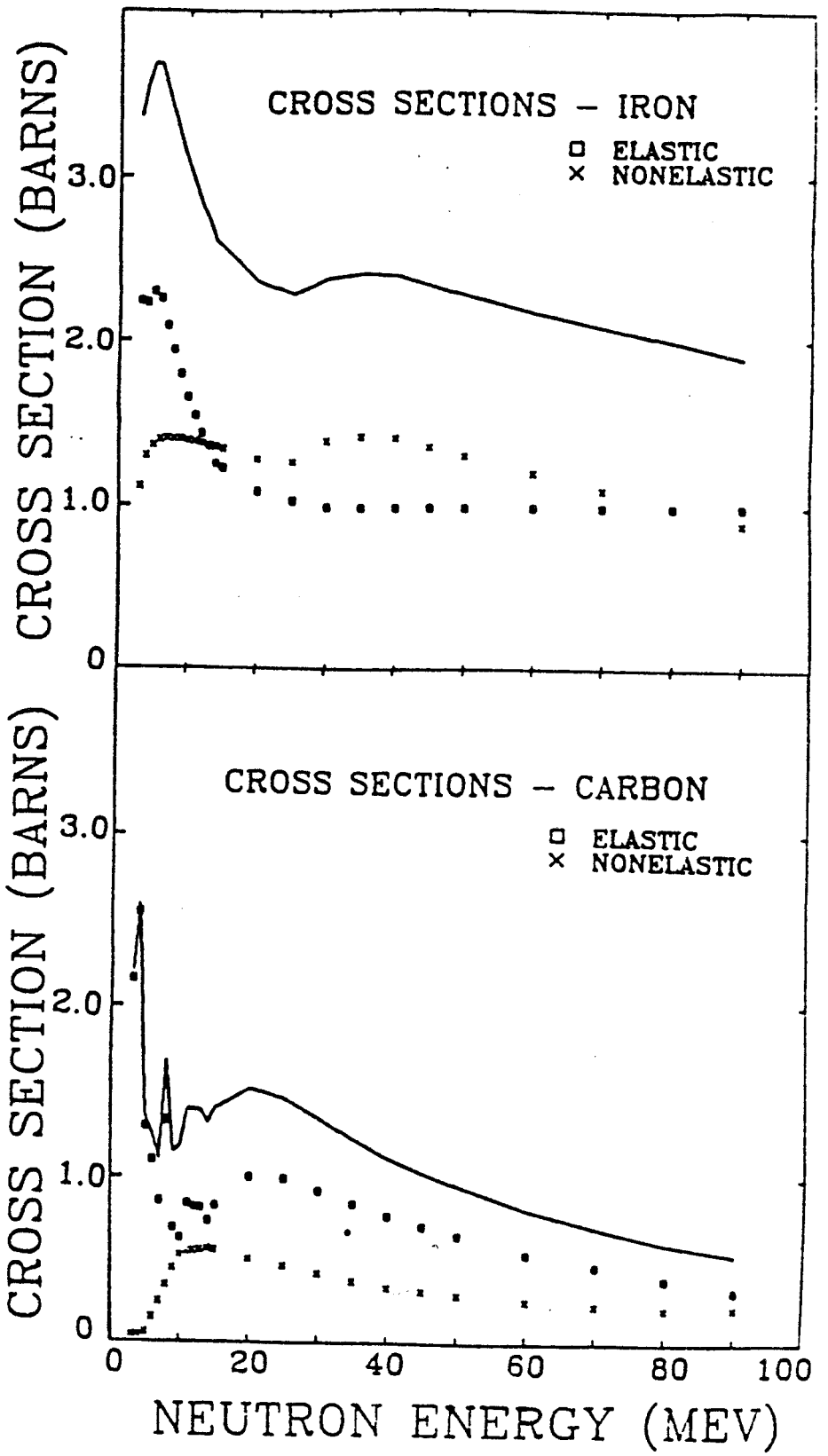

Figure A-22. Cross sections for iron and carbon.

structure in the correction curves at low energies arise from resonances in the total cross section at those energies, especially from carbon. And the sharp increase of the correction curve for energies of 0 MeV to about 10 MeV arises from the sharp decrease in the total cross section in this energy interval. This is seen in Fig. A-22 to be due mainly to the elastic scattering component of the total cross section.

In using shadow bars to measure the background neutrons detected in the detectors, one needs to consider whether there is any transmission of neutrons through the shadow bar. One way of estimating this is to assume that the shadow bar is divided up into, say, four separate pieces and do an "outscattering/inscattering" calculation as described above. Another method is to assume that neutrons traveling through the shadow bar undergo enough interactions that a multiple scattering calculation can be used. For 84 MeV neutrons traveling through copper (Br 50), the average number of collisions is about six, suggesting that a multiple scattering calculation might be worth trying. Both approaches were tried, but before discussing the results, the multiple scattering relationship will be developed.

The multiple scattering relation can be derived as follows. The probability that a neutron undergoing multiple scattering is deflected through an angle of θ is given by

$$P_{(\theta)}d\Omega = \frac{1}{\pi \langle \theta^2 \rangle} e^{-\theta^2/\langle\theta^2\rangle} d\Omega \quad ,$$

where $\langle\theta^2\rangle$ is the average squared deflection angle due to multiple scattering (equation 2-7.9 in Ref. Se 77). But $\langle\theta^2\rangle$ can be related to $\langle\theta^2_{\text{single}}\rangle$, where $\langle\theta^2_{\text{single}}\rangle$ is the average squared deflection angle due to single scattering. Let θ and α represent the angles of deflection arising from multiple scattering and single scattering, respectively. Then

$$\langle\theta^2\rangle = \langle \sum_{i=1}^{N} \alpha_i^2 \rangle \quad ,$$

where the average is taken over independent particles incident upon the scatterer, and the sum is taken over the N collisions each such particle undergoes. If one assumes each of the N collisions is independent of all the others, i.e., if one assumes incoherent collisions, then

$$\langle\theta^2\rangle = \sum_{i=1}^{N} \langle \alpha_i^2 \rangle \quad ,$$

$$\langle\theta^2\rangle = \sum_{i=1}^{N} \langle \alpha^2 \rangle \quad ,$$

$$\langle\theta^2\rangle = N \langle \alpha^2 \rangle \quad ,$$

$$\langle\theta^2\rangle = N \langle \theta^2_{single} \rangle \quad ,$$

where N is the number of collisions. So by using the measured angular distribution for 84 MeV neutrons on copper (Br 50), one can obtain $\langle\theta^2_{single}\rangle$, hence $\langle\theta^2\rangle$ and then $P(\theta)d\Omega$. The fraction of neutrons multiply scattered through a small enough angle that they still enter the neutron detector is given by

$$F_{ms} = \int_{\theta=0}^{\theta_o} P(\theta) 2\pi \sin\theta d\theta \quad ,$$

where θ_o is the angle subtended by the neutron detector at the shadow bar. Then the fraction of the neutrons incident upon the front face of the shadow bar that reach the detector is given by

$$F_{trans} = e^{-n\sigma_T x} + F_{ms} \quad .$$

Both the multiple scattering calculation and the "outscattering/inscattering" calculation were done assuming a Cu shadow bar 11.625" long, and the results are presented

in Fig. A-23. The four points from the multiple scattering calculation are indicated in the figure by arrows. The transmission through the shadow bar is less than 5% for all but the highest neutron energies. For a 100 MeV neutron, there is about 10% transmission. At $\theta_n \geq 70°$, though, there were no 100 MeV neutrons and at smaller θ_n longer shadow bars were used, as mentioned above. So in subtracting the shadow bar data from the raw data, the effect of transmission through the shadow bar was neglected.

It should be noted that all cross sections used were the most recent values available and were obtained upon request from the neutron cross section data bank maintained at the National Nuclear Data Center at Brookhaven National Laboratory (BNL 84).

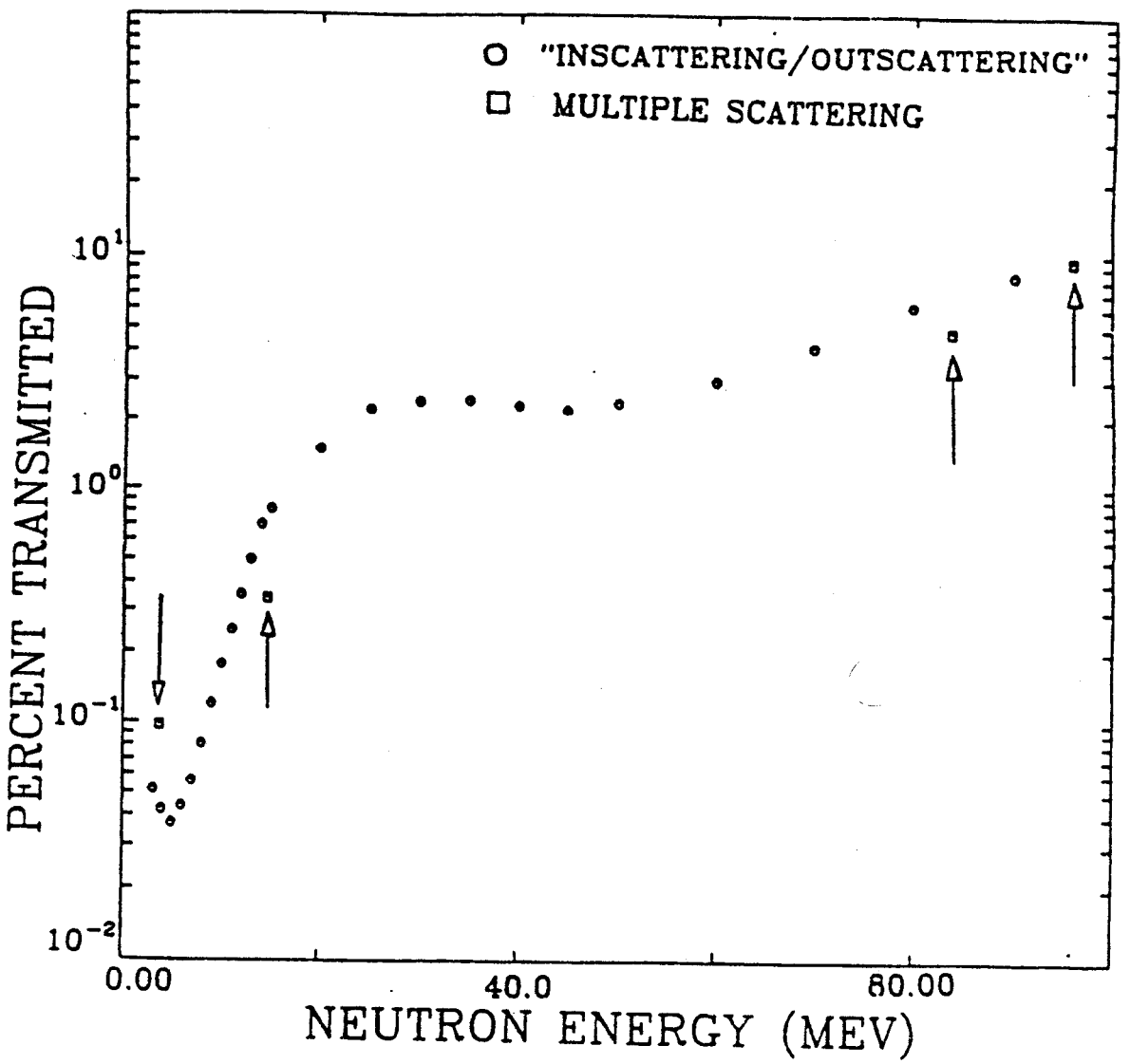

Figure A-23. Neutron transmission through the shadow bar.

A-VIII. Shadow Bar Beam Time

Let R_1 and R_2 be the data acquisition rates without and with shadow bars, respectively. Also let T_1 and T_2 be the length of time spent taking data without and with shadow bars. So $T = T_1 + T_2$ is the total time spent taking data. Assuming T, R_1, and R_2 are constants, an equation will be derived that indicates how T should be divided between T_1 and T_2 such as to minimize the fractional uncertainty of the data after subtraction of the shadow bar data.

Assume for a given channel that N_1 is the number of counts from the data taken without a shadow bar and N_2 is the number of counts taken with the shadow bar in place. Then the corrected number of counts is

$$N = N_1 - N_2(T_1/T_2) \quad .$$

The uncertainty in the corrected number of counts is given by

$$\Delta N = \{(\Delta N_1)^2 + (\Delta N_2\ T_1/T_2)^2\}^{\frac{1}{2}} \quad ,$$

$$\Delta N = \left\{ R_1 T_1 + (T_1/T_2)^2 R_2 T_2 \right\}^{\frac{1}{2}} \quad ,$$

having substituted $(\Delta N_i)^2 = (\sqrt{N_i})^2 = R_i T_i$ for $i = 1,2$. Then the fractional uncertainty is

$$\frac{\Delta N}{N} = \frac{\left\{ R_1 T_1 + (T_1/T_2)^2 R_2 T_2 \right\}^{\frac{1}{2}}}{R_1 T_1 - (T_1/T_2) R_2 T_2} \quad ,$$

$$\frac{\Delta N}{N} = \frac{1}{R_1 - R_2} \left\{ \frac{R_1}{T_1} + \frac{R_2}{T - T_1} \right\}^{\frac{1}{2}} \quad ,$$

having rearranged and substituted $T - T_1$ for T_2. To minimize $\Delta N/N$ with respect to T_1, it is sufficient to minimize only that which is contained within the braces in the last relation, so

$$0 \underset{\text{set}}{=} \frac{\partial}{\partial T_1} \left\{ \frac{R_1}{T_1} + \frac{R_2}{T - T_1} \right\} \quad ,$$

$$0 = \frac{-R_1}{T_1^2} - \frac{R_2(-1)}{(T - T_1)^2} \quad .$$

Upon resubstituting T_2 for $T - T_1$, this solves to give

$$\frac{T_1}{T_2} = \left\{ \frac{R_1}{R_2} \right\}^{1/2} ,$$

which is the desired relation.

A-IX. Nuclear Temperature Formulations.

The moving-source parameterization is predicated upon the model of thermal evaporation of nucleons from a "hot" nucleus, first introduced by Weisskopf in 1937 (We 37). This model has since been extended (Le 59) and refined (Fr 83), but the basic idea remains, and will be developed below.

Figure A-24 schematically illustrates the situation where, as a result of a nuclear interaction, a nucleus is left in an excited state at excitation energy E_0. It then emits a neutron of kinetic energy ε, thus forming a daughter nucleus at excitation

$$E = E_0 - \varepsilon - s_n \quad ,$$

where s_n is the neutron binding energy. The probability of a neutron of energy ε being emitted, $N(\varepsilon)\, d\varepsilon$, depends upon the product of the probability of forming the final state times the density of states at that final state. So

$$N(\varepsilon)d\varepsilon \propto P(E,\varepsilon)\rho(E)d\varepsilon \quad ,$$

where $P(E,\varepsilon)$ is the probability of this particular final state, $\rho(E)$ is the density of final states at this

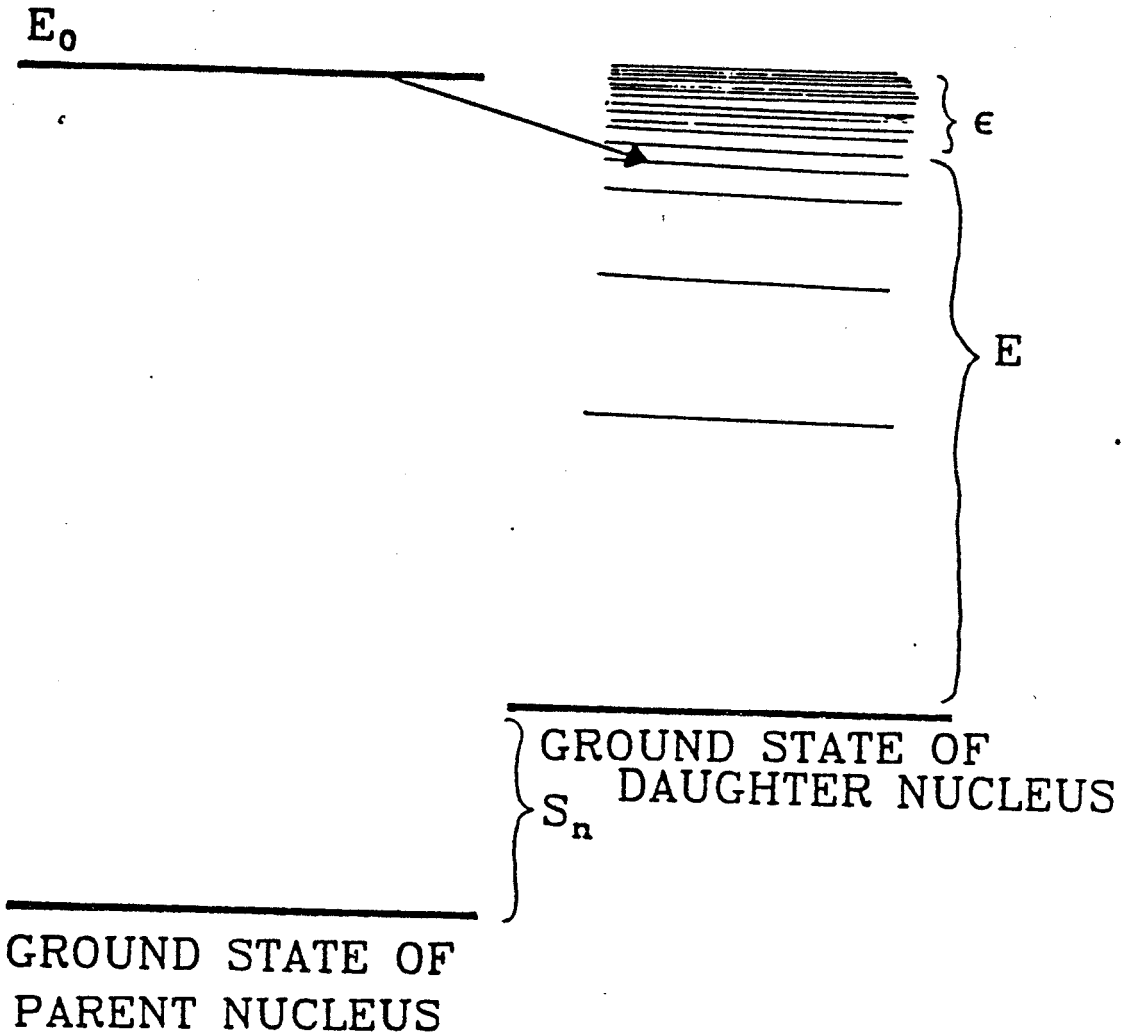

Figure A-24. Energy level diagram for neutron evaporation.

particular state and $d\varepsilon$ is the resolution for detecting a neutron of energy ε.

First treating the density of states, the concept of entropy, S(E), is introduced by

$$S(E) = \ell n\ \rho(E) \quad ,$$

thus,

$$\rho(E) = e^{S(E)} \quad .$$

Next, the entropy is expanded about S_0, the entropy that would result if the daughter nucleus had the maximum excitation energy possible, i.e., for the case that the neutron carries away no kinetic energy. This gives

$$S(E) = S_0 - \frac{\partial S(E)}{\partial E}\,\varepsilon \quad ,$$

where the Taylor expansion has been truncated at first order. The first order truncation is a reasonable approximation if, at daughter excitation energy E, the variation of the density of states in energy interval ε is small. This generally is true if $\varepsilon << E$. At this point, the thermodynamic definition of temperature can be introduced, i.e.,

$$\frac{1}{T} = \frac{\partial S(E)}{\partial E} \quad .$$

Recognizing that $S_0 = S(E_0 - s_n)$ is a constant for the given reaction being considered, then this constant factor can be incorporated in an overall normalization, A, giving

$$\rho(E) = Ae^{-\varepsilon/T} \quad .$$

So the concept of a nuclear temperature arises from the density of states and is a measure of the temperature of the daughter nucleus.

Another useful expression for the density of states can be arrived at by invoking the third law of thermodynamics, which states that as temperature approaches absolute zero, entropy smoothly approaches a constant value. Then from the relation for specific heat,

$$C_v = T \left(\frac{\partial S}{\partial T}\right) \quad ,$$

one sees that specific heat goes to zero as T goes to zero. But from the definition of specific heat,

$$C_v = \left(\frac{\partial E}{\partial T}\right)_v \quad ,$$

it is clear that as T goes to zero, so also does $\frac{\partial E}{\partial T}$ go to zero. If excitation energy is expanded in a power series in temperature, in the low temperature limit one can neglect higher order terms in T. So

$$E = \sum_{n=0}^{\infty} a_n T^n \quad ,$$

$$E \approx a_0 + a_1 T + a_2 T^2 \quad .$$

The assumption that $E_{(T) \underset{T \to 0}{\dashrightarrow} 0}$ requires that $a_0 = 0$, and

$C_v = \frac{\partial E}{\partial T} \underset{T \to 0}{\dashrightarrow} 0$ requires that $a_1 = 0$. So

$$E \approx a_2 T^2 = aT^2 \quad .$$

Then using the definition of entropy, $dS = dE/T$, one can write

$$S(E) = \int \frac{dE}{T} \quad ,$$

$$S(E) = \int \frac{dE}{\sqrt{(E/a)}} \quad ,$$

$$S(E) = 2\sqrt{(aE)} + \text{const} \quad .$$

So the density of states can also be expressed as

$$\rho(E) = Be^{2\sqrt{(aE)}} \quad .$$

Returning to the derivation of the neutron emission probability density, $N(\varepsilon)$, one needs to consider the factor $P(E,\varepsilon)$, i.e., the probability of forming the final state given by a neutron of energy ε and a daughter nucleus of excitation energy E. Here one makes use of the reciprocity theorem which relates a reaction to its inverse reaction. It can be shown (Bl 79) that the factor $P(E,\varepsilon)$ only introduces an additional factor of ε in front of the exponential temperature factor. So from simple statistical and thermodynamical arguments, one arrives at the following form for the neutron energy spectrum:

$$N(E) = A\varepsilon e^{-\varepsilon/T} \quad .$$

In this equation, temperature T is assumed to be in units of energy. Notice that the the temperature of the daughter nucleus completely parameterizes the shape of the neutron energy spectrum. This relation characterizes what is called the Maxwellian surface evaporation spectrum (Go 78), because

it has the same functional form as the energy spectrum of molecules evaporated from the surface of a hot object.

It is interesting to go one step further and consider the functional form one would get by simply sampling a Maxwell-Boltzmann gas. Starting with Maxwell's velocity distribution for an ideal gas in equilibrium, one can write the probability of finding a molecule with velocity $\vec{v}$ contained within d^3v as

$$P(\vec{v}) = f(\vec{v})d^3v \quad ,$$

$$P(\vec{v}) = Ae^{-\varepsilon/KT}d^3v \quad ,$$

where $A = (m/2\pi KT)^{\frac{3}{2}}$ and $\varepsilon = \frac{1}{2}mv^2$. To put this in a form that is independent of the direction of the velocity, one can write

$$P(v) = f_v dv \quad ,$$

$$P(v) = Ae^{-\varepsilon/KT}4\pi v^2 dv \quad .$$

So

$$f_v = 4\pi Av^2 e^{-\varepsilon/KT} \quad ,$$

where $f_v dv$ is the probability that $|\vec{v}|$ is between v and v+dv. If one defines $f_\varepsilon d\varepsilon$ as the probability that the kinetic energy of the molecule is between ε and $\varepsilon+d\varepsilon$, then

$$f_\varepsilon d\varepsilon = f_v dv$$

such that

$$f_\varepsilon = \left(\frac{dv}{d\varepsilon}\right) f_v \quad ,$$

and

$$f_\varepsilon = \left(\frac{dv}{d\varepsilon}\right)(4\pi A v^2 e^{-\varepsilon/KT}) \quad .$$

Noting that

$$\frac{d\varepsilon}{dv} = \frac{d}{dv}\left(\tfrac{1}{2}mv^2\right) = mv \quad ,$$

then

$$f_\varepsilon = \frac{1}{mv}\, 4\pi A v^2 e^{-\varepsilon/KT} \quad ,$$

$$f_\varepsilon = B\sqrt{\varepsilon}\; e^{-\varepsilon/KT} \quad ,$$

and

$$N(E) = A \sqrt{\varepsilon}\, e^{-\varepsilon/KT} \quad ,$$

which is commonly referred to as the Maxwellian volume emission spectrum (Go 78). In an extension of the above statistical arguments first put forth by Weisskopf, LeCouteur and Lang (Le 59) considered a temperature description for the case of multiple neutron emission. The temperature would be lowered after each neutron emission, hence they introduced an effective temperature parameter τ. The derived functional form for the neutron energy spectrum can then be written as

$$N(E) = A\varepsilon^{5/11} e^{-\varepsilon/\tau} \quad .$$

Here τ is a temperature parameter related to the temperature of the daughter nucleus after the first neutron emission by $T = (12/11)\tau$.

A-X. The Neutron Data

This section contains all the neutron data. The moving source fit parameters are contained in the tables in Section A, the neutron spectra are contained in the figures in Section B, and the LF contribution in Section C.

A. The Moving Source Fit Parameters

1. The Ho Target

Table 1-A displays the fit parameters for a two-moving-source fit to the neutron spectra taken with the Ho target. In the first column is listed which energy gate (HE for high energy or LE for low energy) was set across the fragment and which fragment (Li, Be, B, or C) was selected. In the second column is the angle of the fragment (7°, 10°, 15°, 18°, or 23°), where the angles are all in the horizontal plane. (The neutron spectra in coincidence with fragments at 14° out-of-plane were not studied with the moving-source parameterization). The third column lists the source (TLS for target-like source or IRS for intermediate-rapidity source). The remaining four columns list the associated multiplicity (see main text, Section V), temperature, kinetic-energy/nucleon and angle of the source, respectively.

Table 1-A. The neutron spectra fit parameters for the Ho target

LF	θ(Deg)	Source	Mult	Temp(MeV)	E/A(MeV)	θ(Deg)
HE-Li	7	TLS	3.580	1.767	0.011	-7.500
		IRS	0.984	6.045	5.070	0.000
HE-Be	7	TLS	3.086	1.946	0.018	15.000
		IRS	0.658	7.745	7.341	-6.294
HE-B	7	TLS	1.608	2.028	0.007	-14.530
		IRS	0.582	8.000	9.000	-10.000
HE-C	7	TLS	0.520	2.476	0.000	-3.000
		IRS	0.24	9.334	9.105	-18.340
LE-Li	7	TLS	3.981	2.358	0.011	-29.840
		IRS	1.373	6.497	5.541	0.000
LE-Be	7	TLS	2.056	3.753	0.010	20.000
		IRS	0.155	10.220	10.110	0.000
LE-B	7	TLS	2.359	3.000	0.020	-17.500
		IRS	0.777	9.175	9.127	0.197
LE-C	7	TLS	1.883	2.254	0.024	11.880
		IRS	0.964	7.973	7.915	-1.245
HE-Li	10	TLS	3.746	2.663	0.043	-20.000
		IRS	1.155	8.240	8.734	0.000
HE-Be	10	TLS	2.267	2.989	0.016	-21.990
		IRS	0.770	9.209	7.552	-4.994
HE-B	10	TLS	2.026	2.265	0.016	-35.0004
		IRS	0.657	8.639	9.562	-10.990
HE-C	10	TLS	1.125	2.260	0.024	-39.890
		IRS	0.455	9.170	9.933	-20.000
LE-Li	10	TLS	5.200	2.704	0.014	-26.010
		IRS	1.722	7.238	5.571	0.000
LE-Be	10	TLS	3.751	3.098	0.010	-15.000
		IRS	1.492	7.596	6.241	0.000
LE-B	10	TLS	4.939	2.433	0.012	-13.660
		IRS	1.602	8.304	8.507	-2.386
LE-C	10	TLS	3.385	3.104	0.011	-10.000
		IRS	1.667	7.011	8.839	0.000

Table 1-A. (continued)

LF	θ(Deg)	Source	Mult	Temp(MeV)	E/A(MeV)	θ(Deg)
HE-Li	15	TLS	3.235	2.845	0.036	-7.786
		IRS	1.224	7.928	8.497	3.042
HE-Be	15	TLS	3.175	2.931	0.038	-24.580
		IRS	1.206	8.851	7.855	0.000
HE-B	15	TLS	4.177	2.049	0.049	-10.000
		IRS	0.935	8.670	8.934	0.000
HE-C	15	TLS	1.805	2.430	0.009	-12.650
		IRS	0.959	8.345	8.692	0.000
LE-Li	15	TLS	5.541	3.012	0.093	-3.734
		IRS	1.551	9.377	6.575	3.350
LE-Be	15	TLS	5.500	2.931	0.043	-4.257
		IRS	1.951	8.984	7.823	0.000
LE-B	15	TLS	7.506	2.104	0.027	-2.264
		IRS	2.165	8.594	6.372	0.000
LE-C	15	TLS	5.036	2.588	0.012	-34.220
		IRS	2.016	7.358	5.251	0.000
E-Li	18	TLS	5.366	3.161	0.090	-11.000
		IRS	1.212	10.220	9.235	0.000
HE-Be	18	TLS	3.829	3.000	0.060	-15.480
		IRS	1.002	11.510	7.304	-5.828
HE-B	18	TLS	4.446	2.355	0.040	-25.750
		IRS	0.891	9.349	8.753	0.000
HE-C	18	TLS	4.159	2.111	0.052	-9.000
		IRS	1.356	11.310	6.504	0.000
LE-Li	18	TLS	6.469	3.233	0.087	-21.620
		IRS	1.374	8.008	5.446	0.000
LE-Be	18	TLS	7.354	2.817	0.050	-15.000
		IRS	1.315	10.000	7.000	0.000
LE-B	18	TLS	8.611	2.251	0.028	-37.410
		IRS	2.248	9.167	7.688	6.268
LE-C	18	TLS	5.120	2.611	0.023	-47.670
		IRS	2.171	8.458	6.210	0.000

Table 1-A. (continued)

LF	θ(Deg)	Source	Mult	Temp(MeV)	E/A(MeV)	θ(Deg)
HE-Li	23	TLS	5.253	2.601	0.072	-11.600
		IRS	1.679	9.043	4.752	4.000
HE-Be	23	TLS	5.705	2.603	0.050	-20.000
		IRS	1.583	9.659	7.495	0.000
HE-B	23	TLS	5.573	2.226	0.108	-3.239
		IRS	0.811	10.000	6.000	5.000
HE-C	23	TLS	3.267	2.084	0.028	-45.000
		IRS	0.798	8.500	5.000	0.000
LE-Li	23	TLS	7.507	2.726	0.071	-14.380
		IRS	2.318	10.520	5.177	2.325
LE-Be	23	TLS	7.899	3.165	0.061	4.351
		IRS	1.890	9.159	7.653	0.000
LE-B	23	TLS	7.487	2.607	0.047	0.412
		IRS	2.884	10.900	5.221	0.000
LE-C	23	TLS	6.310	3.316	0.105	-4.041
		IRS	3.185	12.610	4.356	0.000

2. The Ni Target

Table 2-A presents the moving-source fit parameters for the neutron spectra taken with the Ni target. The format of the table is the same as that for Table 1-A.

Table 2-A. The neutron spectra fit parameters for the Ni target

LF	θ(Deg)	Source	Mult	Temp(MeV)	E/A(MeV)	θ(Deg)
HE-Li	7	TLS	0.741	2.748	0.100	-4.509
		IRS	0.403	8.131	11.010	0.000
HE-Be	7	TLS	0.711	3.088	0.200	-10.330
		IRS	0.392	9.427	10.990	0.000
HE-B	7	TLS	0.513	2.553	0.071	-4.010
		IRS	0.360	8.728	11.120	0.000
HE-C	7	TLS	0.350	3.105	0.118	-18.500
		IRS	0.343	10.000	11.000	-10.540
LE-Li	7	TLS	0.933	2.927	0.034	0.000
		IRS	0.851	7.641	5.891	0.000
LE-Be	7	TLS	0.835	3.655	0.200	0.000
		IRS	0.665	8.126	6.559	-4.000
LE-B	7	TLS	1.065	3.225	0.229	-25.250
		IRS	0.713	8.189	7.003	-3.412
LE-C	7	TLS	1.041	3.845	0.198	0.0004
		IRS	0.436	11.000	8.850	0.000
HE-Li	10	TLS	0.746	3.098	0.153	-13.440
		IRS	0.404	8.769	11.320	0.000
HE-Be	10	TLS	0.985	2.669	0.206	-15.670
		IRS	0.481	10.130	11.160	0.000
HE-B	10	TLS	0.476	3.009	0.070	-30.000
		IRS	0.357	10.110	11.950	0.000
HE-C	10	TLS	0.373	3.209	0.182	-33.200
		IRS	0.309	11.420	12.000	-3.000
LE-Li	10	TLS	0.884	3.717	0.174	-4.498
		IRS	0.701	9.006	8.019	0.000
LE-Be	10	TLS	1.165	2.865	0.164	-25.490
		IRS	0.831	10.190	8.045	0.000
LE-B	10	TLS	0.813	3.353	0.074	-16.230
		IRS	0.836	8.716	7.698	0.000
LE-C	10	TLS	1.107	3.302	0.260	-12.920
		IRS	0.659	9.475	9.104	0.000

Table 2-A. (continued).

LF	θ(Deg)	Source	Mult	Temp(MeV)	E/A(MeV)	θ(Deg)
HE-Li	15	TLS	1.166	3.342	0.323	-6.257
		IRS	0.425	10.350	12.530	-3.328
HE-Be	15	TLS	1.054	2.934	0.357	-25.130
		IRS	0.544	11.230	12.430	0.000
HE-B	15	TLS	0.853	3.000	0.264	-24.800
		IRS	0.443	8.402	12.000	0.000
HE-C	15	TLS	0.908	2.880	0.156	-30.000
		IRS	0.566	9.748	11.450	0.000
LE-Li	15	TLS	1.323	3.064	0.320	-1.913
		IRS	0.896	9.355	9.133	0.000
LE-Be	15	TLS	1.080	3.652	0.297	-7.500
		IRS	0.955	10.340	9.039	0.000
LE-B	15	TLS	1.607	2.621	0.261	-11.430
		IRS	1.050	9.551	7.954	0.000
LE-C	15	TLS	1.156	3.745	0.274	-3.809
		IRS	0.993	10.480	9.546	0.000
HE-Li	18	TLS	1.211	3.869	0.359	-16.490
		IRS	0.552	11.380	12.560	0.000
HE-Be	18	TLS	1.197	3.237	0.307	-25.560
		IRS	0.589	10.980	12.090	0.000
HE-B	18	TLS	1.119	3.148	0.288	-22.710
		IRS	0.463	11.510	12.000	4.000
HE-C	18	TLS	1.811	2.608	0.184	-24.760
		IRS	0.415	10.140	12.000	-3.000
LE-Li	18	TLS	1.516	3.280	0.333	-12.180
		IRS	0.532	11.790	11.520	0.000
LE-Be	18	TLS	1.218	3.765	0.391	-20.000
		IRS	0.675	12.000	10.000	0.000
LE-B	18	TLS	1.347	3.119	0.251	-15.000
		IRS	0.983	9.082	9.253	2.216
LE-C	18	TLS	1.285	3.763	0.159	-31.470
		IRS	0.974	9.399	8.990	0.000

Table 2-A. (continued).

LF	θ(Deg)	Source	Mult	Temp(MeV)	E/A(MeV)	θ(Deg)
HE-Li	23	TLS	1.424	4.055	0.668	-7.711
		IRS	0.751	11.980	12.630	0.000
HE-Be	23	TLS	1.618	3.307	0.324	-14.980
		IRS	0.758	10.440	12.170	0.000
HE-B	23	TLS	1.227	3.227	0.355	-22.040
		IRS	0.631	10.230	12.130	0.000
HE-C	23	TLS	1.313	3.463	0.140	-17.590
		IRS	0.486	13.470	14.000	0.000
LE-Li	23	TLS	1.632	4.230	0.575	-7.552
		IRS	1.069	12.270	12.110	0.000
LE-Be	23	TLS	1.883	3.775	0.556	0.000
		IRS	0.571	13.000	12.580	0.000
LE-B	23	TLS	1.704	4.204	0.400	-9.000
		IRS	0.909	14.560	13.750	0.000
LE-C	23	TLS	1.202	4.498	0.200	-14.010
		IRS	1.211	13.160	8.765	0.000

B. The Neutron Spectra

1. The Ho Target

Figure A-25 presents the differential neutron multiplicity spectra for the Ho target. For those spectra that were studied with the moving-source parameterization, the fitted curves are displayed along with the data points. For clarity of display, the spectra are offset from one another in symmetric angle pairs by factors of 100, with the spectra at ±10° being at the correct scale. Open symbols and dashed lines correspond to the same side of the beam as the detected fragment, whereas closed symbols and solid lines correspond to the opposite side. The selection of coincident fragment type, energy, and angle is indicated in the title of each spectrum.

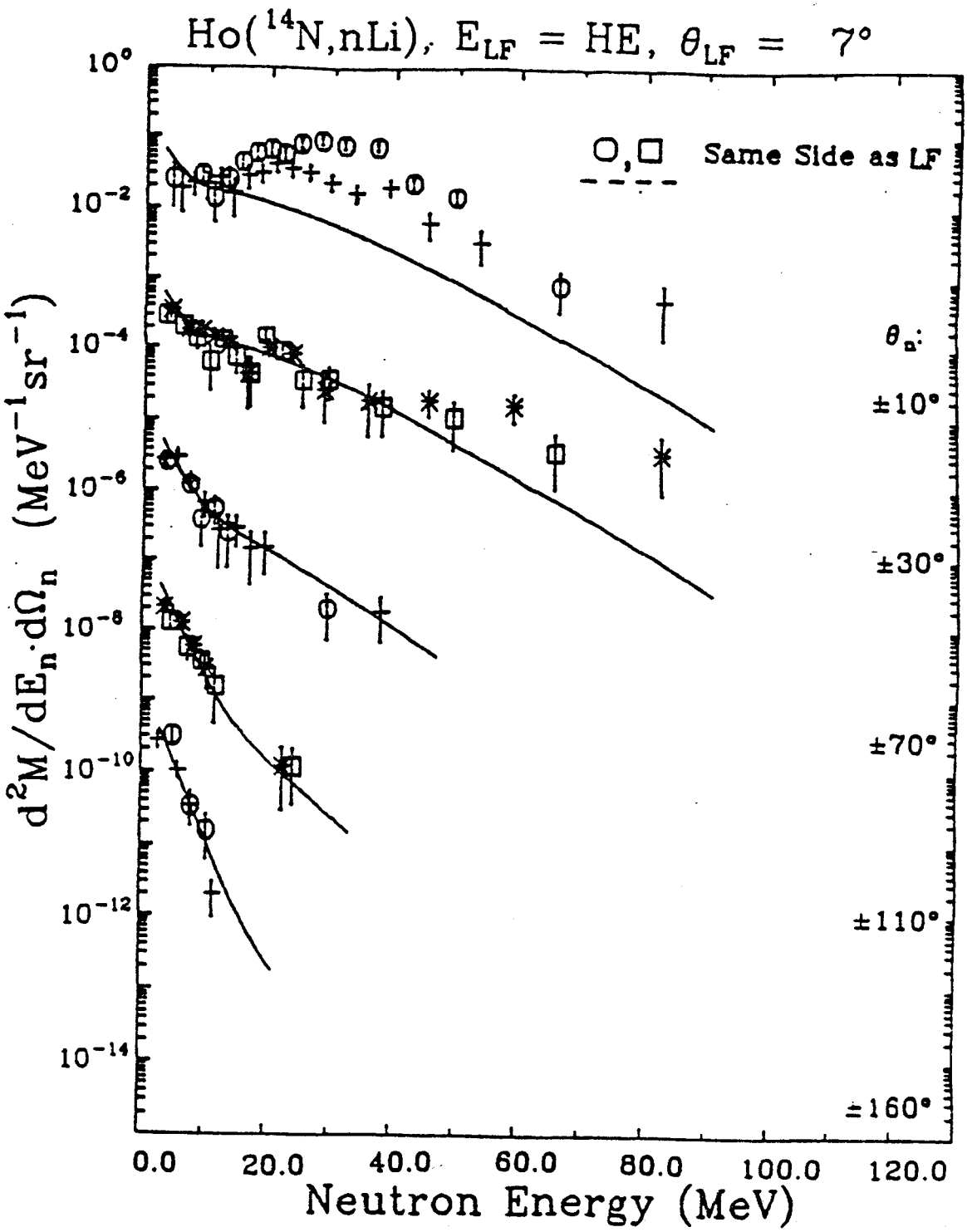

Figure A-25. Neutron spectra for the Ho target.

Figure A-25. (continued)

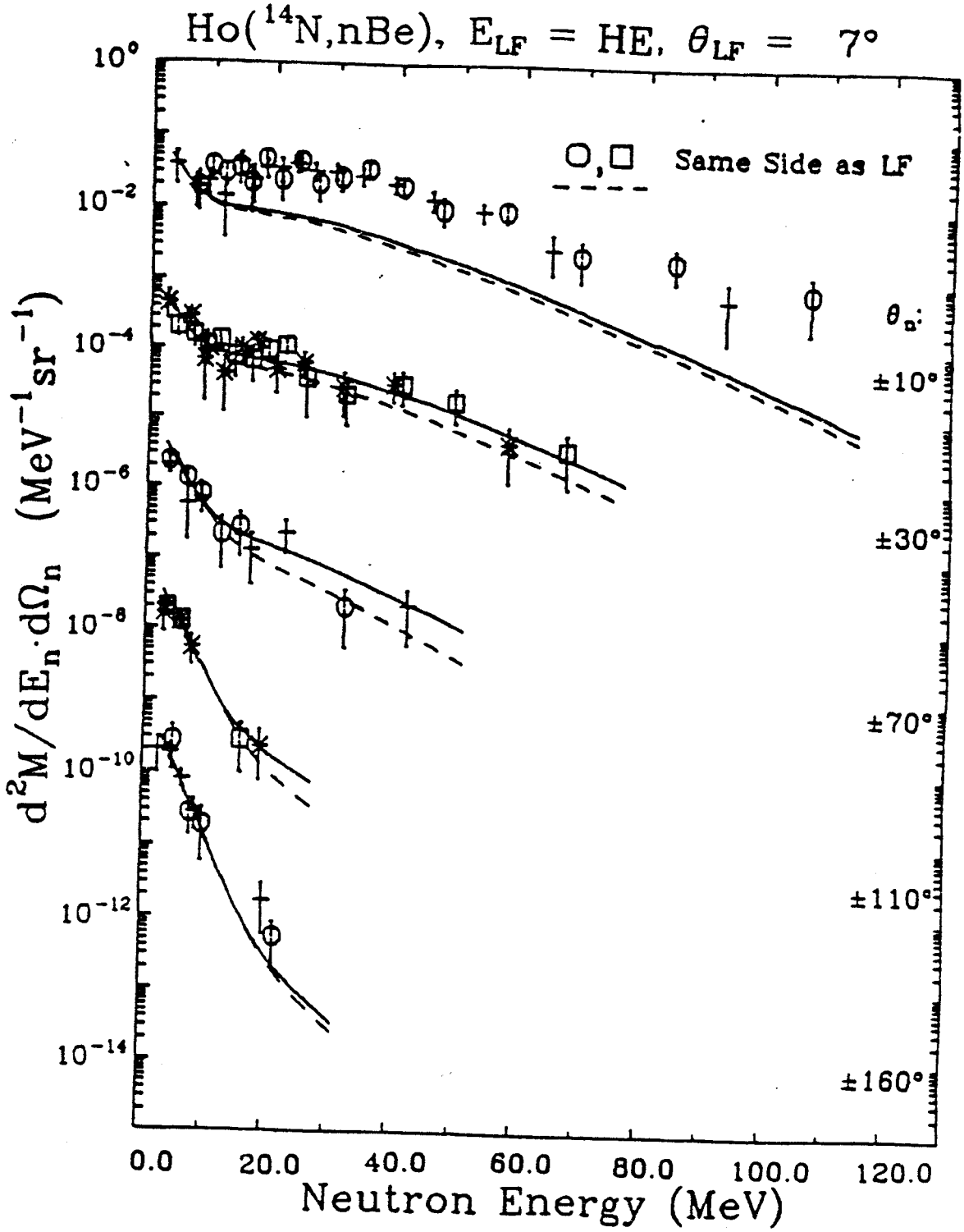

Figure A-25. (continued)

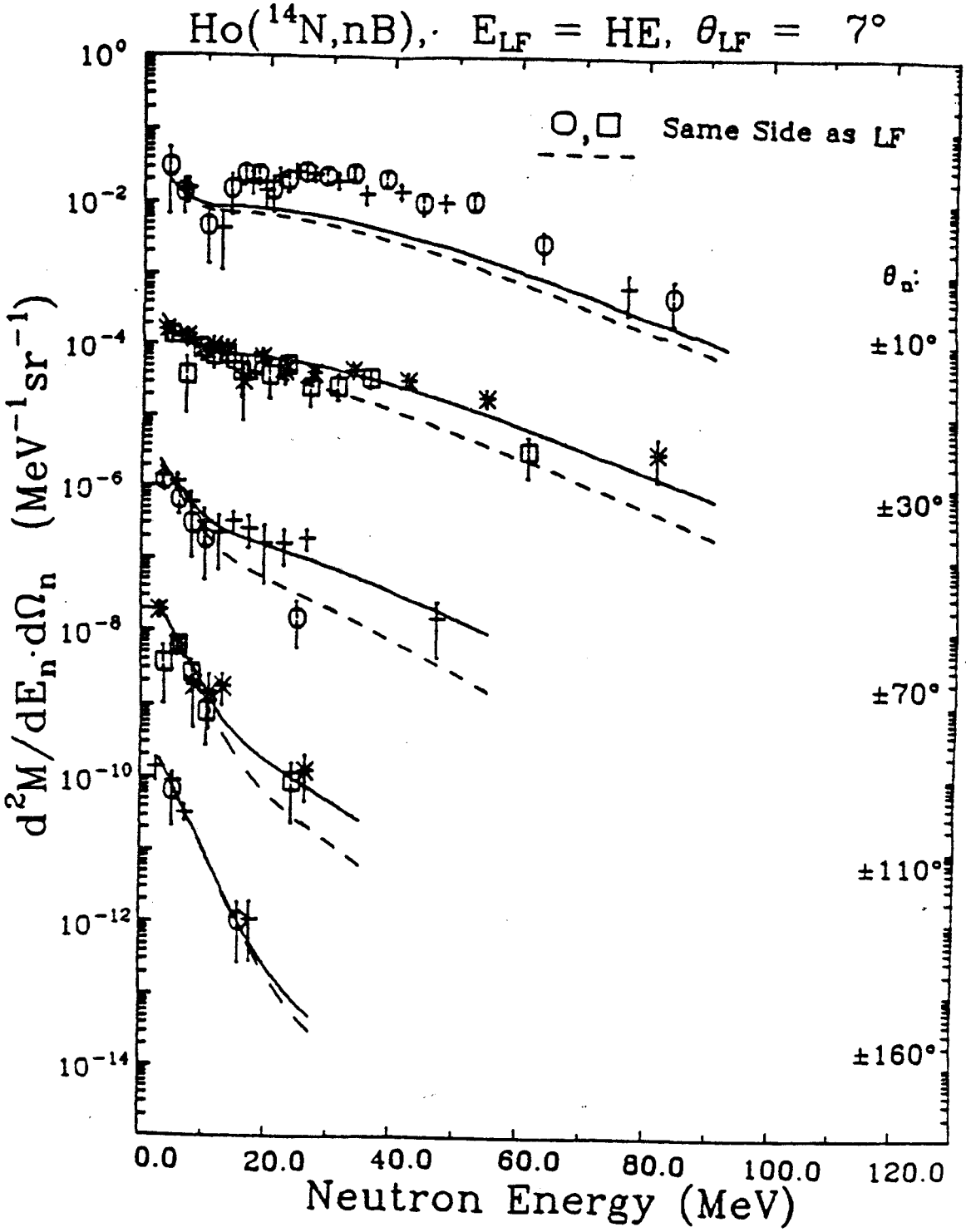

Figure A-25. (continued)

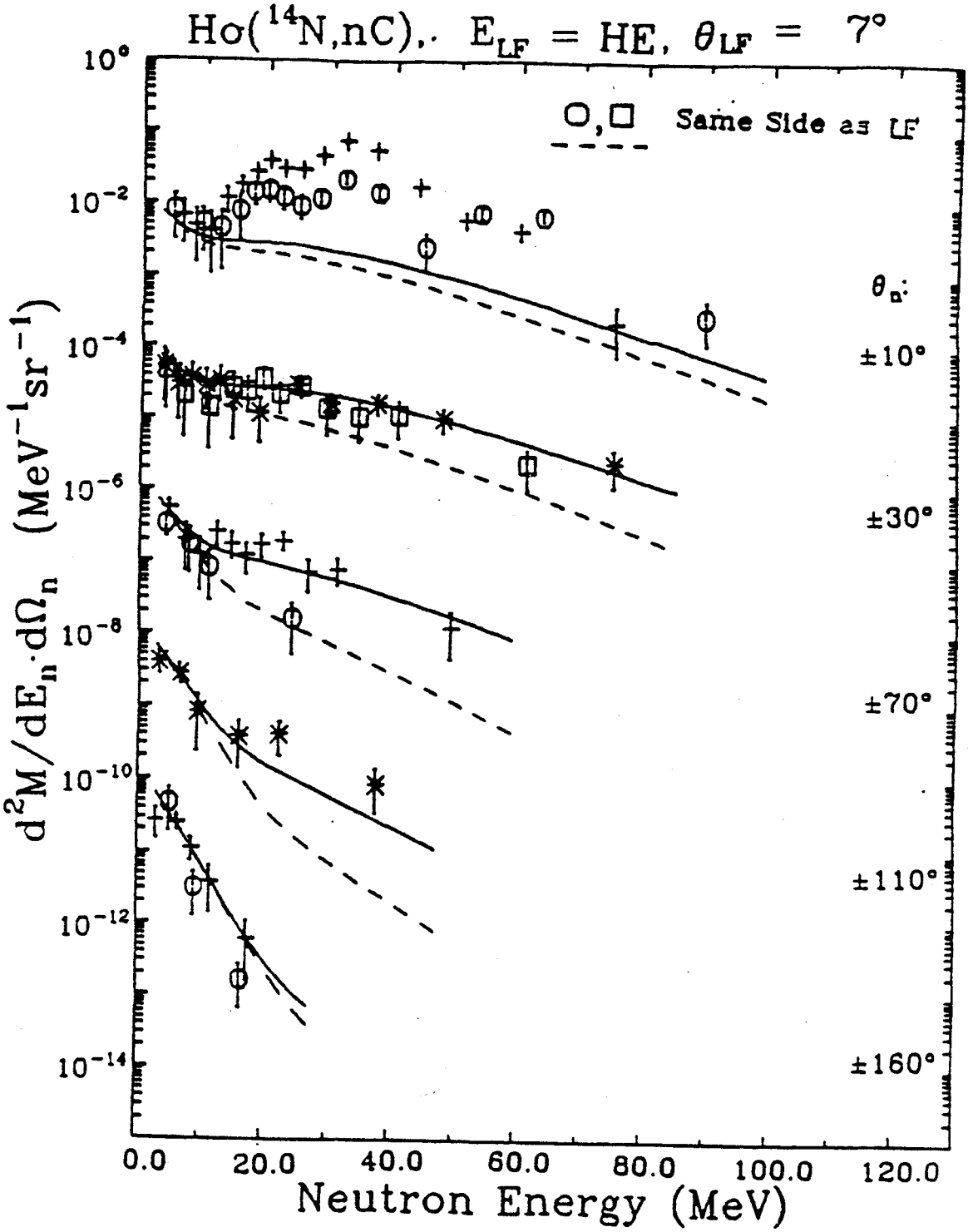

Figure A-25. (continued)

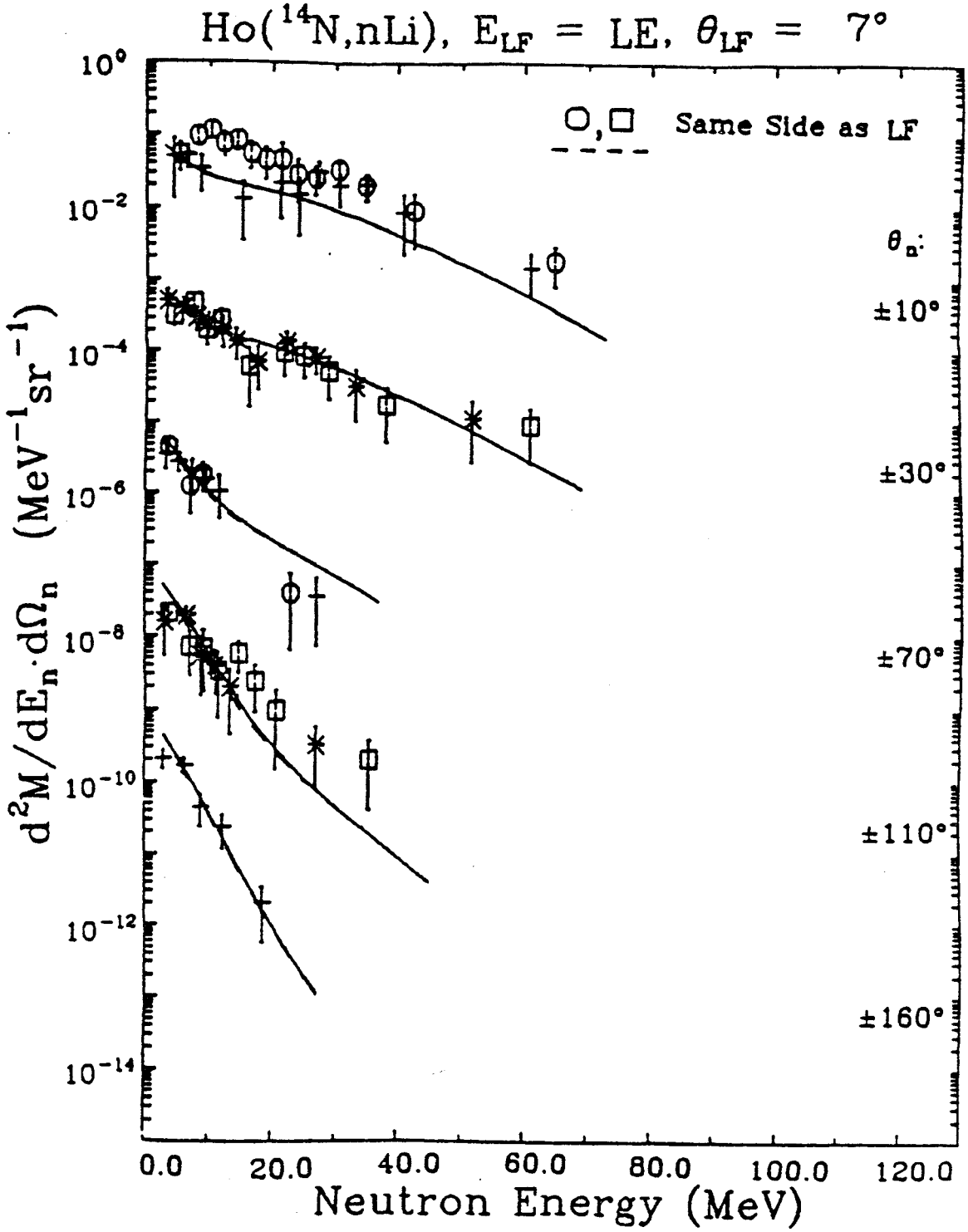

Figure A-25. (continued)

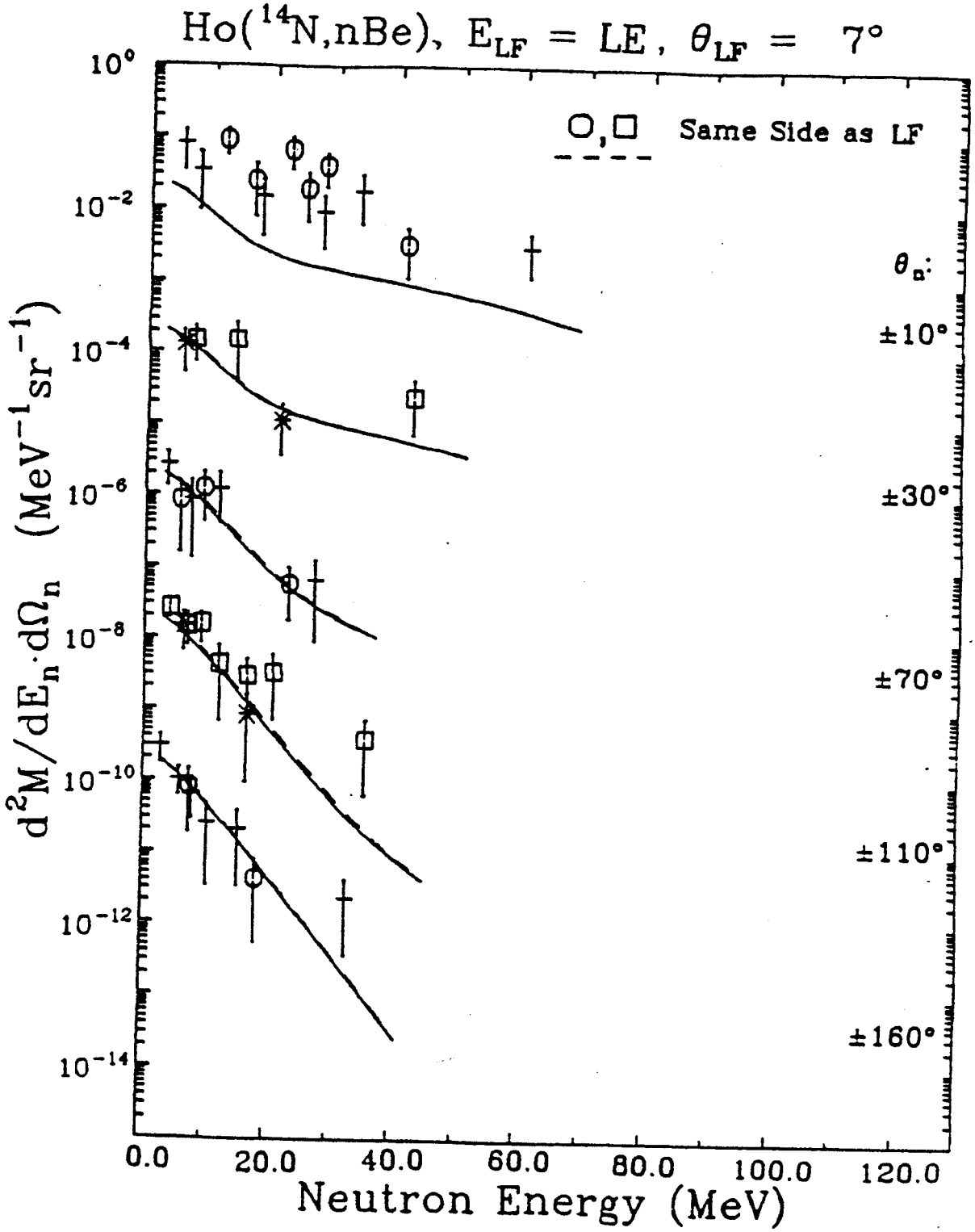

Figure A-25. (continued)

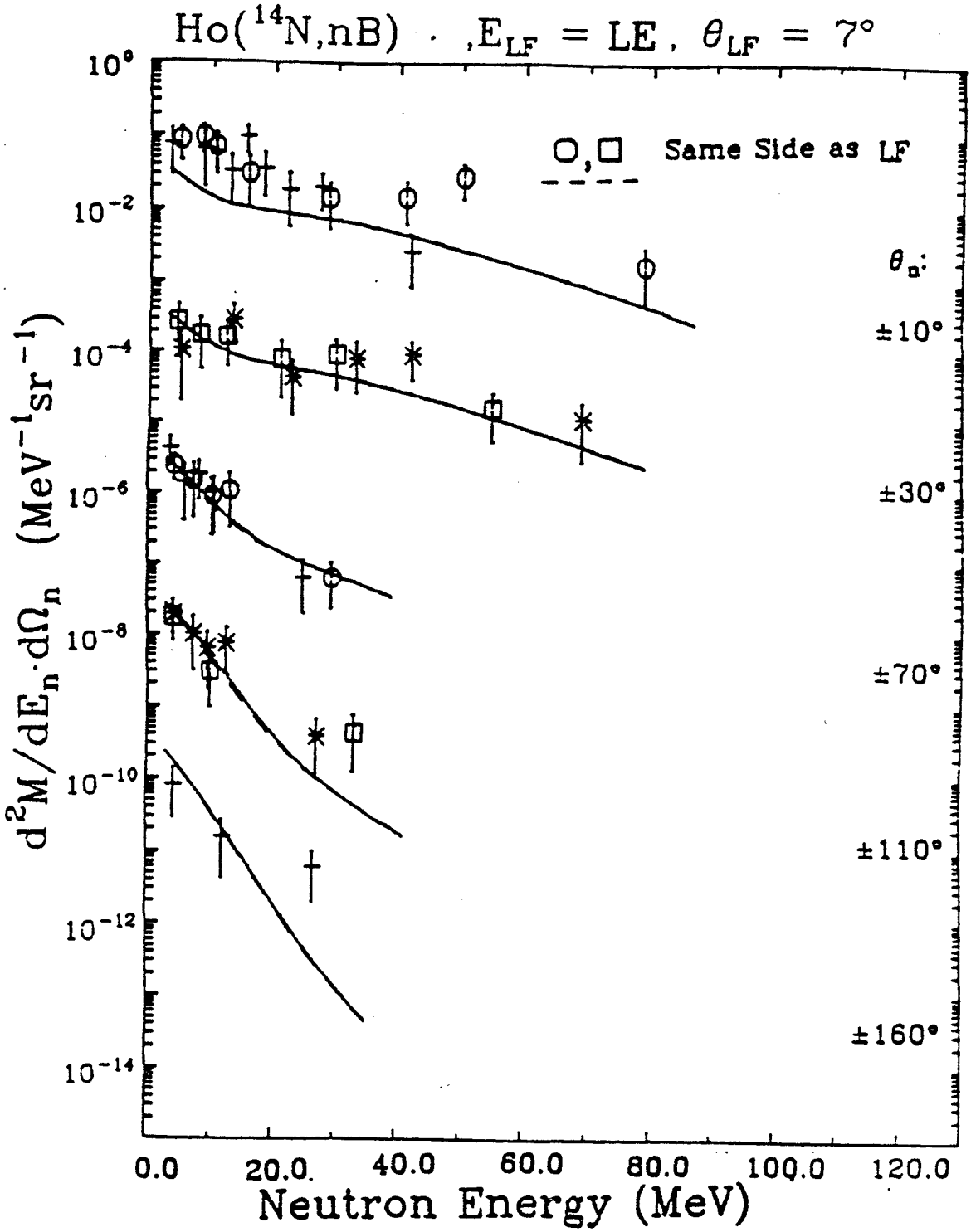

Figure A-25. (continued)

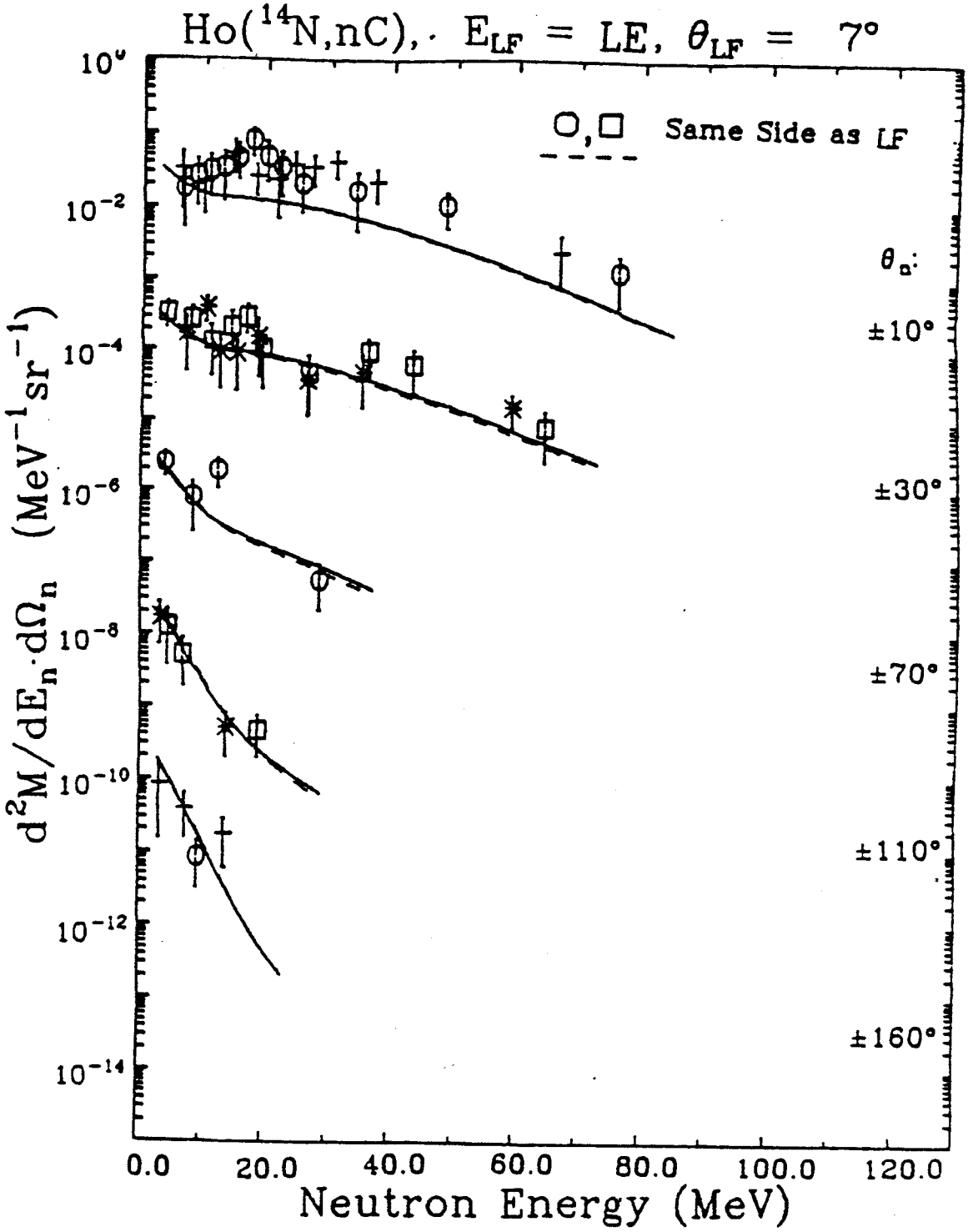

Figure A-25. (continued)

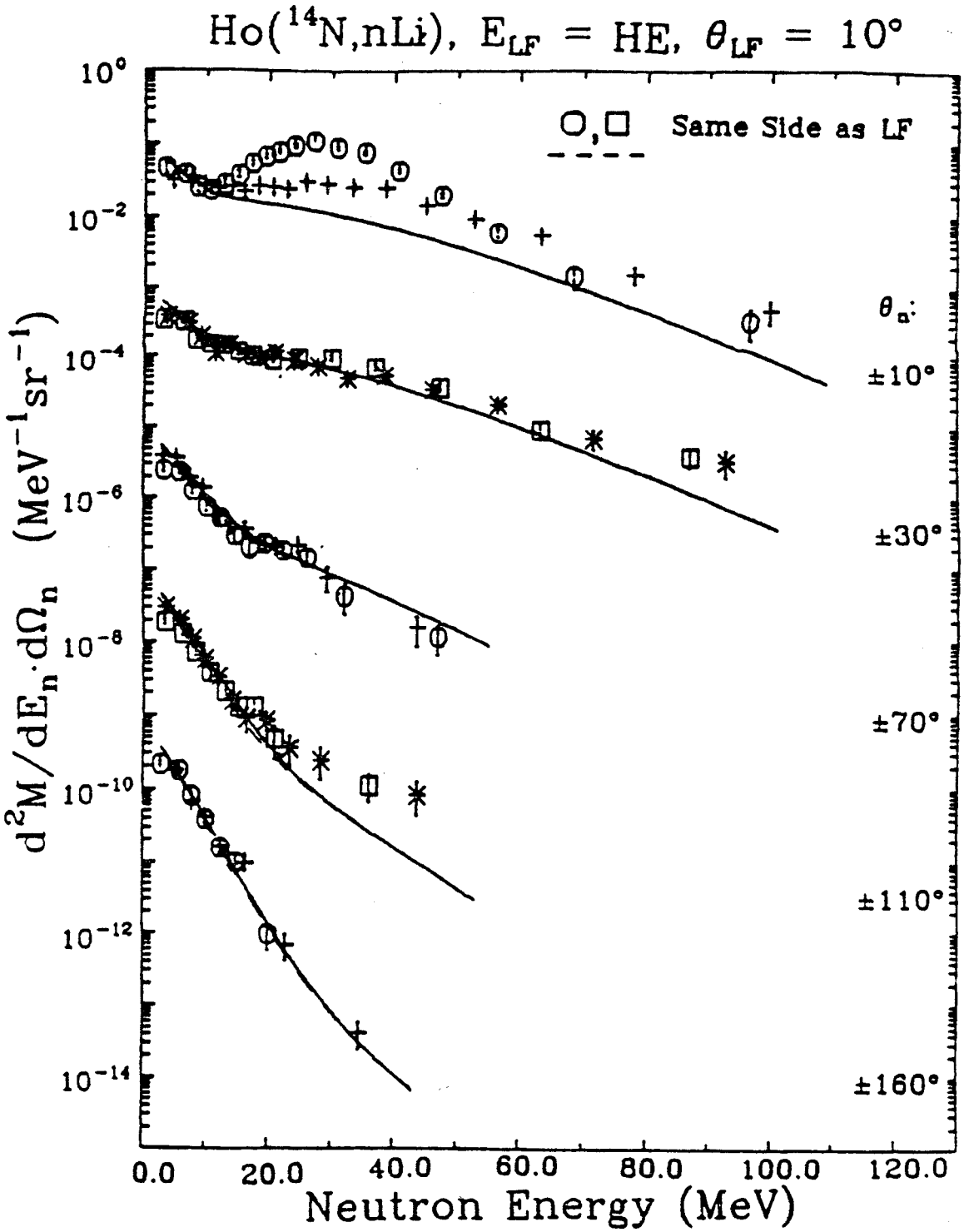

Figure A-25. (continued)

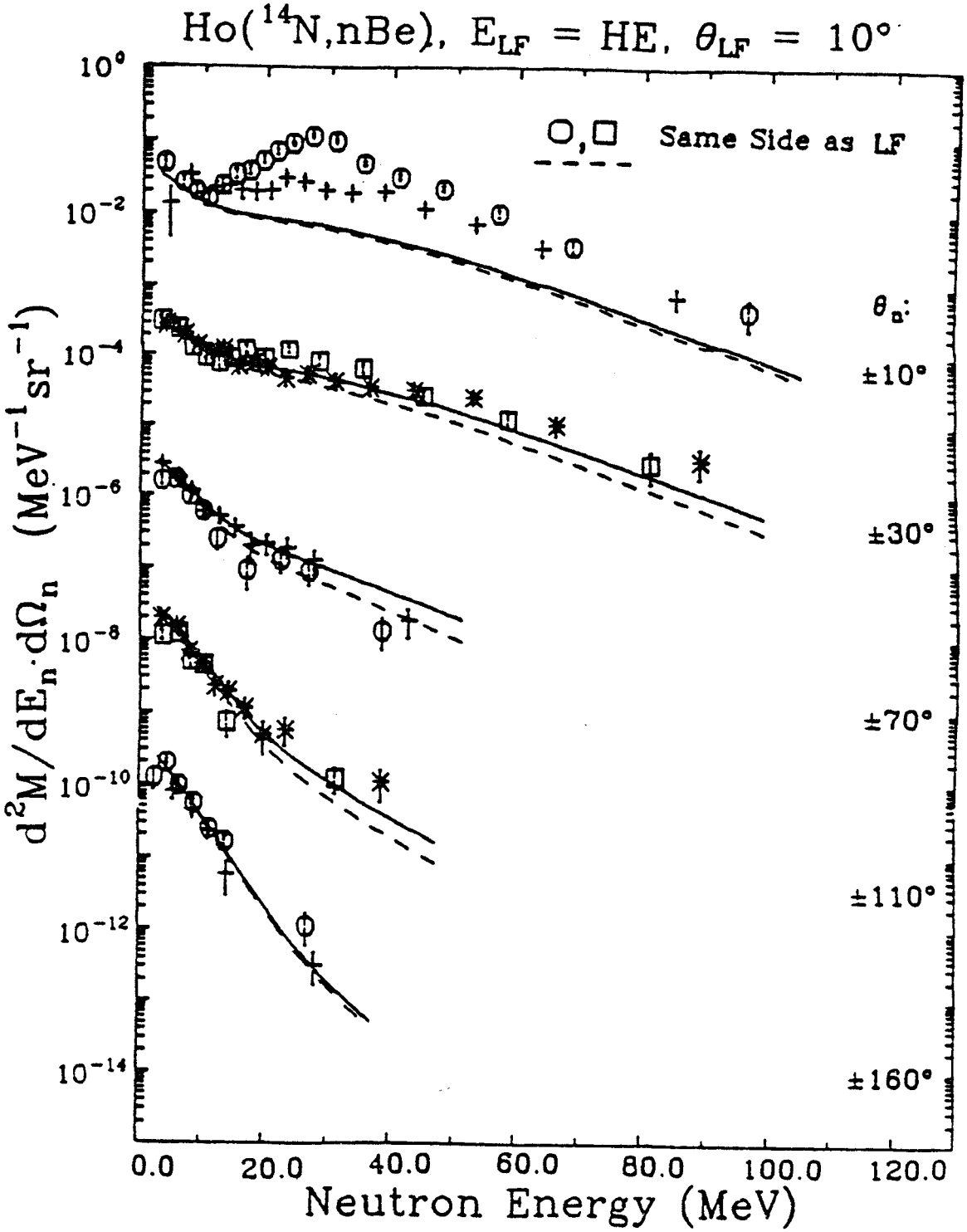

Figure A-25. (continued)

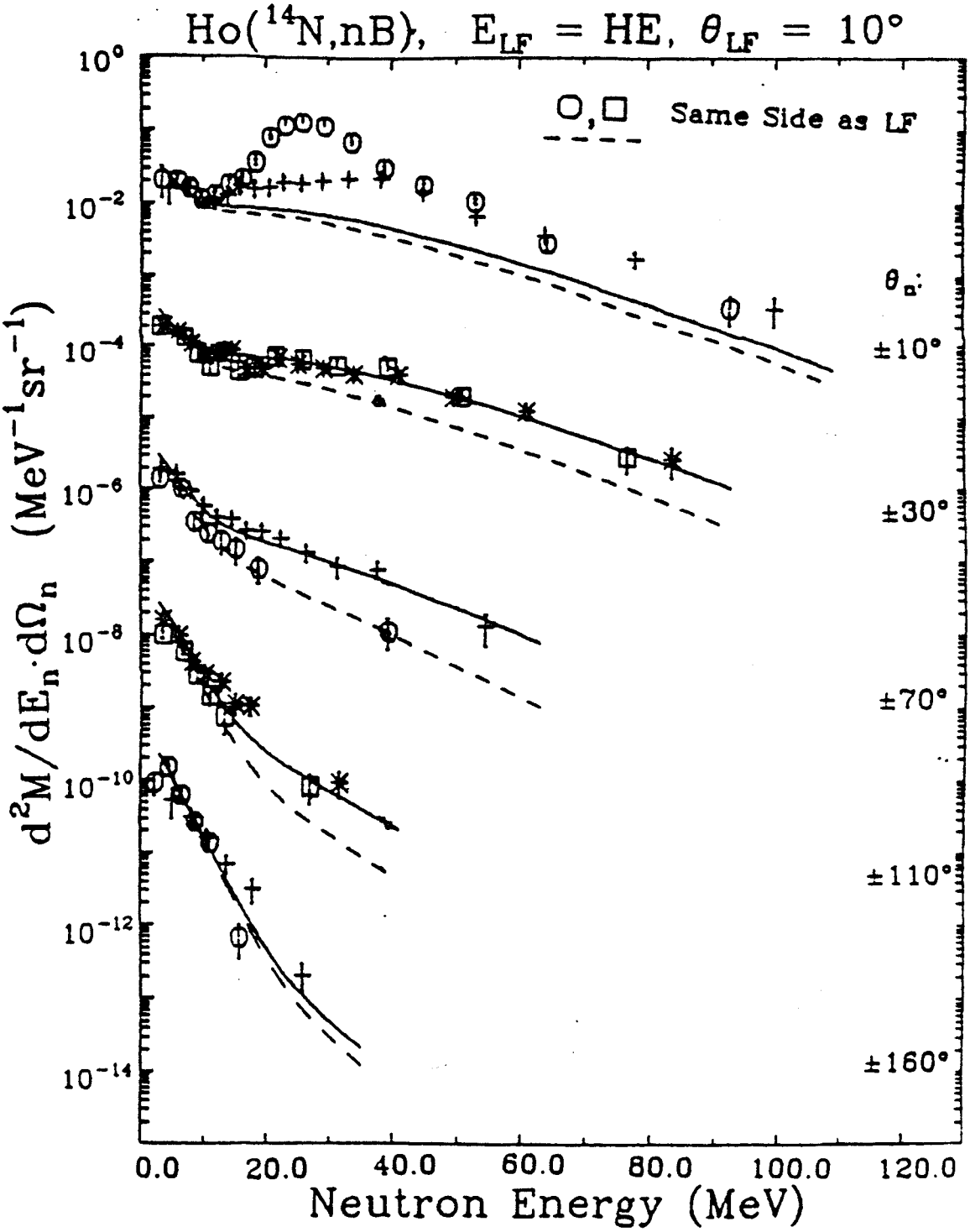

Figure A-25. (continued)

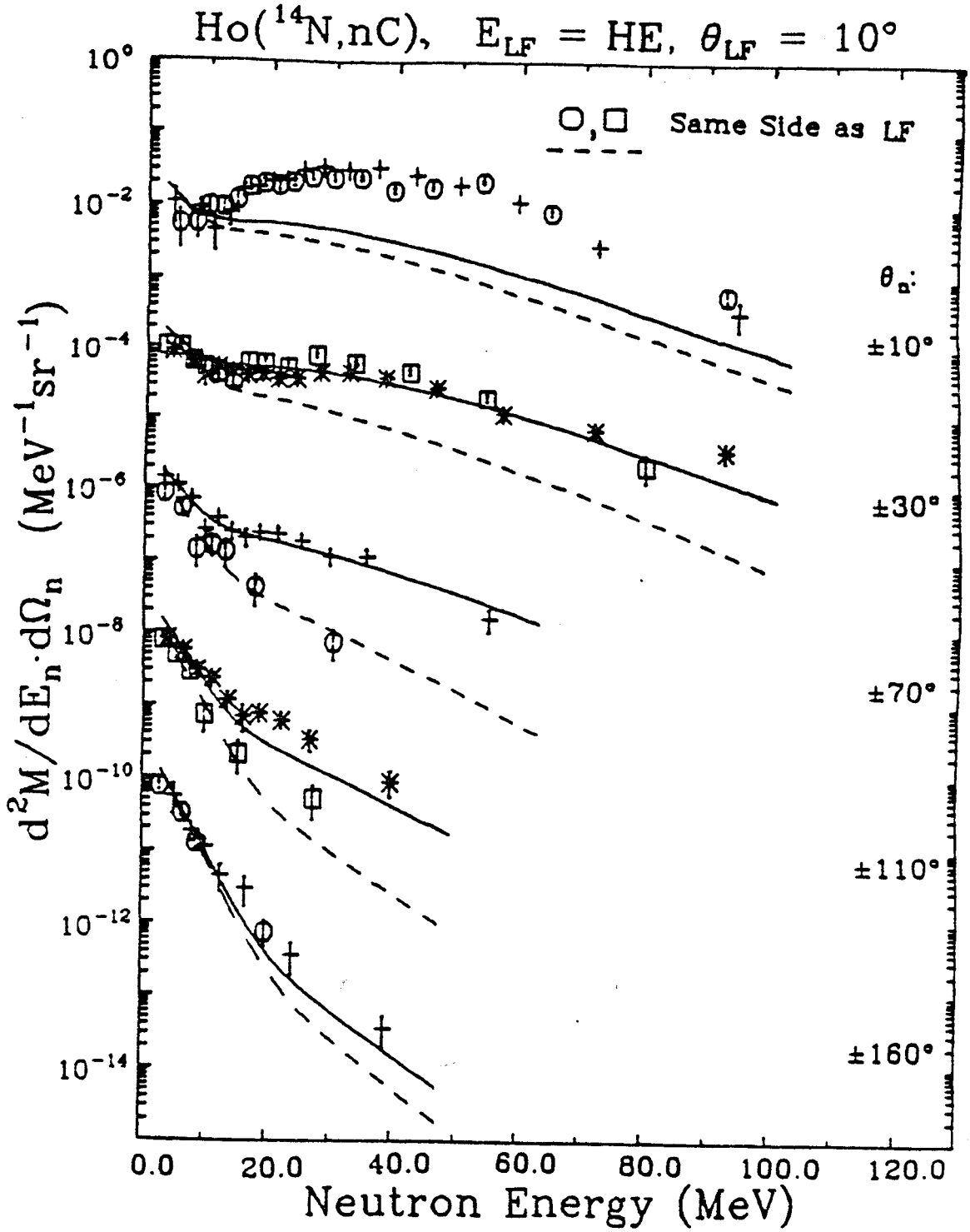

Figure A-25. (continued)

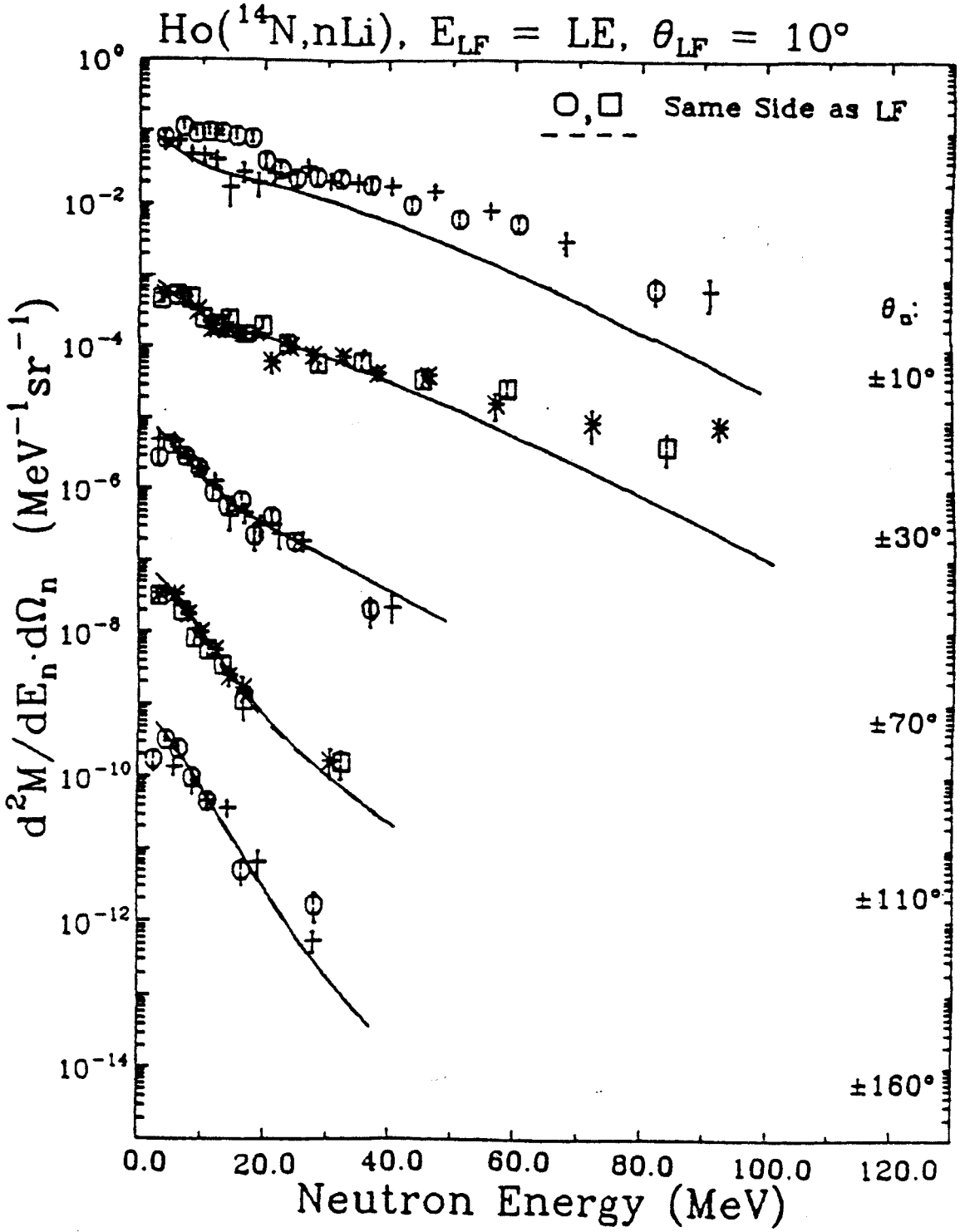

Figure A-25. (continued)

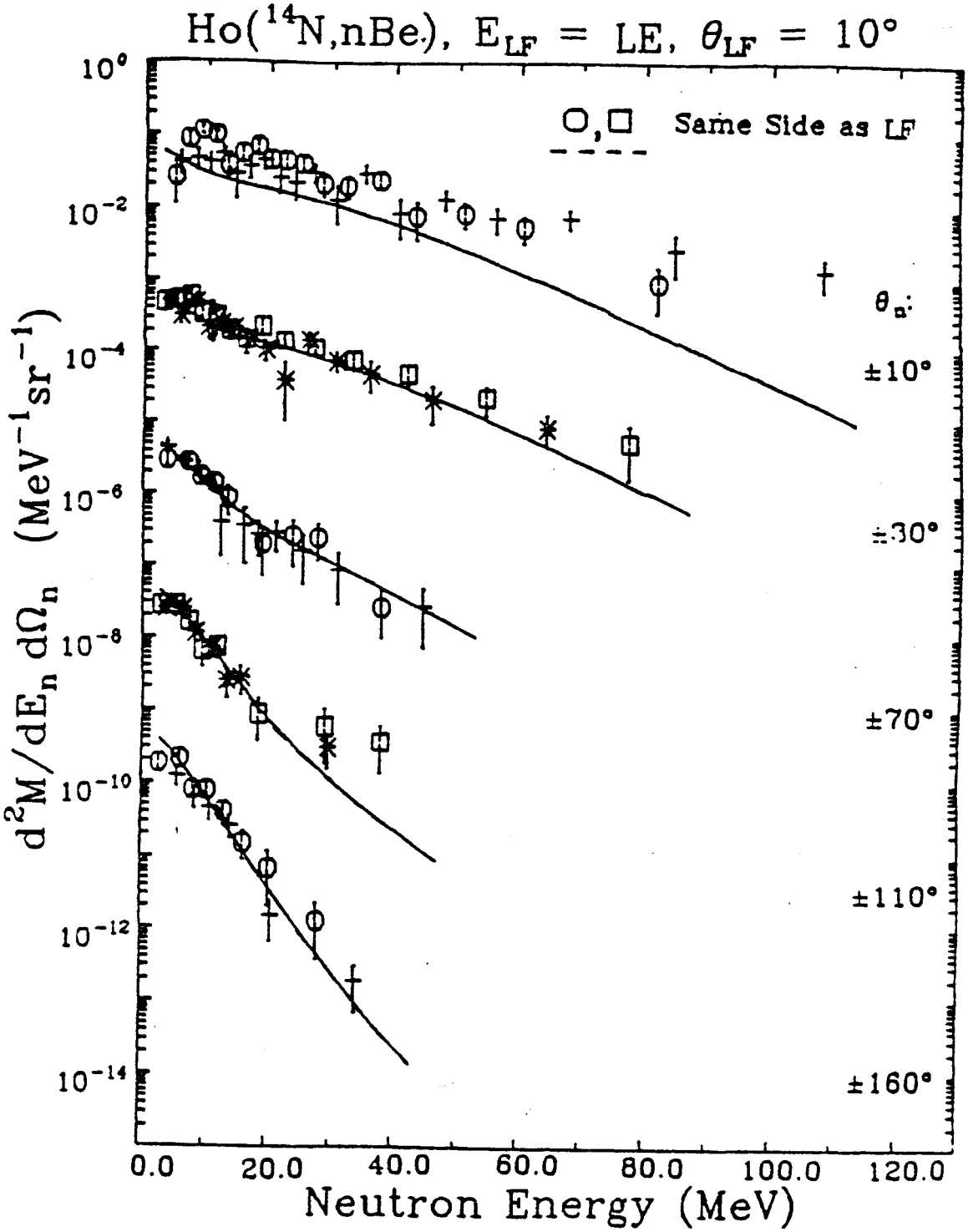

Figure A-25. (continued)

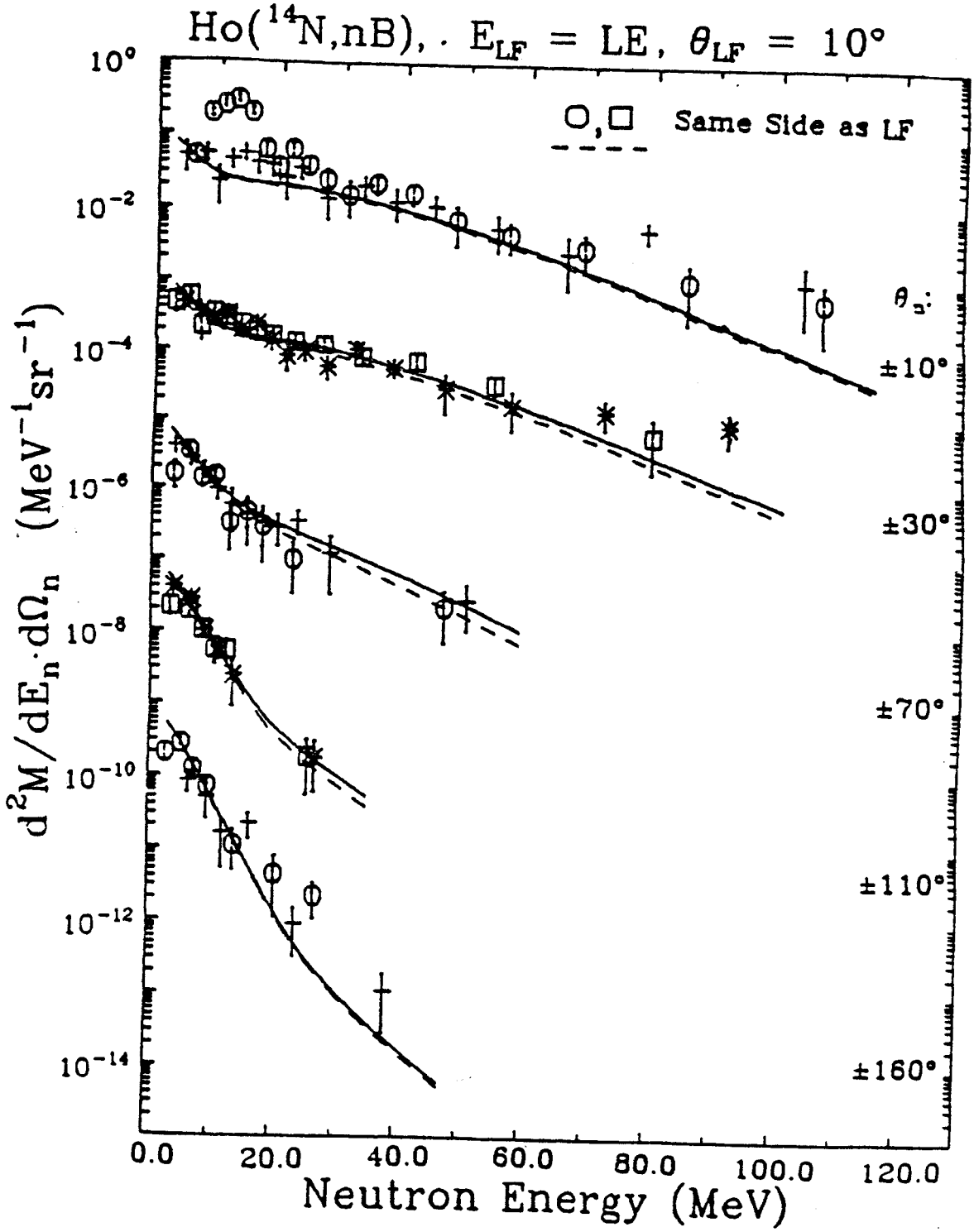

Figure A-25. (continued)

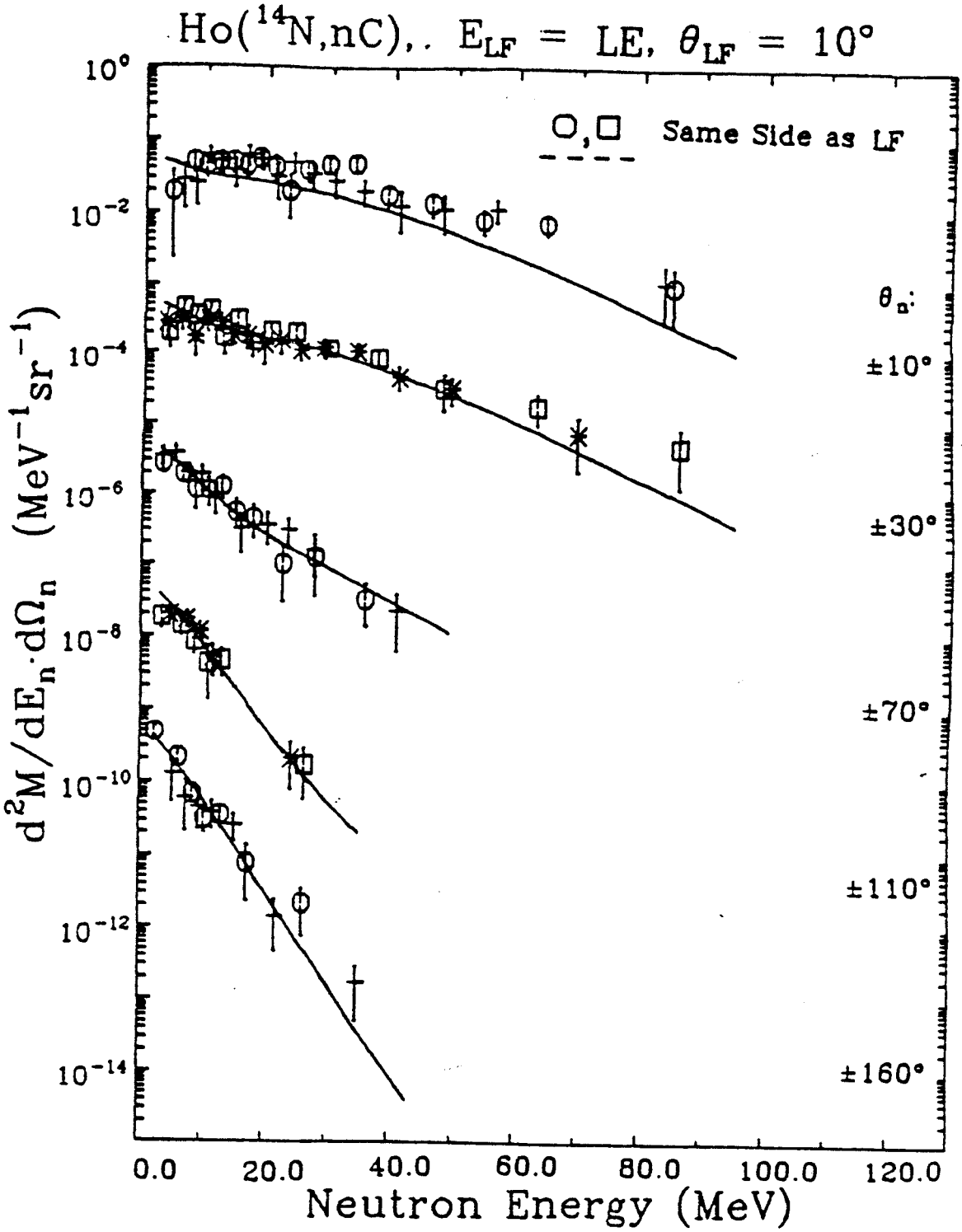

Figure A-25. (continued)

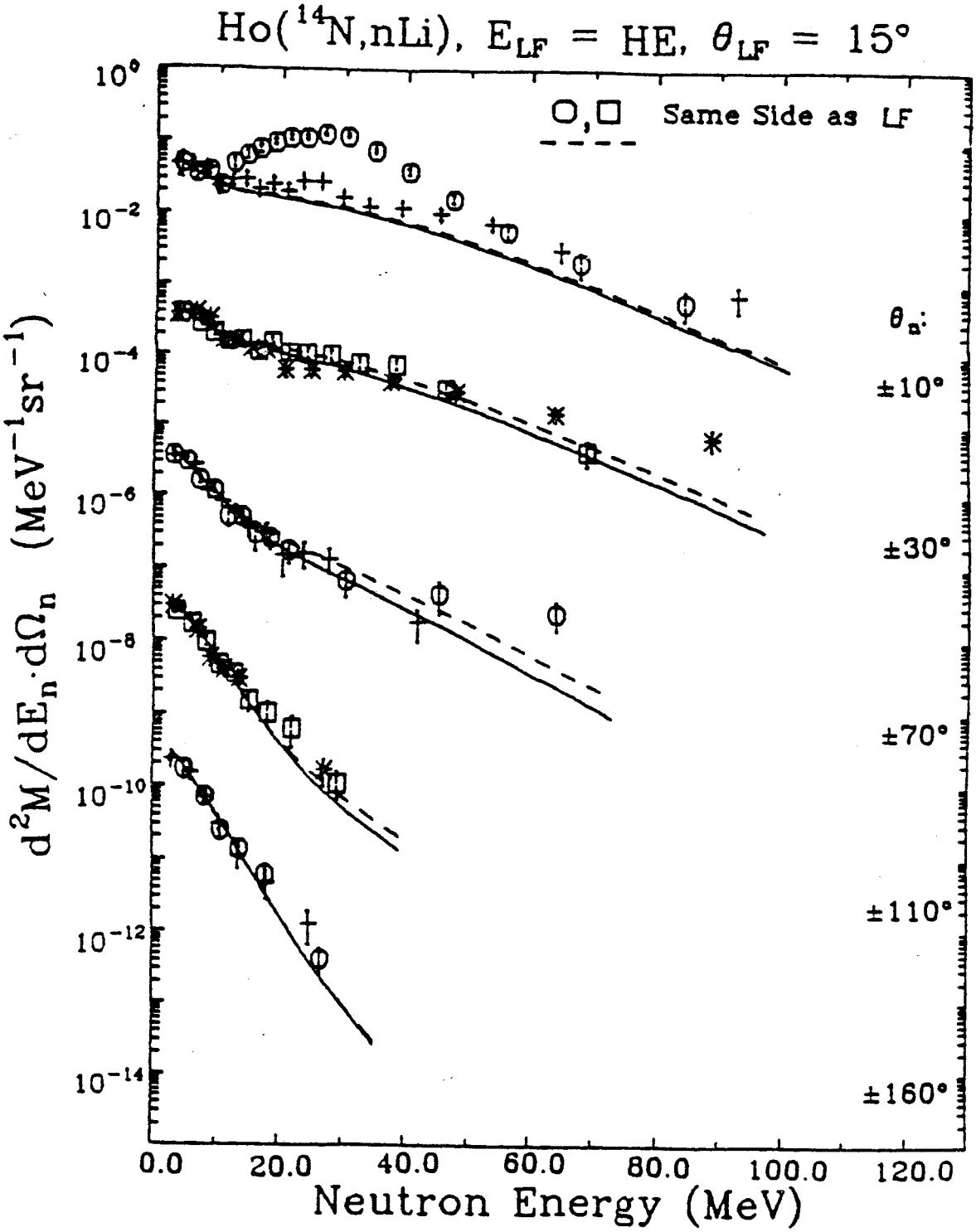

Figure A-25. (continued)

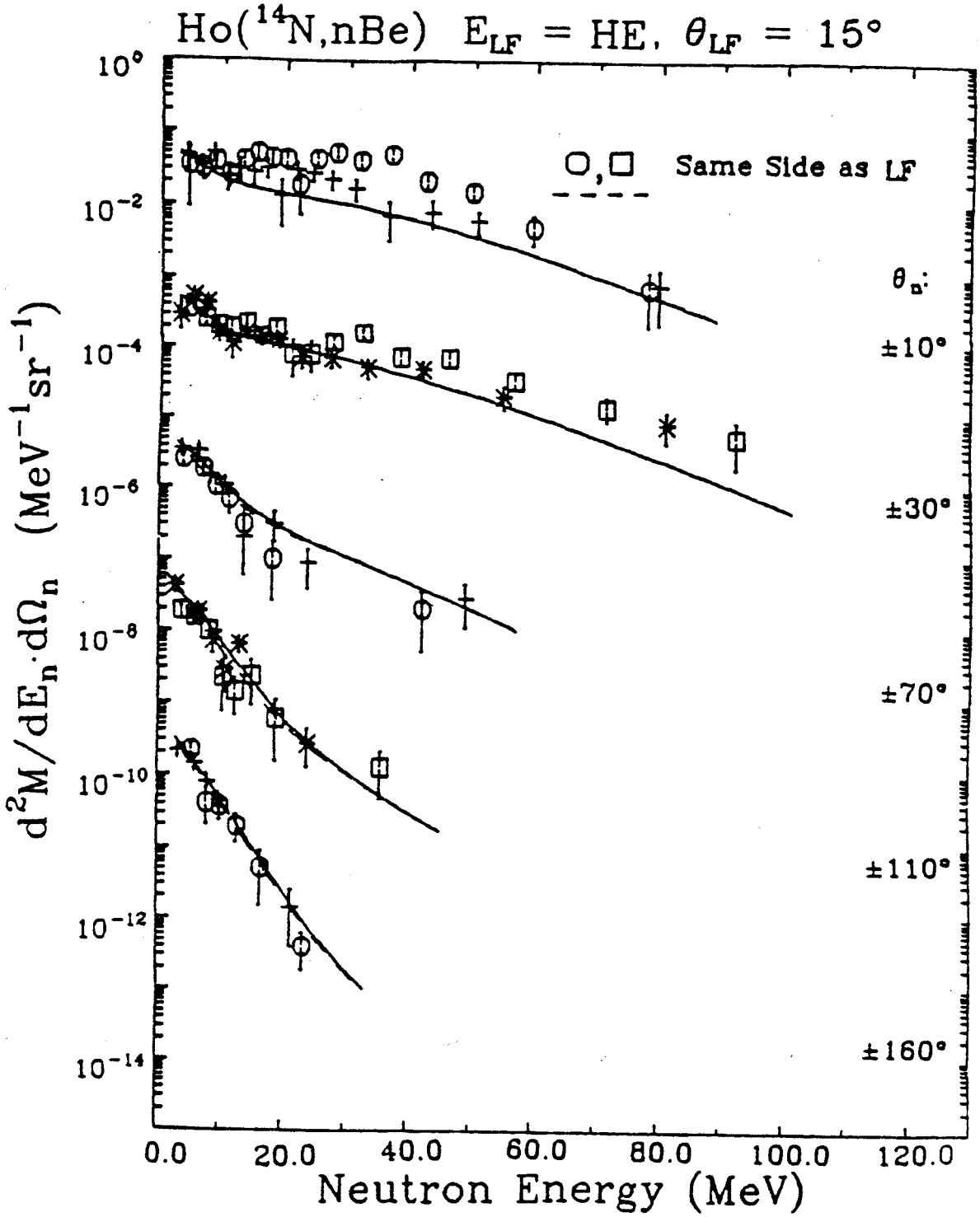

Figure A-25. (continued)

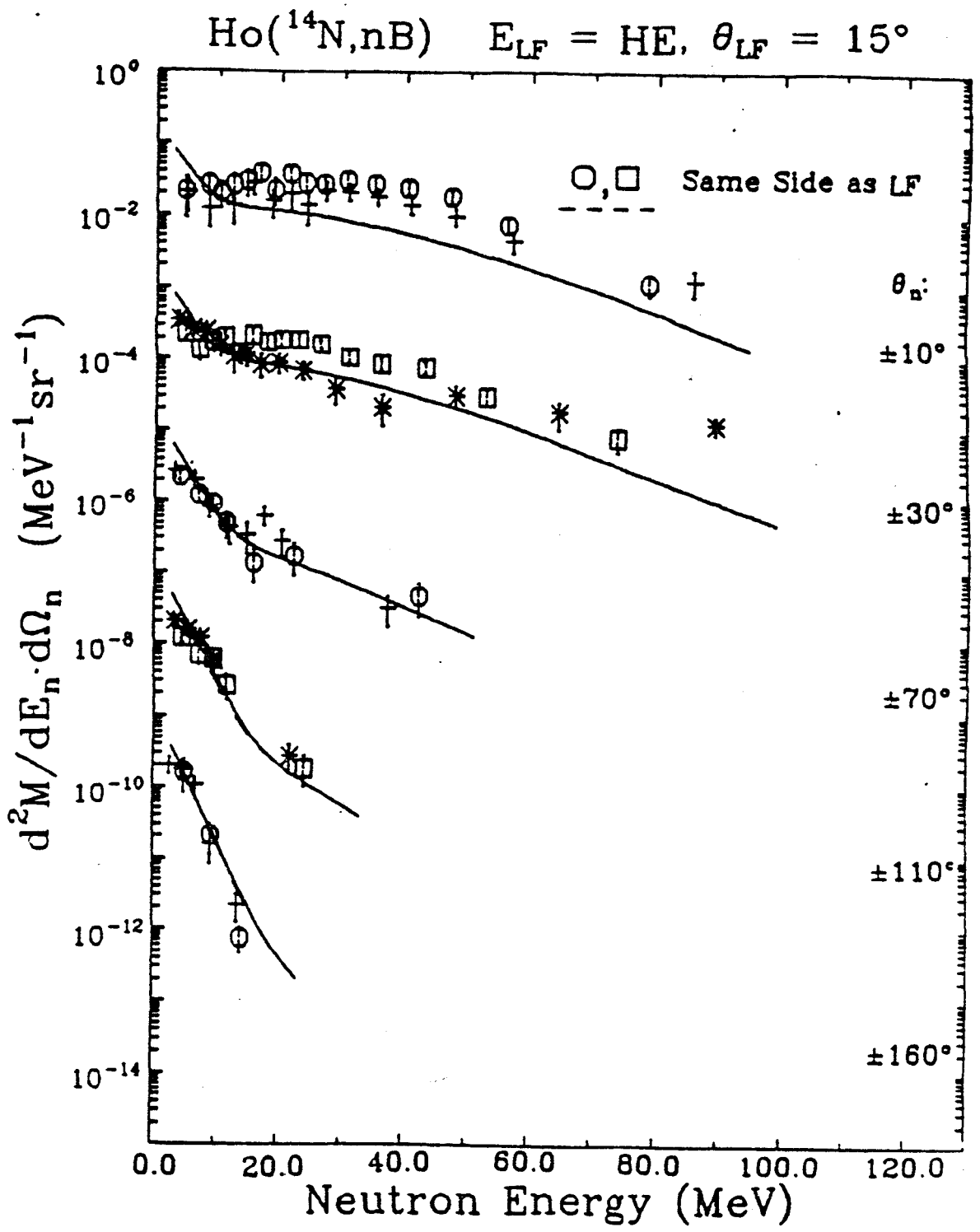

Figure A-25. (continued)

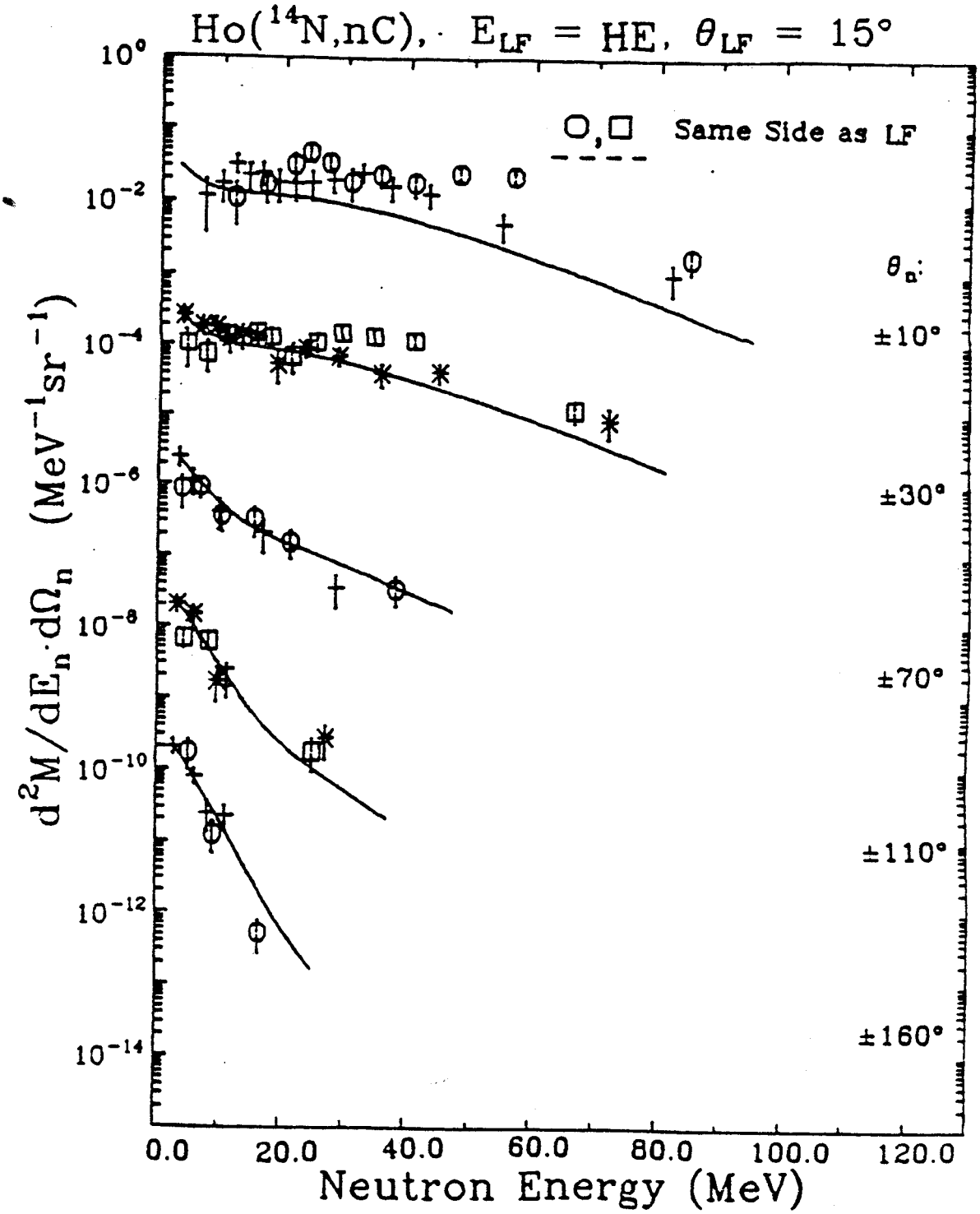

Figure A-25. (continued)

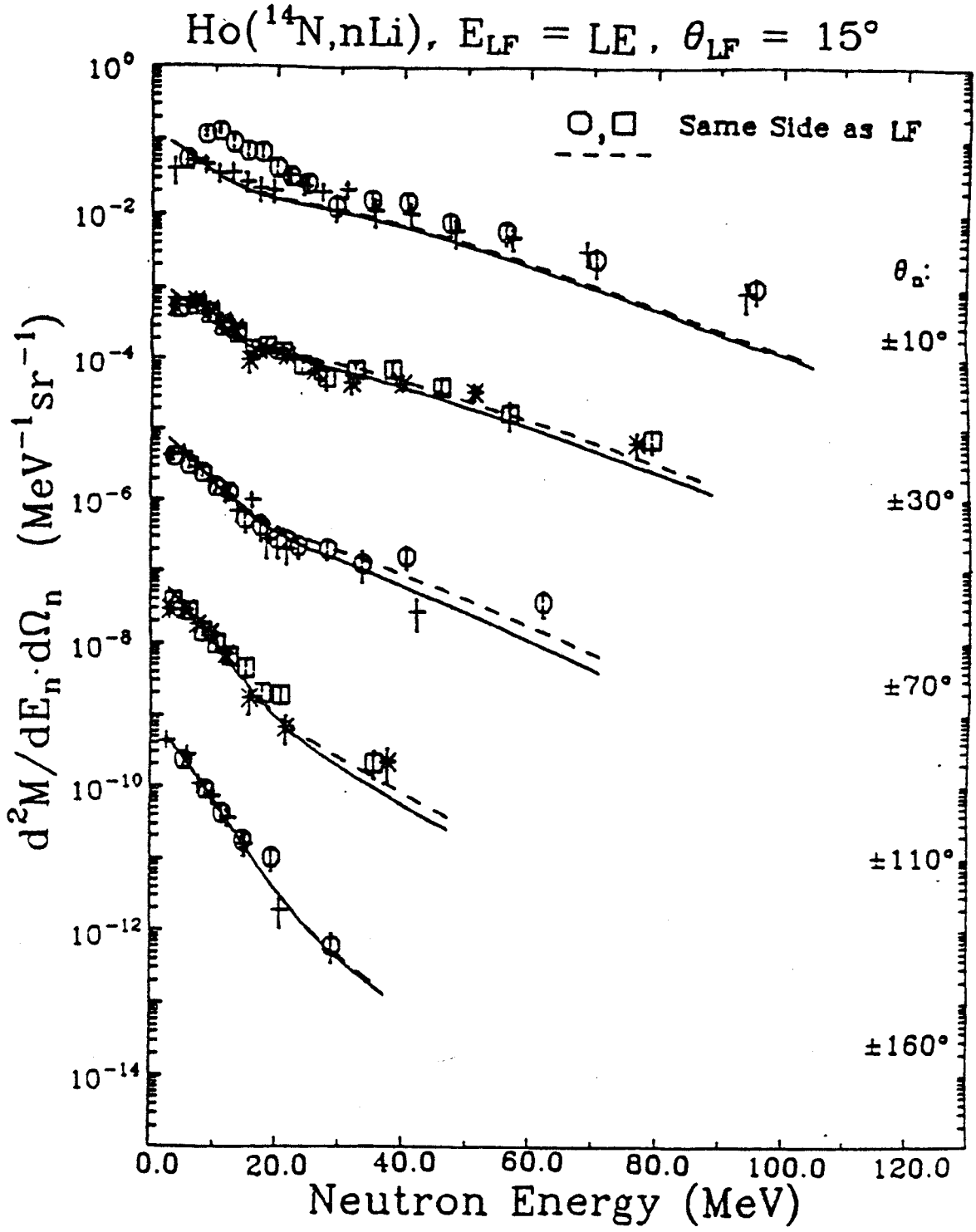

Figure A-25. (continued)

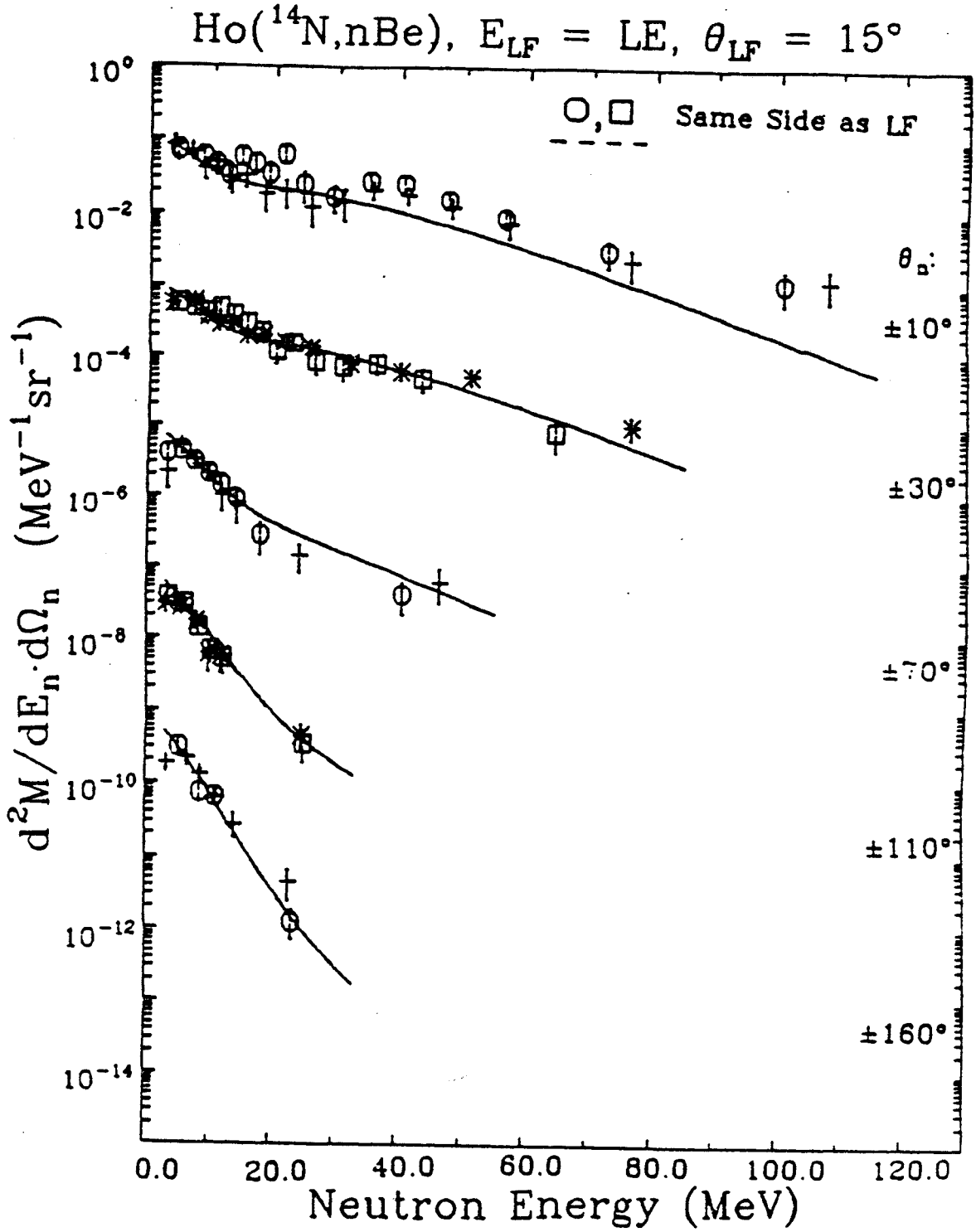

Figure A-25. (continued)

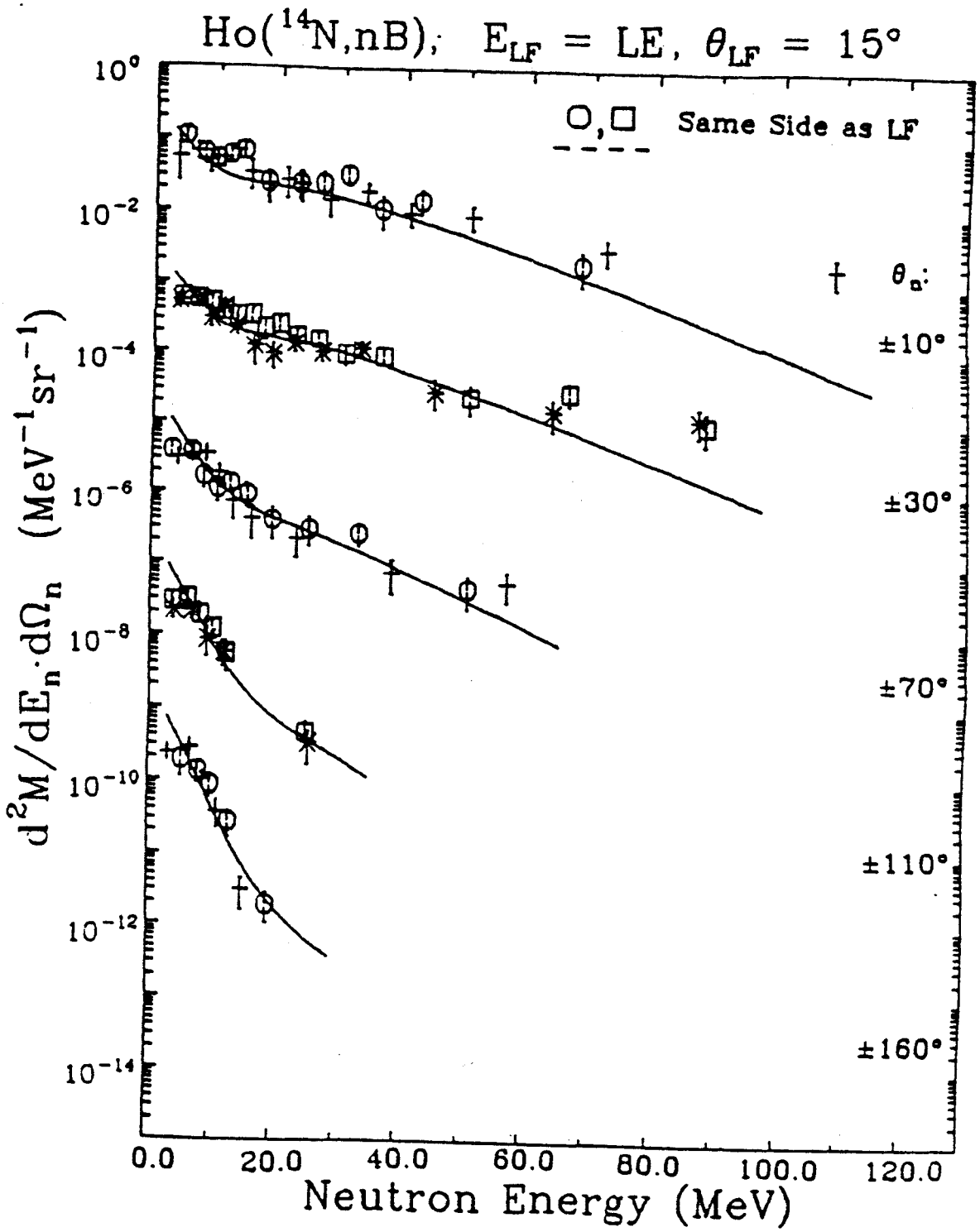

Figure A-25. (continued)

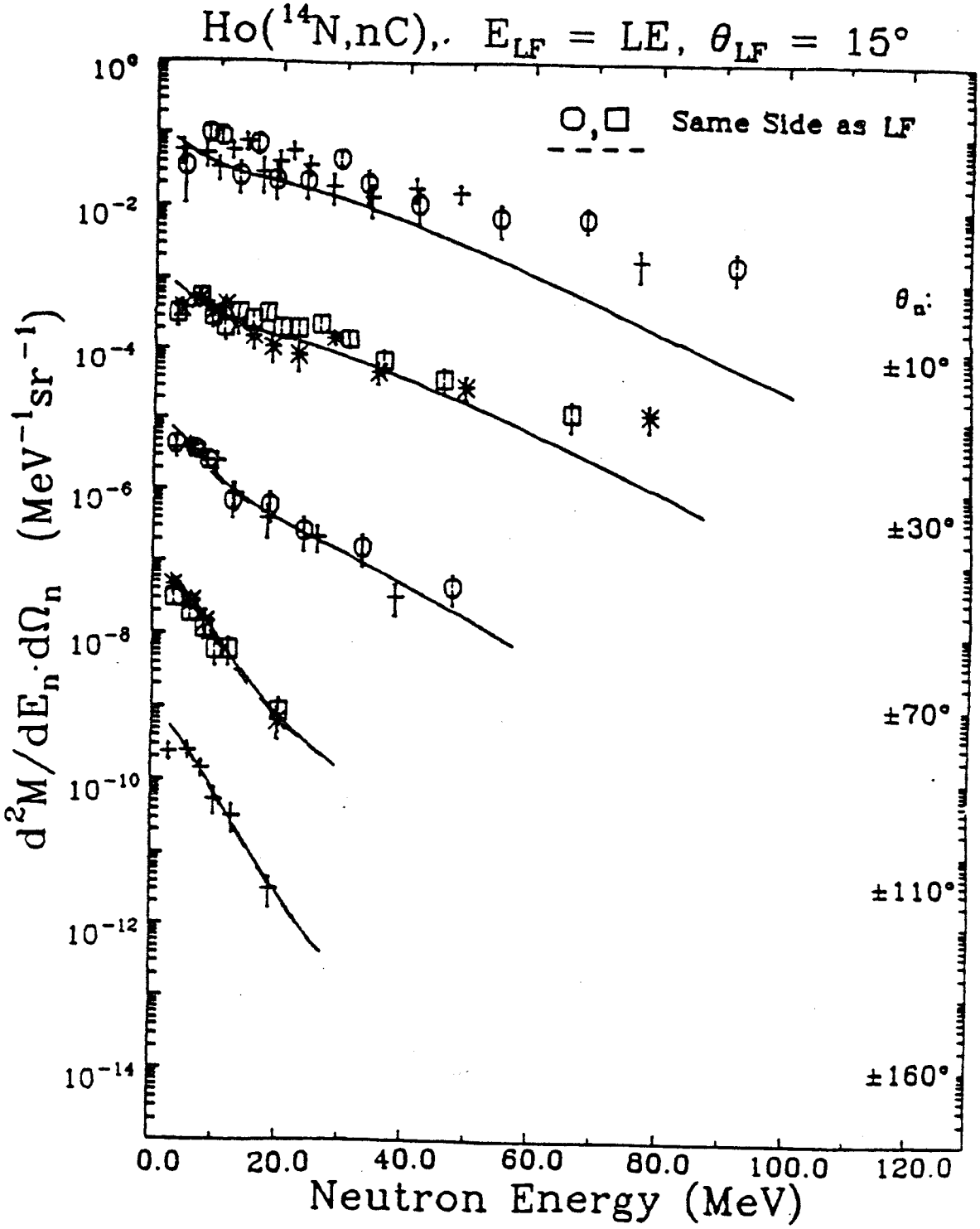

Figure A-25. (continued)

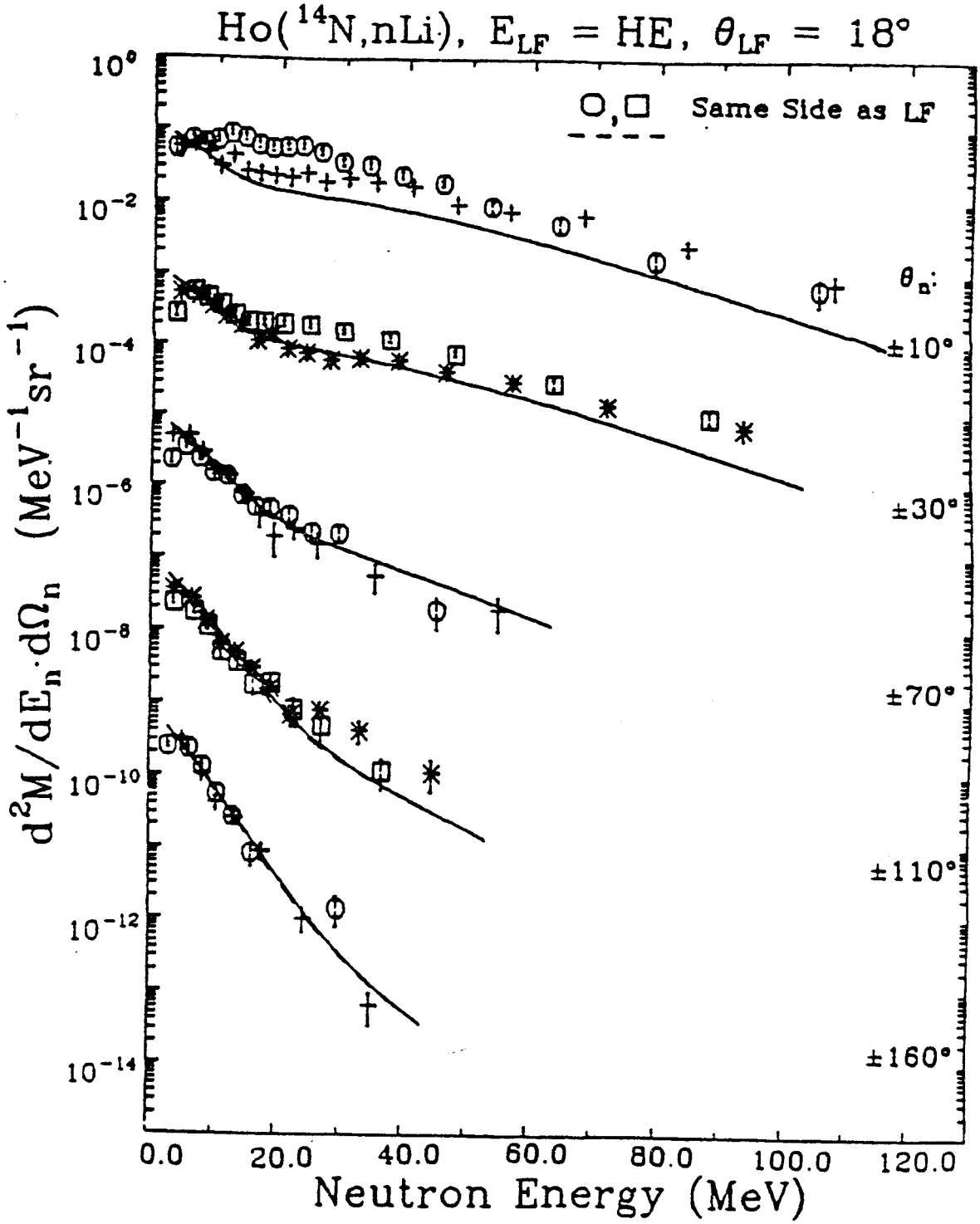

Figure A-25. (continued)

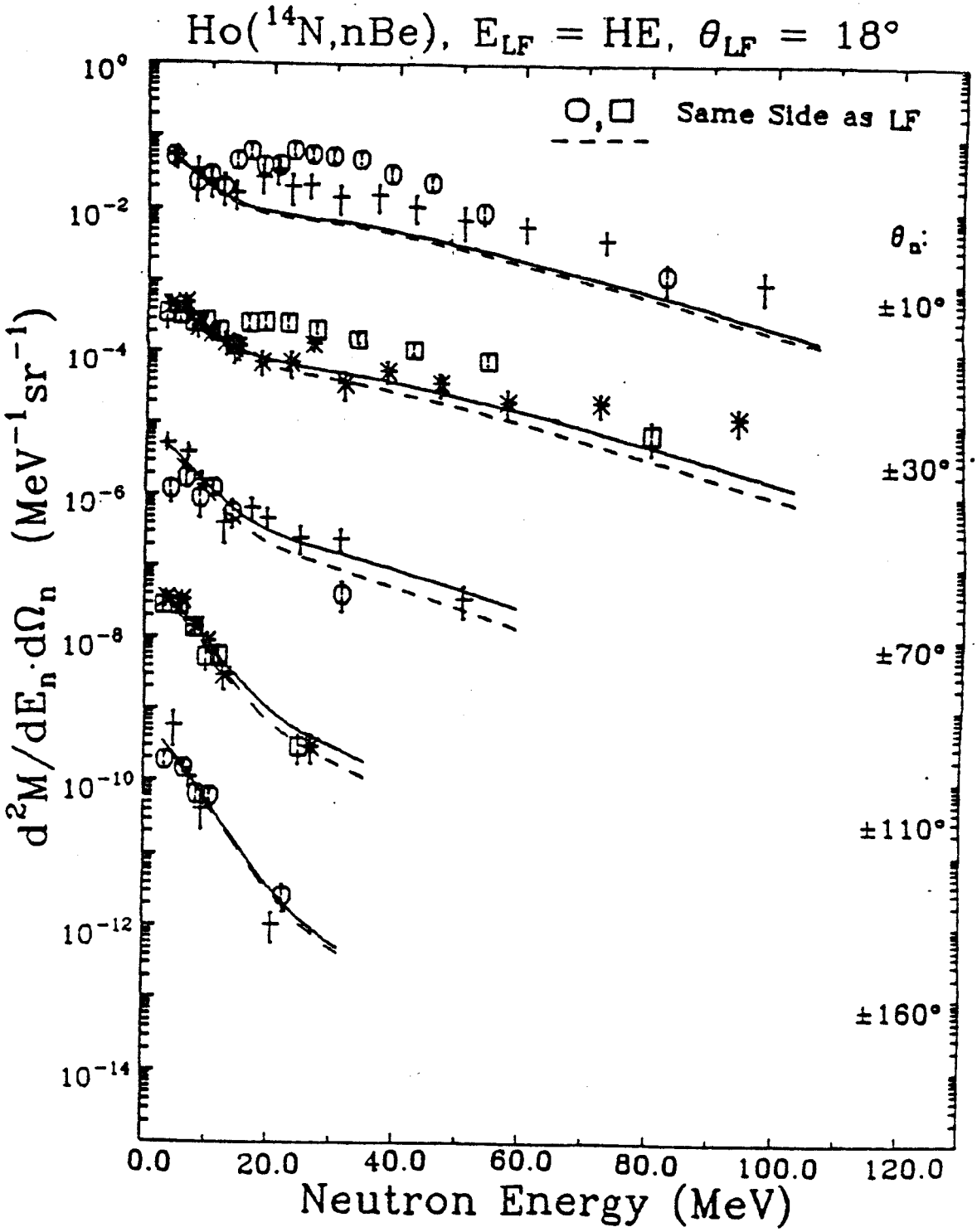

Figure A-25. (continued)

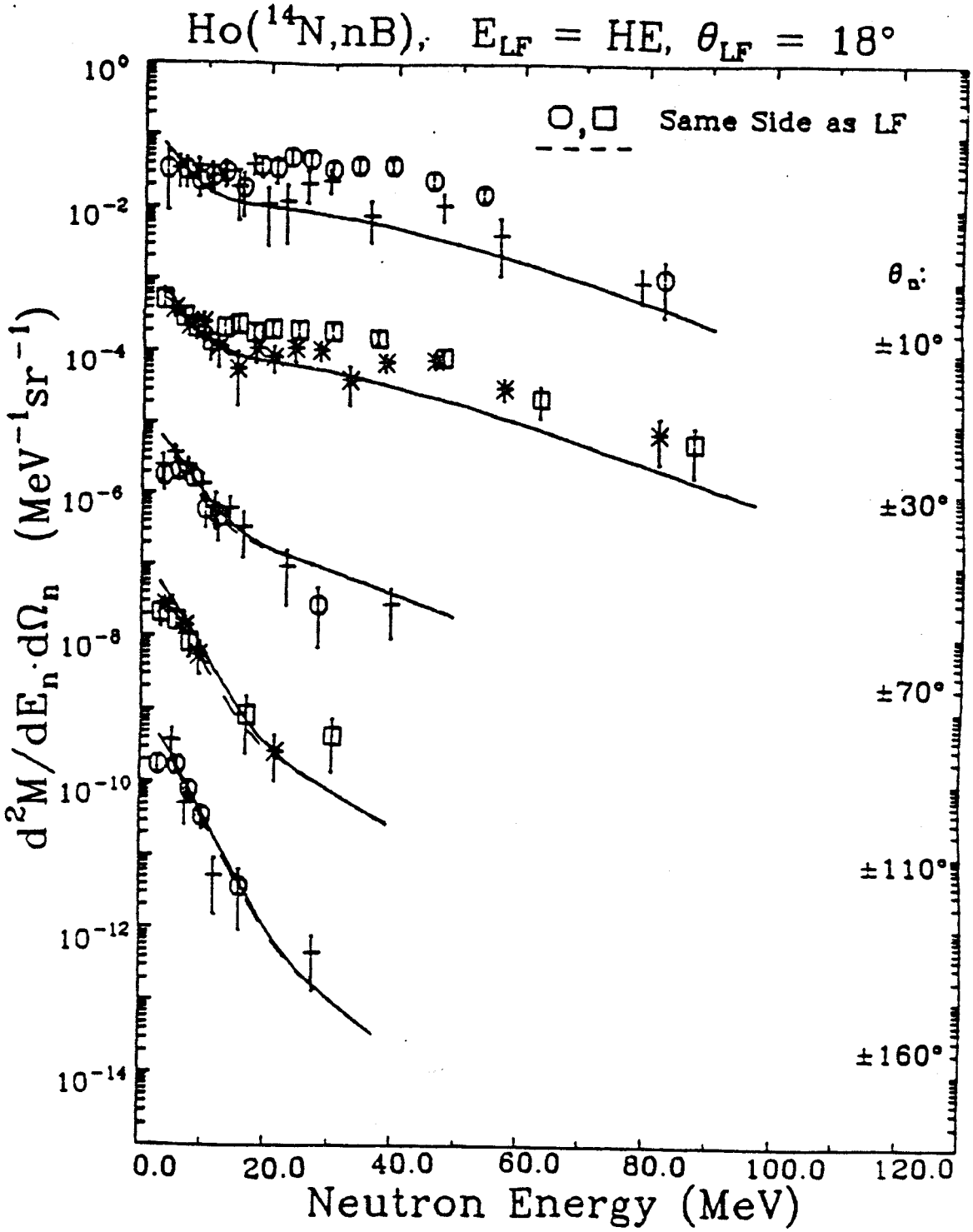

Figure A-25. (continued)

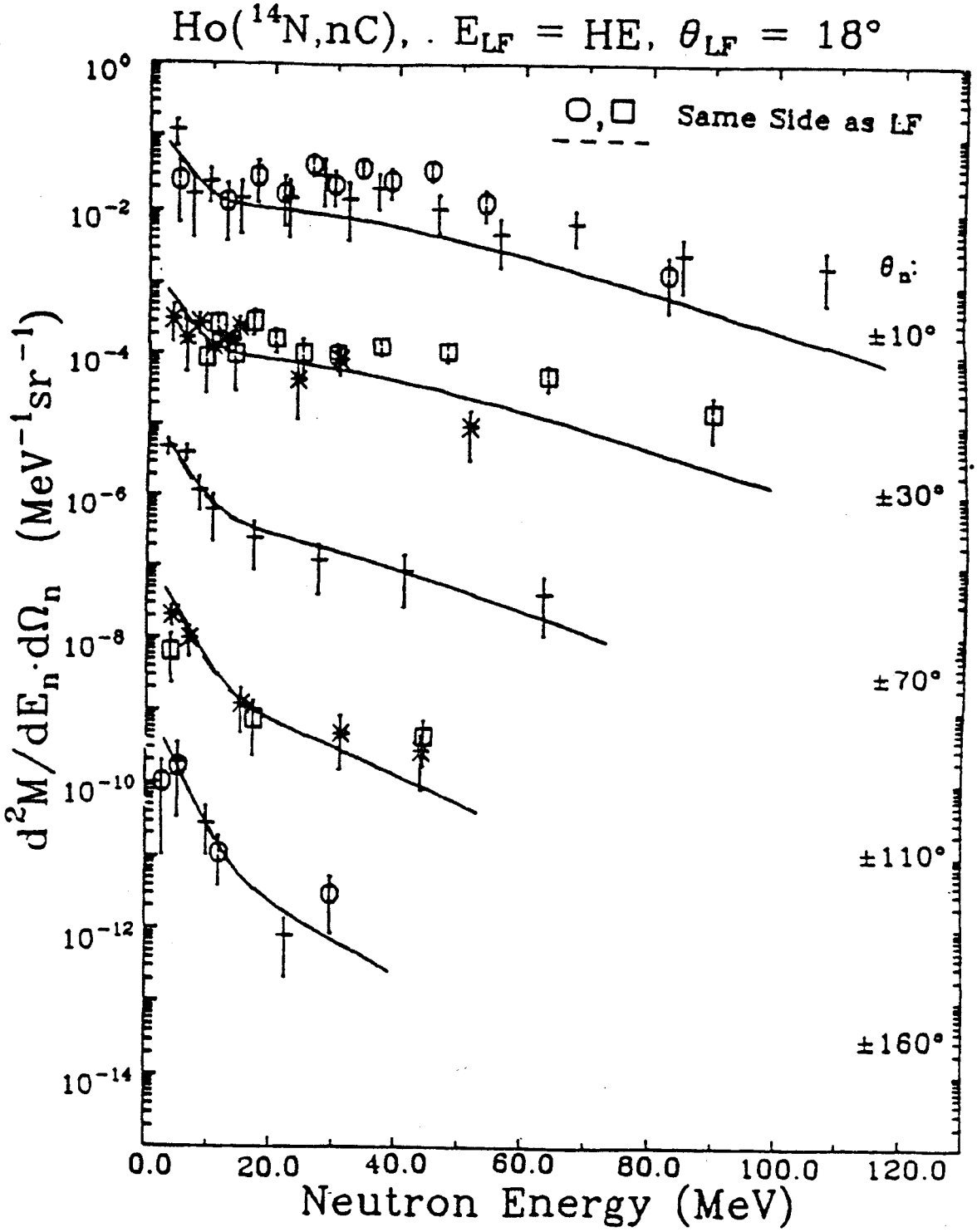

Figure A-25. (continued)

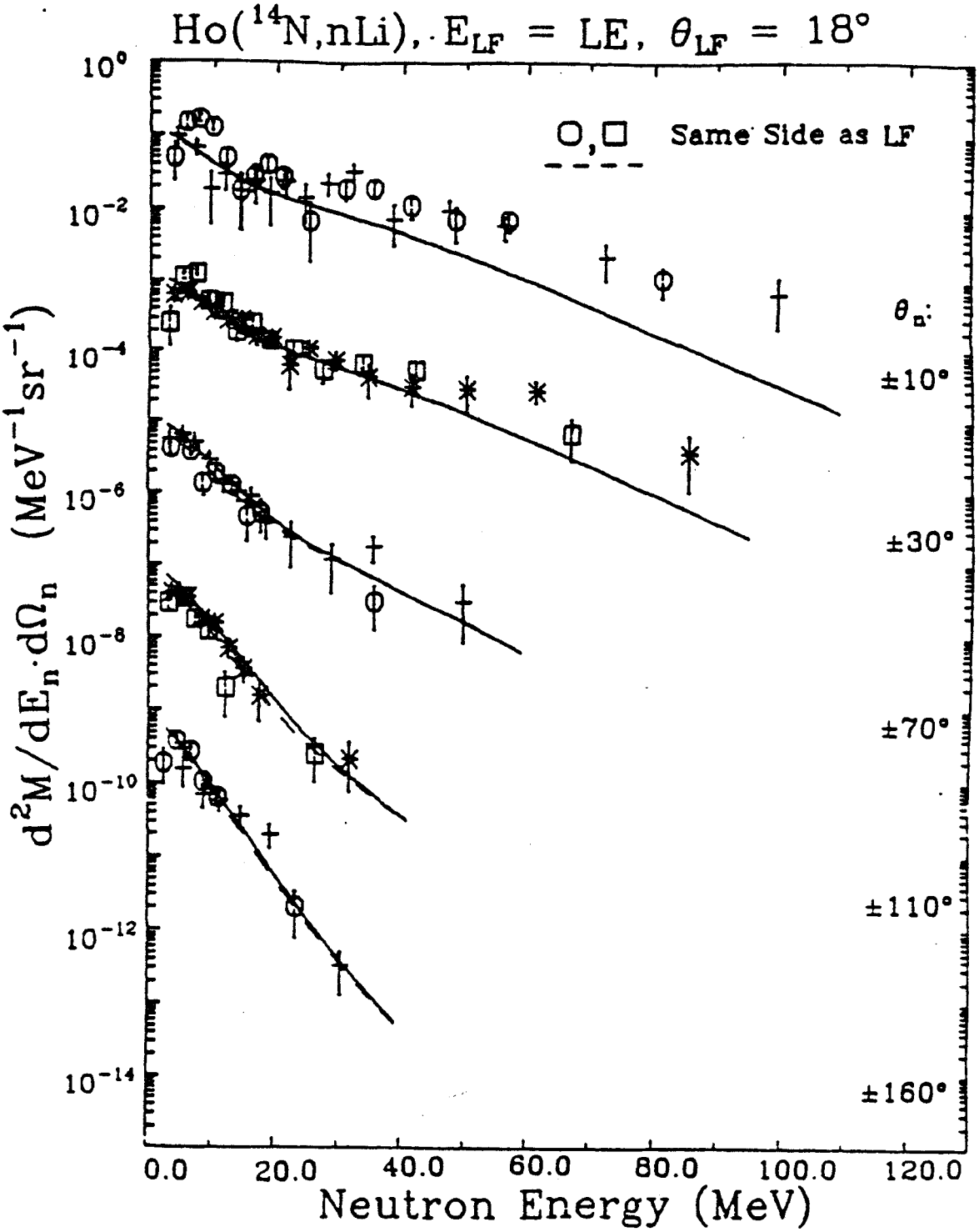

Figure A-25. (continued)

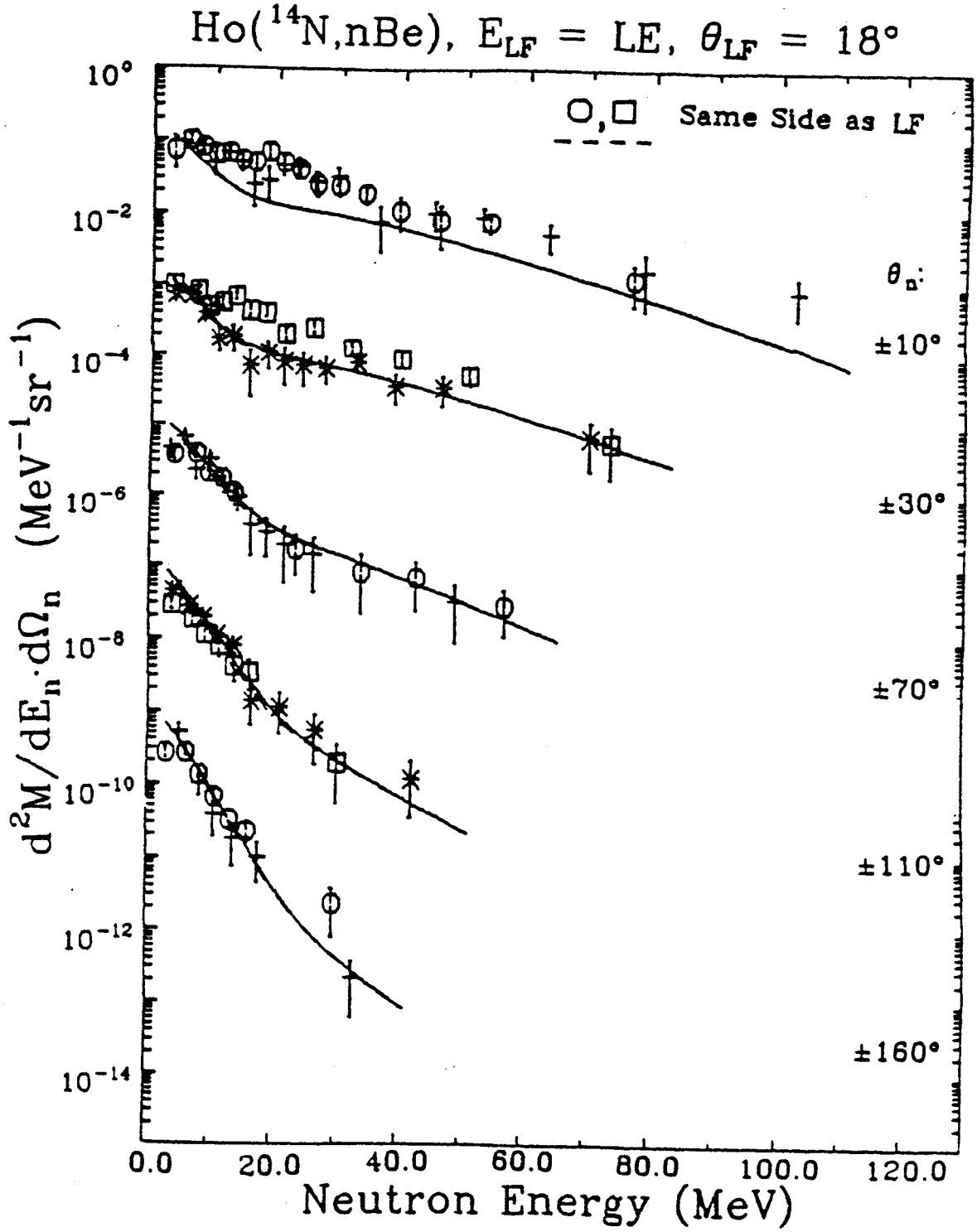

Figure A-25. (continued)

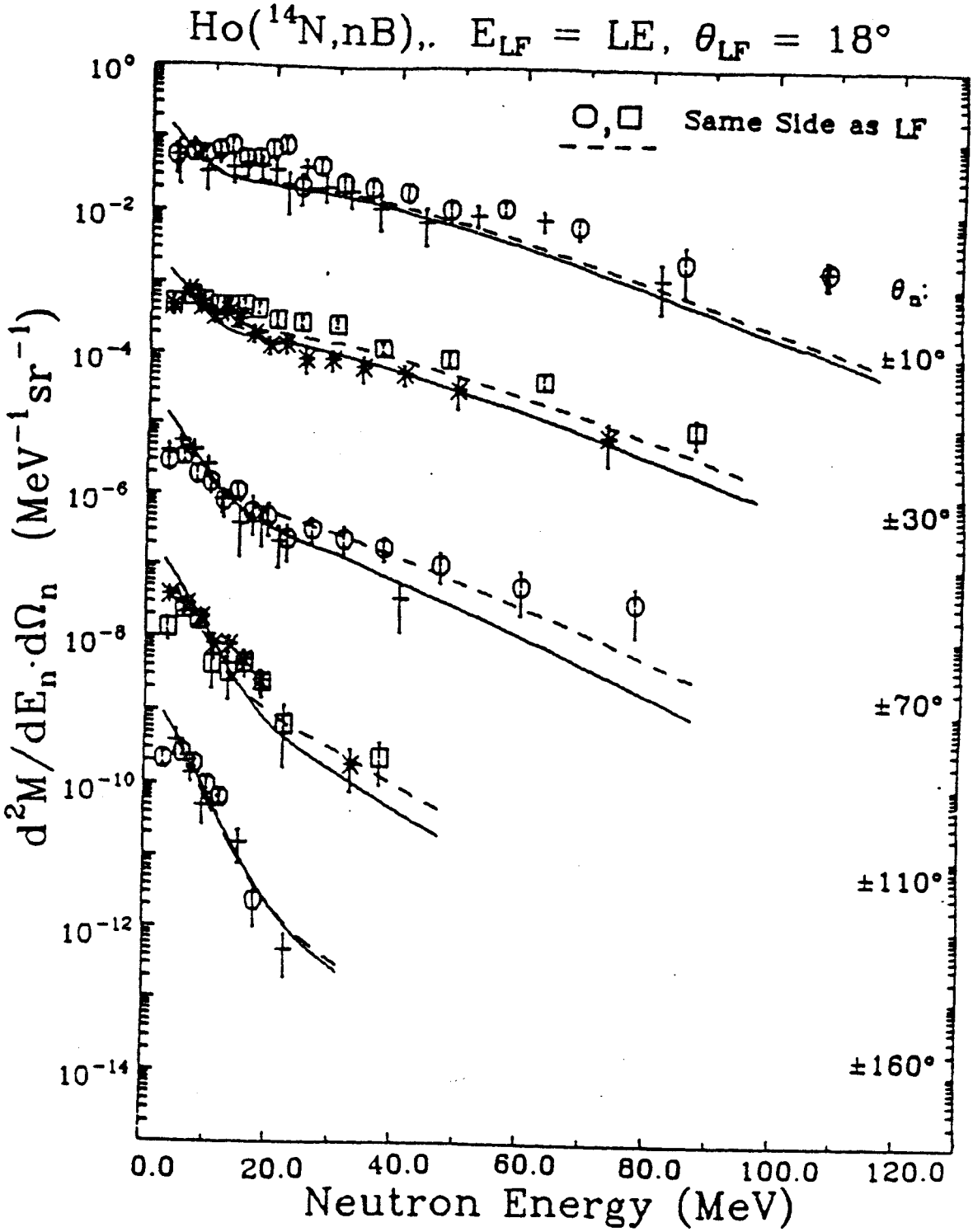

Figure A-21. (continued)

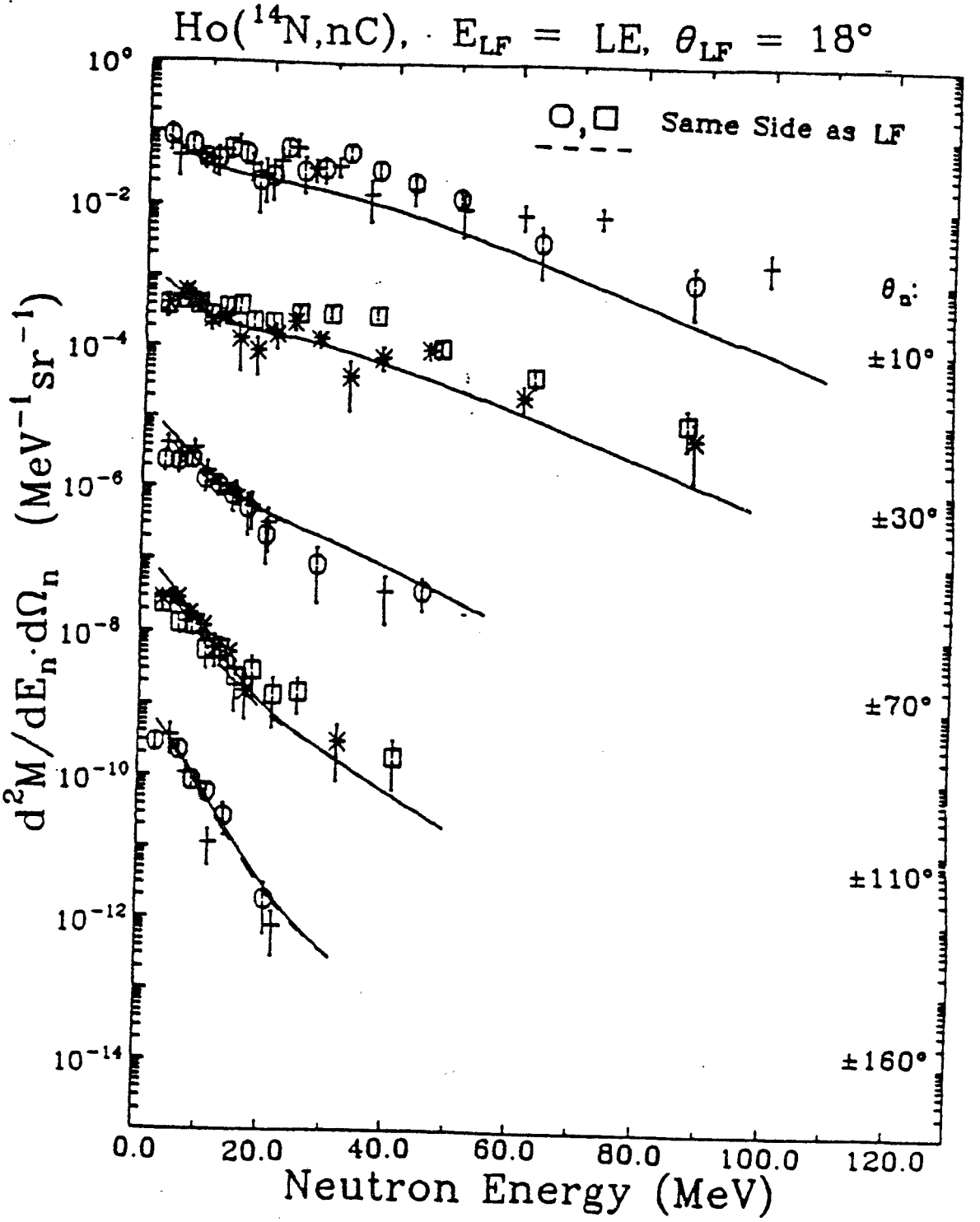

Figure A-25. (continued)

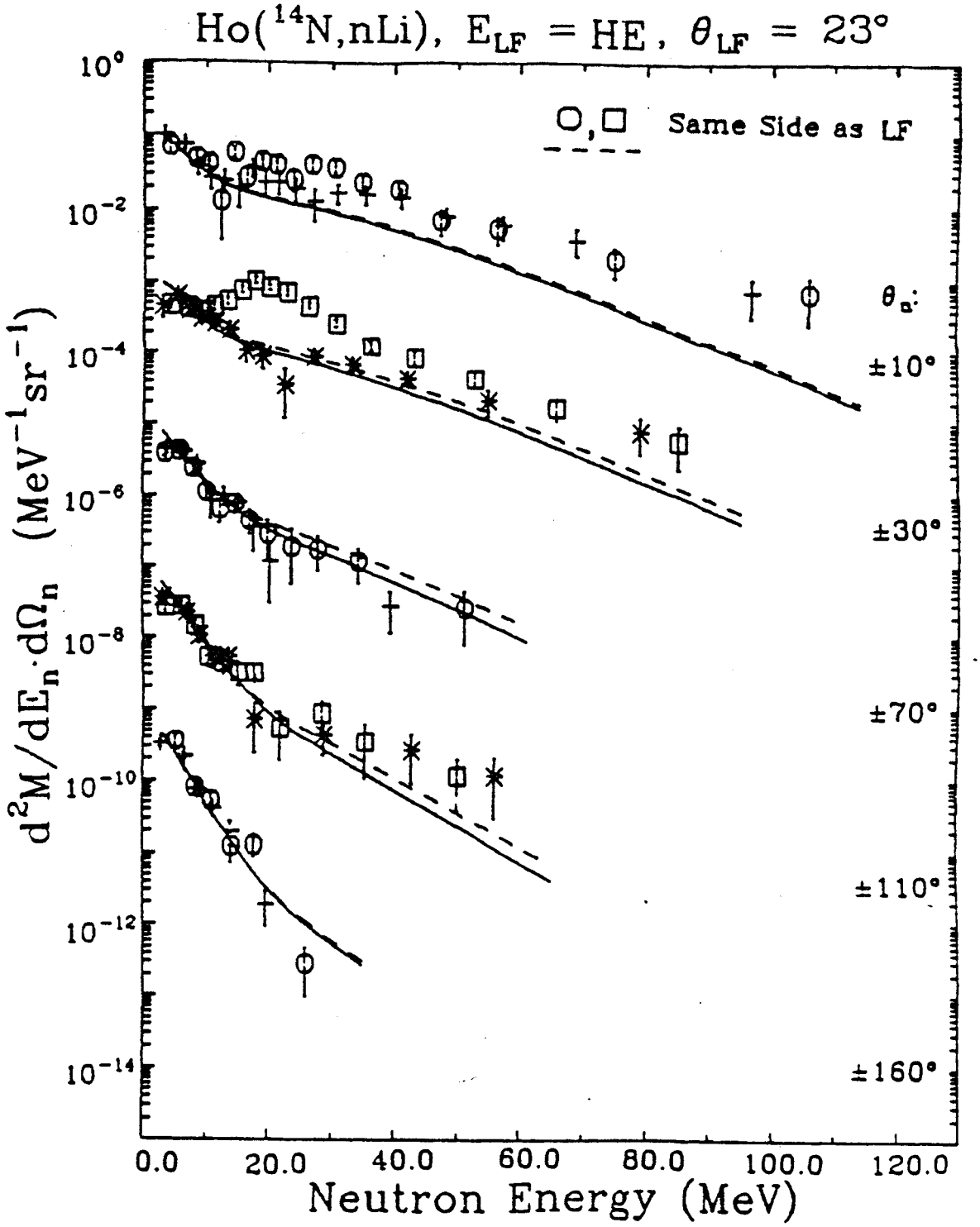

Figure A-25. (continued)

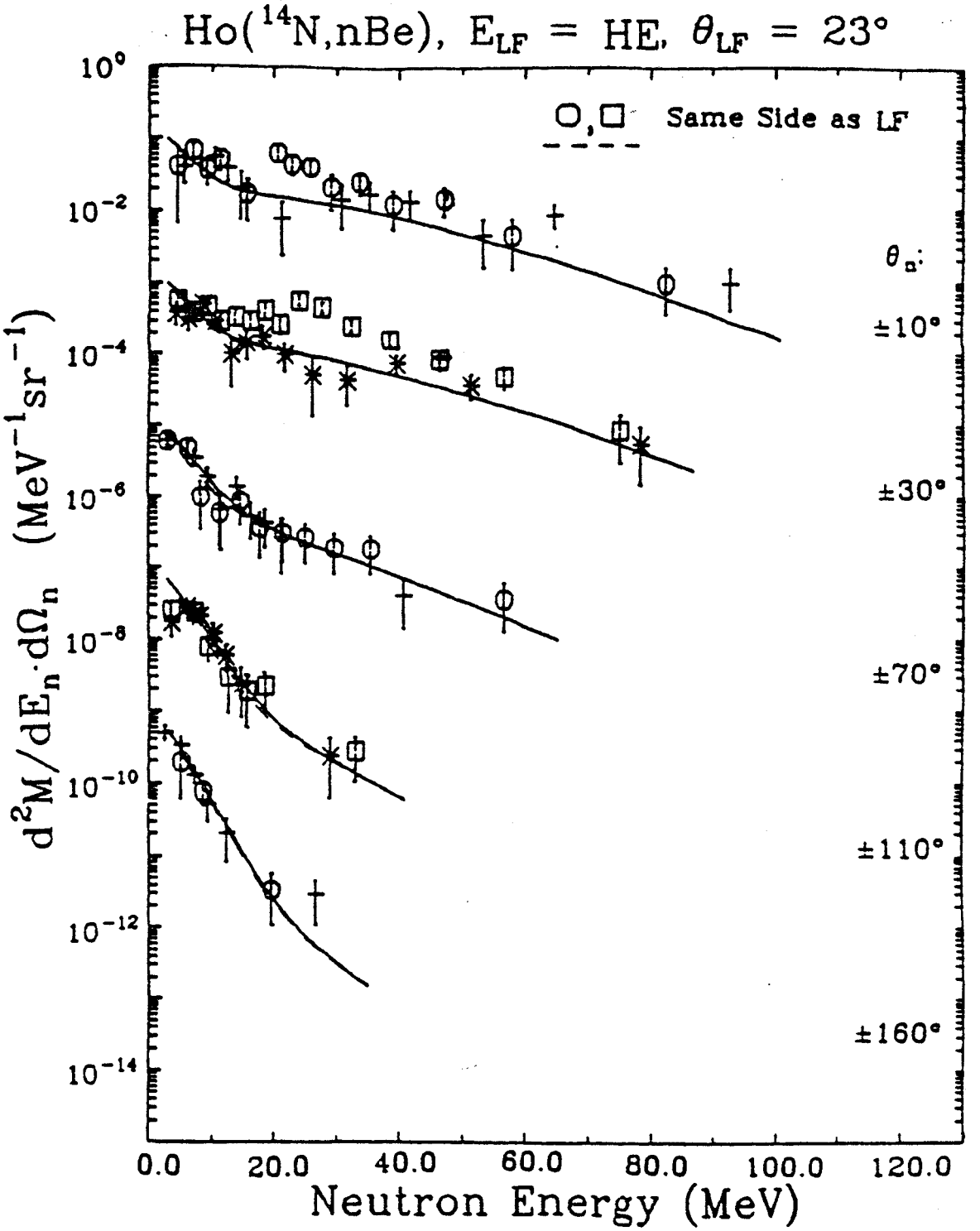

Figure A-25. (continued)

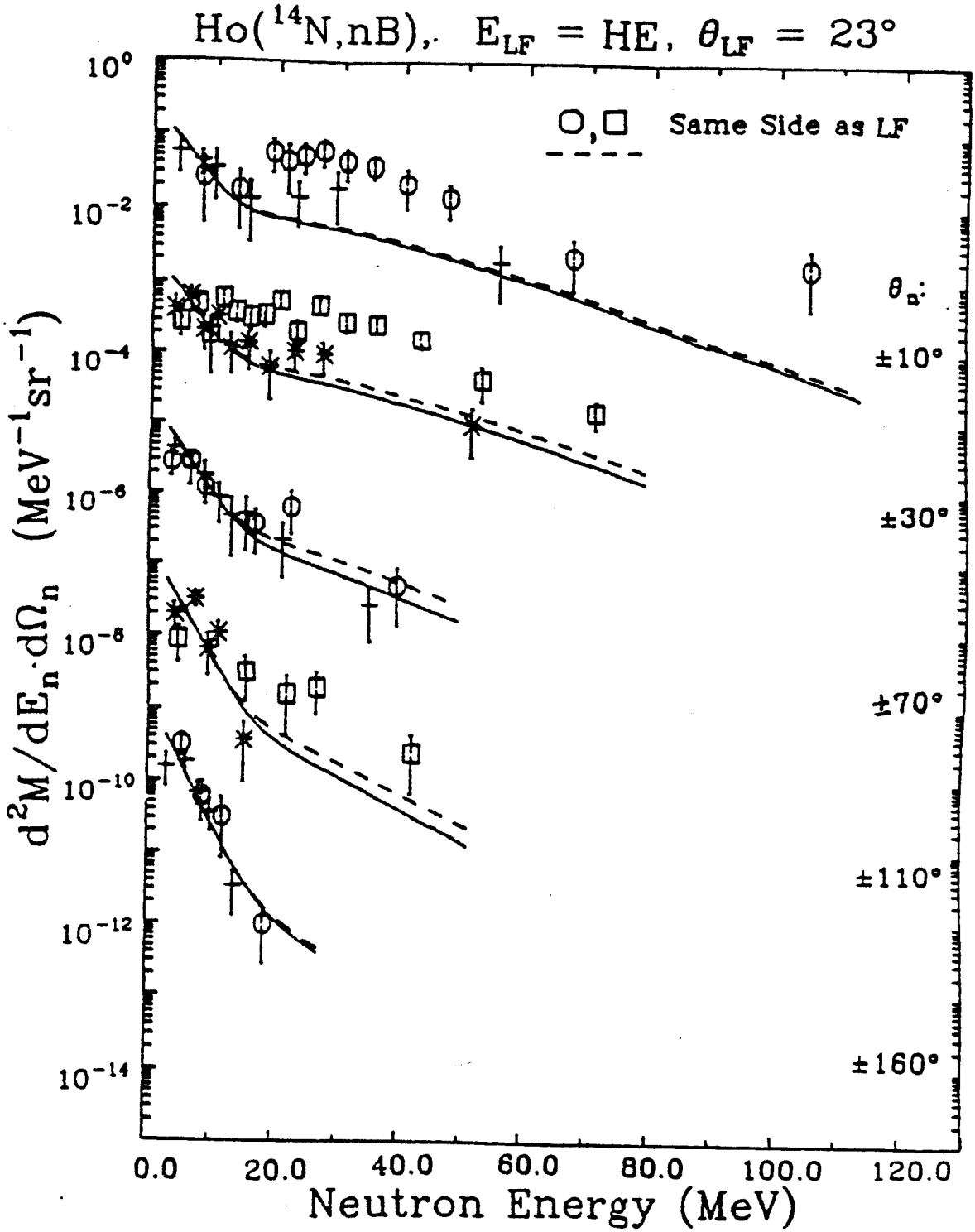

Figure A-25. (continued)

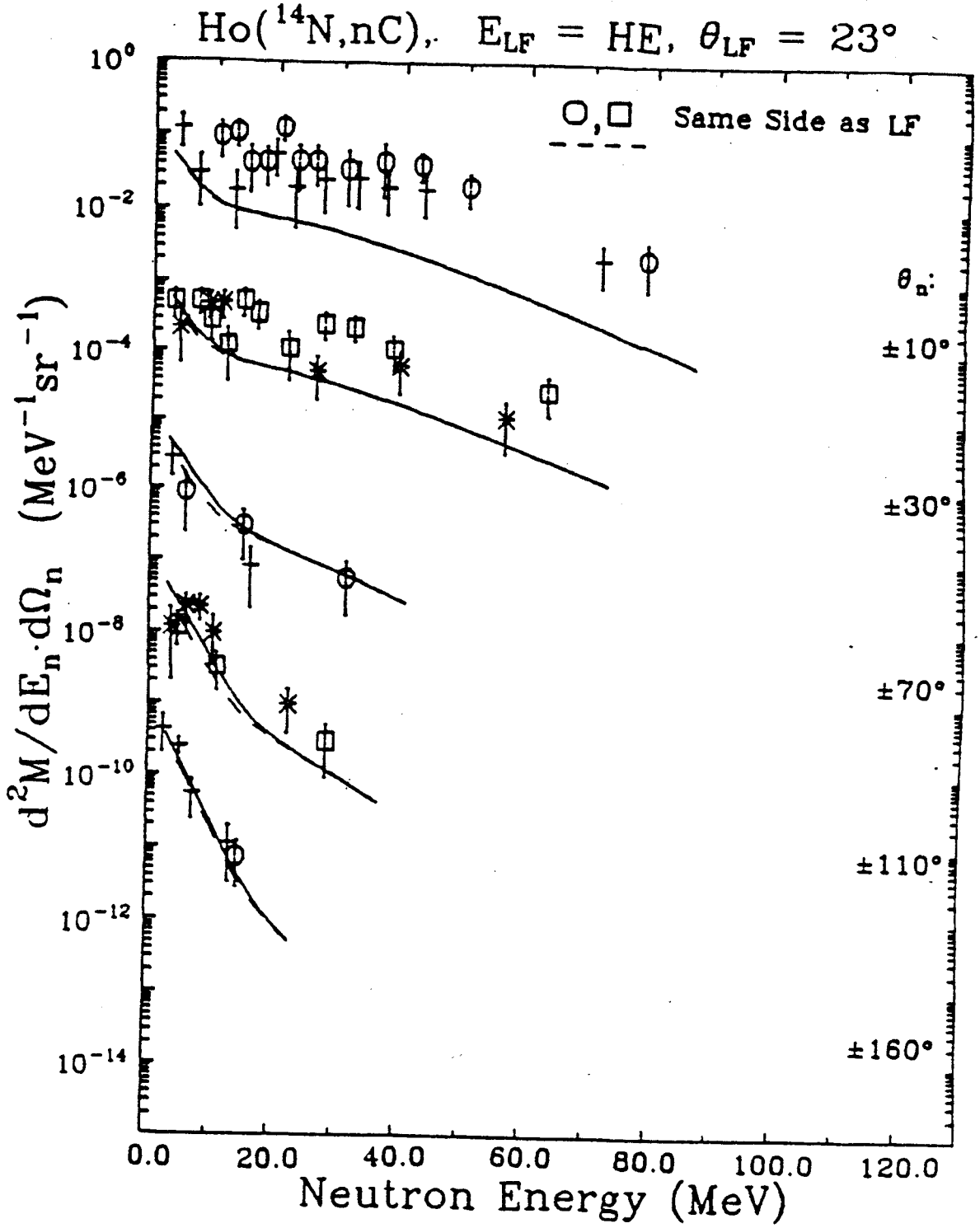

Figure A-25. (continued)

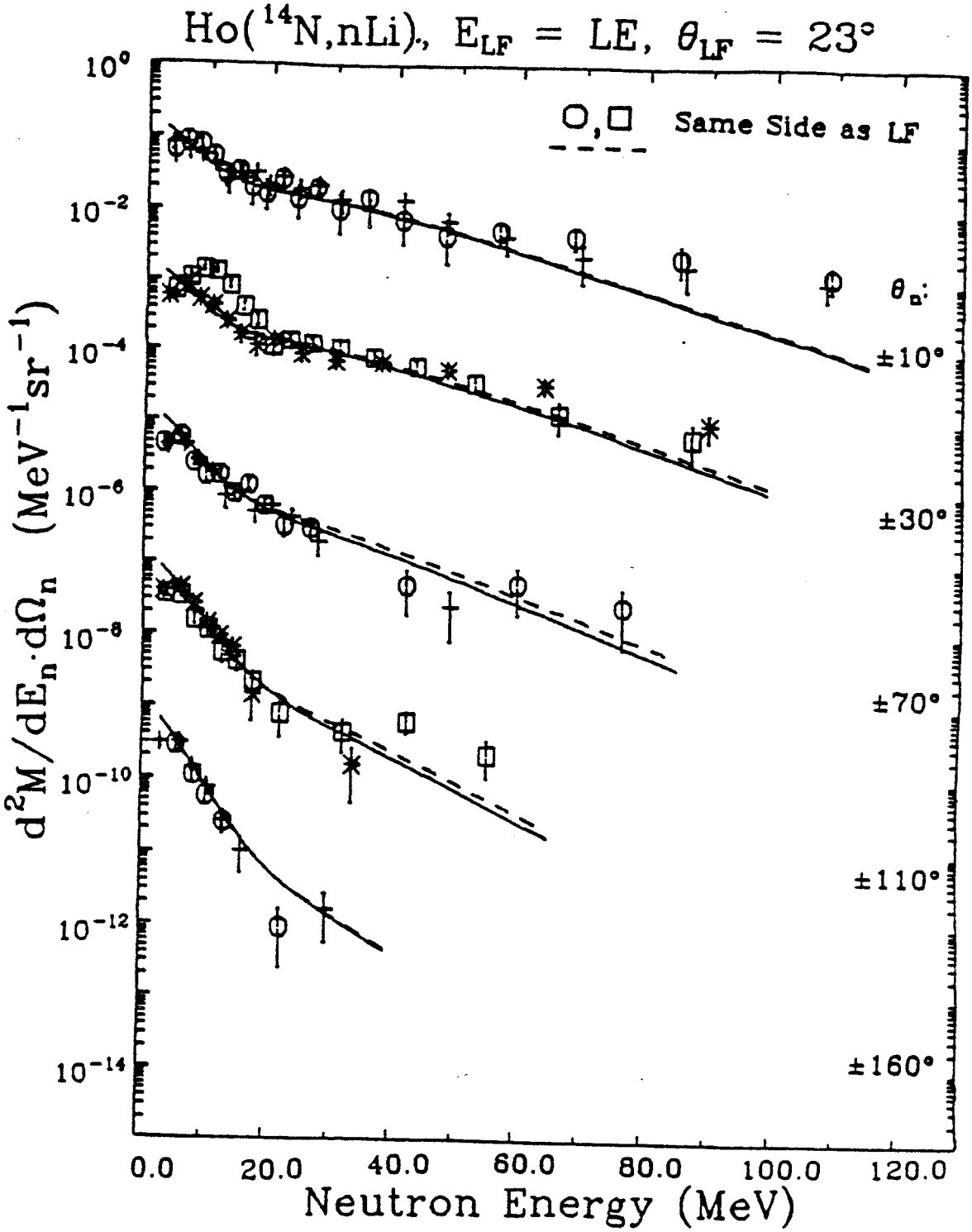

Figure A-25. (continued)

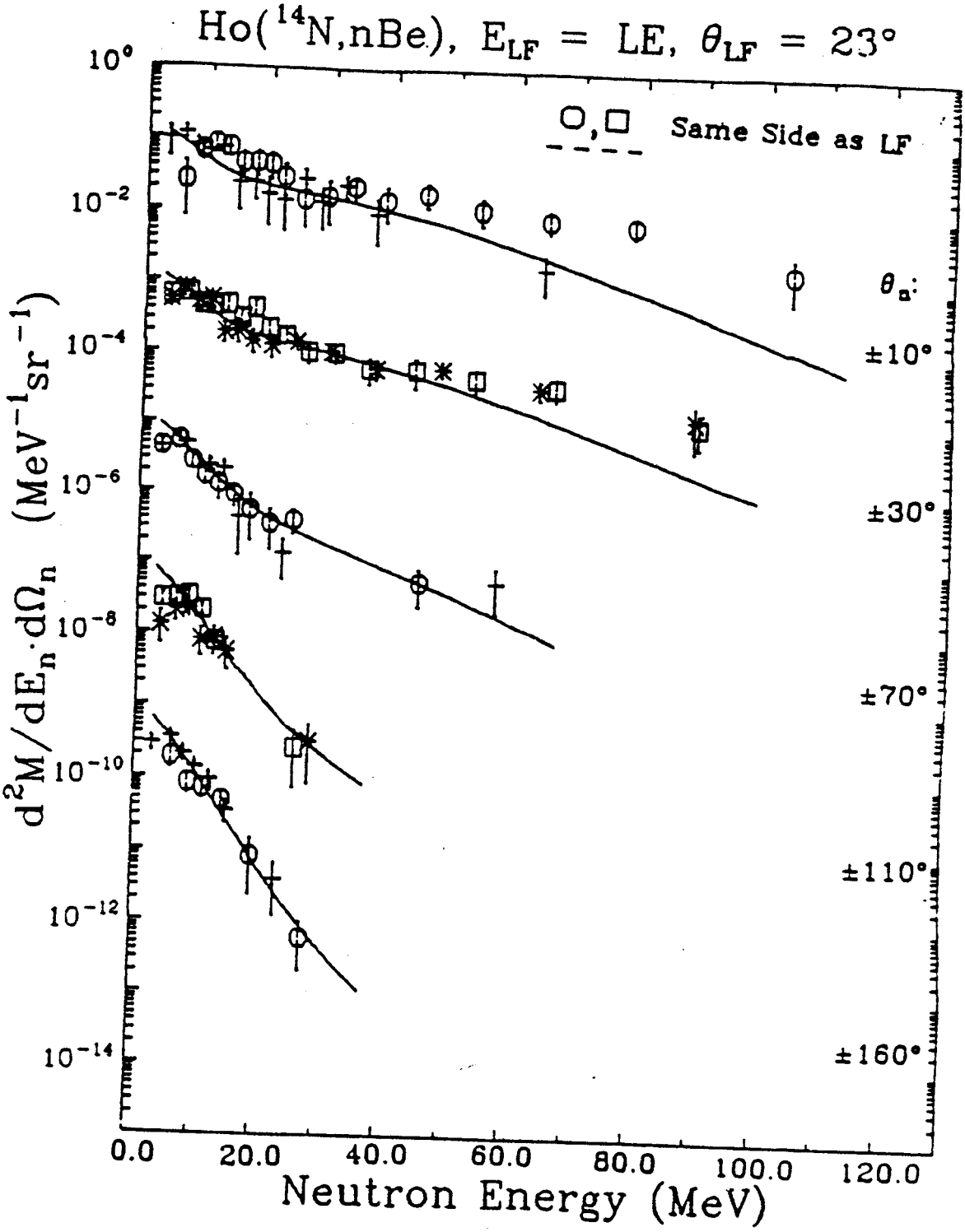

Figure A-25. (continued)

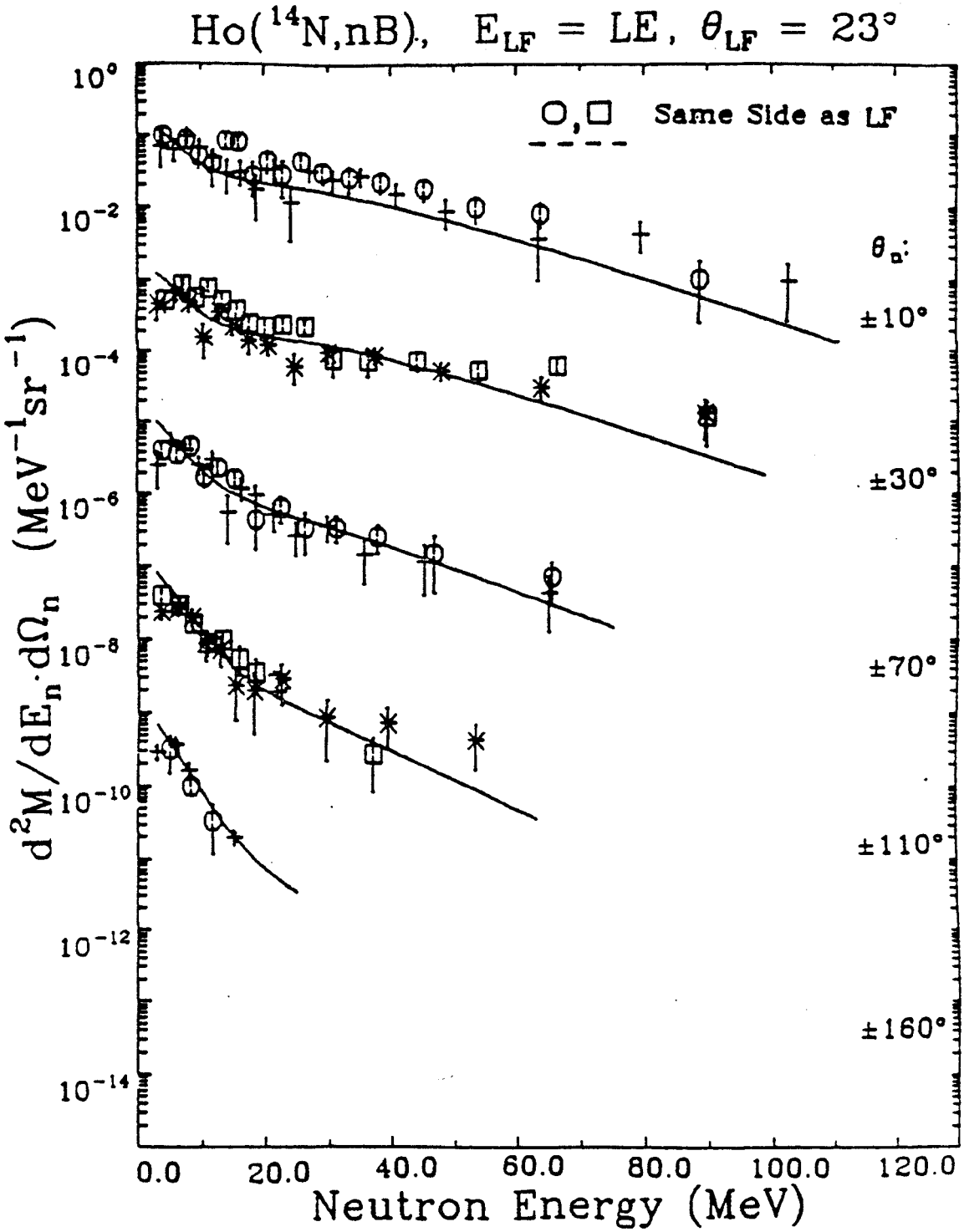

Figure A-25. (continued)

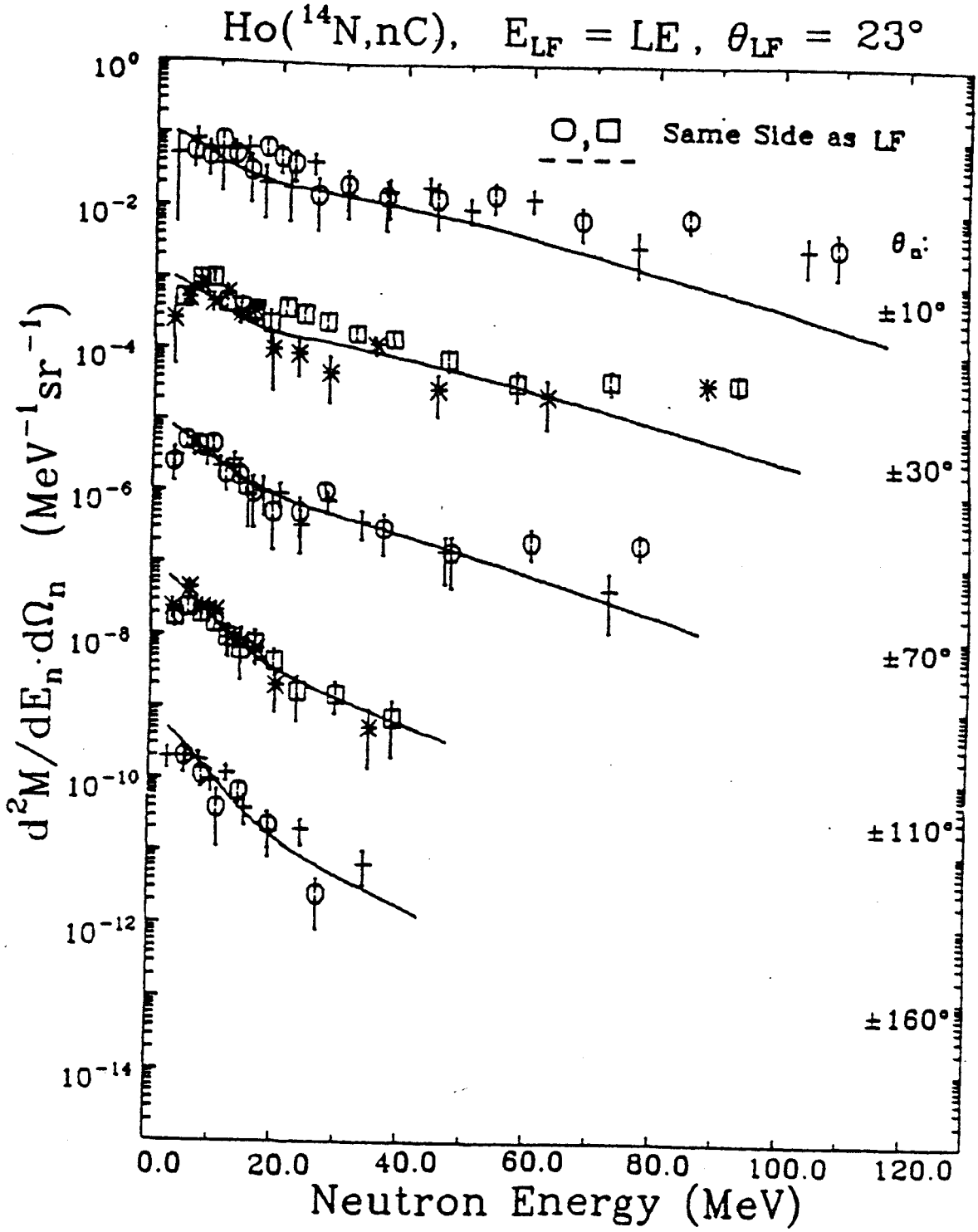

Figure A-25. (continued)

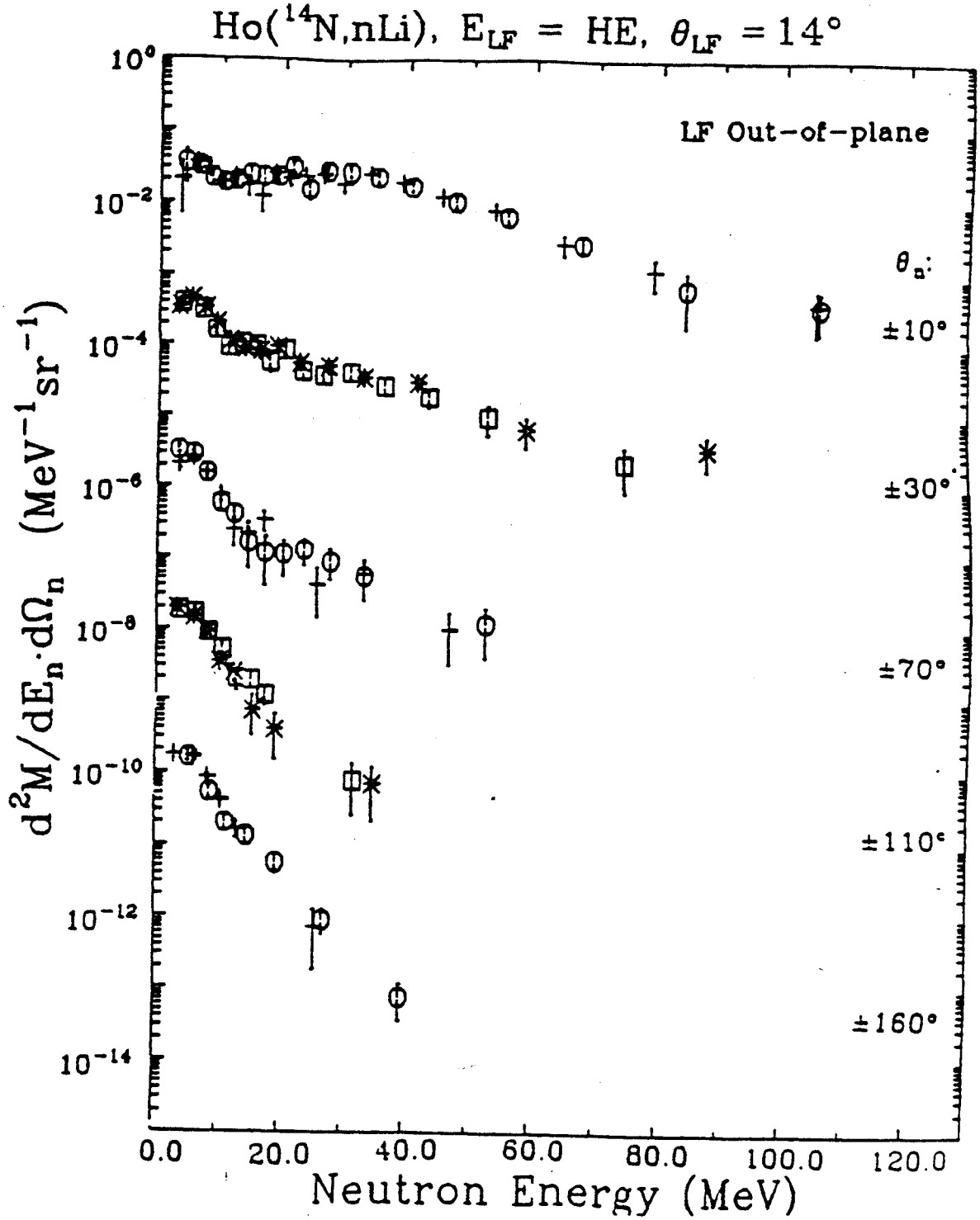

Figure A-25. (continued)

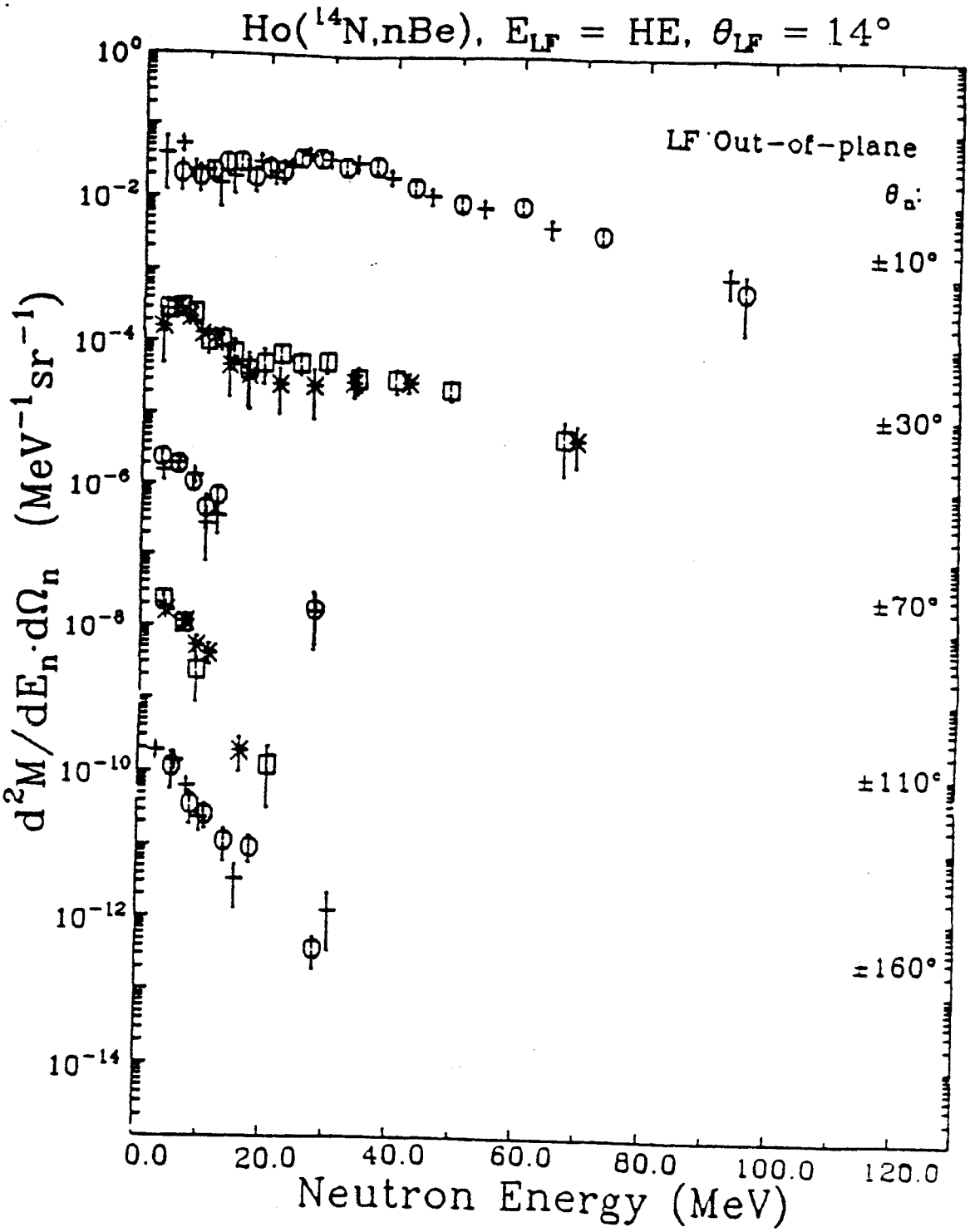

Figure A-25. (continued)

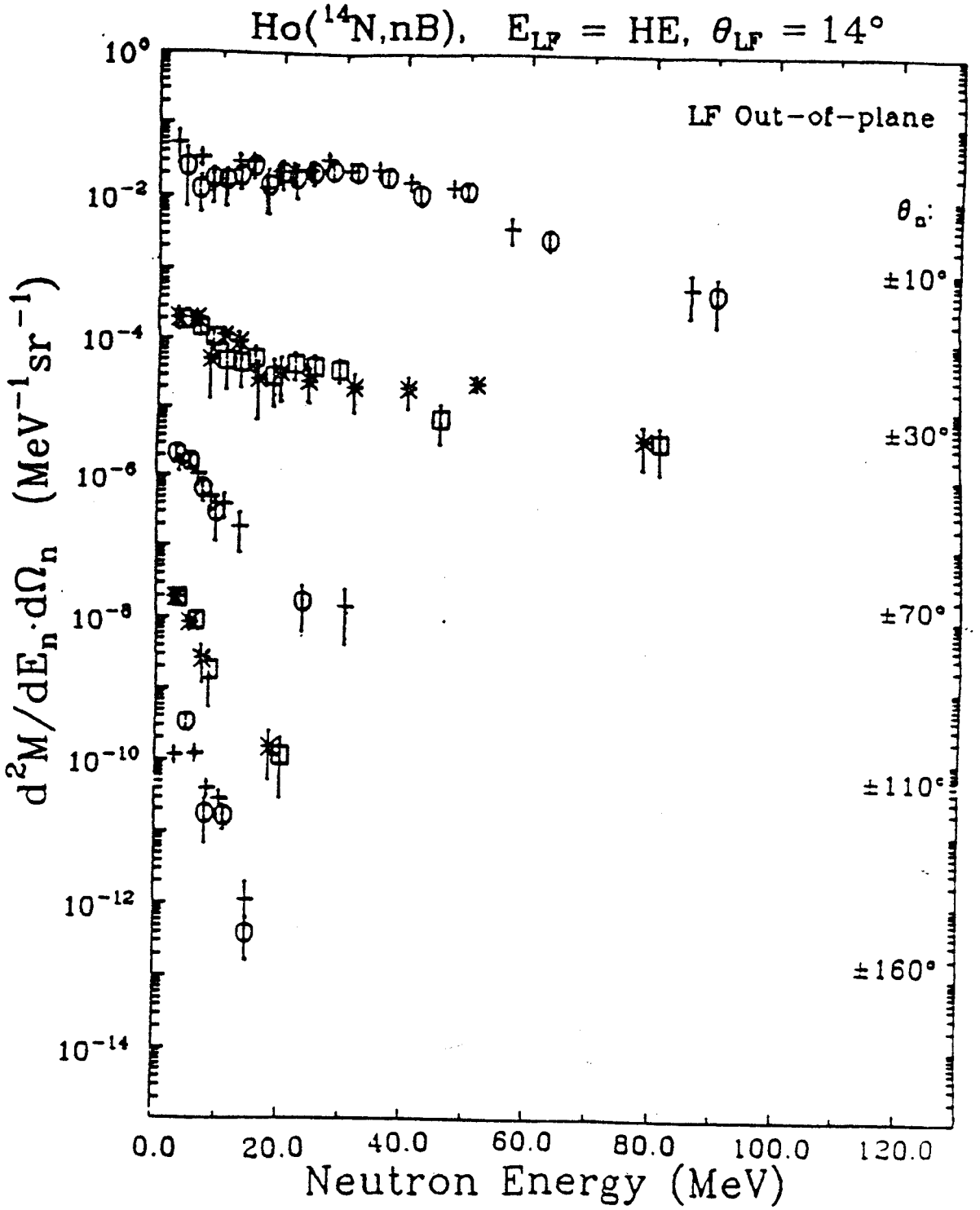

Figure A-25. (continued)

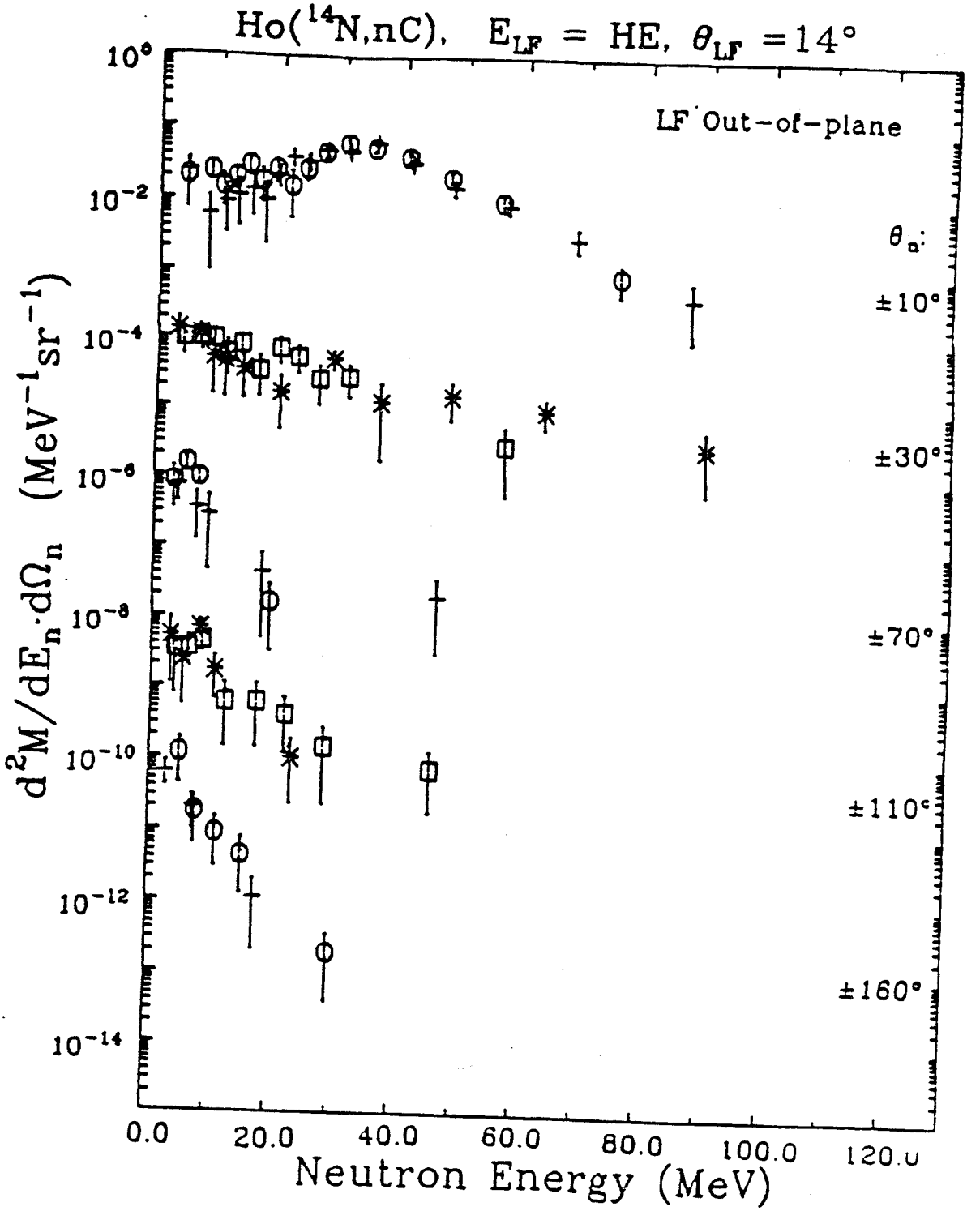

Figure A-25. (continued)

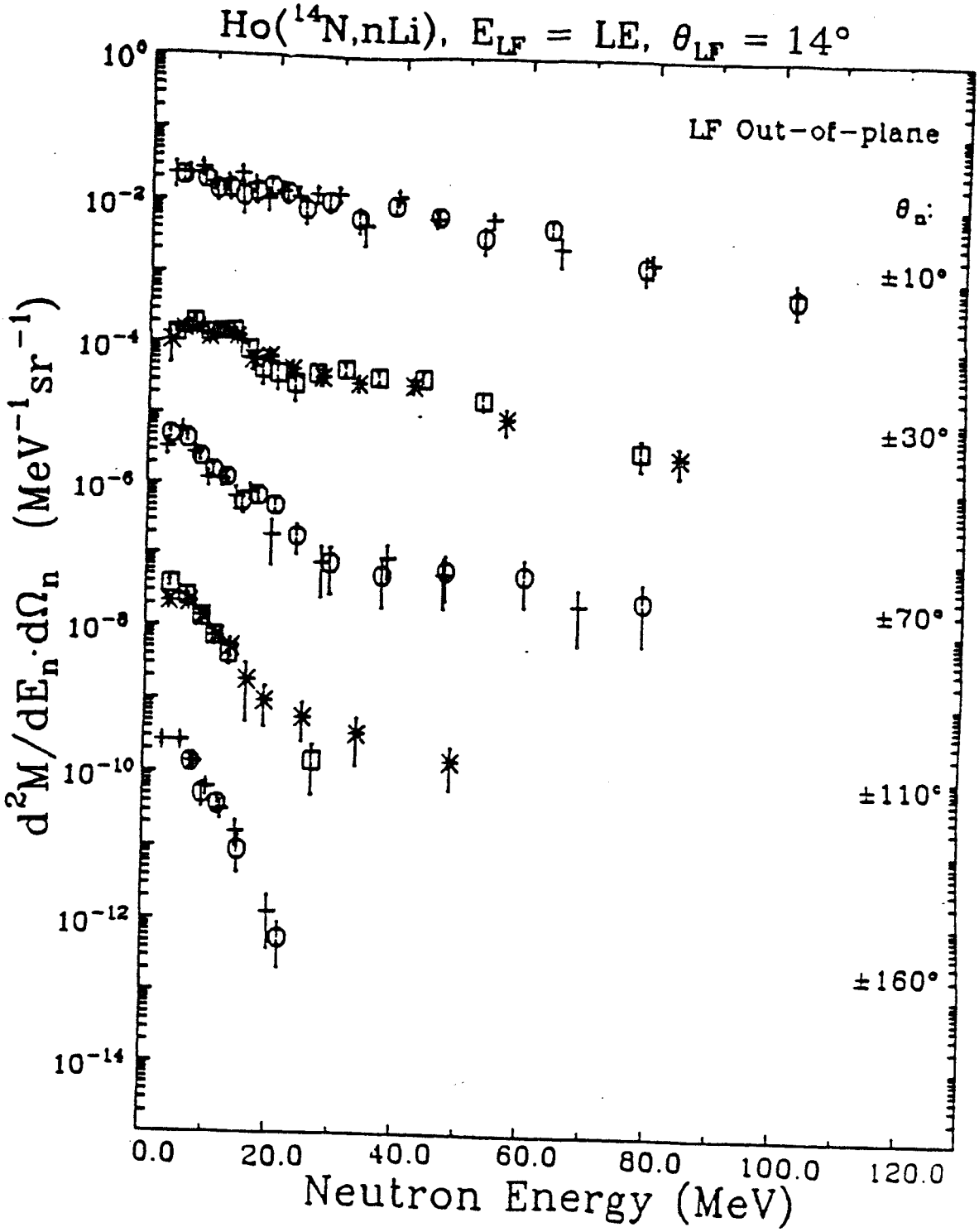

Figure A-25. (continued)

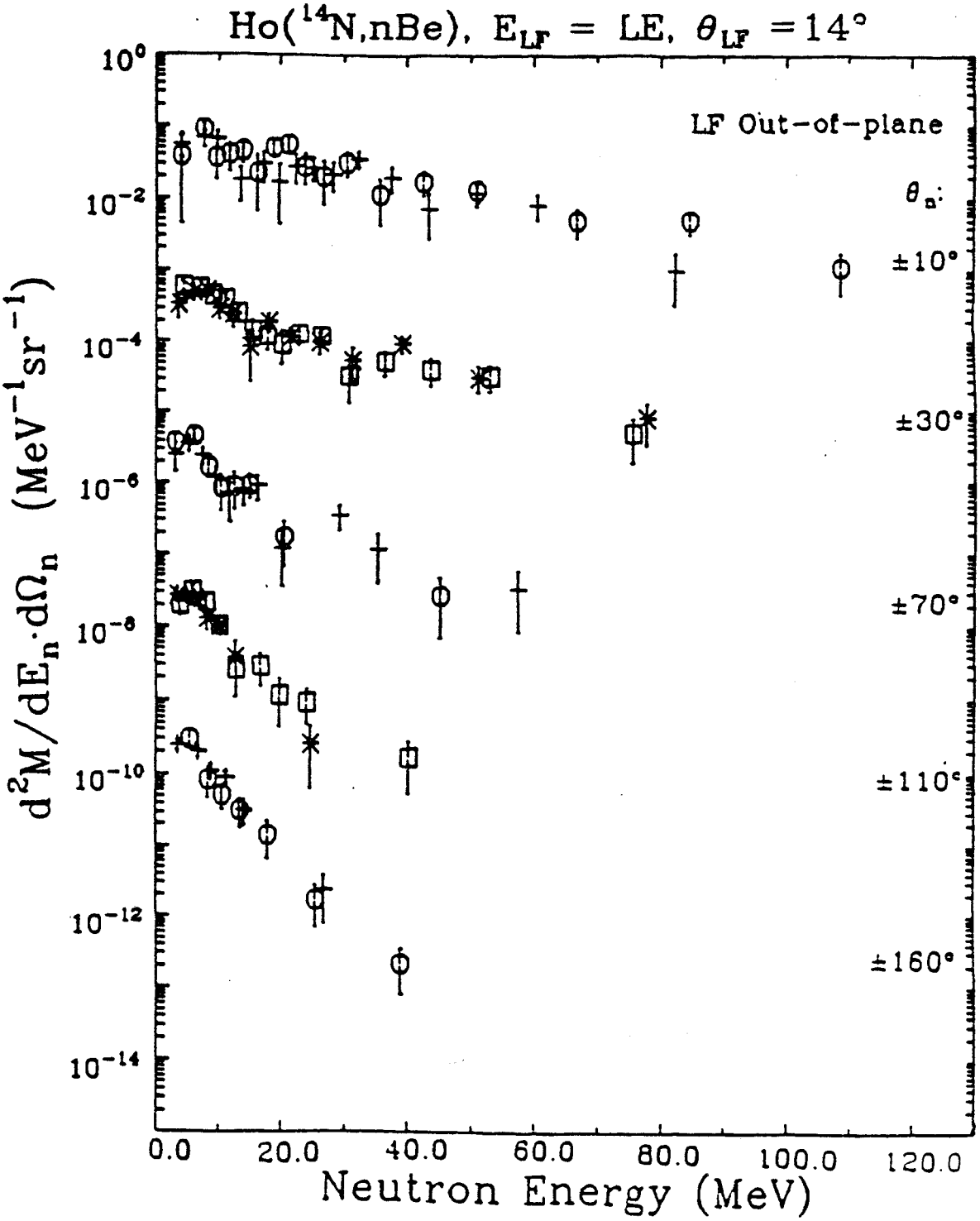

Figure A-25. (continued)

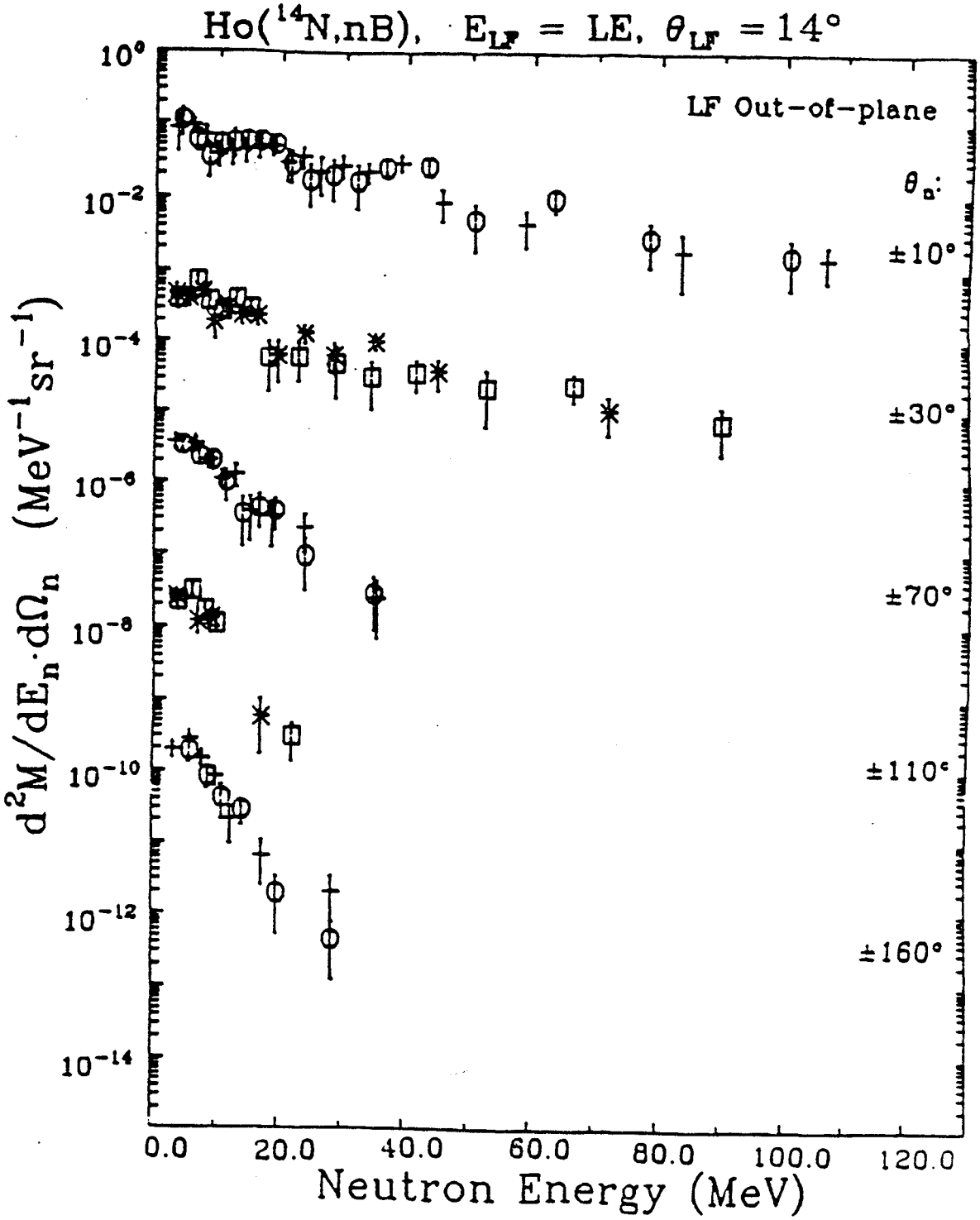

Figure A-25. (continued)

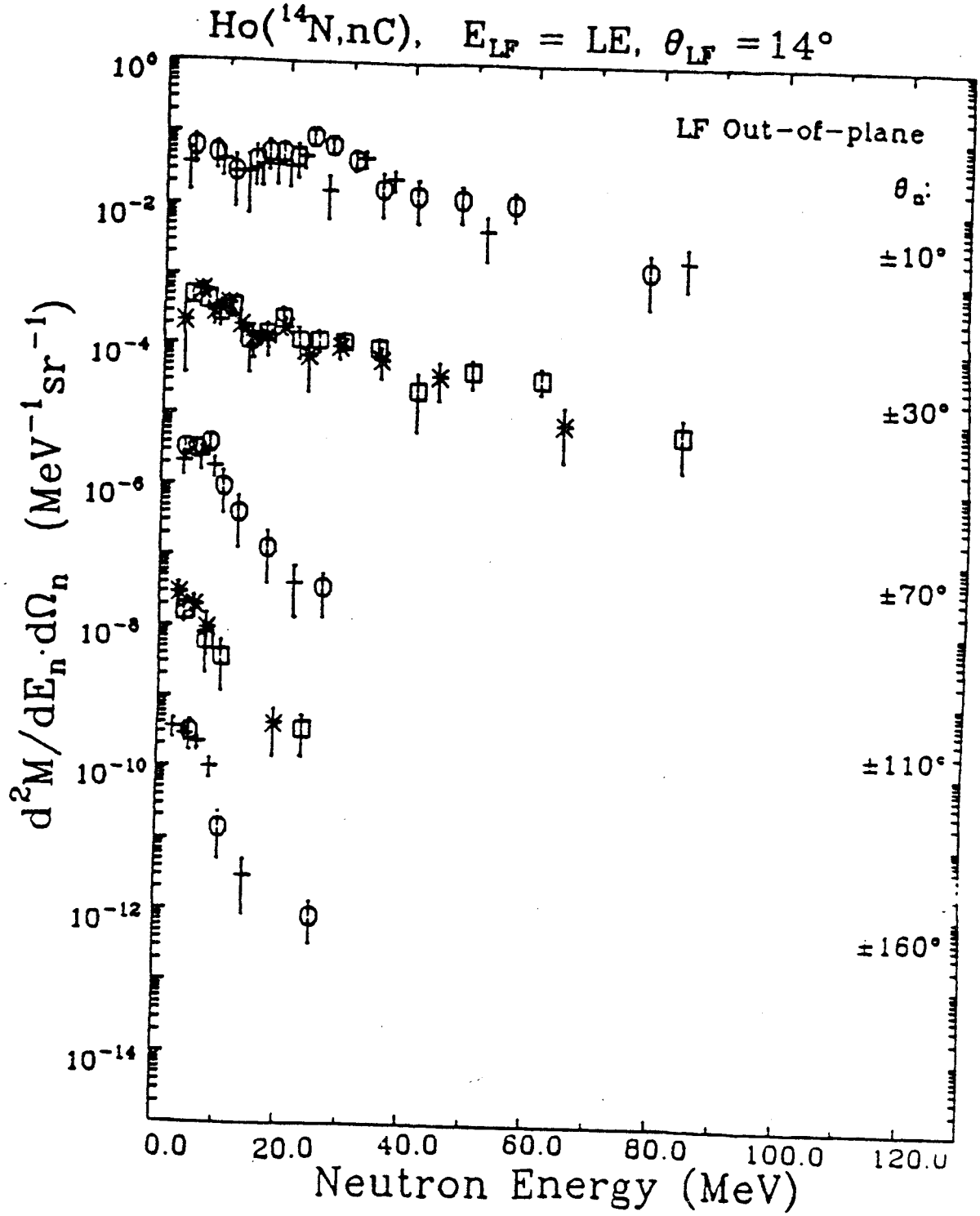

2. The Ni Target

Figure A-26 contains the differential neutron multiplicity spectra for the Ni target. The format of the figure is the same as that for Fig. A-25.

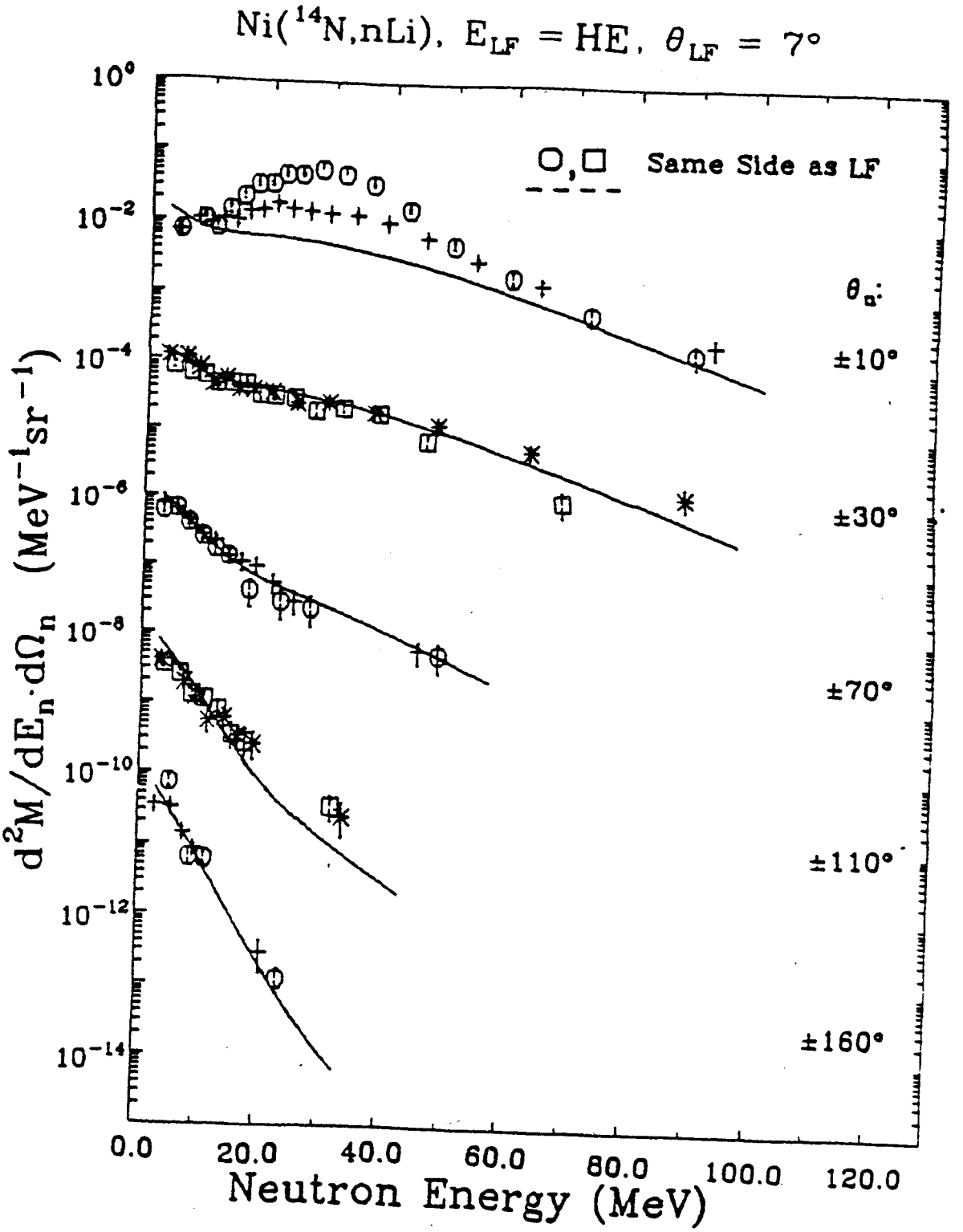

Figure A-26. Neutron spectra for the Ni target.

Figure A-26. (continued)

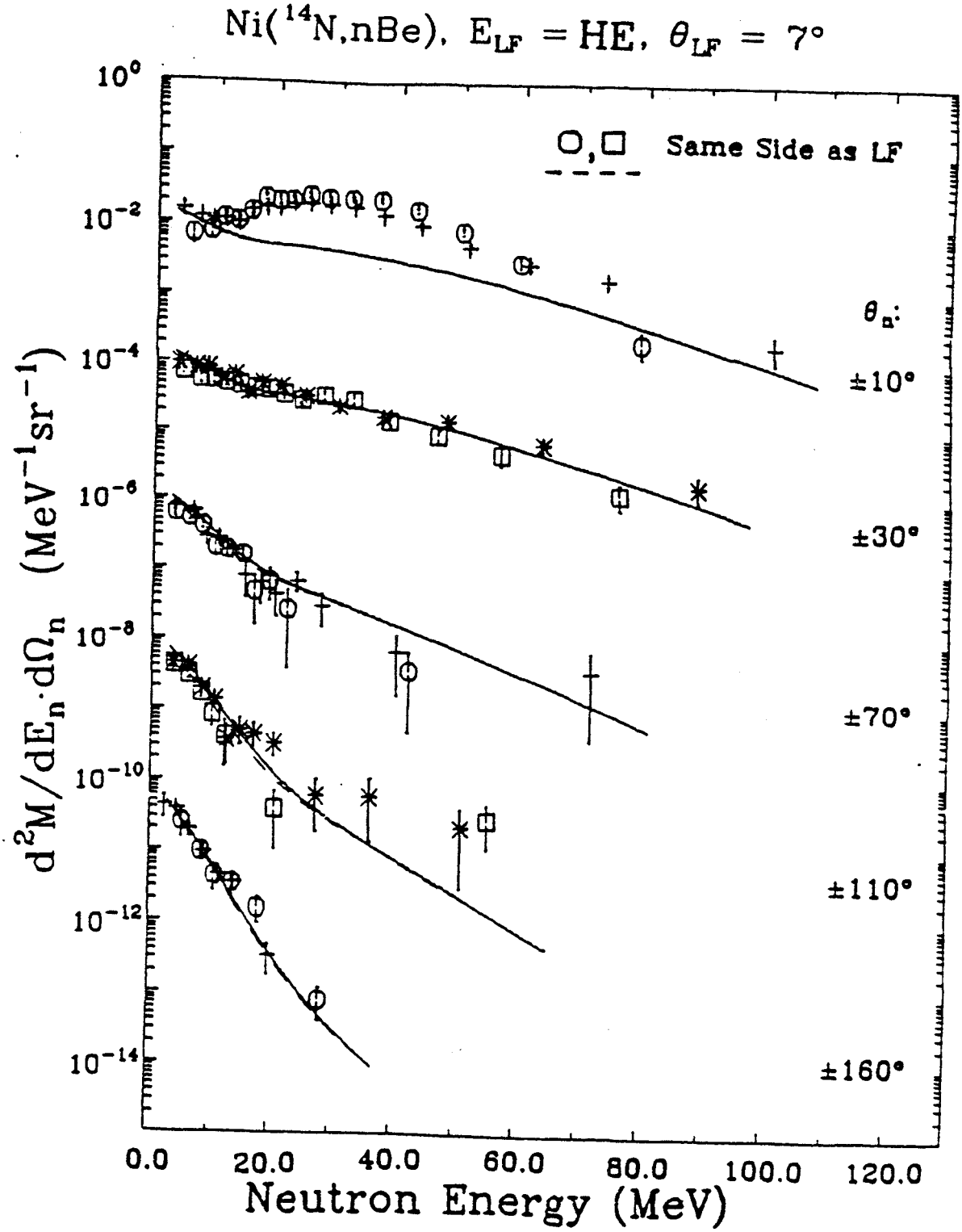

Figure A-26. (continued)

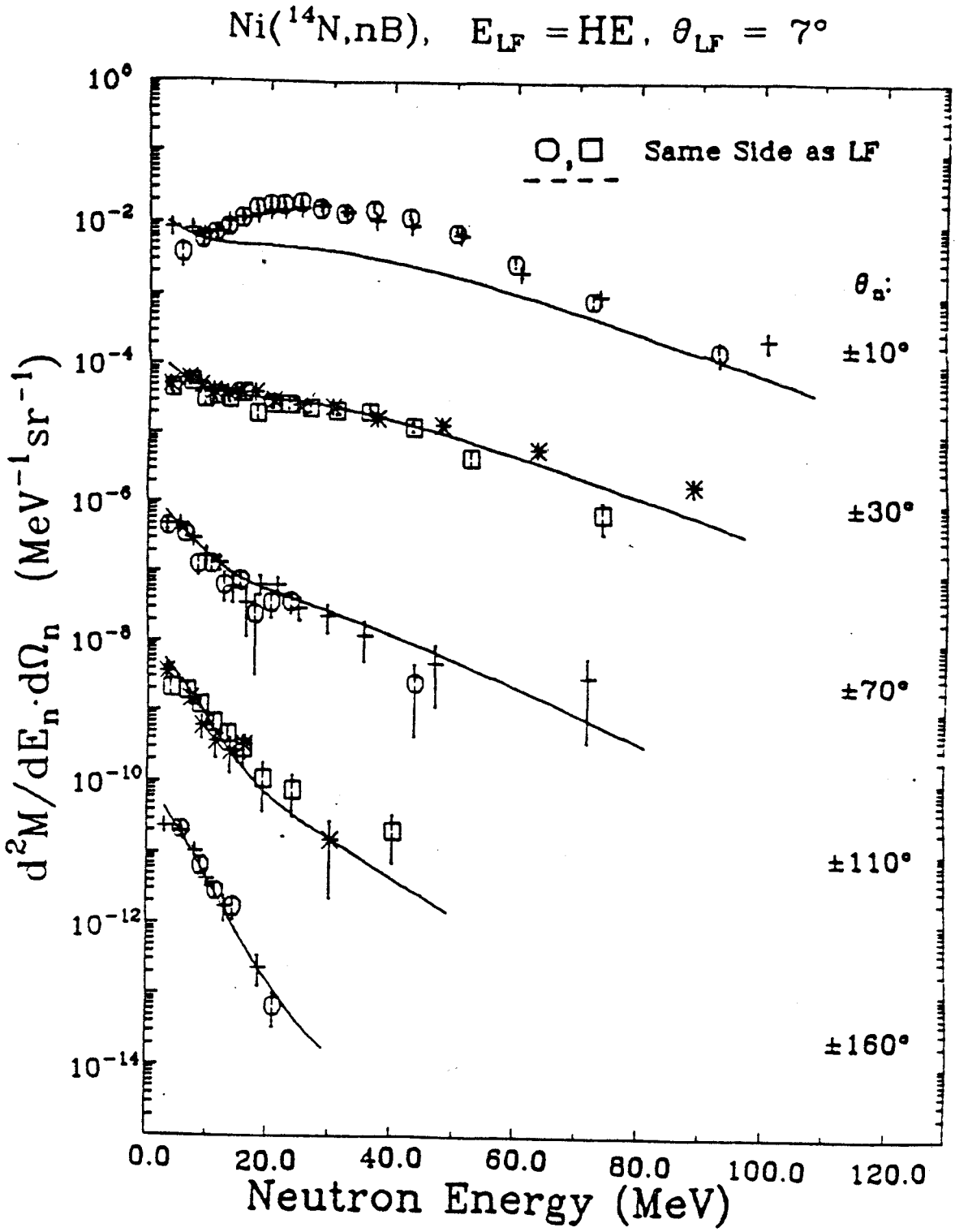

Figure A-26. (continued)

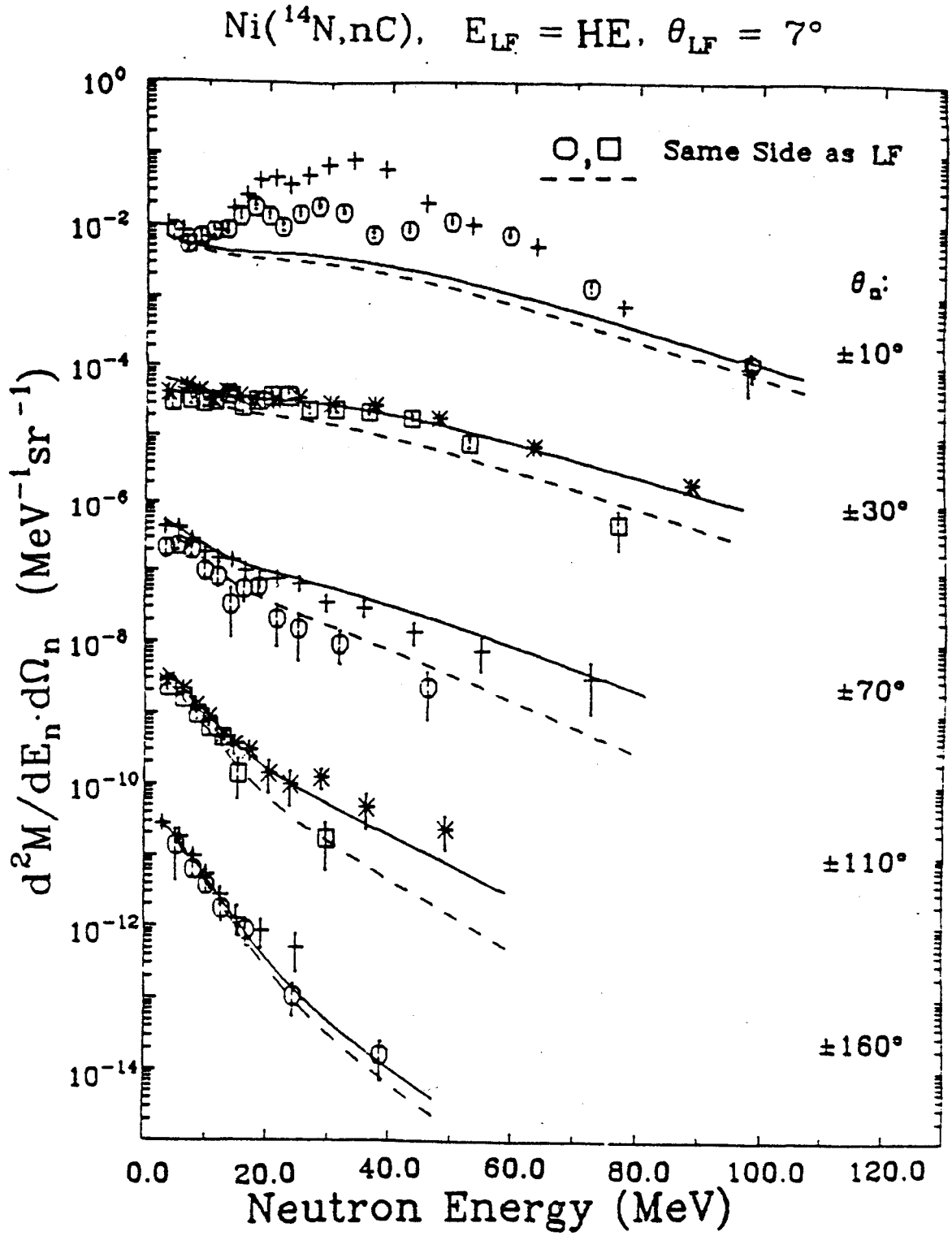

Figure A-26. (continued)

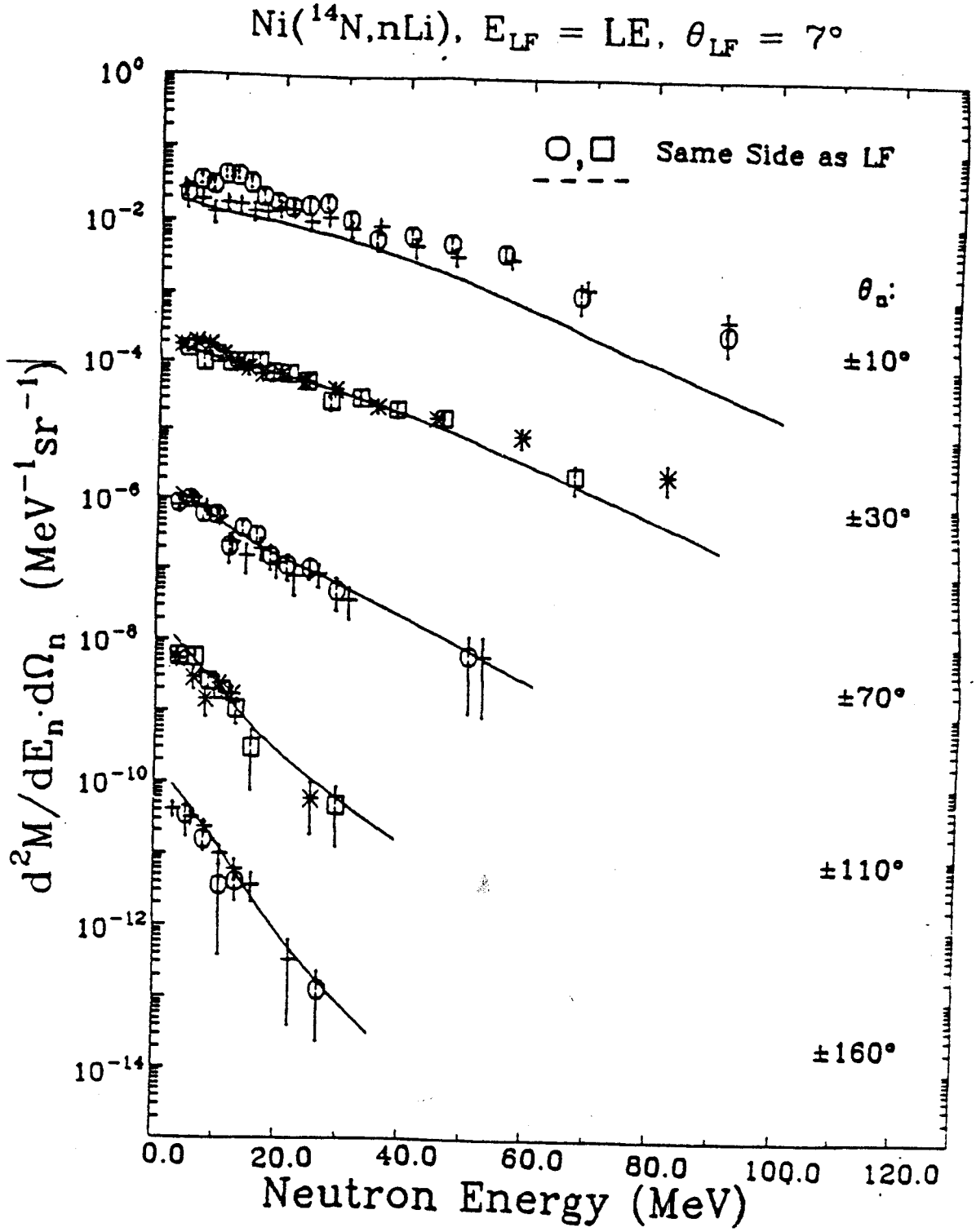

Figure A-26. (continued)

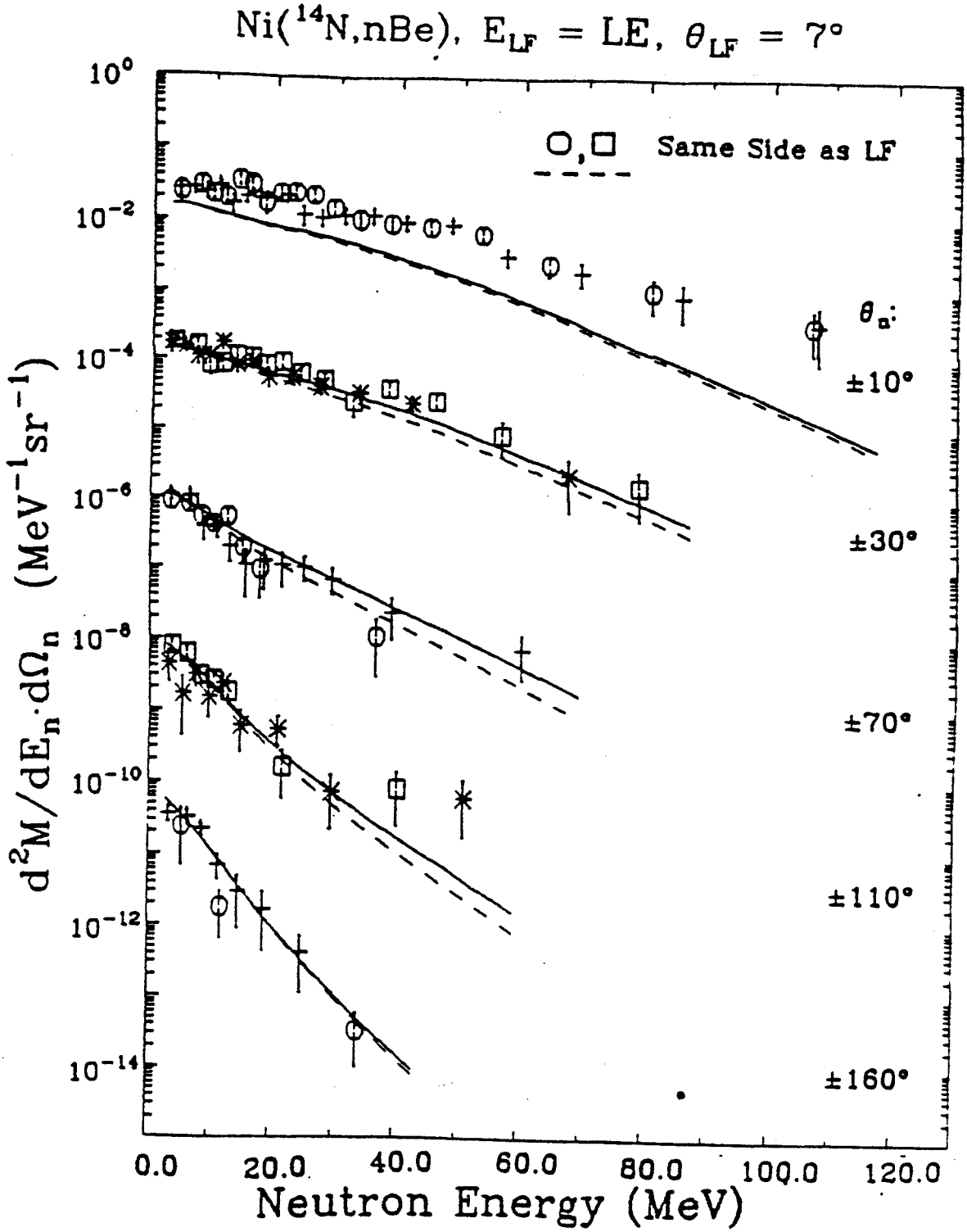

Figure A-26. (continued)

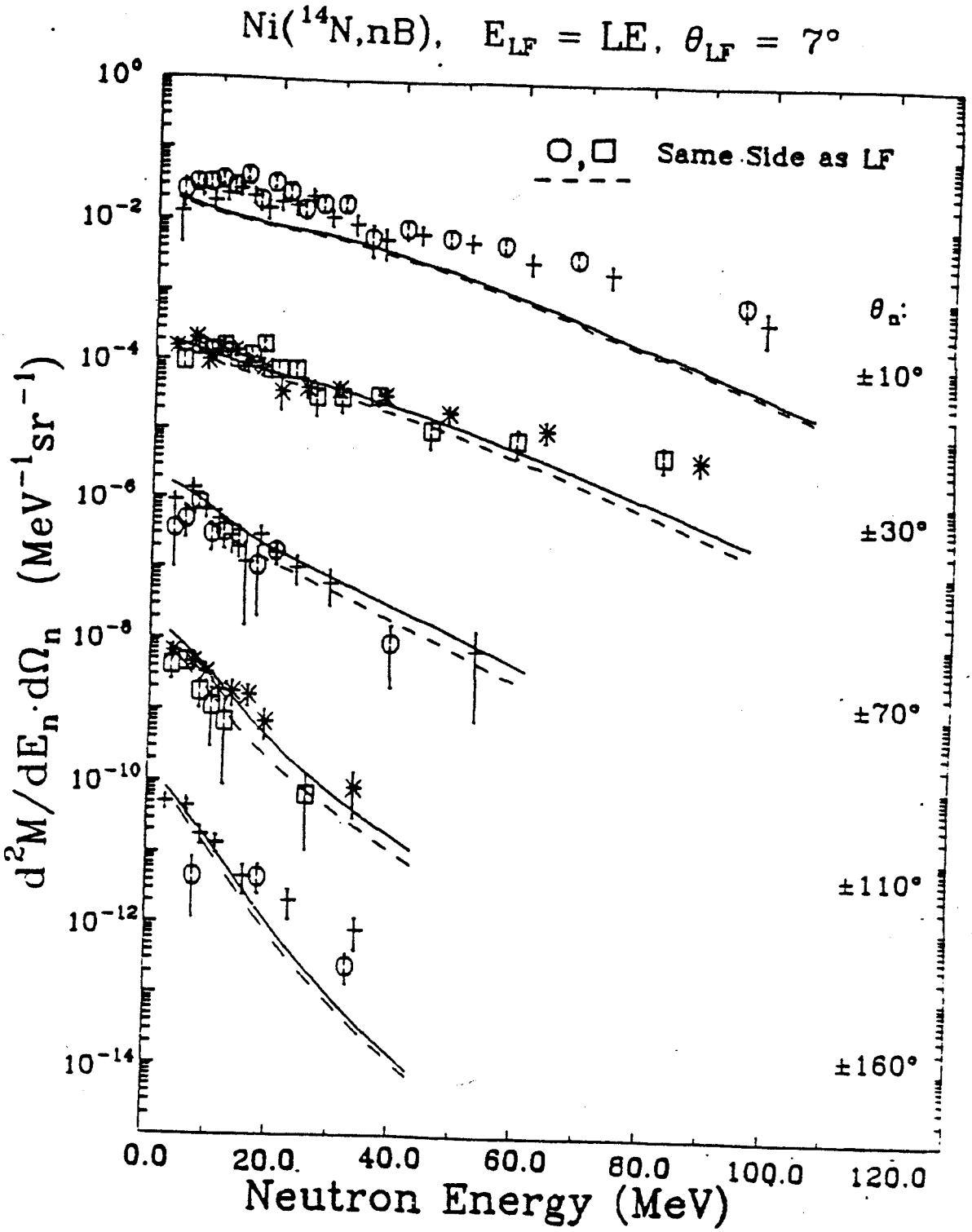

Figure A-26. (continued)

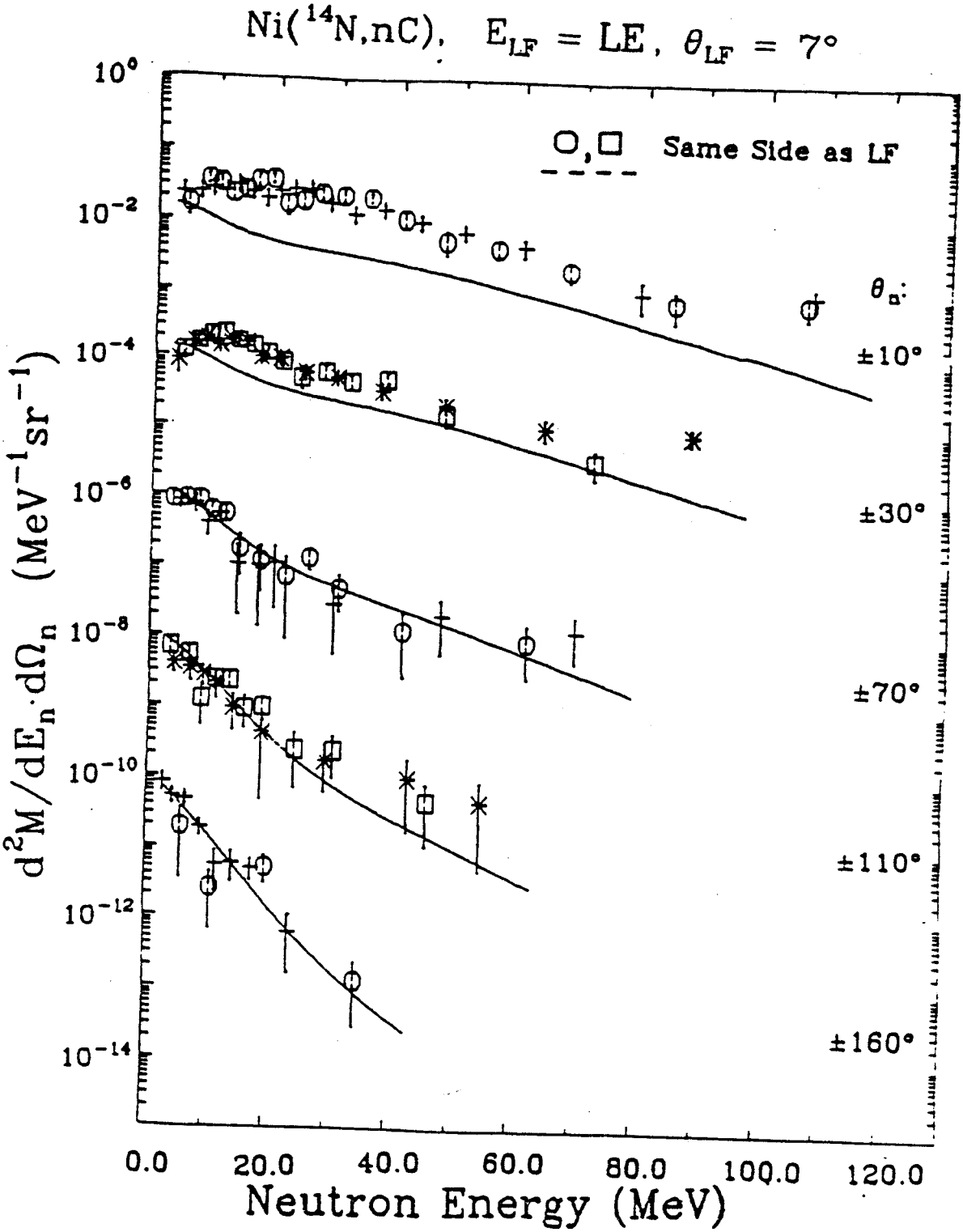

Figure A-26. (continued)

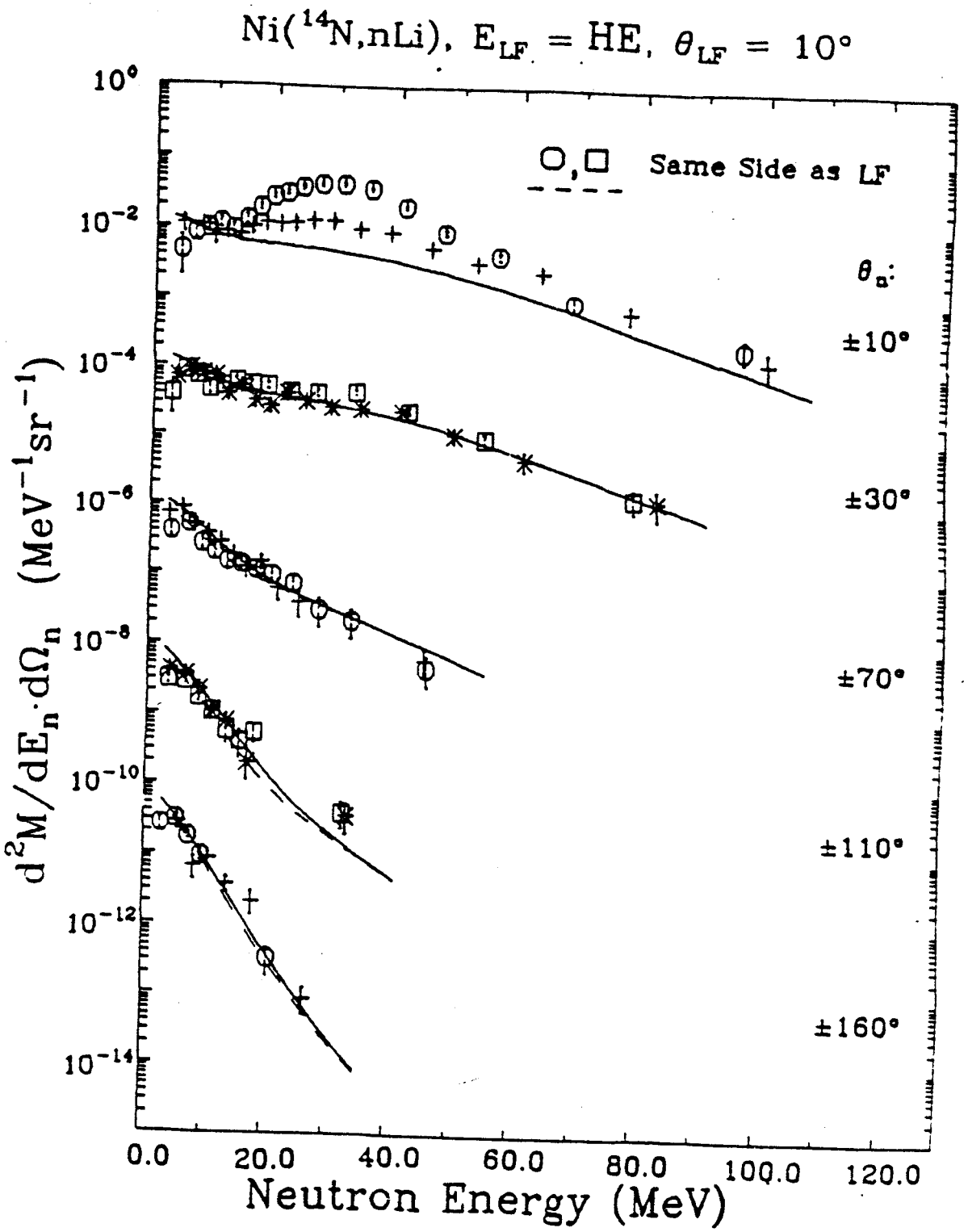

Figure A-26. (continued)

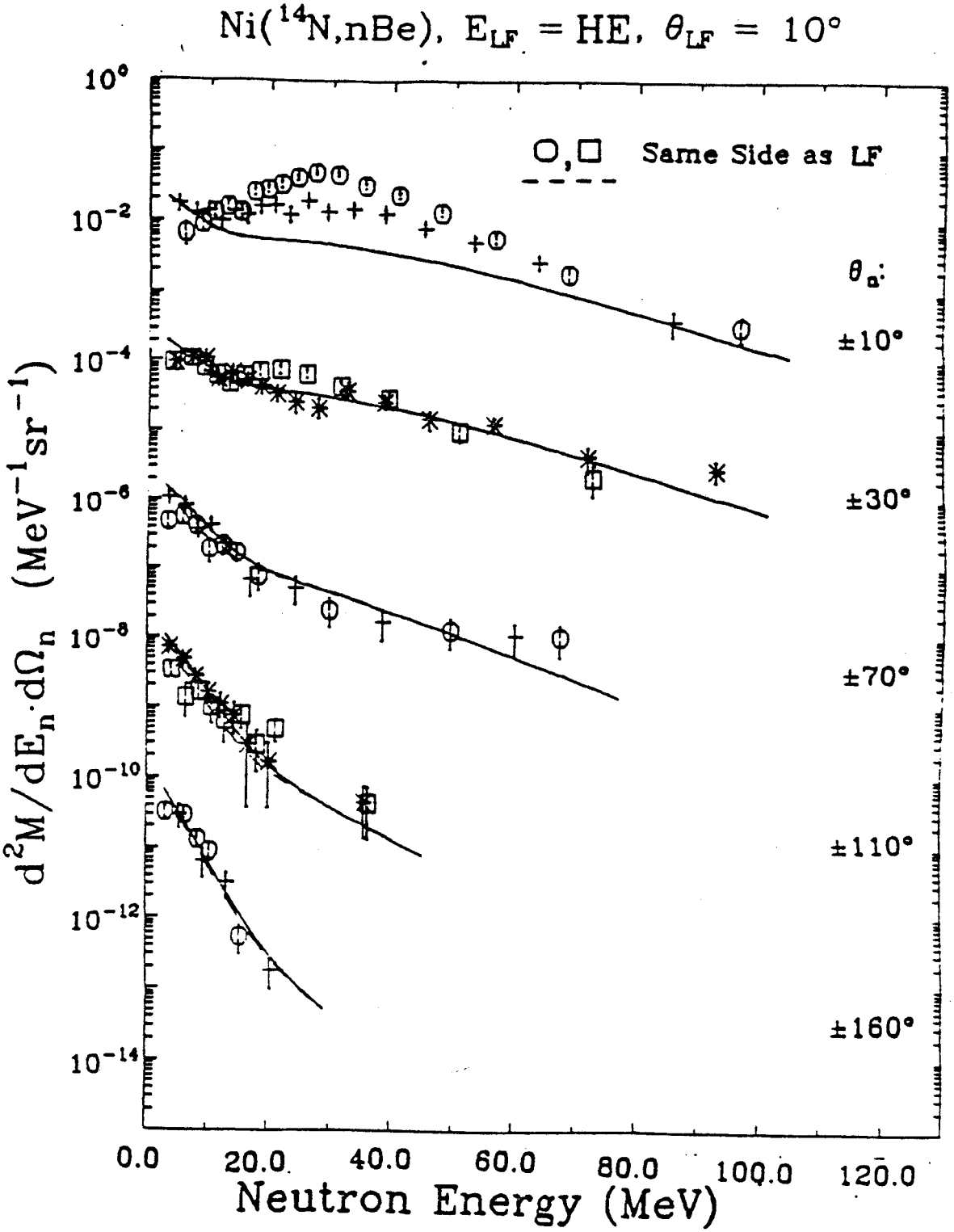

Figure A-26. (continued)

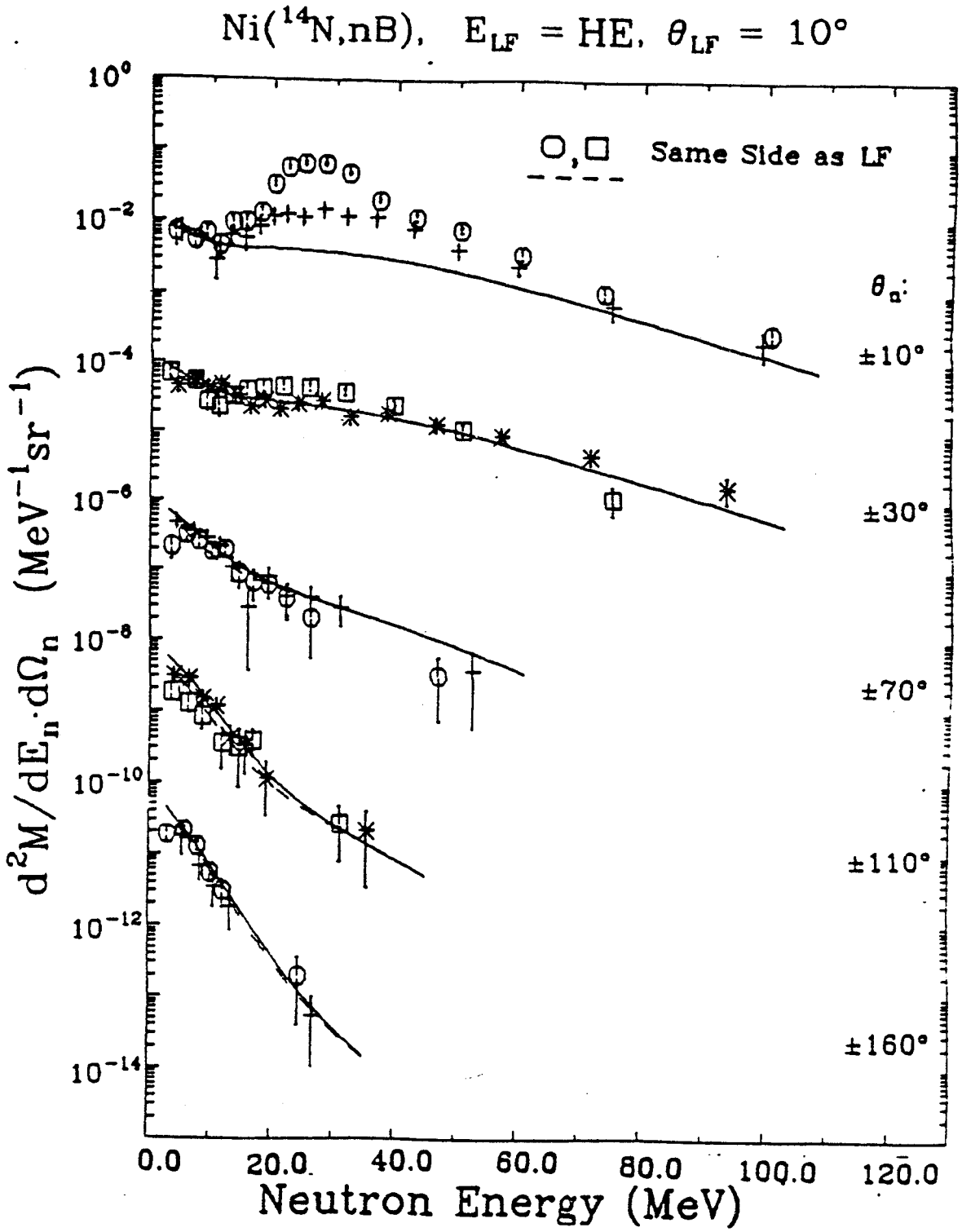

Figure A-26. (continued)

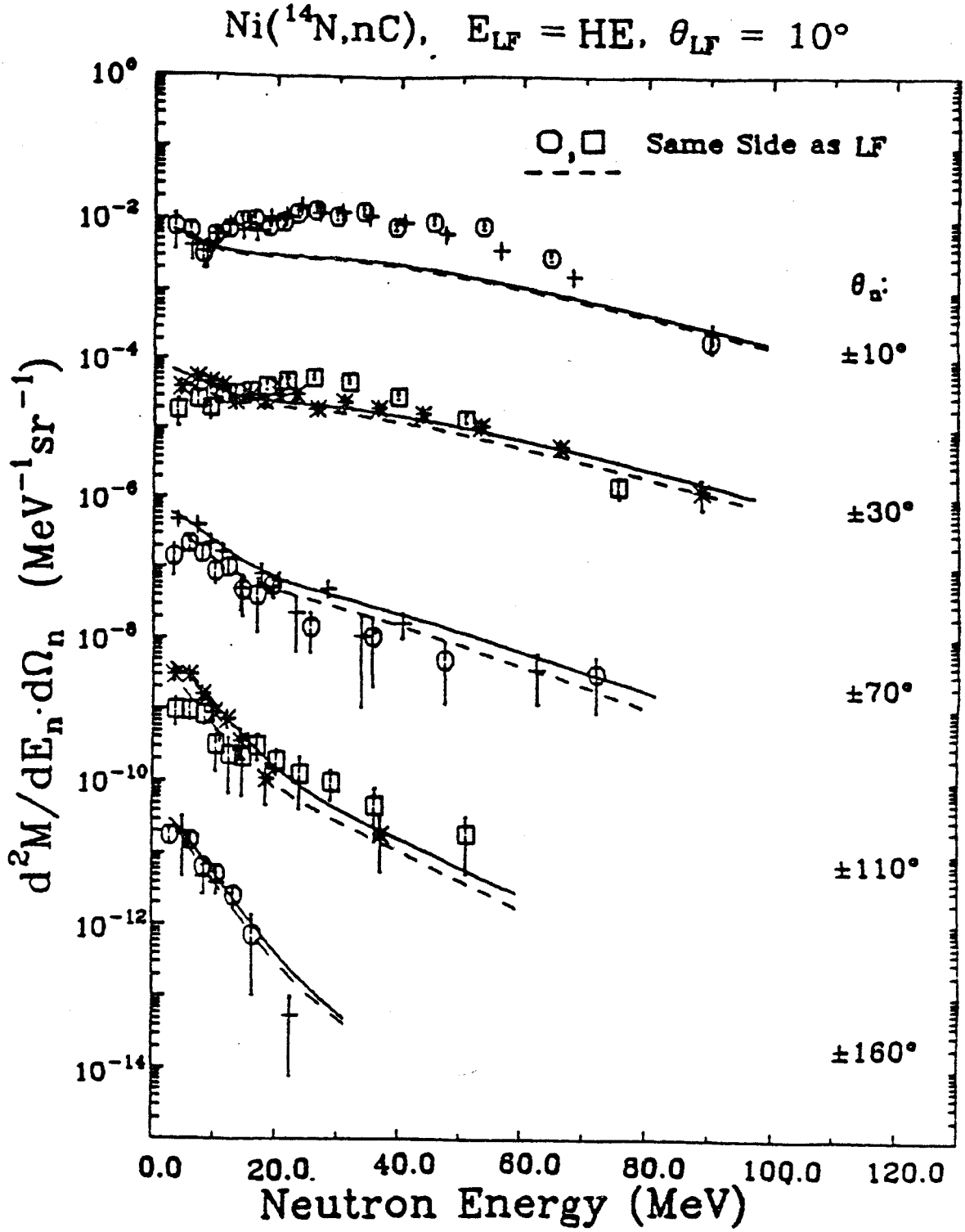

Figure A-26. (continued)

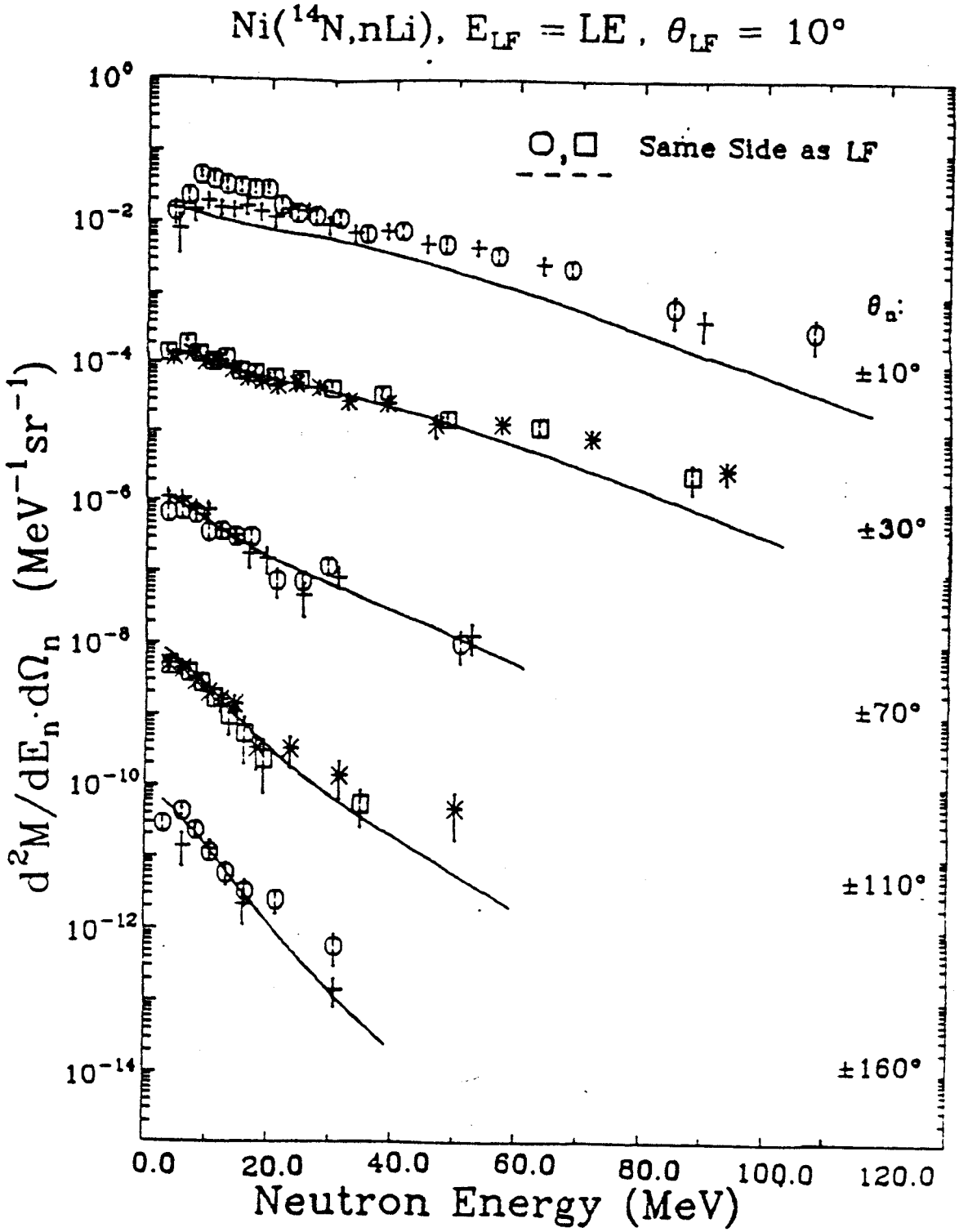

Figure A-26. (continued)

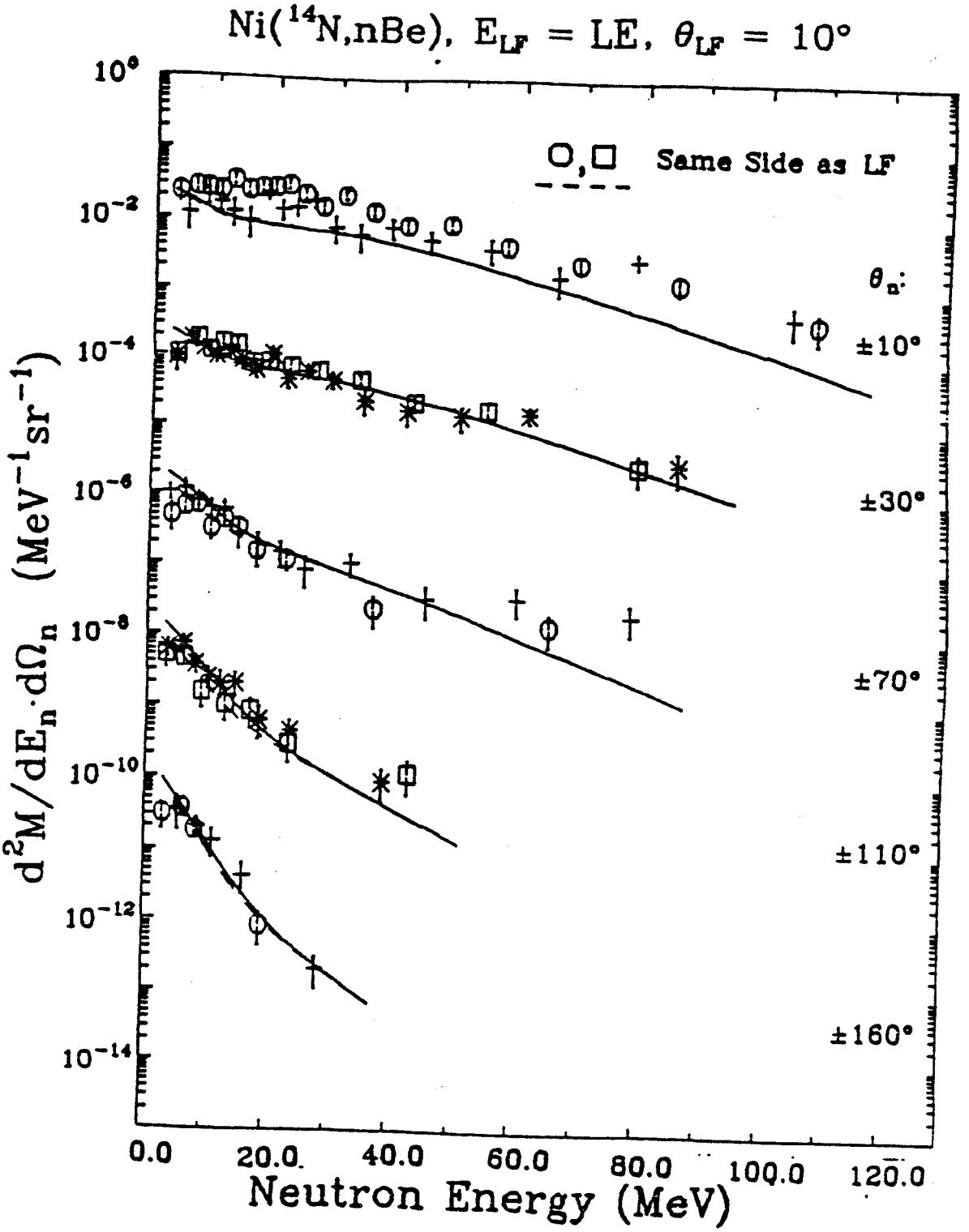

Figure A-26. (continued)

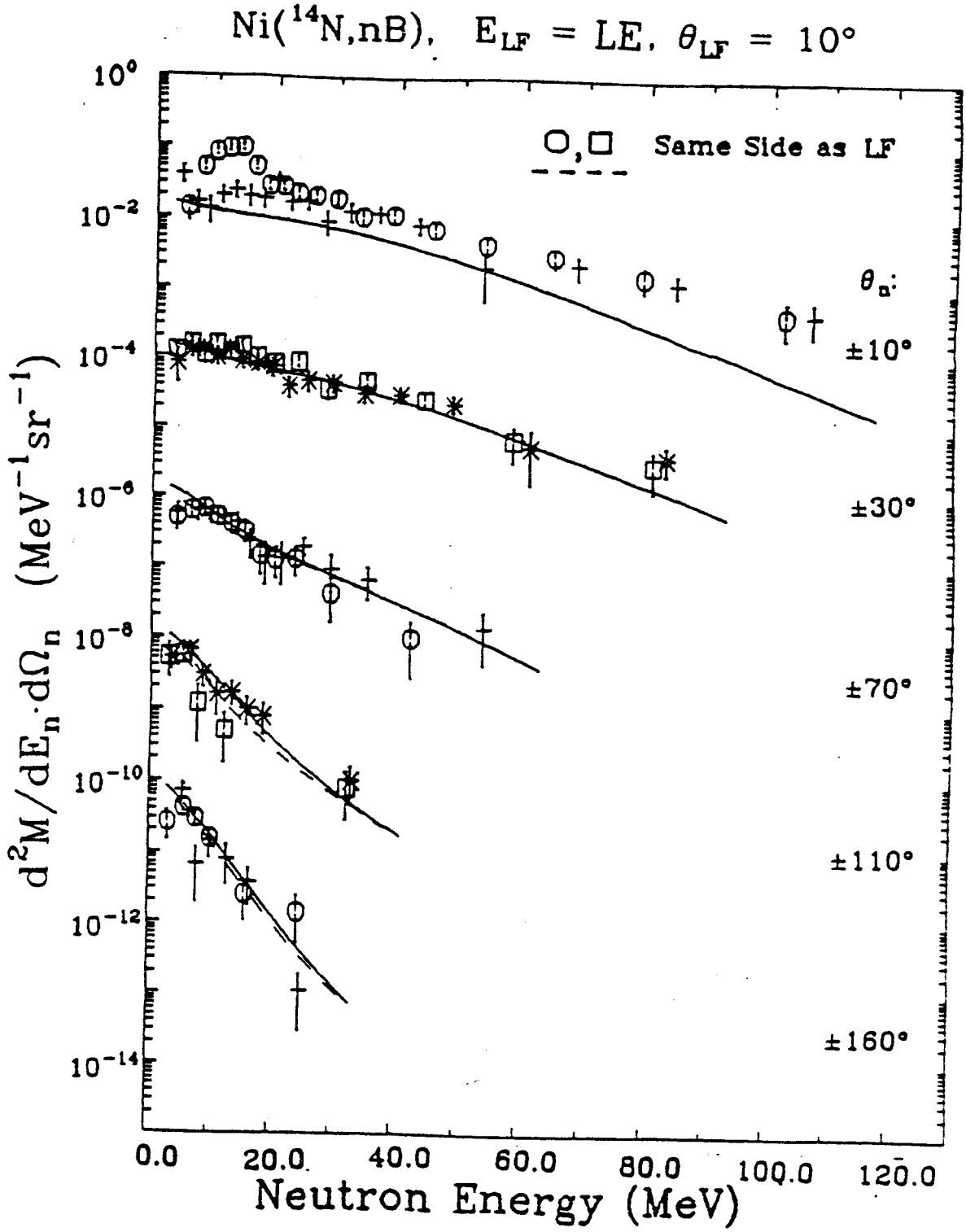

Figure A-26. (continued)

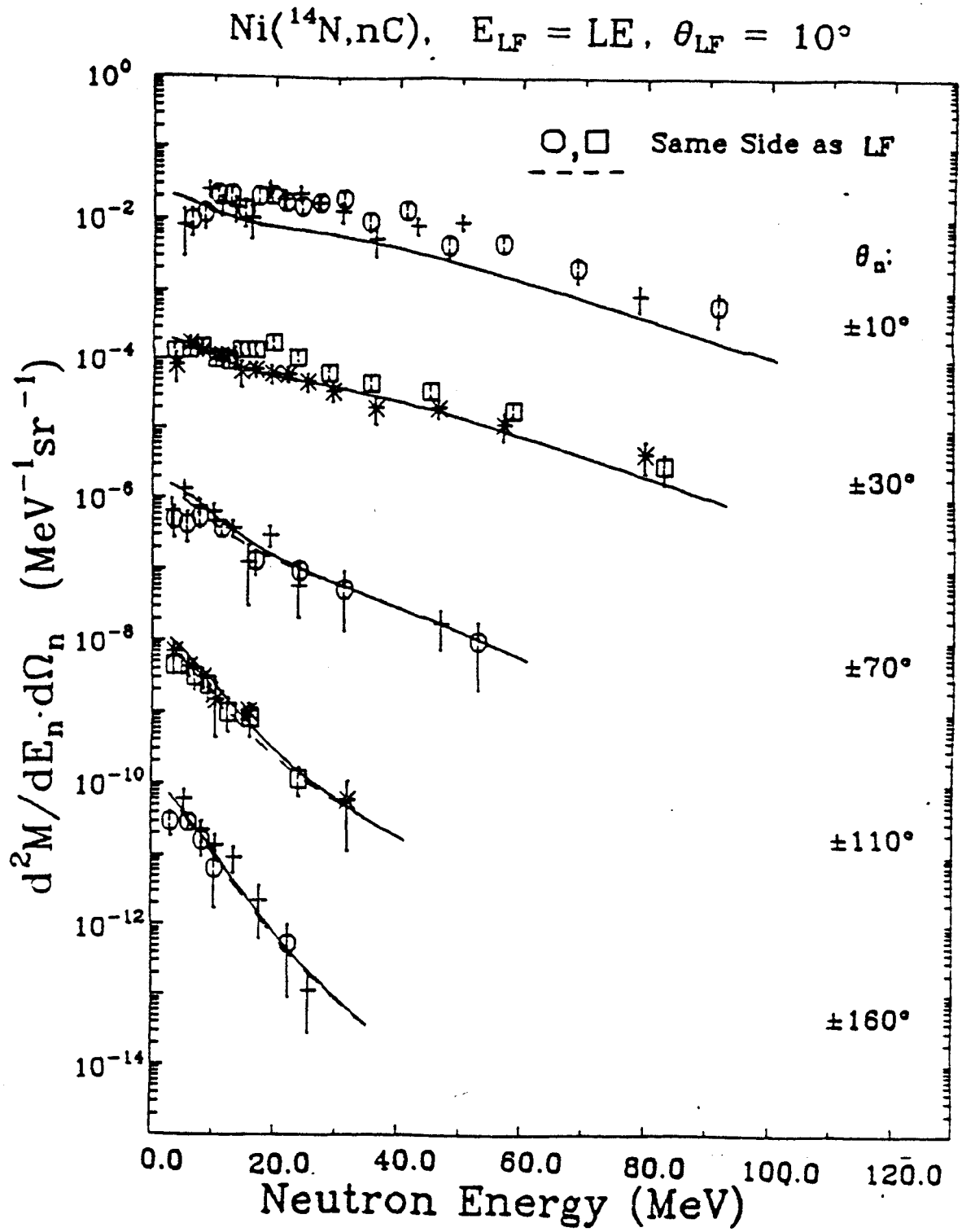

Figure A-26. (continued)

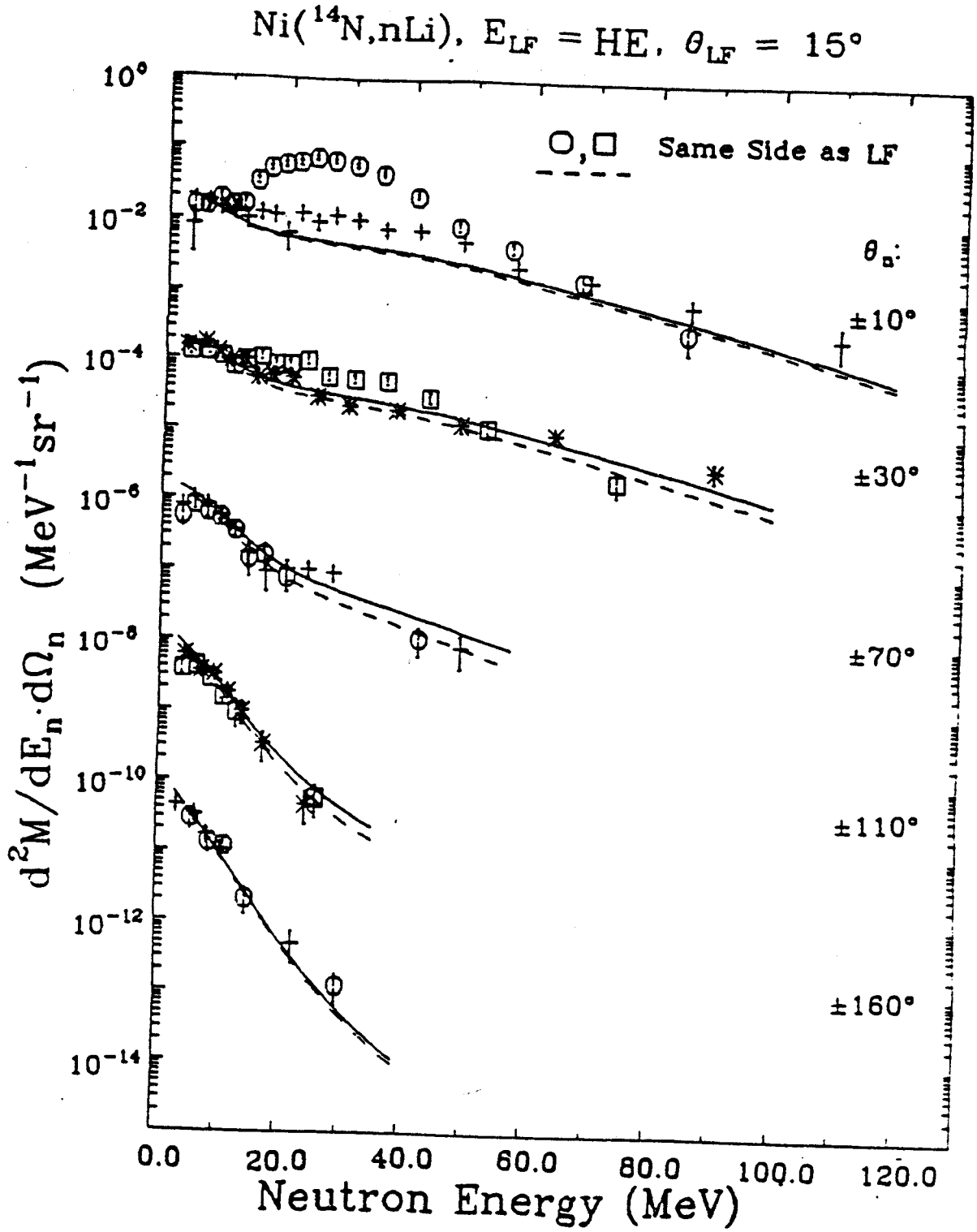

Figure A-26. (continued)

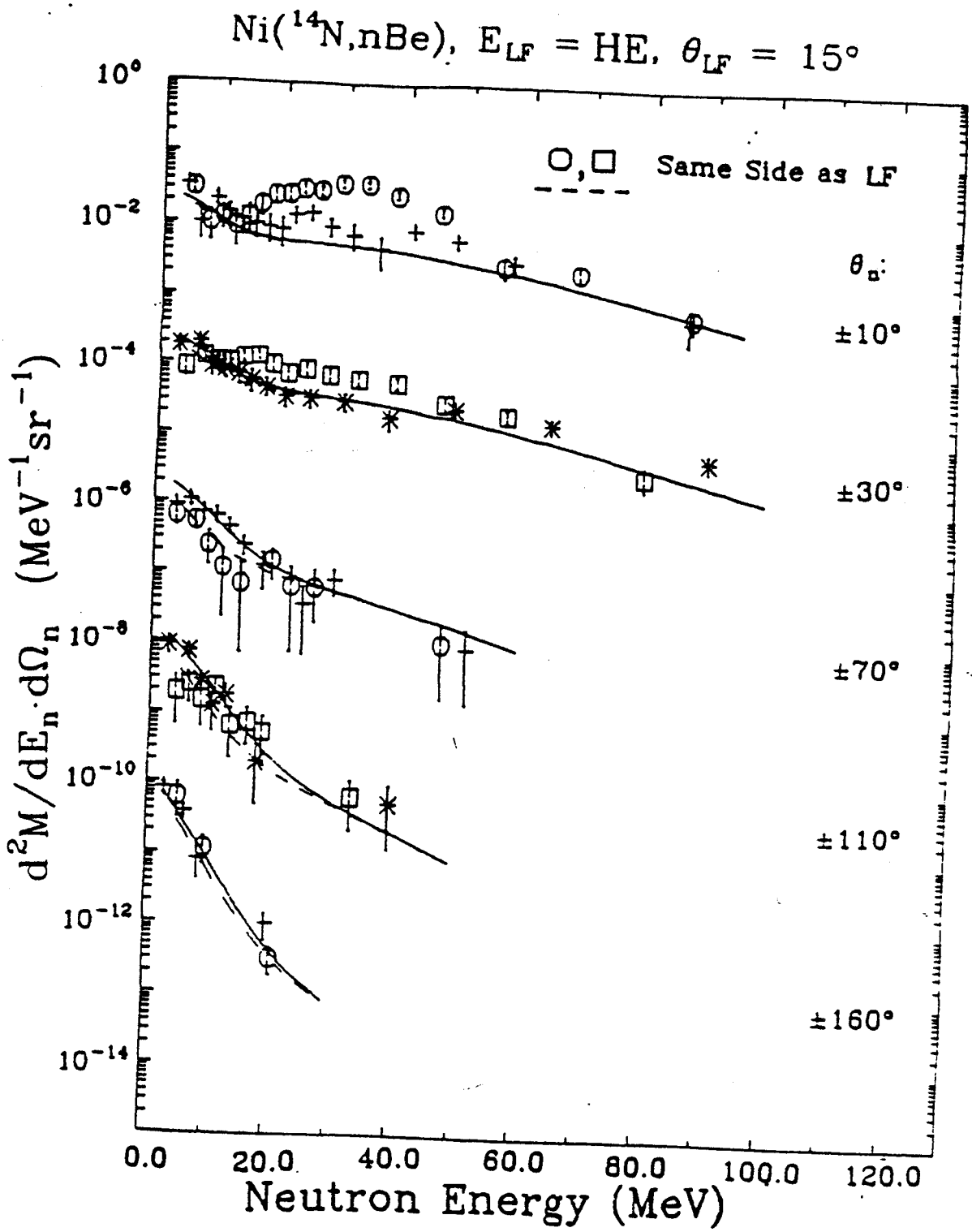

Figure A-26. (continued)

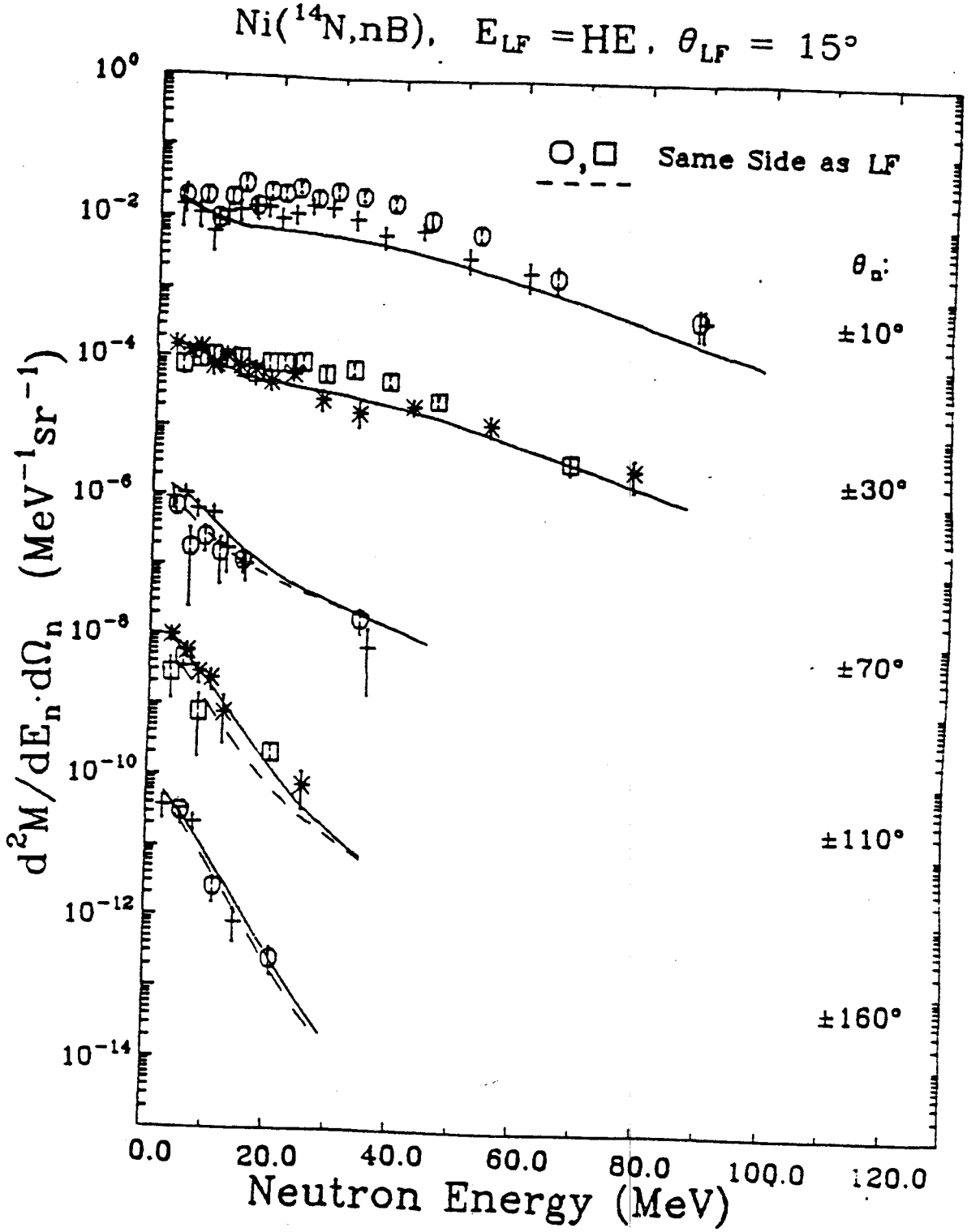

Figure A-26. (continued)

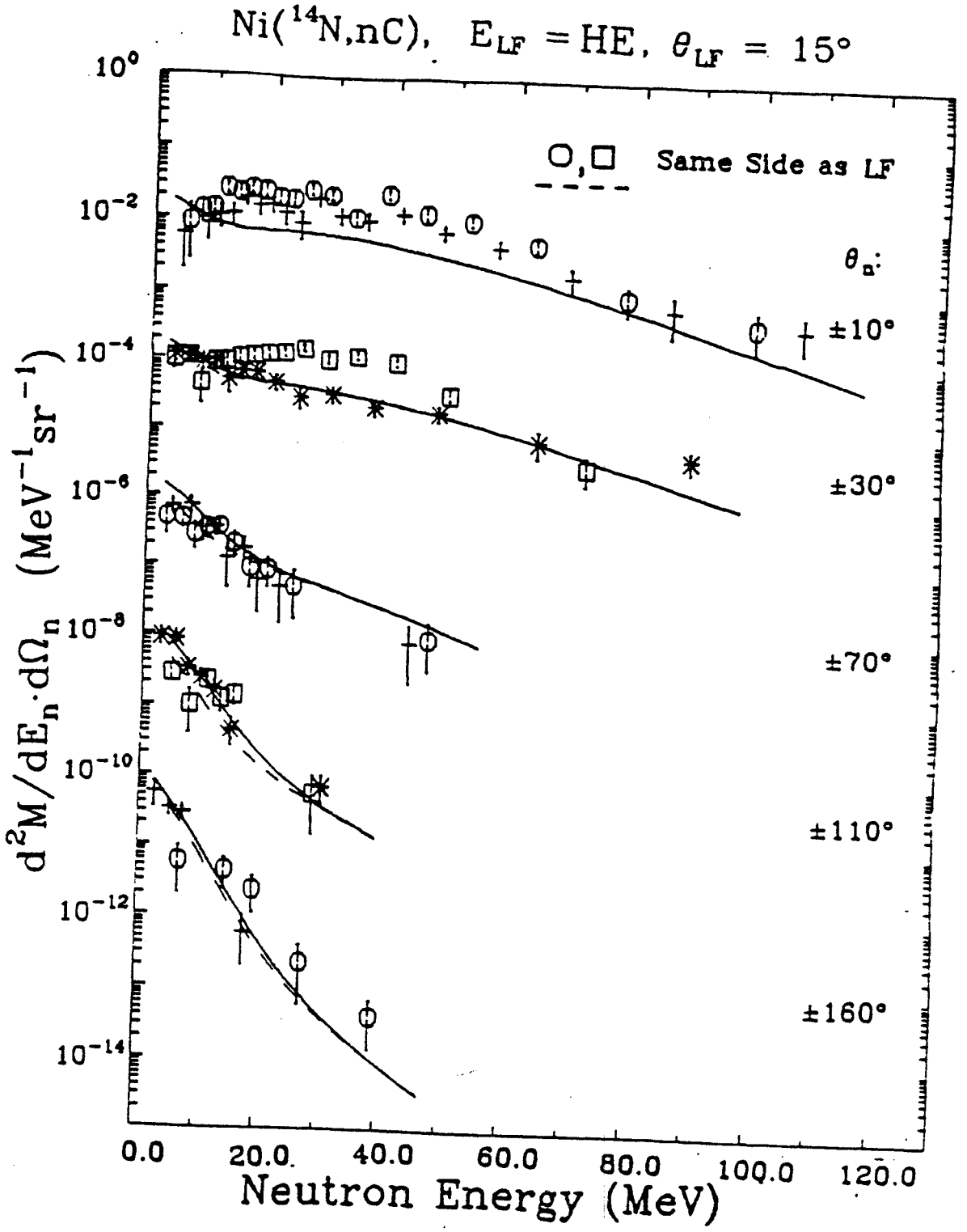

Figure A-26. (continued)

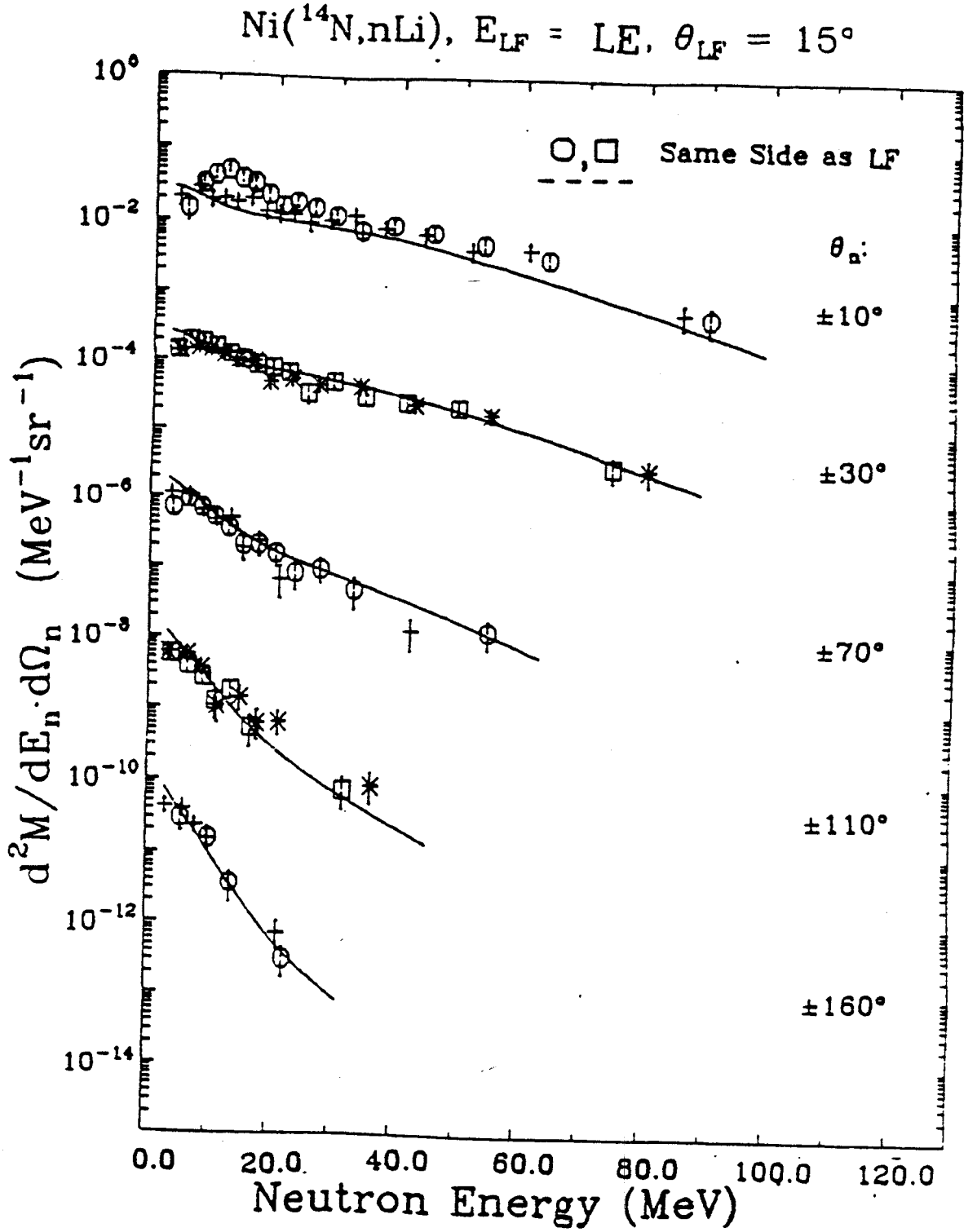

Figure A-26. (continued)

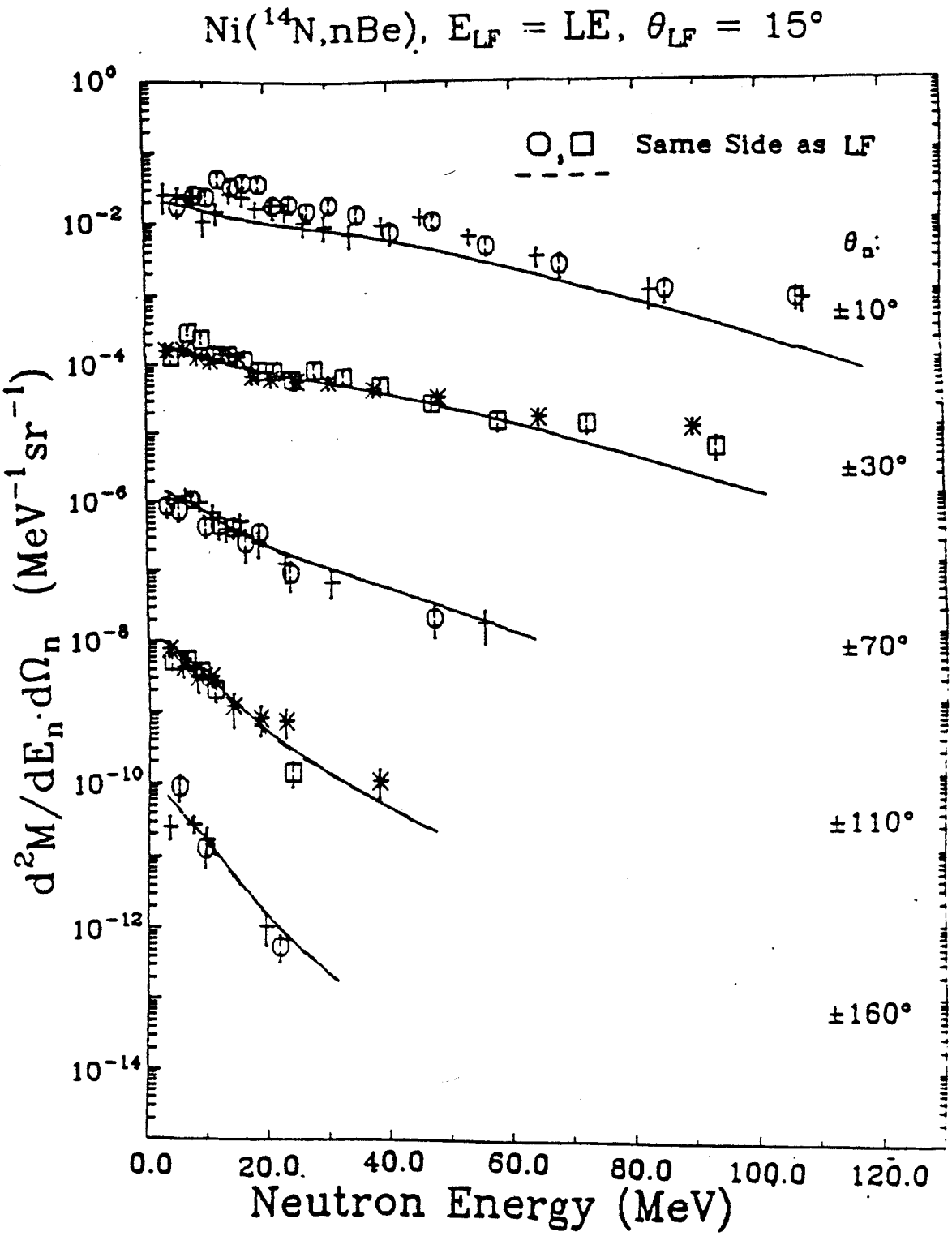

Figure A-26. (continued)

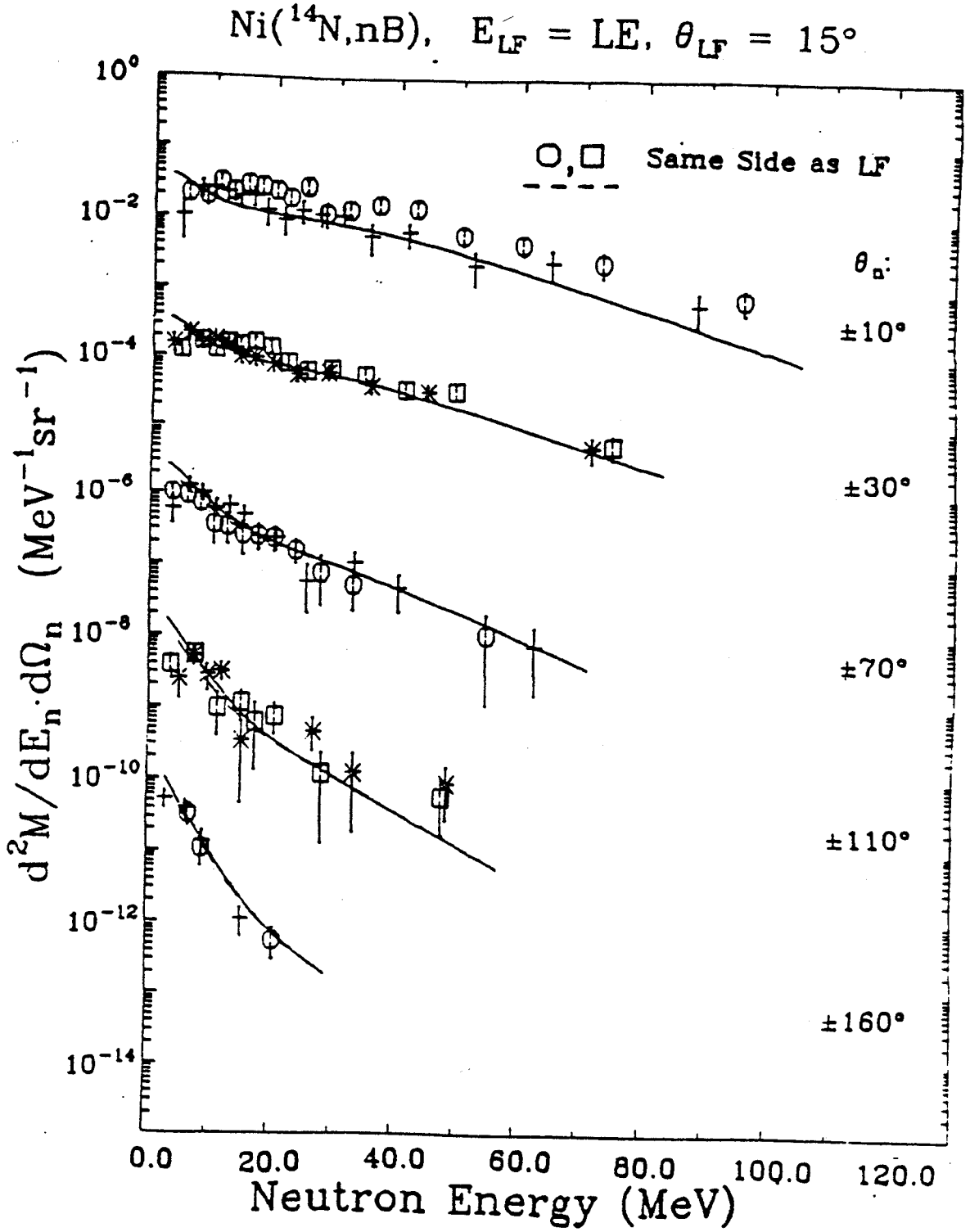

Figure A-26. (continued)

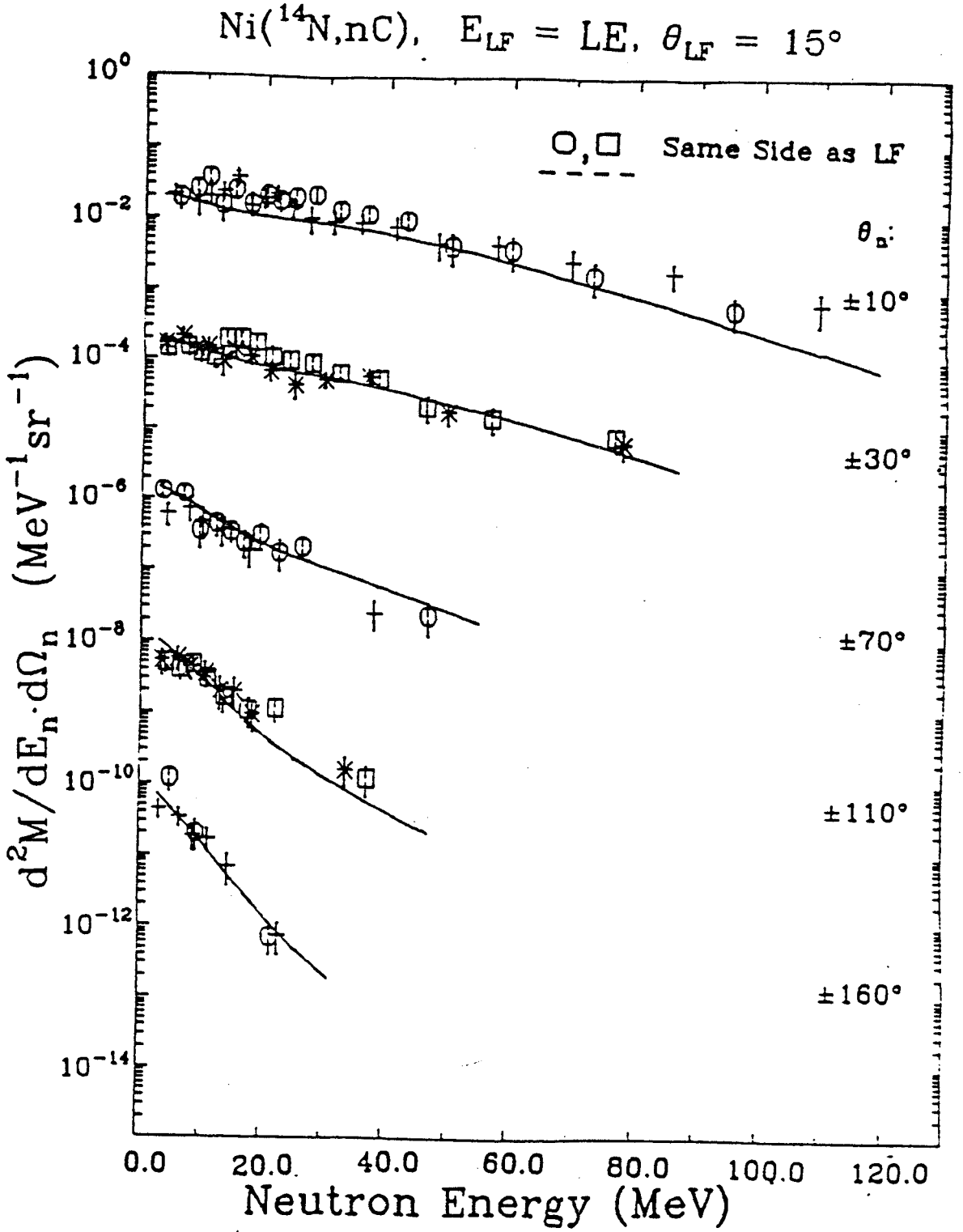

Figure A-26. (continued)

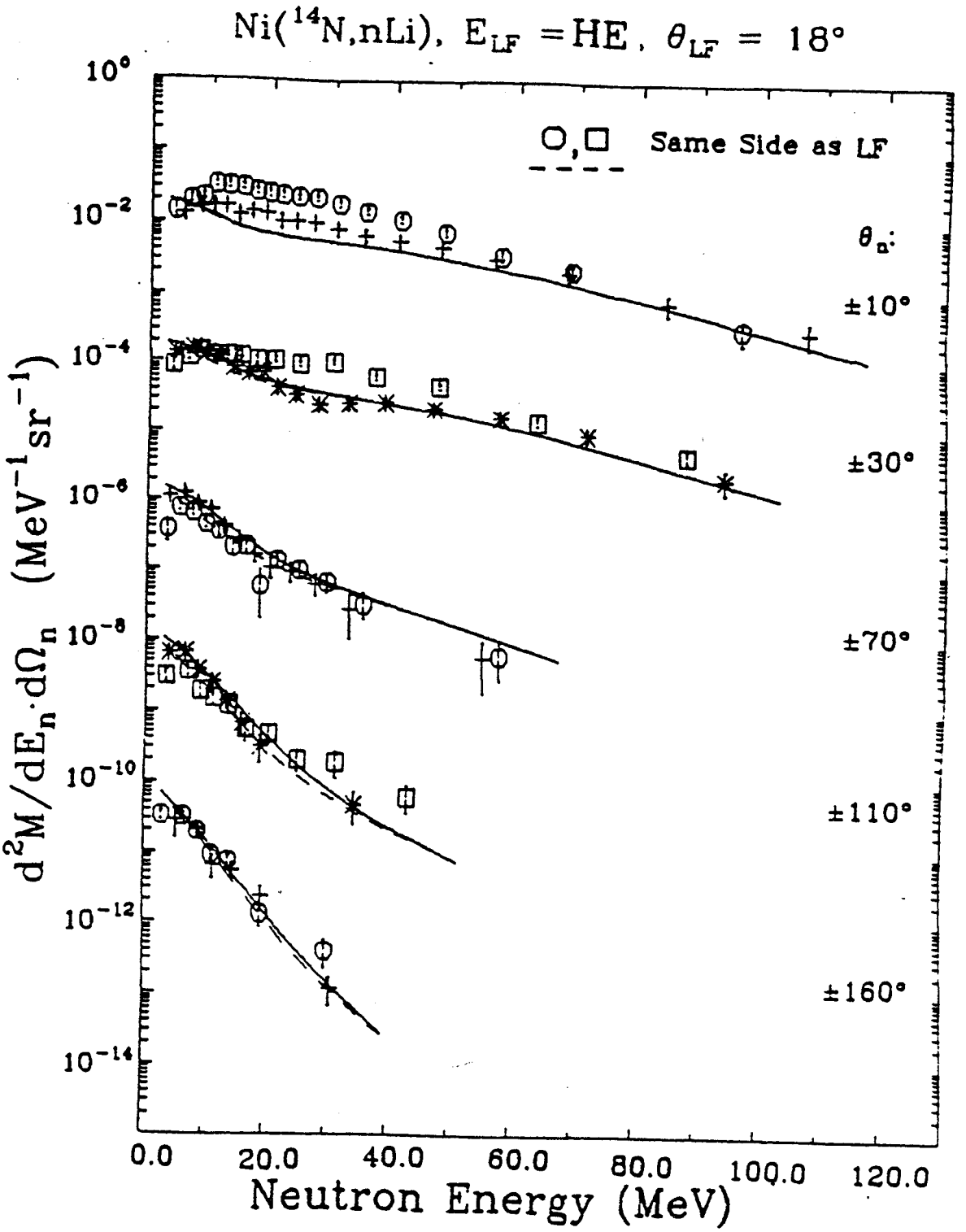

Figure A-26. (continued)

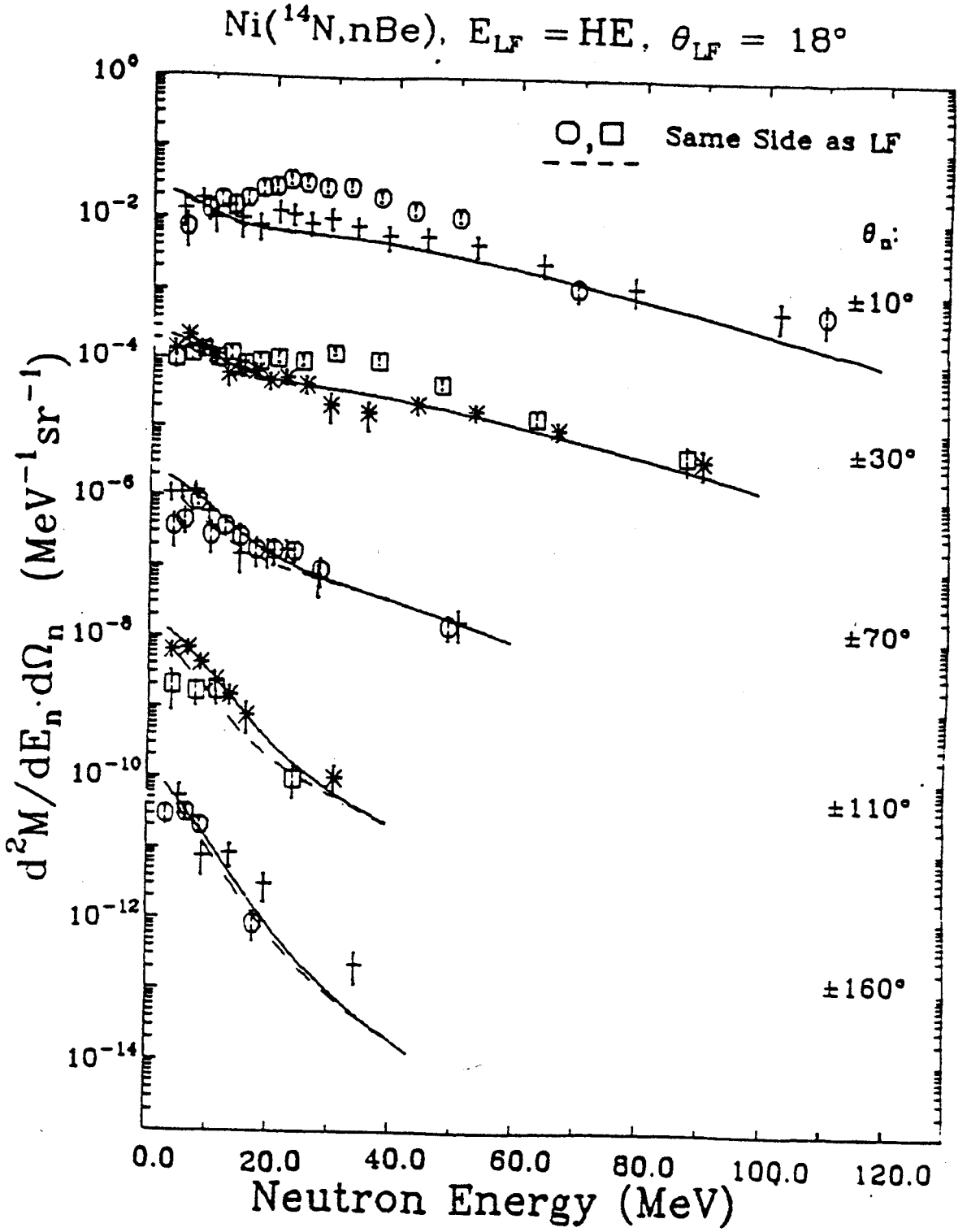

Figure A-26. (continued)

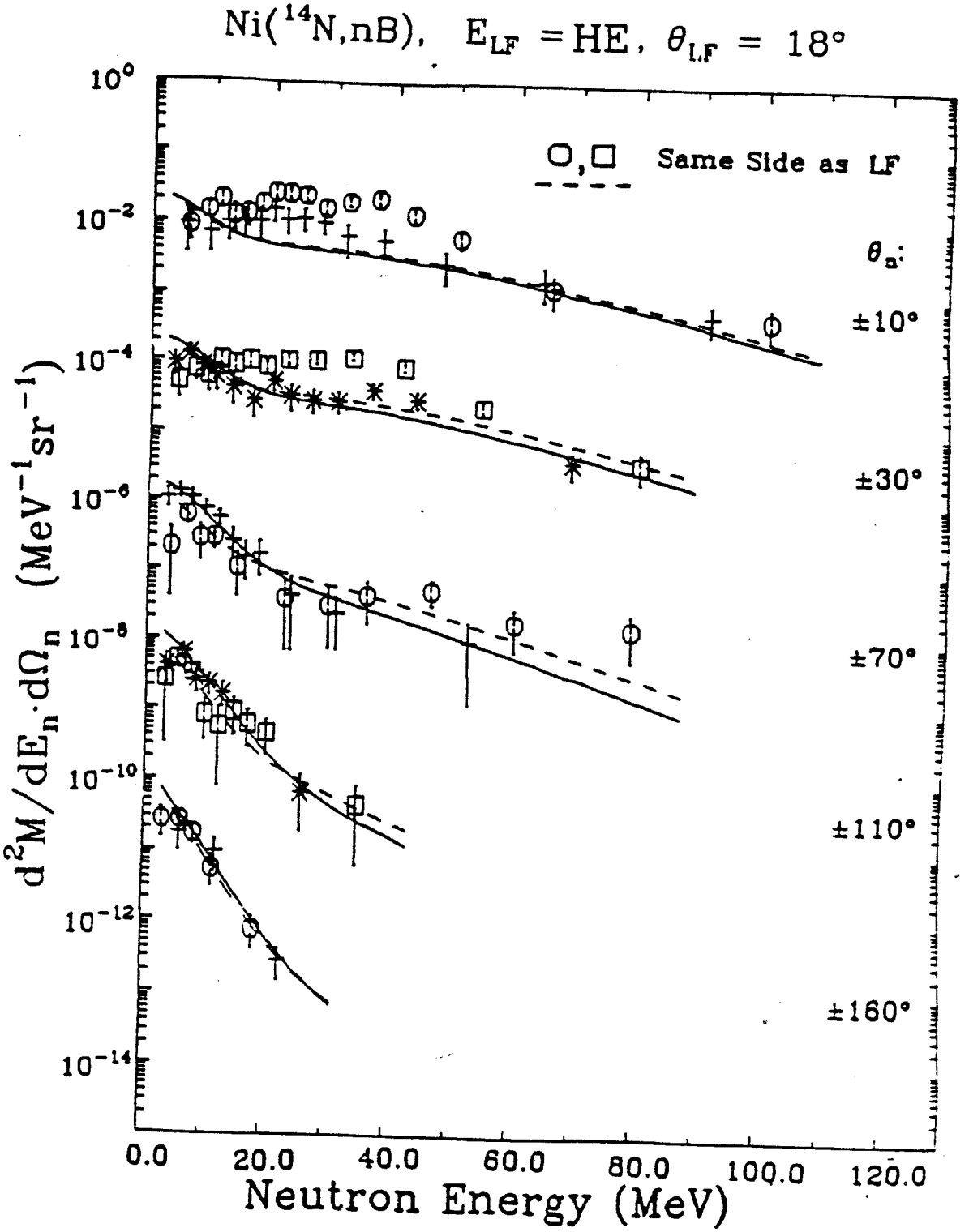

Figure A-26. (continued)

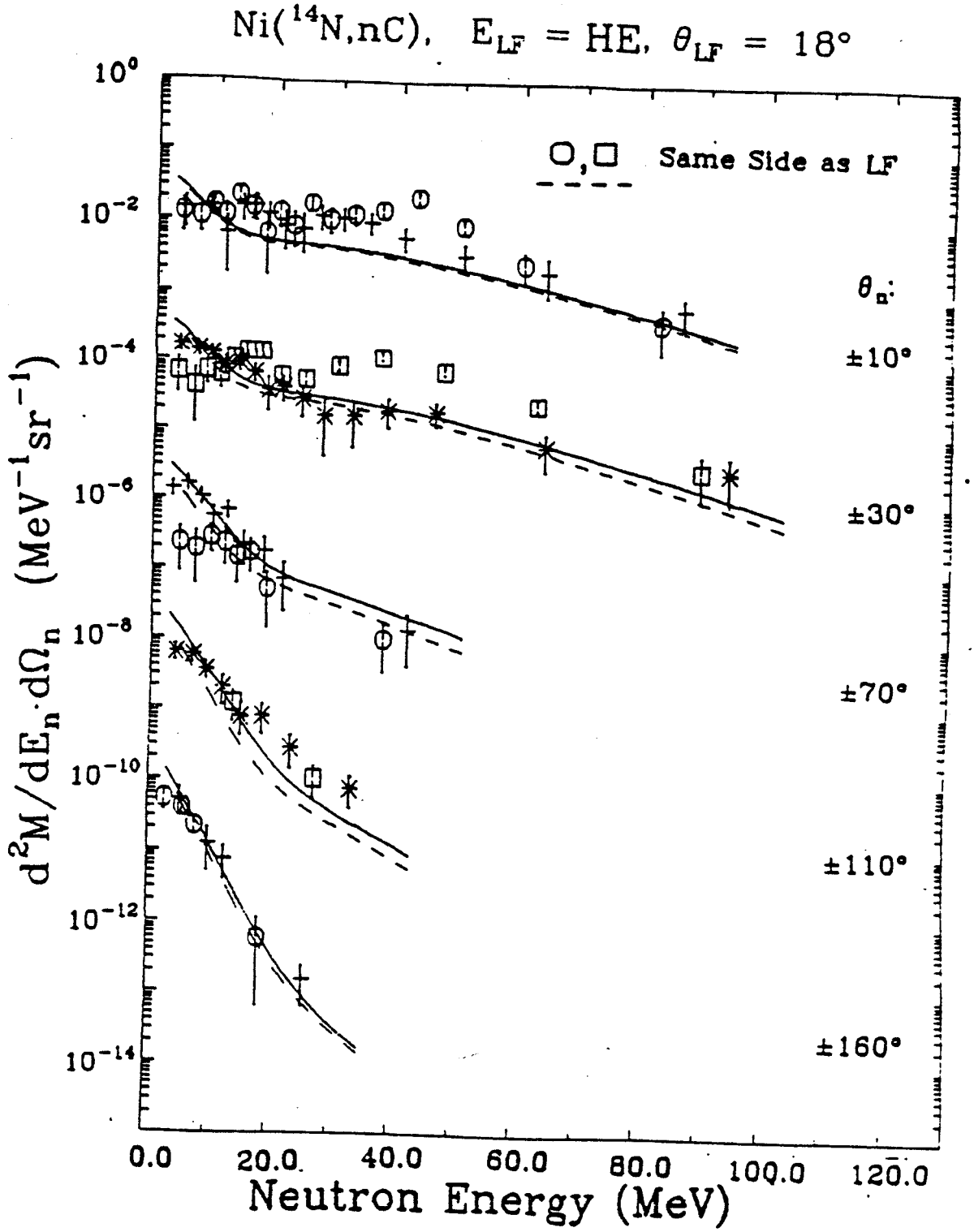

Figure A-26. (continued)

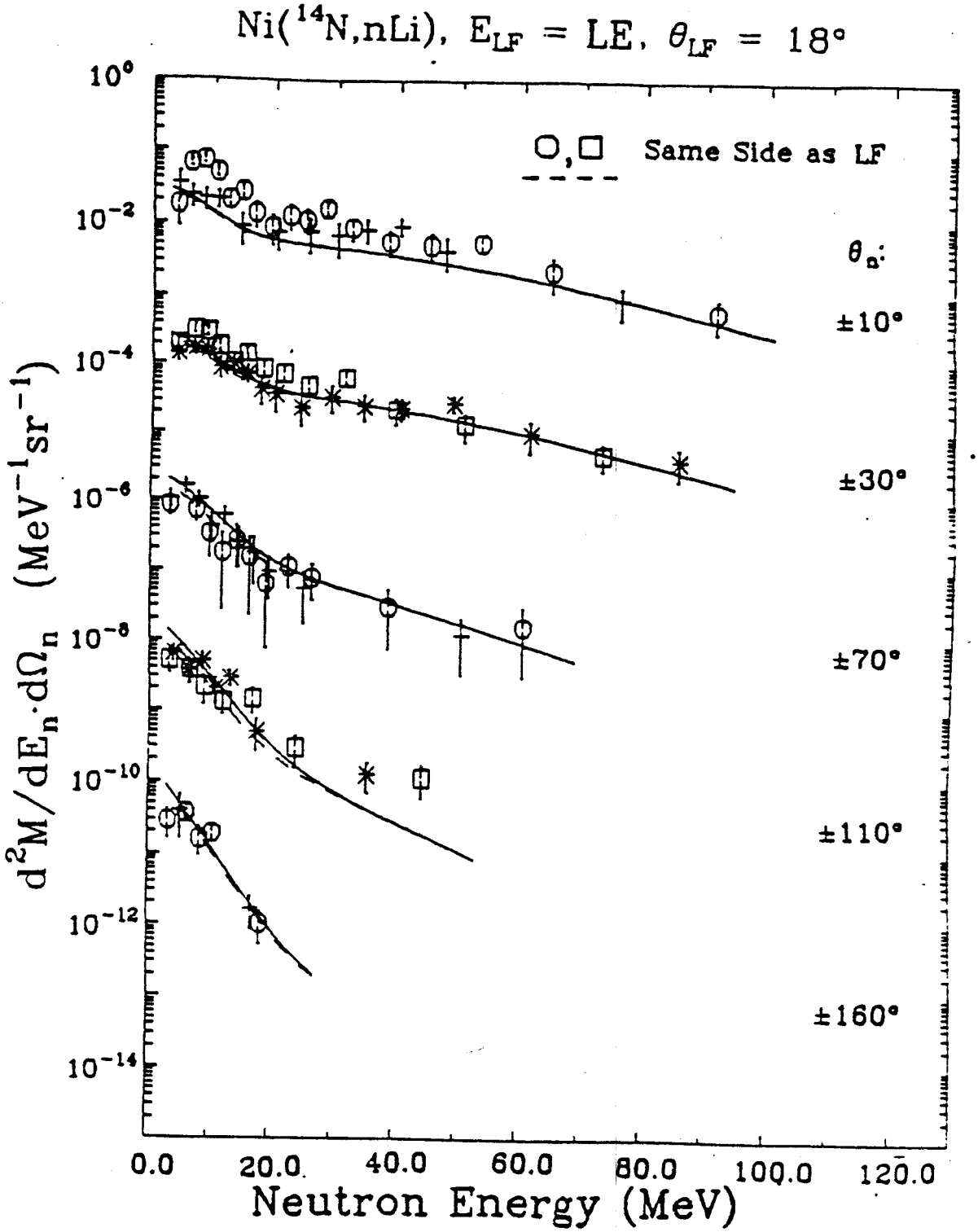

Figure A-26. (continued)

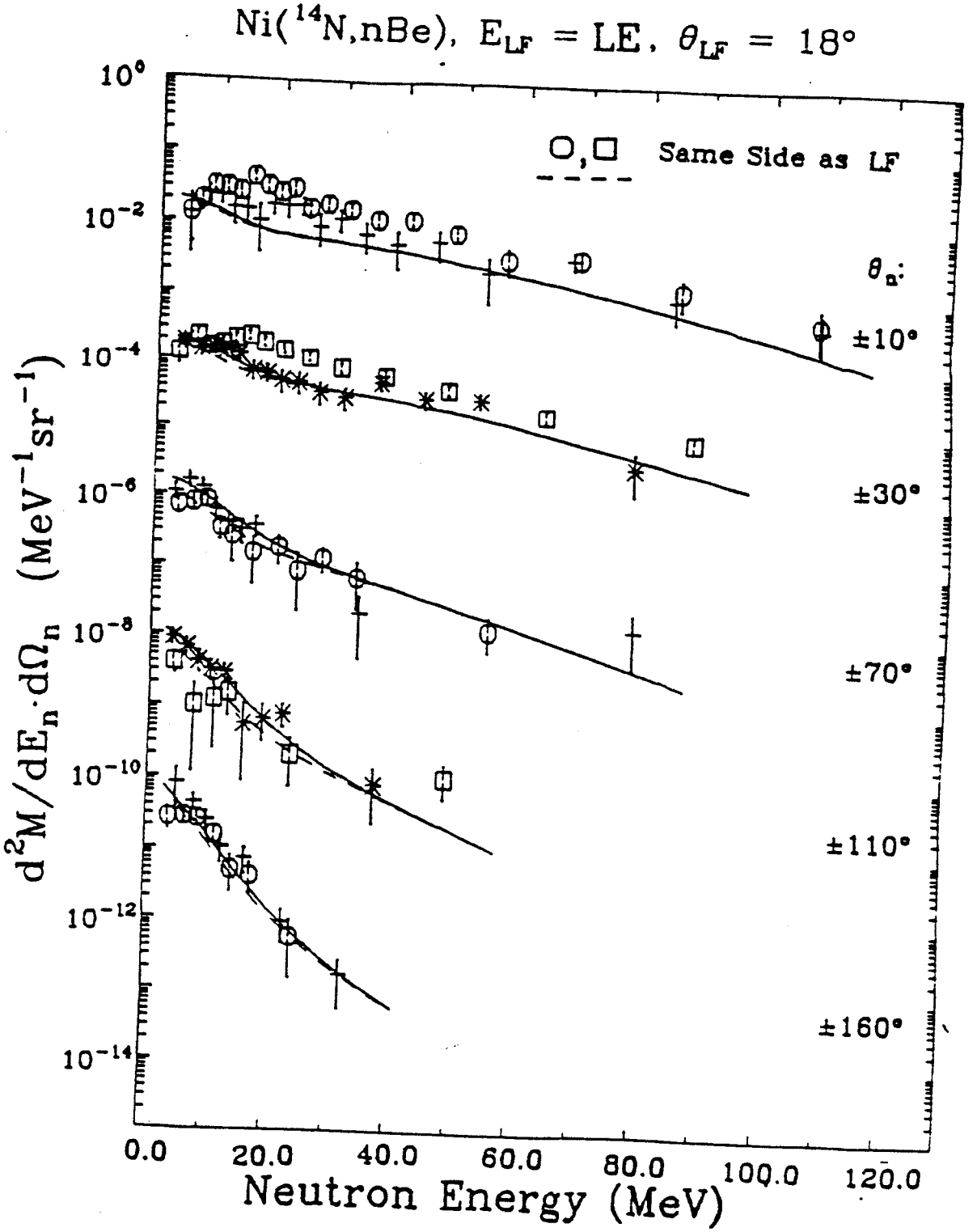

Figure A-26. (continued)

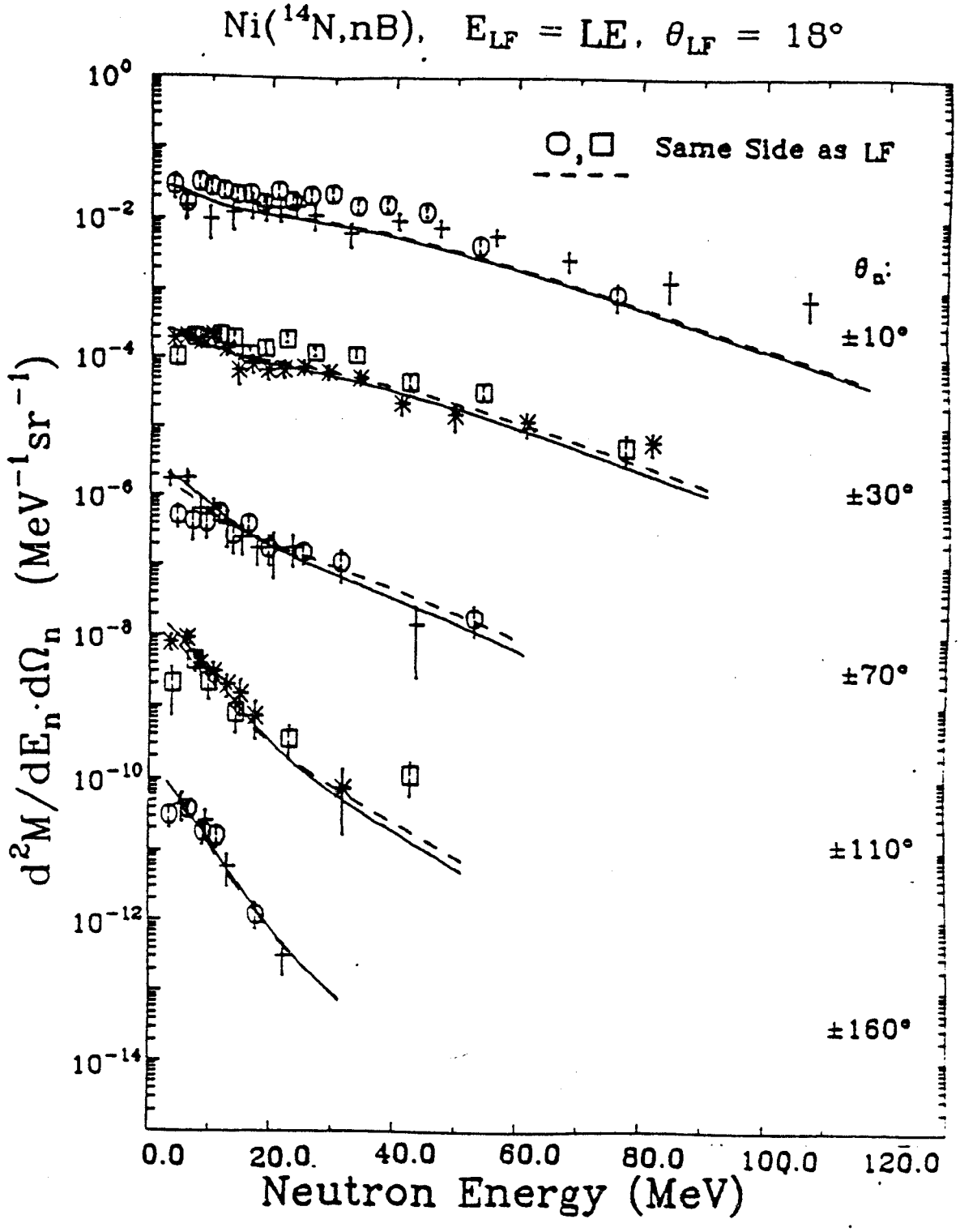

Figure A-26. (continued)

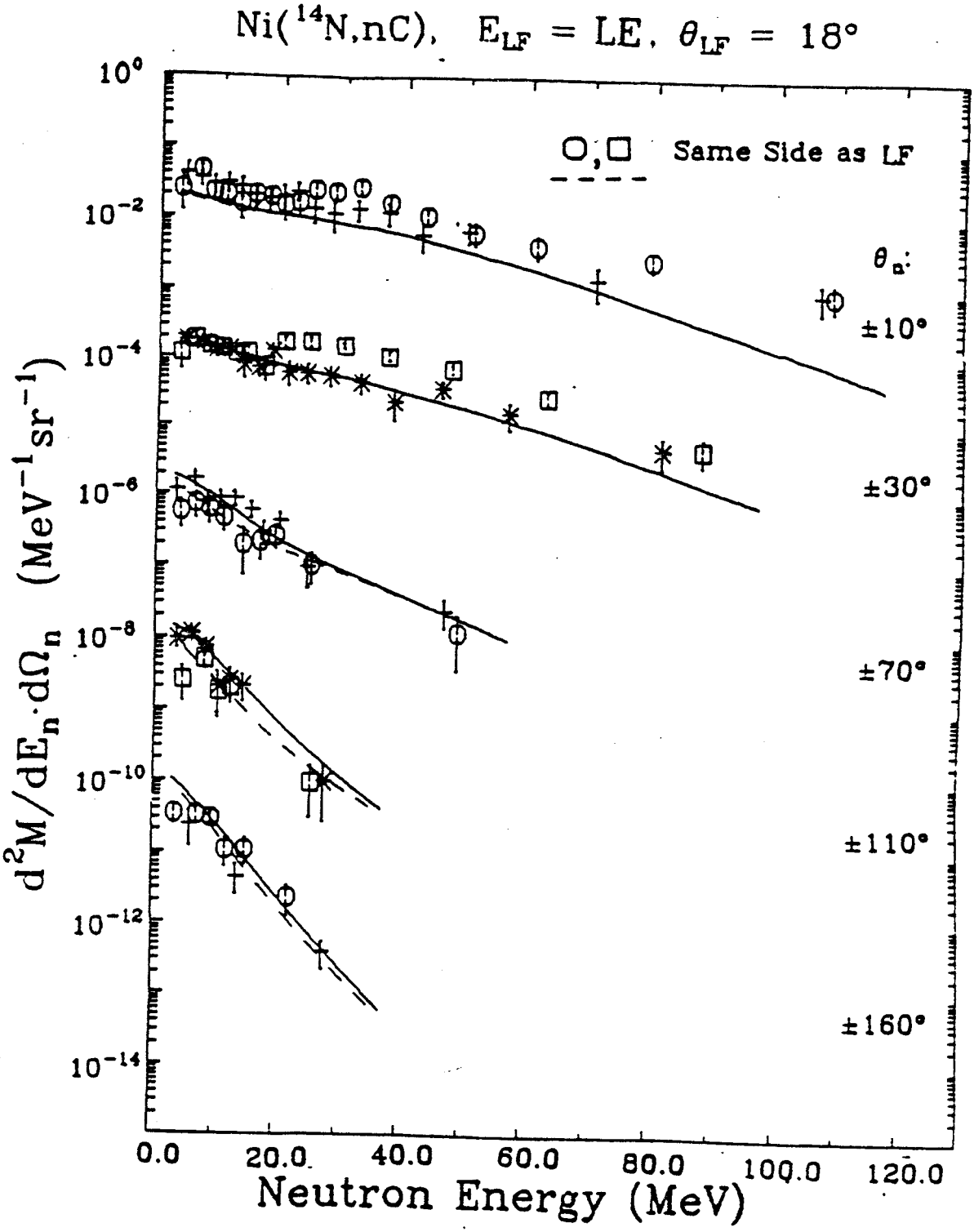

Figure A-26. (continued)

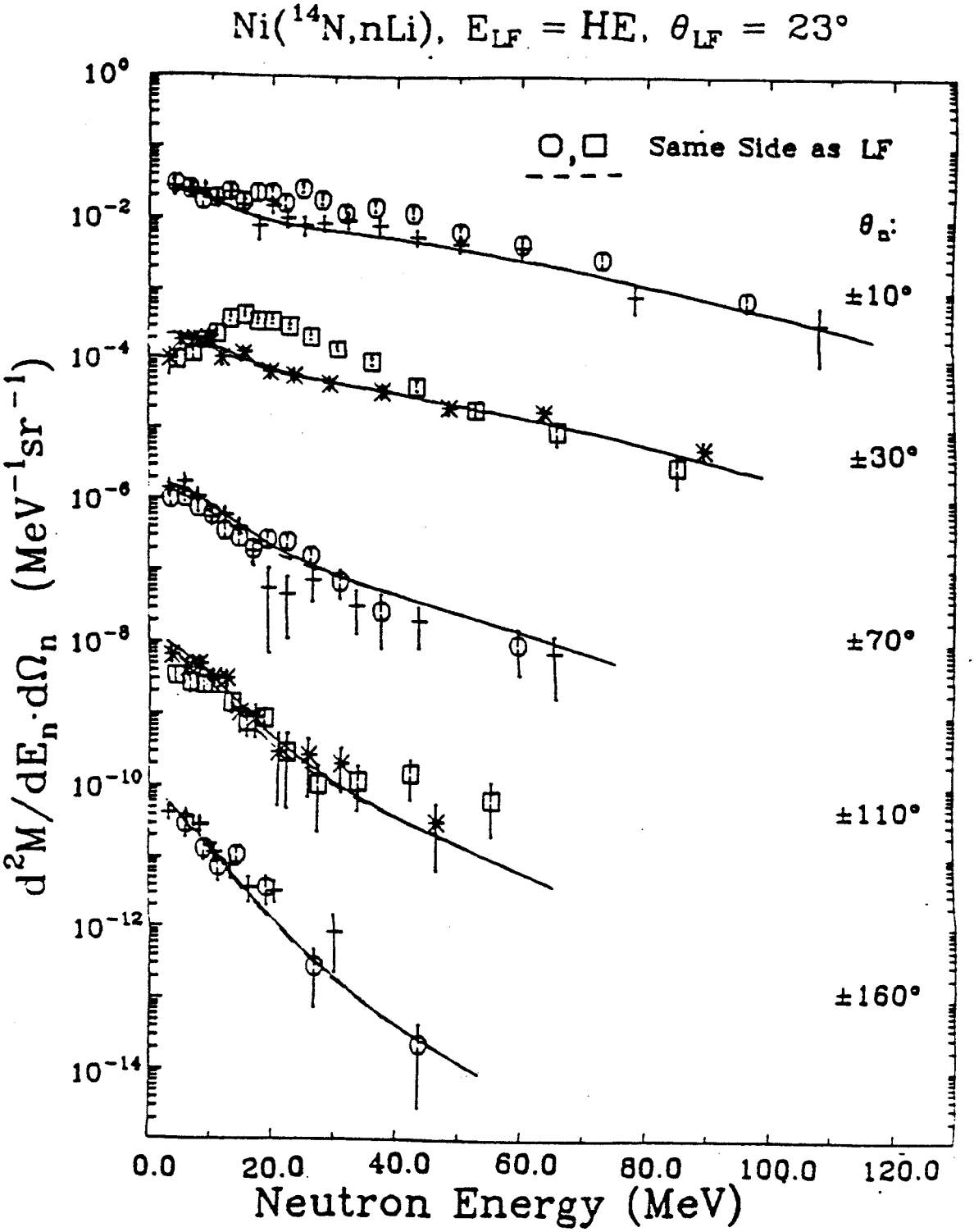

Figure A-26. (continued)

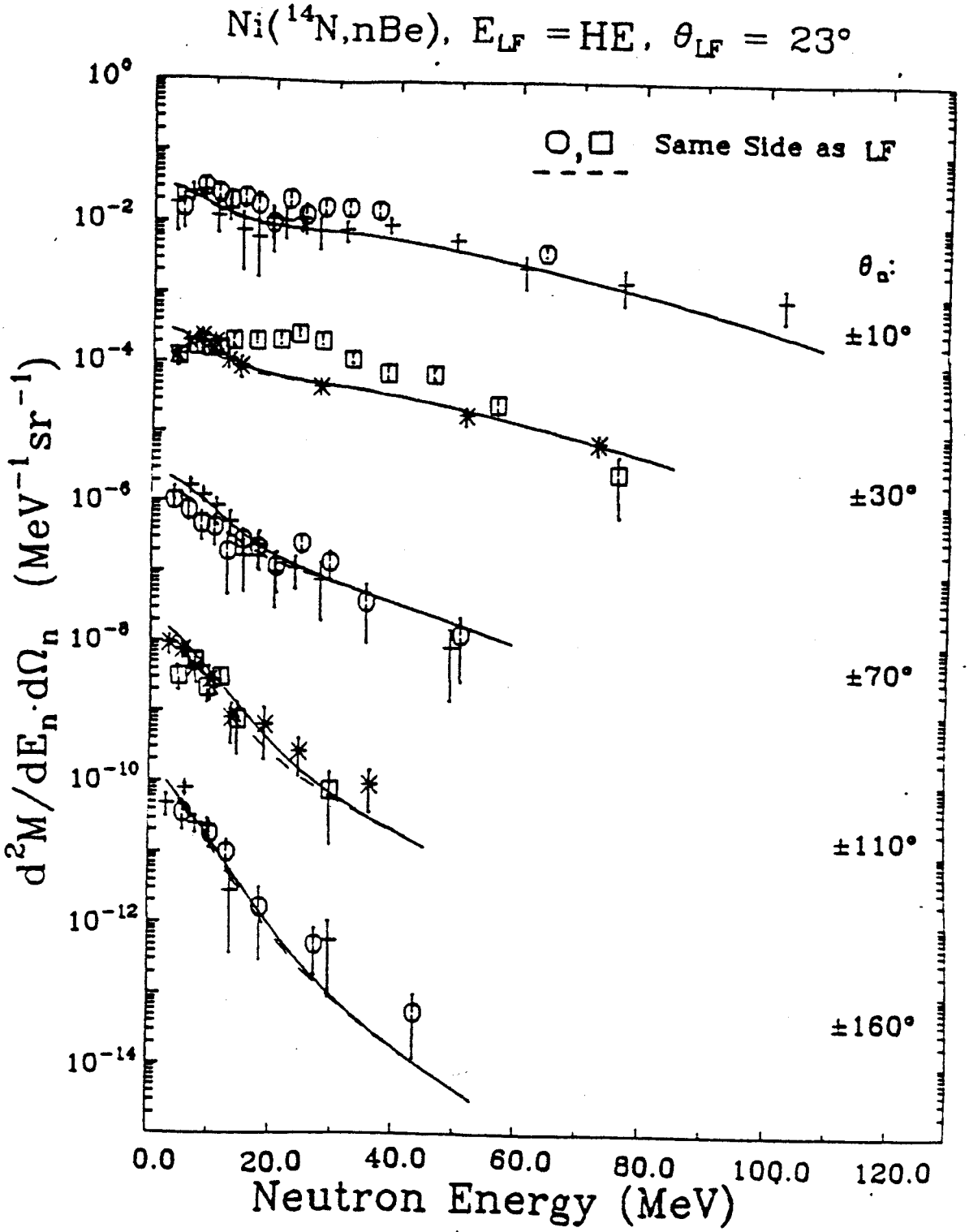

Figure A-26. (continued)

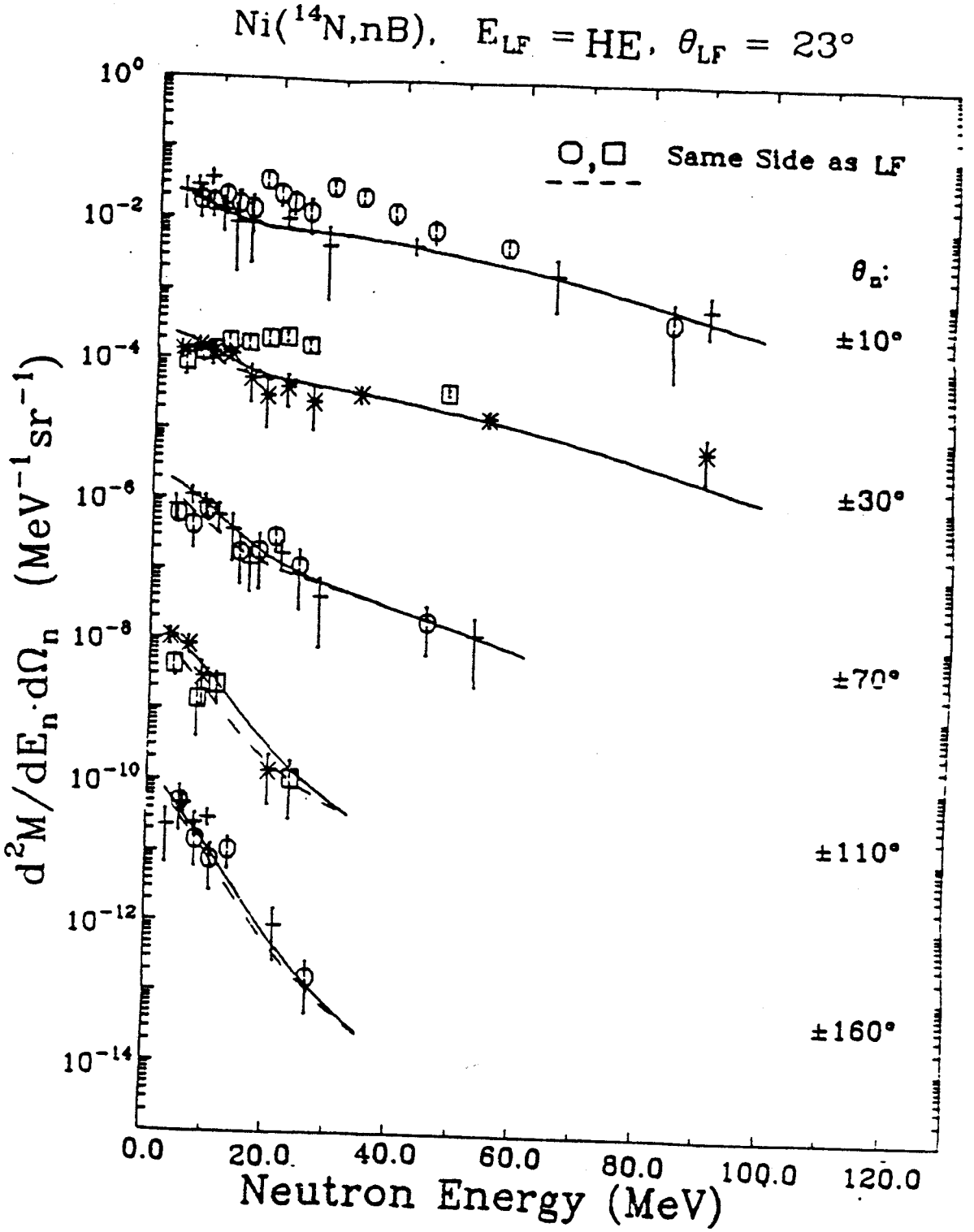

Figure A-26. (continued)

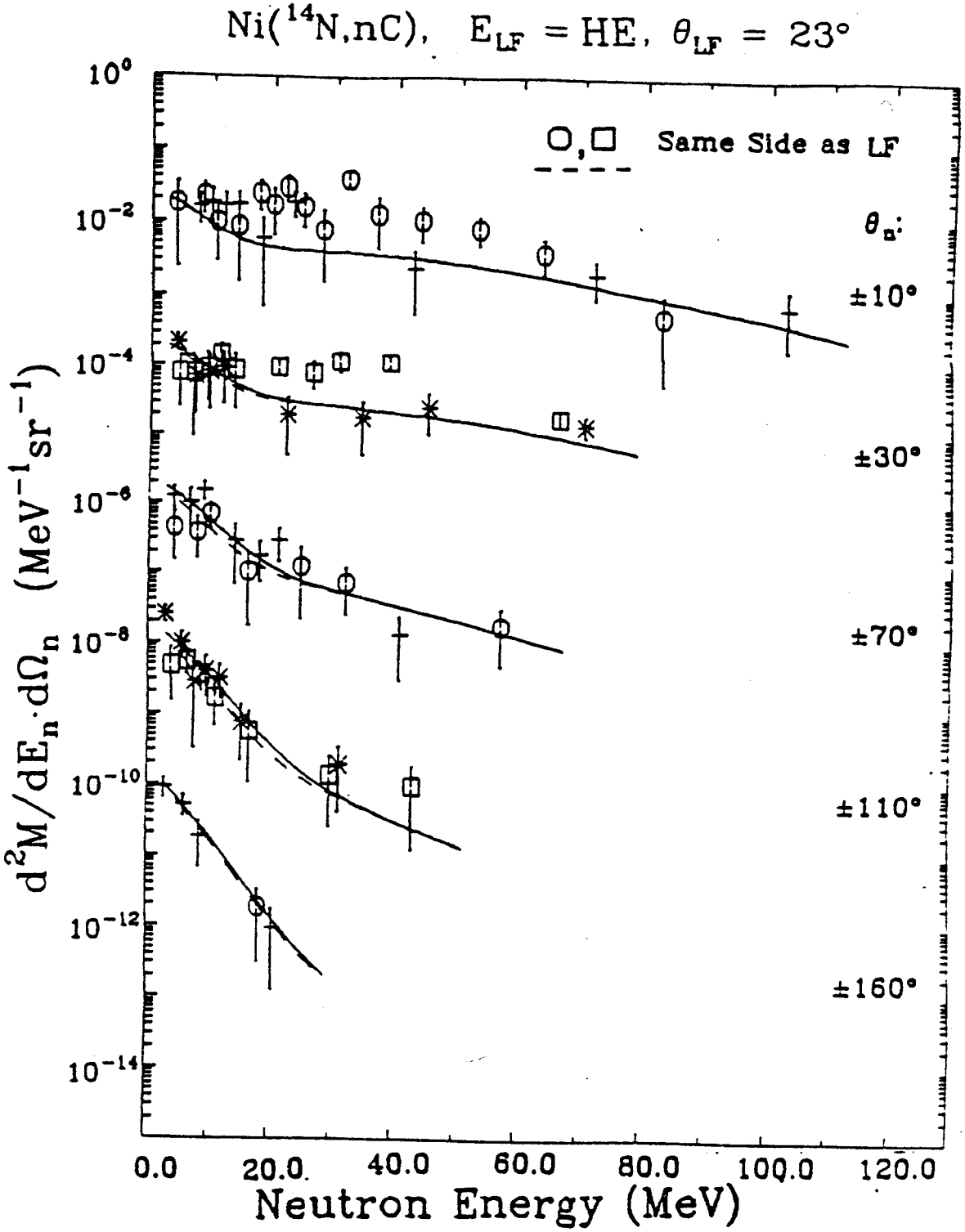

Figure A-26. (continued)

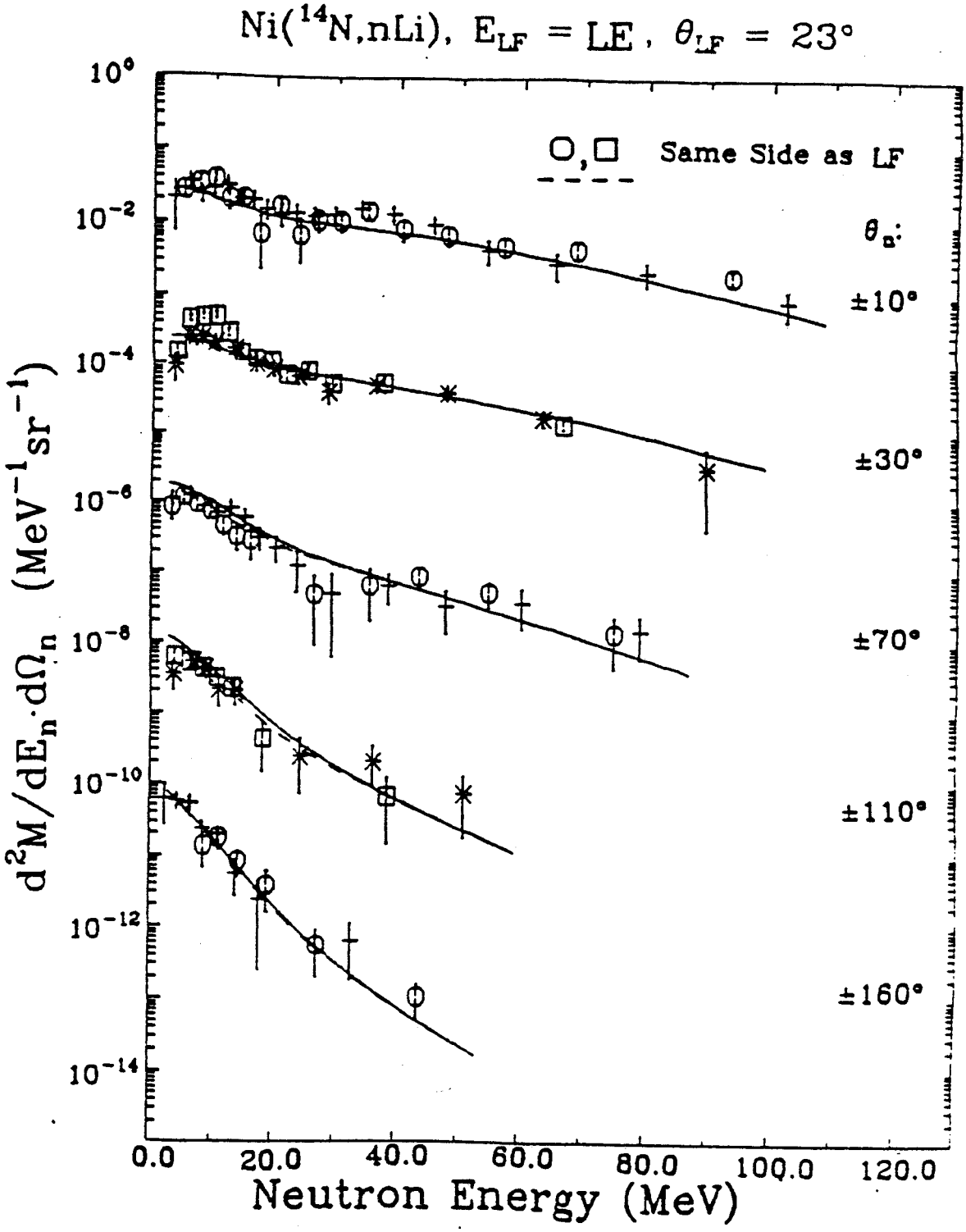

Figure A-26. (continued)

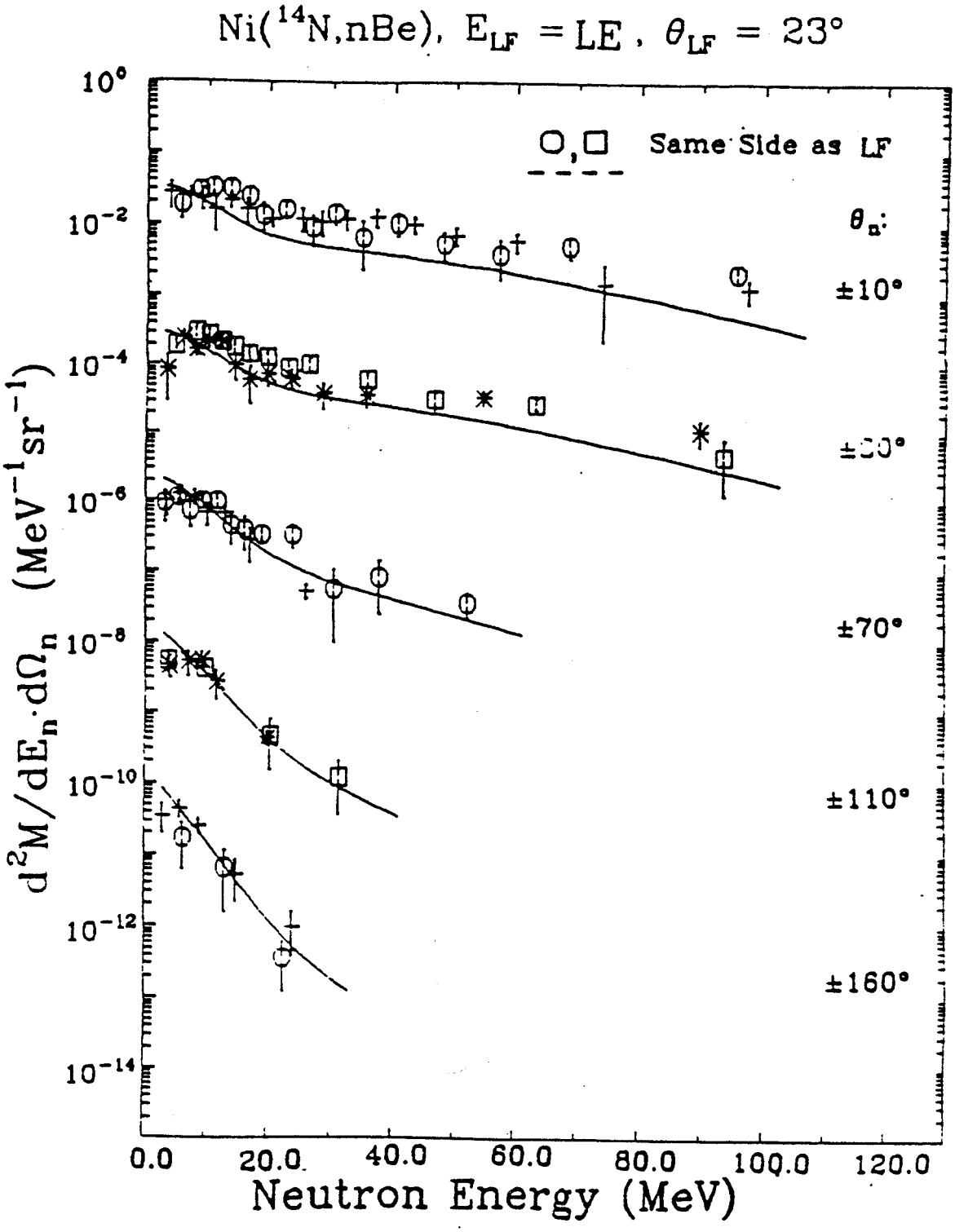

Figure A-26. (continued)

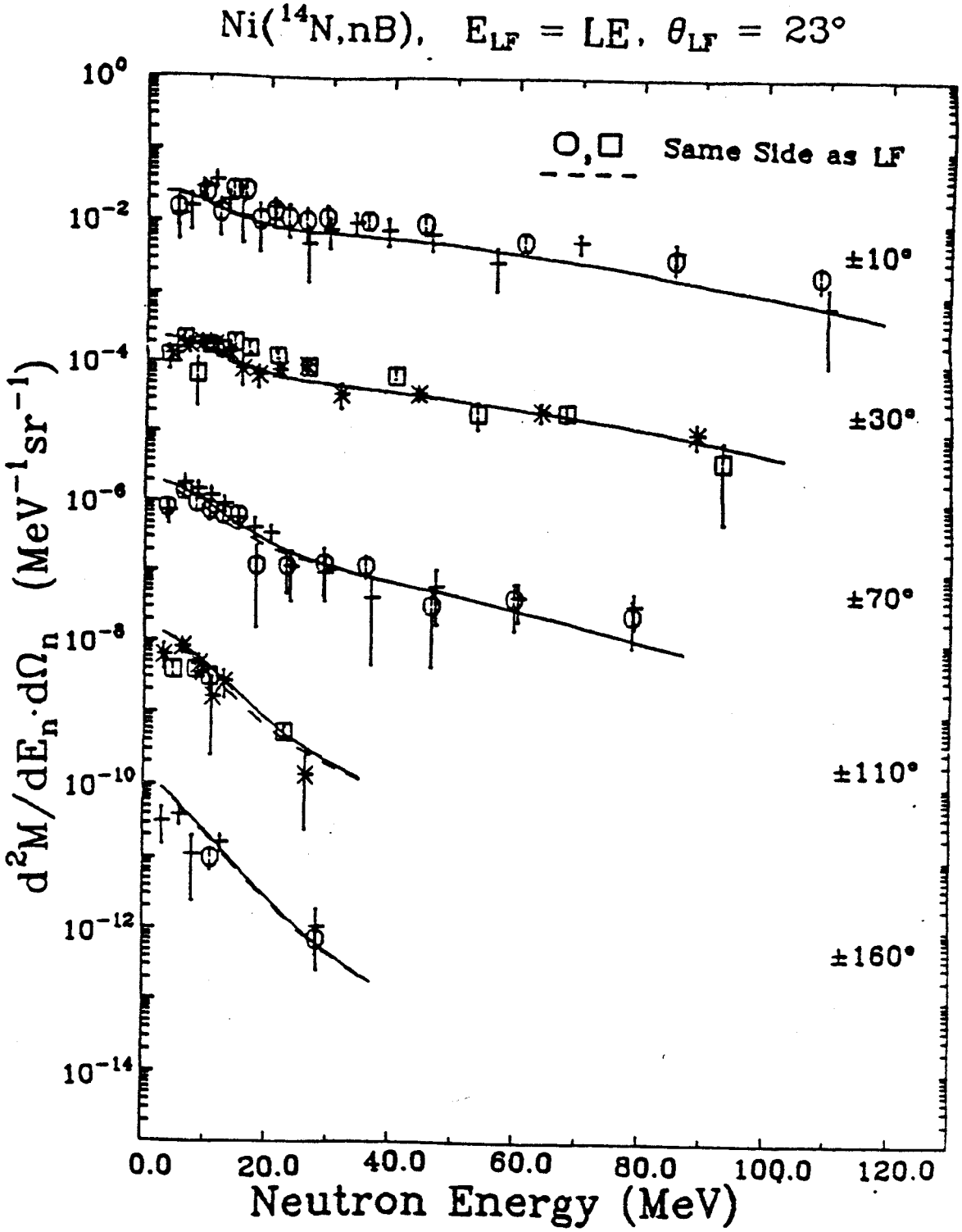

Figure A-26. (continued)

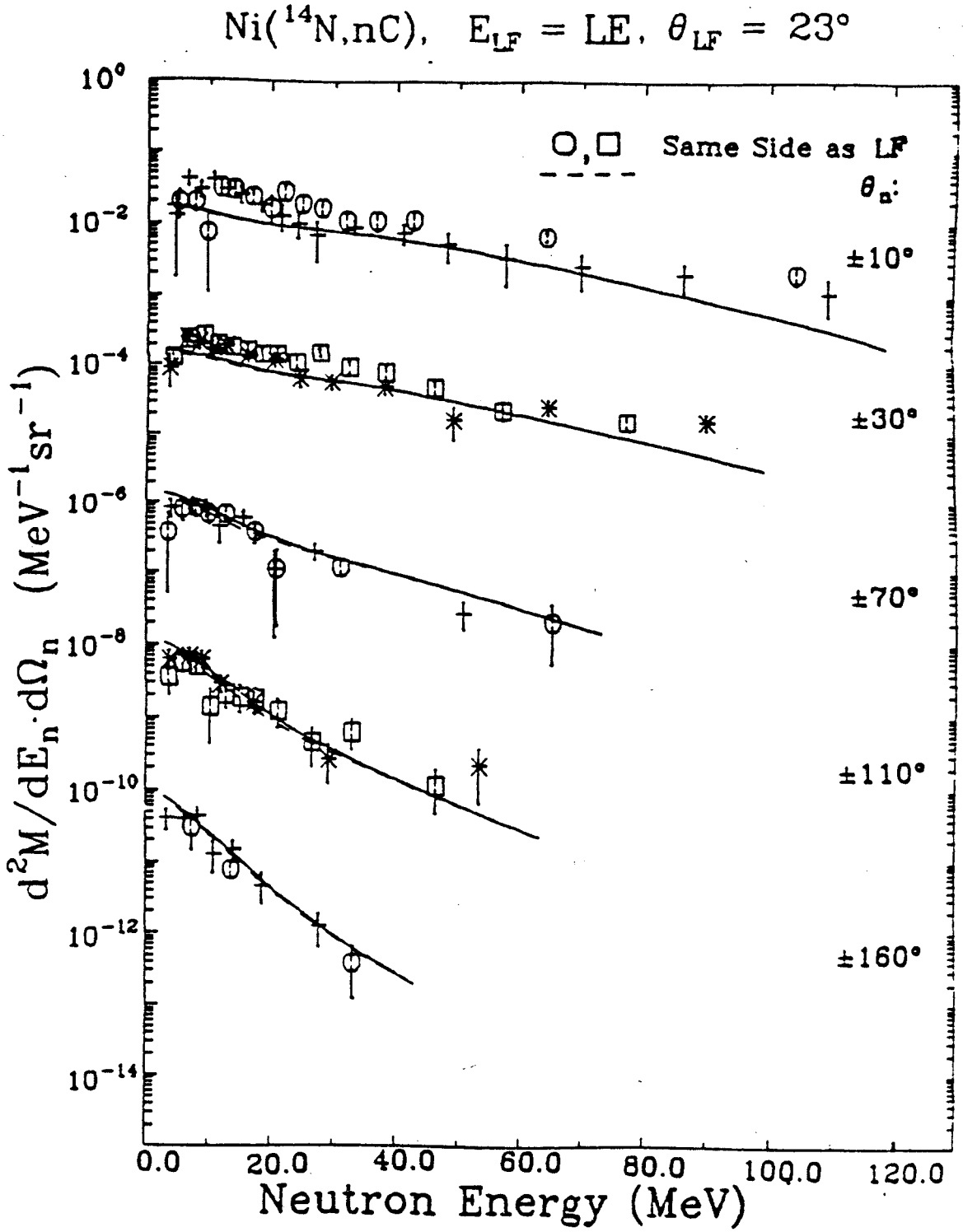

Figure A-26. (continued)

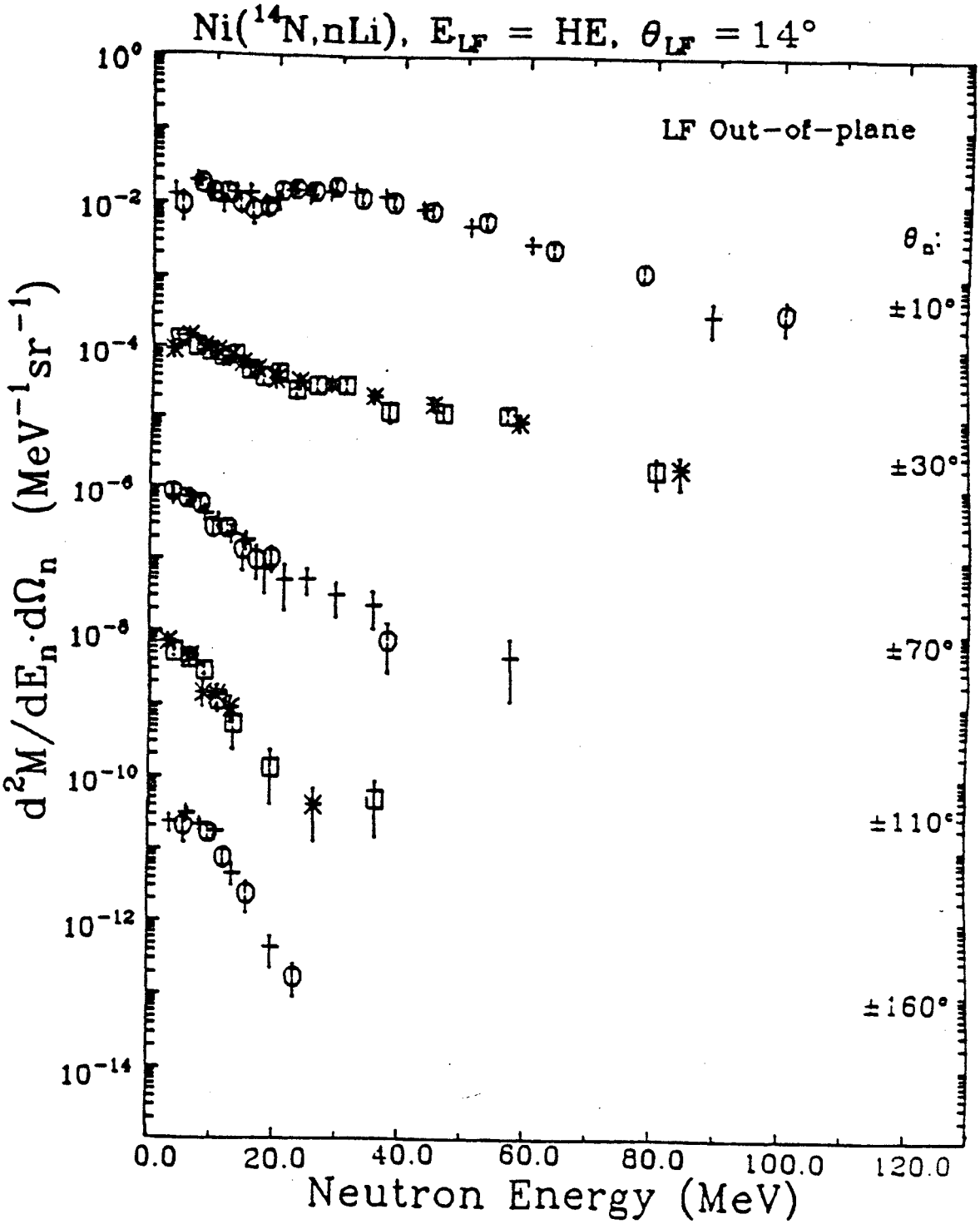

Figure A-26. (continued)

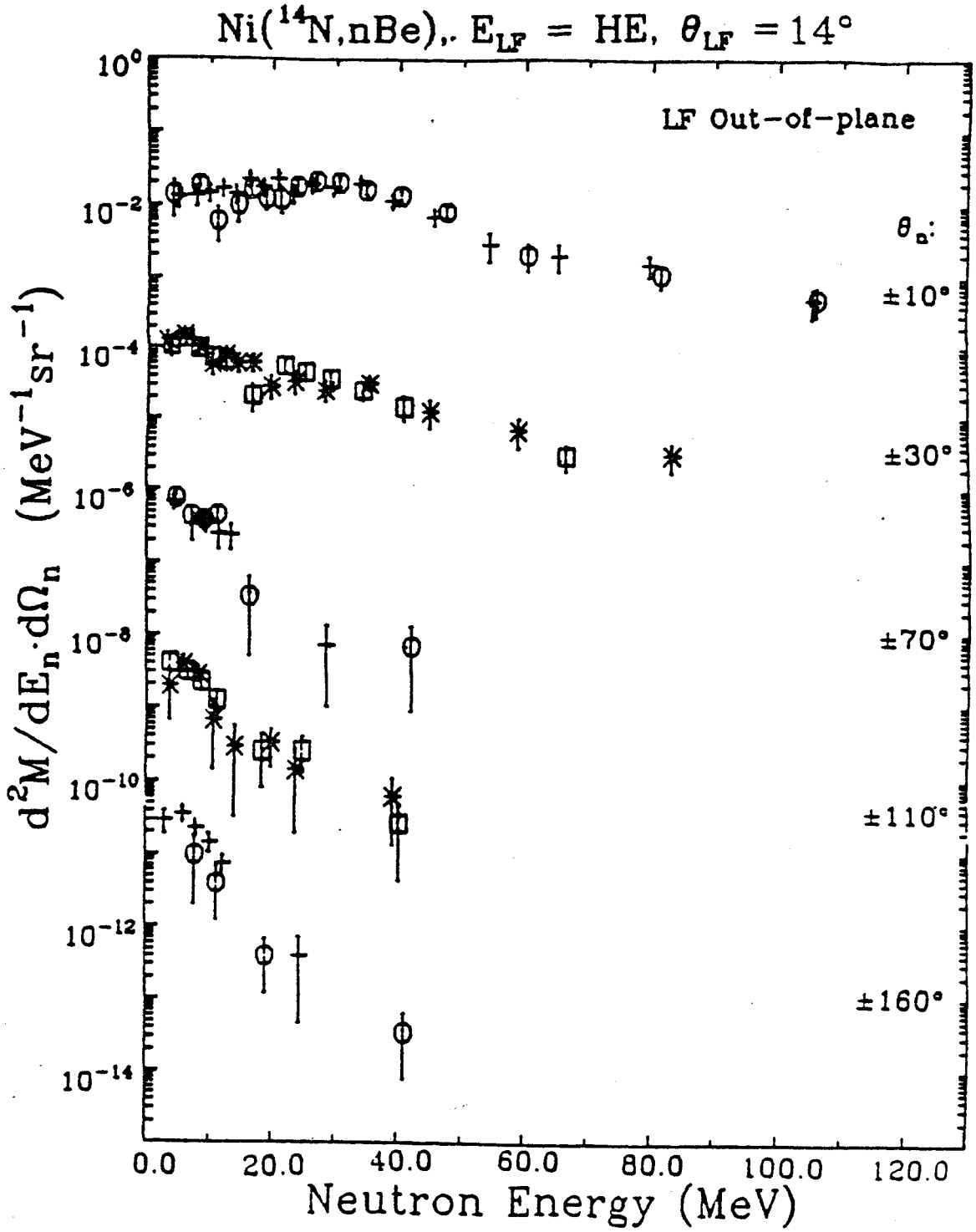

Figure A-26. (continued)

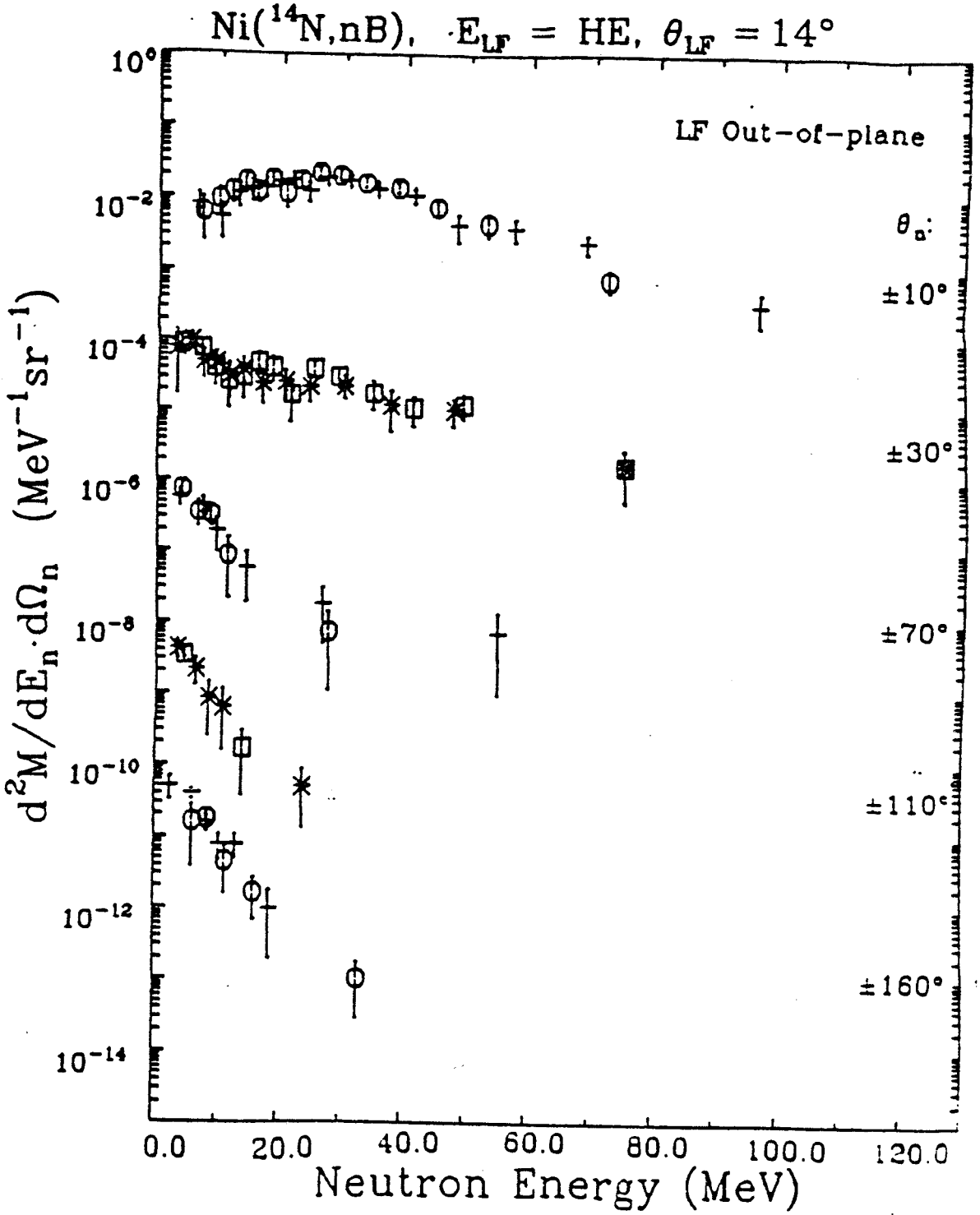

Figure A-26. (continued)

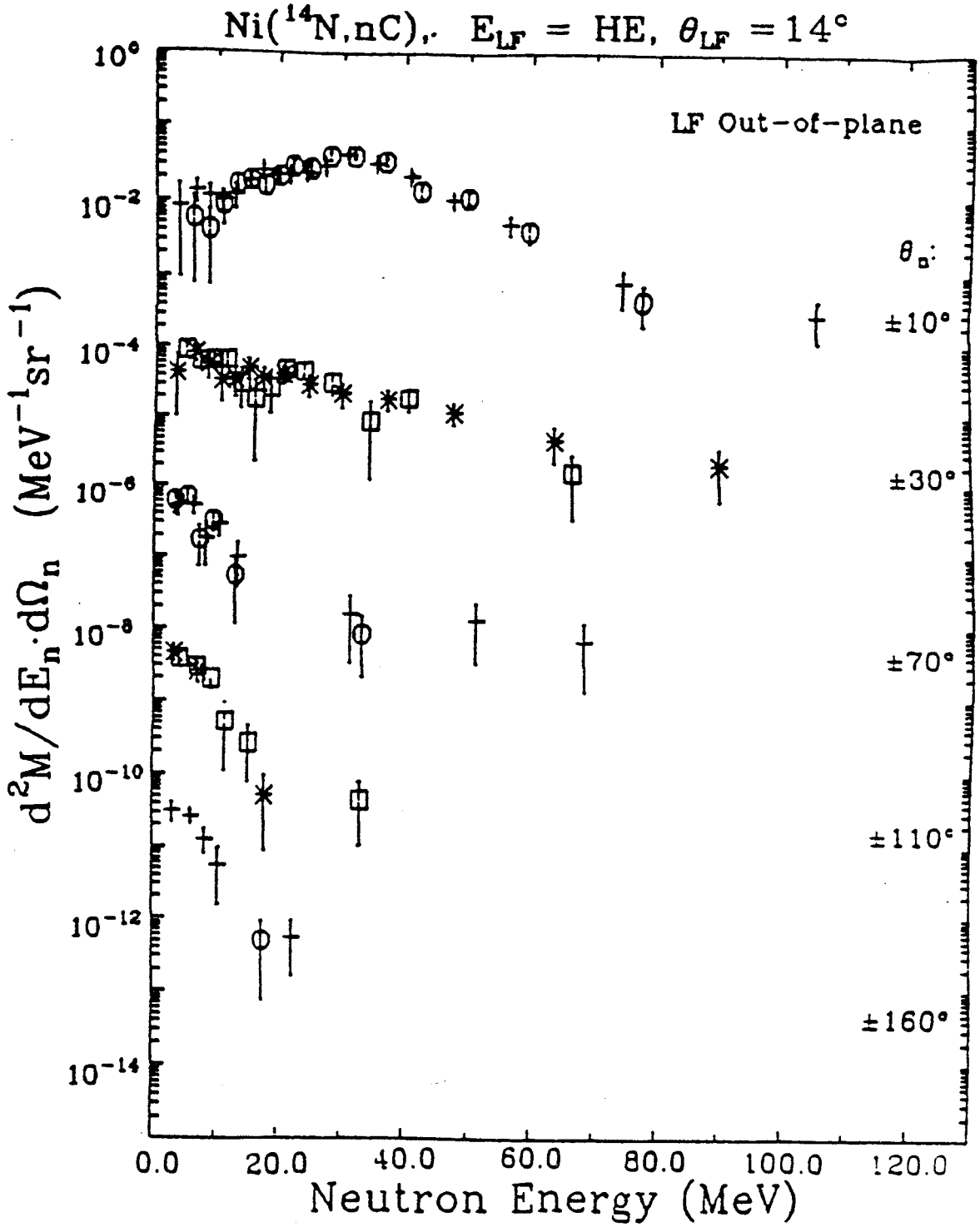

Figure A-26. (continued)

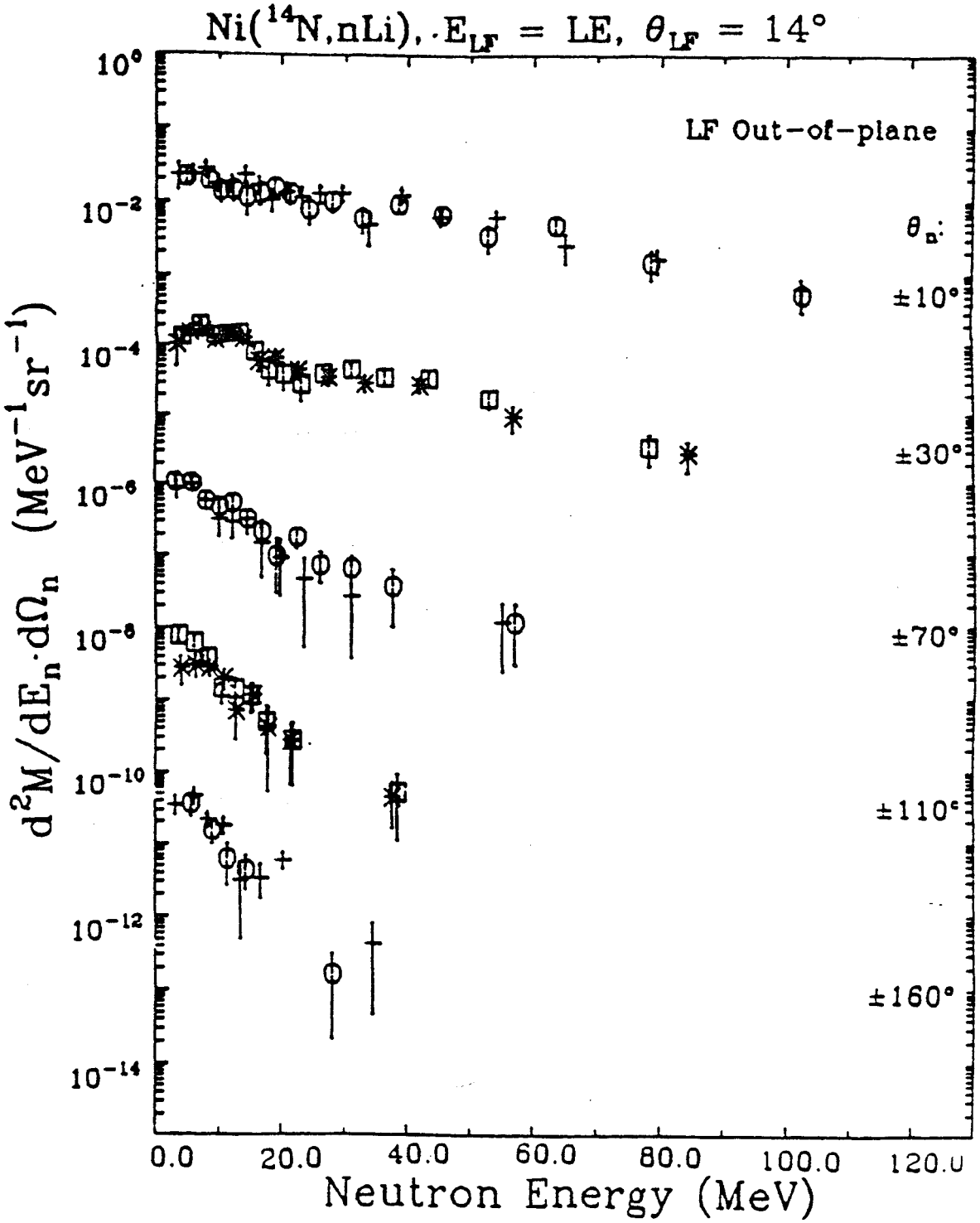

Figure A-26. (continued)

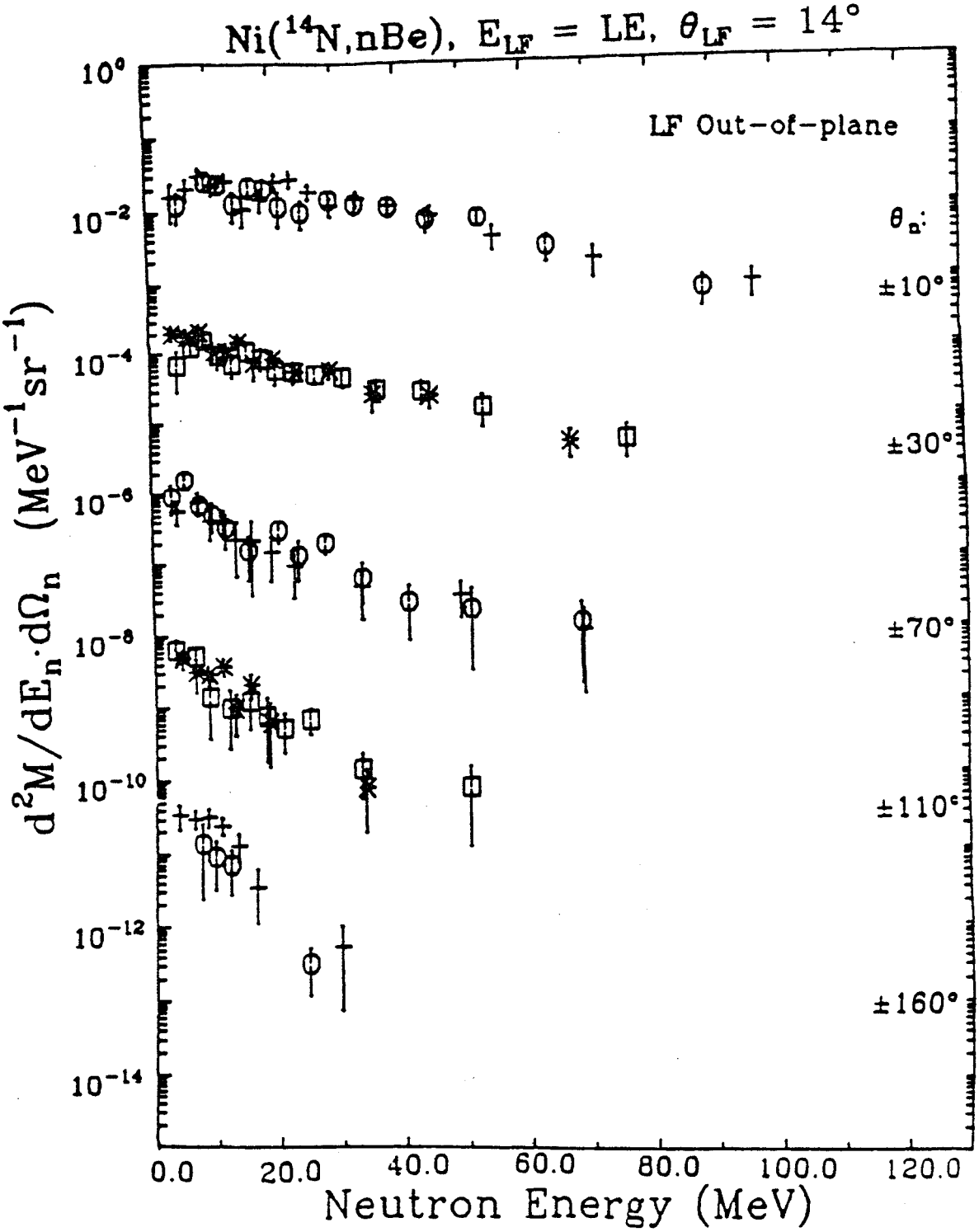

Figure A-26. (continued)

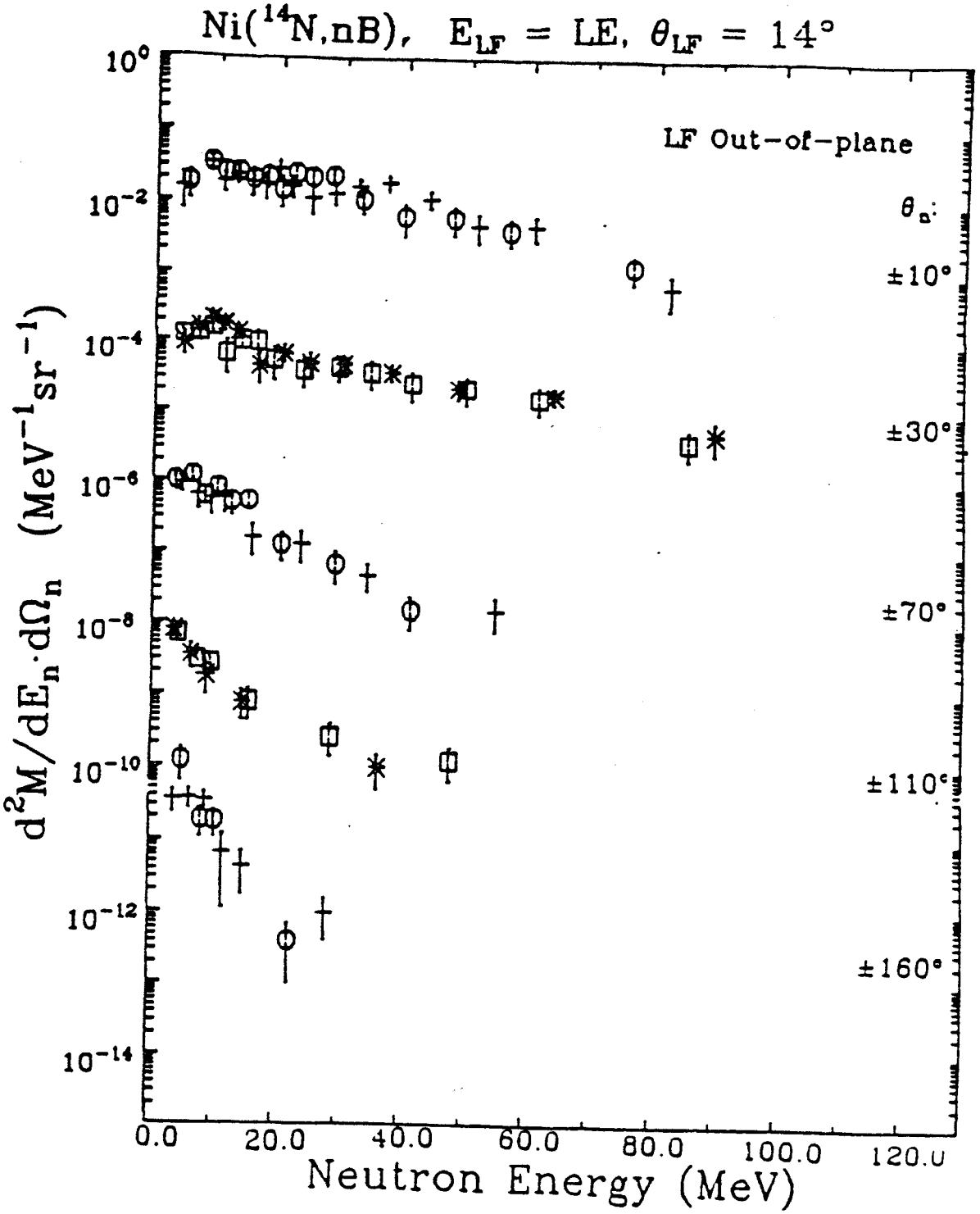

Figure A-26. (continued)

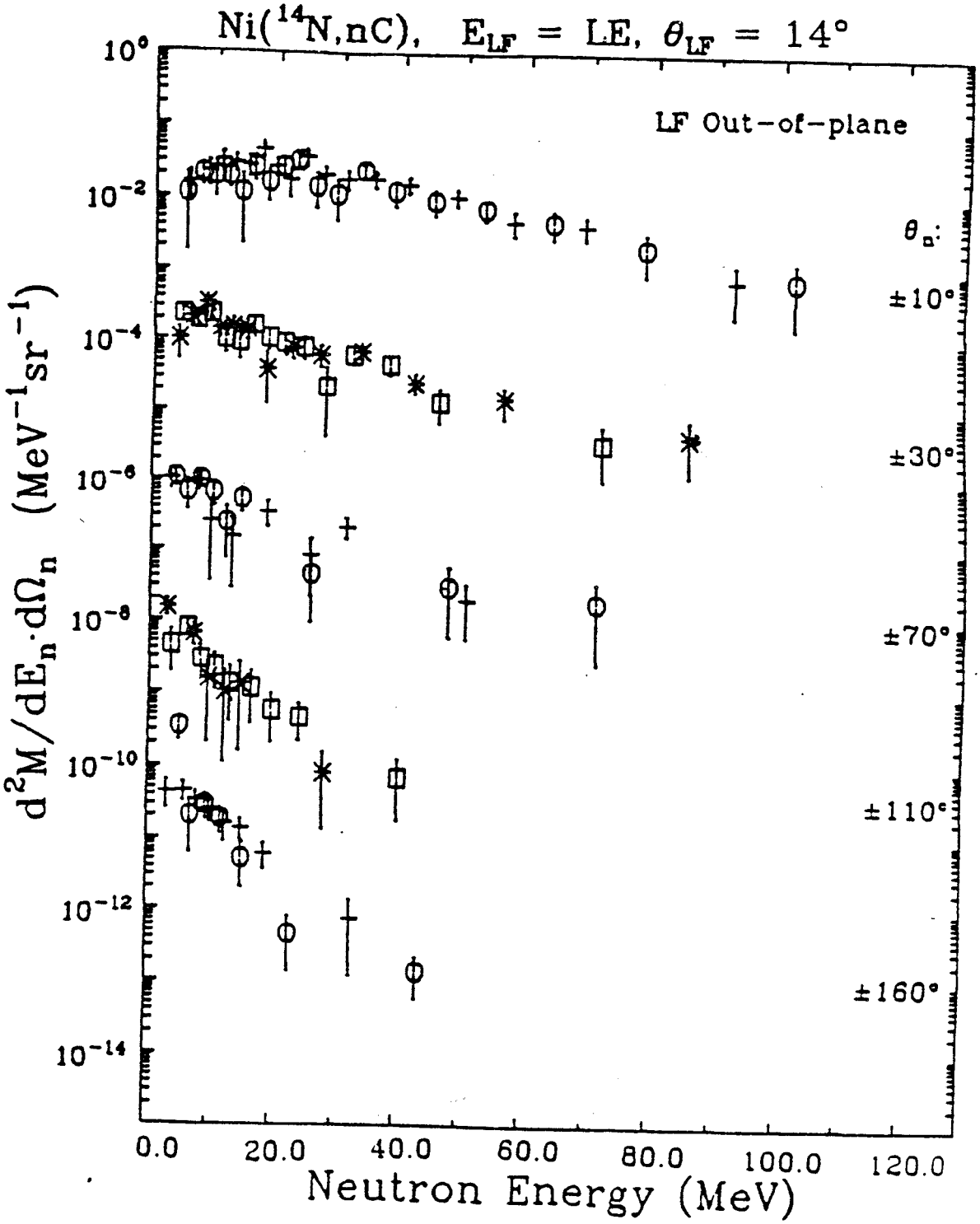

3. The C Target

Figure A-27 contains the differential neutron multiplicity spectra for the C target. The format of the figure is the same as that for Fig. A-25. The neutron data from the C target were not studied with the moving-source parameterization, hence no fitted curves are displayed with the data.

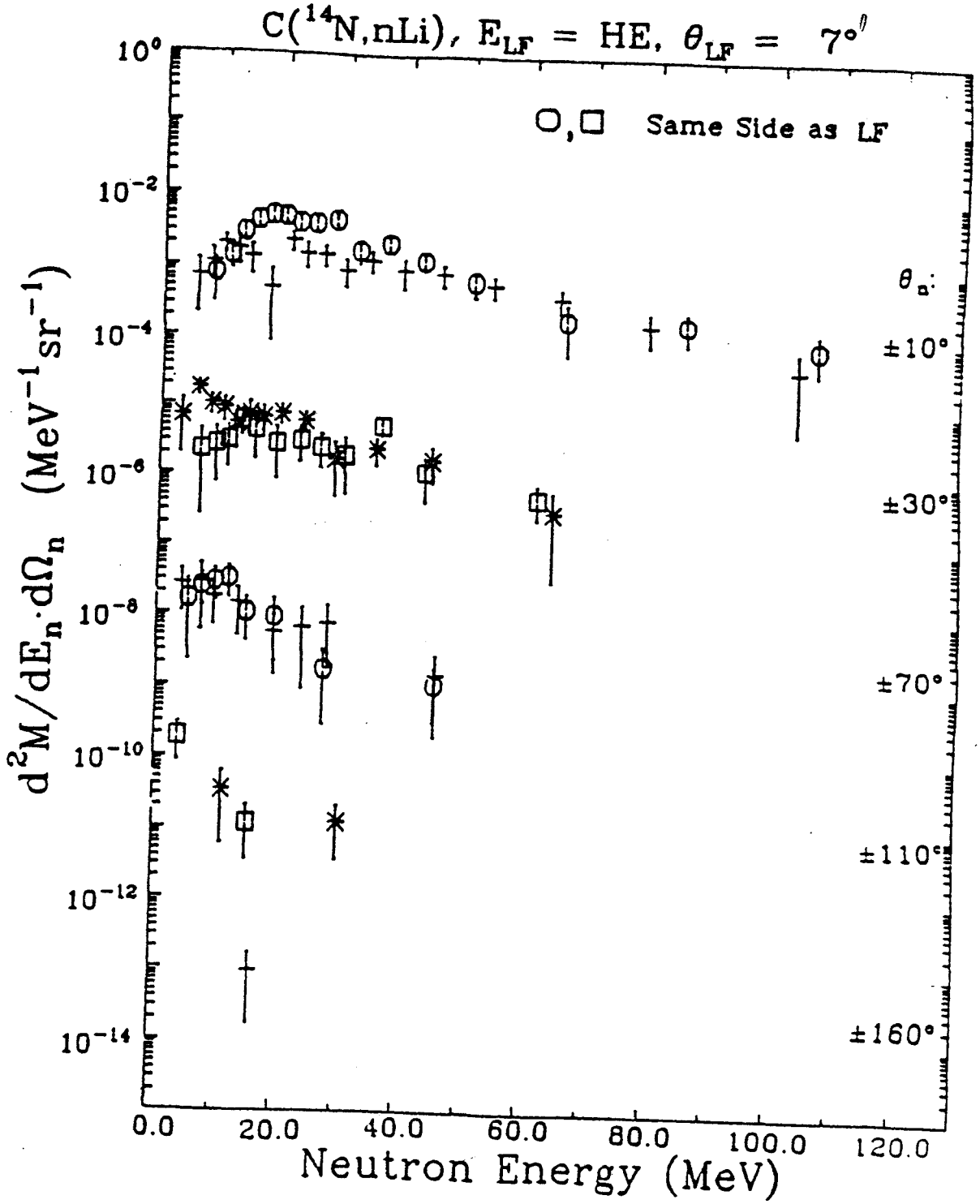

Figure A-27. Neutron spectra for the C target.

Figure A-27. (continued)

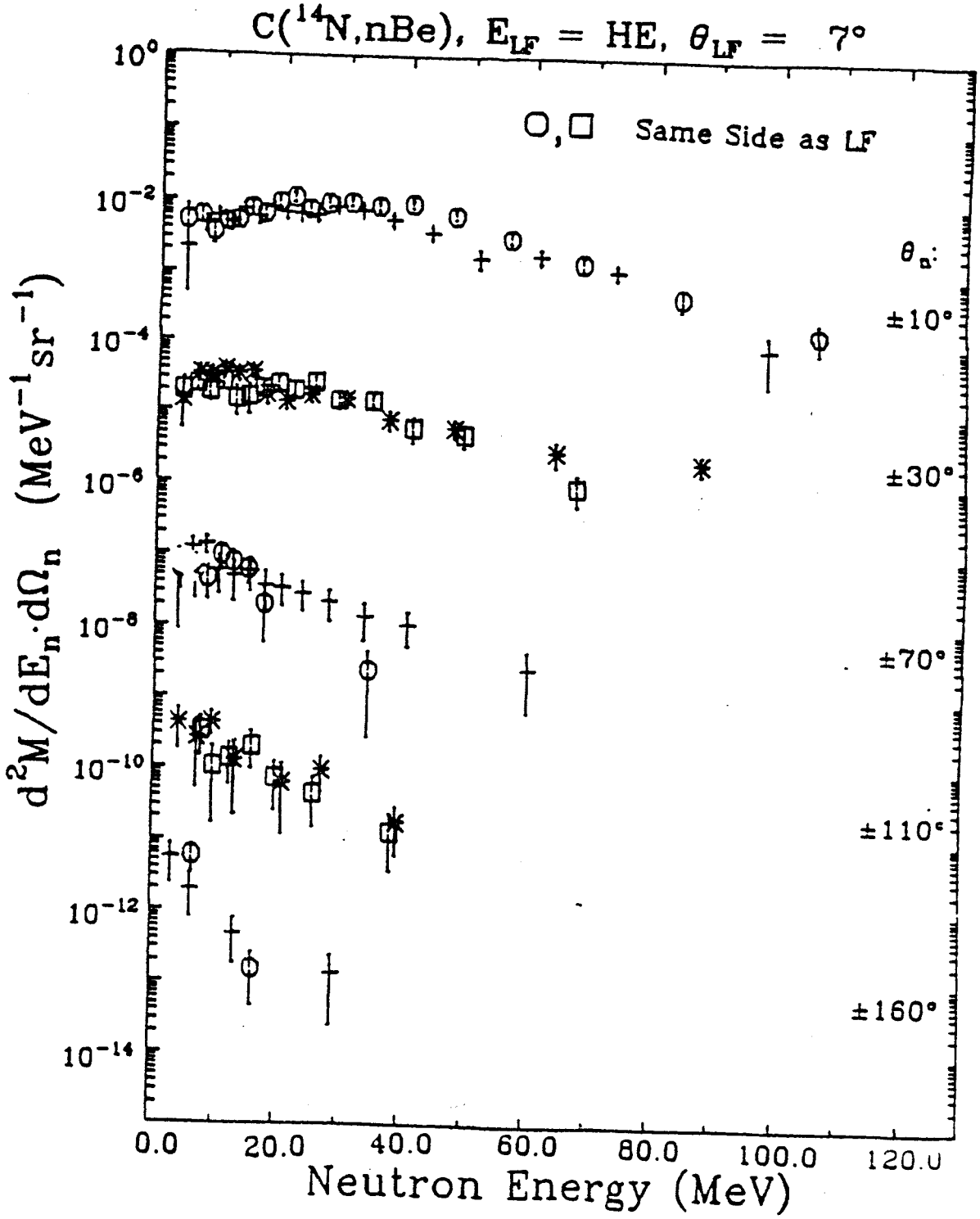

Figure A-27. (continued)

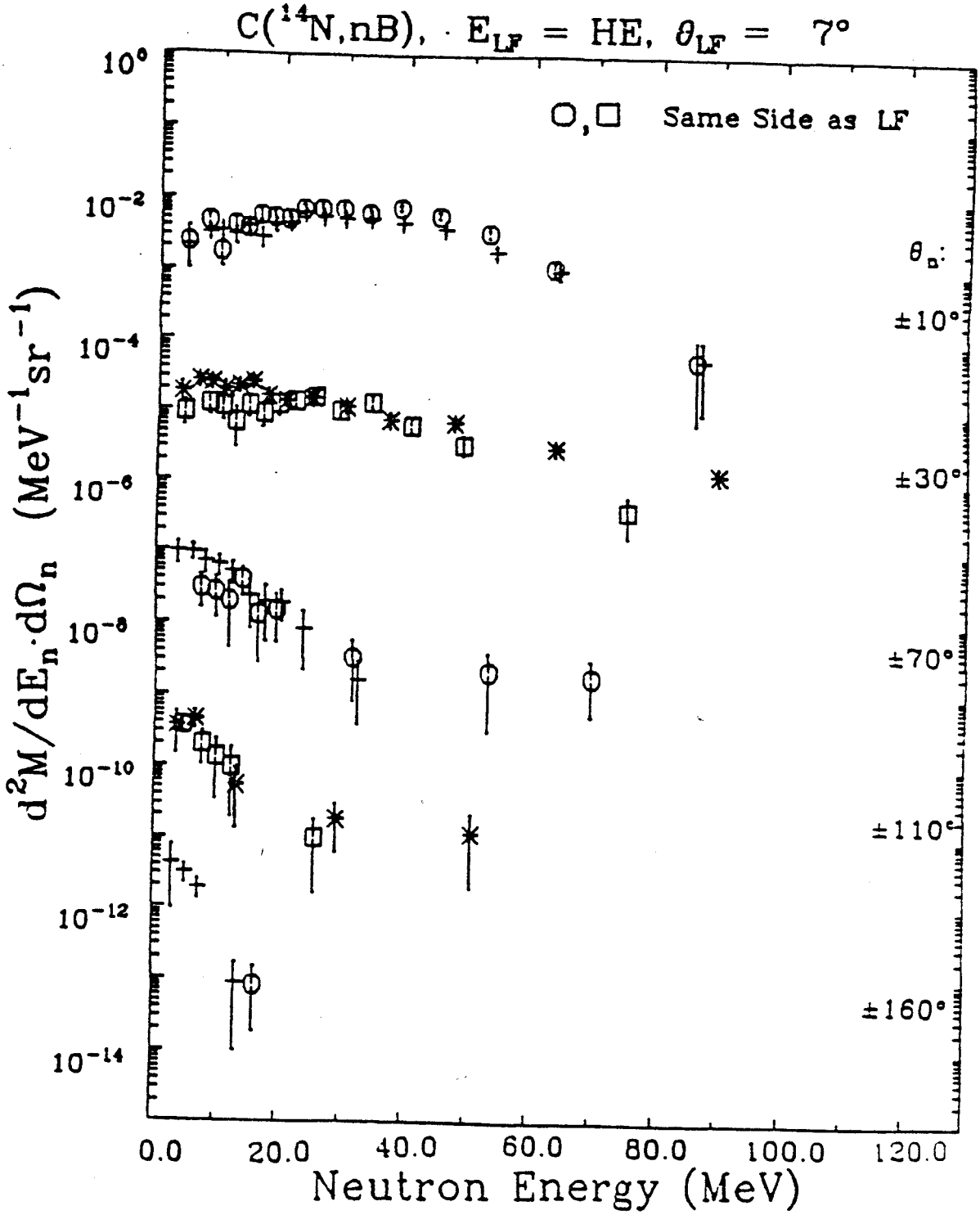

Figure A-27. (continued)

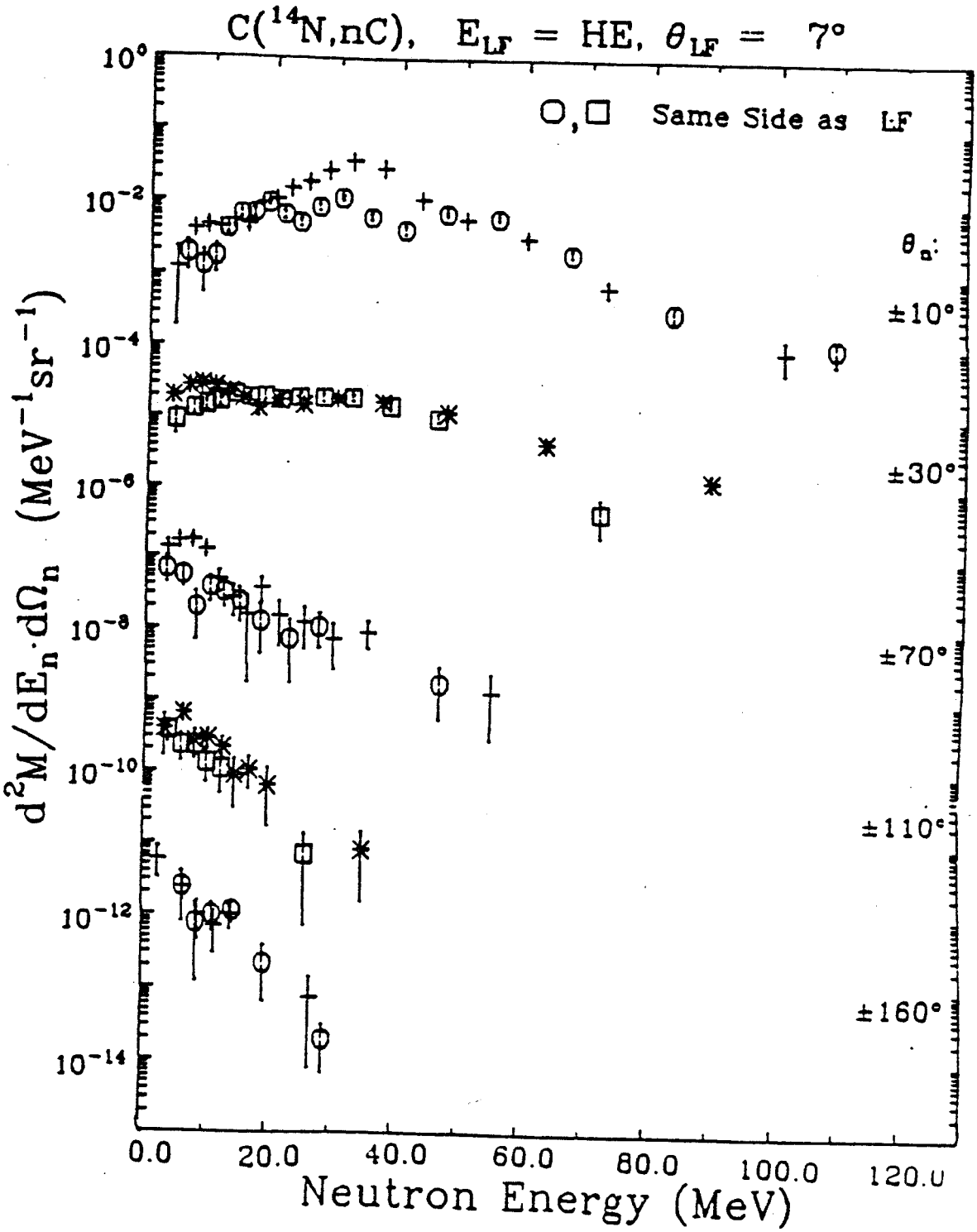

Figure A-27. (continued)

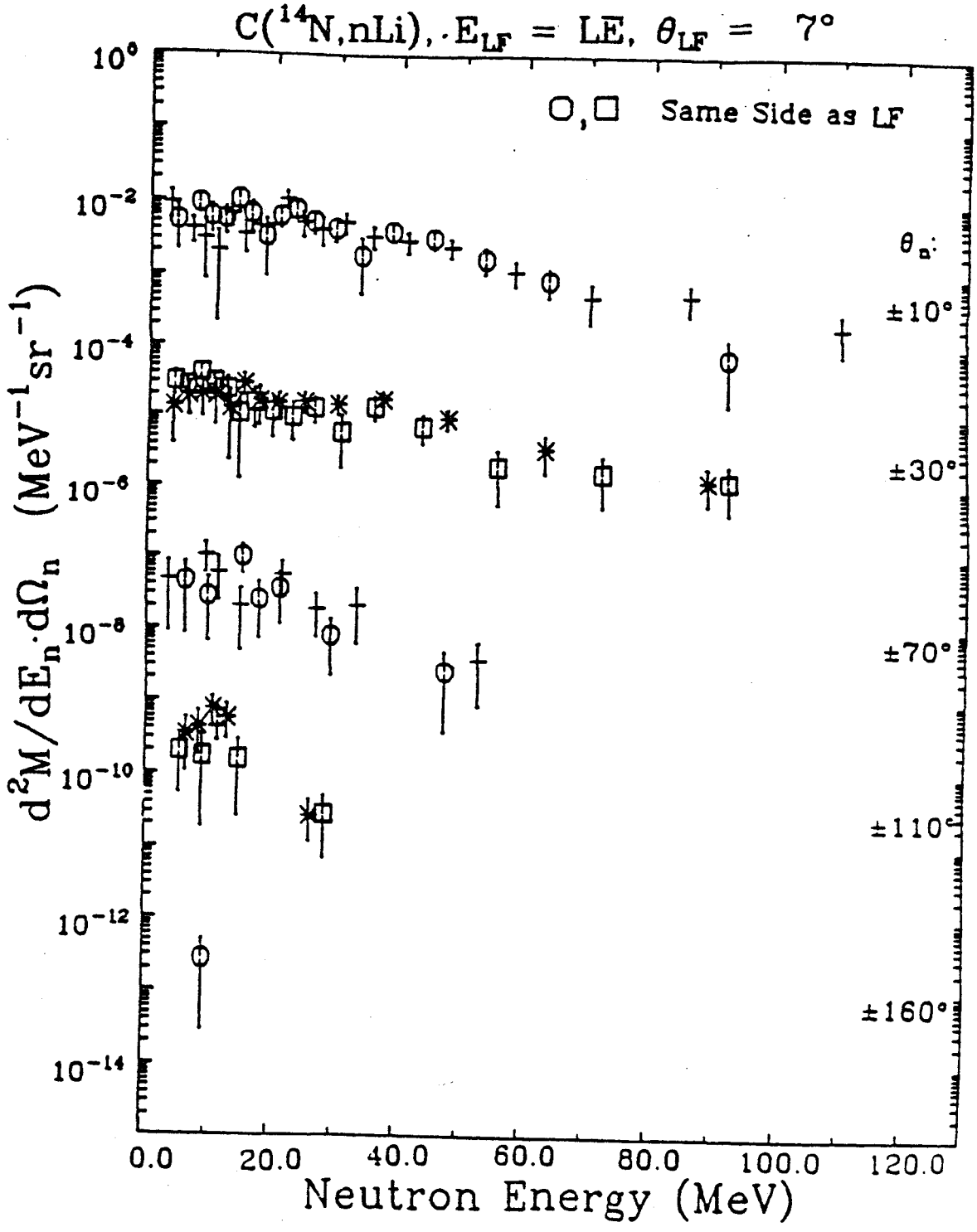

Figure A-27. (continued)

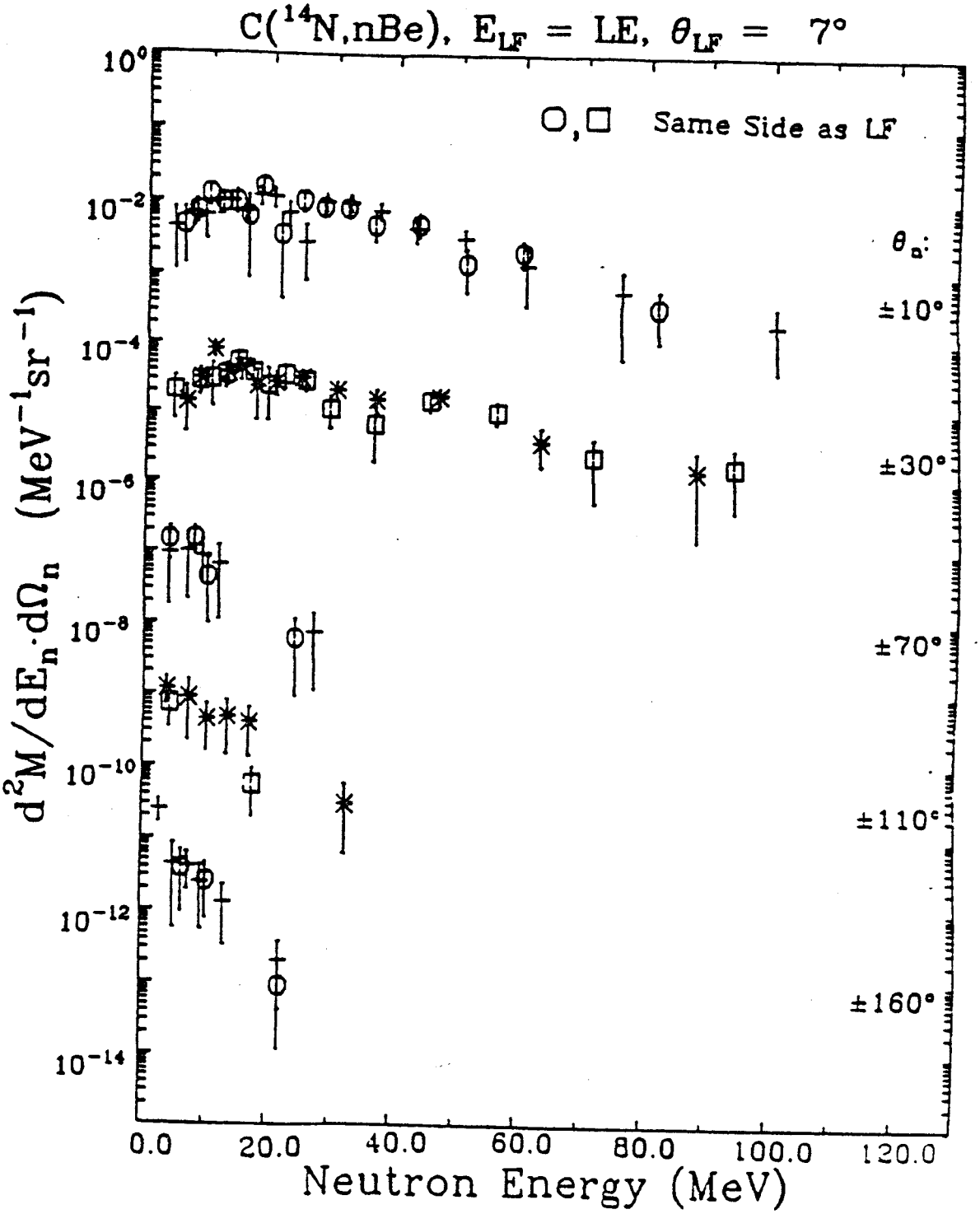

Figure A-27. (continued)

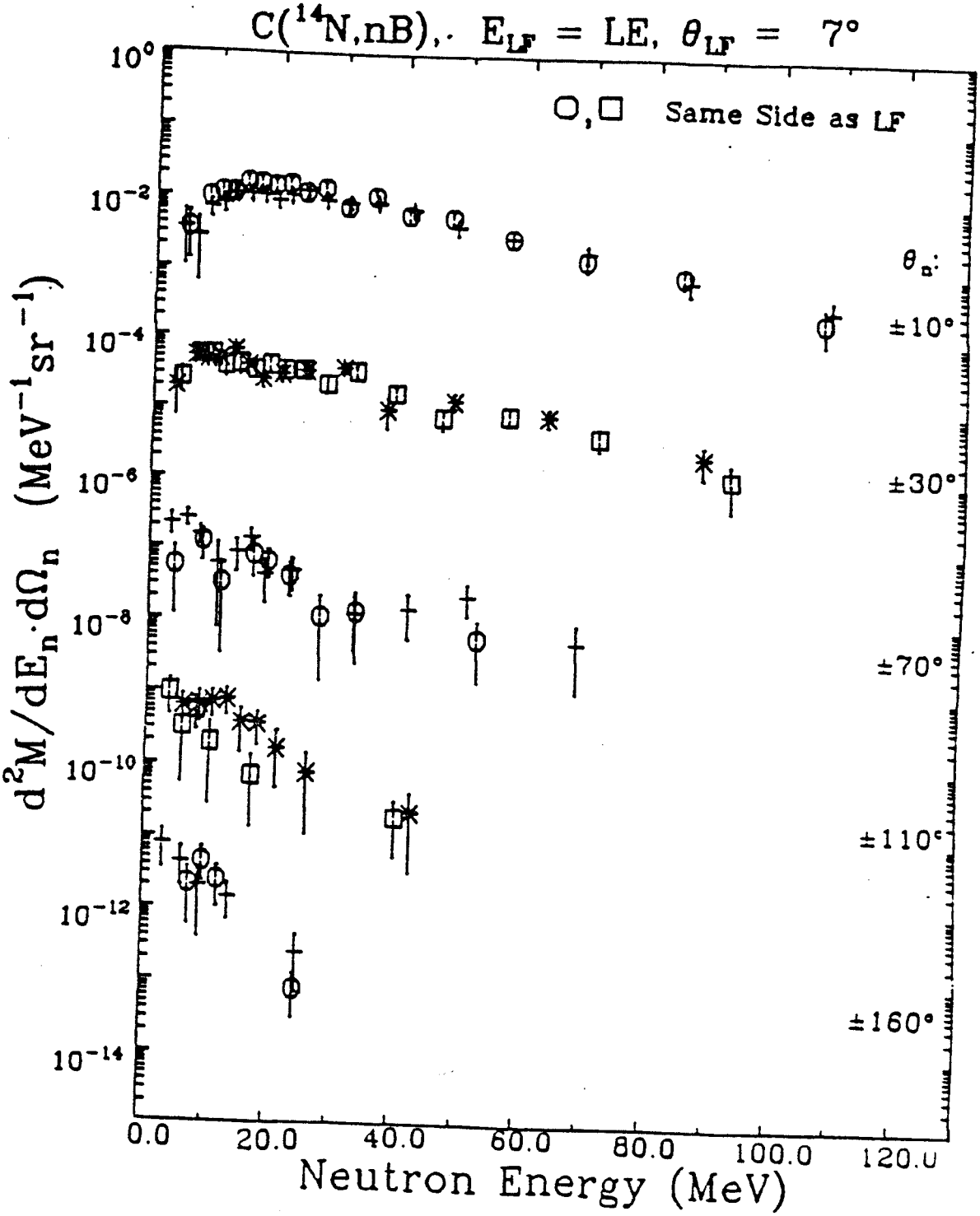

Figure A-27. (continued)

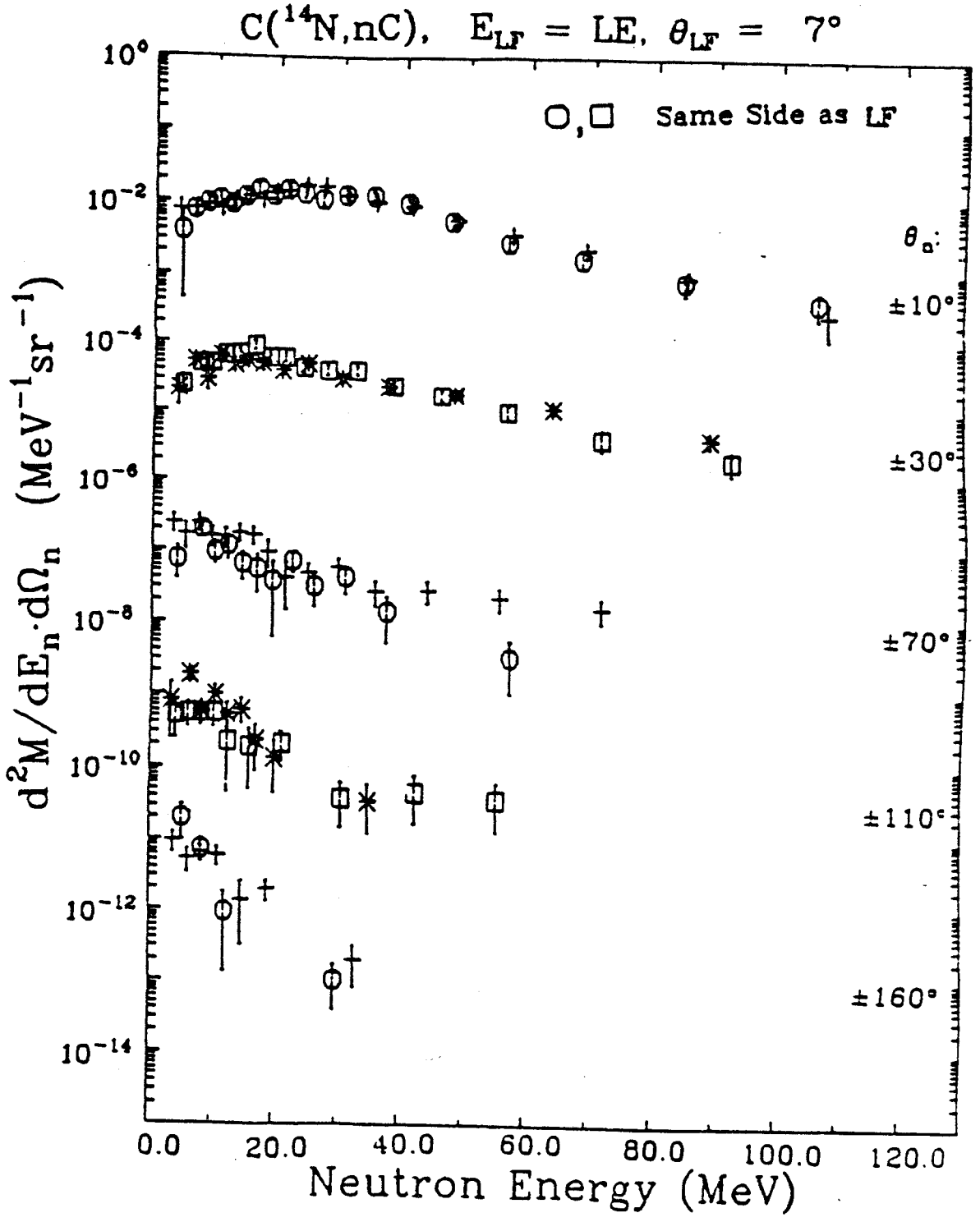

Figure A-27. (continued)

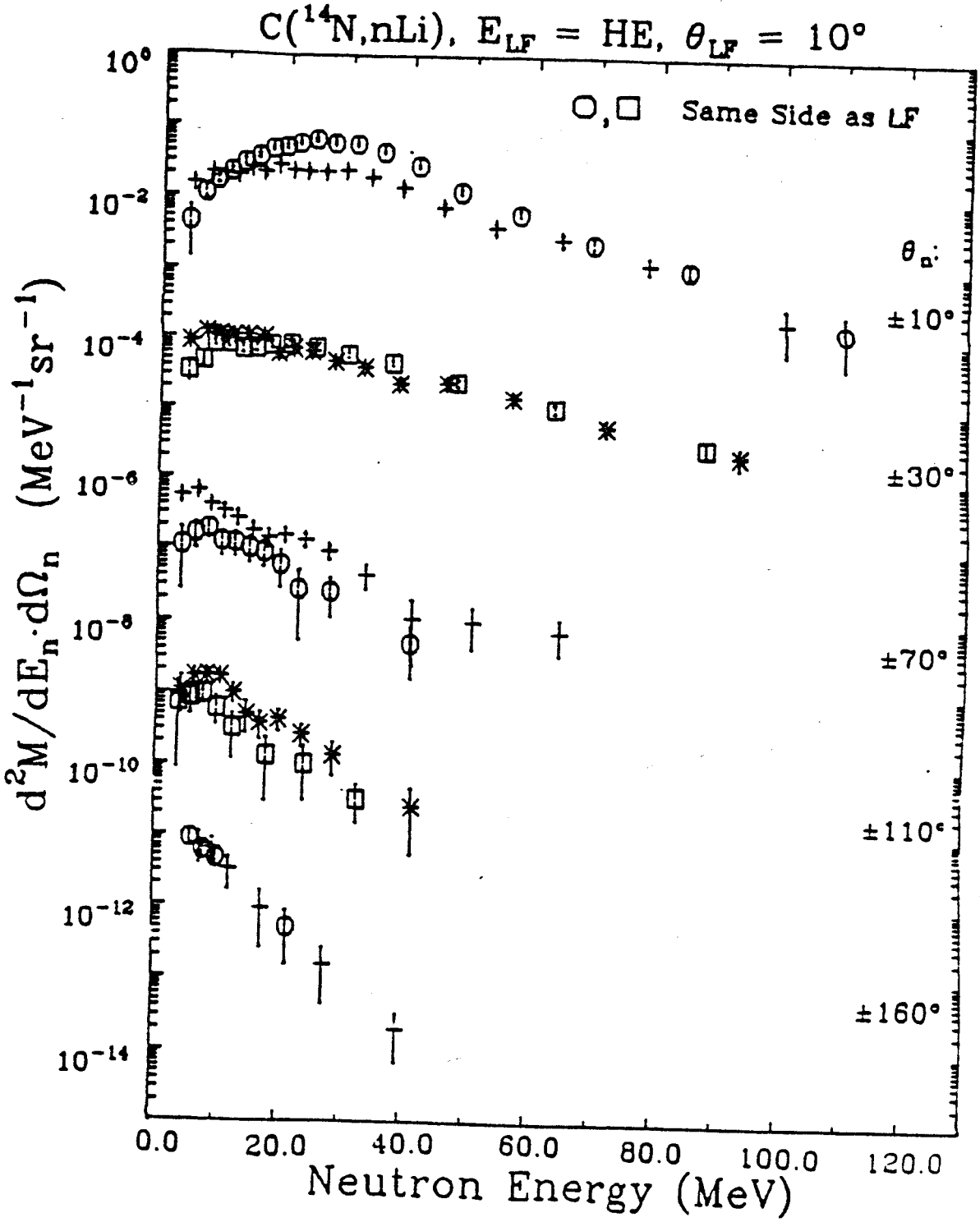

Figure A-27. (continued)

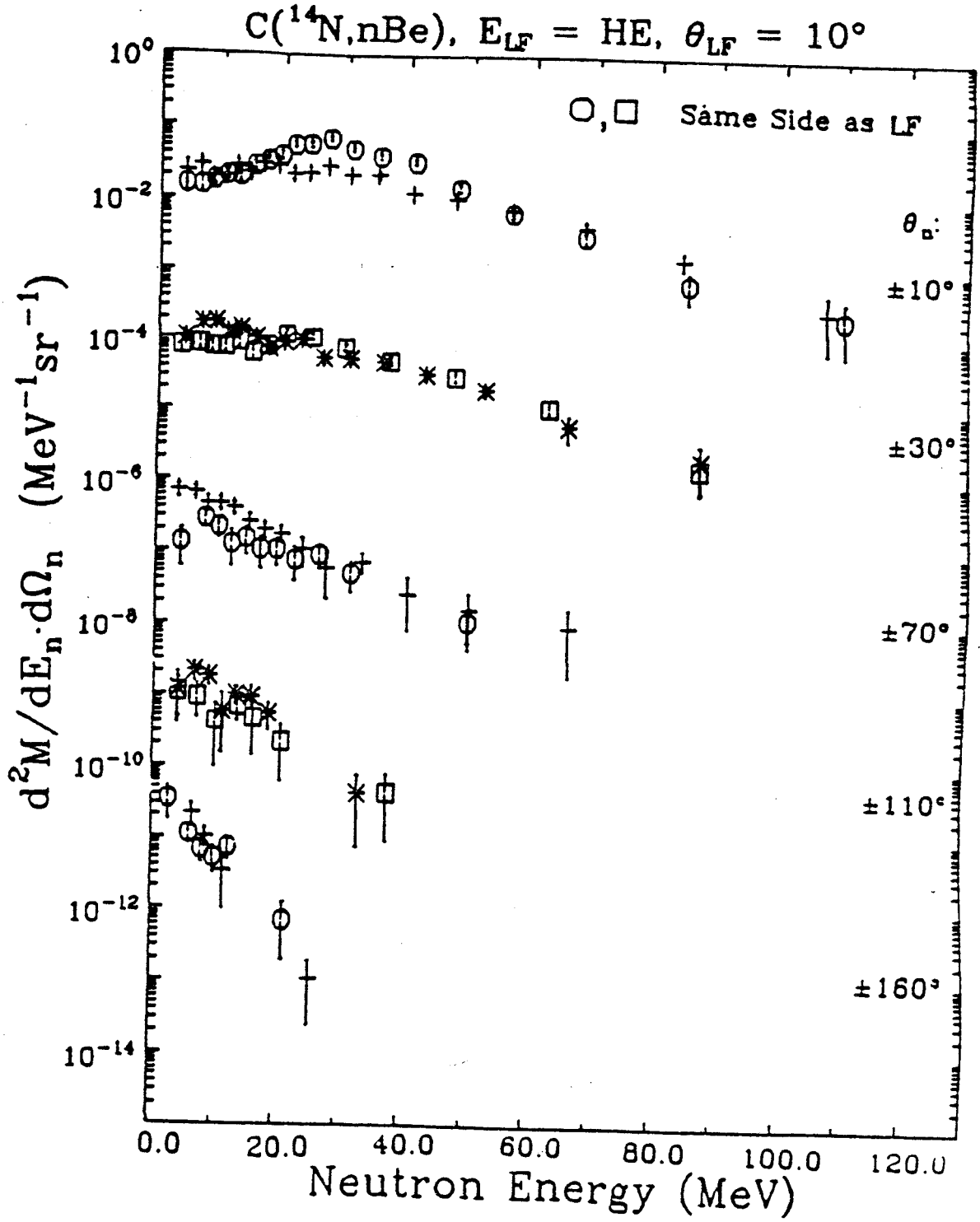

Figure A-27. (continued)

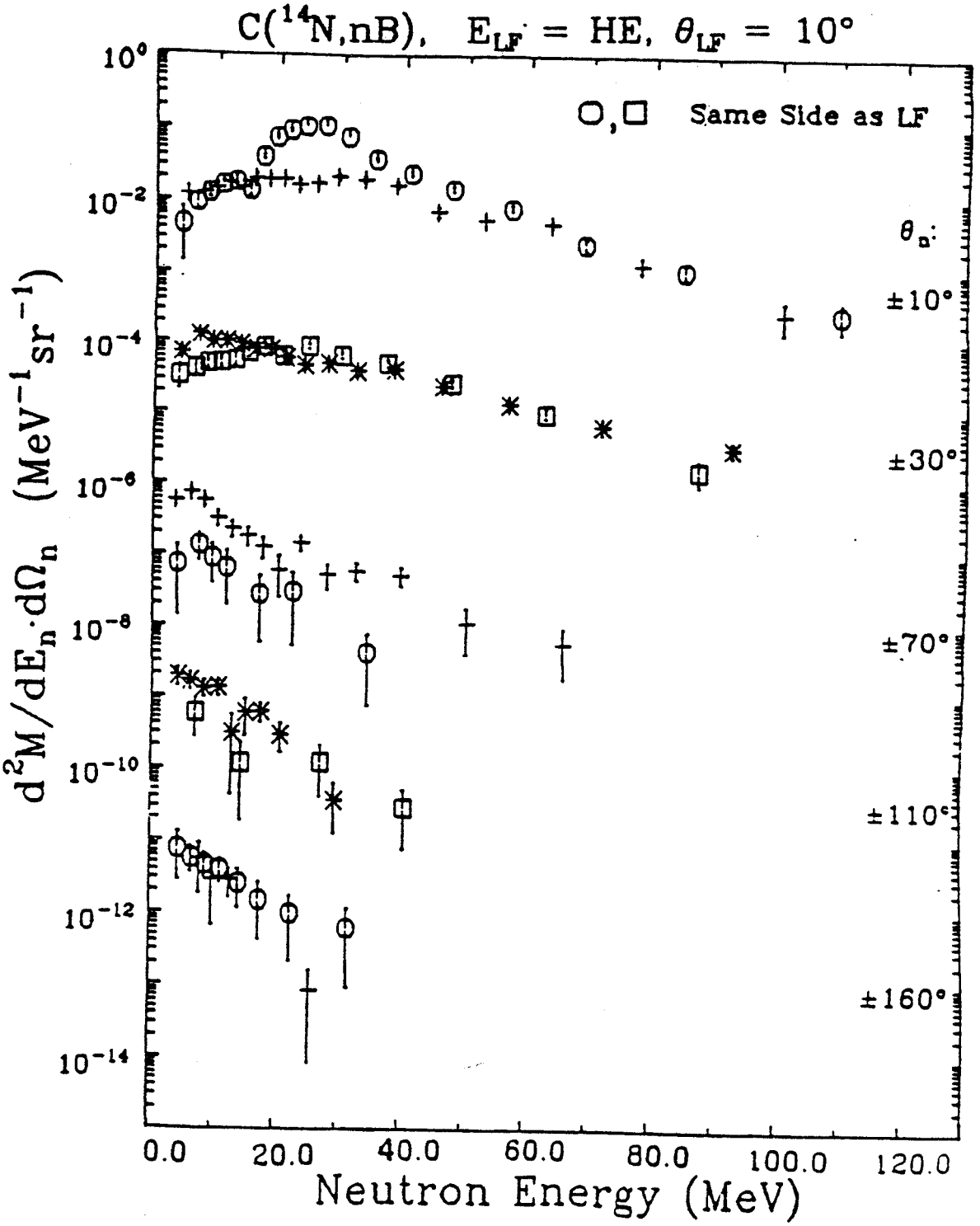

Figure A-27. (continued)

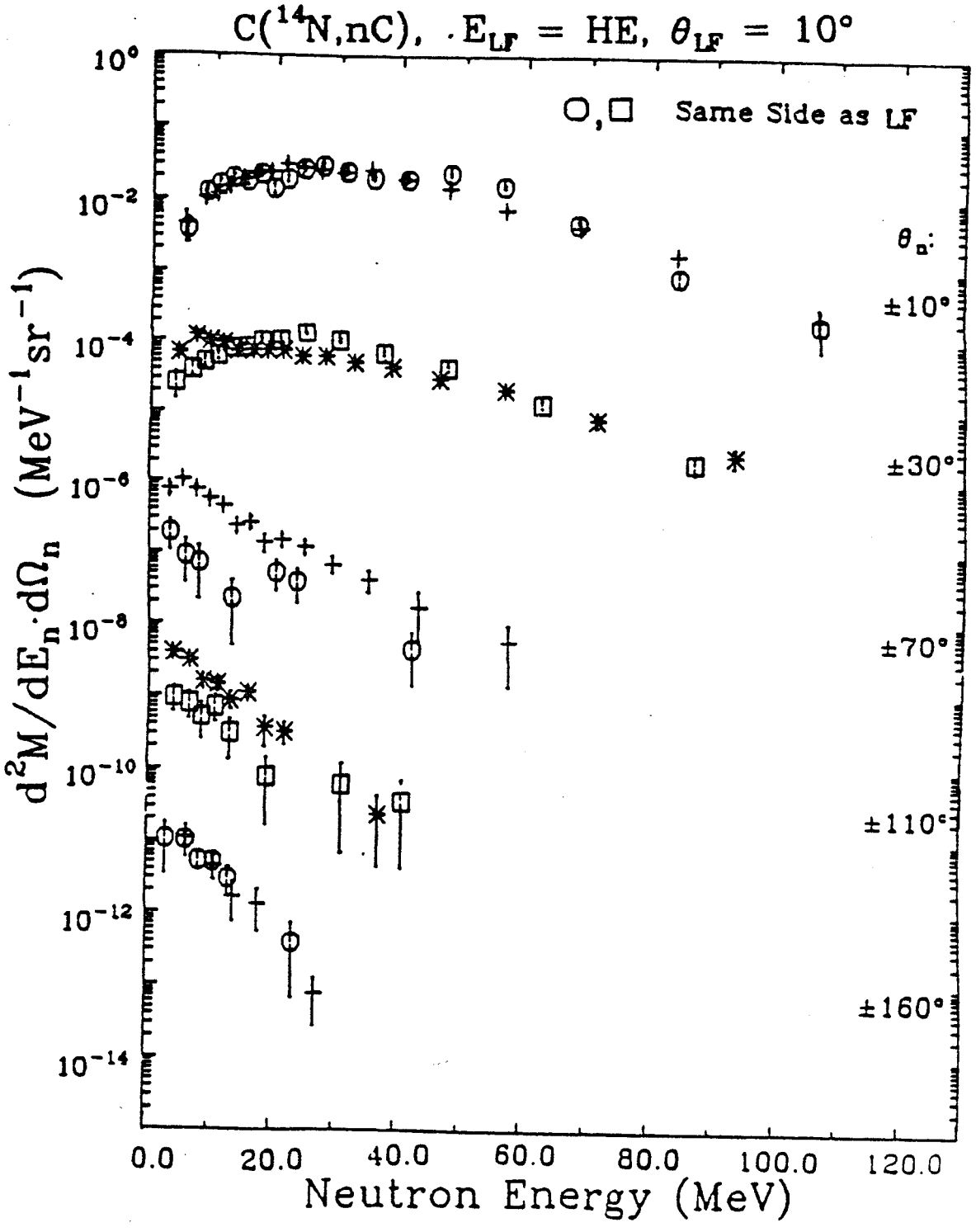

Figure A-27. (continued)

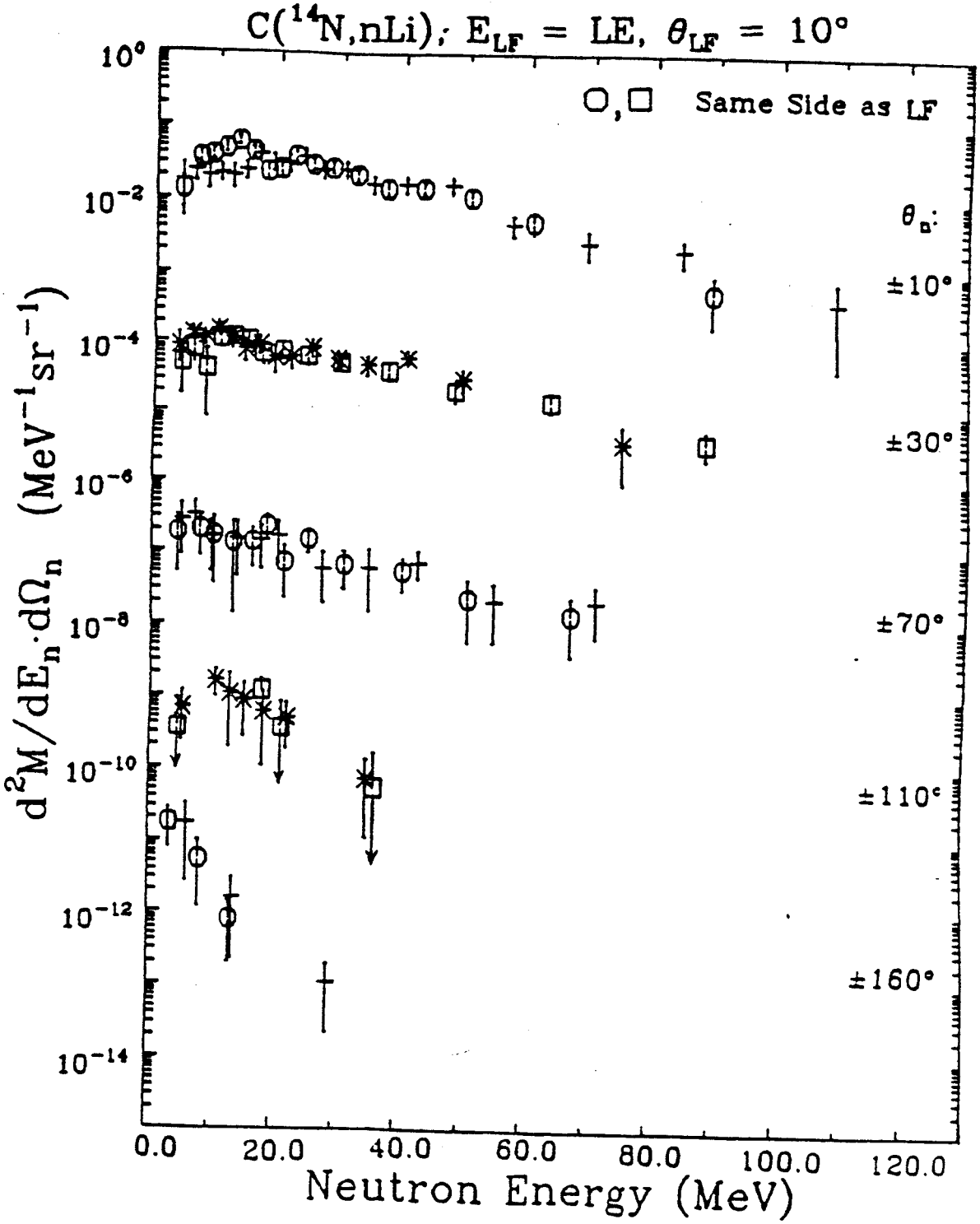

Figure A-27. (continued)

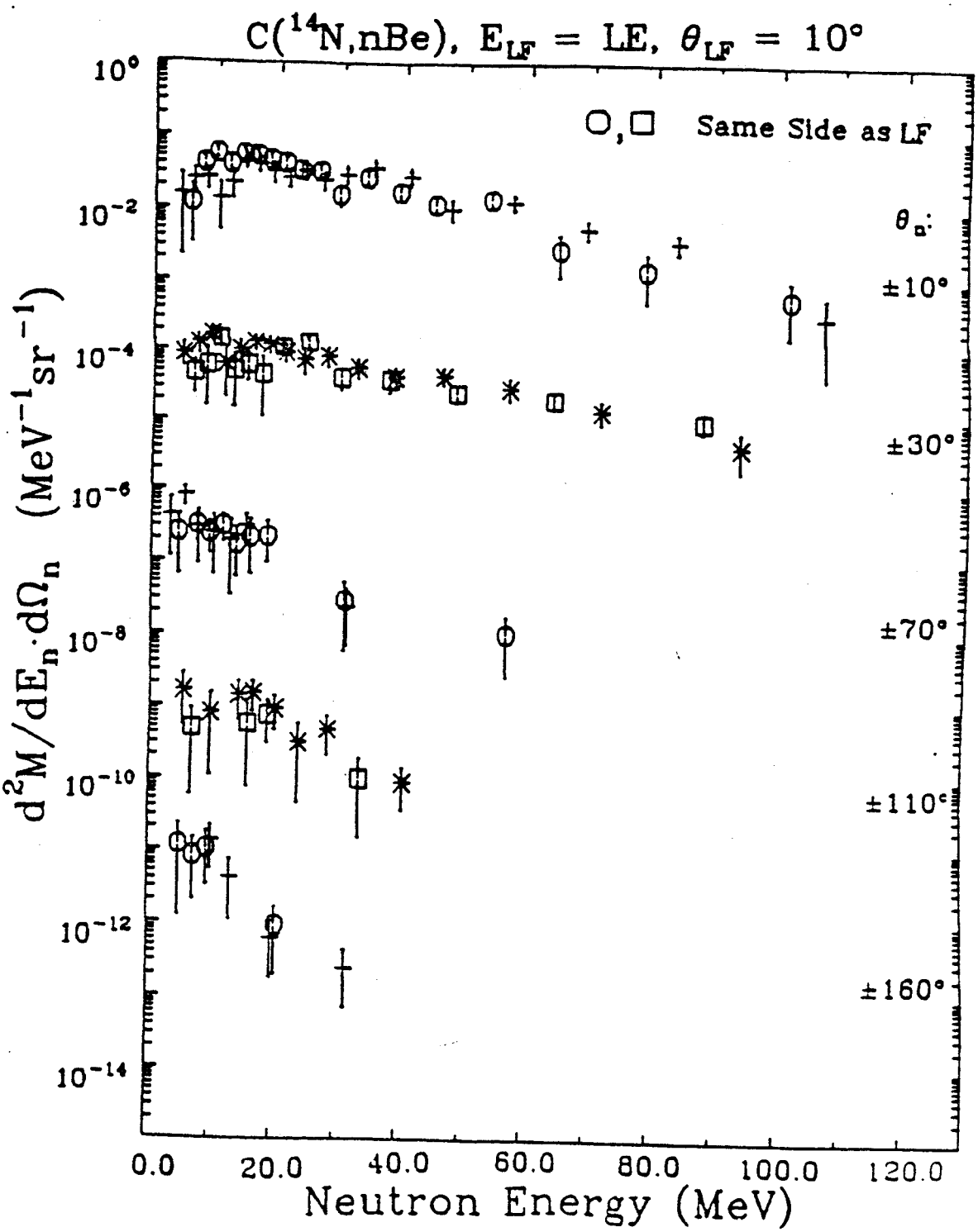

Figure A-27. (continued)

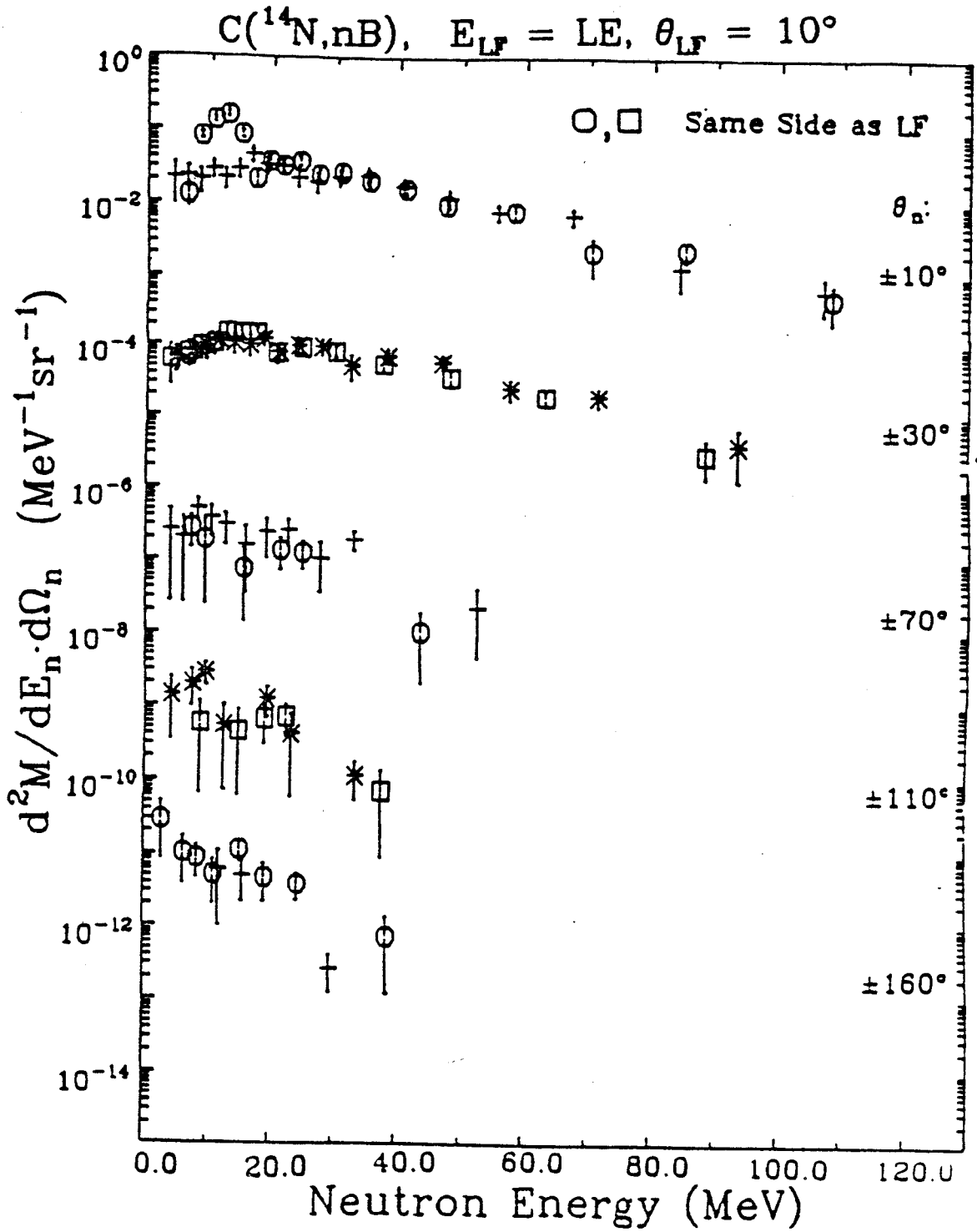

Figure A-27. (continued)

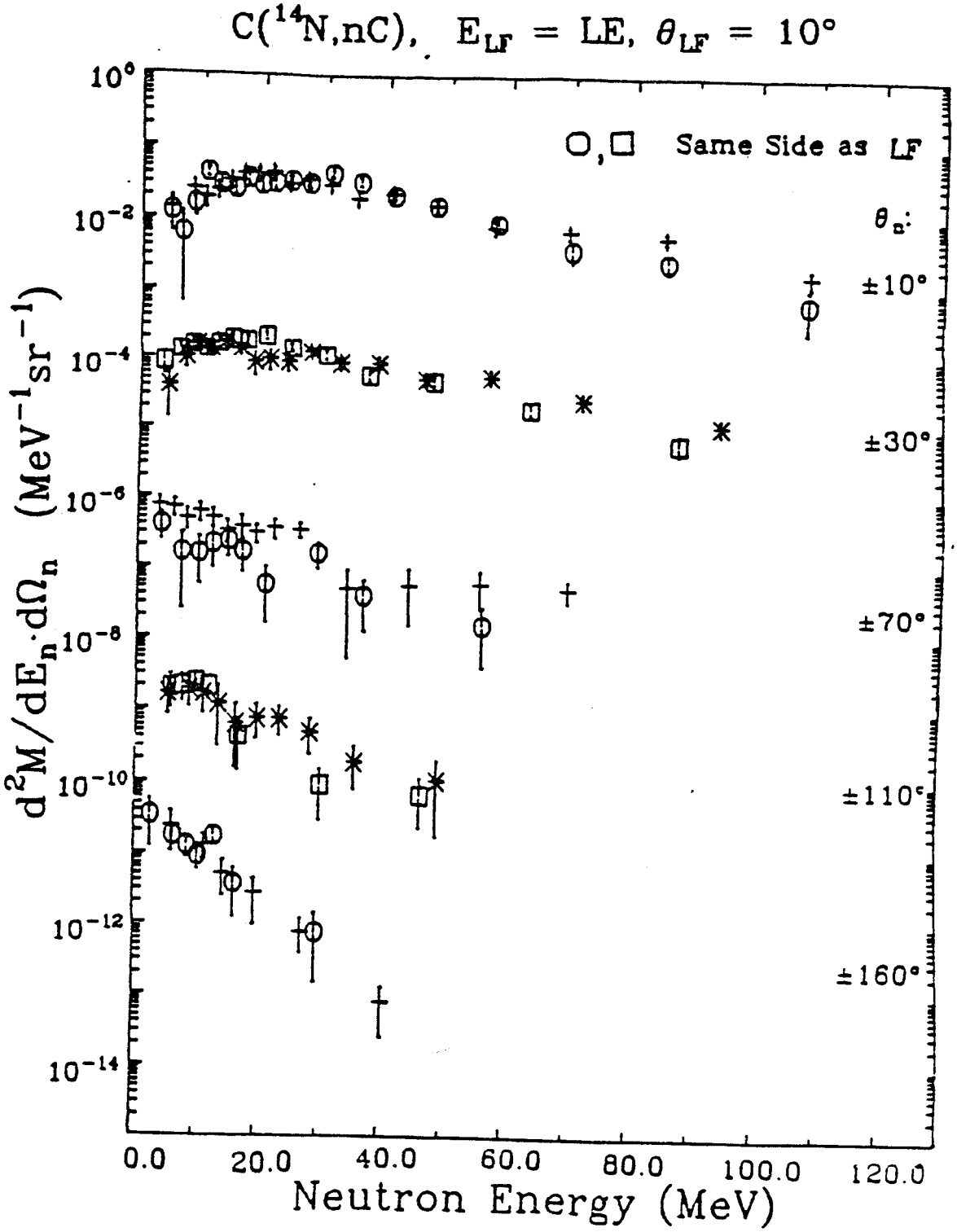

Figure A-27. (continued)

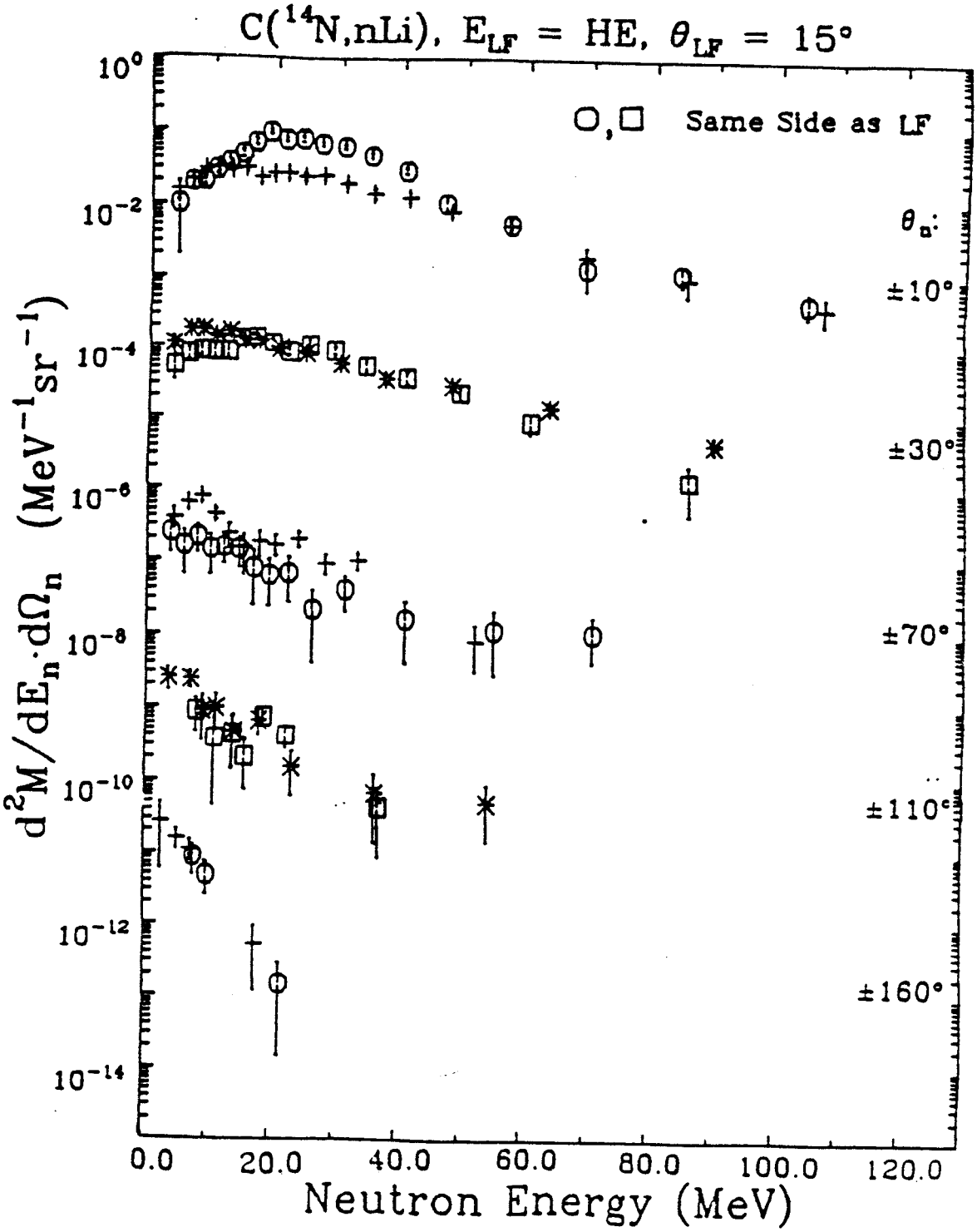

Figure A-27. (continued)

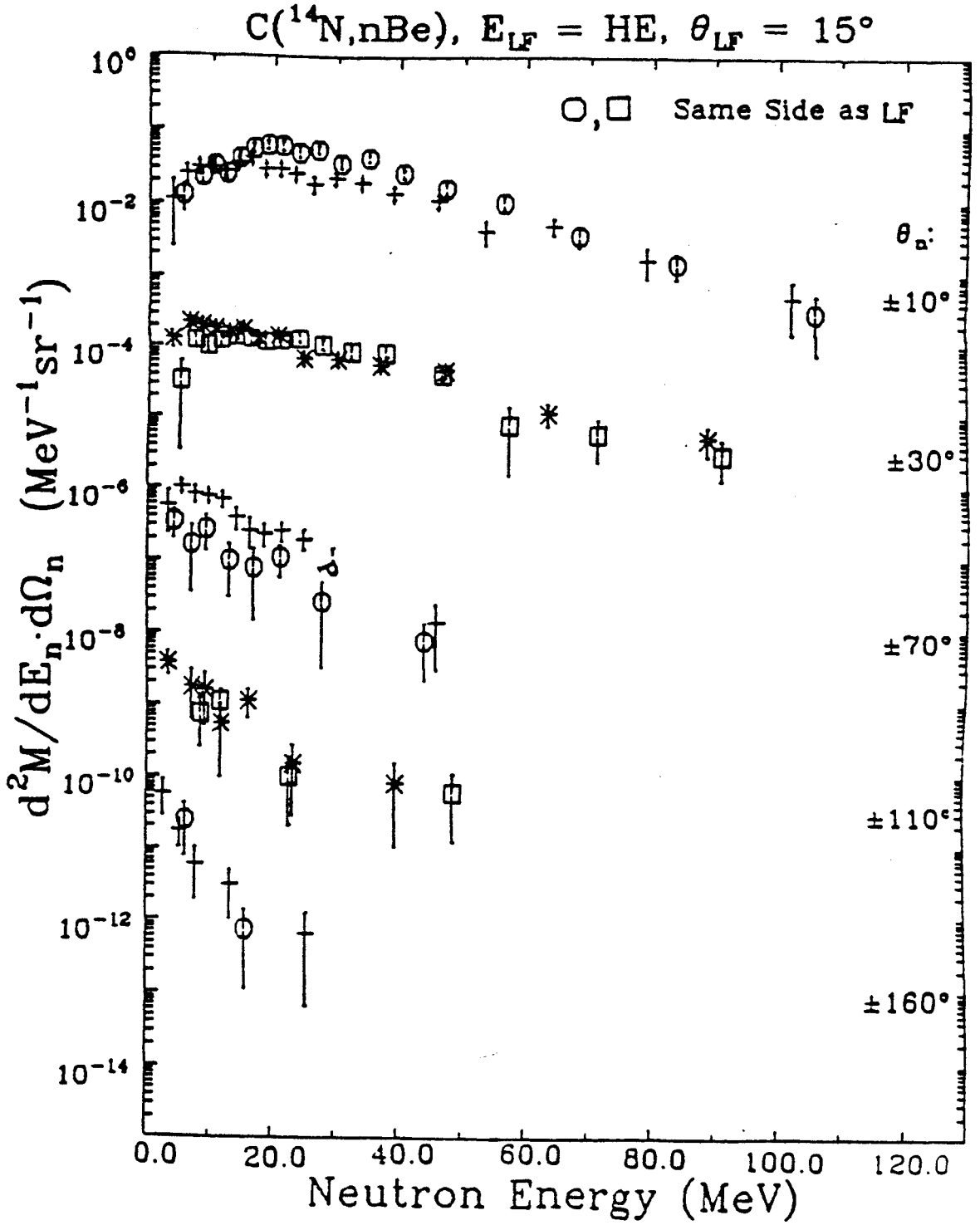

Figure A-27. (continued)

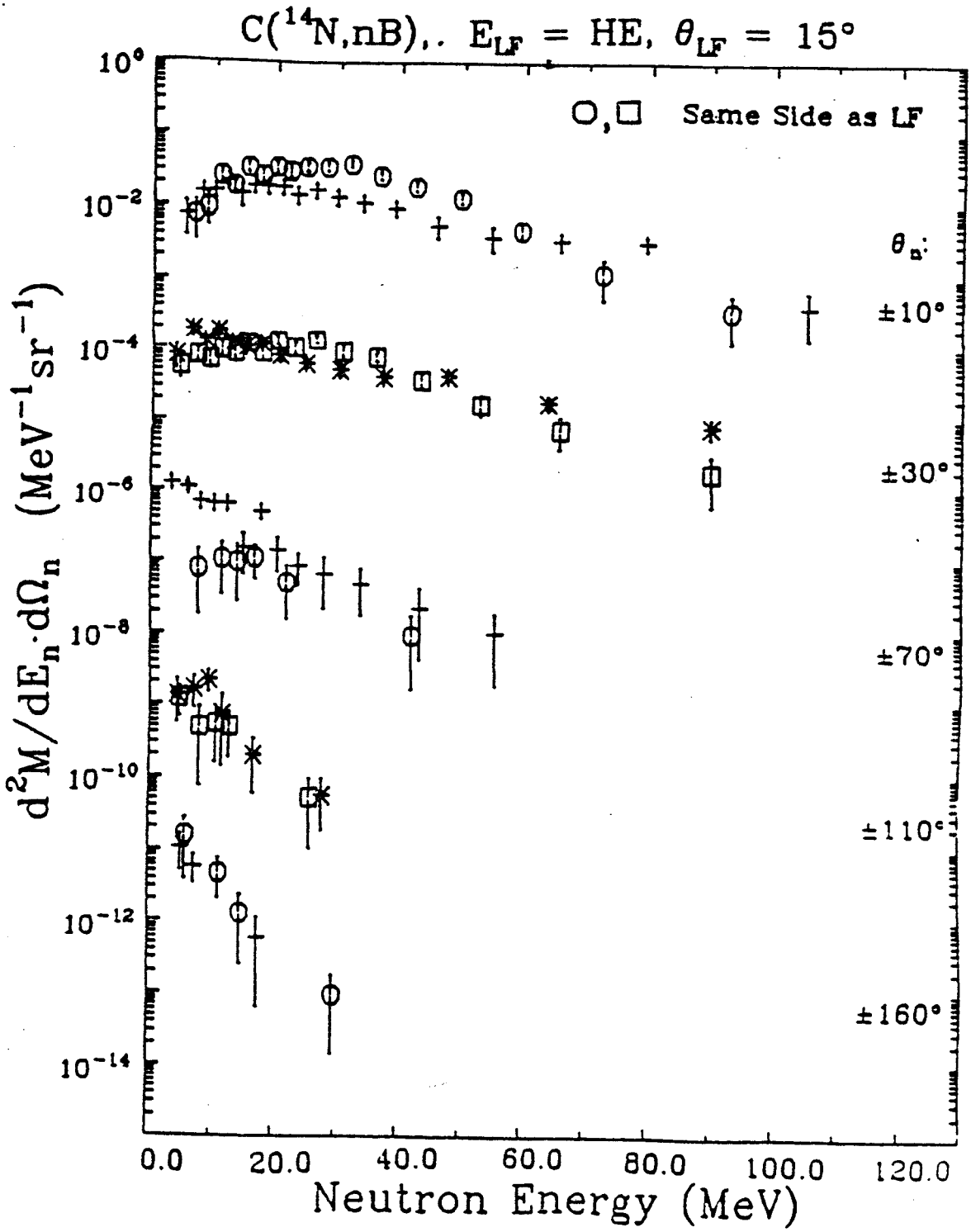

Figure A-27. (continued)

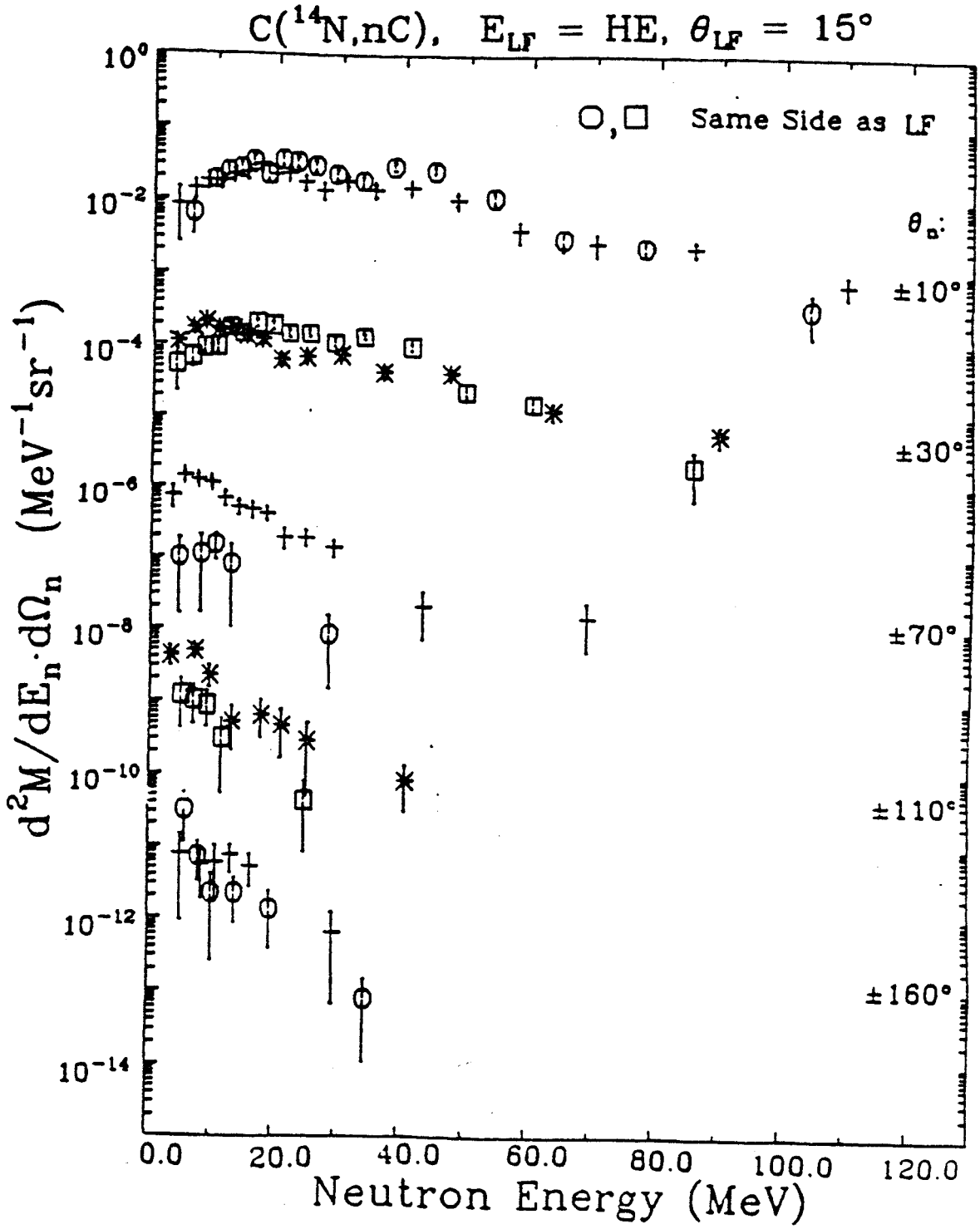

Figure A-27. (continued)

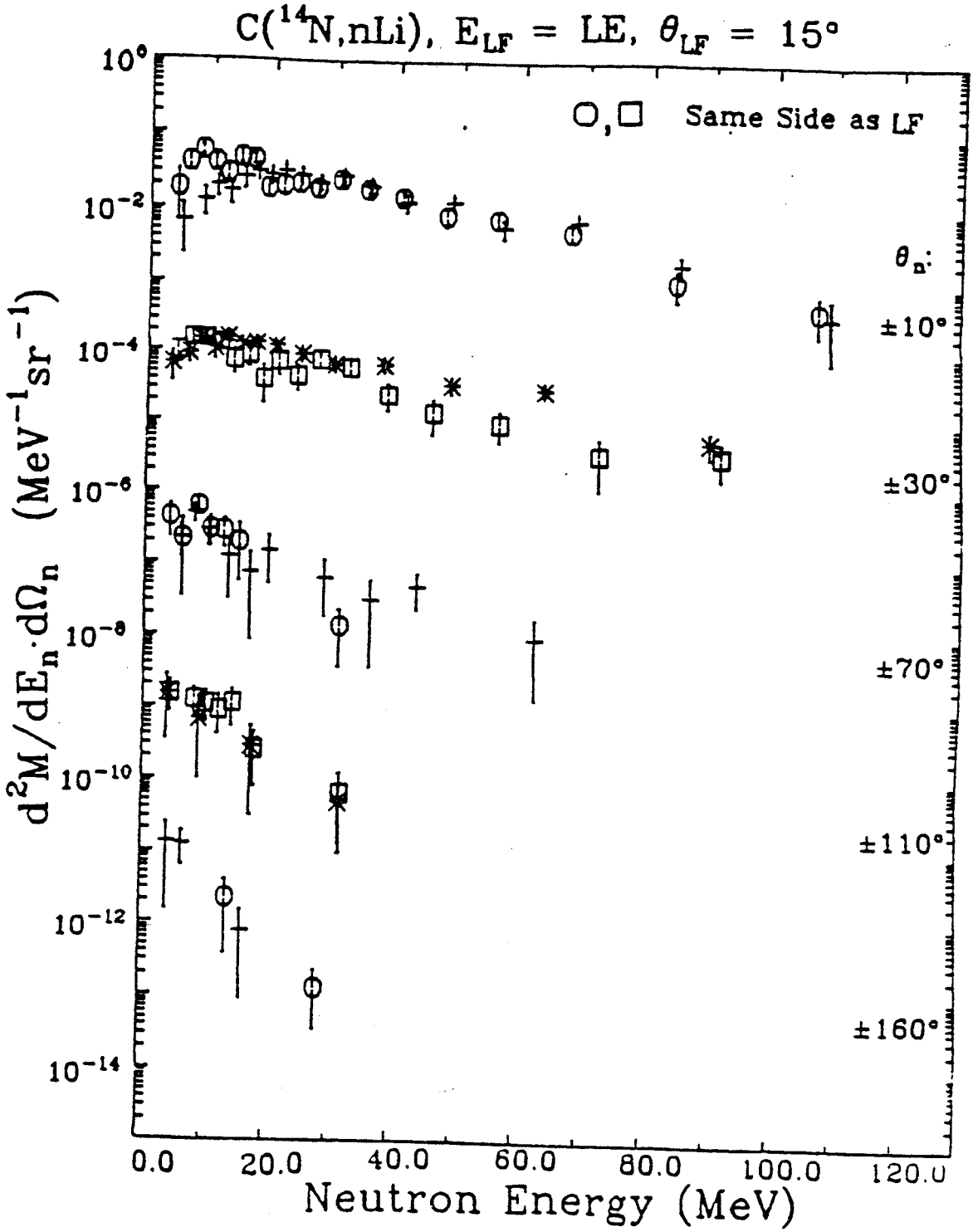

Figure A-27. (continued)

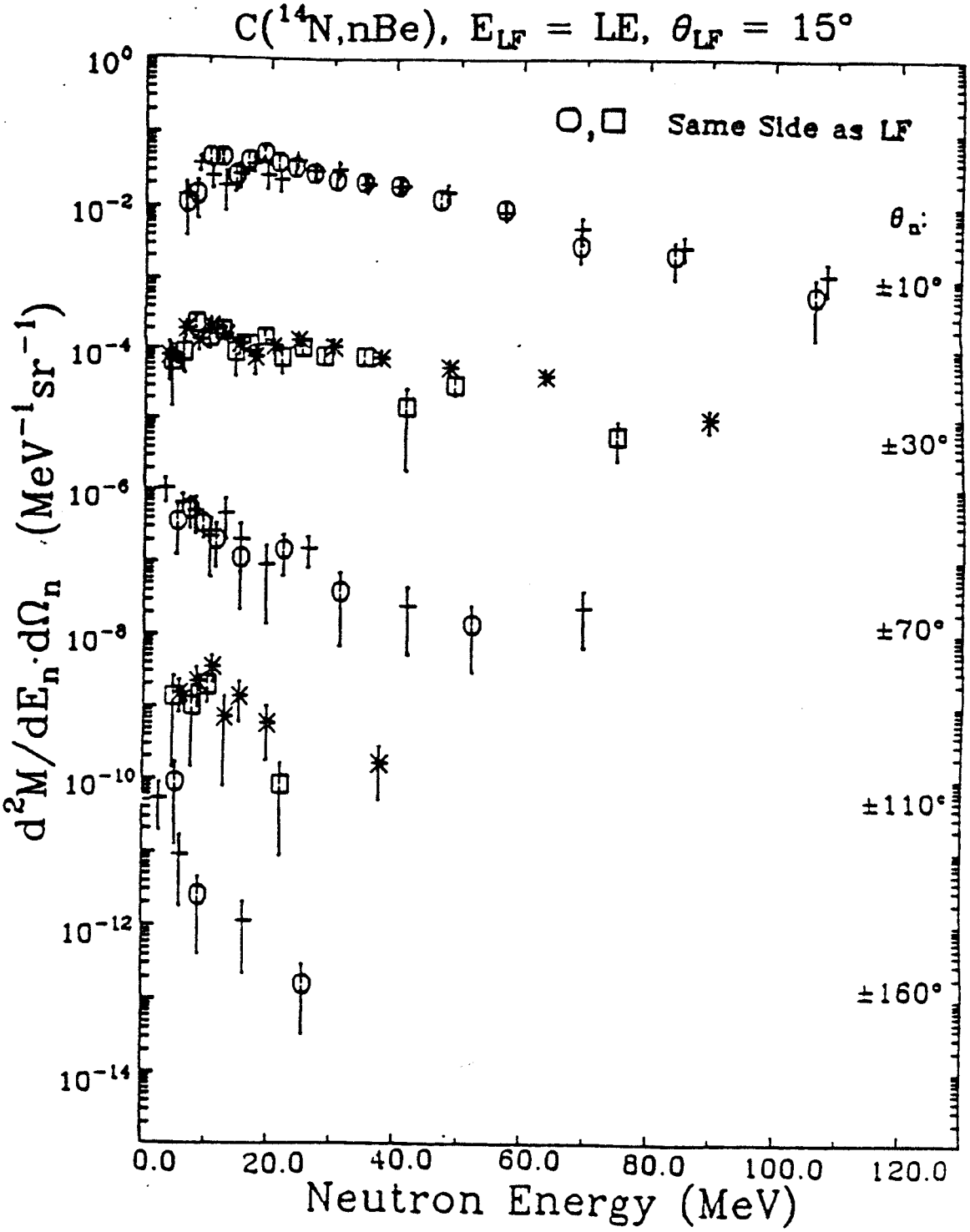

Figure A-27. (continued)

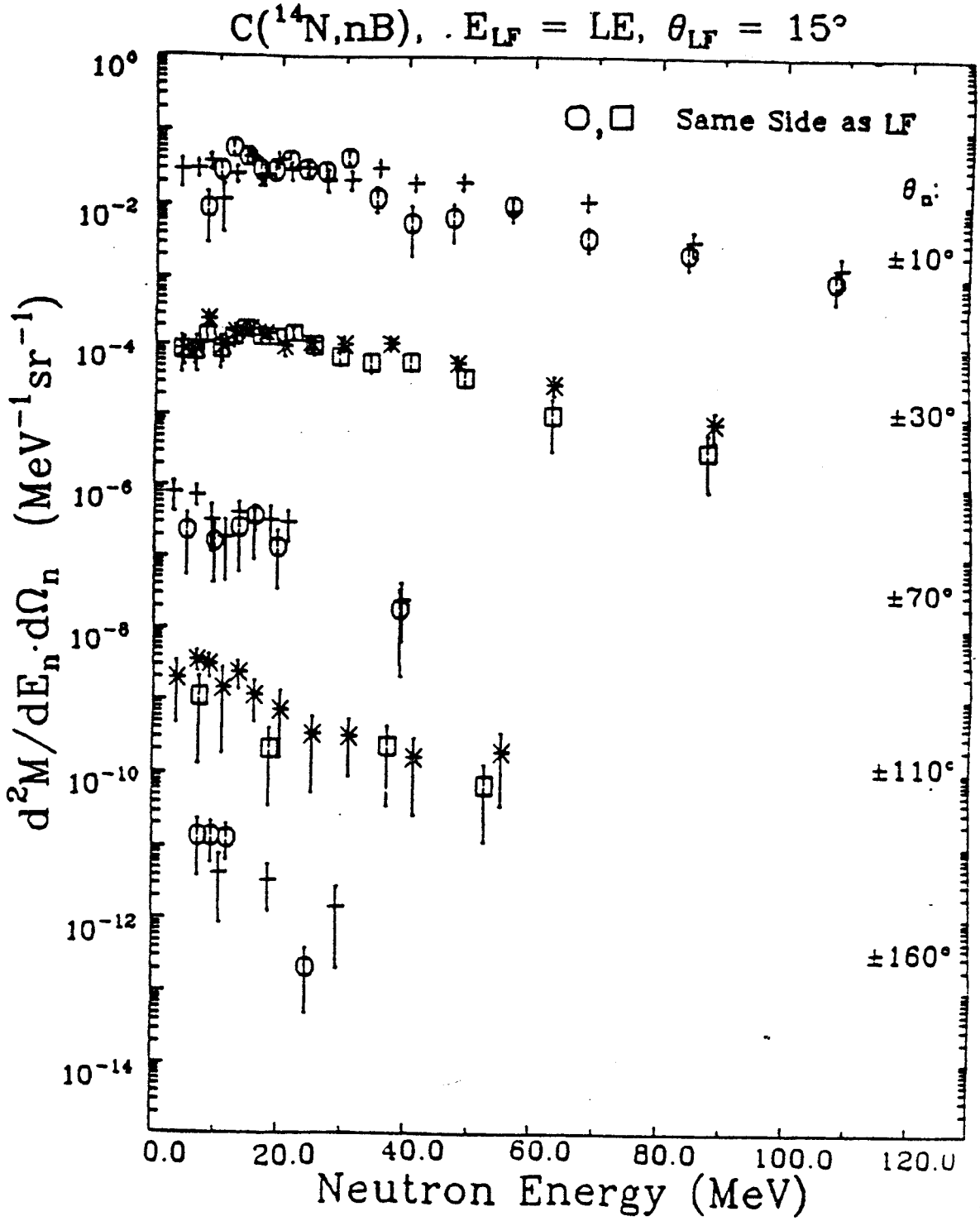

Figure A-27. (continued)

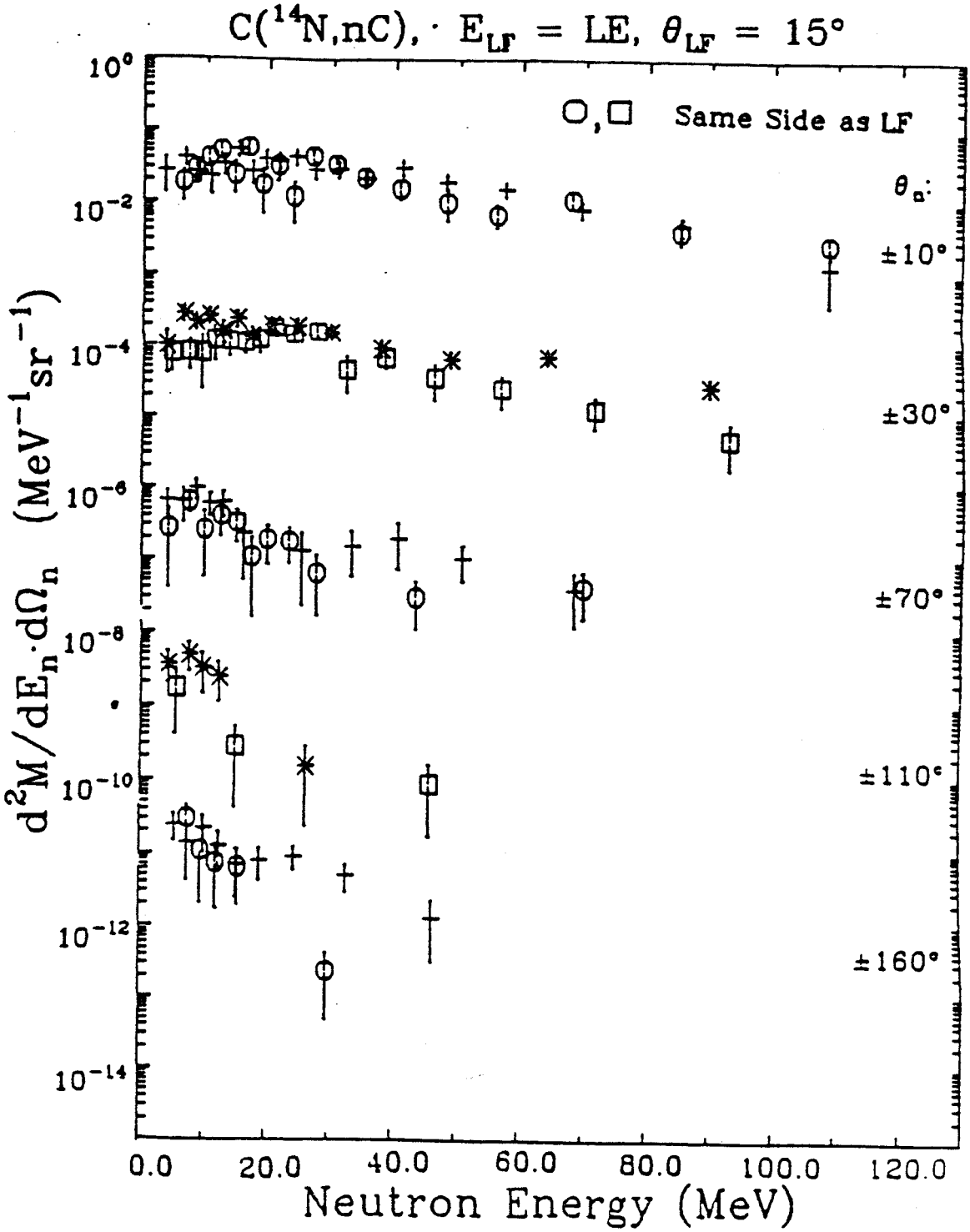

Figure A-27. (continued)

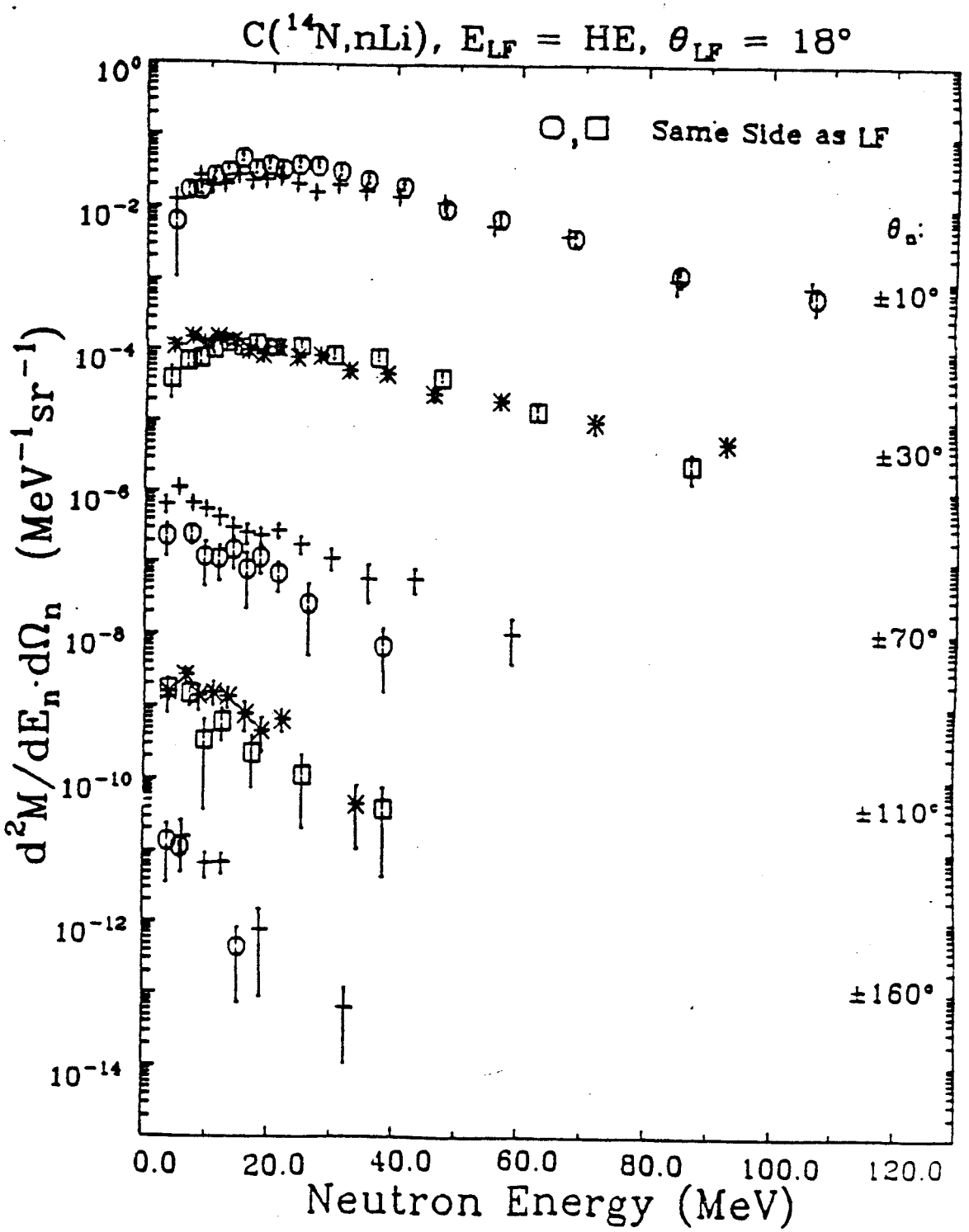

Figure A-27. (continued)

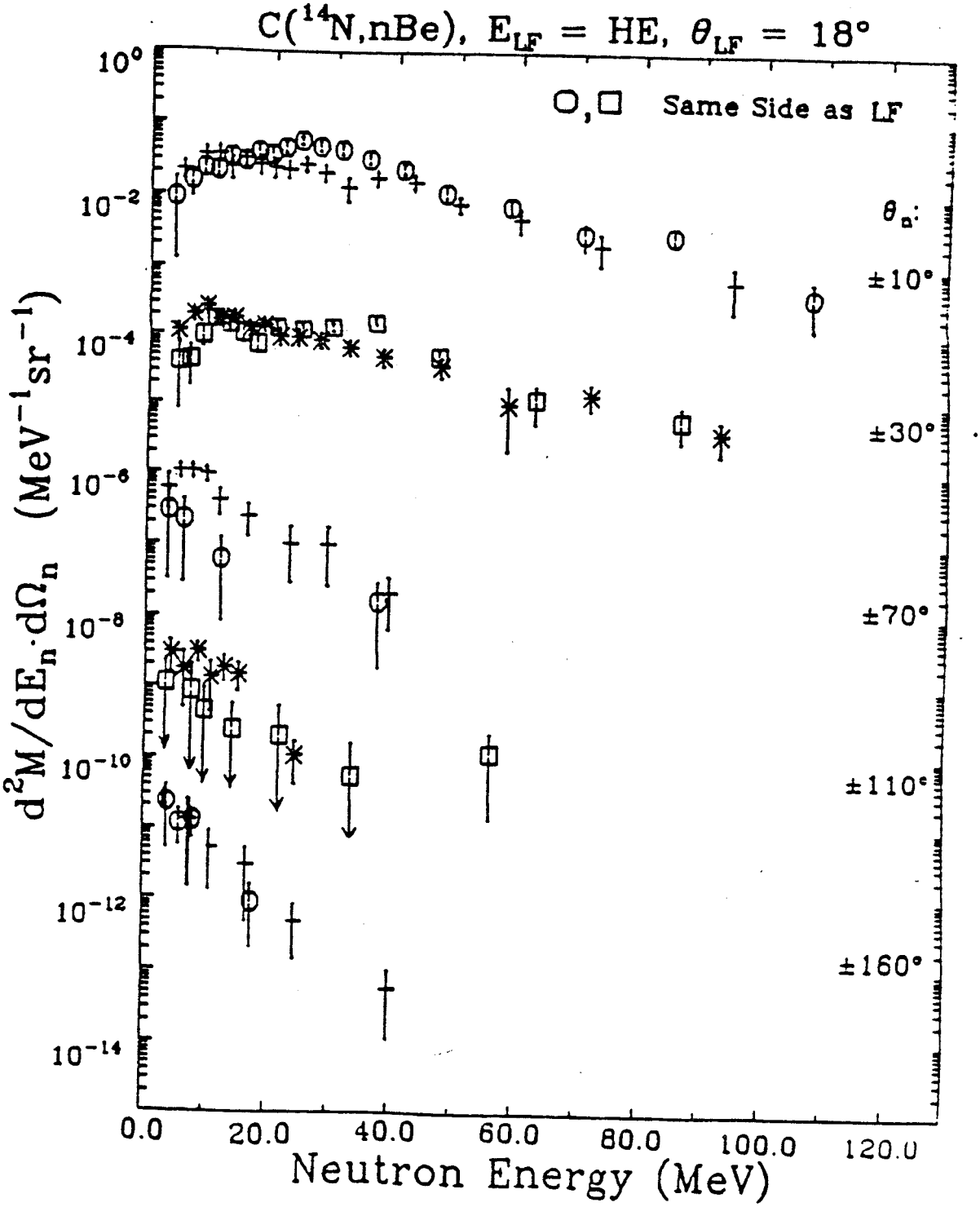

Figure A-27. (continued)

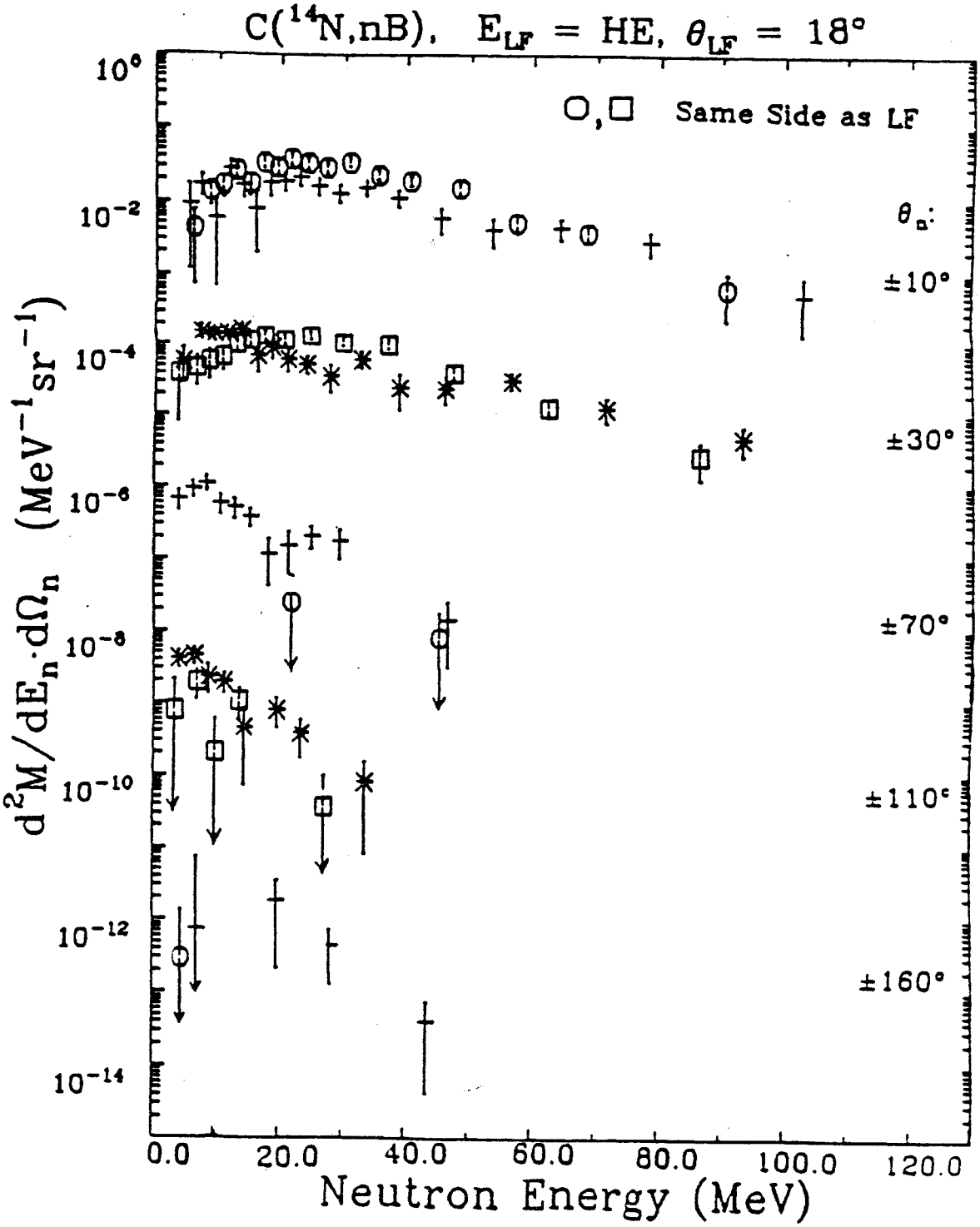

Figure A-27. (continued)

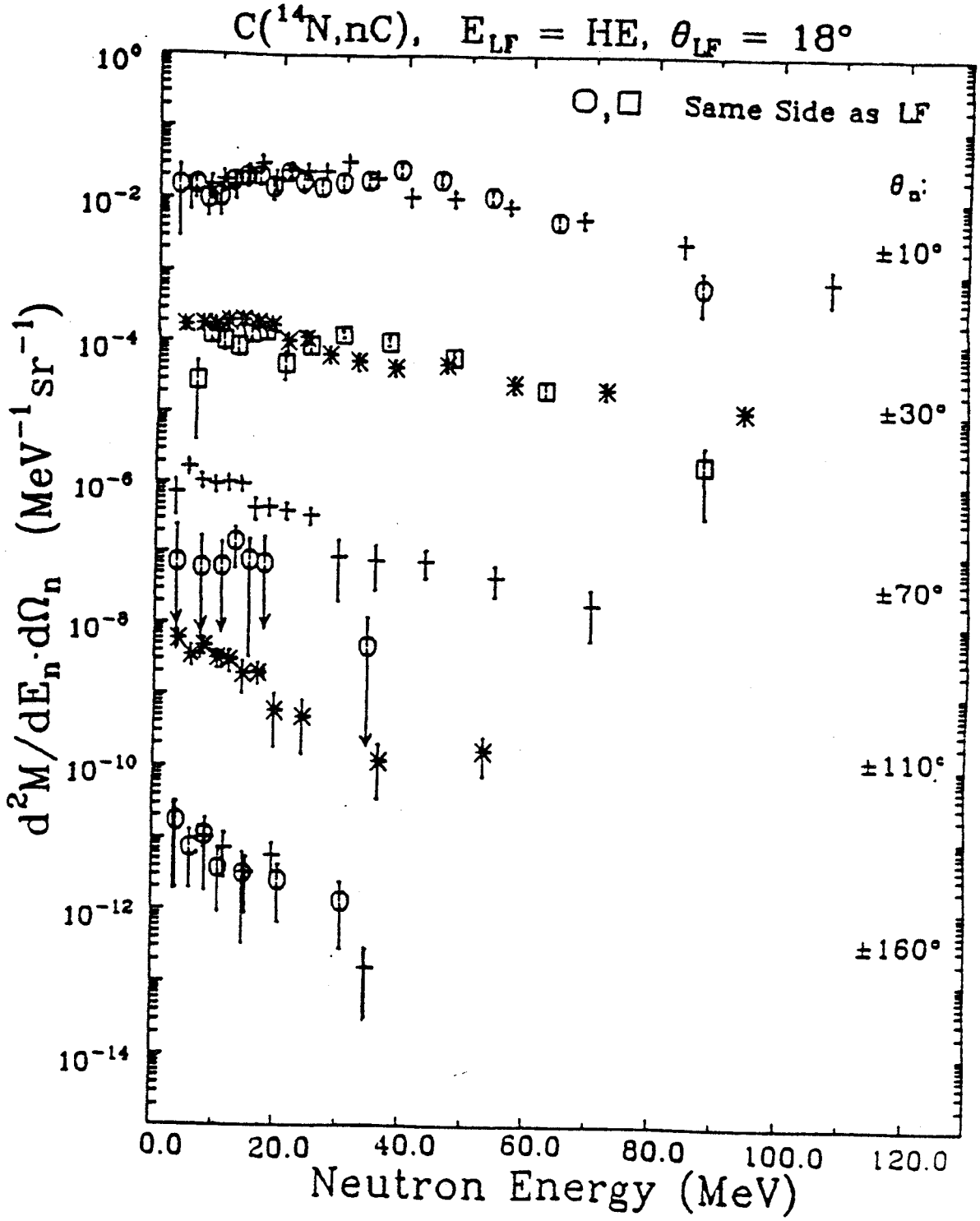

Figure A-27. (continued)

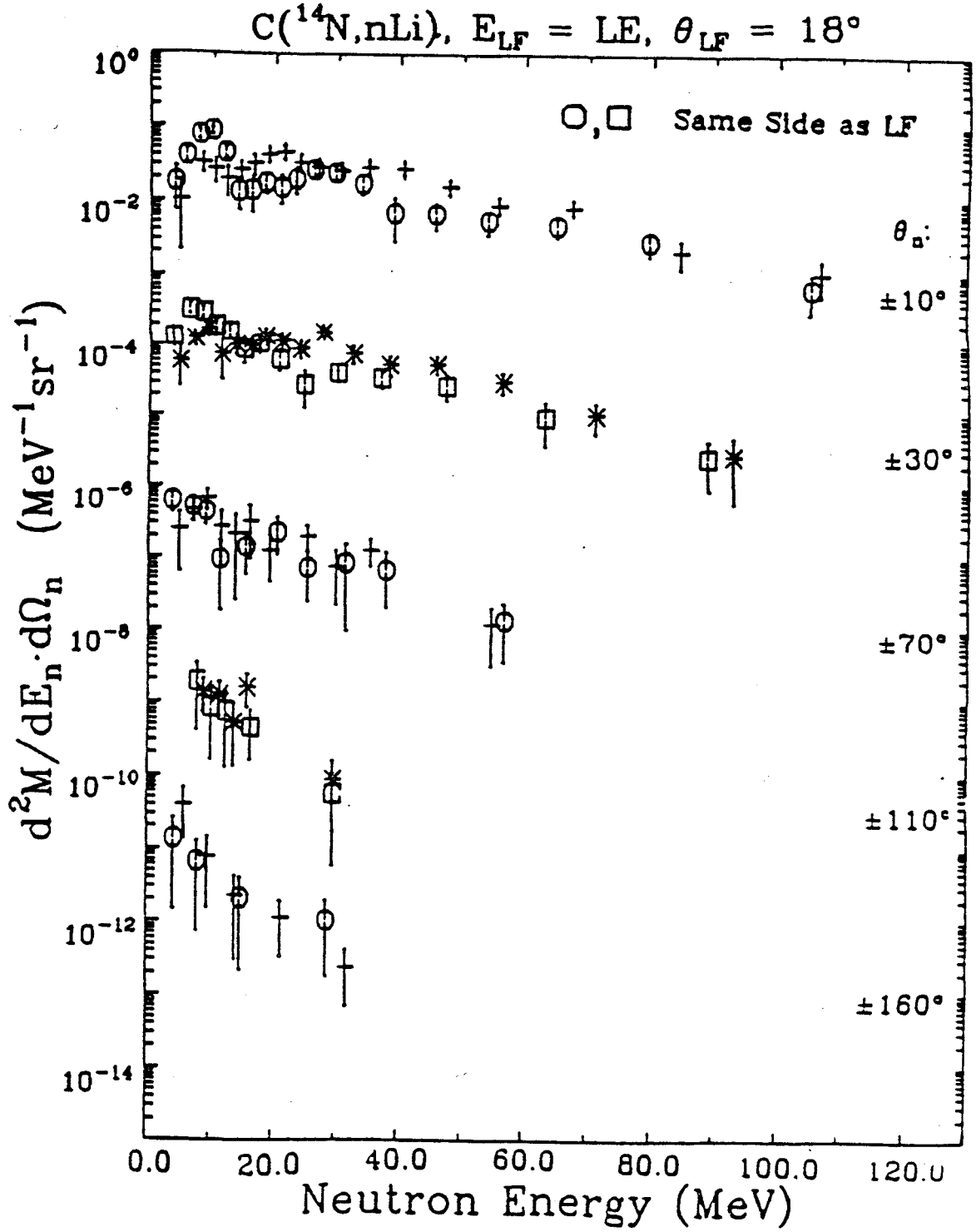

Figure A-27. (continued)

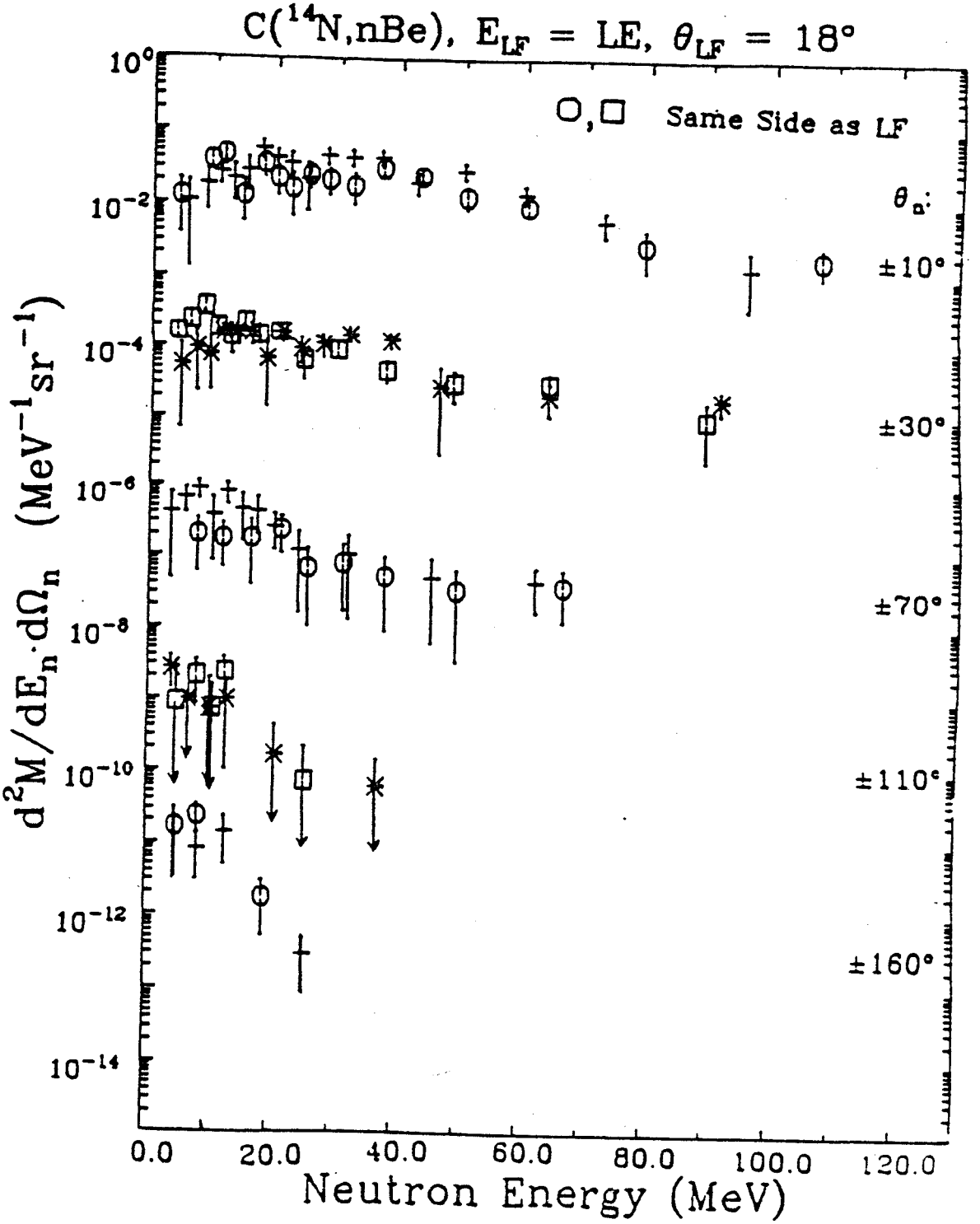

Figure A-27. (continued)

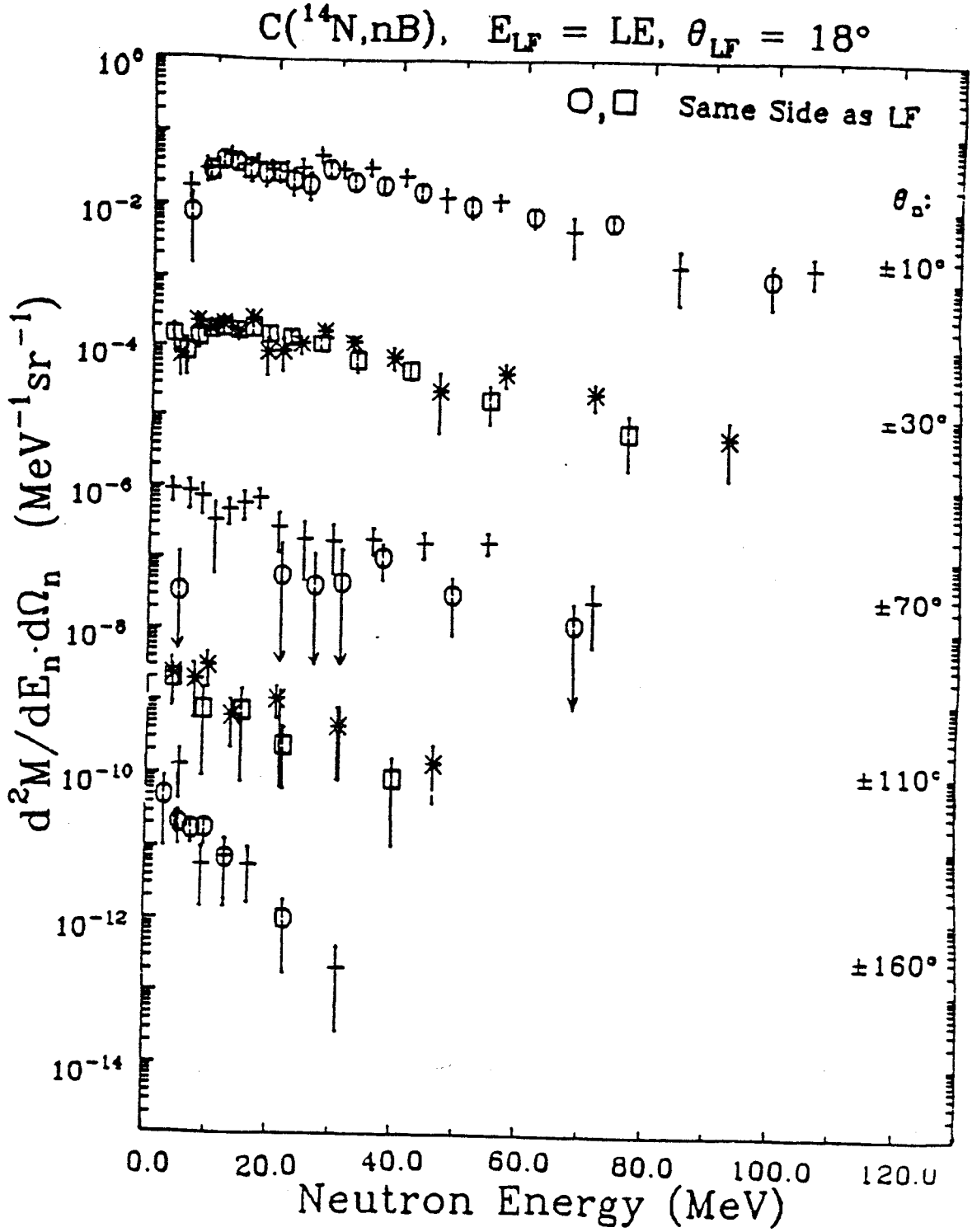

Figure A-27. (continued)

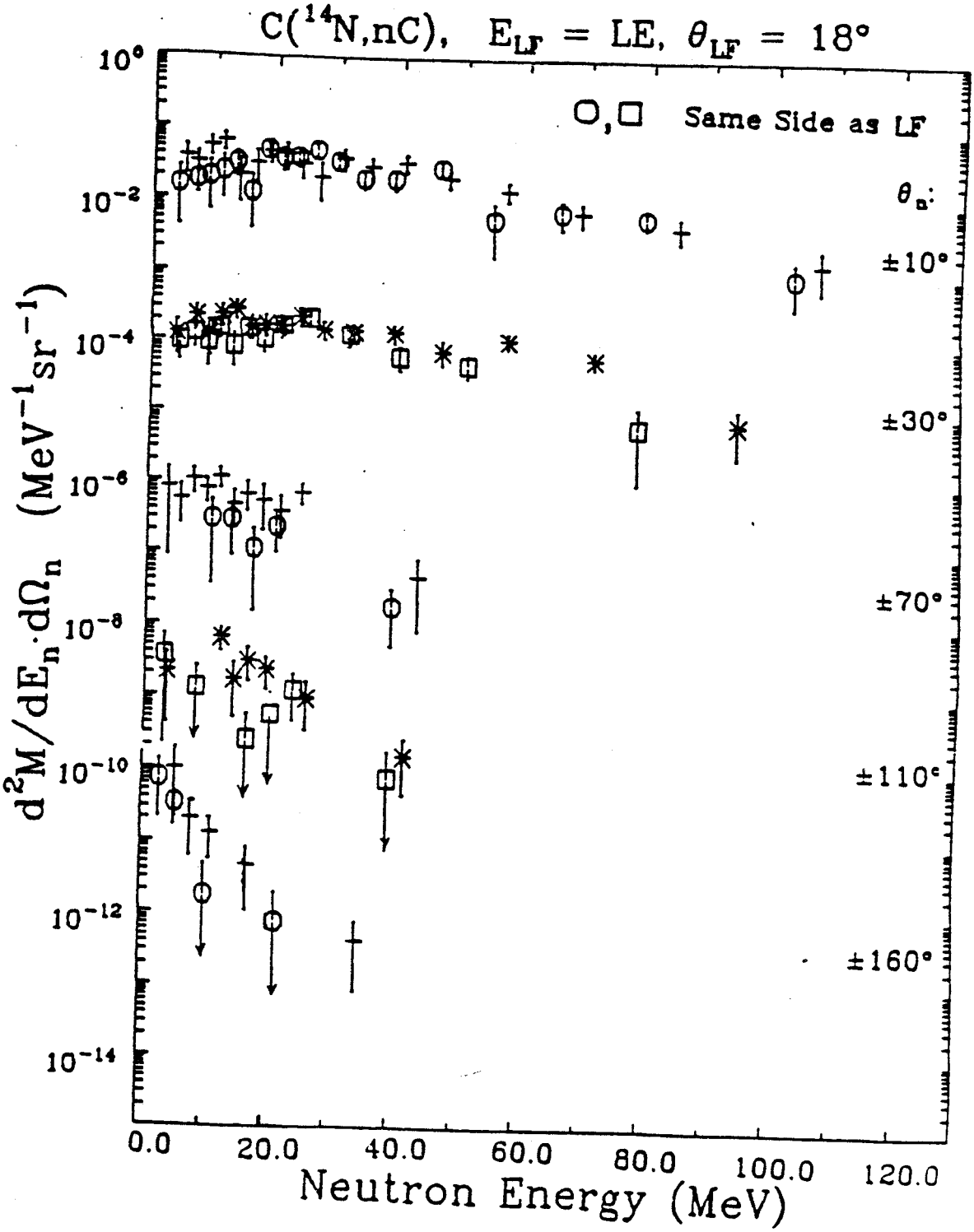

Figure A-27. (continued)

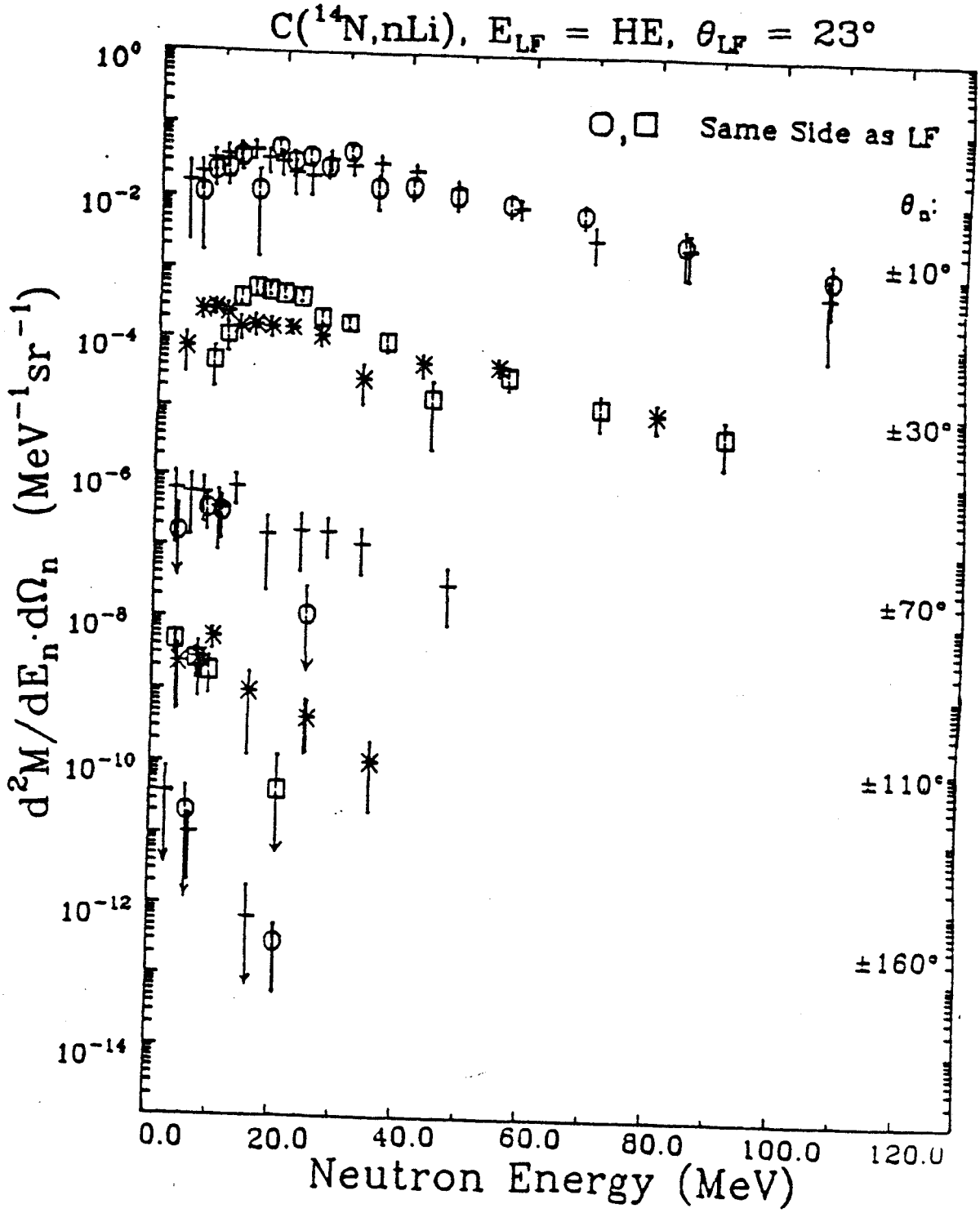

Figure A-27. (continued)

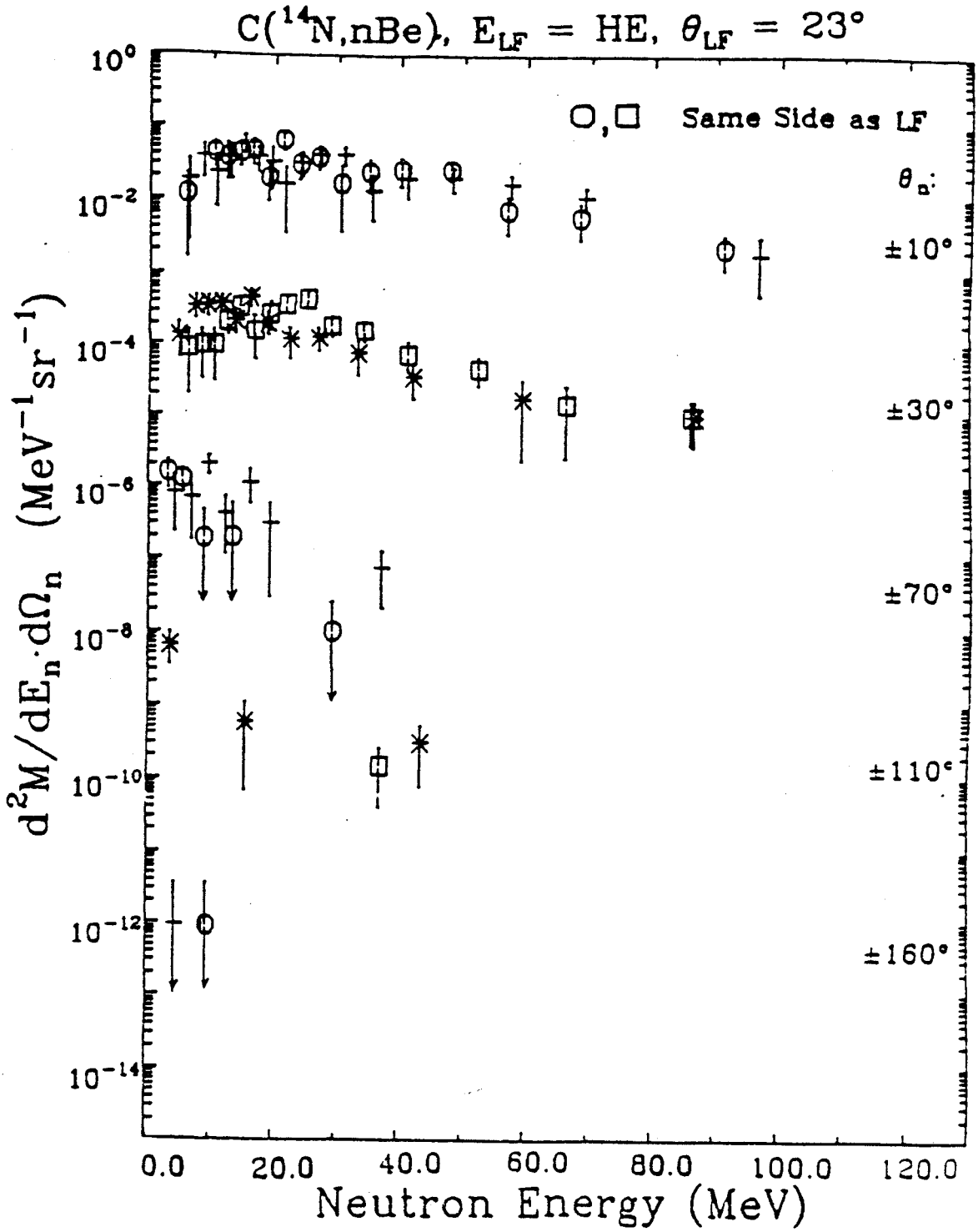

Figure A-27. (continued)

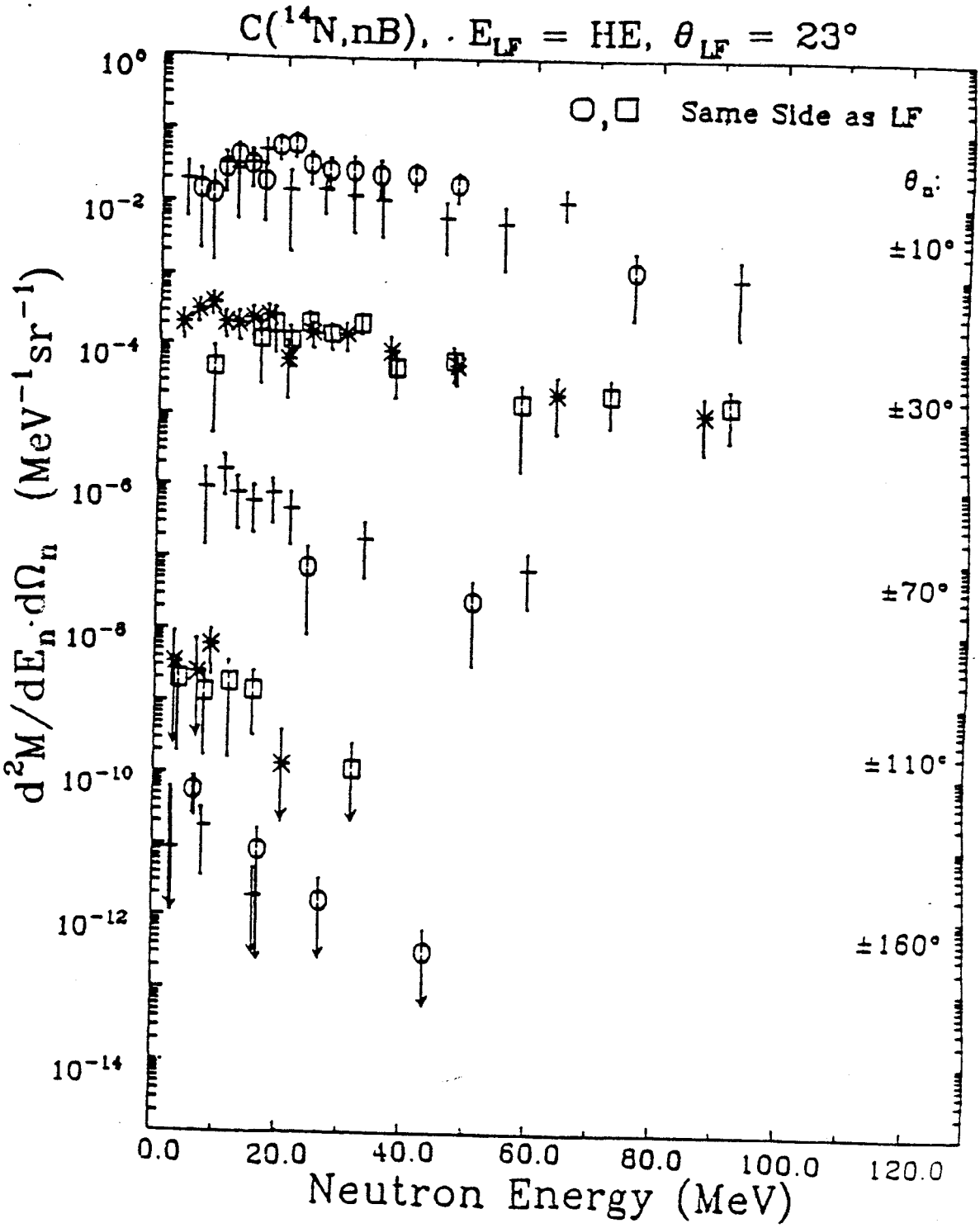

Figure A-27. (continued)

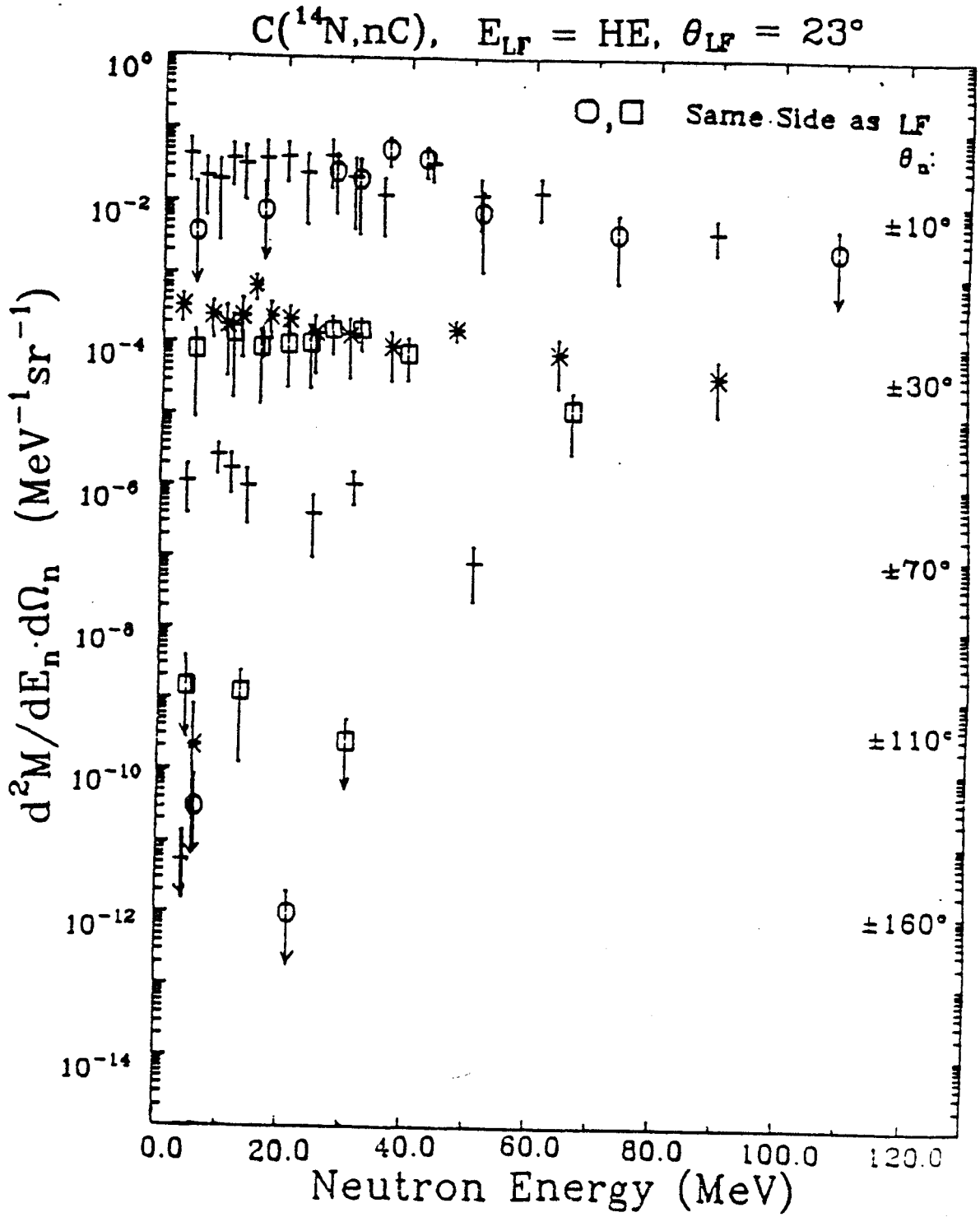

Figure A-27. (continued)

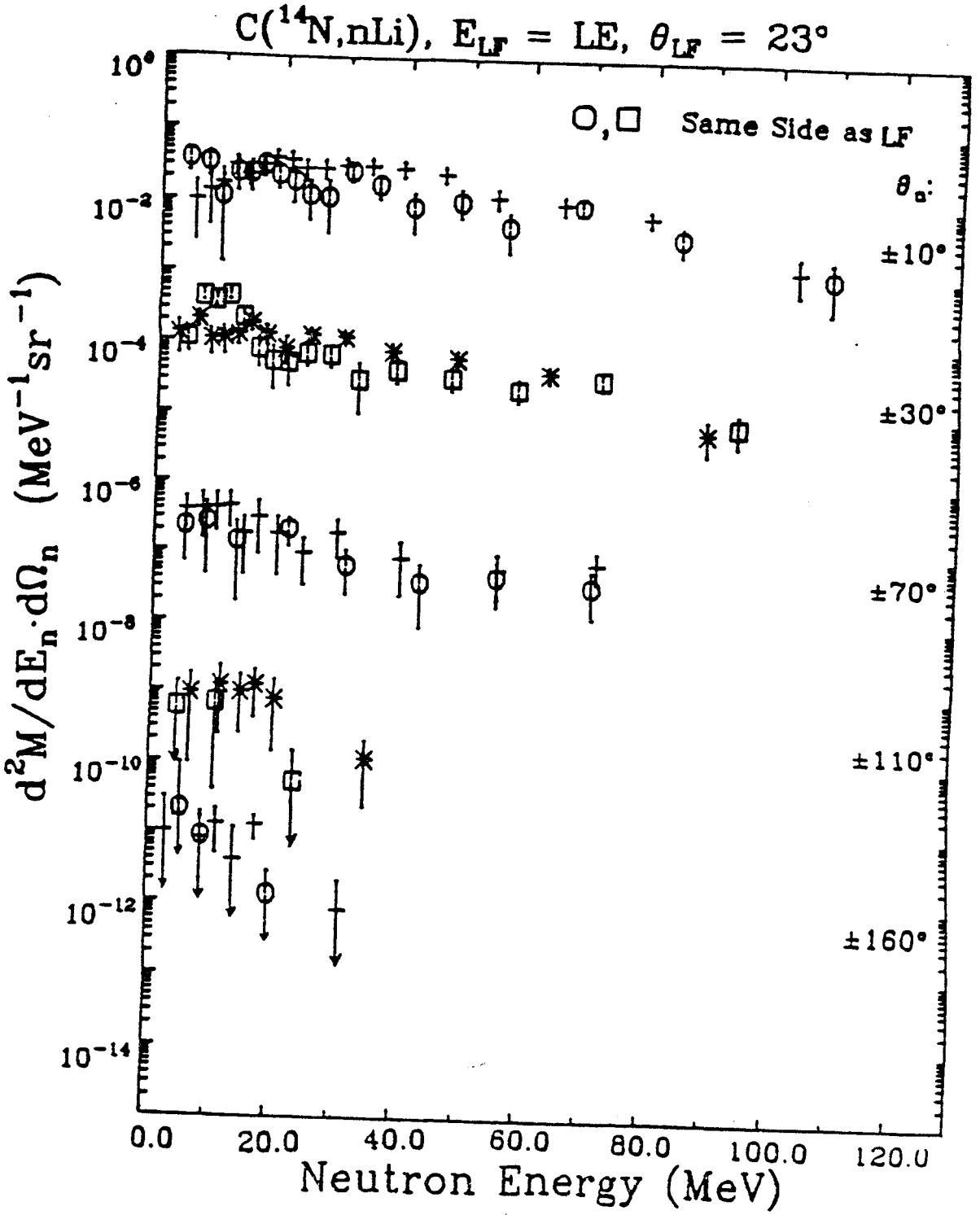

Figure A-27. (continued)

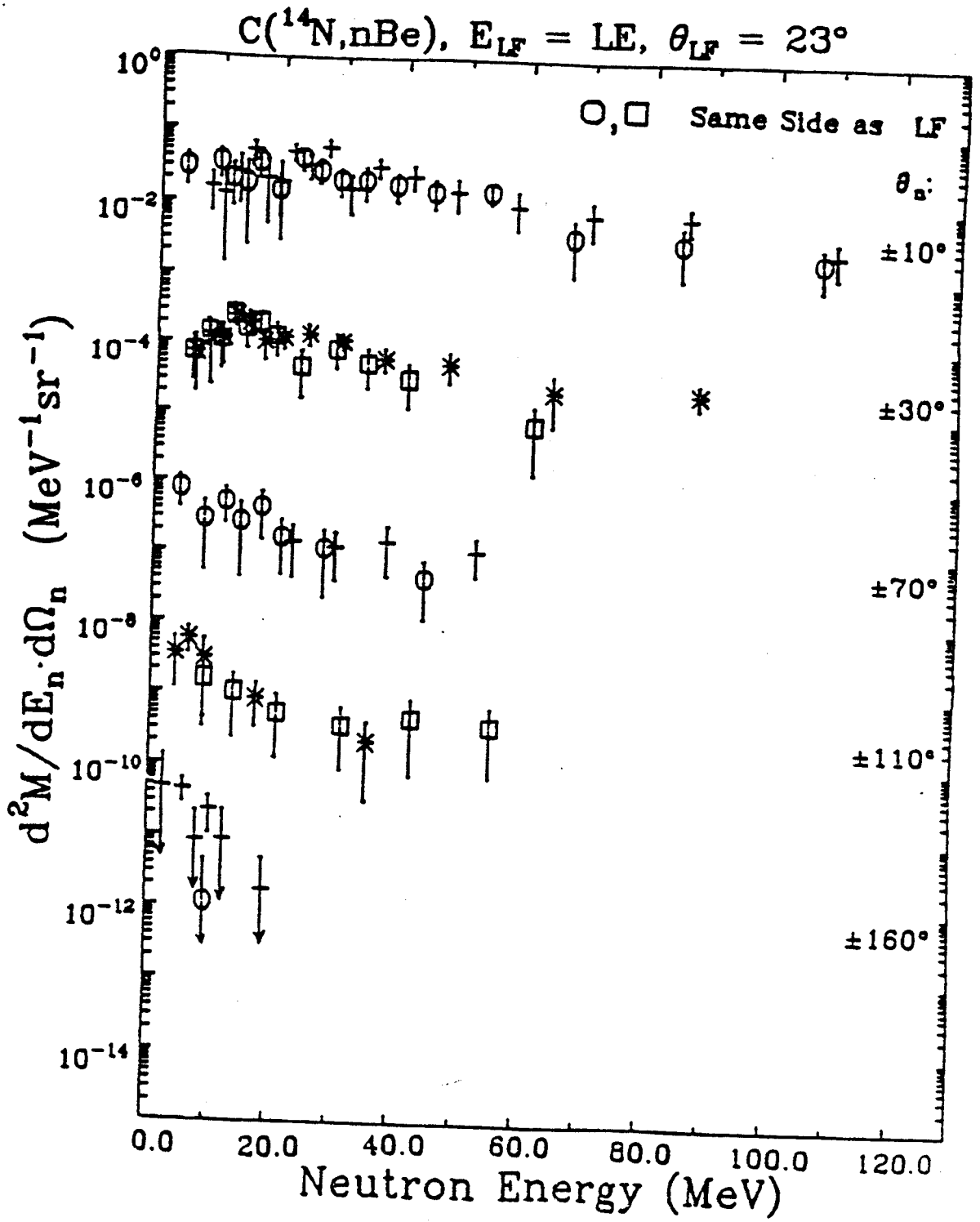

Figure A-27. (continued)

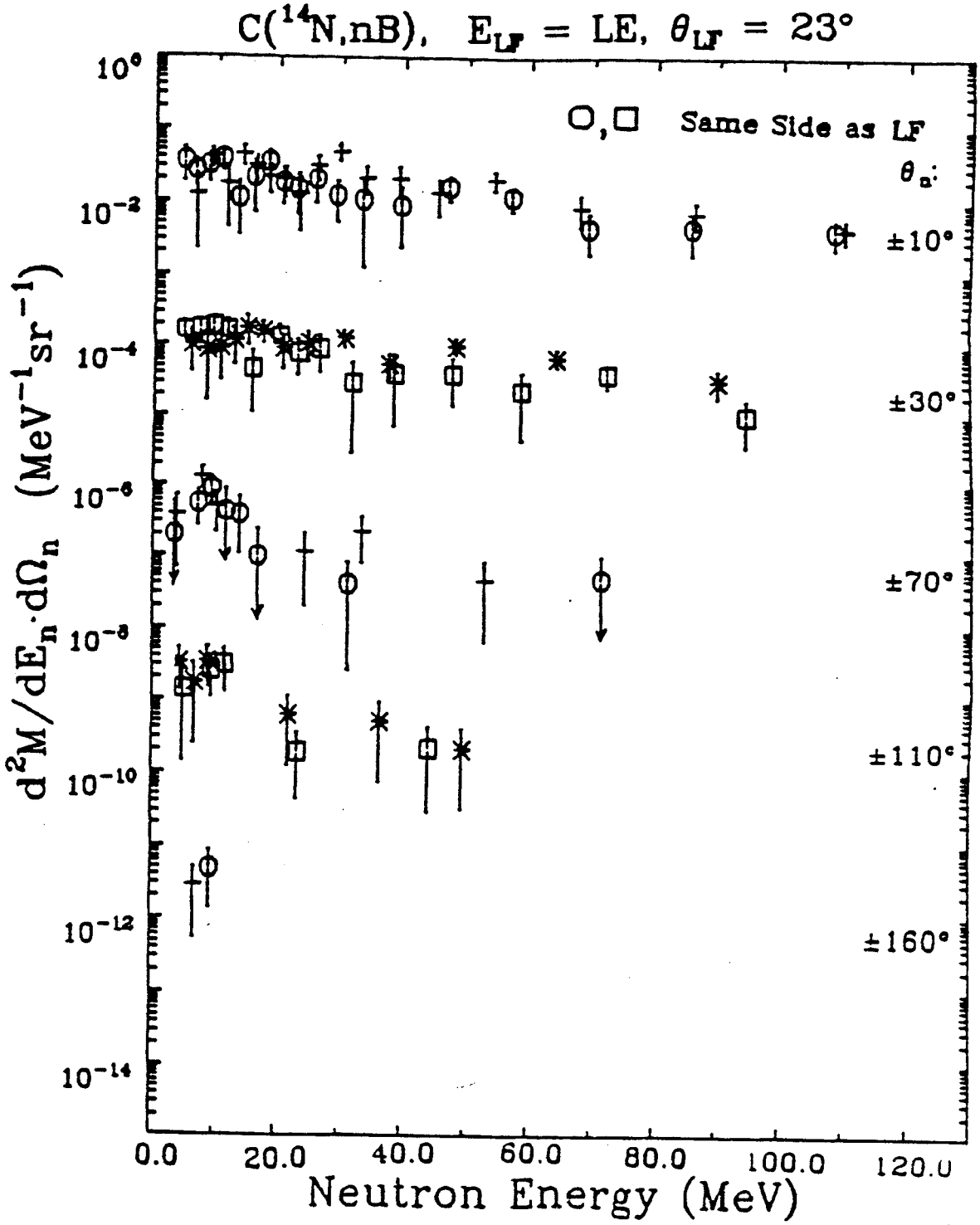

Figure A-27. (continued)

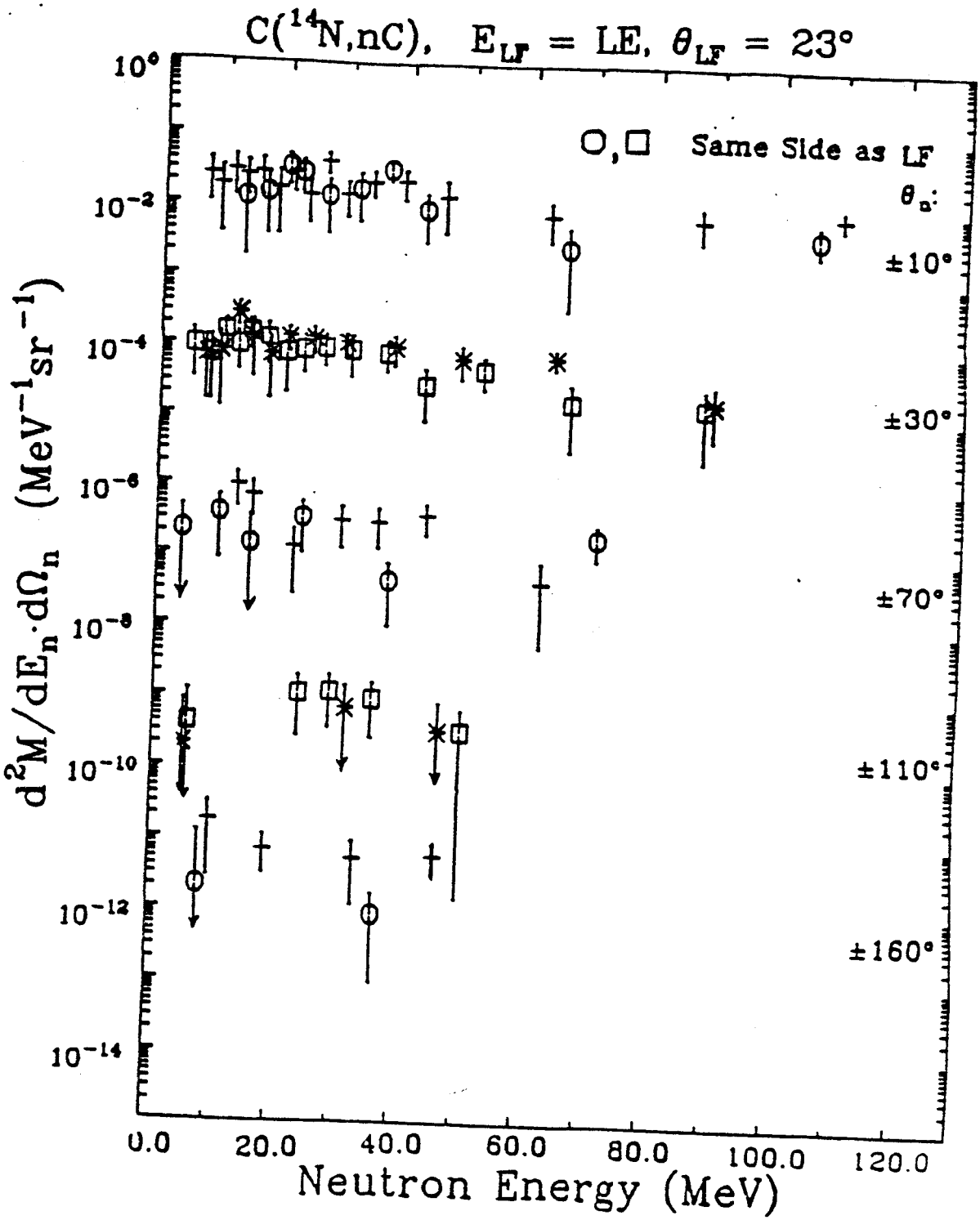

Figure A-27. (continued)

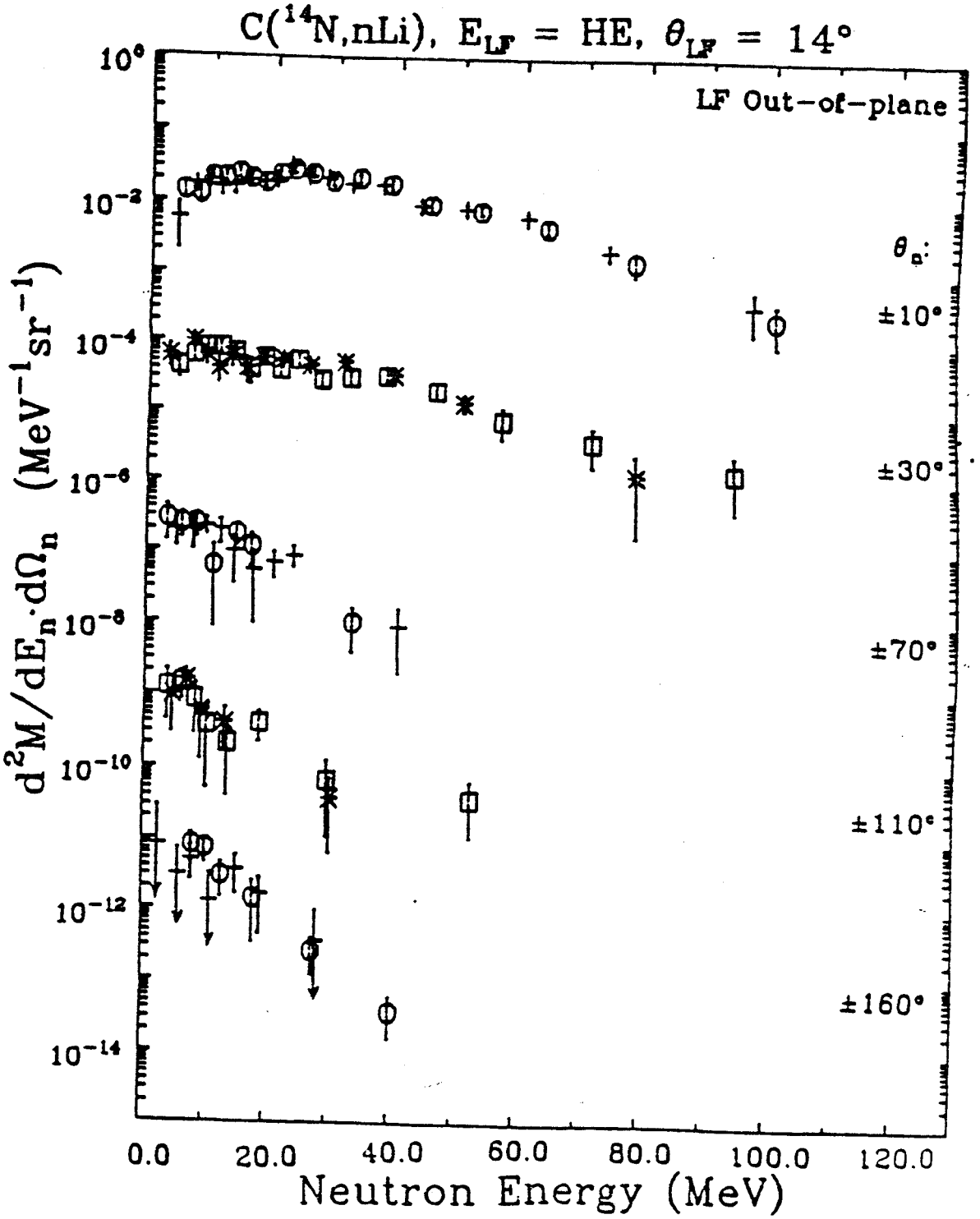

Figure A-27. (continued)

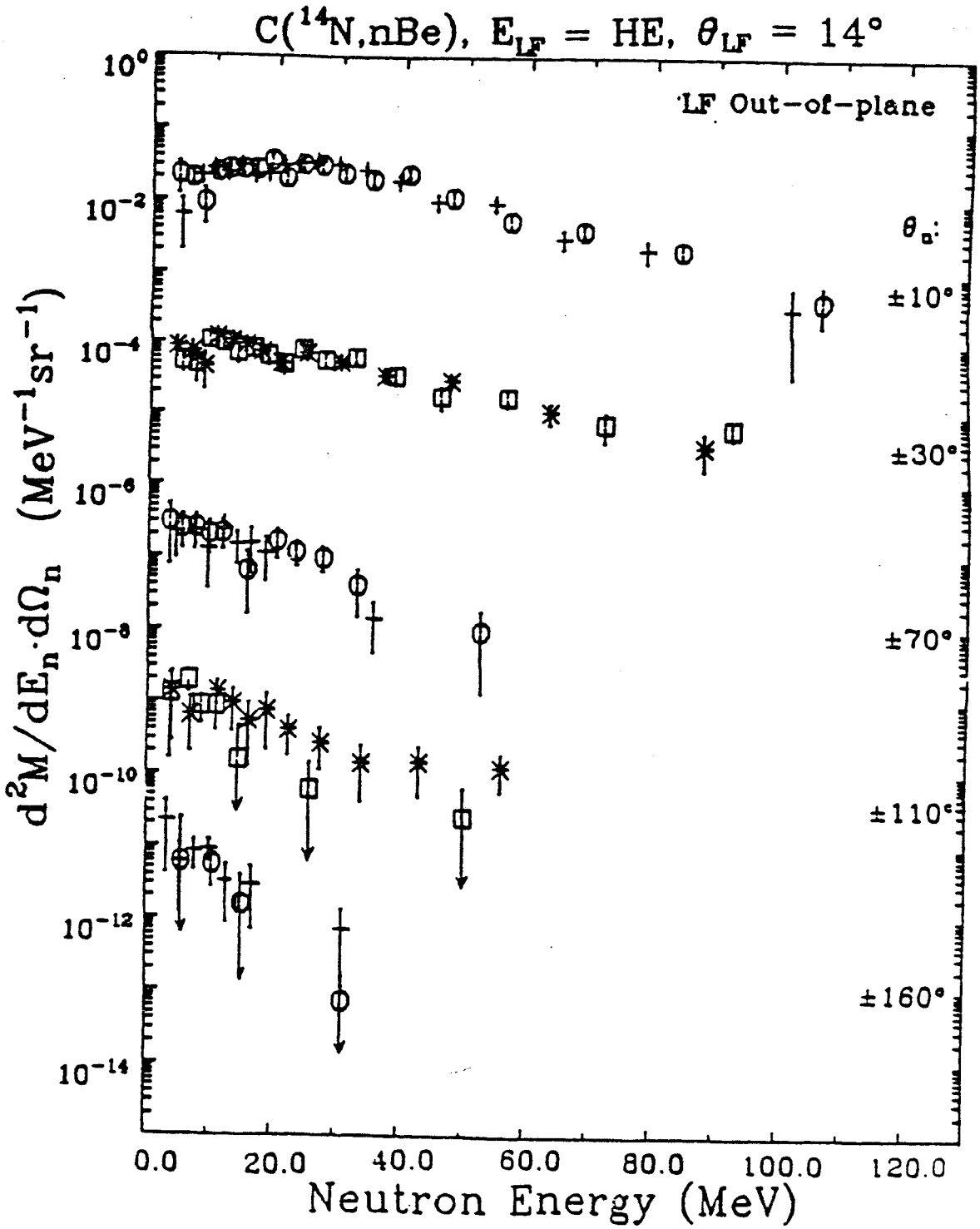

Figure A-27. (continued)

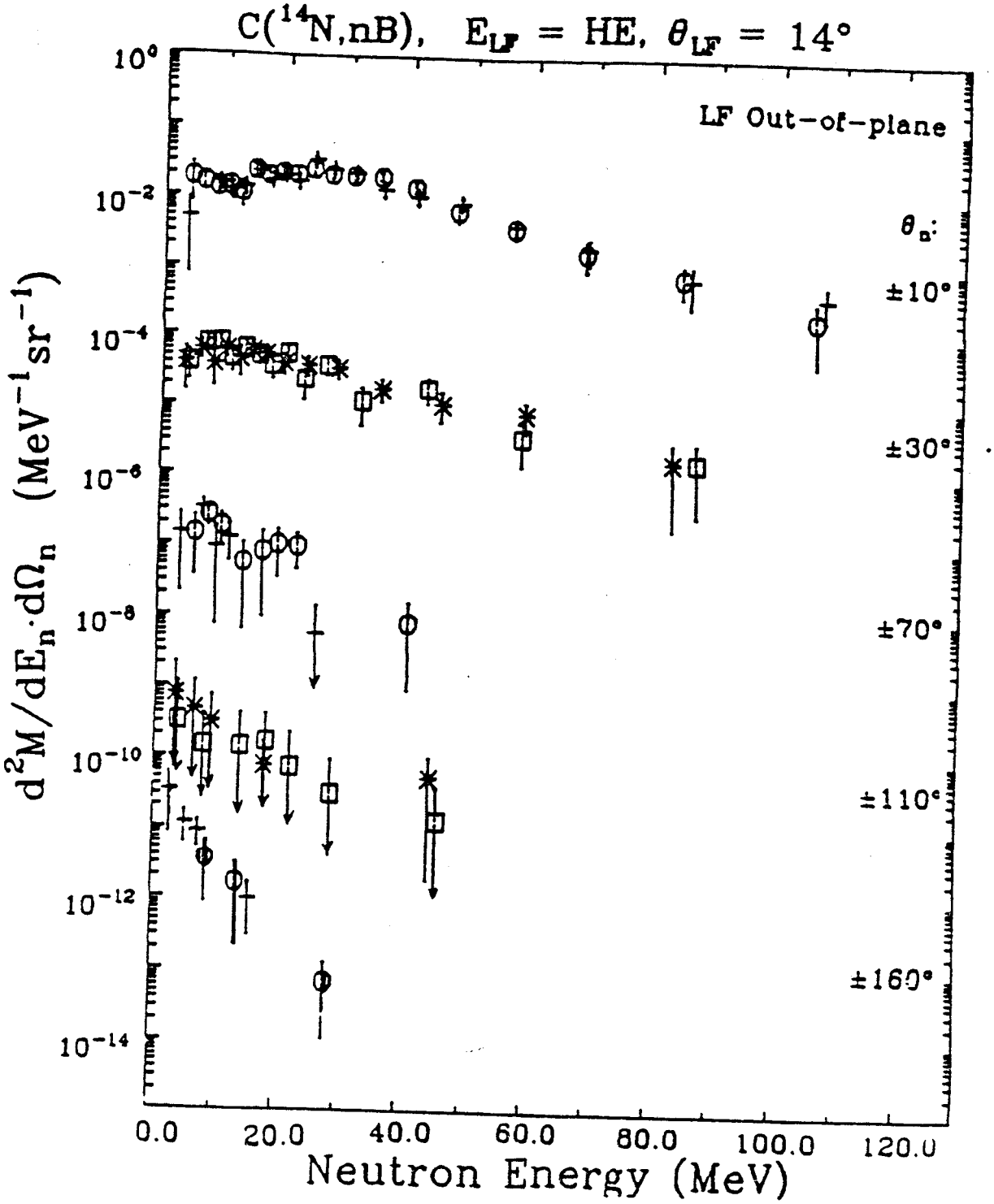

Figure A-27. (continued)

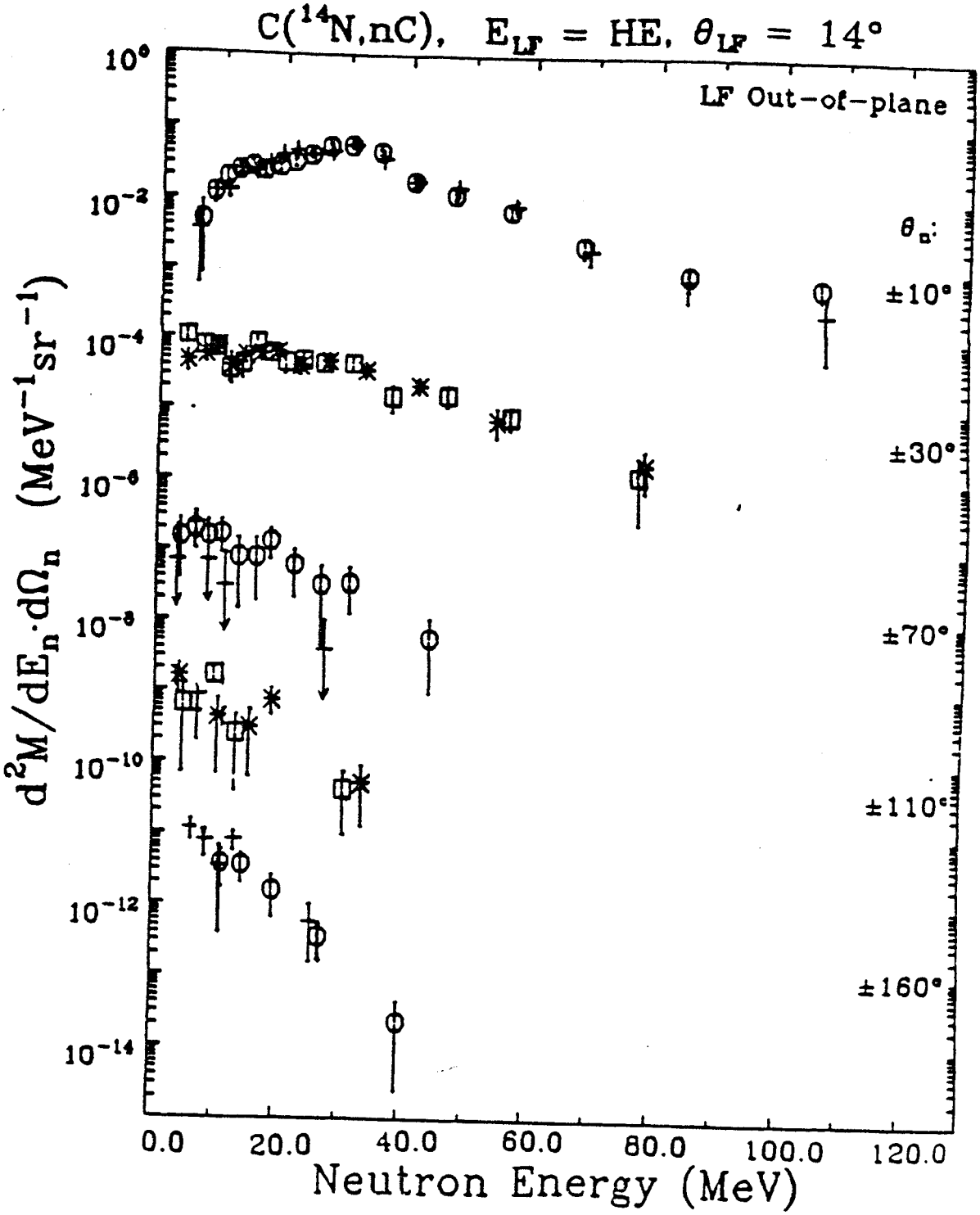

Figure A-27. (continued)

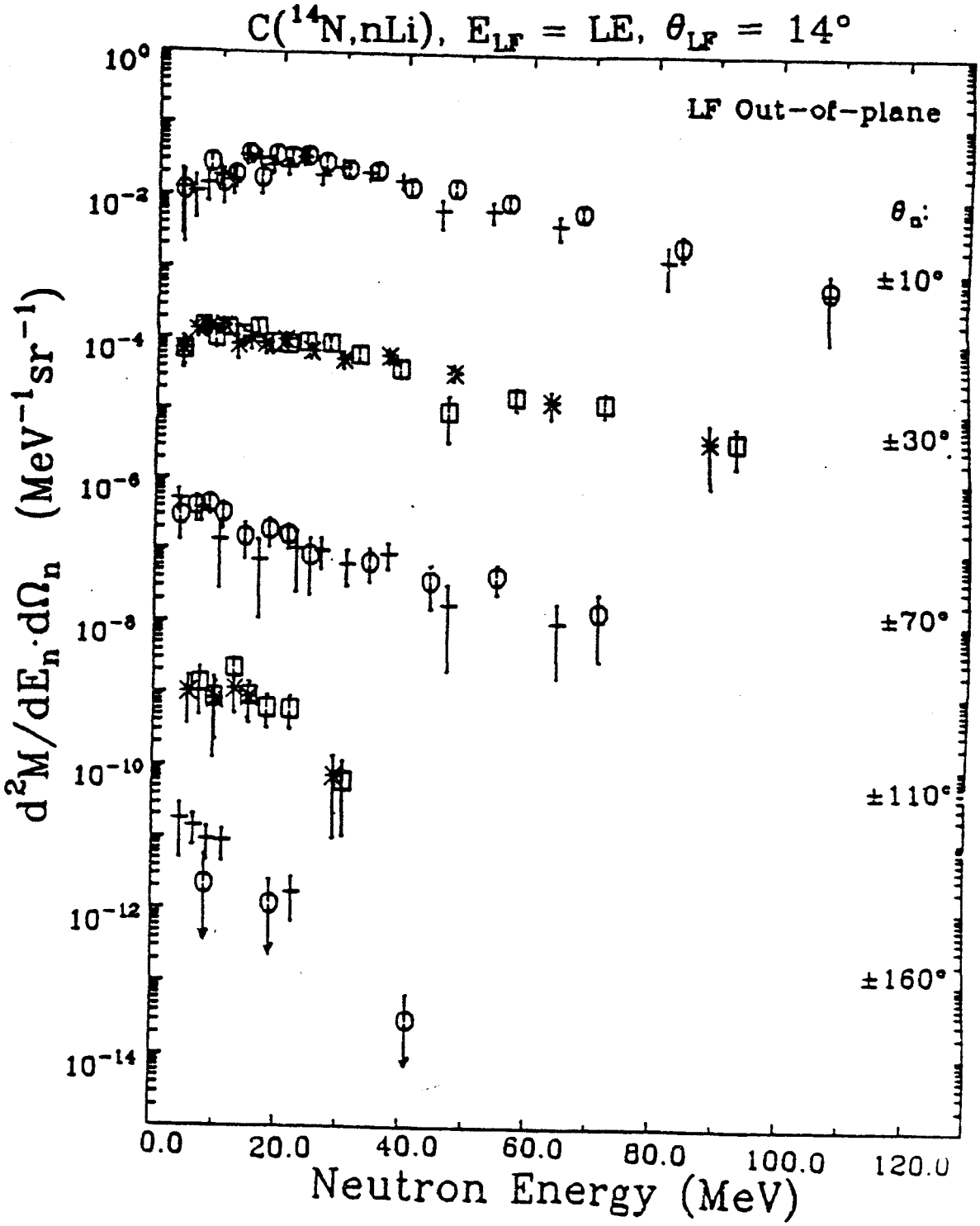

Figure A-27. (continued)

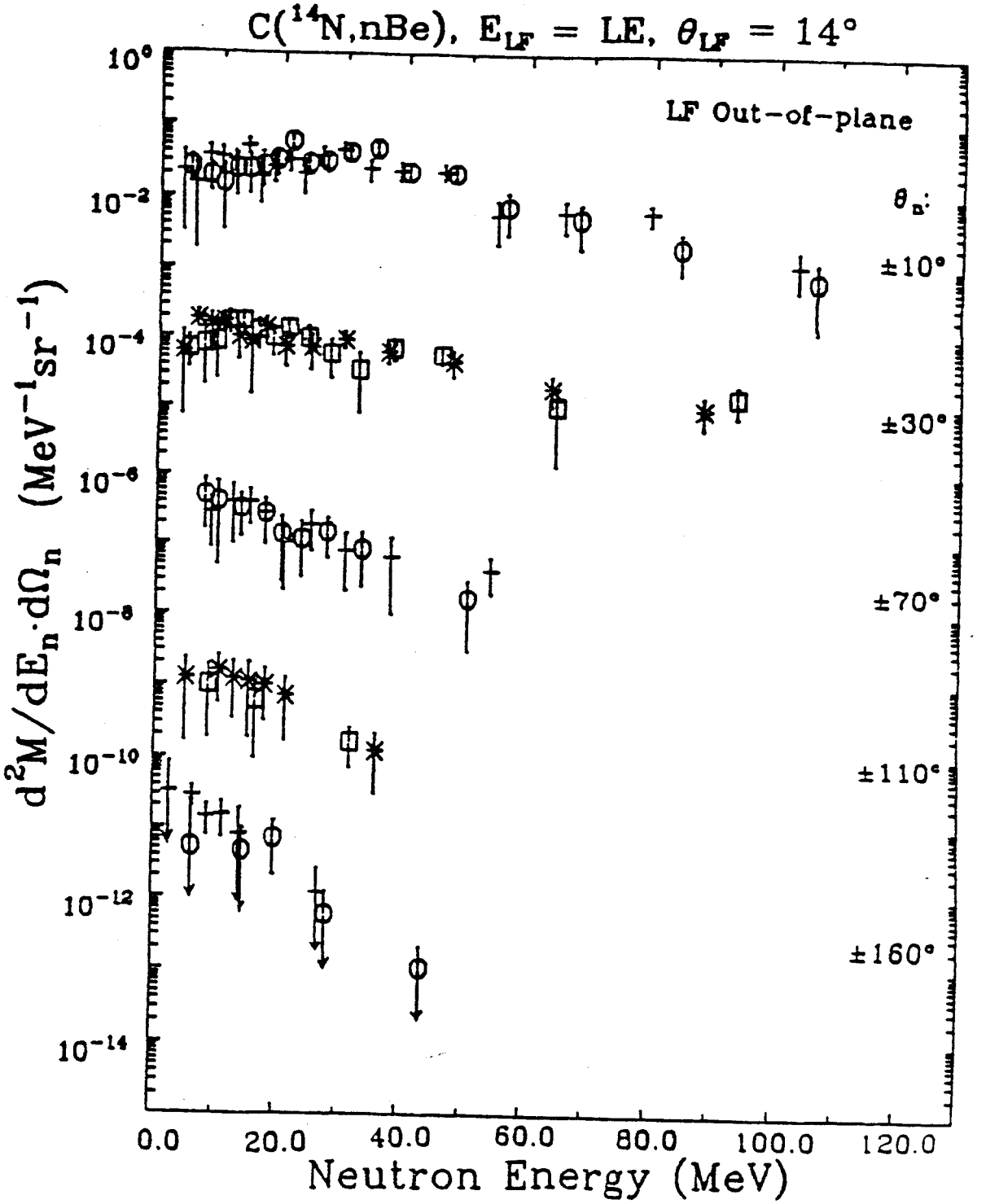

Figure A-27. (continued)

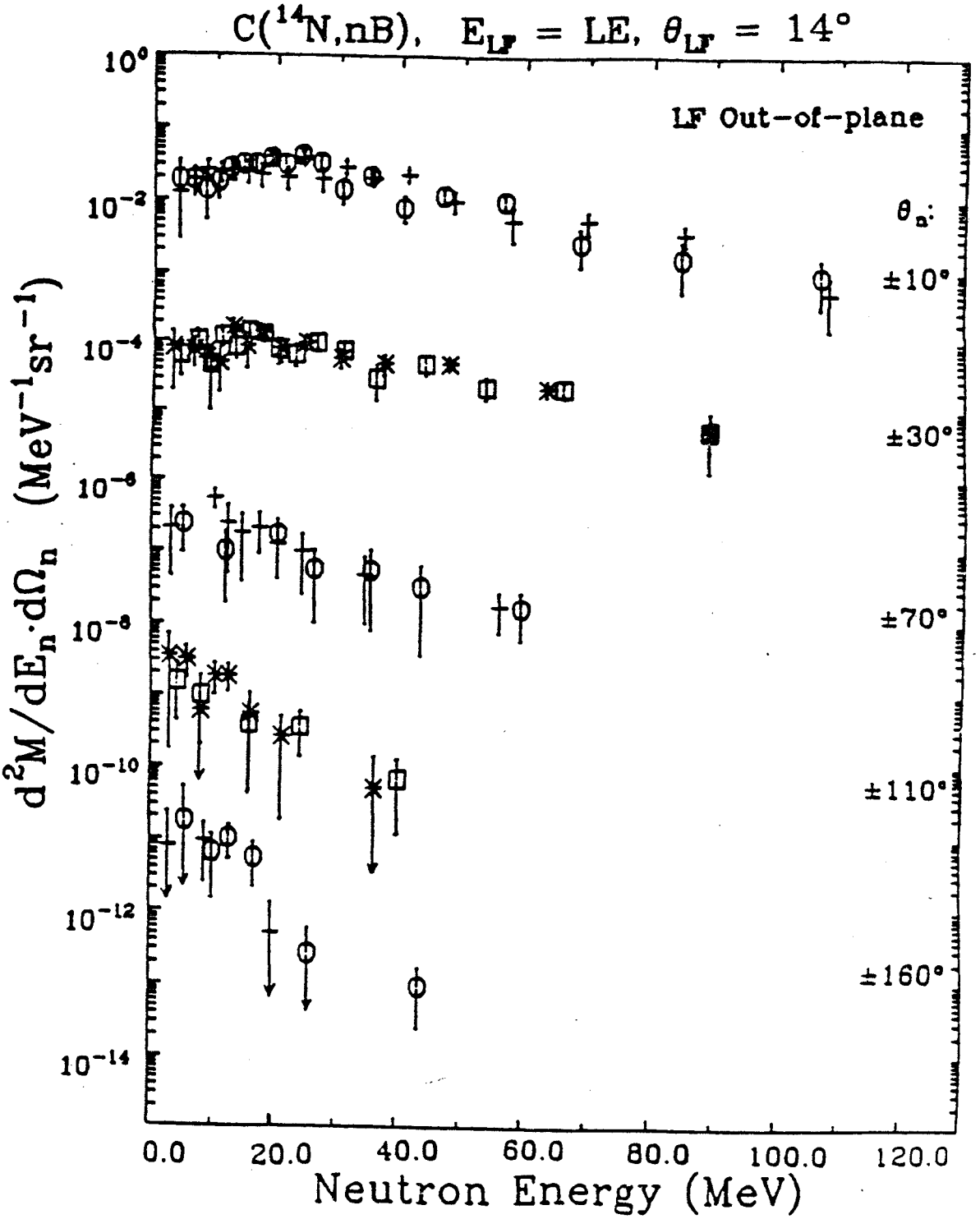

Figure A-27. (continued)

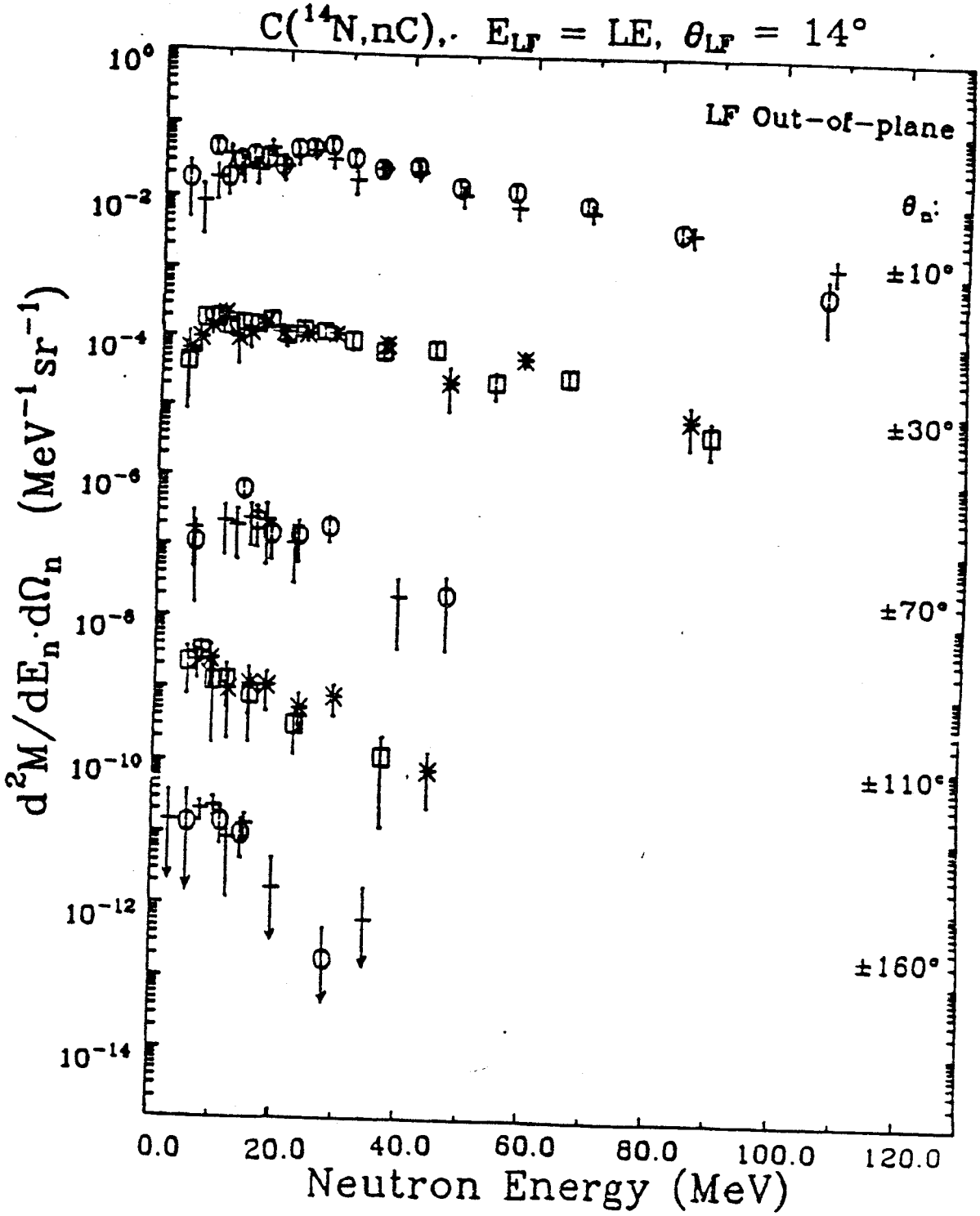

C. The LF Contribution

Figure A-28 shows the neutron spectra at ±10° and ±30° for coincident HE boron light fragments (LF) at Θ_{LF} = +10° for the Ho and Ni target. The solid and dashed curves are results from fits which will be discussed below. The prominent bump in the Θ_n = +10° spectrum corresponds to the neutron detector located directly behind the +10° fragment telescope. One can attempt to use the moving thermal-sources picture to incorporate the contribution to the neutron spectra from the LF. Figures A-25 and A-26 in the previous subsections show the results of fitting the spectra with two moving sources, the TLS and IRS, in the manner described in Section IV of the main text. The parameters for these fits are listed in Tables 1-A and 2-A. In general, the middle and backward angle neutron spectra are reproduced very well, but the spectra at the three angles closest to the direction of the LF are quite different from the predicted result. Using the parameters of the TLS and IRS as determined from a two-source fit and holding them fixed, one can introduce a third source, one at low temperature (0.957 MeV) and moving at the velocity of the detected LF. As shown by the solid and dashed lines in Fig. A-28(a) for the Ho target, the conspicuous bump at +10° can then be reproduced. But the high energy tails at ±10° and the spectrum at -30° is not predicted correctly. If,

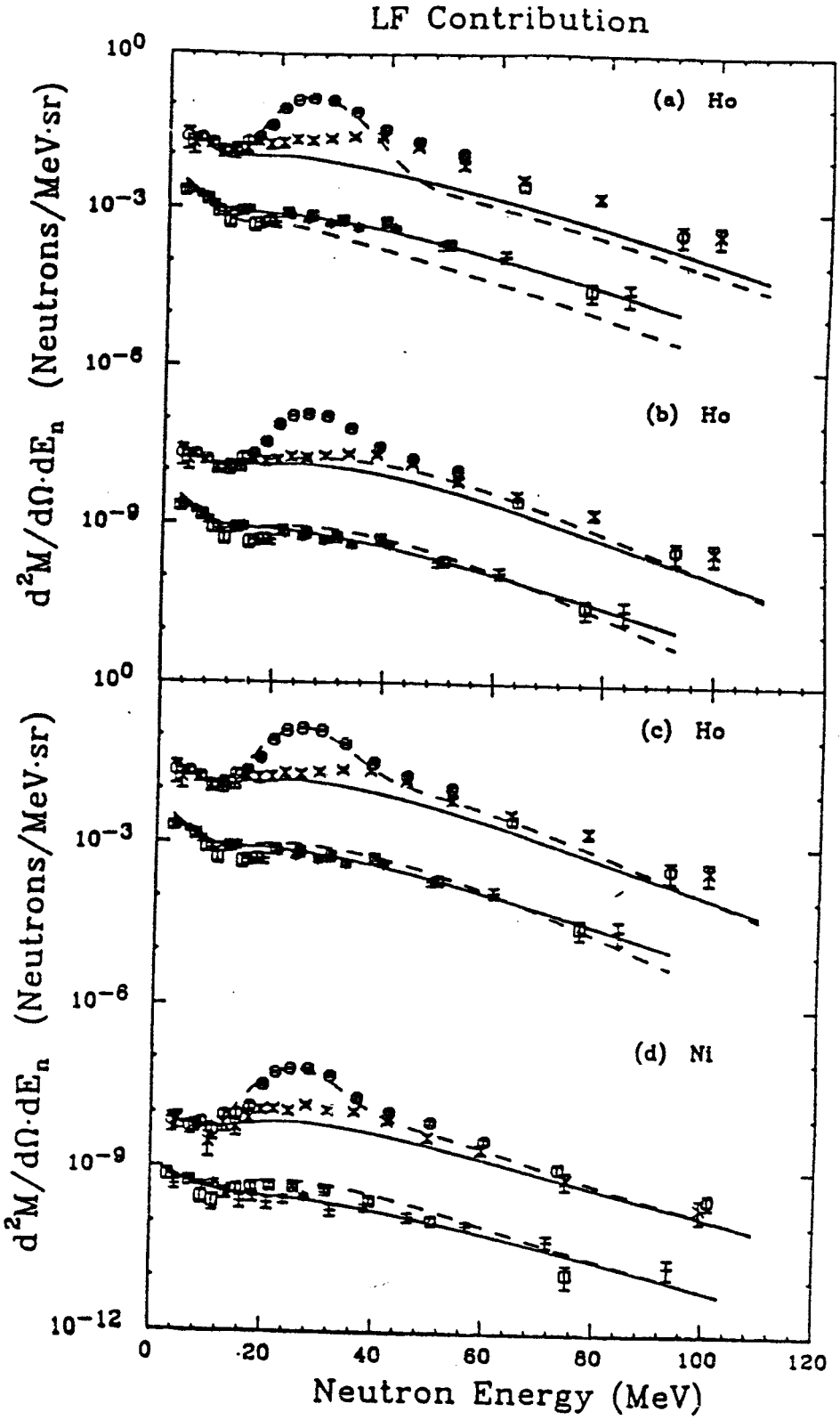

Figure A-28. LF contribution to neutron spectra at ±10° and ±30°.

instead, one lets the temperature of the third source be higher (3.96 MeV), then the high energy tails are more correctly predicted, as shown in Fig. A-28(b), but now the "low-temperature bump" is not reproduced. To satisfactorily reproduce the entire energy and angular distribution with thermal sources, one needs to use four sources: a TLS, an IRS, and two LF sources. One of the LF sources requires a low temperature (0.547 MeV) and the other a higher temperature (3.96 MeV) and both move at the velocity of the detected LF. The result of such a fit for the Ho target is presented in Fig. A-28(c) and one sees quite satisfactory agreement between the parameterization and the data. Figure A-28(d) shows the neutron spectra and four thermal source fit for the same LF gate only for the Ni target and again one has good agreement between the parameterization and the data. The fit parameters for Fig. A-28 are given in Table 3-A.

The prominent "low-temperature" bump is independent of the target. This observation is strengthened by looking at Fig. A-27 for the neutron spectra in coincidence with HE boron fragments at +10° for the C target and noticing that these data too have the "low-temperature bump". This independence of target indicates that the "structure" at θ_n = +10° is associated with the projectile and not the target nucleus. Using two thermal LF sources moving at the same velocity to produce the "structure" at θ_n = +10° is

Table 3-A. The fit parameters for Fig. 28

Fig	Source	Mult	Temp(MeV)	E/A(MeV)	Angle(Degrees)
A-28(a)	TLS	2.026	2.27	0.016	-35.0
	IRS	0.657	8.64	9.562	-11.0
	LF_1	0.120	0.55	25.010	+10.0

Fig	Source	Mult	Temp(MeV)	E/A(MeV)	Angle(Degrees)
A-28(b)	TLS	2.026	2.27	0.016	-35.0
	IRS	0.657	8.64	9.562	-11.0
	LF_2	0.213	3.96	25.010	+10.0

Fig	Source	Mult	Temp(MeV)	E/A(MeV)	Angle(Degrees)
A-28(c)	TLS	2.02	2.27	0.016	-35.0
	IRS	0.657	8.64	9.562	-11.0
	LF_1	0.103	0.55	25.010	+10.0
	LF_2	0.213	3.96	25.010	+10.0

Fig	Source	Mult	Temp(MeV)	E/A(MeV)	Angle(Degrees)
A-28(d)	TLS	0.476	3.01	0.070	-30.0
	IRS	0.357	10.11	11.950	0.0
	LF_1	0.050	0.56	24.780	+10.0
	LF_2	0.093	3.22	24.780	+10.0

equivalent to having a single LF source, but one having two temperatures and different relative weights. The requirement of a thermal LF source at two different temperatures indicates that one should instead consider a source emitting neutrons from multiple discrete states to reproduce the "structure" at $\Theta_n = +10°$.

The fact that the LF source contributes strongly through discrete neutron-emitting levels at angles close to the direction of the detected LF has been noted before (Ga 81, Lü 85, Ho 83, Ch 83, Hi 83, Re 85, Ki 86). One way to identify which levels of the LF are contributing is with a relative velocity plot (Re 85, Ki 86). Figure A-29 shows the neutron velocity spectrum at $\Theta_n = +10°$ for a ^{12}C LF detected at $\Theta_{LF} = +10°$ for the Ho target. The neutron velocities are calculated relative to a ^{13}C rest frame. One can clearly see four spikes centered symmetrically about $V_{rel} = 0$ cm/ns. Each pair of peaks corresponds to neutrons emitted into the forward and backward hemisphere from discrete neutron-emitting states of ^{13}C. The symmetric pair of peaks at low relative velocity ($V_{rel} = \pm 0.4$ cm/ns) corresponds to the decay of the 9.50 MeV $9/2^+$ state of ^{13}C (Aj 84) to the first excited state of ^{12}C. The two peaks at larger relative velocity ($V_{rel} = \pm 2.1$ cm/ns) correspond to

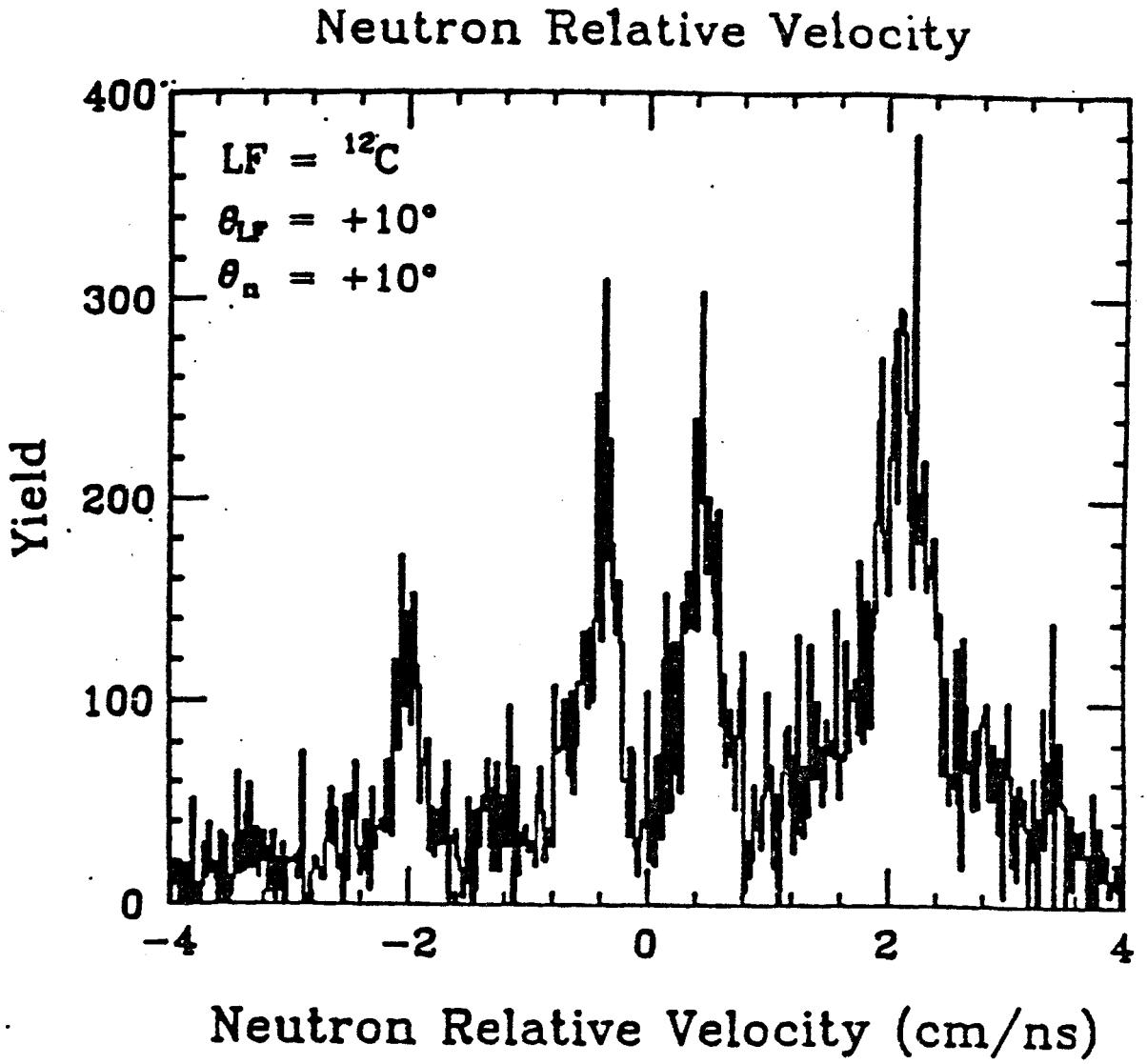

Figure A-29. Neutron relative velocity plot for ^{12}C LF.

the decay of the 6.86 MeV $5/2^+$ state as well as the 7.49, 7.55 and 7.67 MeV states of ^{13}C to the ground state of ^{12}C. The neutron detector efficiencies have been folded into the spectrum in event mode sorting, but the kinematic solid angle "efficiency" has not been corrected for. The solid angle effect is why symmetric peaks do not have the same height and width. Indeed the solid angle "efficiency" falls off extremely rapidly with increasing neutron relative velocity. If this efficiency were folded into Fig. A-29, the low velocity peaks at ±0.4 cm/ns would be much smaller than the peaks at ±2.1 cm/ns. Figure A-30 shows a neutron relative velocity plot for detected ^{11}B LFs. The single peak centered about zero relative velocity corresponds to the decay of the 3.388 MeV state of ^{12}B (Aj 85) to the ground state of ^{11}B, yielding a 19 keV neutron in the rest frame of the ^{12}B emitter. If an excited ^{12}B in the 3.388 MeV state decays and is detected as ^{11}B in the +10° telescope, essentially 100% of the emitted 19 keV neutrons are detected in the +10° neutron detector directly behind the telescope, due to the strong kinematic focusing. So only a single peak is observed centered about $V_{rel} = 0$ cm/sec. The width of the peak is due to neutrons moving into the forward or backward hemisphere, with 19 keV corresponding to 0.2 cm/ns.

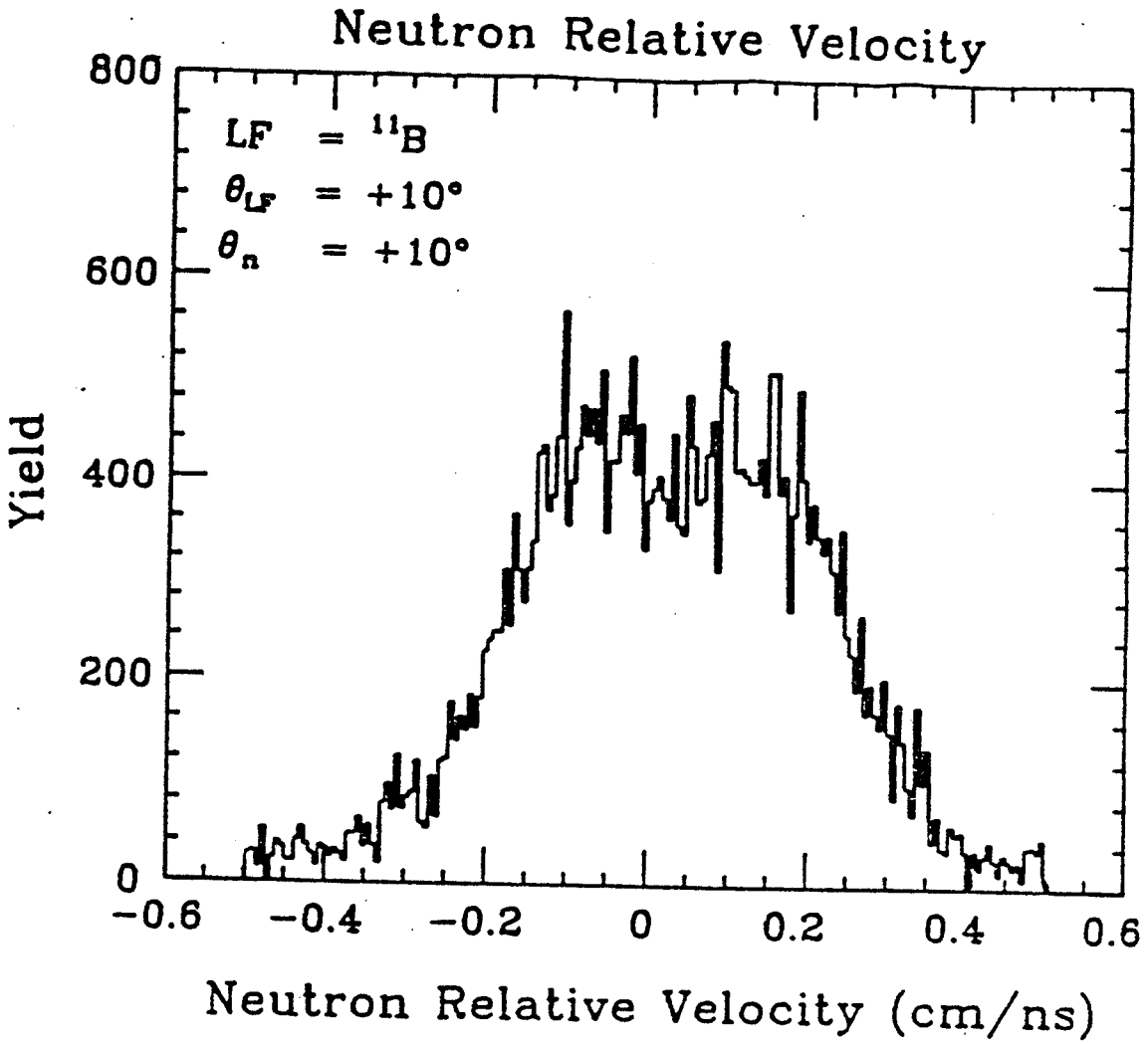

Figure A-30. Neutron relative velocity plot for ^{11}B LF.

A-XI. The Fragment Data

A. The Fragment Energy Gates and Cross Sections

1. The Ho Target

Table 4-A lists the energy gates and cross sections of the fragments for the Ho target. The first column lists which fragment was selected (Li, Be, B, C, N, or O). The second column lists the LE (low energy) gate set on the fragment energy spectrum. The third column gives the cross section of the fragments with the LE gate. This cross section is for fragments recorded in singles mode, i.e., for fragments not in coincidence with a neutron. The final two columns list the HE (high energy) gate and HE cross section, respectively. These cross sections were used in converting differential neutron cross section to differential neutron associated multiplicity. Only neutron spectra in coincidence with Li, Be, B, and C fragments were transformed to multiplicity spectra. So the singles fragment cross sections were not tabulated for N and O fragments.

Table 4-A. The fragment energy gates for the Ho target

LF	LE(MeV)	dσ/dΩ(mb/sr)-LE	HE(MeV)	dσ/dΩ(mb/sr)-HE
θ = 7°		Ho target		
Li	20-110	219.5	146-250	972.5
Be	34-50, 100-156	75.6	190-340	586.2
B	50-120, 204-210	61.5	270-420	1405.4
C	60-220	96.1	372-480	3045.0
N	80-360		400-500	
O	100-320		400-500	
θ = 10°				
Li	31-105	120.1	136-220	425.7
Be	52-126	42.0	168-315	241.4
B	73-168	40.4	210-399	436.0
C	94-210	27.8	252-472	630.0
N	105-315		441-504	
O	120-370		440-500	
θ = 15°				
Li	20-100	92.1	120-240	191.9
Be	30-140	41.9	160-320	64.7
B	50-160	33.0	200-390	72.9
C	60-200	23.0	260-440	47.3
N	80-300		380-500	
O	100-280		300-500	
θ = 18°				
Li	36-60	35.4	61-232	195.9
Be	58-150	36.2	151-300	39.4
B	80-220	35.0	221-370	28.3
C	100-270	20.5	271-400	12.7
N	126-304		305-450	
O	141-270		271-440	
θ = 23°				
Li	30-96	75.3	100-260	64.8
Be	30-114	28.0	120-340	22.3
B	34-140	26.9	180-380	12.0
C	40-140	17.7	200-400	5.1
N	40-140		160-420	
O	50-124		126-400	

Table 4-A. (continued)

θ = 14° (Out-of-Plane) Ho target

LF	LE(MeV)	dσ/dΩ(mb/sr)-LE	HE(MeV)	dσ/dΩ(mb/sr)-HE
Li	30-110	106.5	126-270	291.3
Be	46-146	42.0	166-350	104.7
B	60-190	41.0	226-410	125.3
C	74-230	25.7	280-460	101.8
N	90-320		380-500	
O	110-320		321-500	

2. The Ni Target

Table 5-A lists the fragment energy gates and cross sections for the Ni target. The format of the table is the same as that of Table 4-A.

Table 5-A. The fragment energy gates for the Ni target

θ = 7°		Ni target		
LF	LE(MeV)	dσ/dΩ(mb/sr)-LE	HE(MeV)	dσ/dΩ(mb/sr)-HE
Li	20-100	145.7	150-260	720.2
Be	30-140	92.0	180-340	437.3
B	48-180	80.0	240-430	880.3
C	60-220	80.9	300-470	1329.5
N	80-320		420-500	
O	96-320		321-500	
θ = 10°				
Li	30-100	115.4	140-250	399.2
Be	40-140	70.0	170-300	166.3
B	60-180	57.1	220-400	306.8
C	74-210	53.0	260-436	405.4
N	95-290		370-500	
O	110-300		340-488	
θ = 15°				
Li	20-100	99.3	120-250	175.3
Be	30-140	54.9	160-330	71.9
B	50-180	45.6	210-390	75.6
C	60-180	35.6	230-430	75.0
N	80-280		281-483	
O	100-310		311-490	
θ = 18°				
Li	36-60	36.9	61-230	222.1
Be	60-140	43.5	141-300	59.5
B	84-200	58.6	201-370	47.3
C	108-240	30.8	241-400	37.1
N	128-300		301-440	
O	144-270		271-440	
θ = 23°				
Li	20-70	53.3	80-240	93.4
Be	20-100	31.6	110-310	39.2
B	30-140	33.6	146-360	27.6
C	40-200	37.2	220-400	12.5
N	40-200		220-450	
O	50-210		211-420	

Table 5-A. (continued)

θ = 14° (Out-of-Plane) Ni target

LF	LE(MeV)	dσ/dΩ(mb/sr)-LE	HE(MeV)	dσ/dΩ(mb/sr)-HE
Li	30-104	99.7	120-270	240.0
Be	40-140	53.3	150-340	106.6
B	60-200	47.7	220-410	105.0
C	70-220	36.8	260-440	101.2
N	90-320		321-500	
O	110-300		301-500	

3. The C Target

Table 6-A lists the fragment energy gates and cross sections for the C target. The format of the table is the same as that of Table 4-A.

Table 6-A. The fragment energy gates for the C target

LF	LE(MeV)	dσ/dΩ(mb/sr)-LE	HE(MeV)	dσ/dΩ(mb/sr)-HE
θ = 7°		C target		
Li	20-112	170.0	113-270	536.8
Be	30-120	65.3	170-330	275.9
B	50-210	151.1	260-410	562.3
C	60-260	221.0	320-460	840.0
N	80-320		380-500	
O	100-380		400-480	
θ = 10°				
Li	30-80	44.1	100-240	289.0
Be	40-110	29.3	150-290	127.5
B	60-160	42.9	200-380	225.8
C	80-200	52.2	240-430	331.5
N	100-240		340-500	
O	110-290		330-466	
θ = 15°				
Li	20-80	42.4	90-250	132.8
Be	30-120	27.7	130-340	55.7
B	50-160	27.5	180-390	75.6
C	70-180	20.6	220-420	80.0
N	80-260		261-460	
O	100-290		291-444	
θ = 18°				
Li	36-64	23.0	80-220	103.7
Be	36-60	12.6	140-280	32.2
B	76-160	17.9	180-340	38.8
C	104-180	10.7	200-380	37.0
N	132-240		260-440	
O	160-260		261-430	
θ = 23°				
Li	10-80	31.9	84-240	26.5
Be	16-100	15.9	102-330	12.0
B	22-134	14.9	146-350	7.5
C	32-176	10.7	180-380	3.9
N	42-236		237-400	
O	50-220		221-400	

Table 6-A. (continued)

θ = 14°(Out-of-Plane) C target

LF	LE(MeV)	dσ/dΩ(mb/sr)-LE	HE(MeV)	dσ/dΩ(mb/sr)-HE
Li	30-110	60.0	116-270	165.5
Be	40-114	19.6	116-350	92.9
B	60-200	42.9	220-410	104.6
C	80-220	35.8	250-440	128.5
N	96-280		300-480	
O	120-290		291-470	

B. The Fragment Spectra

1. The Ho Target

Figure A-31 presents the fragment energy spectra as a function of angle for the Ho target. These spectra are for fragments recorded in singles mode, i.e., for fragments not in coincidence with a neutron. At 7° and 10° the total number of counts for the elastically scattered N fragments saturated the bin capacity of the spectrum at around 490 MeV, giving the elastic peaks a "flat-top" appearance.

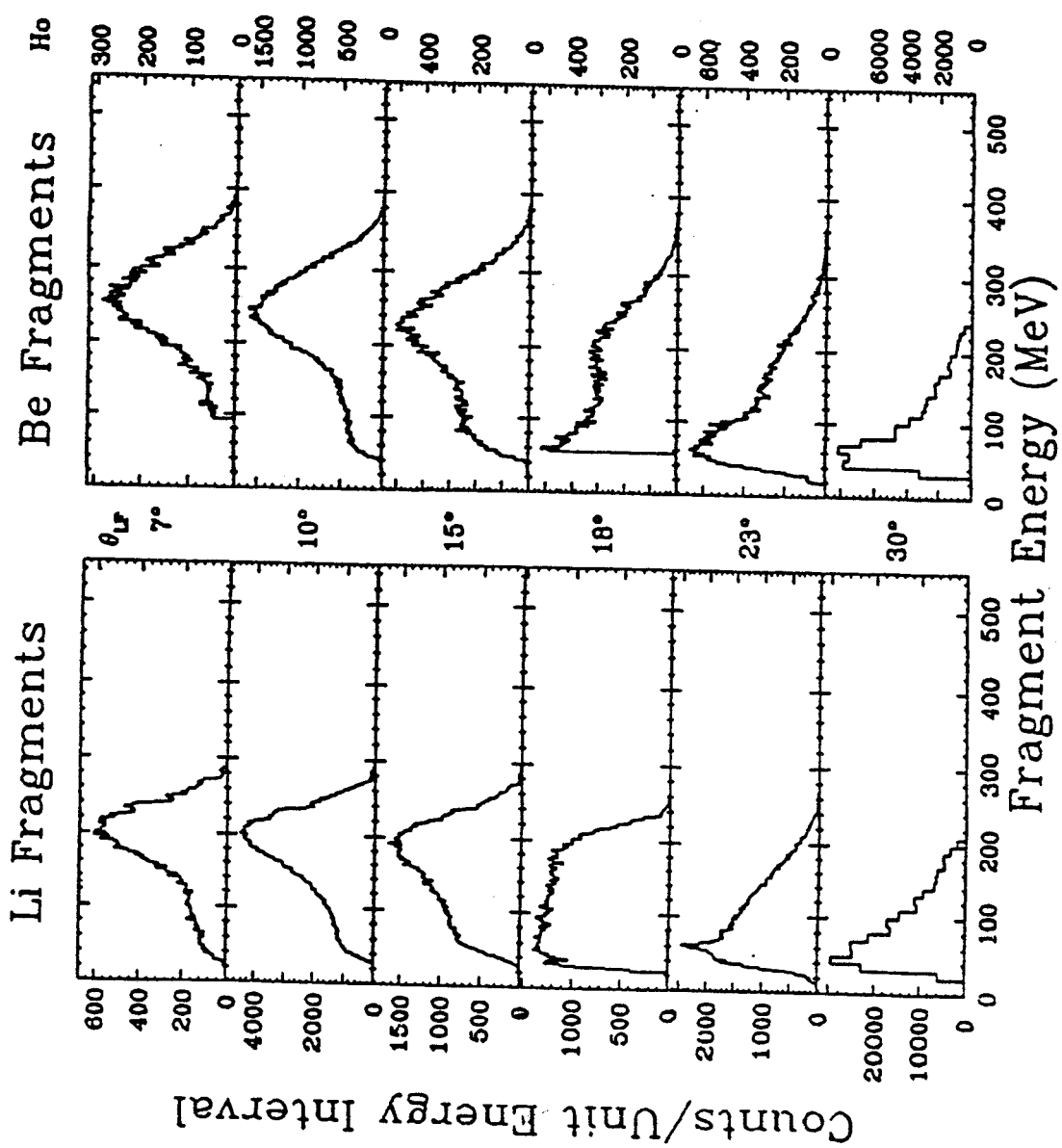

Figure A-31. Fragment spectra for the Ho target.

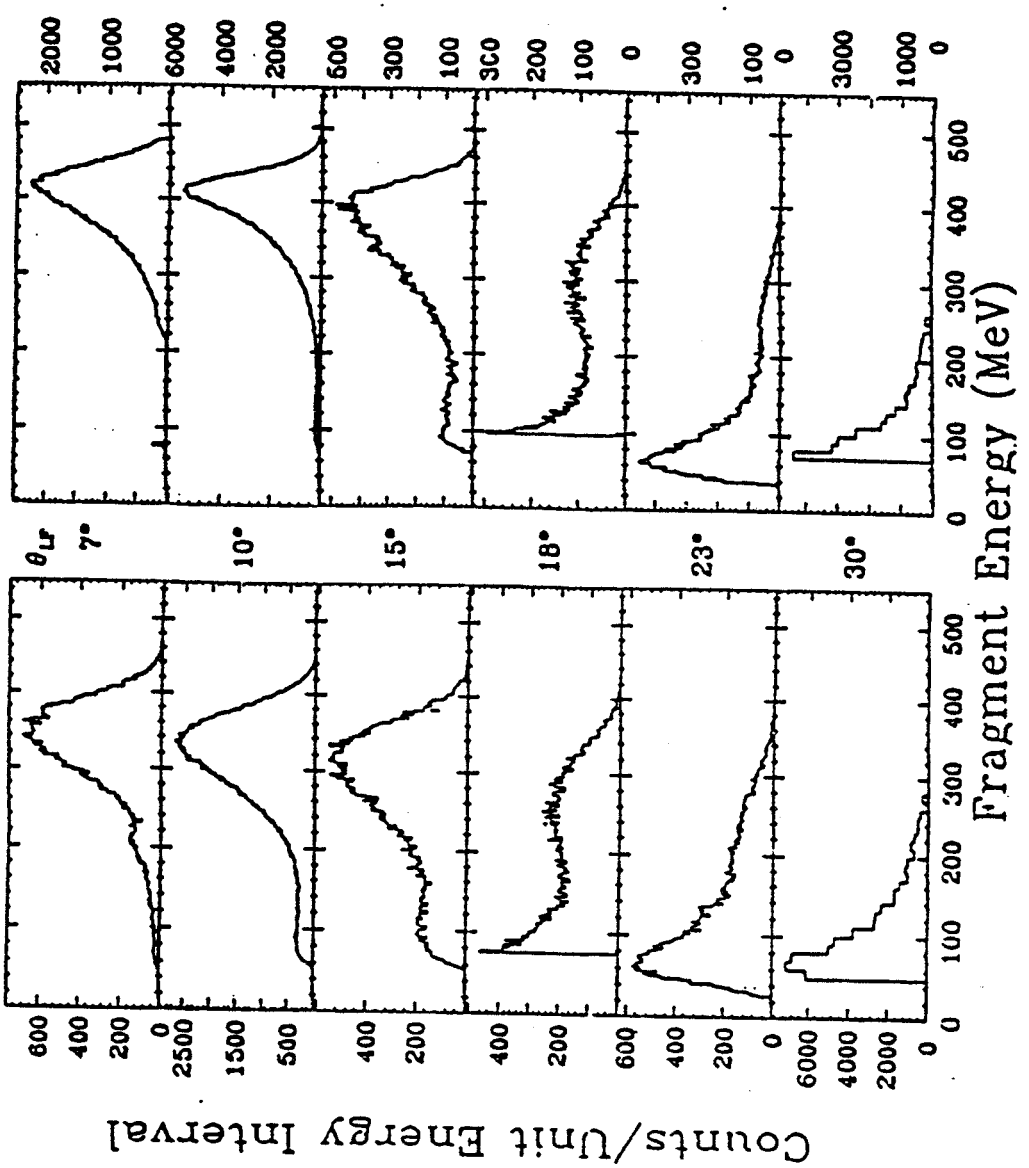

Figure A-31. (continued)

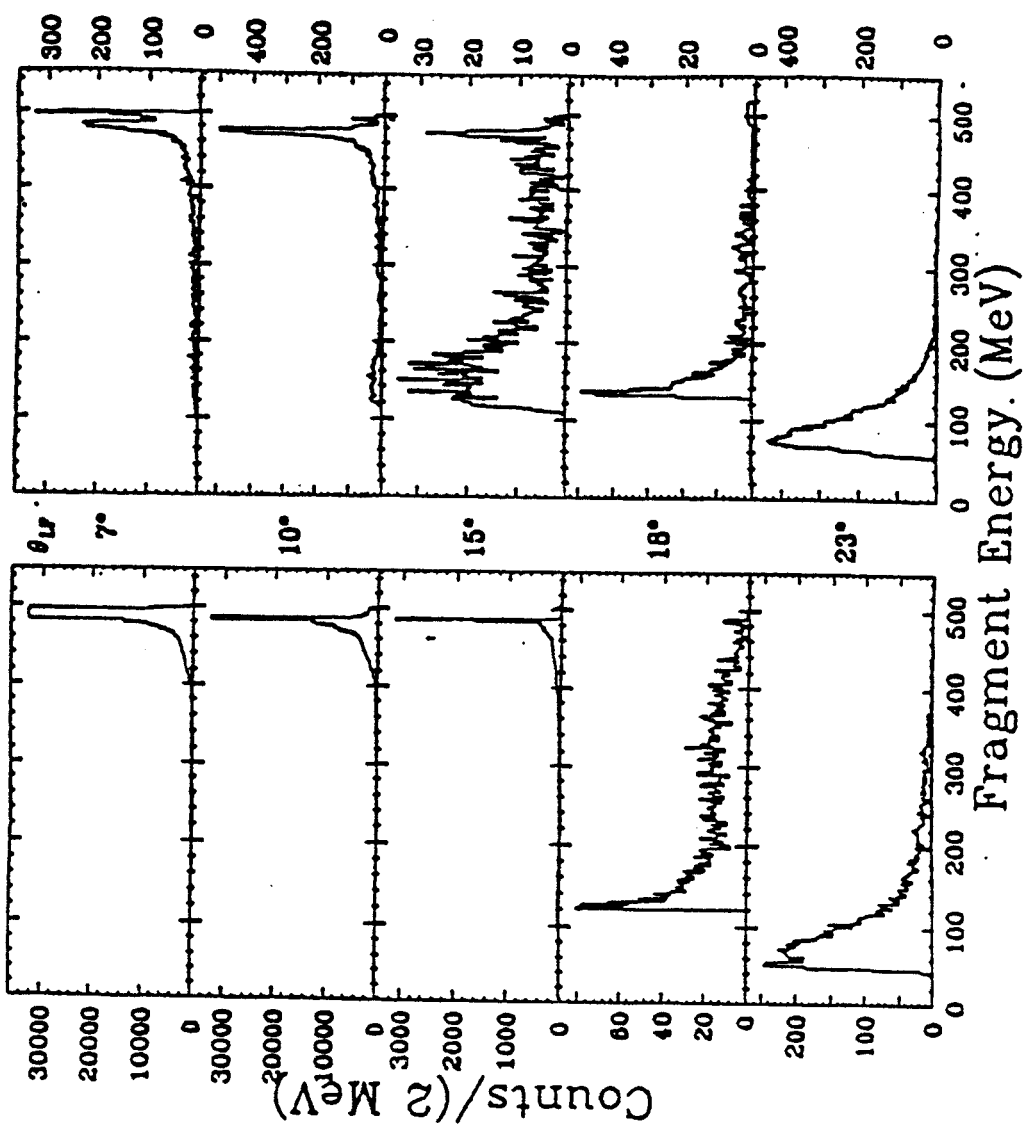

Figure A-31. (continued)

2. The Ni Target

Figure A-32 presents the fragment spectra for the Ni target. The format of the figure is the same as that of Fig. A-31.

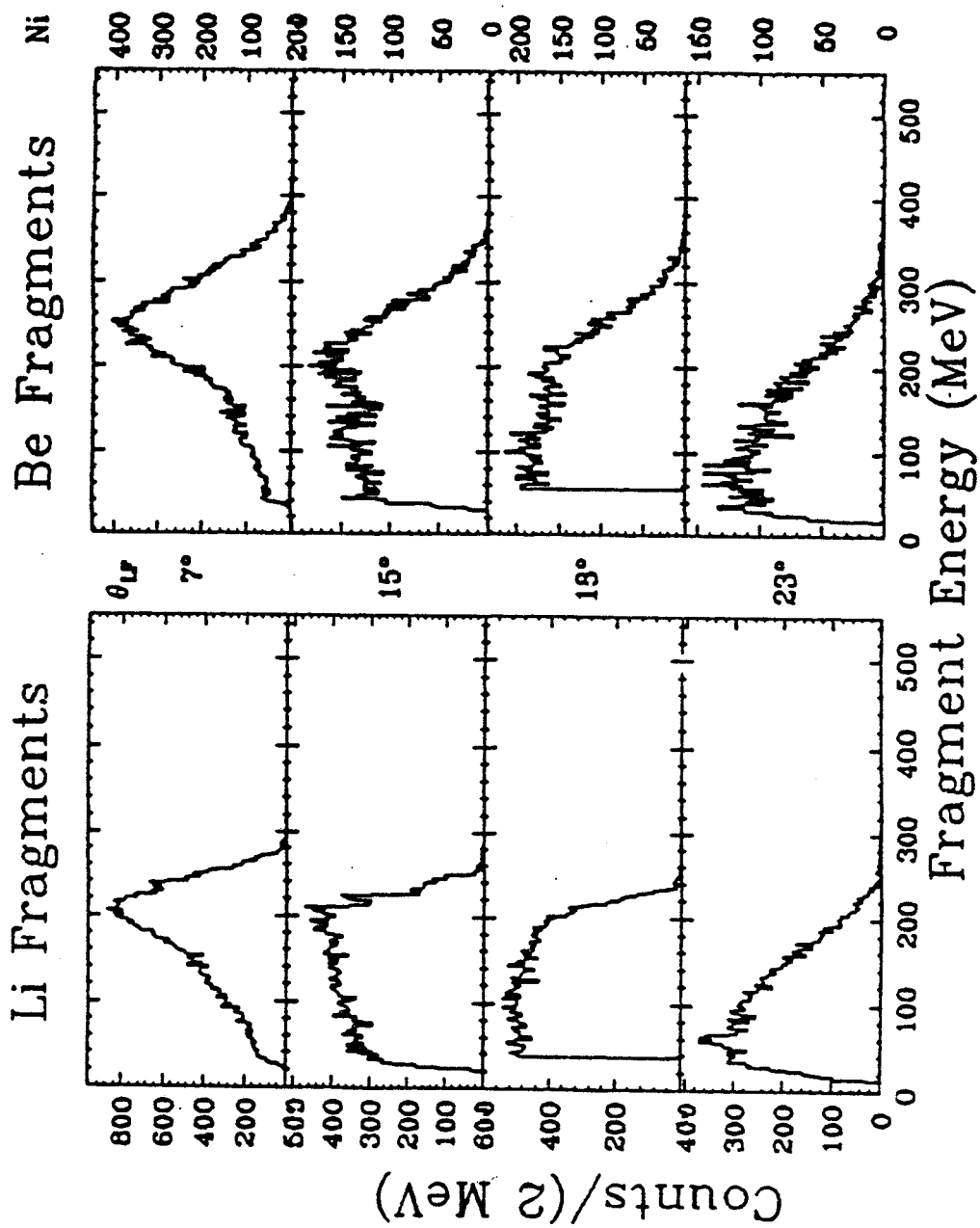

Figure A-32. Fragment spectra for the Ni target.

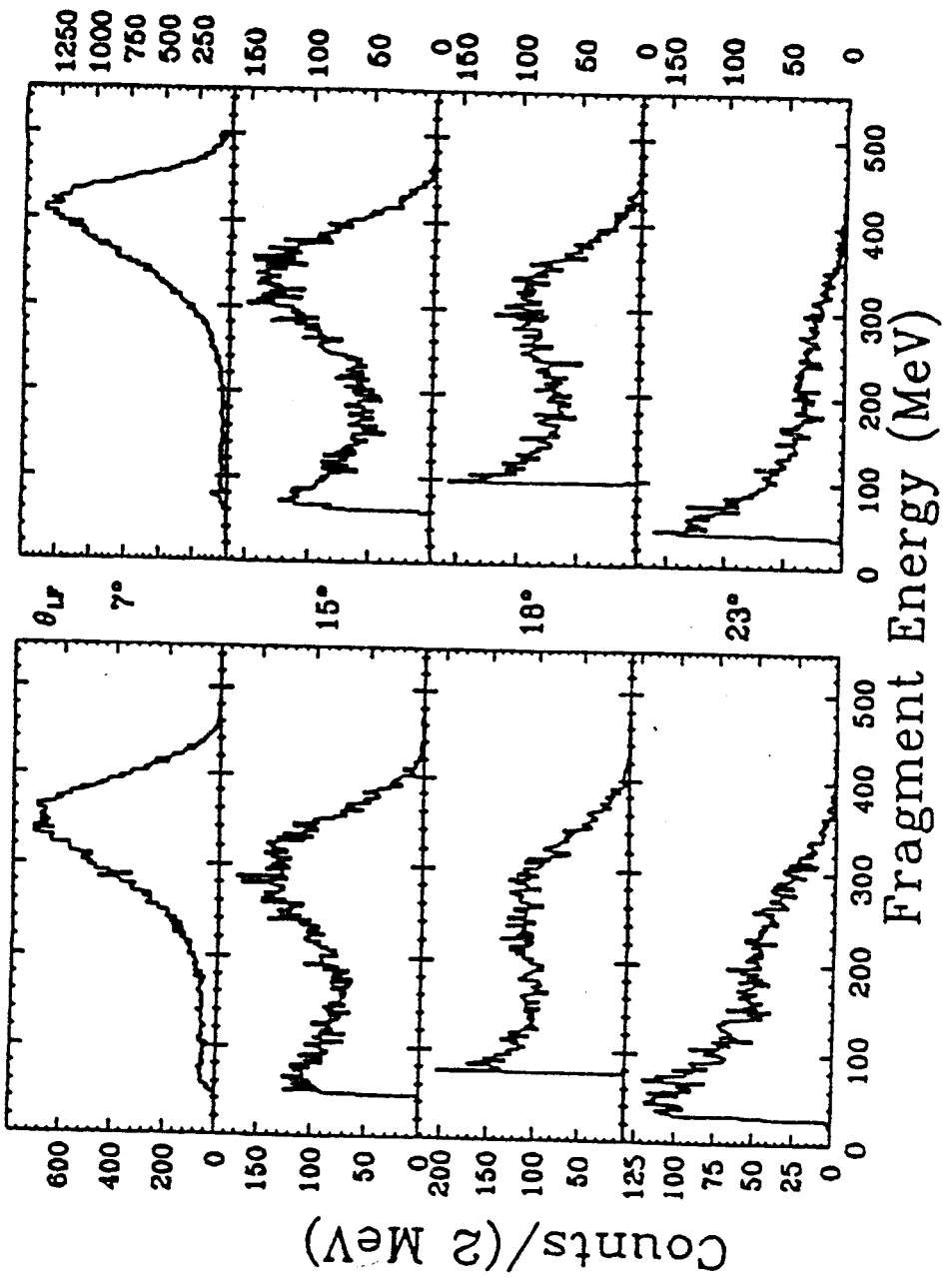

Figure A-32. (continued)

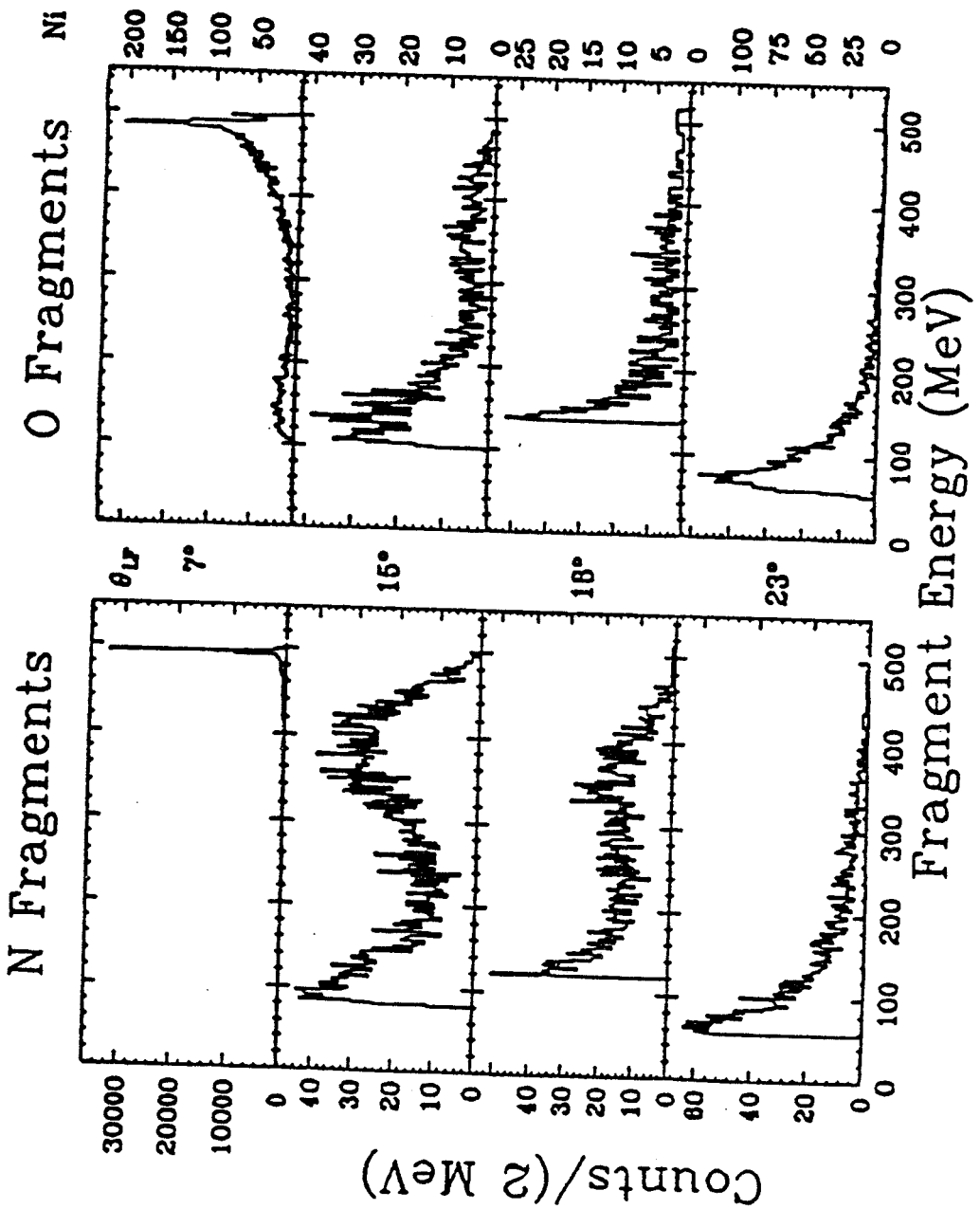

Figure A-32. (continued)

3. The C Target

Figure A-33 shows the fragment spectra for the C target. The format of the figure is the same as that of Fig. A-31.

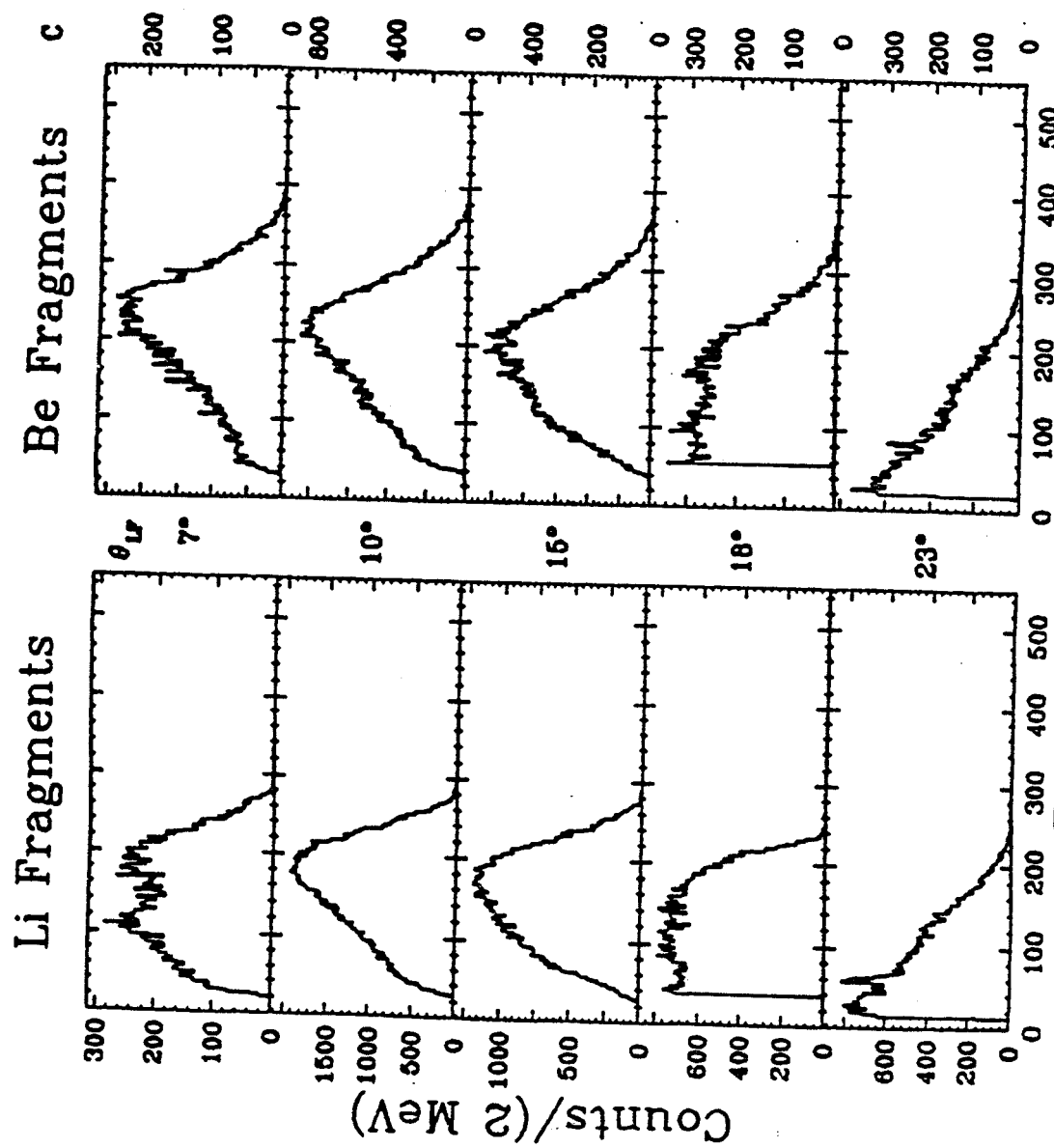

Figure A-33. Fragment spectra for the C target.

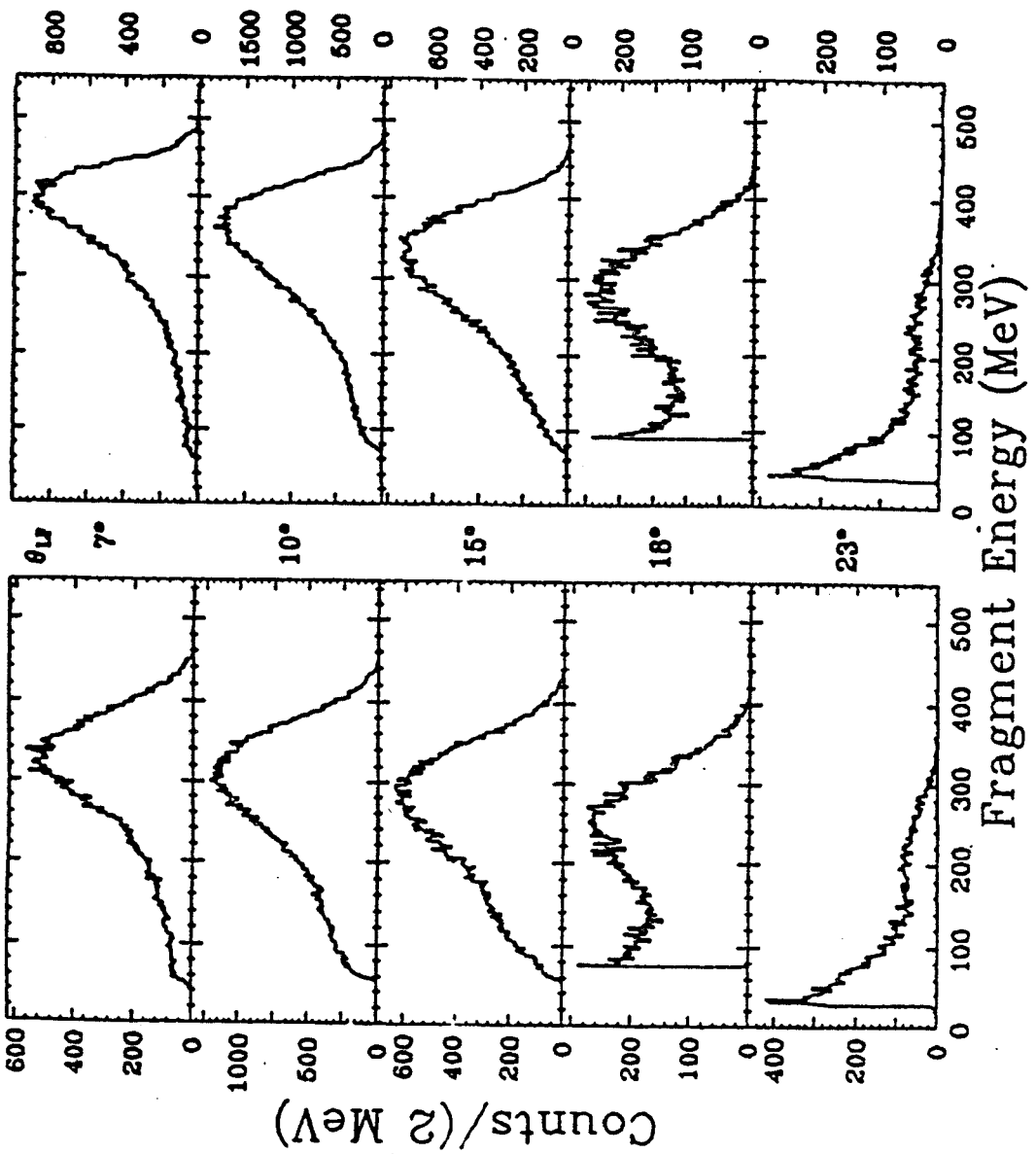

Figure A-33. (continued)

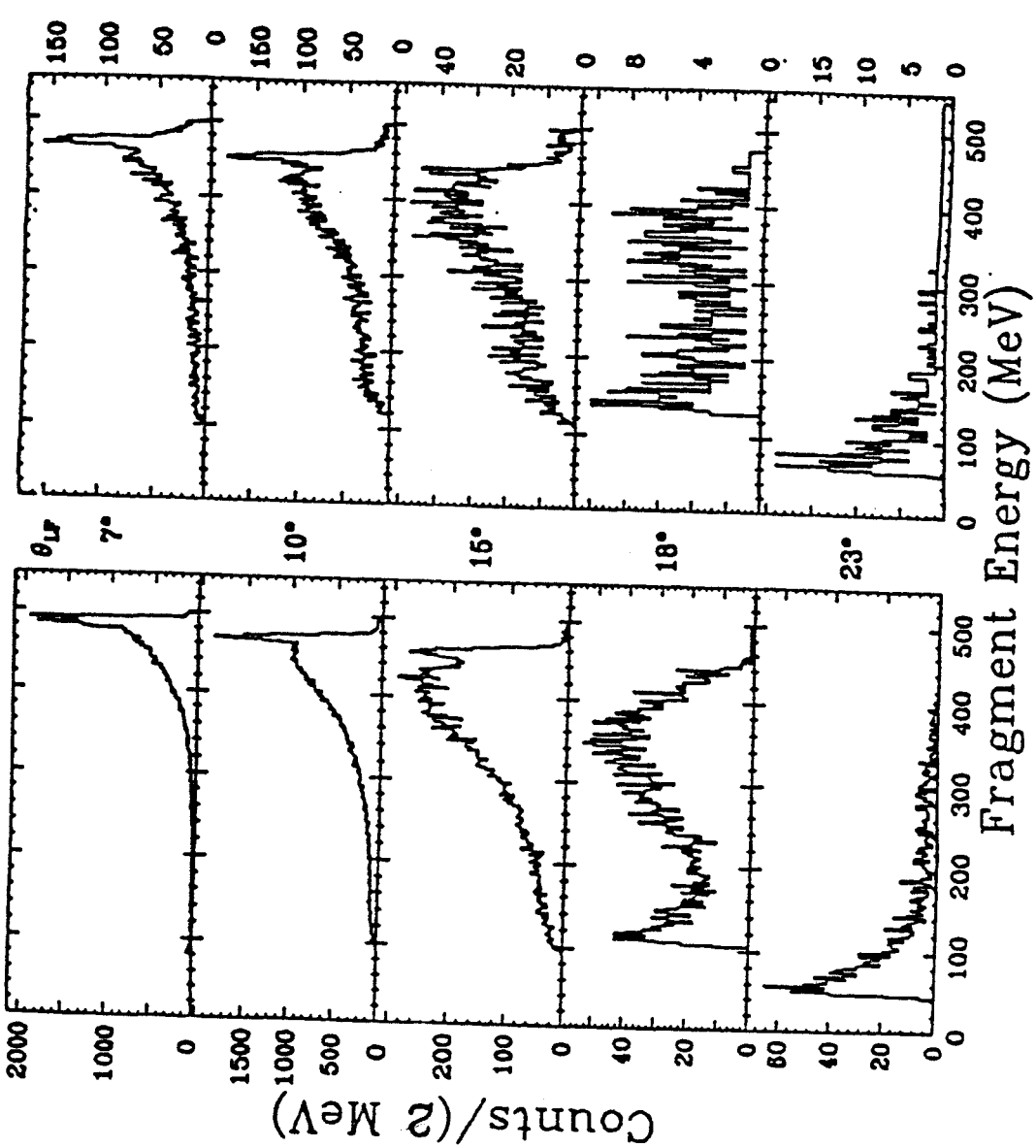

Figure A-33. (continued)

C. The Fragment Angular Distributions

Figure A-34 presents the angular distribution of fragments for the Ho target. The fragments were recorded in singles mode, i.e., not in coincidence with neutrons. The yield in Fig. A-34 is in arbitrary units. Each spectrum is offset from adjacent spectra by a factor of 10. Figures A-35 and A-36 show the fragment angular distributions for the Ni and C targets, respectively. The solid lines are fits with the functional form

$$\text{YIELD} = e^{a+b\theta+c\theta^2}$$

and serve only to guide the eye. For the Ni target there are no data points at $\theta = 10°$, as mentioned in Section III of the main text.

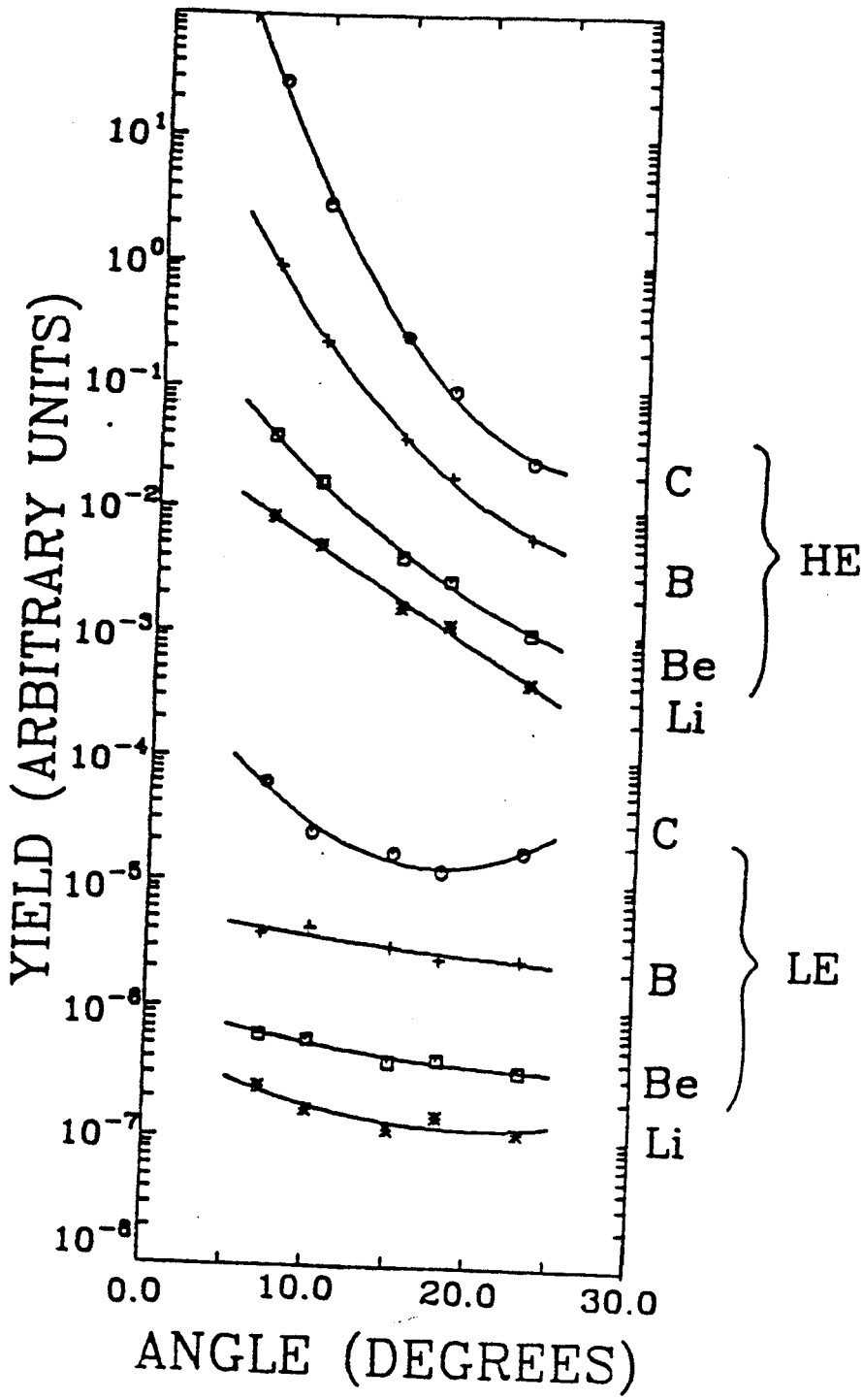

Figure A-34. Fragment angular distribution for the Ho target

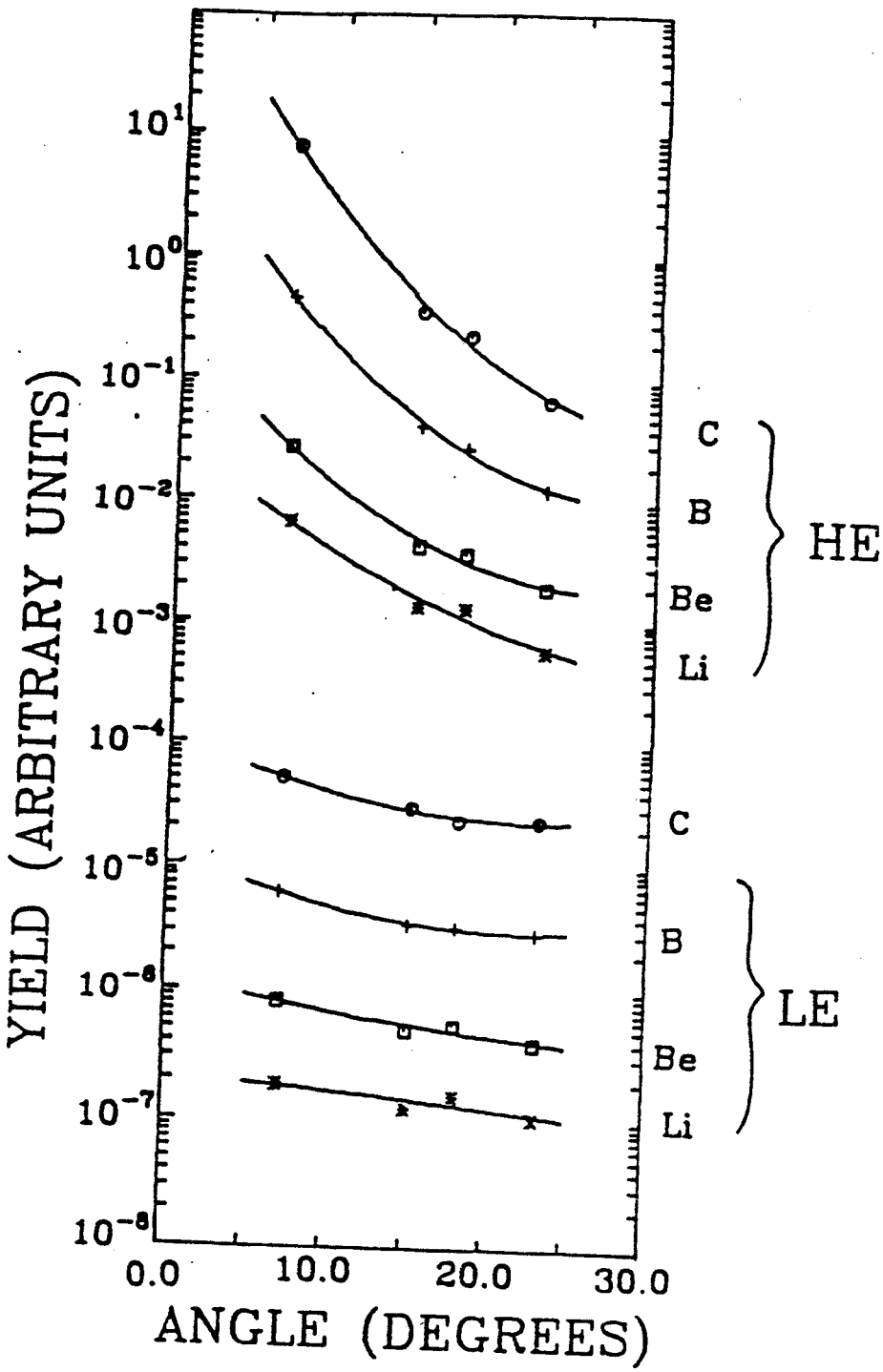

Figure A-35. Fragment angular distribution for the Ni target.

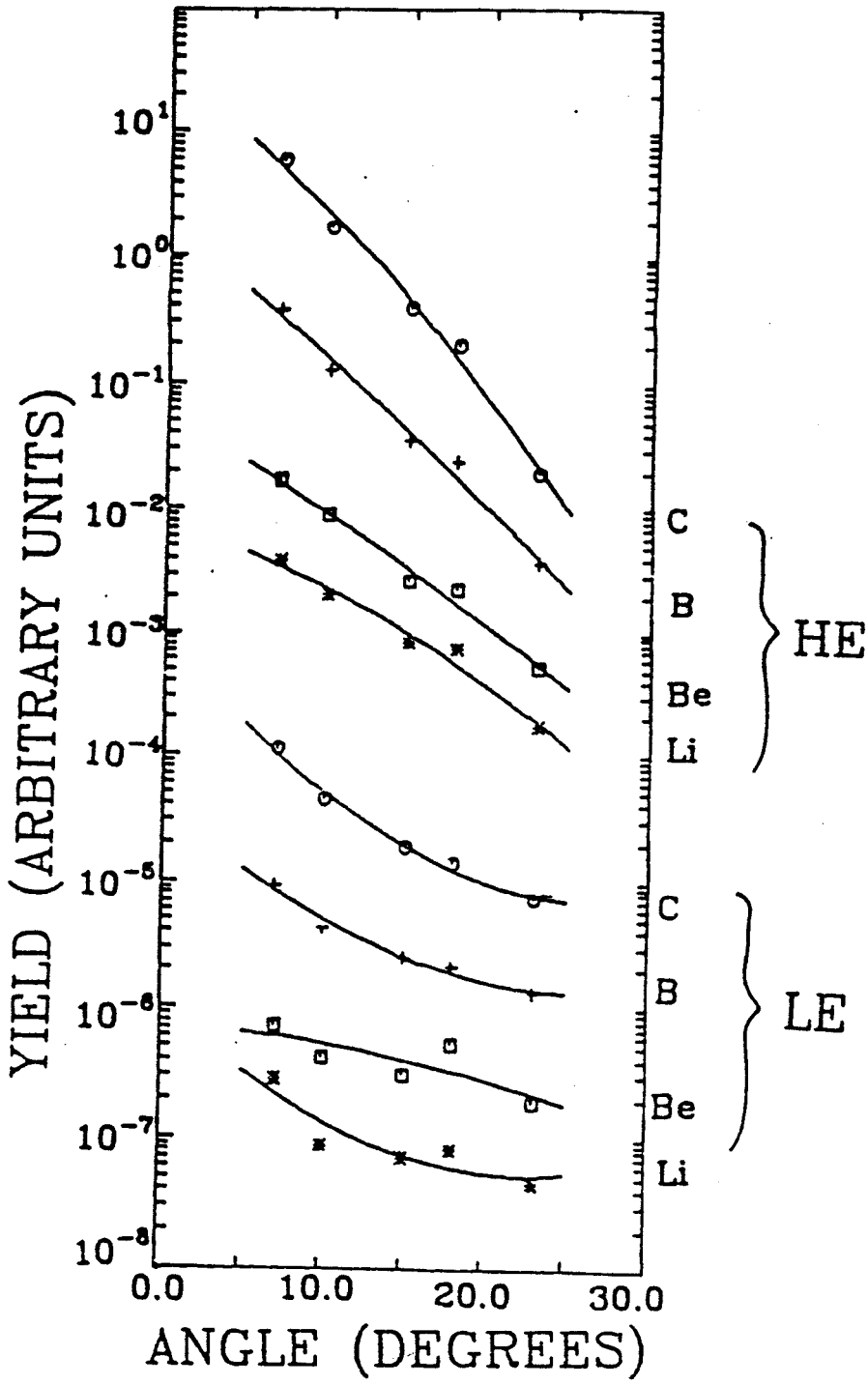

Figure A-36. Fragment angular distribution for the C target.

REFERENCES

a) Current address: Physics Department, Rose-Hulman Institute of Technology, Terre Haute, IN 47803.

b) Current address: LeCroy Research Systems Corporation, Spring Valley, NY 10977.

(Ai 85) J. Aichelin and G. Bertsch, Phys. Rev. C 31, 1730 (1985).

(Aj 84) F. Ajzenberg-Selove, Nucl. Phys. A413, 1 (1984).

(Aj 85) F. Ajzenberg-Selove, Nucl. Phys. A433, 1 (1985).

(Aw 79) T.C. Awes, C.K. Gelbke, B.B. Back, A.C. Mignerey, K.L. Wolf, P. Dyer, H. Breuer, and V.E. Viola Jr., Phys. Lett. 87B, 43 (1979).

(Aw 81) T.C. Awes, G. Poggi, S. Saini, C.K. Gelbke, R. Legrain, and G.D. Westfall, Phys. Lett. 103B, 417 (1981).

(Aw* 81) T.C. Awes, G. Poggi, C.K. Gelbke, B.B. Back, B.G. Glagola, H. Breuer and V.E. Viola, Jr., Phys. Rev. C 24, 89 (1981).

(Aw 82) T.C. Awes, S. Saini, G. Poggi, C.K. Gelbke, D. Cha, R. Legrain and G.D. Westfall, Phys. Rev. C 25, 2361 (1982).

(Aw 84) T.C. Awes, R.L. Ferguson, R. Novotny, F.E. Obenshain, F. Plasil, S. Pontoppidan, V. Rauch, G.R. Young, and H. Sann, Phys. Rev. Lett. 52, 251 (1984).

(Ba 80) B.B. Back, K.L. Wolf, A.C. Mignerey, C.K. Gelbke, T.C. Awes, H. Breuer, V.E. Viola, Jr., and P. Dyer, Phys. Rev. C 22, 1927 (1980).

(Be 38) H. Bethe, Phys. Rev. 53, 675 (1938).

(Be 85) A recent experiment (NSCL Experiment #85003) by W. Benenson et al. looking at neutron-fragment coincidences with beams of 20 MeV/nucleon and 35 MeV/nucleon ^{14}N on Ag used the method of two QDCs for neutron--gamma-ray discrimination.

(Bl 75) M. Blann, Ann. Rev. Nucl. Sci. 25, 123 (1975).

(Bl 79) J.M. Blatt and V.F. Weisskopf, Theoretical Nuclear Physics, (Springer-Verlag, New York, 1979) pg. 365.

(Bl 81) M. Blann, Phys. Rev. C 23, 205 (1981).

(Bl 85) M. Blann, Phys. Rev. C 31, 1245 (1985).

(BNL 84) Cross sections were obtained from the National Nuclear Data Center, Brookhaven National Laboratory.

(Bo 80) J.P. Bondorf, J.N. De, G. Fai, A.O. Karvinen, B. Jakobsson, and J. Randrup, Nucl. Phys. A333, 285 (1980).

(Br 50) A. Bratenahl, S. Fernbach, R.H. Hildebrand, C.E. Leith and B.J. Moyer, Phys. Rev. 77, 597 (1950).

(Ca 85) G. Caskey, A. Galonsky, B. Remington, M.B. Tsang, C.K. Gelbke, A. Kiss, F. Deak, Z. Seres, J.J. Kolata, J. Hinnefeld, and J. Kasagi, Phys. Rev. C 31, 1597 (1985).

(Ca* 85) G. Caskey, Bull. Am. Phys. Soc. Vol. 30, No. 4, 746, (1985).

(Ce 79) R.A. Cecil, B.D. Anderson, and R. Madey, Nucl. Instr. and Meth. 161, 439 (1979).

(Ch 80) M. Chemtob and B. Schürmann, Nucl. Phys. A336, 508 (1980).

(Ch 83) B. Chambon, D. Drain, C. Pastor, A. Dauchy, A. Giorni, C. Morand, Z. Phys. A312, 125 (1983).

(Ch 85) C.B. Chitwood, C.K. Gelbke, J. Pochodzalla, Z. Chen, D.J. Fields, W.G. Lynch, R. Morse, M.B. Tsang, D.H. Boal and J.C. Shillcock, Nat. Sup. Cyc. Lab. Internal Report No. MSUCL-543, (1985).

(Cu 82) J. Cugnon, Phys. Rev. C 22, 1885 (1980).

(Da 84) K.T.R. Davies, K.R.S. Devi, S.E. Koonin, and M.R. Strayer, in Heavy-Ion Science, edited by D.A. Bromley (Plenum, New York, 1984).

(De 86) F. Deak, A. Kiss, Z. Seres, G. Caskey, A. Galonsky, B. Remington, C. Gelbke, B. Tsang, and J.J. Kolata, to be submitted to Phys. Rev. C.

(Dy 79) P. Dyer, T.C. Awes, C.K. Gelbke, B.B. Back, A. Mignerey, K.L. Wolf, H. Breuer, V.E. Viola, Jr., and W.G. Meyer, Phys. Rev. Lett. 42, 560 (1979).

(Fi 84) D.J. Fields, W.G. Lynch, C.B. Chitwood, C.K. Gelbke, M.B. Tsang, H. Utsunomiya, and J. Aichelin, Phys. Rev. C 30, 1912 (1984)

(Fl 63) R. Fletcher and M.J.D. Powell, Comp. J. 6, 163 (1963).

(Fr 83) W.A. Friedman, Phys. Rev. C 27, 569 (1983).

(Ga 80) S.I.A. Garpman, D. Sperber, and M. Zielinska-Pfabe, Phys. Lett. 90B, 53 (1980).

(Ga 81) A. Gavron, J.R. Beene, R.L. Ferguson, F.E. Obenshain, F. Plasil, G.R. Young, G.A. Petitt, K. Geoffroy Young, M. Jääskeläinen, D.G. Sarantites, and C.F. Maguire, Phys. Rev. C 24, 2048 (1981).

(Ga* 81) A. Gavron, R.L. Ferguson, Felix E. Obenshain, F. Plasil, G.R. Young, G.A. Petitt, K. Geoffroy Young, D.G. Sarantites, and G.F. Maguire, Phys. Rev. Lett. 46, 8 (1981).

(Ga 83) A. Gavron, J.R. Beene, B. Cheynis, R.L. Ferguson, F.E. Obenshain, F. Plasil, G.R. Young, G.A. Pettit, C.F. Maguire, D.G. Sarantites, M. Jääskeläinen and Geoffroy-Young, Phys. Rev. C 27, 450 (1983).

(Ge 77) C.K. Gelbke, M. Bini, C. Olmer, D.L. Hendrie, J.L. Laville, J. Mahoney, M.C. Mermaz, D.K. Scott, and H.H. Wieman, Phys. Lett. 71B, 83 (1977).

(Ge 78) C.K. Gelbke, C. Olmer, M. Buenerd, D.L. Hendrie, J. Mahoney, M.C. Mermaz and D.K. Scott, Physics Reports 42, No. 5, 311 (1978).

(Ge 79) C.K. Gelbke in Proc. of the International Symposium on Continuum Spectra of Heavy Ion Reactions held in San Antonio, Texas, edited by T. Tamura, J.B. Natowitz and D.H. Youngblood (Harwood Academic Publishers, New York, (1979).

(Ge 80) H. Gemmeke, P. Netter, Ax. Richter, L. Lassen, S. Lewandowski, W. Lücking, and R. Schreck, Phys. Lett. 97B, 213 (1980).

(Go 74) A.S. Goldhaber, Phys. Lett. 53B, 306 (1974).

(Go 77) P.-A. Gottschalk and W. Weström, Phys. Rev. Lett. 39, 1250 (1977).

(Go 78) A.S. Goldhaber, Phys. Rev. C 17, 2243 (1978).

(Gr 67) J.J. Griffin, Phys. Lett. 24B, 5 (1967).

(Gr 77) D.H.E. Gross and J. Wilczynski, Phys. Lett. 67B, 1 (1977).

(Ha 68) G.D. Harp, J.M. Miller and B.J. Berne, Phys. Rev. 165, 1166 (1968).

(Ha 79) R.L. Hatch and S.E. Koonin, Phys. Lett. 81B, 1 (1979).

(Ha 85) B.E. Hasselquist, G.M Crawley, B.V. Jacak, Z.M Koenig, G.D. Westfall, J.E. Yurkon, R.S. Tickle, J.P. Dufour and T.J.M. Symons, Phys. Rev. C 32,145 (1985).

(Hi 79) D. Hilscher, J.R. Birkelund, A.D. Hoover, W.U. Schröder, W.W. Wilcke, J.R. Huizenga, A.C. Mignerey, K.L. Wolf, H.F. Breuer, and V.E. Viola, Jr., Phys. Rev. C 20, 576 (1979).

(Hi 81) D. Hilscher, E. Holub, U. Jahnke, H. Orf, and H. Rossner, in Dynamics of Heavy-ion Collisions, edited by N. Cindro, R.A. Ricci and W. Greiner, (North-Holland Publishing Co., 1981).

(Hi 83) D. Hilscher, E. Holub, G. Ingold, U. Jahnke, H. Orf, and H. Rossner, Lecture presented by D. Hilscher at the XV Masurian Summer School on Nuclear Reactions, Mikolajke, Poland, 5-17 Sept. 1983.

(Hi 84) D. Hilscher, E. Holub, G. Inglold, U. Jahnke, H. Orf, H. Rossner, W.U. Schröder, H. Gemmeke, K. Keller, L. Lassen, and W. Lücking, in Conf. Prec. from Workshop on Coincidence Particle Emission from Continuum States at Bad Honnef, 1984.

(Ho* 83) H. Ho, P.L. Gonthier, G.-Y. Fan, W. Kühn, A. Pfoh, L. Schad, R. Wolski, J.P. Wurm, J.C. Adloff, D. Disdier, A. Kamili, V. Rauch, G. Rudolf, F. Scheibling, and A. Strazzeri, Phys. Rev. C 27, 584 (1983).

(Ho 83) E. Holub, D. Hilscher, G. Ingold, U. Jahnke, H. Orf, and H. Rossner, Phys. Rev. C 28, 252 (1983).

(Hü 77) J. Hüfner and J. Knoll, Nucl. Phys. A290, 460 (1977).

(Hu 81) C. Hurlbut, private communication.

(Ja* 83) U. Jahnke, G. Ingold, H. Homeyer, M. Bürge, Ch. Egelhaaf, H. Fuchs and D. Hilscher, Phys. Rev. Lett. 50, 1246 (1983).

(Ja 83) B.V. Jacak, G.D. Westfall, C.K. Gelbke, L.H. Harwood, W.G. Lynch, D.K. Scott, H. Stöcker, and M.B. Tsang, Phys. Rev. Lett. 51, 1846 (1983).

(Ka 81) J. Kasagi, S. Saini, T.C. Awes, A. Galonsky, C.K. Gelbke, G. Poggi, D.K. Scott, K.L. Wolf, and R.L. Legrain, Phys. Lett. 104B, 434 (1981).

(Ka 85) J. Kasagi, B. Remington, A. Galonsky, F. Haas, J.J. Kolata, L. Satkowiak, M. Xapsos, R. Racca, and F.W. Prosser, Phys. Rev. C 31, 858 (1985).

(Kh 85) Teng-Lek Khoo (private communication). Measured particle multiplicities from the O + Nd system at 60-70 MeV excitation were compared with predictions from CASCADE with agreement at the 5% level.

(Ki 86) A. Kiss, F. Deak, Z. Seres, G. Caskey, A. Galonsky, L. Heilbronn, B. Remington, J. Kasagi, submitted to Phys. Rev. Lett.

(Ko 77) Steven E. Koonin, Phys. Rev. Lett. 39, 680 (1977).

(Kr 85) H. Kruse, B.V. Jacak, J.J. Molitoris, G.D. Westfall, and H. Stöcker, Phys. Rev. C 31, 1770 (1985).

(Ku 64) R.J. Kurz, University of California Radiation Lab Internal Report No. UCRL-11339, (1964).

(La 78) C. Lauterbach, W. Dünnweber, G. Graw, W. Hering, H. Puchta, and W. Trautmann, Phys. Rev. Lett. 41, 1774 (1978).

(Le 85) S. Leray, G. La Rana, and C. Ngo. Z. Phys. A320, 383 (1985).

(Le 59) K.J. Le Couteur and D.W. Lang, Nucl. Phys. 13, 32 (1959).

(Lü 85) W. Lücking, R. Schreck, K. Keller, L. Lassen, A. Nagel, and G. Gemmeke, Z. Phys. A320, 585 (1985).

(Ma 76) G. Mantzouranis, H.A. Weidenmüller, and D. Agassi, Z. Phys. A276, 145 (1976).

(Mo 80) W.W. Morison, S.K. Samaddar, D. Sperber and M. Zielinska-Pfabe, Phys. Lett. 93B, 379 (1980).

(Na 79) S. Nagamiya, L. Anderson, W. Brückner, O. Chamberlain, M.-C. Lemaire, S. Schnetzer, G. Shapiro, H. Steiner, and I. Tanihata, Phys. Lett. 81B, 147 (1979).

(Ne 82) J. Negele, Rev. Mod. Phys. 54, 913 (1982).

(On 75) R. St. Onge, A. Galonsky, R.K. Jolly, and T.M. Amos, Nucl. Instr. and Meth. 126, 391 (1975).

(Pa 76) D.M. Patterson, R.R. Doering and A. Galonsky, Nucl. Phys. A263, 261 (1976).

(Pe 79) L.J. Perkins and M.C. Scott, Nucl. Instr. and Meth. 166, 451 (1979).

(Pe 85) G.A. Petitt, A. Gavron, J.R. Beene, B. Cheynis, R.L. Ferguson, F.E. Obenshain, F. Plasil, G.R. Young, M. Jääskeläinen, D.G. Sarantites and C.F. Maguire, Phy Rev. C 32, 1572 (1985).

(Pü 77) F. Pühlhofer, Nucl. Phys. A280, 267 (1977).

(Ra 82) J. Randrup, Nucl. Phys. A383, 468 (1982).

(Re 85) B.A. Remington, G. Caskey, A. Galonsky, C.K. Gelbke, M.B. Tsang, Z. Seres, F. Deak, A. Kiss, J. Kasagi and J.J. Kolata, in Proc. of the 4th International Conf. on Nuclear Reaction Mechanisms held in Varenna, Italy, edited by E. Gadioli (Univ. of Milan Press, 1985), (Ricerca Scientifica Educazione Permanente, Supplemento N. 46, 1985).

(Sc 78) W.U. Schröder, J.R. Birkelund and J.R. Huizenga, Phys. Reports 45, No. 5, 301 (1978).

(Sc 81) D.K. Scott, M.S.U. Cyclotron Internal Report No. MSUCL-359, 7 (1981).

(Se 77) E. Segrè, Nuclei and Particles, (W. A. Benjamin, Inc., 1977).

(Si 79) K. Siwek-Wilczynska, E.H. du Marchie van Voorthuysen, J. van Popta, R.H. Siemssen, and J. Wilczynski, Phys. Rev. Lett. 42, 1599 (1979).

(Si 84) J.D. Silk, Doctoral Thesis, PP#-85-028, Univ. of Maryland Dept. of Physics and Astronomy, 153 (1984).

(Si 85) K. Siwek-Wilczynska, R.A. Blue, L.H. Harwood, R.M. Ronningen, H. Utsunomiya, J. Wilczynski and D.J. Morrisey, Phys. Rev. C 32, 1450 (1985).

(Sp 74) P. Sperr, H. Spieler, M.R. Maier, and D. Evers, Nucl. Instr. and Meth. 116, 55 (1974).

(St 77) R.G. Stokstad, Proc. of Topical Conference on Heavy Ion Collisions, Fall Creek Falls State Park, Pikeville, TN, June 13-17, 1977.

(St 85) R.G. Stokstad in Treatise on Heavy-Ion Science, Vol. 3, edited by D.A. Bromley (Plenum, New York, 1985), pg. 94.

(St* 85) In ref. St 85 on pg. 172 are presented data and evaporation calculations for charged particle emission from ^{194}Hg ($E^* = 98$ MeV, $\ell_{max} = 46\hbar$). The calculations slightly underpredict the data indicating that there might be a commensurate overprediction of the neutron emission.

(Sy 80) T.J.M. Symons, P. Doll, M. Bini, D.L. Hendrie, J. Mahoney, G. Mantzouranis, D.K. Scott, K. Van Bibber, Y.P. Viyogi and H.H. Wieman, Phys. Lett. 94B, 131 (1980).

(Ta 70) I. Taylor and J. Kalyna, Nucl. Instr. Meth. 88, 767 (1970).

(Ts 82) I. Tserruya, A. Breskin, R. Chechik, A. Fraenkel, S. Wald, N. Zwang, R. Bock, M. Dakowski, A. Gobbi, H. Sann, R. Bass, G. Kreyling, R. Renfordt, K. Stelzer, and U. Arlt, Phys. Rev. C 26, 2509 (1982).

(Va 85) A. Vander Molen, R. Au, R. Fox and T. Glynn, Nucl. Instr. Meth. A236, 359 (1985).

(Ve 68) V. Verbinski, W. Burrus, T. Love, W. Zobel, N. Hill and R. Textor, Nucl. Instr. Meth. 65, 8 (1968), and references therein.

(Wa 83) S. Wald, I. Tserruya, Z. Fraenkel, G. Doukellis, H. Gemmeke and H.L. Harney, Phys. Rev. C 28, 1538 (1983).

(We 76) G.D. Westfall, J. Gosset, P.J. Johansen, A.M. Poskanzer, W.G. Meyer, H.H. Gutbrod, A. Sandoval, and R. Stock, Phys. Rev. Lett. 37, 1202 (1976).

(We 77) R. Weiner and M. Weström, Nucl. Phys. A286, 282 (1977).

(We 82) G.D. Westfall, B.V. Jacak, N. Anantaraman, M.V. Curtin, G.M. Crawley, C.K. Gelbke, B. Hasselquist, W.G. Lynch, D.K. Scott, M.B. Tsang, M.J. Murphy, T.J.M. Symons, R. Legrain, and T.J. Majors, Phys. Lett. 116B, 118 (1982).

(We 84) G.D. Westfall, Z.M. Koenig, B.V. Jacak, L.H. Harwood, G.M. Crawley, M.W. Curtin, C.K. Gelbke, B. Hasselquist, W.G. Lynch, A.D. Panagiotou, D.K. Scott, H. Stöcker, and M.B. Tsang, Phys Rev. C 29, 861 (1984).

(We 37) V. Weisskopf, Phys. Rev. 52, 295 (1937).

(Wi 73) J. Wilczynski, Phys. Lett. 47B, 484 (1973).

(Wi 85) T. Williams, Doctoral Thesis, Department of Physics, University of Birmingham, 1985.

(Wo 74) G.J. Wozniek, N.A. Jelley and Joseph Cerney, Nucl. Instr. and Meth. 120, 29 (1974).

(Yo 80) G.R. Young, R.L. Ferguson, A. Gavron, D.C. Hensley, Felix E. Obenshain, F. Plasil, A.H. Snell, M.P. Webb, G.F. Maguire and G.A. Petitt, Phys. Rev. Lett. 45, 1389 (1980).